Uranium Thiocyanate Compounds in Multiple Oxidation States

A thesis presented to the University of Dublin,

Trinity College for the degree

of

Doctor of Philosophy in Chemistry

by

Stefano Nuzzo

Under the supervision of Prof. Robert J. Baker

School of Chemistry

Trinity College Dublin

2019

Declaration

I hereby declare that this thesis has not been submitted as an exercise for a degree at this or any other university and it is entirely my own work.

I agree to deposit this thesis in the University's open access institutional or allow the library to do so on my behalf, subject to Irish Copyright Legislation and Trinity College Library conditions of use and acknowledgement.

…

…….

Stefano Nuzzo

Summary

In this thesis a series of high symmetry uranium(IV) and thorium(IV) thiocyanate complexes of the type $A_4[An(NCS)_8]$ (An = Th, U; A = Cs, Me_4N, Et_4N, $^nPr_4N$) have been structurally and spectroscopically characterized. It was shown that the size and shape of the counter cation determine the coordination symmetry around the actinide ion. Interestingly, this effect proved to have a significant influence on the magnetic properties of the $[U(NCS)_8]^{4-}$ ion, as revealed by SQUID and specific heat capacity measurements. Inelastic neutron scattering and far-infrared spectroscopic measurements have been performed on the uranium compounds to examine the corresponding low-lying energy level electronic structures, while a computational approach using the CONDON framework has been used to quantify these energy states. Overall, the experimental and computational data suggest that the energy gap between the ground and the first excited state varies considerably so that for A = Et_4N a magnetic singlet ground state is predicted; however, a distortion of the coordination geometry from cubic toward square antiprismatic reduce this energy gap such that a magnetic triplet ground state is observable for A = Cs at low temperatures. This represents the first example of a triplet electronic ground state for a uranium(IV) compound; thus, this study underlines the importance of the coordination geometry to understand the magnetic properties of uranium(IV) compounds. Moreover, a spectroscopic and magnetic analysis has been carried out also on two uranium(IV) selenocyanate complexes of the type $A_4[U(NCS)_8]$ (A = Et_4N, $^nPr_4N$); however, no significant differences in the electronic structure have been observed with respect to the equivalents thiocyanate compounds.

The reactivity of the $[U(NCS)_8]^{4-}$ ion has also been examined in organic media of diverse polarity and with several different counter cations. From oxidation processes of $Cs_4[U(NCS)_8]$, two mixed-valent uranium compounds have been isolated and structurally characterized. A spectroscopic, magnetic and computational analysis has been performed to unequivocally delineate the electronic configuration of these systems; a photophysical study also revealed the presence of both uranium(IV) and uranyl(VI) together in one compound. A reaction between $Na_4[U(NCS)_8]$ and $[Co(bipy)_3][PF_6]_2$ led to the formation of a compound of formula $[Co(bipy)_3][U(NCS)_8]$ for which spectroscopic and magnetic properties suggest the presence of a pentavalent uranium(V) ion, but the mechanism of the synthesis is not clear. The synthesis of homoleptic uranium(III) thiocyanate complexes, from reductions of uranium(IV) precursors, have also been attempted, but

without success; however, a spectroelectrochemistry study on $[U(NCS)_8]^{4-}$ has shown that the addition of one electron to the metal ion causes the dissociation of all the π-donor $[NCS]^-$ ligands and decomposition of the sample. Theoretical calculations have also revealed an enhanced ionicity for the U(III)–N compared to the U(IV)–N bond, which can explain the observed decomposition.

A series of uranyl(VI) thiocyanate $[NCS]^-$ and selenocyanate $[NCSe]^-$ complexes, of the type $[R_4N]_3[UO_2(NCS)_5$ (R_4 = ^{n}Bu$_4$, Me$_3$Bz, Et$_3$Bz), $[Ph_4P][UO_2(NCS)_3(NO_3)]$ and $[R_4N]_3[UO_2(NCSe)_5]$ (R_4 = Me$_4$, ^{n}Pr$_4$, Et$_3$Bz) have also been described. X-ray crystallography, NMR, vibrational and photoluminescence spectroscopy and theoretical methods have been used to explore the non-covalent interactions present in the structures of these compounds, namely: charge assisted C—H···O=U and C—H···S(e) hydrogen bonding, and Se···Se or S···S chalcogenide interactions. Chalcogenide interactions have been observed in some of the structures and were more prevalent in the $[NCSe]^-$ series than in the $[NCS]^-$. Charge assisted hydrogen bonding to the –yl oxygens were also noticed, but they were weak and not able to strongly influence the spectroscopic properties of the uranyl moiety.

Finally, a detailed structural, spectroscopic and theoretical study on a series of 10-[(4-halo-2,6-diisopropylphenyl)imino]phenanthren-9-ones and derivatives of the phenanthrene-9,10-dione ligand has been discussed. Particular attention has been reserved on the analysis of the supramolecular non-covalent interactions exhibited by the structures of these molecules, such as "π–π stacking", C–H···π, C–X lone pair···π, C–X···H–C and C–X···X–C. DFT and AIM analysis have also been used to compare the strength of these interactions. It was found that the lone pair···π interactions were the dominant halogen type interactions and a computational study showed that these were stabilizing and of the same order of magnitude as interactions from lone pairs deriving from oxygen or nitrogen donor atoms. However, among all the interactions, the most important one appeared to be a weak hydrogen bond between the C–H of a phenanthrene and the carbonyl oxygen. These ligands were also reduced by reaction with potassium metal to form iminoalkoxy semiquinone radical anions. A spectroscopic analysis confirmed the formation of radical species, but these were isolated as powders only and it was not possible to grow single crystals. Reactions between UCl_4, as source of U(IV), and these radicals have been also attempted. However, the desired compounds, that could potentially show magnetic coupling interactions between the radical and the uranium metal, have not been isolated.

Acknowledgement

Firstly, I would like to express my sincere gratitude to my supervisor Prof. Robert James Baker for his continuous support during my PhD study and related research, for his enormous patience with my mistakes. His guidance helped me in all the time of research and writing of this thesis. Thank you very, very much.

Besides my supervisor, I would like to thank Dr. Brendan Twamley for his enormous contribute throughout my project; thank you for all the crystal structures that you refined for me, for your help in the lab and your encouragements. I also would like to thank Dr. John O' Brien for being the "NMR god" and, of course, Dr. Manuel Ruether for "simply" being the king of the spectroscopic instruments; thank you both for being always present. Obviously, I also want to thank all the members of the stuff in the School of Chemistry of Trinity College.

My sincere thanks go also to Professor Michael Probert from University of New Castle for welcoming me in his group even if for a short period, for diffracting two of my single crystals at 4 K and for explaining me how a single crystal can be diffracted at different pressures. Moreover, I would like to express my gratitude to Dr. Marco Evangelisti and Dr. Giulia Lorusso (from University of Saragoza), for measuring the magnetic properties of my samples, to Dr. Duc Lee and Dr. Helen C. Walker (from the ISIS facility) for the INS experiments, to Silvia Capelli (from ISIS Neutron and Muon Facility) for the single-crystal neutron diffraction analysis, to Dr. Milan Orlita (from Grenoble) for the FIR measurements, to Dr. James a. Platts (from Cardiff University) and Dr. A. Kerridge (from Lancaster university) and Dr. P. Kögerel (from Aachen University) for the computational calculations.

I thank my fellow labmates, in particular Dr. Harrison Omorodin and Samuel Edwards, for their help in the lab and for all the fun we have had in the last four years. A big thank goes in particular to Dr. Saptarshi Biswas for simply being Saptarshi and for his suggestions and helps during difficult experiments. I wish to thank all my friends in Dublin, in particular Luca and Imma, and the members of the Colavita group: Khairul, Adam, Federico, Johana, James, Ronan, Guido, Alessandro, Carlota and Letizia for being a very nice office-mates.

Last but not the least, I want to thank my family: my parents, my brothers and my sister for their support throughout my project and during the writing of this thesis.

Table of Contents

List of Appendices

Appendix 1

Appendix 2

Appendix 3

Appendix 4

List of Figures

201

List of Tables

List of Schemes

List of Symbols and Abbreviations

α	alpha
β	beta
γ	gamma
δ	chemical shift in ppm
ε	Molar Extinction coefficient
ζ	spin-orbit coupling constant
θ	theta
φ	phi
f	oscillator strength
°C	degrees Celsius
λ_{max}	wavelength of maximum absorption
λ_{ex}	excitation wavelength
λ_{em}	emission wavelength
τ	lifetime
a.u.	arbitrary units
Å	Angstrom
AIM	atoms in molecules
An	actinide
B	applied magnetic field
BCP	bond critical points
Bipy	2,2′-bipyridine
BTBPs	6,6′-bis(5,6-dialkyl-1,2,4-triazin-3-yl)-2,2′-bipyridines
ca.	circa
CASSCF	complete active space self-consistent field

CCIs	cation-cation interactions
CFT	crystal field theory
CFS	crystal field splitting
CLSM	Confocal Laser Scanning Microscopy
CCR	Cryo-Cooled Refrigerating
CT	charge transfer
CV	cyclic voltammetry
DFT	density functional theory
DCM	dichloromethane
DME	dimethoxyethane
DMF	dimethylformamide
DMSO	dimethyl sulfoxide
DPA	dipicolinate
DRIFT Spectroscopy	Diffuse Reflectance Infrared Fourier Transform
ENDOR	electron nuclear double resonance
EPR	electron paramagnetic spectroscopy
ESEEM	electron spin echo envelope modulation
EXAFS	extended X-ray absorption fine structure
Fc	ferrocene
Fc*	decamethylferrocene
HOMO	highest occupied molecular orbital
HRPD	High Resolution Powder Diffractometer
INS	inelastic neutron scattering
j	angular momentum of a single electron
J	total angular momentum

K	kelvin
L	total orbital angular momenta
ℓ	orbital angular momentum of a single electron
LMCT	ligand to metal charge transfer
Ln	lanthanide
LUMO	lowest unoccupied molecular orbital
LS	Russell-Saunders
M	Molarity (mol/L)
M_m	molar magnetization
MCD	magnetic circular dichroism
MeCN	acetonitrile
MEP	molecular electrostatic potential
MLCT	metal to ligand charge transfer
mmol	millimoles
mg	milligrams
MPt	melting point
FIR	far infrared spectroscopy
NBO	natural bonding orbital
NIR	near infrared spectroscopy
PES	photoelectron spectroscopy
PhMe	toluene
Py	pyridine
S	total spin angular momenta
s	spin angular momentum of a single electron
s	second
µs	microseconds

ns	nanoseconds
SAP	square antiprismatic
SEC	Spectroelectrochemistry
SMM	single molecular magnet
SNF	Spent Nuclear Fuels
SQUID	superconducting quantum interference device
T	tesla
TBAH	Tetrabutylammonium hexafluorophosphate
TDD	triangular dodecahedron
TIP	temperature independent paramagnetism
THF	tetrahydrofuran
TLCV	Thin-Layer Cyclic Voltammetry
TM	transition metals
TRLIFS	time-resolved laser induced fluorescence spectroscopy
UV-vis	ultraviolet-visible
VSM	Vibrating Sample Magnetometer
V	volt
WIPP	Waste Isolation Pilot Plant
XANES	X-ray absorption near edge structure
Z_{eff}	effective nuclear charge

List of Publications

➢ Oxidation of Uranium(IV) Thiocyanate Complexes: Mixed Valent and Cation-Cation Interactions in Uranium Compounds. S. Nuzzo, J. van Leusen, B. Twamley, J. A. Platts, P. Kögerler and Robert J. Baker, *Chem. Commun.*, submitted.

➢ Pseudohalide Tectons within the Coordination Sphere of the Uranyl Ion: Experimental and Theoretical Study of C−H···O, C−H···S, and Chalcogenide Noncovalent Interactions. S. Nuzzo, B. Twamley, J. A. Platts and Robert J. Baker, *Inorg. Chem.*, 2018, **57**, 3699-3712.

➢ Structural variability of 4f and 5f thiocyanate complexes and dissociation of uranium(III)-thiocyanate bonds with increased iconicity. S. Biswas, S. Ma, S. Nuzzo, B. Twamley, A. T. Russel, J. A. Platts, F. Hartl and Robert J. Baker, *Inorg. Chem.*, 2017, **56**, 14426-14437.

➢ N-Aryl-9,10-phenanthreneimines as scaffolds for exploring non-covalent halogen bond interactions. D. Farrell, D. Tungulin, S. Nuzzo, B. Twamley, J. A. Platts and R. J. Baker, *Eur. J. Org. Chem.*, 2017, **37**, 5597-5609.

➢ Characterization of isothiocyanic acid, HNCS, in the solid state: trapped by hydrogen bonding. S. Nuzzo, B. Twamley, J. A. Platts and R. J. Baker, *Chem. Commun.*, 2016, **52**, 13296-13298.

➢ Cl...Cl and Cl...H Interactions in the Chlorinated Hydocarbon 1,1,1,2,2,3,3-Heptachloropropane: A Structural Study. S. Nuzzo, B. Twamley and R. J. Baker, *J. Chem. Crystallogr.*, **47**, 182-186.

➢ A structural and spectroscopic study of the first uranyl selenocyanate, [Et4N]3[UO2(NCSe)5]. S. Nuzzo, M. P. Browne, B. Twamley, M. E. G. Lyons and R. J. Baker, *Inorganics*, 2016, **4**, 4-8. (invited f-block chemistry issue).

Chapter 1

Introduction

1.1 Overview

The electronic structure and magnetic behaviour of the complexes of the d-block transition metals (TM) is by now well explored,[1] with few exceptions represented for example by manganese whose complicated magnetic behaviour is still being investigated.[2] f-block metal complexes in contrast are still the focus of numerous discussions due to a much more complicated chemical and physical behaviour.[3] The *4f* (lanthanide) and *5f* (actinide) series reflect TM in some of their aspects. For instance, the existence of coloured metal-ligand complexes due to *f-f* electronic transitions (*d-d* in TM), the possibility of having the metal ion in many oxidation states for the relatively low energy of the valence *f* orbitals (*d* in TM) and the formation of paramagnetic compounds due to the presence of unpaired *f* electrons (*d* in TM).[4] However, while the chemistry of lanthanides has seen much progress over the last few years,[3l-t] knowledge of actinide chemistry is still lacking. Despite all the studies on many actinide compounds, there are still several key questions to be answered: for example, the number of electrons in the valence shells, the magnetic behaviour and the character of the metal-ligand bonding.

All actinides are radioactive and release energy upon radioactive decay. They exist as either primarily α emitters, such as Th, U, Np, Pu, Am, Cm, Es and Fm, with thorium and uranium the only naturally occurring, or primarily β^- emitters, such as Ac, Bk, Pa, Cf. Of all of these metals, thorium and uranium are the most amenable to experimental work[5] and the majority of the reported studies on actinide chemistry has been centred on uranium chemistry; instead, the higher toxicity and increased nuclear instability of the other actinides make them more difficult and expensive to study experimentally.[6] For instance, compounds that contain isotopes of actinides with half-lives of less than hundreds of thousands of years undergo rapid degradation; this is because the high energetic and ionizing nature of nuclear decay processes can be up to million times larger than the strength of any chemical bonding. Thus, the absence of a considerable number of useful experimental data has led to increased theoretical work on actinide chemistry.[7]

Among the actinides, uranium (and more recently thorium)[8] can be used as fuel in nuclear reactors to generate nuclear energy. In 2011, nuclear energy provided 10% of the world's electricity[9] which fell to 4.3% after the Fukushima nuclear disaster.[9] Nowadays, there are many debates over the safety of nuclear power plants and the radioactive waste produced, which represents the major environmental concern especially for the presence of α emitters with very long half-lives.[10] This makes studying the chemistry of the

actinides both environmentally [11] and scientifically important. Spectroscopically, investigations of the chemical and physical properties of the actinides have seen progress over the past few years.[3a-j] For example, a recent review on neptunium chemistry [12] summaries the properties of the very few neptunium complexes reported and fully characterized since the foundation of organometallic neptunium chemistry, highlighting the main differences between neptunium and its closest neighbours, uranium and plutonium.

The availability of more sensitive techniques allowed scientists to better comprehend the unique properties of actinide compounds and their interaction mechanism in aqueous, mineral and organic phases. Advanced spectroscopic techniques such as X-ray Photoelectron Spectroscopy (XPS), [13] Diffuse Reflectance Infrared Fourier Transform Spectroscopy (DRIFT) [14] and X-ray Absorption Spectroscopy (XAS), [15] with the two subsets Extended X-ray Absorption Fine Structure (EXAFS)[15,16] and X-ray Absorption Near Edge Structure (XANES),[15] provided solid basis to understand the structural differences between actinide metal ions and their compounds, ultimately leading to a better approach toward the radioactive waste treatment. Quantum chemistry has also received numerous improvements in the field of actinide chemistry and has been used extensively to support experimental results.[7, 17] Computational methods, such as the Density Functional Theory (DFT),[18] and the *ab-initio* method "Complete Active Space Self-Consistent Field" (CASSCF)[19] provide information for determining the ground state wave function,[20] considering the core electrons, and for predicting the contribution of *5f* electrons in chemical bonding.[21]

To fully elucidate the electronic structure of actinide compounds, photoluminescence spectroscopy has become an important spectroscopic tool.[3k] Remarkable are the studies on the luminescent properties of curium(III) compounds, despite their high radioactivity and limited availability.[22] The photophysical properties of the uranyl(VI) ion, $[UO_2]^{2+}$, both in solid and in aqueous solution, has been also well explored. [23] However, in comparison with lanthanides[3l-t] and TM,[1] actinide photoluminescent properties are still poorly understood and, only recently, they have begun to be explored in more detail.[24]

1.2 Actinides and Nuclear Energy

In recent years there has been a renewed global interest in electricity production from nuclear power and several countries are announcing plans for new reactors construction,[25]

in order to reduce the consumption of fossil fuels and the associated greenhouse gas emissions. Some studies have shown that nuclear energy can indeed be considered as a clean energy supply and it has been predicted that if nuclear energy became the prime source of energy supply, then the carbon dioxide emission could be significantly reduced.[26] However, concerns regarding the safety of nuclear power plants and the radioactive waste produced after nuclear fission processes are still far from being resolved.[10, 27] Nuclear waste is usually divided into categories. In UK, for example, there are three types of nuclear fission waste: Low-level Waste (LLW) in the form of contaminated material,[27] Intermediate-Level Waste (ILW) and the more serious High-Level Waste (HLW). This latter includes Spent Nuclear Fuels (SNF), Transuranic Waste (TRUW) and by-products of nuclear reprocessing, which comprise different isotopes of highly radioactive actinides, such as neptunium-237 and plutonium-239 with very long half-lives.[27] Table 1.1 lists the known isotopes of the actinide elements, from Ac to No, and the half-life of the most long-lived isotope.

Table 1.1. Masses of existing isotopes of actinides, from Ac to No, and half-life of the most long-lived isotope (shown in year for Ac – Fm, m: million and b: billion).[5]

Early Actinides							
Metal	**Ac**	**Th**	**Pa**	**U**	**Np**	**Pu**	**Am**
Isotopes	225, 227-228	226-232, 234-235	231, 233-236	232-240	237-240	238-240, 242, 244	241-245
Longest-lived Isotope	227	232	232	238	237	244	243
Half-life/year	21.8	14 b	32500	4.47 b	2.14 m	80.8 m	7370
Later Actinides							
Metal	**Cm**	**Bk**	**Cf**	**Es**	**Fm**	**Md**	**No**
Isotopes	242-249	249-250	249-253	252	257	258	259
Longest-lived Isotope	247	247	251	252	257	258	259
Half-life/year	15.6 m	1400	900	1.29	100.5	52 days	58 min

After neutron irradiation, the mass of the Spent Nuclear Fuel is mostly consisted by 95% ^{238}U, 1% ^{235}U, 1-2% Pu isotopes, 2-3% radioactive fission products and less than 0.1% other trans-uranic elements.[9] Handling the SNF is a complex issue and the waste can either be disposed of or reprocessed.

Currently, in United States, nuclear waste is disposed in cooling pools of nitric acid and in dry storage casks at nuclear power plants,[28] with the most famous nuclear waste repository being at Yucca mountain in Nevada. In 1987, the site was designated as a deep geological repository storage for SNF and other high level radioactive waste in the United States.[29] However, the funding decreased significantly in 2011 and the project started to be highly contested by the non-local public, the Western Shoshone peoples, and many politicians.[30] In 2010, the U.S. government had also found an alternative deep geological repository in New Mexico, known as Waste Isolation Pilot Plant (WIPP);[31] however, on February 5th 2014, an incident caused the leakage of airborne radiation consisting of americium and plutonium particles and 21 people were exposed.[32] This event raised the question of whether or not WIPP could be a safe replacement for the Yucca Mountain nuclear waste repository, as a destination for all the waste generated at U.S. commercial nuclear power plants.

An alternative strategy to nuclear waste repositories is to reprocess and re-use the fissile material to ultimately reduce both the volume and the activity of high level radioactive nuclear waste. In UK, for example, for several years this process had taken place at the Sellafield site with the new waste, generated after the reprocessing, being finally vitrified and sealed in stainless steel containers for dry storage.[33] However, the current policy of the UK government is to manage the nuclear waste through geological disposal.[34]

Reprocessing can theoretically recover up to 95% of the fissile material in Spent Nuclear Fuel.[35] However, firstly, the fissionable material needs to be isolated from the SNF and therefore several separation processes have to be performed. One example is the PUREX solvent extraction[36] (Plutonium and Uranium Reduction EXtraction) which uses tri-*n*-butyl phosphate (TBP) as extracting ligand to extract uranium and plutonium (and with slight modifications neptunium also) from SNF, so that they can be recycled as MOX (mixed oxide) fuels. After the PUREX separation, the remaining waste of a highly radioactive raffinate contains over 99.9% of the fission product including lanthanide isotopes, ^{137}Cs, ^{90}Sr, ^{99}Tc and the minor actinides ^{237}Np, ^{243}Am and ^{247}Cm.[37] This must then be further divided to finally recycle the spent nuclear fuel as proposed in the "Partitioning and Transmutation" (PT) strategy:[38] the actinides have to be separated from the lanthanide fission products and then neutron irradiation can be executed. The separation is crucial, because the lanthanides have a high neutron absorption cross-section so that they can effectively compete with the actinides during neutron irradiation.[38] Achieving this separation is, however, extremely difficult due to the many chemical

similarities between lanthanides and actinides.[38] This is particularly evident with some minor actinides such as Am and Cm; they tend to resemble the lanthanides, with their *5f* orbitals dropping in energy and becoming more core-like to a greater extent compared to the early actinides. This different chemical behaviour within the actinide series will be illustrated in more detail in section 1.3.

Despite several difficulties, extraction processes have already been established for a correct separation of the material in the PUREX raffinate and some are listed in Scheme 1.1. The UREX[39] (URanium EXtraction) method for the extraction of the remaining uranium and technetium from the nitric acid solution of the dissolved PUREX raffinate, the UNEX[40] procedure (UNiversal EXtraction) for the simultaneous separation of caesium, strontium and some actinides from radioactive acidic raffinate solutions, and finally the SANEX[39e,f] (Selective ActiNide EXtraction), the TRUEX[41] (TRansUranic EXtraction) and the DIAMEX[42] (DIAMide Extraction) processes that help to separate the trivalent actinides (americium and curium) and lanthanides from high acidity PUREX raffinate solutions.

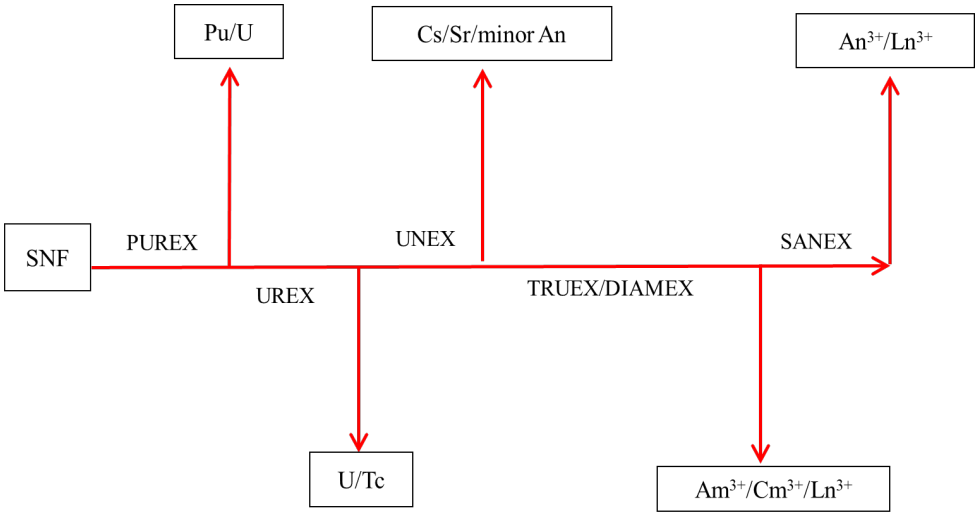

Scheme 1.1. Schematic diagram showing the separation processes of SNF.

The most successful techniques adopted by the above methods are centred on liquid-liquid separations, taking advantage of selective binding of an actinide and/or lanthanide to specific ligands. For example, different N-heterocyclic chelating ligands such as the 6,6′-bis(5,6-dialkyl-1,2,4-triazin-3-yl)-2,2′-bipyridines (BTBPs) (with an example reported in Figure 1.1(a)), the 2,9-bis(1,2,4-triazin-3-yl)-1,10-phenanthroline (BTPhen) (Figure 1.1(b)) and the 2,6-bis(5,6-di-*n*-propyl-1,2,4-triazin-3-yl)pyridine (^{n}Pr-BTP, R1) or 2,6-bis(5,6-di-*iso*-propyl-1,2,4-triazin-3-yl)pyridine (^{i}Pr-BTP, R2) (Figure 1.1, (c)),

have demonstrated extraction abilities towards Am(III) and Cm(III) with high selectivity over Ln(III) from nitric acid solutions.[43]

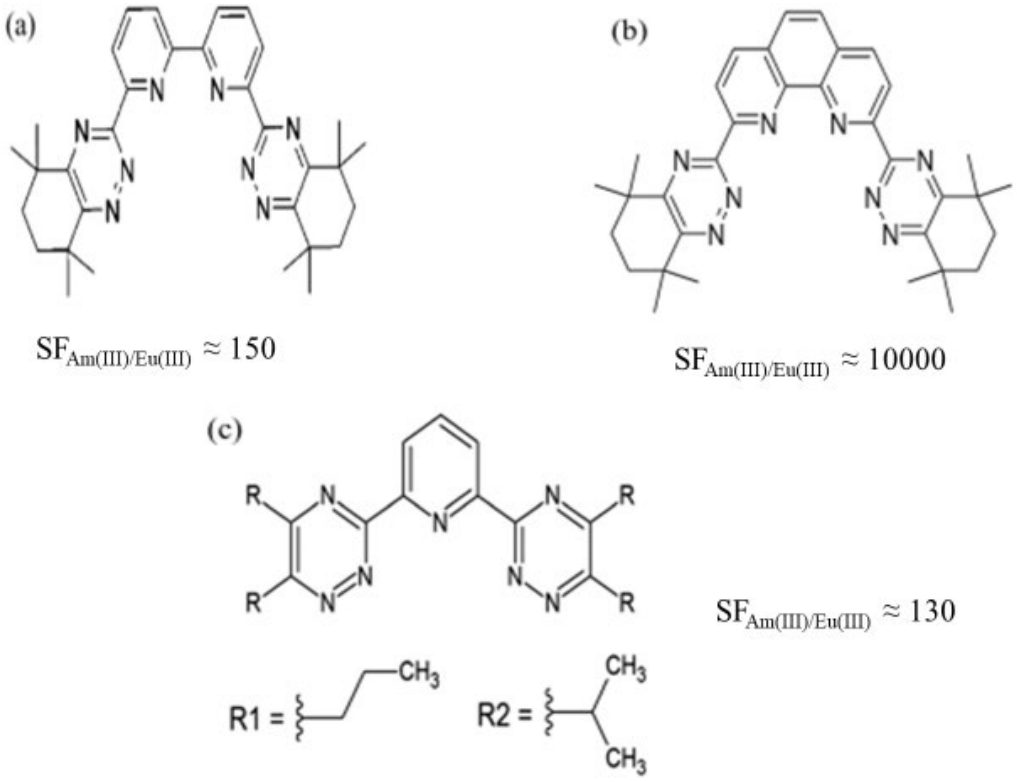

Figure 1.1. Examples of N-heterocyclic ligands for extraction of radioactive minor actinides from lanthanides in SNF and corresponding separation factors for separation between Am(III) and Eu(III) from nitric acid solution, (a) example of a 6,6′-bis(5,6-dialkyl-1,2,4-triazin-3-yl)-2,2′-bipyridine ($CyMe_4$-BTBP), (b) 2,9-bis(1,2,4-triazin-3-yl)-1,10-phenanthroline (BTPhen);[43a] (c) 2,6-bis(5,6-di-*n*-propyl-1,2,4-triazin-3-yl)pyridine (^{n}Pr-BTP, R1) and 2,6-bis(5,6-di-*iso*-propyl-1,2,4-triazin-3-yl)pyridine (^{i}Pr-BTP, R2).[43]

The above N-donor ligands show high positive values for the separation factors $SF_{Am(III)/Eu(III)}$ for Am(III) and Eu(III). These are given by the ratios between the distribution ratios $D_{Am(III)/Eu(III)}$ for Am(III) and Eu(III), where a distribution ratio (D) is defined as the ratio of the solute's (*i.e.*, the metal ion extracted) concentration in the organic phase over its concentration in the acidic aqueous phase after extraction ($D_M = [M]_{org}/[M]_{aq}$).

The higher affinity of these ligands towards An(III) ions over Ln(III) ions can be explained considering that the slightly higher charge density of the lanthanides makes them a little harder compared to actinides; thus, soft nitrogen donor ligands will preferentially coordinate to trivalent actinides over trivalent lanthanides.[43] This selectivity

may also be traced to the fact that An-ligand bonds have a covalent character generally greater compared to the principally ionic Ln-ligand bonds.[44]

In turn, the higher covalency in An-ligand bonds, especially for the early actinides, is partially explainable considering the larger radial extension of the *5f* orbitals of the actinides compared to the more contracted *4f* orbitals of the lanthanides. Thus, there is possibility of an orbital overlap between the *5f* orbitals of the actinides and the π^* molecular orbitals of these N-heterocyclic ligands.[43] However, recent computational studies raised some doubts about the origin of this perceived covalency. For example, it has been suggested that the greater affinity of the BTBPs ligands for trivalent actinides over trivalent lanthanides, particularly for the isoelectronic pair Am(III)/Eu(III), can be explained considering a coincidental energy match between ligand and actinide orbitals. In this case, the covalency in An-ligand bonds is driven by "orbital energy degeneracy" rather than "spatial orbital overlap".[45] The covalency in actinide complexes will be discussed in more detail in section 1.3.

In conclusion, the nature of the interactions between the extractant ligands and the *4f* lanthanide and *5f* actinide ions represents an attractive and challenging subject, and its understanding is crucial to improve the efficiency of the PT strategy.[38]

1.3 Chemical Characteristics of Actinides

The f-block elements have interesting electronic structures which play a key role in their chemical and physical behaviour. The principal differences in the chemical behaviour between lanthanides and actinides can be understood comparing the *4f* and *5f* electron shells[46] and considering that the *5f* orbitals have an additional radial node.

In order to fully comprehend the electronic structures of actinide metals, relativistic effects must be considered. For lighter chemical elements, the velocity of the electrons is negligible compared to the speed of light, but this is not true for heavy elements, such as actinides and, to a lesser extent, lanthanides. In actinides the core electrons travel close to the speed of light and this results in an increasing of their relativistic mass and in a contraction of the orbitals, in accordance with the Einstein's relativity theory. This effect is particularly pronounced with *s* orbitals, which have no node at the nucleus and so their electrons must have very high speeds to prevent their capture by the nucleus. Thus, in the actinide series, there is a contraction of all *s* and (to a slightly less extent) *p* orbitals, which is known as "relativistic orbital contraction",[47] with a stabilization of all *s* and *p* electrons.

In contrast, the *d* and *f* orbitals undergo a radial expansion, due to the increased shielding of the nuclear charge by the more contracted *s* and *p* orbitals, as evidenced in Figure 1.2.[48]

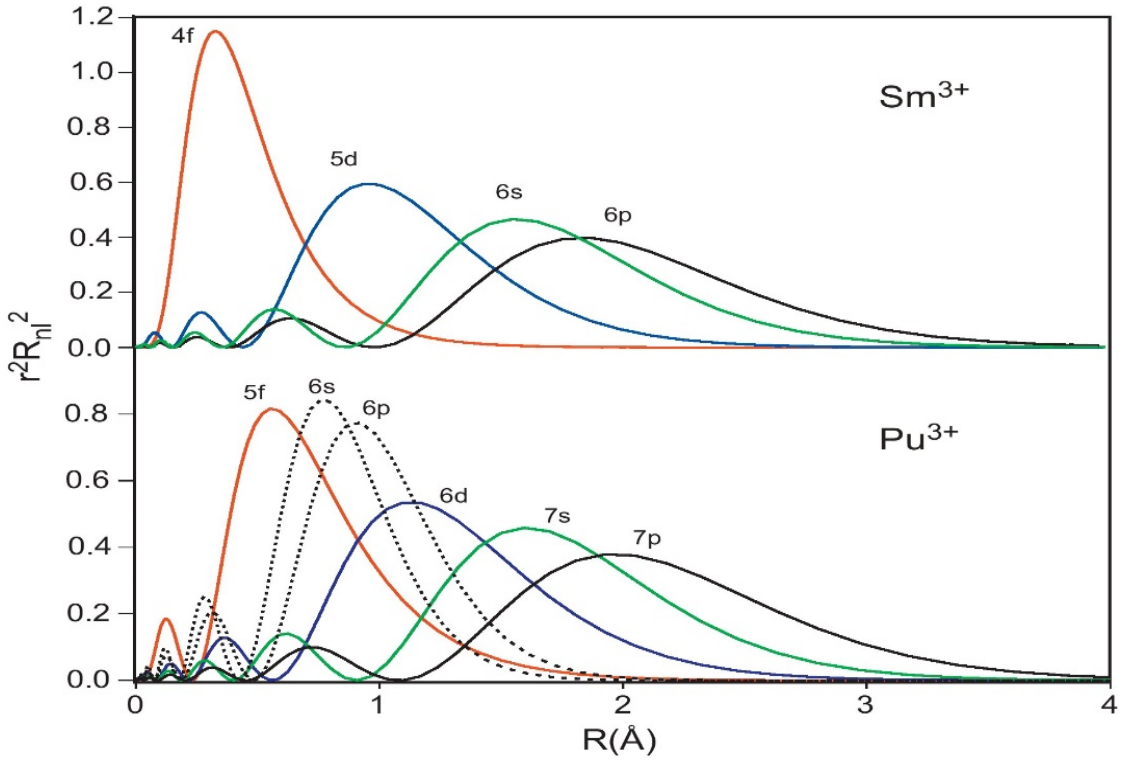

Figure 1.2. Relativistic Radial Distribution Functions for *f*, *d*, *s* and *p* orbitals for Sm^{3+} (top) and Pu^{3+} (bottom). Reproduced from reference 48.

Furthermore, the *5f* orbitals of the actinides are less shielded by the filled *6s* and *6p* orbitals than the *4f* orbitals of the lanthanides by the filled *5s* and *5p* orbitals. As a consequence, the actinides (especially the early actinides) are more inclined to form covalent-type bonds by "spatial orbital overlap" than the lanthanides whose chemical behaviour is mostly ionic.[3] Nevertheless, in the literature there are some examples of covalency in lanthanide complexes. For example, very informative is a recent review by Anwander *et al.*[49] which provides an overview of the historic and current progress of the organometallic chemistry of Ce(IV). Among the tetravalent lanthanide ions, indeed, only Ce(IV) forms stable coordination compounds (*e.g.* $(NH_4)_2[Ce(NO_3)_6]$). Regarding organocerium(IV) chemistry, useful are also the XAS studies conducted by Löble *et al.*,[50] the results by Kapur *et al.*[51] on borohydride derivatives of Cp_3Ce^{IV}, or the analyses on cyclopentadienyl[52] and carbene[53] cerium(IV) complexes. These studies demonstrate that Ce(IV) has a chemical behaviour generally more covalent than the reduced Ce(III) analogue.

In the actinide series, it is generally established that covalency due to orbital overlap is more favourable earlier in the series, where the *6d* and *5f* orbitals are less core-like, but it decreases crossing the series. In fact, as the *5f* orbitals do not efficiently shield each other from the effective nuclear charge, Z_{eff}, the increasing of the atomic number causes the *5f* orbitals dropping rapidly in energy, becoming more core-like and thus resembling the *4f* orbitals of the lanthanides. However, this decreasing in energy of the *5f* orbitals through the series could lead to a degeneracy in energy between the actinide *5f* orbitals and the molecular orbitals of a specific ligand, giving rise to a covalency driven by "orbital energy degeneracy".[45, 54]

Many researchers have started to explore in more detail this new type of covalency. For example, recent reports have noted the ability for californium borates and dipicolinates to participate in more significant covalent interactions than comparable systems of the earlier actinides, such as plutonium, americium, and curium.[6, 22h, 55] Notable is the study by Kelly *et al*.[56] on actinide-dipicolinate (DPA) complexes $[An(DPA)_3]^{3-}$ (An = Am, Cm, Bk, and Cf), where they observed a steady ingrowth of covalency, while moving from Am to Cf, confirmed by a parallel increasing of the measured actinide-dipicolinate stability constants across the series.[56] The trend was also consistent with electronic structure calculations: moving across the series, the An *5f* orbitals drop in energy and tend to become degenerate with the DPA ligand orbitals, resulting in increased orbital mixing and more delocalized *5f* character bonding interactions with the ligands.[56] Thus, the participation of the *5f* orbitals in the Bk- and Cf-DPA complexes is a significant difference from the earlier actinides, which instead are known as having mostly the *6d* orbitals dominating the metal-ligand interactions while the *5f* orbitals remain more unaffected.[57]

Thus, the early actinides such as uranium, neptunium and plutonium, can exhibit covalency arising predominantly from metal-ligand orbital overlap, although maybe involving *6d* rather than *5f* orbitals. In contrast, heavier actinides, with more contracted *5f* and *6d* orbitals, tend to resemble the lanthanides in their ionic chemical behaviour;[58] however, the dropping in energy of the *5f* orbitals, with a possible degeneracy with ligand molecular orbitals, could lead to a covalency driven by "orbital energy degeneracy".[45, 54] The equilibrium between these two forms of covalency is still an intriguing mystery.

Actinides exhibit large ionic radii and, thanks to a small energy gap between *7s*, *6d* and *5f* states, support a wide range of oxidation states, from +2 to +7, compared to lanthanides (mostly +3) and a maximum coordination number higher than observed in TM complexes.[3] Table 1.2 lists the oxidation states of the actinide ions.[3]

Table 1.2. Oxidation states of actinide ions.[3]

Ac	Th	Pa	U	Np	Pu	Am	Cm	Bk	Cf	Es	Fm	Md	No	Lr
	+2		+2	+2	+2	+2	+2		+2	+2	+2	+2	+2	
+3	+3	+3	+3	+3	+3	+3	+3	+3	+3	+3	+3	+3	+3	+3
	+4	+4	+4	+4	+4	+4	+4	+4	+4					
		+5	+5	+5	+5	+5	+5							
			+6	+6	+6	+6								
				+7	+7	+7								

An = only found in solid state; An = most stable oxidation state in aqueous solution

Redox potentials can be used to explain the stability of the oxidation states. Scheme 1.2 shows standard reduction potentials of selected actinide ions in 1 M $HClO_4$ solution (values in volt *vs* standard hydrogen electrode).[59]

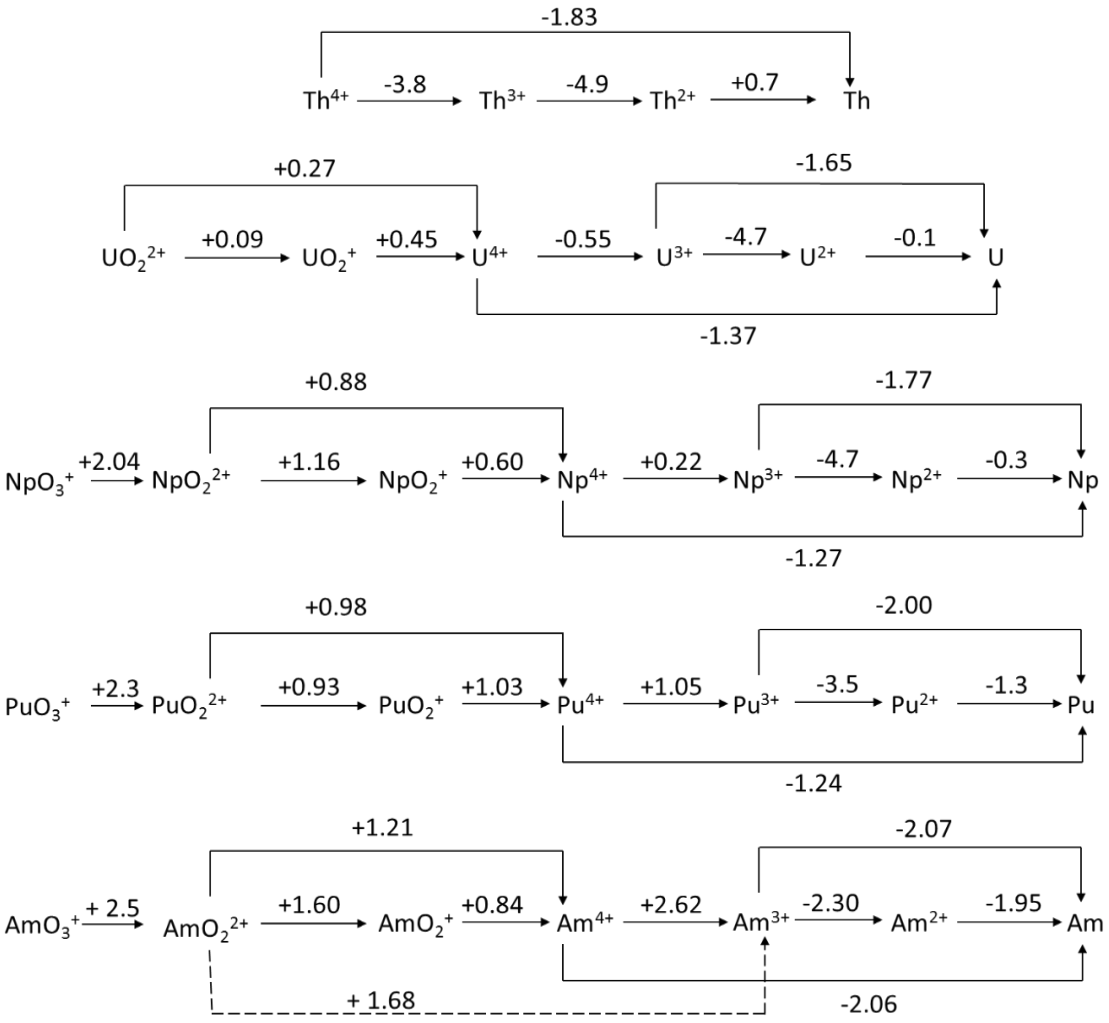

Scheme 1.2. Standard reduction potentials of selected An ions in 1 M $HClO_4$ solution (values in volt versus Standard Hydrogen Electrode).[59]

As can be seen from Scheme 1.2, there is a variety of oxidation states for the early An, due to a low energy gap between *5f* and *6d* orbitals. In acidic solution, thorium clearly has a very stable +4 oxidation state, which is very difficult to reduce and, according to these redox potentials, Th(II) should not be stable in aqueous media. From uranium to americium the situation is more intricate, as there is a higher number of oxidation states that can be reached. For uranium, in particular, the values of the corresponding reduction potentials (Scheme 1.2) suggest that in solution the uranyl(VI) ion, $[UO_2]^{2+}$, represents the most stable oxidation state in uranium chemistry, while a disproportionation of the uranyl(V), $[UO_2]^{+}$, to U^{4+} and $[UO_2]^{2+}$, is favoured in acidic conditions. Moreover, the value −4.7 V for the semicouple U(III)/U(II) highlights the instability of the U^{2+} ion. It is therefore very interesting the recent identification of the formal +2 oxidation state of uranium in the molecular complex $[K(2.2.2\text{-Cryptand})][(C_5H_4SiMe_3)_3U]$, reported by

Evans *et al.*,[60] with a $5f^3 6d^1$ quintet ground state for uranium(II) in the $[(C_5H_4SiMe_3)_3U]^-$ anion.[60] Perhaps more fascinating is the recent isolation of a formal Np^{2+} ion, with a $5f^4 6d^1$ ground state electronic configuration, achieved in the crystallographically characterized molecular complex $[K(crypt)][Np^{II}Cp''_3]$ [crypt = 2.2.2-cryptand, $Cp'' = C_5H_3(SiMe_3)_2$],[61] or the debated possibility of forming a Np^{2+} ion, upon reduction of a Np^{3+} complex with the supporting ligand *trans*-calix[2]benzene[2]pyrrole.[62] Even more remarkable, in light of its very complicated chemical behaviour, is the identification of plutonium in a formal +2 oxidation state in the molecular complex $\{Pu^{II}[C_5H_3(SiMe_3)_2]_3\}$.[63]

Scheme 1.3 shows the standard redox potentials of the semicouples An^{4+}/An^{3+} and An^{3+}/An^{2+} for the actinide series in acidic solution.[59] It is clear that, traversing the actinide series, the 4+ ion becomes destabilised with respect to the 3+ ion, with the exception of Bk(IV) ($5f^7$), and for heavier An the +2 oxidation state tends to be more stable than the +3, with the exception of Cm(III) ($5f^7$).

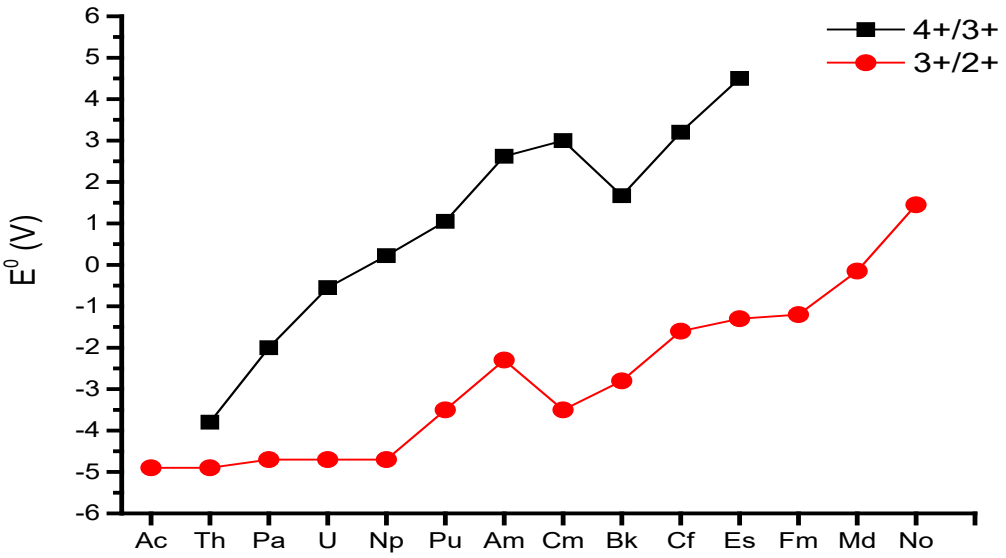

Scheme 1.3. Plot of the redox potentials for the semicouples An^{4+}/An^{3+} and An^{3+}/An^{2+} in 1 M $HClO_4$ solution (values in Volt vs standard hydrogen electrode).[59]

The electronic configurations of gas-phase actinide atoms, determined by electronic spectroscopy, are summarized in Table 1.3.[64] In the element thorium ($6d^2\ 7s^2$), the *6d* orbitals are still lower in energy than the *5f* and so thorium, unlike its lanthanide analogue cerium, has no valence *f* electrons. Crossing the series, with the increasing of Z_{eff}, the energy gap between the *5f* and *6d* orbitals changes progressively until the energies invert, with the *5f's* becoming lower in energy than the *6d's*.[64] This has been explained

theoretically by Bursten *et al.*,[64] as shown in Scheme 1.4 for the "base-free" tris(η^5-cyclopentadienyl) actinide complexes Cp_3An (An = Th, Pa, U, Np, Pu).

Table 1.3. Ground state electronic configurations of actinides.[59]

Actinide	Electronic configuration	Actinide	Electronic configuration
Ac (actinium)	$6d^1\ 7s^2$	Bk (berkelium)	$5f^9\ 7s^2$
Th (thorium)	$6d^2\ 7s^2$	Cf (Californium)	$5f^{10}\ 7s^2$
Pa (protactinium)	$5f^2\ 6d^1\ 7s^2$	Es (einsteinium)	$5f^{11}\ 7s^2$
U (uranium)	$5f^3\ 6d^1\ 7s^2$	Fm (fermium)	$5f^{12}\ 7s^2$
Np (neptunium)	$5f^4\ 6d^1\ 7s^2$	Md (mendelevium)	$5f^{13}\ 7s^2$
Pu (plutonium)	$5f^6\ 7s^2$	No (nobelium)	$5f^{14}\ 7s^2$
Am (americium)	$5f^7\ 7s^2$	Lr (lawrencium)	$5f^{14}\ 6d^1\ 7s^2$
Cm (curium)	$5f^7\ 6d^1\ 7s^2$		

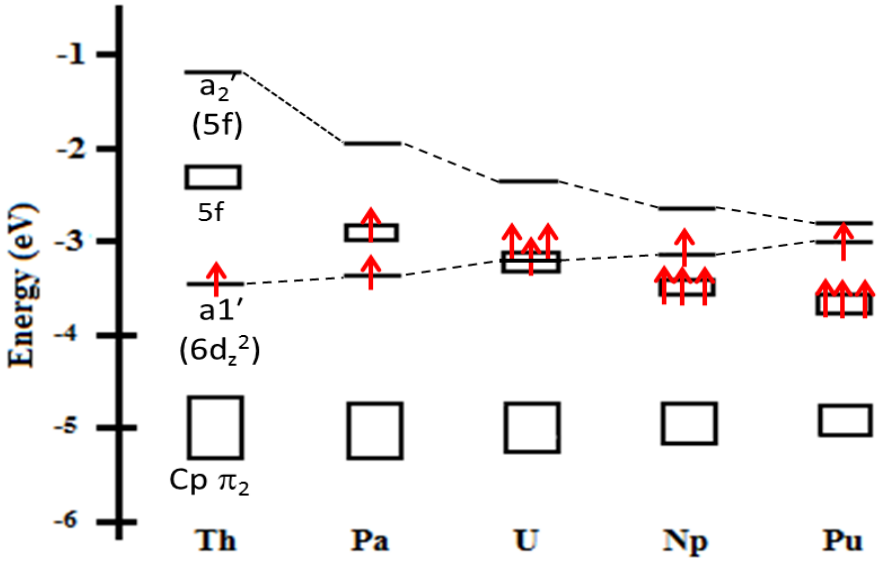

Scheme 1.4. Metal-based orbital energies for the $5f^{n-1}\ 6d^1$ ground state electron configurations of planar Cp_3An (An = Th, Pa, U, Np, Pu) complexes.[64]

Spectroscopic methods are very useful in quantifying the covalency in metal-ligand bonding for TM complexes,[65] but the subject is much more intricate with An complexes, where the degree of orbital overlap is strongly dependent on the oxidation state of the metal and the nature of the ligand.[66] In this regard, remarkable is the work conducted by

Albrecht-Schmitt *et al.,*[67] which shows that the *5f*, *6d* and *7p* orbitals are all involved in bonding in a Cf(III) borate complex.

Generally, useful information can be obtained from measurements of Electron Paramagnetic Resonance (EPR) Spectroscopy, which can give insight into the delocalization of the electron spin density within the ligand valence orbitals,[68] and PhotoElectron Spectroscopy (PES) which offers information on the energies of the occupied molecular orbitals of the metal complex.[69] Mössbauer Spectroscopy and X-ray Absorption Spectroscopy (XAS) are also useful to study actinide compounds. Mössbauer Spectroscopy can help to estimate the shielding of *s* orbitals by valence electrons,[70] although this technique is only valid for certain elements with Mössbauer-active nuclei, such as ^{237}Np.[70] XAS, in turn, allows to quantify the degree of covalency in a metal-ligand bonding by looking at the amount of ligand *p* character in the primarily metal-based anti-bonding orbitals.[71]

1.3.1 Spin-Orbit Coupling

Spin-orbit coupling and electron correlation effects are extremely important to understand spectroscopic properties of metal ions.[57b, 72] As discussed above, for the early An, ligand-metal bonding can take place through ligand interactions with the *6d* orbitals of the metal, which are strongly split by the ligand field, and with the slightly more contracted *5f* orbitals that show a weaker splitting.[73] The ground state electronic configurations are thus guided by the filling of these closely spaced *5f* orbitals, which leaves unpaired electrons that may couple to the open shell ground states.[73] In the Hamiltonian used for electronic structure calculations, angular momenta of multi-electron systems can be coupled by the Russell-Saunders (*LS*) and/or *j-j* coupling scheme.

For transition metals, where the spin-orbit coupling is reasonably weak (*ca.* 200 cm^{-1}) and crystal-field splitting dominates instead ($\Delta_o \approx 15000 - 25000$ cm^{-1}),[1] the *LS* coupling scheme holds well and atoms exhibit Hund's rule ground states with maximum values of both the total orbital angular momentum *L* (sum of the orbital angular momenta of the all electrons, ℓ) and total spin angular momentum *S* (sum of the spin angular momenta of the all electrons, *s*).[74] Thus, for TM, *L* couples to *S* to give the total angular momentum *J*. For the lanthanides, crystal-field effects are smaller (*ca.* 100 cm^{-1}), spin-orbit coupling is more significant (*ca.* 1000 cm^{-1}), but inter-electronic repulsions dominate.[75] For the actinides, inter-electronic repulsion is still greatest, but spin-orbit coupling is now also relatively

larger (*ca*. 2000 cm^{-1} for uranium, for example).[75] Therefore, for the actinides, the *j-j* coupling should become the right scheme to calculate energetic levels, where each electron orbital, ℓ, and spin angular momentum, *s*, couple to form individual electron angular momentum, *j*, which then couples to the other electron angular momenta to give the total angular momentum, *J*.[76] However, this is not straightforward since for the actinides crystal-field effects are also appreciable (*ca*. 1000 cm^{-1} for uranium, for example)[75] and, more importantly, are of the same order of magnitude as spin-orbit coupling; in this case, the accuracy of both *LS* and *j-j* coupling depends on the electronic configuration of the ion. For instance, uranium is considered the heaviest element that falls into the *LS* coupling curve.[75] Its strong spin-orbit coupling, *ca.* 2000 cm^{-1}, is partially cancelled by the degree of localization of the *5f* orbitals and so uranium in its +4 and +6 oxidation state follows the *LS* coupling to about 80% and 90% respectively.[75, 77] This *LS* scheme gives rise to term symbols $^{(2S+1)}L_J$, which are $^5I_4$, $^4I_{9/2}$, $^3H_4$, $^2F_{5/2}$, and $^1S_0$ for uranium(II) (assuming the [Rn]$5f^4$ and not [Rn]$5f^3 6d^1$ electronic configuration), uranium(III) ([Rn]$5f^3$), uranium(IV) ([Rn]$5f^2$), uranium(V) ([Rn]$5f^1$), and uranium(VI) ([Rn]$5f^0$), respectively. This method assumes that the ground state is well separated from the excited states, that is, there is no mixing of *J* levels. The electronic structure of uranium in different oxidation states will be illustrated with more details in section 1.4.

Moreover, progressing across the actinide series, the spin-orbit coupling becomes even larger than 2000 cm^{-1}. Therefore, for the later actinides, due to the interplay between large crystal-field splitting and strong spin-orbit coupling, an intermediate scheme between *LS* and *j-j* coupling must be used to estimate energetic levels.[21, 75, 78]

1.4 Photophysical Properties of Actinides

The photophysical properties of transition and lanthanide metals have been well defined, providing insight into their electronic structure and chemical behaviour.[79] Moreover, during the last decade, the luminescence properties of transition and lanthanide metals have aroused interest, due to potential applications in the exploitation of the solar energy,[80] optical imaging techniques[81] and protein biology.[82] Assigning the electronic transitions in the absorption spectra of lanthanide complexes is generally not very difficult, since for lanthanides the spin-orbit coupling (*ca*. 1000 cm^{-1}) dominates over crystal-field effects (*ca.* 100 cm^{-1}).[75]

For the actinides the greater radial extension of the *5f* orbitals (Figure 1.2), especially for the early actinides, results in larger crystal-field splitting; but the spin-orbit coupling is also considerably greater. As a consequence, in actinide complexes there is often considerable overlap between different energetic levels and so the interpretation of UV-vis-NIR spectra is difficult. Nevertheless, understanding both the absorption and emission profiles of actinide compounds is very important, since it gives insight into the degree of covalency in An-ligand bonding to increase the efficiency of the PT strategy.[38]

The electronic transitions in the absorption spectra of both lanthanides and actinides are characterized by lower extinction coefficients compared to those of transition metals. Laporte forbidden *f-f* transitions are often visible in the near infrared region (NIR) as sharp bands for both lanthanides and actinides, although for the lanthanides they are generally weaker. In actinide compounds, instead, vibronic coupling is greater and so slightly higher extinction coefficients can be reached (molar absorptivity $\varepsilon \approx 10 - 80$ M^{-1} cm^{-1} with simple σ-donor ligands).[3k] In addition, metal-ligand interactions are commonly greater in actinide than in lanthanide complexes and a stronger nephelauxetic effect can be noted in absorption spectra of actinide complexes.[83]

In addition to the narrow *f-f* transitions in the NIR region (*ca.* $E < 15000$ cm^{-1}), two other types of absorption bands can be commonly seen at higher energy in the absorption spectra of actinide complexes. For the early actinides, Laporte allowed *5f-6d* transitions generally occur above 20000 cm^{-1} (222 nm) and are more intense and broad than the *f-f* bands (*ca.* $E < 15000$ cm^{-1}).[3k] Ligand-Metal Charge Transfer (LMCT) and Metal-Ligand Charge Transfer (MLCT) transitions are also detectable in the UV region and are very intense.[3k,75] The *d–d* transitions are also Laporte forbidden, but *d* orbital mixing with ligand frontier orbitals of opposite parity "switches on" these transitions so that appreciable intensities can be observed, although they are not of the same magnitude as LMCT or MLCT transitions. [3k, 75] Moreover, for imido and ketimido complexes of U(IV), as reported by Morris *et al.*,[84] the *f-f* transitions intensity can increase to ~ 50 – 400 M^{-1} cm^{-1}. This interesting effect can be understood in the context of an "intensity stealing mechanism" from the charge transfer (CT) excited states, that reflects an enhanced degree of covalency between the actinide metal and nitrogen-donor ligand systems.[84] Solvation has also an important effect upon the relative energies of the *5f* and *6d* states. For example, in the case of the free U^{3+} ion, the $5f^2 6d^1$ excited state is over 30000 cm^{-1} (absorption band at $\lambda_{max} = 333$ nm) above the $5f^3$ ground state, while in $U^{3+}_{(aq)}$ the CT transitions start around 24000 cm^{-1} (absorption band at $\lambda_{max} = 416$ nm).[85]

For many years, emission spectroscopy has been applied in the field of actinide chemistry and the most well defined is the green emission of the uranyl $[UO_2]^{2+}$ ion.[86] However, understanding the emission profile of actinide ions and their compounds in solution is still a complex subject, due to their complicated spectroscopic properties when compared to transition or lanthanide metals.

1.4.1 Structures and Photophysical Properties of Uranyl(VI) Ion

The structure of actinide ions depends strongly on the oxidation state. From +2 to +4 oxidation states, they adopt a spherical symmetry and the final structure is subject to the steric demand of the ligands. In contrast, the +5 and +6 ions generally exist as an actinyl unit, $[AnO_2]^+$ or $[AnO_2]^{2+}$, which usually displays a mostly linear O=An=O fragment and a bipyramidal coordination geometry, with the ligands located on the equatorial plane.[3f] The metal-ligand bonding is predominantly ionic, but, as already discussed, covalency is possible and the U=O bonding in the uranyl units ($[UO_2]^+$ or $[UO_2]^{2+}$) is an important example. The uranyl(VI) ion, $[UO_2]^{2+}$, is the most common form of uranium in the environment and, among all the actinide ions, it has been studied in great detail due to its role in the nuclear fuel cycle.[3] The molecular orbital diagram of the uranyl(VI) ion, shown in Figure 1.3, is both experimentally and theoretically understood.[3, 87] Uranyl(VI) has a bond order of three, arising from interactions of matching symmetries (*e.g.* σ and π); a U–O σ bond is formed by interaction of the oxygen $2p\sigma$ orbitals with the uranium $6d_{z^2}$ orbitals (σ_g) and a hybrid metal orbital formed by mixing uranium $5f_z^3$ with the semicore $6p_z$; a U–O π bond is formed by interaction of oxygen $2p\pi$ orbitals with uranium $6d\pi$ (π_g) and $5f\pi$ (π_u) orbitals. The $5f\,\delta_u$ and φ_u are non-bonding *5f* orbitals, as they have no symmetry match with the ligand orbitals, and are the Lowest Unoccupied Molecular Orbitals (LUMO).[87] Interestingly, the π orbitals are lower in energy than the σ orbitals and this has been proved experimentally (Figure 1.3) due to a small destructive overlap between the *2p* and $5f_z^3$ orbitals.[87]

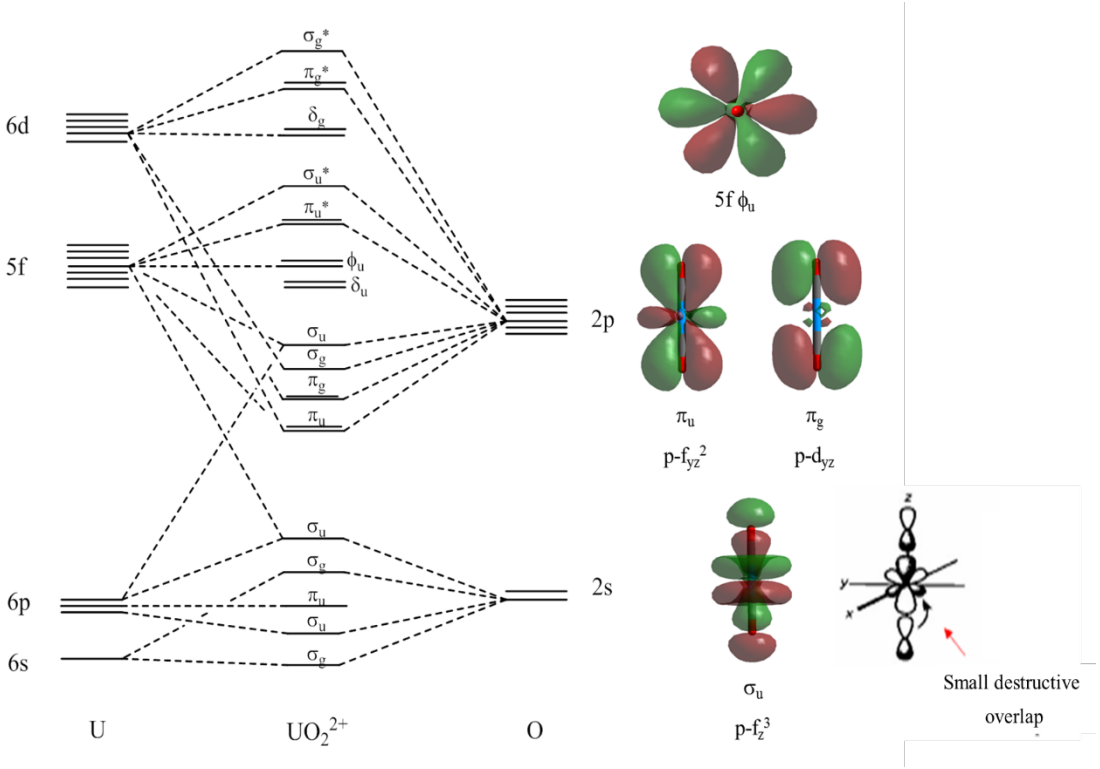

Figure 1.3. Qualitative MO diagram for the bonding in the free uranyl ion, $[UO_2]^{2+}$, and graphical representations of selected molecular orbitals.[3, 87] In the free uranyl ion, $[UO_2]^{2+}$, the π bonding orbitals are lower in energy than the σ bonding orbitals, due to a small destructive overlap between the *2p* and $5f_z^3$ orbitals (bottom right).

A detailed Jabłoński diagram of the uranyl(VI) aquo ion is shown in Figure 1.4. The absorption spectrum of the free uranyl(VI) ion can show a maximum of twelve bands, with a vibrationally resolved pattern from 450 to 500 nm, arising from LMCT transitions with the promotion of an electron from a bonding -yl oxygen orbital (σ_u, σ_g, π_u and π_g) to a non-bonding uranium $5f_\delta$ and $5f_\varphi$ orbital.[87, 88] The de-excitation from the $^3\Pi_u$ triplet excited state produces the characteristic green emission at *ca.* 510 nm, with up to six structurally resolved bands both in solution and solid state,[89] as illustrated in Figure 1.4. A number of examples of absorption and emission spectra of uranyl(VI) compounds are shown in Chapter 4.

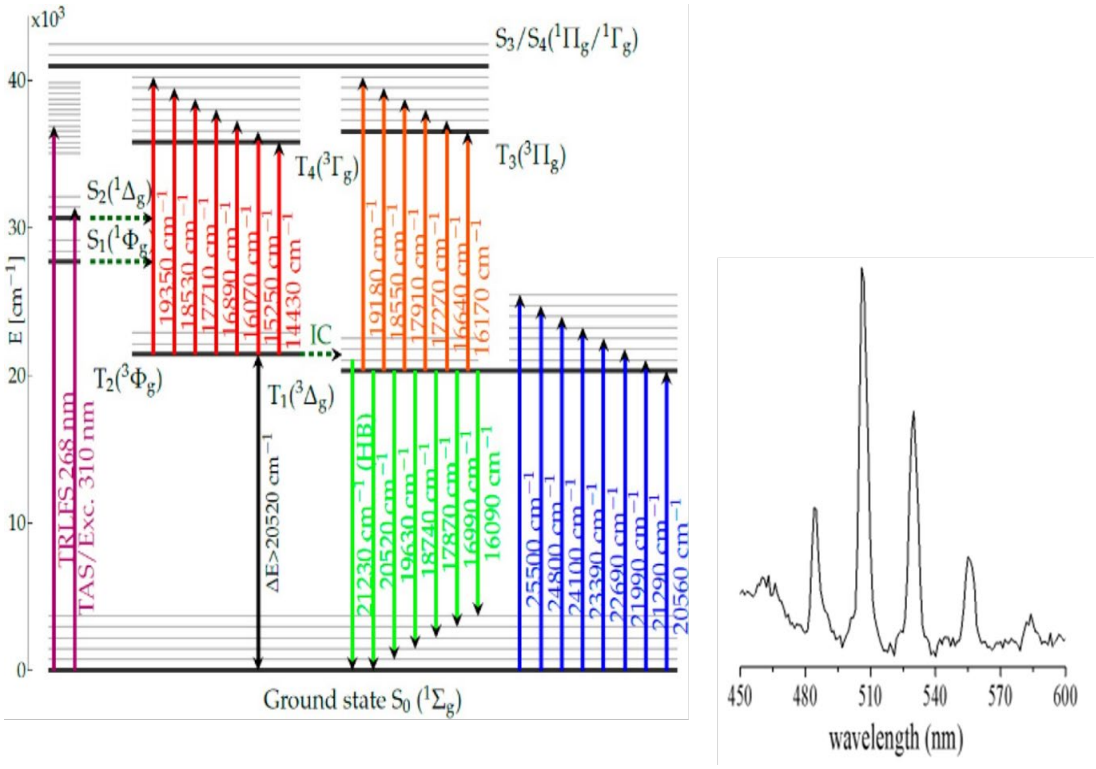

Figure 1.4. (Left) Proposed Jabłoński diagram of the uranyl(VI) aquo ion based on data obtained from UV-vis (blue), Time Resolved Laser induced Fluorescence Spectroscopy (TRLFS) (green), transient absorption (red, orange), and luminescence excitation scan (purple) measurements, taken from reference 90. (Right) solid-state emission spectrum of $UO_2(NO_3)_2{\cdot}6H_2O$ acquired at 77 K (λ_{ex} = 340 nm).

Visible on the absorption and emission profile is the vibronic progression arising from strong coupling of the ground state Raman active symmetric vibrational O=U=O (ν_1) mode, normally seen between 780 and 900 cm^{-1}, with the $^3\Pi_u$ electronic triplet excited state.[91]

A number of studies that investigate the chemical behaviour of the uranyl(VI) ion using luminescence spectroscopy have been reported in the literature. The uranyl(VI) ion can undergo hydrolysis at different pH values forming monomeric hydroxides, dimeric hydroxides and oligomers,[89] and some spectroscopic techniques have been proven to be powerful to study these distinct species in aqueous solution.[89a] In particular: the aqua ion $[UO_{2(aq)}]^{2+}$ has an absorption maximum at λ_{max} = 413.8 nm and a diagnostic emission at λ_{em} = 488 nm, with lifetime of about (τ = 0.9 ± 0.3 μs), the hydroxide $[UO_2(OH)_2]$ shows an absorption at λ_{max} = 421.8 nm and an emission at λ_{em} = 427 nm, with a lifetime of (τ = 2.9 ± 0.3 μs), and the oligomer $[(UO_2)_3(OH)_5]^+$ appears with an absorption band at λ_{max} = 429 nm.[89]

The emission character of the uranyl(VI) ion has been accurately explored in aqueous solutions, where it has been proved that the electronic excited states are long-lived with lifetimes of hundreds of microseconds in the solid state and ten of microseconds to nanoseconds in solution.[92] In contrast, not many experimental data are available in organic media, where most of the actinide ions are known to be non-emissive at room temperature.[93] However, this can be considered as principally due to the low values of the radiative lifetime of the electronic excited states, which in actinide compounds are also strongly influenced by the nature of coordinative ligands and solvent. For example, Yayamura *et al.*[94] reported on the influence of different coordination environments on the energy of the LMCT transitions in a series of $[UO_2]^{2+}$ β-diketonate complexes in organic media. They showed that, at room temperature, the absorption bands from LMCT transitions of the uranyl(VI) were masked by the intra-ligand CT absorption bands of the β-diketonate ligands and that the lifetime of the uranyl(VI) emission was dependent on the nature of the ligands and the solvent. Indeed, a reduction in the lifetime from 484 ns to 0.9 ns for the uranyl(VI) emission, was found by changing the hexafluoroacetylacetone (hfac) ligand with the β-diketonate acetylacetone.[94] This lowering of the lifetime of the uranyl(VI) emission is in line with the complexing strength of the bidentate ligands. The increase in the ligand strength favours a reduction of the U=O bond distance; thus the interaction between the atomic orbitals of the oxygens and uranium in forming the uranyl molecular orbitals (Figure 1.3) increases, this leads to a lowering in the energy gap between the occupied and unoccupied orbitals within the $[UO_2]^{2+}$ ion with a consequent reduction of the lifetime of the emission.[94] Other examples are the photoluminescent study conducted by Hashem *et al.*[95] on the complexes *trans*-$[UO_2X_2(O{=}PPh_3)_2]$ (X = Cl, Br, I) or the measurements performed by Natrajan *et al.* on the *trans*-$[UO_2Cl_2L_2]$ (L = $Ph_3P{=}NH$, $Ph_3P{=}O$ and $Ph_3As{=}O$).[96] In particular, for the first series, the photoluminescent properties of the uranyl(VI) ion do not vary changing the halogen bonded to the uranyl ion,[95] but, within the second group, a red shift in the $O_{yl} \rightarrow U$ LMCT band was noted, in line with the increased donor strength of the ligand.[96]

The high sensitivity of the LMCT of the uranyl(VI) ion to the surrounding environment, such as pH in aqueous solutions[87a] and/or coordinating solvent in organic media,[24a] makes luminescence spectroscopy a suitable tool to follow the chemical behaviour of uranyl(VI) compounds solutions. In addition, understanding the type of interactions between a particular ligand and the uranyl(VI) cation could give a significant contribution to enhance the efficiency of extraction processes in the PT strategy.[38]

Moreover, as well as being photo-luminescent, the uranyl ion is also photo-reactive and the photo-excited uranyl ion, $[UO_2]^{2+*}$, is highly oxidising as well as reducing,[97] and can readily undergo photo-reduction in protic solvents. However, the photo-excited uranyl(V) radical pair, $[UO_2]^{+*}$, can be obtained more favourably than the photo-reduced uranyl(V) and the LMCT emission is partially precluded by electron transfer processes in the photo-excited radical pair.[98] A detailed structural, spectroscopic and theoretical study on a series of uranyl(VI) thiocyanate and selenocyanate complexes will be discussed in Chapter 4.

1.4.2 Photophysical Properties of Uranyl(V) Ion

The occurrence of the actinyl(V) species $[AnO_2]^+$ (An = U,[99b] Np, Pu,) in the natural environment, as a result of the storage of nuclear waste, makes studying their physiochemical behaviour very important.[99] For example, the most stable oxidation state of neptunyl in aqueous solution is the +5,[100] and few $[NpO_2]^+$ compounds have also been isolated and crystallographically characterized.[101] Compounds based on U(V) and Pu(V) ions, instead, are less common, since they are unstable and undergo disproportionation to U(IV) and $[UO_2]^{2+}$ and to Pu(IV) and $[PuO_2]^{2+}$ in protic media.[102] However, the uranyl $[UO_2]^+$ cation can be obtained by chemical, electrochemical and photochemical reduction from the hexavalent $[UO_2]^{2+}$ parent ion.[103] For example, the photoreduction of $5f^0$ $[UO_2]^{2+}$ to $5f^1$ $[UO_2]^+$ can be monitored spectroelectrochemically,[104] following the decrease of the CT bands in the UV-vis region and the formation of a broad feature at higher energy, along with a series of sharp *f-f* transitions at approximately 1818, 1600, 1400, 990 and 760 nm, with very low extinction coefficients ($\varepsilon \sim 1$ - 10 M^{-1} cm^{-1}).[105]

The first luminescence study on pentavalent uranyl $[UO_2]^+$ was published by Steudner *et al.*[106] Irradiation of U(VI) in aqueous perchlorate solution, with a mercury-vapour lamp at λ_{ex} = 245 nm, and monitoring with absorption spectroscopy over time revealed the formation of a band at 255 nm which was assigned to U(V). The corresponding fluorescence emission spectrum, acquired using TRLIFS, showed a band at 440 nm with a radiative lifetime of 1.1 μs. Grossmann *et al.*[107] also investigated the surface alteration of uraninite, UO_2, and uranium tetrachloride, UCl_4, under aerobic conditions, by using a combined technique of laser induced fluorescence spectroscopy and Confocal Laser Scanning Microscopy (CLSM). They found that excitation at 408 nm led to a fluorescence signal in the wavelength range of 415-475 nm, which was indicative of a metastable uranium(V) species, as a result of a one electron oxidation process of UO_2 to $[UO_2]^+$. A

second electron oxidation process, as effect of exposure to air and laser source, could produce $[UO_2]^{2+}$ with a fluorescence signal in the range of 480-560 nm. In addition, the oxidation process of UCl_4 in aqueous solution at pH 0.3 was visualized by CLSM and $[UO_2]^{+}$ was fluorescence spectroscopically identified.

An example of mixed-valent uranyl(VI)-uranyl(V)-uranium(IV) compound will be shown in Chapter 3. In that Chapter an unusual mixed-metal cobalt-uranium compound will be also described, for which preliminary spectroscopic results are indicative of a Co(III)-U(V) configuration.

1.4.3 Photophysical Properties of Actinide(IV) Ions

There are only few examples of spectroscopic studies on actinide(IV) compounds both in solution and solid state, principally because an absolute assignment of the electronic transitions in open shell tetravalent actinide compounds is not straightforward. In fact, for tetravalent actinide ions the involvement of *5f* orbitals in chemical bonds makes the electronic structure very complex to investigate,[3] although the Russell-Saunders coupling scheme can be used as a good initial approximation.

In actinide(IV) complexes the position and the intensity of the *f-f* electronic transitions can be significantly influenced by the ligand field, the symmetry and the polarity of the solvent.[3] An example explaining the influence of the symmetry is shown in Figure 1.5, where the energies of the electronic states of the free U(IV) ion change considerably moving to an octahedral environment.[108]

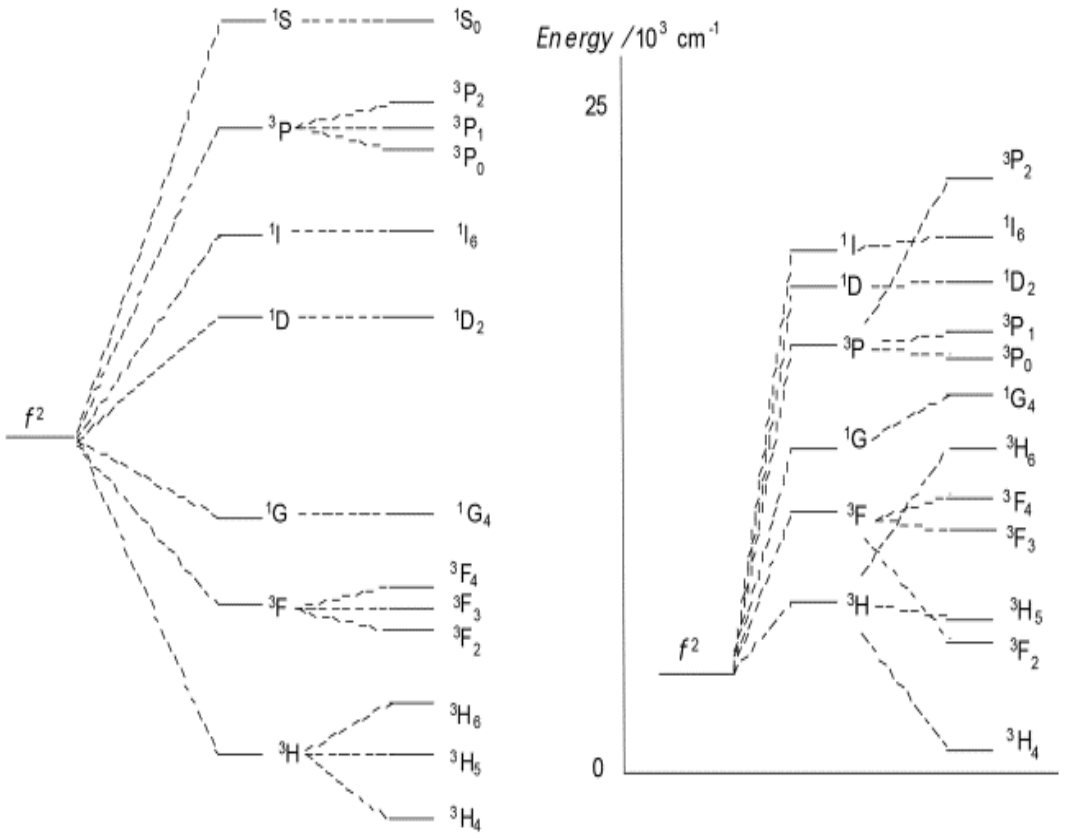

Figure 1.5. (Left) A qualitative energy-level diagram for the free U^{4+} ion showing successively the effects of electrostatic repulsion and spin-orbit coupling; (right) an energy level diagram for the U^{4+} ion in an octahedral crystal-field.[108]

Uranium(IV) represents a challenging model for its complex electronic structure; while it has a strong spin-orbit interaction, its *5f* orbitals are delocalized enough to create an *LS*-like situation due to mixing of the $J = 5/2$ and 7/2 levels, which are split due to relativistic effects.[78] The spin-orbit coupling pushes the *5f* electrons toward the *j-j* coupling scheme, where the early actinides preferentially fill the $J = 5/2$ level and the later actinides fill the $J = 7/2$ level.[109] However, in the case of uranium(IV), hybridisation results in increased mixing of $J = 7/2$ character and hence reduced spin-orbit interaction. Therefore, while uranium follows *LS* coupling, it also has strong spin-orbit interaction, which is partially masked by the degree of delocalization of the *5f* states.[109]

U(IV) organic complexes are generally known to be non-emissive. However, there are few examples in the literature that have tried to elucidate the electronic structure of tetravalent uranium compounds by examining emission profiles. In the solid state, for example, for the doped systems U^{4+} in $LiYF_4$,[110] $ThCl_4$ and $ThSiO_4$,[111] and Cs_2ZrBr_6,[112] with a cubic geometry, the emission bands, observed in the visible region and originated from CT bands in the UV-vis region, were assigned to $5f^1 6d^1 \rightarrow 5f^2$ electronic transitions

from the lowest excited state to different levels of the $5f^2$ manifold. These were produced from a redistribution of valence electrons in the *5f* sub-shell, with a radiative lifetime of tens of nanoseconds at both room temperature and low temperature (77 K). In addition, for single crystals of $LiYF_4:U^{4+}$, an absorption band observed at 240 nm has seven corresponding emission bands at 262, 282, 304, 328, 334, 438 and 492 nm.[110] They were assigned as transitions between the $^3F_2$ ($5f^1 6d^1$) excited state and $^3H_4$ ($5f^2$ manifold) ground state, with a radiative lifetime of approximately 17 ns at both 300 and 77 K.[110]

In this regard, Kiplinger *et al.*[113] showed that, if U(IV) complexes have ligands that exhibit CT bands extended until the visible region, then the emission through the *5f* orbital manifold is very difficult to observe, being in the picoseconds domain.

A remarkable example is the luminescence study on U^{4+} ion in aqueous perchlorate medium reported by Kirishima *et al.*[24b] (Figure 1.6). The absorption band observed in the UV region is assigned to the CT transition $^3H_4 \rightarrow {}^1S_0$ and the corresponding emission bands at 525, 409, 394, 345, 338, 320, 318, 291 and 289 nm as transitions from the $^1S_0$ highest lying state to lower lying states $^1I_6$, $^1G_4$, $^3P_0$, $^1D_2$, $^3F_3$, $^3F_4$ and $^3H_5$, with a radiative lifetime for each band of less than 20 ns at room temperature and 149 ns at 77 K.[24c] The emission bands mirrored the absorption bands and the excitation spectrum of all emission bands was identical, suggesting that emission arises from de-excitation of the $^1S_0$ state only. This study underlines the fact that varying the nature of the medium (perchlorate, chloride and sulfate) leads to a small difference in the emission profile as consequence of a change in local symmetry and crystal-field effect. In other words, the spectroscopic profile of uranium(IV) complexes is influenced by the coordinating environment and solvent.

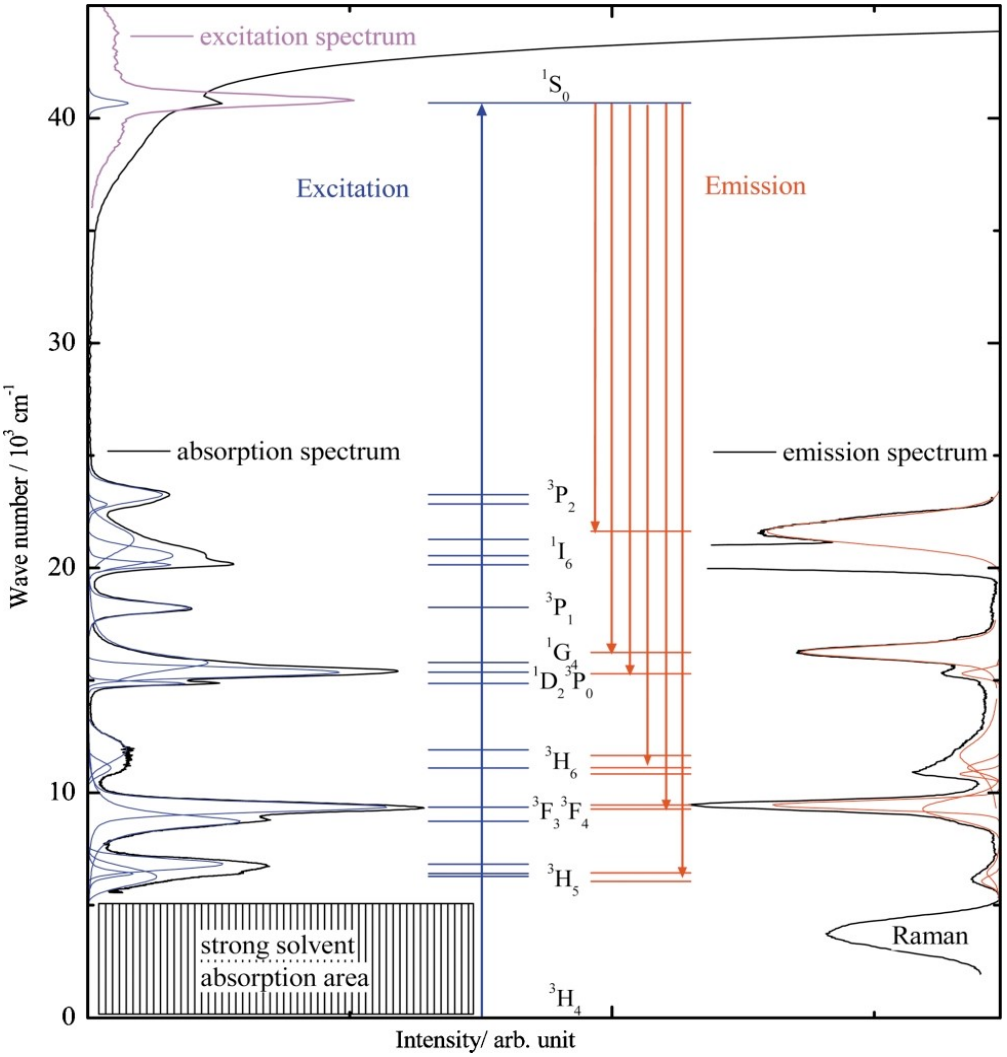

Figure 1.6. Transition energies of the U^{4+} ion in aqueous perchlorate medium reported by Kirishima.[24b]

It is noteworthy also the spectroscopic study conducted on simple U(IV) coordination compounds by Hashem *et al.*[24a] The absorption spectra of the compounds $[Li(THF)_4][UX_5(THF)]$ (X = Cl, Br, I), $[Et_4N]_2[UCl_6]$ and UCl_4 were acquired in THF and the electronic transitions were interpreted with the aid of computational methods, Figure 1.7. Excitation into a band of *f-d* and *LMCT* character, followed by energy transfer into the *5f*-orbital manifold, leads to a radiative de-excitation observed in the UV-vis region of the emission spectrum.[24a] The emission bands were assigned to transitions from the excited $5f^1 6d^1$ electronic configuration to a mixture of states arising from the ground state $5f^2$ electronic configuration.[24a, 114] In summary, one can predict that any U(IV) compound, that does not have CT bands extended in the visible region, could be emissive. A recent spectroscopic study has also reported unusual fluorescence properties from a Th(IV) complex, both in solution and solid state.[115]

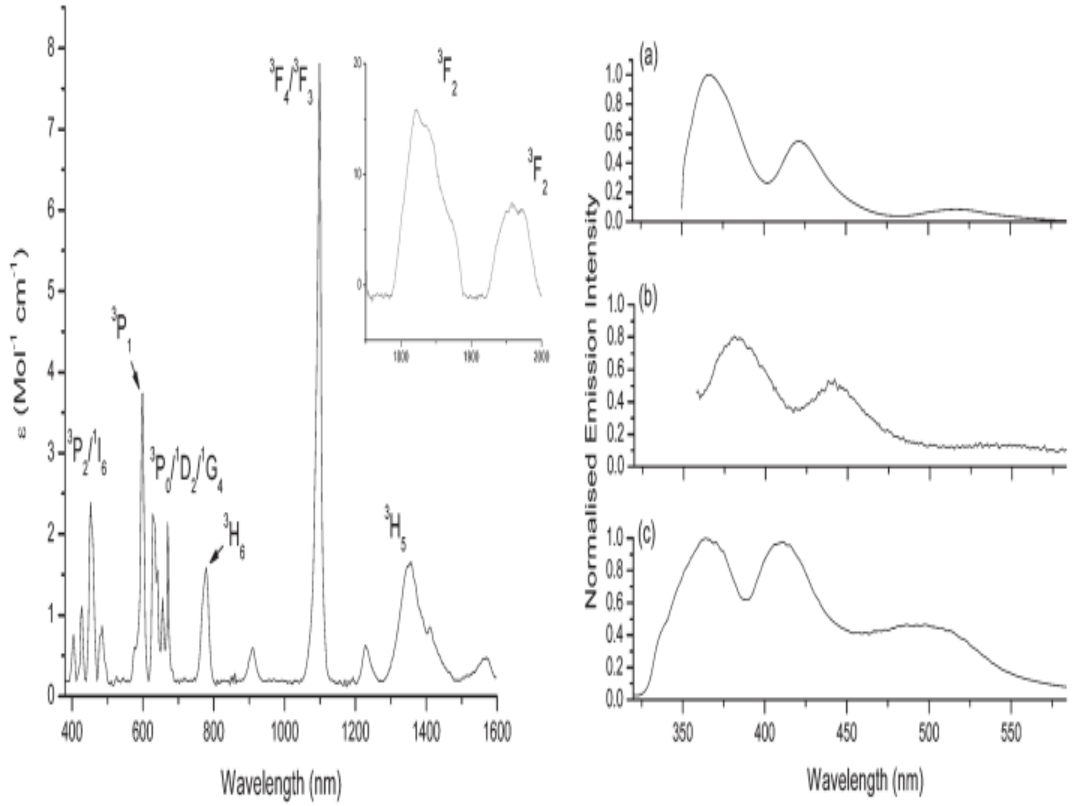

Figure 1.7. (Left), assignment of intra-configurational *f–f* transitions of $[Li(THF)_4][UCl_5(THF)]$ in THF (insert shows bands in the region 1750–2000 nm); (right), emission spectra of (a) $[Li(THF)_4][UCl_5(THF)]$ (λ_{ex} = 303 nm), of (b) $[Li(THF)_4][UBr_5(THF)]$ (λ_{ex} = 325 nm), of (c) $[UCl_4(THF)_3]$ (λ_{ex} = 290 nm), all measured in THF at 298 K.[24a]

1.4.4 Photophysical Properties of Actinide(III) Ions

Trivalent actinides can be found in SNF and their chemical similarities with the analogue trivalent lanthanides, another major product of SNF, make exploring their electronic structure very important. The absorption spectra of trivalent *5f* ions are dominated by intra-configurational *f-f* transitions.[116] These are Laporte forbidden by the electric dipole operator, however some are magnetic dipole and/or electric quadrupole allowed, because of the mixing of the *f* and *d* orbitals and mixing of spin-orbit coupled states.[116] The higher spin-orbit coupling and the mixing of the *J* states in trivalent actinide compounds lead to a significant reduction of the overall energy range between different electronic states, with respect to the analogue lanthanide compounds.[117] Therefore, for trivalent actinides the energy gaps between *J* states are small compared to trivalent lanthanides, and the radiative lifetime of the emissive states are lowered by fast non-radiative de-excitation through the *5f*-manifold mediated by photons.[24]

Luminescence spectroscopy has proven to be useful in analysing and detecting trivalent actinides from environmental samples, especially in the case of Cm(III)[118] or Am(III)[119]. To date, there is no emission spectrum reported for any U(III) compounds, but absorption spectroscopy can be used to identify U(III) samples. For U(III), indeed, the *5f-6d* energy gap is smaller than for higher uranium oxidation states; consequently, the corresponding Laporte allowed *5f-6d* transitions can be observed around 500 - 700 nm, while with higher oxidation states they usually shift into the UV region.[75]

1.5 Magnetic Properties of Actinide Ions

The magnetic properties of actinide ions and relative compounds derive from the spin and orbital angular momenta of unpaired electrons[21] and in 1932 Van Vleck published the theoretical basis for understanding these properties.[120] However, the interpretation of the magnetic data for actinide samples is still challenging and accurate theoretical models are needed. This is principally due to the fact that spin-only approximation, that works well for the first-row TM, loses its validity for actinides because of larger spin-orbit coupling and relativistic effects.[121]

Ideally, magnetic susceptibility measurements need to be presented together with optical spectroscopic data to have clear information on the electronic structure of actinide compounds. Optical data can be used to resolve the symmetry, then information on the ground state and on the low-lying states can be obtained from magnetic data, such as temperature-dependent magnetic susceptibility and EPR measurements. Moreover, the nature of the metal-ligand bonding can be investigated by focusing on the ligand superhyperfine coupling, using double resonance (electron nuclear double resonance, ENDOR) and pulsed (electron spin echo envelope modulation, ESEEM)[68] EPR methods. Thus, it is possible to estimate the delocalization of the electron spin density into the ligand orbitals, in order to gain useful information on the degree of covalency into the metal-ligand bonding.[122]

1.5.1 Magnetic Susceptibility of Uranium Ions

Closed shell systems, such as Th^{4+}, Pa^{5+}, U^{6+} and $[UO_2]^{2+}$ are expected to be diamagnetic, due to their $^1S_0$ (f^0) ground state. However, compounds like UF_6 and some uranyl complexes can exhibit temperature-independent paramagnetism (TIP), due to some covalency in metal-ligand bonding. Magnetic susceptibility measurements, reported by

Eisenstein and Pryce,[123] concluded that in UF_6 there is a coupling of paramagnetic excited states with the diamagnetic ground state and probably this is a consequence of a partial covalent character in the U–F bonding. Similarly, the weak paramagnetism in $[UO_2]^{2+}$, reported by Denning *et al.*,[124] is attributed to the coupling between different states and to particular characteristics of the U=O bonding.

Uranium has several paramagnetic oxidation states, $5f^1$ U^{5+}, $5f^2$ U^{4+}, and $5f^3$ U^{3+}, therefore an useful analytical method for characterizing uranium complexes is the measurement of magnetic susceptibilities.

Uranium(V) compounds are, as expected for a $5f^1$ system, paramagnetic, usually exhibiting Curie-Weiss behaviour, with large Weiss constants.[125] The absence of electron repulsion makes the magnetic data relatively simple to interpret and the magnetic susceptibility is generally reduced by the mixing of higher states and by orbital-reduction effects (covalency).[125] Experimental *g*-values are, for example, 1.2 in Na_3UF_8 and 0.71 in $CsUF_6$.[125]

Magnetic susceptibility measurements are often used to confirm the oxidation state of uranium. However, at room temperature, the μ_{eff} values of 3.62 and 3.58 μ_B, often chosen to distinguish the magnetism for U(III) and U(IV), respectively, are close enough to be within the experimental error of typical measurements.[3i, 126] Moreover, the histogram in Figure 1.8(d) clearly shows that the range of the room-temperature magnetic moments for each of the common paramagnetic uranium ions is large and the overlap is wide.[127] As a consequence, any room-temperature magnetic moment between 1.75 and 3.77 μ_B could be claimed to be within the full range of U(III), U(IV) or U(V).

The electronic population of the energetic sublevels is also strongly influenced by the temperature and the low temperature depopulation of the sublevels leads to a concomitant decrease in the magnitude of the angular momentum vector which is manifested as a decrease in the magnetic susceptibility.[111b, 128] Thus, considering that the variable temperature magnetic behaviours are distinct and possibly revealing of the oxidation state, and the exact shape of the magnetization response can be quite informative on crystal-field splitting,[129] it is preferable to obtain magnetic data at variable temperature with a Superconducting QUantum Interference Device (SQUID).[130] In fact, normally, the susceptibility of a $5f^2$ U(IV) ion drops drastically toward a diamagnetic ground state at low temperature (typically around 50 K). In fact, as the temperature is lowered, the two unpaired *5f* electrons of a U(IV) ion become spin paired in first approximation, leading to the observation of a single magnetic ground state.[127] This does not occur instead with half-

integral $5f^3$ U(III) and $5f^1$ U(V) ions.[127] However, the trend of the data is not always consistent with a given ion.[131]

The magnetic profile of a uranium compound is indeed strictly dependent upon the electronic configuration of the uranium ion. For example, as anticipated, the magnetic profile of $5f^2$ U(IV) compounds can be qualitatively summarized considering a non-degenerate singlet (S = 0) ground state with Temperature Independent Paramagnetism (TIP) at low temperatures (to ~ 100 K), followed by a region of temperature-dependent paramagnetism (Figure 1.8b).[127, 129] However, this temperature-dependent paramagnetism is also dependent on the coordination symmetry.[127] For example, in an octahedral geometry, O_h, there is no contribution to the paramagnetic susceptibility from the first-order Zeeman term and only the second-order Zeeman term is observed. Species like the $[UCl_6]^{2-}$ ion (and the isoelectronic PuF_6) display TIP, caused by the second-order Zeeman term mixing the T_{1g} excited state with the ground state A_g. Instead, when the symmetry is lowered from O_h to D_{4h}, it has been shown that the 1st excited state changes from a triplet T_{1g} to a doublet E_g and both the first- and second-order Zeeman terms contribute to the susceptibility. In this case, temperature-paramagnetism depends on the splitting of the T_{1g} excited state, on the value of ΔE and on the thermal population of these excited states.[127, 129] Scheme 1.5 illustrates the crystal-field splitting on the electronic ground state for a $5f^2$ configuration in two different symmetries.[85]

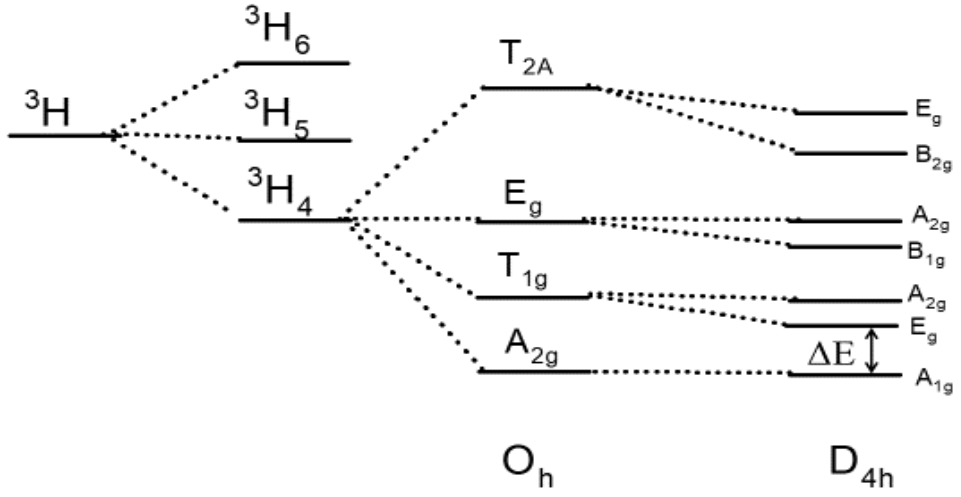

Scheme 1.5. Qualitative energy-level diagram showing the crystal-field effect on the electronic ground state for a O_h and D_{4h} symmetry.[85]

Figure 1.8 displays typical variable-temperature magnetic profiles for a) uranium(III), b) uranium(IV) and c) uranium(V).

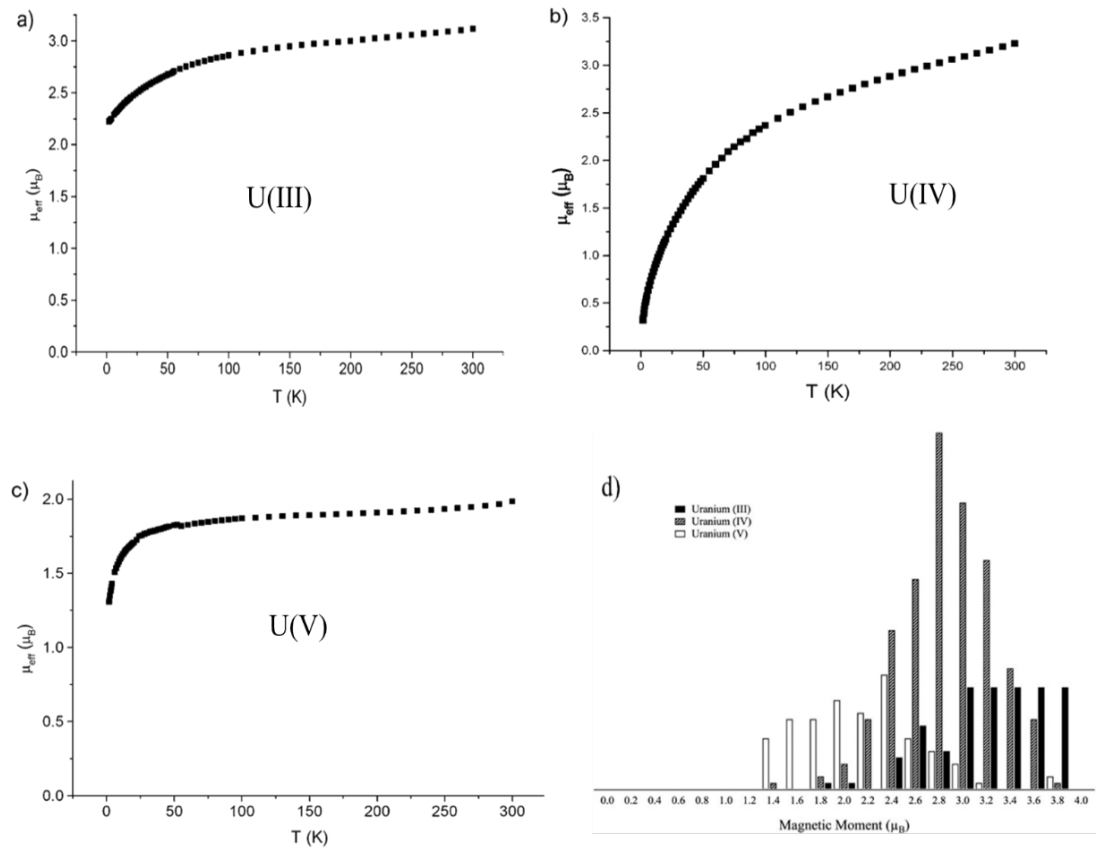

Figure 1.8. Representative μ_{eff} (μ_B) versus temperature (K) plots for a) U(III), b) U(IV) and c) U(V).[75] d) Histogram of room-temperature magnetic moments for some uranium monometallic complexes of the three common oxidation states with U(III), U(IV), and U(V) in white, grey, and black, respectively. Histogram bin widths are 0.20 μ_B.[127]

A typical uranium(III) magnetic profile decreases only slowly until at low temperature, where a drop in the magnetic moment occurs as low-lying states are depopulated, and the uranium ion exhibits an orbital doublet (S = 2) ground state. Notably, however, the magnetic moment is usually higher than what would be expected for the equivalent system with one unpaired electron because some low-lying states are not completely depopulated, even at low temperature. In contrast, uranium(IV) commonly presents a monotonous decrease in the magnetic moment, and the curve tends to zero at low temperatures. At 2 K, there is usually a residual magnetic moment of approximately 0.3 – 0.5 μ_B, which is due to TIP. The magnetism of uranium(V) tends to exhibit a more flat line with small variations in the magnetic moment from room temperature (calculated moment of 2.54 μ_B) to approximately 50 K; below this temperature, there is a rapid drop due to the depopulation of low-lying states, but an appreciable value (*ca.* 1.1 μ_B) tends to remain

because $5f^1$ uranium(V) is always an orbital doublet (S = 2). However, the moment is usually smaller than for uranium(III) because there is less mixing with excited states.

Moreover, it is important to underline that experimentally observed magnetic moments of uranium complexes frequently deviate below ideal behaviour. In Figure 1.8, the magnetic moments at 298 K for uranium(III) and uranium(IV) are approximately 3 μ_B, whereas for uranium(V) it is about 2 μ_B. This effect might be attributed to partial quenching of *L* by the crystal-field, which would invoke covalency. However, numerous factors contribute to the observed magnetism in each case, and their inter-relationships are complex and non-linear; therefore, accrediting the unusual magnetism of some uranium complexes as only due to an enhanced covalency is too simplistic.[75, 131]

The magnetic properties of uranium compounds have attracted interest because a number of $5f^3$ U(III) compounds, with a $^5I_{9/2}$ ground state, show Single Molecular Magnetic (SMM) behaviour,[132] and some $5f^1$ uranyl(V) compounds can also exhibit unusual magnetic behaviour.[133] Most interestingly it appears that SMM behaviour is an intrinsic property of the U(III) ion.[134] A recent computational study[135] has suggested that also $5f^2$ U(IV) compounds could present unusual magnetic behaviour, particularly in tetragonal or trigonal prismatic geometries with the correct ground state.

1.6 The Thiocyanate Ion

Thiocyanate is the anion $[SCN]^-$. It can be considered as the conjugate base of the thiocyanic acid HSCN, which exists as a tautomer with isothiocyanic acid HNCS (Scheme 1.6). The *iso*– form is usually more stable than the *thio*– one with the material being about 95% isothiocyanic acid in the vapor phase.[136]

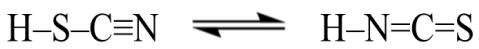

Scheme 1.6. Tautomerism between thiocyanic acid (left) and isothiocyanic acid (right).

The $[SCN]^-$ ion is a π-donor ligand and can be considered as a pseudohalide ion, since its chemistry resembles that of true halides ions. The negative charge is approximately equally distributed between sulfur and nitrogen; thus, the thiocyanate ion can act as ambidentate ligand being nucleophile at either sulfur or nitrogen; resonances forms: $[^-N=C=S] \leftrightarrow [N–C\equiv S^-]$. Nevertheless, experimental and theoretical studies have

indicated that hard metal acids tend to form *N*–bonded thiocyanate complexes, whereas soft metal acids are more incline towards *S*–bonded thiocyanate complexes.[74, 137]

The thiocyanate ion has also attracted interest in the field of the Partition and Transmutation process. It can be successfully used in liquid-liquid extractions[138] or as a component of ionic liquids for separating trivalent actinides from trivalent lanthanides for advanced fuel cycles.[139] Am(III), Cm(III) and Cf(III) have exhibited a tendency to form thiocyanate complexes greater than the corresponding lanthanides; it has been reported, for example, that the thermodynamic stability constant of higher-order complexes $[Am(NCS)_2]^+$ is higher than that for the corresponding Eu complex [$\beta_2 = 4.19$ for Am(III) and 1.93 for Eu(III)].[139] Moreover, [A336][SCN] (A336 = tricaprylmethylammonium) is a task-specific ionic liquid of sufficiently low viscosity that can be used in water solutions as potential extracting agent for thorium and uranium, although the mechanism is unknown.[140]

In order to give insight into the chemical interactions between the thiocyanate ligand and actinide ions, a spectroscopic characterization of the uranyl thiocyanate $[UO_2(NCS)_5]^{3-}$ ion in ionic liquids[141] has been reported and some structural and Raman spectroscopic studies have given useful information on these species.[142] More recently the properties of the uranium(IV) thiocyanate complexes $[^nBu_4N]_4[U(NCS)_8]$, $[Et_4N]_4[U(NCS)_8]$, $Cs_4[U(NCS)_8]$ have been studied in non-aqueous environments using a number of spectroscopic and spectroelectrochemical techniques and DFT calculations.[143] For these complexes, in particular, SQUID magnetic data have revealed that the local coordination geometry has an important influence on the low-temperature magnetic susceptibility.

1.7 Aims of the Project

Understanding the different contribution of the *4f* and *5f*/*6d* orbitals in forming bonds in lanthanide and actinide complexes is currently the subject of numerous investigations. As well as exploring the fundamental behaviour of the *f* orbitals, these studies are aimed to increase the efficiency of the "Partition and Transmutation" strategy.[38]

My PhD project can be considered as part of this large study and the principal goal was to study the electronic structures of some high symmetry uranium thiocyanate and selenocyanate complexes in different oxidation states. For this reason, a number of new compounds have been synthesised and characterized using several spectroscopic

techniques. Moreover, the experimental results have been explored also with the aid of computational calculations.

In addition, a series of iminoalkoxy semiquinone radical anions have been synthesised and reacted with UCl_4, as source of U(IV), with the aim of synthesizing complexes that could potentially exhibit magnetic coupling interactions between the $5f^2$ U(IV) metal centre and the coordinated radical ligand.

1.7 References

[1] J. B. Berscker, *Electronic Structure and Properties of Transition Metal Compounds*, Wiley, New York, 1996

[2] D. Hobbs, J. Hafner and D. Spišák, *Phys. Rev. B*, 2003, **68**, 014407

[3] For example, a) R. J. Baker, *Coord. Chem. Rev.,* 2012, **256**, 2843; b) O. P. Lamb and K. Meyer, *Polyhedron.*, 2012, **32**, 1; c) P. L. Arnold, *Chem. Commun.*, 2011, **47**, 9005; d) O. T. Summerscales and F. G. N. Cloke, *Struct. Bonding*., 2008, **127**, 87; e) O. P. Lam, C. Anthon and K. Meyer, *Dalton Trans.*, 2009, 9677; f) T. W. Hayton, *Dalton Trans.*, 2010, **39**, 1145; g) S. T. Liddle and D. P. Mills, *Dalton Trans.*, 2009, 5592; h) S. T. Liddle, *Proc. R. Soc. A.*, 2009, **465**, 1673; i) I. Castro-Rodriguez and K. Meyer, *Chem. Commun.*, 2006, 1353; j) M. Ephritikhine, *Dalton Trans.*, 2006, 2501; k) L. S. Natrajan, *Coord. Chem. Rev.*, 2012, **256**, 1583; l) C. M. Sturza, R. Boscencu and V. Nacea, *Farmacia*, 2008, **3**, 326; m) A. K. Gschneider and L. Eyring, *Handbook of the Physics and Chemistry of Rare Earths*, 1978, Vol 1, North-Holland, Amsterdam; n) W. K. Wong, X. Zhu and W. X, *Coord. Chem. Rev.*, 2007, **251**, 2386; o) I. Kostova, G. Momekov, T. Tzanova and M. Karaivanova, *Bioinorg. Chem. Appl.*, 2006, 25651; p) J. -C. G. Bünzli, *Chem. Rev.*, 2010, **110**, 2729; q) K. N. Allen and B. Imperiali, *Curr. Opin. Chem. Biol.*, 2010, **14**, 247; r) E. G. Moore, A. P. S. Samuel and K. N. Raymond, *Acc. Chem. Res.*, 2009, **42**, 542; s) C. M. G. dos Santos, A. J. Harte, S. J. Quinn and T. Gunnlaugsson, *Coord. Chem. Rev*., 2008, **252**, 2512; t) J. -C. G. Bünzli and S. V. Eliseeva, *J. Rare Earths*, 2010, **28**, 824; u) J. Rocha, L. D. Carlos, F. A. Almeida Paz and D. Ananias, *Chem. Soc. Rev.*, 2011, **40**, 926; v) M. D. Ward, *Coord. Chem. Rev.*, 2010, **254**, 2634; w) S. Faulkner, L. S. Natrajan, W. S. Perry and D. Sykes, *Dalton Trans*., 2009, 3890.

[4] N. Kaltsoyannis and P. Scott, *The f-elements*, Oxford Chemistry Primer, 1999

[5] L. R. Morss, N. M. Edelstein and J. Fuger, *The Chemistry of the Actinide and Transactinide Elements*, 4th edition, Springer, 2010, Chapter 1

[6] M. A. Silver, S. K. Cary, J. A. Johnson, R. E. Baumbach, A. A. Arico, M. Luckey, M. Urban, J. C. Wang, M. J. Polinski, A. Chemey, G. Liu, K.-W. Chen, S. M. Van Cleve, M. L. Marsh, T. M. Eaton, L. J. van de Burgt, A. L. Gray, D. E. Hobart, K. Hanson, L. Maron, F. Gendron, J. Autschbach, M. Speldrich, P. Kögerler, P. Yang, J. Braley and T. E. Albrecht-Schmitt, *Science*, 2016, **353**, 3762

[7] a) D. Reta, F. Ortu, S. Randall, D. P. Mills, N. F. Chilton, R. E. P. Winpenny, L. Natrajan, B. Edwards and N. Kaltsoyannis, *J. Organomet. Chem.*, 2017, **1**; b) N. Kaltsoyannis, *Chem. Soc. Rev.*, 2003, **32**, 9; c) G. Schreckenbach and G. A. Shamov, *Acc. Chem. Res.*, 2010, **43**, 19; d) L. Gagliardi and B. O. Roos, *Chem. Soc. Rev.*, 2007, **36**, 893; e) I. Kirker and N. Kaltsoyannis, *Dalton Trans.*, 2011, **40**, 124; f) M. J. Tassell and N. Kaltsoyannis, *Dalton Trans*., 2010, **39**,

6719; g) P. L. Arnold, Z. R. Turner, N. Kaltsoyannis, P. Pelekanaki, R. M. Bellabarba and R. P. Tooze, *Chem. Eur. J.*, 2010, **16**, 9623; h) D. Wang, W. F. van Gunsterenb and Z. Chai, *Chem. Soc. Rev.*, 2012, **41**, 5836; i) A. E. Clark, J. L. Sonnenberg, P. J. Hay and R. L. Martin, *J. Chem. Phys.*, 2004, **121**, 2563; j) L. Petit, L. Joubert, P. Maldivi and C. Adamo, *J. Am. Chem. Soc.*, 2006, **128**, 2190; k) V. Vallet, U. Wahlgren and I. Grenthe, *J. Phys. Chem. A.*, 2012, **116**, 12373; l) B. M. Gardner, D. Patel, A. D. Cornish, J. McMaster, W. Lewis, A. J. Blake and S. T. Liddle, *Chem. Eur. J.*, 2011, **17**, 11266

[8] The international Thorium Energy Committee, CERN, Geneva Switzerland, October, 2013, https://indico.cern.ch/event/222140

[9] Key World Energy Statistics 2012 Publication, http://alofatuvalu.tv/FR/12_liens/12_articles_rapports/IEA_rpt_2012_us.pdf

[10] a) K. Maher, J. Bargar and G. E. Brown, *Inorg. Chem.*, 2013, **52**, 3510; b) A. B. Kersting, *Inorg. Chem.*, 2013, **52**, 3533

[11] R. A. Peterson, E. C. Buck, J. Chun, R. C. Daniel, D. L. Herting, E. S. Ilton, G. J. Lumetta and S. B. Clark, *Environ. Sci. Technol.*, 2018, **52**, 381

[12] P. L. Arnold, M. S. Dutkiewicz and O. Walter, *Chem. Rev.*, 2017, **117**, 11460

[13] a) J. Terry, R. K. Schulze, J. D. Farr, T. Zocco, K. Heinzelman, E. Rotenberg, D. K. Shuh, G. van der Laan, D. A. Arena and J. G. Tobin, *Surf. Sci*, 2002, **499**, L141; b) K. I. Maslakov, A. Y. Teterin, K. E. Ivanov, S. V. Yudintsev and S. V. Stefanovskii, *Radiochemistry*, 2012, **54**, 115

[14] a) C. Zeine and J. Grobe, *Microchimica Act.*, 1997, **125**, 279; b) M. M. Herron, S. Herron, A. Charsky and R. Akkurt, *PCT. Int. Appl.*, 2013, WO 2013025679 A2 20130221; c) R. A. Zehnder, D. L. Clark, B. L. Scott, R. J. Donohoe, P. D. Palmer, W. H. Runde and D. E. Hobart, *Inorg. Chem*., 2010, **49**, 4781

[15] A) D. C. Konningsberger and R. Prins, *X-Ray Absorption: Principles, Application, Techniques of EXAFS, SEXAFS, XANES,* John Wiley and Sons, USA 1988; b) G. Bunker, *Introduction to XAFS: A Practical Guide to X-ray Absorption Fine Structure Spectroscopy*, Cambridge University Press, 2010

[16] a) G. Vlaic and L. Olivi, *Croat. Chem. Acta.*, 2004, **77**, 427; b) B. K. Teo, *EXAFS*: *Basic Principles and Data Analysis, Inorganic Chemistry Concepts*, 1986 Vol. 9, Springer-Verlag, Berlin

[17] A. Marjolin, C. Gourlaouen, C. Clavaguera, P. Y. Ren, J. C. Wu, N. Gresh, J. P. Dognon and J. P. Piquemal, *Theor. Chem. Acc.*, 2012, **131**, 1198

[18] a) X. D. Wen, R. L. Martin, T. M. Henderson and G. E. Scuseria, *Chem. Rev.*, 2013, **113**, 1063; b) D. Wang, W. F. van Gunsterenb and Z. Chaia, *Chem. Soc. Rev.*, 2012, **41**, 5836; c) P. Pyykko, *Chem. Rev.*, 1988, **88**, 563

[19] a) B. O. Roos, P. R. Taylor and P. E. M. Siegbahn, *Chem Phys.*, 1980, **48**, 157; b) K. Andersson, P. A. Malmqvist and B. O. Roos, *J. Chem. Phys.*, 1992, **96**, 1218

[20] W. Koch and M. C. Holthausen, *A Chemist's Guide to Density Functional Theory*, Second Ed., Wiley, New York, 2001

[21] K. T. Moore and G. van der Laan, *Rev. Mod. Phys.*, 2009, **81**, 235

[22] a) N. M. Edelstein, R. Klenze, T. Fanghanel and S. Hubert, *Coord. Chem. Rev.*, 2006, **250**, 948; b) G. K. Liu and J. V. Beitz, *Phys. Rev. B: Condens. Matter Mater. Phys.*, 1990, **41**, 6201; c) G. X. Tian, Z. Y. Zhang, R. L. Martin and L. F. Rao, *Inorg. Chem.*, 2015, **54**, 1232; d) M. Sturzbecher-Hoehne, B. Kullgren, E. E. Jarvis, D. D. An and R. J. Abergel, *Chem. - Eur. J.*, 2014, **20**, 9962; e) M. Sturzbecher-Hoehne, C. Goujon, G. J. P. Deblonde, A. B. Mason and R.

J. Abergel, *J. Am. Chem. Soc.*, 2013, **135**, 2676− 2683; f) G. L. Law, M. C. Andolina, D. J. Xu, V. Luu, P. X. Rutkowski, G. Muller, D. K. Shuh, J. K. Gibson and K. N. Raymond, *J. Am. Chem. Soc.* 2012, **134**, 15545; g) A. Bremer, A. Geist and P. Panak, *J. Dalton Trans*. 2012, **41**, 7582; h) M. J. Polinski, S. Wang, E. V. Alekseev, W. Depmeier, G. K. Liu, R. G. Haire and T. E. Albrecht-Schmitt, *Angew. Chem., Int. Ed.*, 2012, **51**, 1869; i) G. X. Tian, N. M. Edelstein and L. F. Rao, *J. Phys. Chem. A*, 2011, **115**, 1933; j) Z. Assefa, R. G. Haire and R. E. Sykora, *J. Solid State Chem.*, 2008, **181**, 382; k) R. E. Sykora, Z. Assefa, R. G. Haire, T. E. Albrecht-Schmitt, *Inorg. Chem.* 2005, **44**, 5667−5676; l) T. Vercouter, P. Vitorge, B. Amekraz, E. Giffaut, S. Hubert and C. Moulin, *Inorg. Chem.*, 2005, **44**, 5833

[23] G. Meinrath, *J. Radioanal. Nucl. Chem.*, 1998, **232**, 179

[24] a) E. Hashem, A. N. Swinburne, C. Schulzke, R. C. Evans, J. A. Platts, A. Kerridge, L. S. Natrajan and R. J. Baker, *RSC Adv.*, 2013, **3**, 4350; b) Kirishima, T. Kimura, O. Tochiyama and Z. Yoshida, *Chem. Commun.*, 2003, 910; c) A. Kirishima, T. Kimura, R. Nagaishi and O. Tochiyama, *Radiochim. Acta.*, 2004, **92**, 705; d) R. Bradshaw, D. Sykes, L. S. Natrajan, R. J. Taylor, F. R. Livens and S. Faulkner, *Mater. Sci. Eng.*, 2010, **9**, 012047; e) T. Eeckelaars, S. J. A. Pope, A. J. Hynes, R. Copping, R. J. Taylor, S. Faulkner, D. Sykes, F. R. Livens and I. May, *J. Am. Chem. Soc.*, 2007, **129**, 2442

[25] a) B. J. Mincher, *Nuclear Energy and the Environment*, ed. C. M. Wai and B. J. Mincher, ACS Symposium Series, ACS, Washington DC, 2010, chapter 1, pp. 3-10; b) Nuclear Fission, The Energy Research Partnership Technology Report, The Energy Research Partnership, London, 2010, www.energyresearchpartnership.org.uk; c) Fuel Cycle Stewardship in a Nuclear Renaissance, The Royal Society Science Policy Centre Report 10/11, The Royal Society, London, 2011 (ISBN: 978-0-85403-891-6); d) Assessing the Sustainability of Nuclear Power in the UK, Sustainability Assessment of Nuclear Power: An Integrated Approach, SPRING Report, The University of Manchester, 2011, www.springsustainability.org

[26] H. Nifenecker, *Rep. Prog. Phys.*, 2011, **74**, 12

[27] M. Lenzen, *Energ. Convers. Manag.*, 2008, **49**, 2178

[28] J. Gray, S. Jones and A. Smith, *J. Radiol. Prot.*, 1995, **15**, 99

[29] *Nuclear waste Policy Act*, January 7, 1983, http://www.energy.gov/sites/prod/files/edg/media/nwpa_2004

[30] J. Johnson, *Talk*, *No Action on Nuclear Waste Plan*; in C&EN, 2012, **40**, 44

[31] Certification and Recertification of WIPP, 2010 https://www.epa.gov/radiation/certification-and-recertification-wipp

[32] Managers Blamed in Nuclear Leak, *WSJ*, 29 April 2014

[33] a) J. Johnson, *Reprocessing Key to Nuclear Plan;* in C&EN, 2007, **85**, 48

[34] NDA Report no. NDA/RWM/146, rwm.nda.gov.uk

[35] N. Baldwin, *Remediating Sellafield,* WM'03 Conference, Tucson, AZ, 2003

[36] J. Mathur, M. Murali and K. Nash, *Solvent Extr. Ion. Exc.*, 2001, **19**, 357

[37] I. S. Denniss and A. P. Jeapes, *in The Nuclear Fuel Cycle*; P. D. Wilson, Ed.; Oxford University Press: Oxford, U.K., 1986

[38] a) H. Nitsche, *Chem. Rev.*, 2013, **113**, 855; b) M. J. Hudson, L. M. Harwood, D. M. Laventine and F. W. Lewis, *Inorg. Chem.*, 2013, **52**, 3414; c) D. Warin, *IOP Conf. Ser. Mater. Sci. Eng.,* 2010, **9**, 012063 d) A. P. Paiva and P. J. Malik, *Radioanal. Nucl. Chem.*, 2004, **261**, 485; e) C. Madic, M. J. Hudson, J. O. Liljezin, J. P. Glatz, R. Nannicini, A. Facchini, Z. Kolarik and R. Odoj, *Prog. Nucl. Energy*, 2002, **40**, 523; f) C. Madic, B. Boullis, P. Baron, F. Testard, M. J.

Hudson, J. O. Liljenzin, B. Christiansen, M. Ferrando, A. Facchini, A. Geist, G. Modolo, A. G. Espartero and J. De Mendoza, *J. Alloys Compd.*, 2007, **444**, 23; g) M. Nilsson and K. Nash, *Solvent Extr. Ion Exc*., 2007, **25**, 665; h) J. P. Grouiller, S. Pillon, C. de Saint Jean, F. Varaine, L. Leyval, L. G. Vambenepe and B. Carlier, *J. Nucl. Mater.,* 2003, **320**, 163; i) M. P. Jensen and A. H. Bond, *J. Am. Chem. Soc.*, 2002, **124**, 9870; j) M. Mazzanti, R. L. Wietzke, J. Pecaut, J. M. Latour, P. Maldivi and M. Remy, *Inorg. Chem.*, 2002, **41**, 2389; k) T. Mehdoui, J. C. Berthet, P. Thuery and M. Ephritikhine, *Dalton Trans.*, 2004, 579; l) G. R. Choppin, M. P. Jensen, L. R. Morss, N. M. Edelstein, J. Fuger (Eds.), *The chemistry of the Actinide and Transactinide Elements*, vol. **4**, Springer, Berlin, 2006, Chapter 24; m) A. J. Gaunt, B. L. Scott and M. P. Neu, *Angew. Chem. Int. Ed.*, 2006, **45**, 1638

[39] F. Poineau, J. Du Mazaubrun, D. Ford, J. Fortner, J. Kropf, G. Silva, N. Smith, K. Long, G. Jarvinen and K. Czerwinski, *Radiochim. Acta.*, 2008, **96**, 527; b) C. Gong, W. Lukens, F. Poineau and K. Czerwinski, *Inorg. Chem.*, 2008, **47**, 6674

[40] J. Law, S. Herbst, T. Todd, V. Romanovskiy, V. Babainb, V. Esimantovskiy, I. Smirnov and B. Zaitsev, *Solvent Extr. Ion Exc.*, 2001, **19**, 23

[41] E. Horwitza, D. Kalinaa, H. Diamonda, G. Vandergrifta and W. Schulzb, *Solvent Extr. Ion Exc.*, 1985, **3**, 75

[42] D. Serrano-Purroy, P. Baron, B. Christiansen, R. Malmbeck, C. Sorel and J. Glatz, *Radiochim. Acta.*, 2005, **93**, 351

[43] a) F. W. Lewis, L. M. Harwood, M. J. Hudson, M. G. B. Drew, J. F. Desreux, G. Vidick, N. Bouslimani, G. Modolo, A. Wilden, M. Sypula, T. H. Vu and J. P. Simonin, *J. Am. Chem. Soc.*, 2011, **133**, 13093; b) P. J. Panak and A. Geist, *Chem. Rev.*, 2013, **113**, 1199; c) G. Benay, R. Schurhammer and G. Wipff, *Phys. Chem. Chem. Phys.* 2011, **13**, 2922; d) M. R. S. Foreman, M. J. Hudson, A. Geist, C. Madic and M. Weigl, *Solvent Extr. Ion Exch.* 2005, **23**, 645; e) M. Nilsson, S. Andersson, F. Drouet, C. Ekberg, M. R. S. J. Foreman, M. J. Hudson, J. O. Liljenzin, D. Magnusson and G. Skarnemark, *Solvent Extr. Ion Exch.*, 2006, **24**, 299; f) M. Nilsson, C. Ekberg, M. R. S. J. Foreman, M. J. Hudson, J. O. Liljenzin, G. Modolo and G. Skarnemark, *Solvent Extr. Ion Exch*., 2006, **24**, 823; g) A. Fermvik, C. Ekberg, S. Englund, M. R. S. J. Foreman, G. Modolo, T. Retegan and G. Skarnemark, *Radiochim. Acta*, 2009, **97**, 319; h) T. Retegan, C. Ekberg, I. Dubois, A. Fermvik, G. Skarnemark, T. J. Wass, *Solvent Extr. Ion Exch.*, 2007, **25**, 417; i) C. Ekberg, E. Aneheim, A. Fermvik, M. Foreman, E. LöfströmEngdahl, T. Retegan and I. Spendlikova, *J. Chem. Eng. Data*, 2010, **55**, 5133; l) V. Hubscher-Bruder, J. Haddaoui, S. Bouhroum and F. Arnaud-Neu, *Inorg. Chem.*, 2010, **49**, 1363

[44] N. Kaltsoyannis, *Inorg. Chem*., 2013, **52**, 3407

[45] M. P. Kelly, J. Su, M. Urban, M. Luckey, E. R. Batista, P. Yang and J. C. Shafer, *J. Am. Chem. Soc.* 2017, **139**, 9901

[46] J. C. Sullivan, L. R. Morss, K. H. Schmidt, W. A. Mulac and S. Gordon, *Inorg. Chem.*, 1982, **22**, 2338

[47] M. Seth, M. Dolg, P. Fulde and P. Schwerdtfeger, *J. Am. Chem. Soc.*, 1995, **117**, 6597

[48] M. L. Neidig, D. L. Clark and R. L. Martin, *Coord. Chem. Rev.*, 2013, **257**, 394

[49] R. Anwander, M. Dolg and F. T. Edelmann, *Chem. Soc. Rev*., 2017, **46**, 6697

[50] M. W. Löble, J. M. Keith, A. B. Altman, S. C. E. Stieber, E. R. Batista, K. S. Boland, S. D. Conradson, D. L. Clark, J. L. Pacheco, S. A. Kozimor, R. L. Martin, S. G. Minasian, A. C. Olson, B. L. Scott, D. K. Shuh, T. Tyliszczak, M. P. Wilkerson and R. A. Zehnder, *J. Am. Chem. Soc.*, 2015, **137**, 2506

[51] S. Kapur, B. L. Kalsotra, R. K. Multani, B. D. Jain, *J. Inorg. Nucl. Chem*., 1973, **35**, 1689

[52] A. Gulino, M. Casarin, V. P. Conticello, J. G. Gaudiello, H. Mauermann, I. Fragala` and T. J. Marks, *Organometallics,* 1988, **7**, 2360

[53] I. J. Casely, S. T. Liddle, A. J. Blake, C. Wilson and P. L. Arnold, *Chem. Commun.,* 2007, 5037

[54] I. D. Prodan, G. E. Scuseria and R. L. Martin, *Phys. Rev. B.*, 2007, **76**

[55] a) M. J. Polinski, S. Wang, E. V. Alekseev, W. Depmeier, T. E. Albrecht-Schmitt, *Angew. Chem.*, *Int. Ed.*, 2011, **50**, 8891; b) M. J. Polinski, J. T. Stritzinger, T. G. Parker, E. V. Alekseev, S. M. Cleve, W. Depmeier, L. Gagliardi, J. N. Cross, T. D. Green, E. B. Garner, R. Maurice, N. Planas, M. Shatruk, K. L. Knappenberger, G. Liu, S. Skanthakumar, L. Soderholm, D. A. Dixon and T. E. Albrecht-Schmitt, *Nat. Commun.*, 2015, **6**, 6827

[56] M. P. Kelly, J. Su, M. Urban, M. Luckey, E. R. Batista, P. Yang and J. C. Shafer, *J. Am. Chem. Soc.*, 2017, **139**, 9901

[57] a) C. J. Burns and B. E. Bursten, *Comments Inorg. Chem.*, 1989, **9**, 61; b) M. Pepper and B. E. Bursten, *Chem. Rev.*, 1991, **91**, 719

[58] A. F. Cotton and G. Wilkinson, *Advanced Inorganic Chemistry* 1988, 5th ed., New York: New York: Wiley-Interscience, 776-955

[59] R. J. M. Konings, N. M. Edelstein, L. R. Morss and J. Fuger, *The Chemistry of the Actinide and Transactinide Elements*, 4th edition, Springer, 2010, Chapter 19

[60] M. R. MacDonald, M. E. Fieser, J. E. Bates, J. W. Ziller, F. Furche, and W. J. Evans, *J. Am. Chem. Soc.*, 2013, **135**, 13310

[61] J. Su, C. J. Windorff, E. R. Batista, W. J. Evans, A. J. Gaunt, M. T. Janicke, S. A. Kozimor, B. L. Scott, D. H. Woen and P. Yang, *J. Am. Chem. Soc.*, 2018, **140**, 7425

[62] M. S. Dutkiewicz, J. H. Farnaby, C. Apostolidis, E. Colineau, O. Walter, N. Magnani, M. G. Gardiner, J. B. Love, N. Kaltsoyannis, R. Caciuffo and P. L. Arnold, *Nat. Chem.*, 2016, **8**, 797

[63] C. J. Windorff, G. P. Chen, J. N. Cross, W. J. Evans, F. Furche, A. J. Gaunt, M. T. Janicke, S. A. Kozimor and B. L. Scott, *J. Am. Chem. Soc.*, 2017, **139**, 3970

[64] B. E. Bursten, L. F. Rhodes and R. J. Strittmatter, *J. Am. Chem. Soc.*, 1989, **111**, 2151

[65] V. Balzani and F. Scandola. In Comprehensive Supermolecular Chemistry*,* J. L. Atwood, J. E. D. Davis., D. D. Macnicol and F. Vogtle (eds.), Pergamon, Oxford, 1996, 16; b) V. Balzani, A. Credi and M. Venturi, *Chem. Sus. Chem.*, 2008, **1**, 26

[66] a) G. R. Choppin, *J. Alloys Compd.*, 2002, **344**, 55; b) R. M. Diamond, K. Street and G. T. Seaborg, *J. Am. Chem. Soc.*, 1954, **76**, 1461; c) S. G. Thompson, B. G. Harvery, G. R. Choppin and G. T. Seaborg, *J. Am. Chem. Soc.*, 1954, **76**, 6229

[67] M. J. Polinski, E. B. Garner, R. Maurice, N. Planas, J. T. Stritzingler, T. G. Parker, J. N. Cross, T. D. Green, E. V. Alekseev, S. M. Van Cleve, W. Depmeier, L. Gagliardi, M. Shatruk, K. L. Knappenberger, G. Liu, S. Skanthakumar, L. Soderholm, D. A. Dixon and T. E. Albrecht-Schmitt, *Nat. Chem.*, 2014, **6**, 387

[68] A. Formanuik, A. M. Ariciu, F. Ortu, R. Beekmeyer, A. Kerridge, F. Tuna, E. J. L. McInnes and D. P. Mills, *Nat. Chem.*, 2017, **9**, 578

[69] J. P. Clark and J. C. Green, *J. Chem. Soc.*, *Dalton Trans.*, 1977, 505

[70] G. M. Kalvius, *J. Less-Common Met.*, 1986, **121**, 353

[71] E. I. Solomon, B. Hedman, K. O. Hodgson, A. Dey and R. K. Szilagyi, *Coord. Chem. Rev.*, 2005, **249**, 97

[72] a) B. E. Bursten, R. J. Strittmatter, *Angew Chem.*, *Int. Ed. Engl.*, 1991, **30**, 1069; b) R. G. Denning, *Struct. Bond.*, 1992, **79**, 215; c) S. Matsika, Z. Zhang, S. R. Brozell, J. P. Blaudeau, Q. Wang and R. M. Pitzer, *J. Phys. Chem. A.*, 2001, **105**, 3825

[73] N. Kaltsoyannis, P. J. Hay, J. Li, J. P. Blaudeau, B. E. Bursten, in: L. Morss, N. M. Edelstein, J. Fuger (Eds.), *The chemistry of the Actinide and Transactinide Elements*, vol. **3**, Springer, Berlin, 2006, 1893

[74] M. J. Winter, *d-Block Chemistry*, Oxford Chemistry Primers, 1994

[75] S. T. Liddle, *Angew. Chem. Int. Ed.*, 2015, **54**, 8604

[76] a) J. Hafner and D. Hobbs, *Phys. Rev. B.*, 2003, **68**, 014408; b) R. G. Haire, S. Heathman, M. Idiri, T. Lindbaum and J. Rebizant, *Phys. Rev. B*., 2003, **67**, 134101; c) P. Söderling and B. Sadigh, *Phys. Rev. Lett.*, 2004, **92**, 185702; d) A. B. Shick, J. Havela, V. D. Kolorenc, T. Gouder and P. M. Oppenner, *Phys. Rev. B*., 2006, **73**, 104415

[77] a) Y. Baer and J. K. Lang, *Phys. Rev. B*., 1980, **21**, 2060 b) S. B. Nornes and R. G. Meisenheimer, *Surf. Sci.*, 1979, **88**, 191; c) P. Söderlind and K. T. Moore, *Scr. Mater*., 2008, **59**, 1259

[78] a) G. van der Laan, *J. Phys. Condens. Matter.*, 1991, **3**, 7443 b) G. van der Laan, *Phys. Rev. B.*, 1995, **51**, 240

[79] For example a) C. Lincheneau, J. P. Leonard, T. McCabe and T. Gunnlaugsson, *Chem. Comm.*, 2011, **47**, 7119; b) X. Sun, Y. Bian, M. Bai, C. Ma, C. Ma, N. Kobayashi and J. Jiang, *Dyes and Pigments*, 2005, **65**, 145; c) G. Zucchi, R. Scopelliti, P-A. Pittet, J. C. G Bunzli and R. D. Rogers, *J. Chem. Soc.*, *Dalton. Trans.*, 1999, **6**, 931

[80] a) V. Balzani, F. Bolletta, M. T. Gandolfi and M. Mastri, *Top. Curr. Chem.*, 1978, **75**, 1; b) T. J. Meyer, *Acc. Chem. Res.*, 1978, **11**, 94; c) N. Sutin and C. Creutz, *Pure Appl. Chem.,* 1980, 52, 2717; d) T. J. Meyer, *progr. Inorg. Chem.*, 1983, **30**, 389; d) N. Sutin and C. Creutz, *J. Chem. Ed.*, 1983, **60**, 809; N. Serpone: in *Photoinduced electron transfer* (M. A. Fox and M. Chanon, eds.), 1988, Elsevier, Amsterdam, part d, p 47; e) V. Balzani and F. Scandola: in *Photoinduced electron transfer* (M. A. Fox and M. Chanon, eds.), 1988, Elsevier, Amsterdam, part d, p 148; f) C. Gianotti, S. Gaspard and P. Kransz: In Photoinduced electron transfer (M. A. Fox and M. Chanon, eds.), 1988, Elsevier, Amsterdam, part d, p 200

[81] J. C. G. Bunzli, *Chem. Rev.*, 2010, **110**, 2729

[82] P. Brossier, G. Jaouen, B. Limoges, M. Salmain, A. Vessieres-Jaouen and J. P. Yvert, Ann. Biol. Clin., 2001, **59**, 677

[83] A. Barbanel, *Radiochim. Acta.*, 1997, **78**

[84] D. E. Morris, R. E. Da Re, K. C. Jantunen, I. Castro-Rodriguez and J. L. Kiplinger, *Organometallics*, 2004, **23**, 5142

[85] S. Cotton, *Electronic and Magnetic Properties of Actinides*, in: Lanthanide and Actinide Chemistry, John Wiley and Son Ltd, 2006, p 201

[86] E. Rabinowitch and R. L. Bedford, *Spectroscopy and Photochemistry of Uranyl Compounds*, Pergamon Press, Oxford, 1964, **112**

[87] a) R. G. Denning, *J. Phys. Chem. A.,* 2007, **111**, 4125; b) R. J. Baker, *Chem. Eur. J.* 2012, **18**, 16258

[88] V. V. Syt'ko and D. S. Umreiko, *J. Appl. Spectrosc.,* 1998, **65**, 857

[89] a) G. Meinrath, *Freiurg On-line Geosci.,* 1998, **1**, 1; b) C. K. Jorgenson and R. Reisfeld, *Struct. Bond.,* (Heidelberg) 1982, **50**, 122; c) J. L. Sessler, P. Melfi and G. D. Pantos, *Coord. Chem.*

Rev., 2006, **250**, 816; d) R. Ghosh, J. A. Mondal, H. N. Ghosh and D. K. Palit, *J. Phys. Chem. A*., 2010, **114**, 5263; e) G. K Liu, *J. Phys. Chem. A.*, 2011, **115**, 12419

[90] T. Haubitz, S. Tsushima, R. Steudtner, B. Drobot, G. Geipel, T. Stumpf and M. U. Kumke, *J. Phys. Chem. A*, 2018, **122**, 6970

[91] J. R. Plaisier, D. J. W. Ijdo, C. de Mello Donega and G. Blasse, *Chem. Mater.,* 1995, **7**, 738

[92] I. Billard and G. Geipel, *Luminescence Analysis of Actinides: Instrumentation Application, Quauntifications, Future Trend and Quality Assurance:* in Springer Series, Fluorescence, Springer-Verlag Berlin Heidelberg, 2008, **5**, 465

[93] a) F. de Maria Ramirez, S. Varbenev, J. Padilla and J. C. G. Bùnzli, *J. Phys. Chem. B.*, 2008, **112**, 10976; b) S. Kannan, M. A. Moody, C. L. Barns and P. B. Duval, *Inorg. Chem.,* 2006, **45**, 9206; c) A. E. Vaughn, D. B. Bassil, C. L. Barnes, S. A. Tucker and P. B. Duval*, J. Am. Chem. Soc.,* 2006, **128**, 10656

[94] T. Yayamura, S. Iwata, S. I. Iwamaru and H. Tomiyasu, *J. Chem. Soc. Faraday Trans.,* 1994, **90**, 3253

[95] E. Hashem, T. McCabe, C. Schulzkeb and R. J. Baker, *Dalton Trans*., 2014, **43**, 1125

[96] M. P. Redmond, S. M. Cornet, S. D. Woodall, D. Whittaker, D. Collison, M. Helliwell, and L. Natrajan, *Dalton Trans.* 2011, **40**, 3914

[97] a) H. D. Burrows, *Inorg. Chem.*, 1990, **3**, 139; b) H. D. Burrows and T. Kemp, *J. Chem. Soc. Rev.*, 1974, **3**, 139; c) C. Görller-Walrand and K. Servaes, *Helv. Chim. Acta.*, 2009, **92**, 2304; d) R. Ghosh, J. A. Mondal, H. N. Gosh and D. K. Palit, *J. Phys. Chem. A.*, 2010, **114**, 5263; e) R. Nagaishi, Y. Katsumura, K. Ishigure, H. Aoyagi, Z. Yoshida, T. Kimura and Y. Kato, *J. Photochem. Photobiol. A.*, 2002, **146**, 157

[98] a) S. J. Formosinho, H. D. Burrows, M. G. Miguel, M. E. D. G. Azenha, I. M. Saraiva, A. Catarina, D. N. Ribeiro, I. V. Kholyakov, R. G. Gasanov, M. Bolte and M. Sarakhd, *Photochem. Photobiol. Sci.*, 2003, **2**, 569; b) S. Tsushima, *Inorg. Chem.*, 2009, **48**, 4856; c) S. Tsushima, C. Gòtz, K. Fahmy, *Chem. Eur. J.*, 2010, **16**, 8029

[99] a) J. J. Katz, G. T. Seaborg, L. R. Morss*, The Chemistry of the Actinide Elements*, Chapman and Hall, London, 1986; b) "Chemistry and Migration Behaviour of Actinides and Fission Products in the Geosphere": *Radiochim. Acta*, 1996, **76**, 1

[100] D. Cohen, B. Taylor, *J. Inorg. Nucl. Chem.*, 1961, **22**, 151

[101] a) I. A. Charushnikova, N. N. Krot and Z. A. Starikova, *Radiochemistry* 2001, **43**, 24; b) D. L. Clark, D. W. Keogh, P. D. Palmer, B. L. Scott and C. D. Tait, *Angew. Chem*. 1998, **110**, 173; c) J. H. Burns and C. Musikas, *Inorg. Chem.*, 1977, **16**, 1619; d) G. B. Andreev, A. M. Fedosseev, N. A. Budantseva and M. Y. Antipin, *Mendeleev Commun.* 2001, 58

[102] a) D. J. Cohen, *Inorg. Nucl. Chem.*, 1970, **32**, 3425-3711; b) C. Degueldre, *The Chemistry of the Actinide and Transactinide Elements,* Springer, New York, 2006, Vol **5**, 3013

[103] a) T. I. Docrat, J. F. W. Mosselmans, J. M. Charnock, M. W. Whiteley, D. Collins, F. R. Livens, C. Jones and M. Edmiston, *Inorg. Chem.*, 1998, **38**, 1879; b) K. Mizuoka and Y. Ikeda, *Radiochim. Acta.,* 2004, **92**, 631; c) M. S. Sidhu, W. Schabel and J. Radioanal., *Nucl. Chem.*, 1996, **211**, 375

[104] I. B. Polovov, V. A. Volkovich, J. M. Charnock, B. Kralj, R. G. Lewin, H. Kinoshita, I. May and C. A. Sharrad, *Inorg. Chem.*, 2008, **47**, 7474

[105] K. Mizunka, S. Tsushima, M. Hasegawa, T. Hoshi and Y. Ikeda, *Inorg. Chem.*, 2005, **44**, 6211

[106] R. Steudner, T. Arnold, K. Grobmanʁmann, G. Giepel and V. Brendler, *Inorg. Chem. Commun.,* 2006, **9**, 939

[107] a) K. Grossman, T. Arnold, R. Steudtner, S. Weills and G. Bernhard, *Naturwissenschaften.,* 2009, **96**, 963; b) T. Arnold, K. Grossmann and N. Baumann, *Anal. Bioanal. Chem.,* 2010, **396**, 1641

[108] a) H. Hirose, C. Miyake, L.G. H. Du Preez, B. Zeelie, *Inorg. Chim. Acta.,* 1988, **150**, 293; b) C. W. Williams, M. F. Reid, *J. Chem. Phys.,* 1991, **95**, 7194; c) H. Hubert, E. Simoni, M. Genet, *J. Less. Common Met.,* 1986, **122**, 81; d) A. I. Komyak, A. P. Zazhogin, D. S. Umreiko, A. A. Lugovsky, *J. Appl. Spectrosc.,* 2009, **76**, 167

[109] a) P. Söderling, O. Eriksson, B. Johansson, J. M. Wills and A. M. Boring, *Nature,* 1990, **374**, 524; b) K. T. Moore, G. van der Laan, R. G. Haire, M. A. Wall, A. J. Schwartz and P. Söderling, *Phys. Rev. Lett.,* 2007, **98**, 236402

[110] a) S. V. Godbole, A. G. Page, Sangeeta, S. C. Sabharwal, J. Y. Gesland, M. D. Sastry and J. Lumin, *J. Chem. Phys.*, 2001, **93**, 213; b) S. Hubert, E. Simoni, M. Louis, W. T. Zhang and J. Y. Gestland, *J. Lumin.*, 1995, **65**

[111] a) L. Morss, N. Edelsein and J. Fuger, *The Chemistry of the Actinide and Transactinide Elements,* Springer, New York, 2006, Vol **1**, 52 b) M. Genet, P. Delamoye, N. Edelstein and J. Conway, *J. Chem. Phys,* 1977, **67**, 1620

[112] E. Simoni, S. Hubert and M. Genet, *J. Chem. Phys.,* 1988, **49**, 1425; c) C. K. Malek, J. C. Krupa, P. Delamoye and M. Genet, *J. Chem. Phys.*, 1986, **47**, 1763; d) C. D. Flint and P. A. Tanner, *Mol. Phys.*, 1984, **53**, 429; e) C. K. Mallek and J. C. Krupa, *J. Chem. Phys.*, 1986, **84**, 6584; f) B. Ordejòn, V. Vallet, J. P. Flament, L. Seijoa and Z. Barandiaràna, *J. Lumin.*, 2007, **126**, 779; g) B. Ordejòn, M. Karbowiak, L. Seijo and Z. Barandiaràna, *J. Chem. Phys.*, 2006, **125**, 074511

[113] J. L. Kiplinger, D. E. Morris and A. J. Taylor, *J. Phys. Chem. A*, 2008, **112**, 7840

[114] B. Kanellakopulos, T. J. Marks, R. D. E. Fischer, *Organometallics of the f-Elements,* Reidel: Dordrecht, 1979

[115] E. E. Hardy, K. M. Wyss, J. D. Gorden, I. R. Ariyarathna, E. Miliordos and A. E. V. Gorden, *Chem. Comm*., 2017, **53**, 11984

[116] a) G. V. Inova and G. A. Gerasimova, *Russ. Chem. Rev.*, 1992, **62**, 907; b) J. Su and J. Li, *Prog. Chem.*, 2011, **23**, 1329

[117] N. M. Edelstein, *Lanthanide and Actinide Chemistry and Spectroscopy*, 1980

[118] a) G. Tian, T. Kimura, Z. Yoshida, Y. Zhu and L. Rao, *Radiochim. Acta.*, 2004, **92**, 495; b) A. B. Yusov and A. M. Fedoseev, *J. Radio Nucl. Chem.,* 1991, **147**, 201; c) T. Fanghänel and J. I. Kim, *J. Alloys Compd.;* 1998, **728**, 217; d) A. Skerencak, P. J. Panak, W. Hauser, V. Neck, R. Klenze, P. Lindqvist-Reis and T. Fanghänel, *Radiochim. Acta.*, 2009, **97**, 385; e) T. Stumpf, T. Fanghänel and I. Grenthwe, *J. Chem. Soc.*, *Dalton Trans.*, 2002, **20**, 3799; f) M. Morgensten, R. Klenze and J. I. Kim, *Radiochim. Acta.,* 2000, **88**, 7; g) H. Moll and G. Bernhard, *Polyhedron,* 2012, **31**, 759; h) D. Girnt, P. W. Roesky, A. Geist, C. M. Ruff, P. J. Panak and M. A. Denecke, *Inorg. Chem.,*2010, **49**, 9627; i) P. Lindqvist-Reis, C. Walther, R. Klenze, A. Eichohofer and T. Fanghänel, *J. Phys. Chem. B.*, 2006, **110**, 5279

[119] a) J. V. Beitz, G. Jursich and G. Sullivan, *J. Less. Common. Met.*, 1986, **126**, 301; b) A. B. Yusov, *J. Radioanal. Nucl. Chem.*, 1990, **143**, 287

[120] J. H. Van Vleck*, The Theory of Electric and Magnetic Susceptibilities*, Oxford University Press, London 1932

[121] a) B. G. Wybourne, *Spectroscopic Properties of Rare Earths;* Wiley: New York, 1965; b) T. H. Siddell, *Theory and Applications of Molecular Paramagnetism*; Wiley: New York, 1976; c) T. J. Marks and R. D. Fischer, Eds.; NATO Advanced Study Institues Series; D. Reidel, Dordrecht, The Netherlands, 1978; d) A. F. Orchard, *Magnetochemistry*; Oxford University Press Inc.: New York, 2003; e) N. M. Edelstein and G. H. Lander, in *The Chemistry of the Actinide and Transactinide Elements*, 3rd ed.; L. R. Morss, N.M. Edelstein and J. Fuger, Eds.; Springer: Dordrecht, The Netherlands, 2006, **4**, 2225

[122] B. M. McGarvey, *Electron Spin Resonance of Transition-Metal Complexes*, in: R. L. Carlin (Ed.), Trans. Met. Chem., vol. **3**, Marcel-Dekker, 1967, 89

[123] J. C. Eisestein and M. H. L. Pryce, *Proc. R. Soc., A.,* 1960, **255**, 181

[124] R. G. Denning, T. R. Snellgrove and D. R. Woodmark, *Mol. Phys.*, 1979, **37**, 1109

[125] S. Cotton, *Electronic and magnetic properties of actinides*, in: *Lanthanide and Actinide Chemistry*, John Wiley and Son Ltd, 2006

[126] a) J. L. Stewart and R. A. Andersen, *New J. Chem*. 1995, **19**, 587; b) O. P. Lam, F. W. Heinemann and K. Meyer, *C. R. Chim.*, 2010, **13**, 803; c) I. Castro-Rodriguez, H. Nakai and K. Meyer, *Angew. Chem*., *Int. Ed.*, 2006, **45**, 2389; d) C. Camp, V. Mougel, J. Pecaut, L. Maron and M. Mazzanti, *Chem.-Eur. J.*, 2013, **19**, 17528

[127] D. R. Kindra and W. J. Evans, *Chem. Rev.*, 2014, **114**, 8865

[128] L. Morss, N. M. Edelsein and J. Fuger, *The chemistry of the Actinide and Transactinide Element*s, 4th edition, Springer, 2010, Chapter 20

[129] D. P. Halter, H. S. La Pierre, F. W. Heinemann and K. Meyer, *Inorg. Chem.*, 2014, **53**, 8418

[130] a) O. P. Lam, F. W. Heinemann and K. Meyer, *Chem. Sci.*, 2011, **2**, 1538; b) O. P. Lam, F. W. Heinemann and K. Meyer, *Angew. Chem. Int. Ed.*, 2011, **50**, 5965; c) F. Moro, D. P. Mills, S. T. Liddle and J. van Slageren, *Angew. Chem. Int. Ed.*, 2013, **52**, 3430

[131] a) D. M. King, F. Tuna, E. J. McInnes, J. McMaster, W. Lewis, A. J. Blake and S. T. Liddle, *Nat. Chem.*, 2013, **5**, 482; b) L. A. Seaman, G. Wu, N. Edelstein, W. W. Lukens, N. Magnani and T. W. Hayton, *J. Am. Chem. Soc.*, 2012, **134**, 4931; c) B. Kosog, H. S. La Pierre, M. A. Denecke, F. W. Heinemann and K. Meyer, *Inorg. Chem.*, 2012, **51**, 7940; d) B. M. Gardner, J. C. Stewart, A. L. Davis, J. McMaster, W. Lewis, A. J. Blake and S. T. Liddle, *Proc. Natl. Acad. Sci. U.S.A*, 2012, **109**, 9265; e) J. L. Brown, S. Fortier, R. A. Lewis, G. Wu and T. W. Hayton, *J. Am. Chem. Soc.*, 2012, **134**, 15468; f) S. Fortier, J. R. Walensky, G. Wu and T. W. Hayton, *J. Am. Chem. Soc.*, 2011, **133**, 11732; h) S. Fortier, J. R. Walensky, G. Wu and T. W. Hayton, *J. Am. Chem. Soc.*, 2011, **133**, 6894; i) S. Fortier, N. Kaltsoyannis, G. Wu and T. W. Hayton, *J. Am. Chem. Soc.*, 2011, **133**, 14224; l) S. Fortier, B. C. Melot, G. Wu and T. W. Hayton, *J. Am. Chem. Soc.*, 2009, **131**, 15512

[132] a) J. D. Rinehart and J. R. Long, *J. Am. Chem. Soc.*, 2009, **131**, 12558; b) J. D. Rinehart, K. R. Meihaus and J. R. Long*, J. Am. Chem. Soc.*, 2010, **132**, 7572; c) J. D. Rinehart and J. R. Long, *Dalton Trans.*, 2012, **41**, 13572; d) J. T. Coutinho, M. A. Antunes, L. C. J. Pereira, H. Bolvin, J. Marçalo, M. Mazzanti and M. Almeida, *Dalton Trans.*, 2012, **41**, 13568; e) M. A. Antunes, L. C. J. Pereira, I. C. Santos, M. Mazzanti, J. Marçalo and M. Almeida, *Inorg. Chem.*, 2011, **50**, 9915; f) D. P. Mills, F. Moro, J. McMaster, J. van Slageren, W. Lewis, A. J. Blake and S. T. Liddle, *Nat. Chem.*, 2011, **3**, 454

[133] V. Mougel, L. Chatelain, J. Pecaut, R. Caciuffo, E. Colineau, J. C. Griveau and M. Mazzanti, *Nat. Chem.*, 2012, **4**, 1011

[134] F. Moro, D. P. Mills, S. T. Liddle and J. van Slageren, *Angew. Chem. Int. Edn.*, 2013, **52**, 3430

[135] J. J. Baldovì, S. Cardona-Serra, J. M. Clemente-Juan, E. Coronado and A. Gaita-Arino, *Chem. Sci.,* 2013, **4**, 938

[136] C. I. Beard and B. P. Dailey, *J. Chem. Phys.*, 2017, **18**, 1437

[137] S. Cotton, *Coordination Chemistry of the Actinides*, in: *Lanthanide and Actinide Chemistry*, John Wiley and Son Ltd, 2006

[138] K. Takao, T. J. Bell and Y. Ikeda, *Inorg. Chem.*, 2013, **52**, 3459

[139] a) M. Borkowski; S. Lis, S. Siekierski, *J. Alloys Compd.*, 1998, **275**, 754; b) M. Borkowski, J. Krejzler, S. Siekierski, *Radiochim. Acta*, 1994, **65**, 99; c) P. K. Khopkar, J. N. Mathur, *J. Inorg. Nucl. Chem.*, 1980, **42**, 109; d) P. K. Khopkar, J. N. Mathur, *Inorg. Nucl. Chem.*, 1974, **36**, 3819; e) R. Chiarizia, P. R. Danesi, G. Scibona, L. Magon, *J. Inorg. Nucl. Chem*., 1973, **35**, 3595; f) P. K. Khopkar, P. Narayanankutty, *J. Inorg. Nucl. Chem.*, 1971, **33**, 495; g) F. L. Moore, *Anal. Chem*., 1964, **36**, 2158

[140] M. Srncik, D. Kogelnig, A. Stojanovic, W. Korner, R. Krachler and G. Wallner, *Appl. Radiat. Isot.*, 2009, **67**, 2146

[141] a) N. W. Alcock, M. M. Roberts and D. Brown, *Acta Crystallogr.* 1982, **B38**, 2870; b) G. Bombieri, E. Forsellini, R. Graziani and G. C. Pappalardo, *Transition Met. Chem.*, 1979, **4**, 70; c) V. M. Vdovenko, A. I. Skoblo and D. N. Suglobov, *Radiokhimiya*, 1967, **9**, 119

[142] C. E. Rowland, M. G. Kanatzidis and L. Soderholm, *Inorg. Chem.*, 2012, **51**, 11798

[143] E. Hashem, J. A. Platts, F. Hartl, G. Lorusso, M. Evangelisti, C. Schulzke and R. J. Baker, *Inorg. Chem.*, 2014, **53**, 8624

Chapter 2

Structural and spectroscopic investigation of $A_4[U(NCE)_8]$ ($A = Cs, Me_4N, Et_4N, {}^nPr_4N$; $E = S, Se$)

2.1 Introduction

The coordination and organometallic chemistry of uranium has undergone a remarkable revolution over the past decade, and new spectroscopic and theoretical techniques have augmented impressive synthetic breakthroughs.[1] As discussed in Chapter 1, since uranium has several common paramagnetic oxidation states, *i.e.*, $5f^1$ U(V), $5f^2$ U(IV), and $5f^3$ U(III), an analytical technique often chosen for characterizing uranium compounds is the measurement of the magnetic susceptibility,[2] and the data are often used to support assignments of oxidation states.[3] However, understanding the magnetic profiles of uranium compounds is very complicated.

For most $4f^n$ lanthanides, the ground state is defined by a $^{2S+1}L_J$ Russell-Saunders term because spin-orbit coupling is large, but ligand field splitting is relatively small. In this case, room temperature magnetic moments can be approximated by $\mu_J = g[J(J+1)]^{1/2}$ and correlated with oxidation state.[4] For d^n transition metals (TM) complexes, the crystal field splitting (CFS) effect is more important than the spin-orbit coupling and can reduce the contribution from the orbital angular momentum to the effective magnetic moment (orbital quenching). In general, with TM, a "spin-only" approximation, $\mu_S = 2[S(S+1)]^{1/2}$, represents a good starting point to calculate room-temperature magnetic moments, which can be eventually modified including the orbital contribution depending on the d^n configuration and symmetry.[4]

The situation is more elaborate with actinide complexes, as the spin-orbit coupling is of the same order of magnitude as crystal-field splitting. An additional complication is the mixing of excited state terms with the ground state, determined experimentally from analysis of absorption spectroscopy,[1, 5] which means that the Russell-Saunders scheme does not accurately describe actinide electronic structure. This has also been shown theoretically for the U(IV) ion, whose $^3H_4$ ground state has 9% $^1G_4$ character.[6]

For actinide compounds, ligand field effects cannot be considered as perturbations of the spin-orbit coupling (as in the *4f* series), but they can remove the $(2J+1)$ degeneracy of the ground state and form Stark sublevels. The energy of these sublevels is then dependent upon the symmetry of the actinide ion. Moreover, notably, if the actinide ion has an odd number of electrons, the non-Kramers ground state cannot have its degeneracy totally lifted and the resulting complexes may show unusual properties, such as SMM.[1, 7]

Ligand-field effects are more pronounced in actinides than in lanthanides complexes due to the greater radial extension of the *5f* orbitals.[8] Thus, changing the ligand field

strength could offer a way to 'tune' the magnetic properties. An informative example of this behaviour is the influence of donor strength in the homoleptic U(III) complexes of the $[Bc^{Me}]^-$ (dihydrobis(methylimidazolyl)borate) ion *vs* the weaker $[Bp^{Me}]^-$ dihydrobis(methylpyrazolyl)borate), where the slow magnetic relaxation in SMM compounds could be modified.[9] Correlations towards ligand field strength have also been observed, such as in $[(Cp(^{tBu2})_3UX]$ (X = F, μ_{eff} = 3.11 B.M.; X = Cl, μ_{eff} = 3.32 B.M.)[2c] but this is not a generalisable concept as shown by $[\{(Me_3Si)_2N\}_3UX]$ complexes (X = Cl, μ_{eff} = 2.8 B.M.;[10] X = F, μ_{eff} = 2.91 B.M.;[2c] X = Me, μ_{eff} = 2.7 B.M.;[10] X = H, μ_{eff} = 2.6 B.M.) [11] , or in a larger library of tren-based tetravalent uranium complexes, $[\{N(CH_2CH_2NR)\}_3UX]$, where small changes in the ligand substituent R (R = $SiMe_3$,[12] Si^iPr_3,[13] $SiMe_2{}^tBu$[14]) influences the magnetic moments for given X (X = F, Cl, Br, I). On this line, a recent comprehensive survey of the literature has also highlighted that there is no simple correlation between ligand field strength and the measured magnetic moment.[3] Clearly the interplay between spin-orbit coupling, CF splitting and interelectronic repulsion can give an unusual magnetic behaviour, which is difficult to understand using the accepted framework of electronic structure theory.

While much recent emphasis has been placed on the of U(III) and $[UO_2]^+$ for their dynamic magnetic properties,[7] the magnetic behaviour of $5f^2$ U(IV) compounds is also well known. Described in Chapter 1, it can be summarised considering a non-degenerate singlet ground-state with Temperature Independent Paramagnetism (TIP) at low temperatures (to ~ 100 K) followed by a region of temperature dependent paramagnetism; this gives a distinctive shape of the μ vs T curve for assigning the +4 oxidation state (Figure 1.8).[3, 15]

However, there are a few U(IV) compounds that deviate from this description (Scheme 2.1), and a comprehensive survey of the literature showed that the median value for U(IV) at 5 K or below is 0.69 B.M. with a standard deviation of 0.54 B.M.[3] Of these, 5-coordinate trigonal bypramidal geometries with strong ligand fields are prevalent such as $[(tren^{Si\mathit{i}Pr})U{=}NH]$,[16] $[(tren^{Si\mathit{i}Pr})U{=}PH]$[17] or the homoleptic piperidide[18] or homoleptic[19] or heteroleptic[20] alkyl anionic compounds but not all trigonal bypyramidal geometries give unusual magnetic behaviour. [21] Tetrahedral amides of the type $[(R_2N)_3UI]$ [22] and $[Cp^*_2Co][(R_2N)_3U{=}O]$ [23] (R = $SiMe_3$) also show high magnetic moments; however, highlighting the sensitivity of the magnetic moments, the analogous $[Cp^*_2Co][(R_2N)_3U{=}E]$ (E = Se, Te) show normal low temperature magnetic susceptibility of μ_{eff} = 0.96 and 0.79 B.M. at 4 K respectively and the authors suggested that a geometric distortion is

responsible for this effect.[23] Further evidence for subtle changes in ligand structure greatly influencing the magnetic susceptibility are the complexes [U(COT)$_2$] (μ_{eff} = 1.21 B. M. at 5 K)[24] and [(Pn*)$_2$U][25] (μ_{eff} = 1.6 B. M. at 5 K) (COT = C_8H_8 and Pn* = $C_{14}H_8$). Interestingly, for the complex [U(COT)$_2$], the authors also hypothesised about the presence of a doublet electronic ground state, to explain the unusual high low-temperature effective magnetic moment.

An important example is [Cp′$_3$UNO] (Cp′ = C_5Me_4H), which was shown to display TIP up to room temperature; indeed, for this compound the energy of the first excited state was estimated to be greater than 700 cm^{-1} above the ground state, so it is a singlet state at all temperatures studied.[26] Computational studies have suggested that significant covalency in the U–NO bond is responsible for this magnetic behaviour.[27]

A recent computational study has also revealed that the coordination geometry can have an important role; for example, U(IV) compounds could exhibit unusual magnetic properties, particularly in tetragonal or trigonal prismatic coordination geometries and with a specific electronic ground state.[28]

Finally, set of compounds that feature anionic ligand centred radicals have also been prepared where coupling invokes a higher than expected magnetic moment; however, this effect is not always observable, as demonstrated by Bart *et al*[29] for U(IV) complexes bearing redox-active diazabutadiene ligands. These compounds will be briefly discussed in Chapter 5.

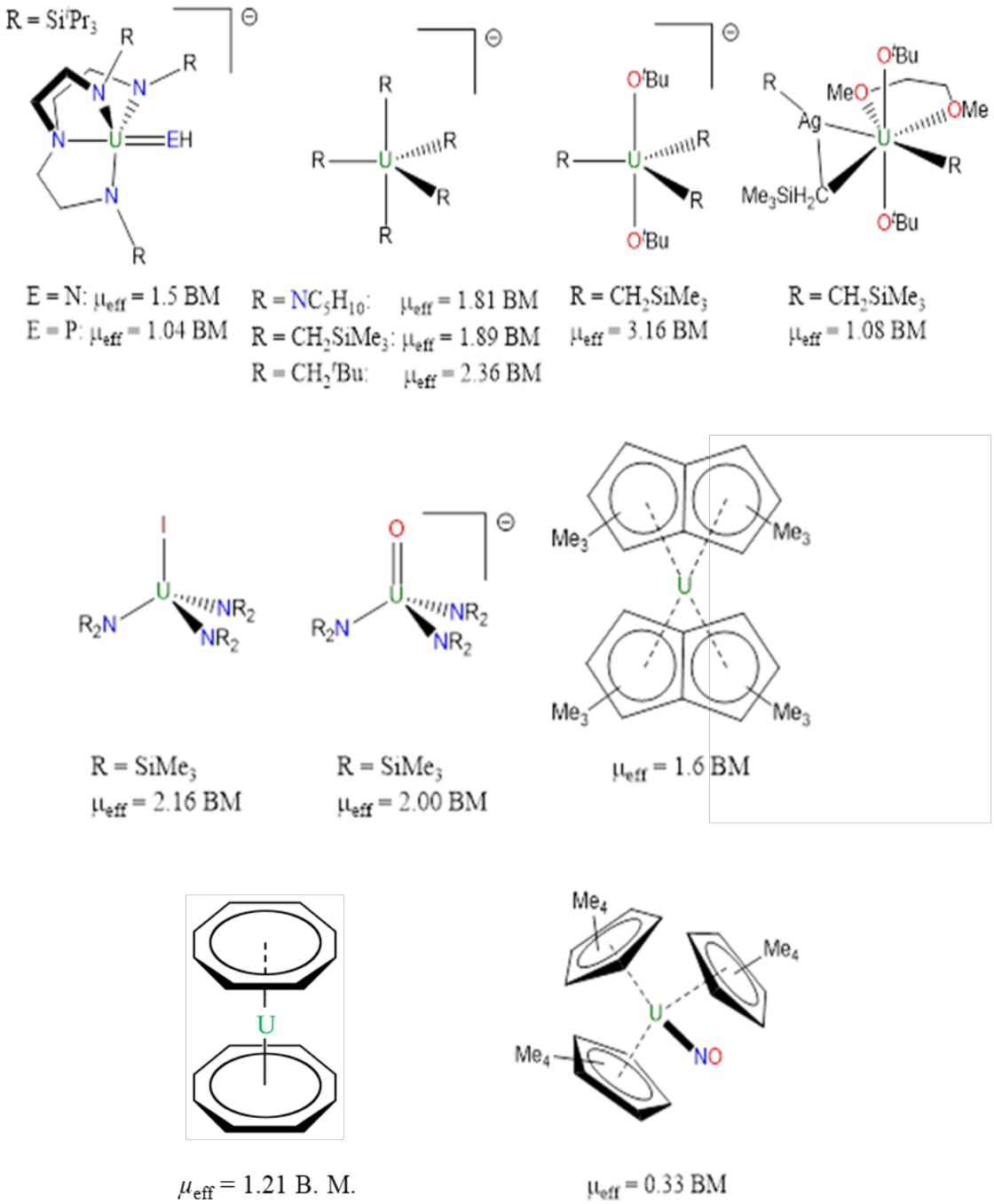

Scheme 2.1. Examples of mononuclear U(IV) complexes that have unusual high magnetic susceptibility (> 1.0 B. M.)[3] at low temperatures (<5 K).

This Chapter contains a comprehensive structural, magnetic and spectroscopic study on a series of high symmetry U(IV) thiocyanate complexes in non-aqueous media. These compounds, of general formula $A_4[U(NCS)_8]$, have been synthesized by simply changing the counter-cation (A) and, systematically, they display a different coordination geometry for the uranium ion. This is the first time that a different coordination geometry has been considered - *i.e.* where the same ligand set is involved but the geometry is different. In

this regard, it is noteworthy that, in the field of lanthanide SMMs, local coordination geometry is an important criterion as this defines the magnetic anisotropy of the system;[30] however, while the ligand field strength can be altered by simple modification of the coordinating ligands, there have been no detailed reports where a different coordination geometry has been considered with the same ligand set. Synthetically this could be an extremely challenging project, but it was possible to gain advantage from the templating effect of different cations on the solid-state structure of the $[U(NCS)_8]^{4-}$ anion.

The first thiocyanate U(IV) compounds were reported in the 1960s;[31] X-ray diffraction studies have shown that, when the cation is Cs^+, the anion $[U(NCS)_8]^{4-}$ has a square antiprismatic (D_{4d}) symmetry,[32] but with $[Et_4N]^+$ the coordination geometry becomes cubic (O_h) due to the templating effect of the ethyl groups.[33] Recently, the structure of $[^nBu_4N]_4[U(NCS)_8]$ has also been reported and in this complex the anion $[U(NCS)_8]^{4-}$ was found in a distorted symmetry from square antiprismatic (D_4).[34] Thus, crystal packing forces are energetically more important than CF splitting in determining the symmetry of the $[U(NCS)_8]^{4-}$ ions in solid state. In solution, however, the templating effect of the counter cation is lost and the U(IV) ion adopts a D_{4d} geometry in all cases; this has also been experimentally proved by $^{13}C\{^1H\}$ NMR and vibrational spectroscopic measurements.[35] Interestingly, previous work in our group have suggested that this structural distortion in the solid state can also influence the low temperature magnetic moment significantly (μ_{eff} = 1.21 B.M. for square antiprismatic and 0.53 B.M. for cubic geometry).[34]

In this chapter, this effect has been further explored, including more examples and adopting a wide set of spectroscopic techniques. The experimental results are also supported by theoretical calculations, which indicate that a different coordination geometry can influence the low-lying energy-level electronic structure of the $[U(NCS)_8]^{4-}$ ion. Finally, the analysis has been expanded changing the ligand field to understand if this behaviour can be thought as general for high symmetry U(IV) complexes. Thus, a structural, magnetic and spectroscopic study on two U(IV) selenocyanate complexes of formula $A[U(NCSe)_8]$ (A = Et_4N, $^nPr_4N$) will be presented and the results have been compared with the ones from the study on the analogue thiocyanate complexes.

2.2 Systematic Structural and Spectroscopic Study of $A_4[An(NCS)_8]$ (An = Th, U; A = Cs, Me_4N, Et_4N, $^nPr_4N$)

2.2.1 Synthesis and Structural Characterization

The $A_4[U(NCS)_8]$ complexes were prepared using UCl_4 as the source of U(IV) and the experimental procedure is not difficult; the syntheses is based on a two-step reaction only, as shown in Scheme 2.2.

$$UCl_4 + 8Na[NCS] \rightarrow Na_4[U(NCS)_8] + 4NaCl$$

$$Na_4[U(NCS)_8] + 4ACl \rightarrow A_4[U(NCS)_8] + 4NaCl$$

Scheme 2.2. Synthesis of $A_4[U(NCS)_8]$, A = Me_4N, Et_4N, $^nPr_4N$, Cs.

The reactions have been performed in dried MeCN and under an inert atmosphere, using standard Schlenk line and glove-box techniques; once isolated, most of the solid samples proved to be stable in air, keeping the same green colour and crystallinity. Some oxidations, however, occurred in solution and these will be described in Chapter 3.

Considering the unusual magnetic behaviour observed with a D_{4d} coordination geometry, as in the case of $Cs_4[U(NCS)_8]$,[34] initially a number of reactions have been performed using alkali or alkaline earth metal ions, such as Na^+, K^+, Mg^{2+}, Sr^{2+} and Ba^{2+}, and also Ti^{4+}. In fact, with these spherical counter cations, the corresponding $[U(NCS)_8]^{4-}$ anion should display a D_{4d} symmetry for the uranium coordination sphere, as in $Cs_4[U(NCS)_8]$. However, from these experiments, it was not possible to isolate crystals suitable for X-ray diffractions and a green gel was constantly the only material obtained. This was isolated and redissolved in solvents of different polarity such as Acetone, DCM, DMSO, THF, EtOH and MeOH; but, in all cases, a green gel was again the only material formed, which was not further analysed.

Given the failures in isolating single crystals from these reactions, a different strategy was followed, in which the encapsulation of the sodium cation from $Na_4[U(NCS)_8]$ was tried using the chelating ligand 18-crown-6 or 2.2.2-cryptand (Scheme 2.3).

$$UCl_4 + 8Na[NCS] \rightarrow Na_4[U(NCS)_8] + 4NaCl$$

$$Na_4[U(NCS)_8] + 4(L) \rightarrow [(L)Na]_4[U(NCS)_8]$$

Scheme 2.3. Synthesis of $[(L)Na]_4[U(NCS)_8]$; L = 18-crown-6 or 2.2.2-cryptand.

With 18-crown-6, a serendipitous oxidation of U(IV) to uranyl(VI) occurred and yellow single crystals of $[(18\text{-C-6})Na]_3[UO_2(NCS)_5]$ were isolated; this compound will be discussed in Chapter 4. When the experiment was performed with 2.2.2-cryptand, the desired U(IV) complex with the Na^+ cation trapped by the 2.2.2-cryptand ligand was not obtained; instead, the reaction afforded hydrolysis of the encapsulating cation and the compound $[H_2(2.2.2\text{-cryptand})]_2[U(NCS)_8]$ was isolated as a few single crystals, but no magnetic measurements were possible. The X-ray structure of $[H_2(2.2.2\text{-cryptand})]_2[U(NCS)_8]$ is shown in Figure 2.1; it suffers of significant disorder in both the $[U(NCS)_8]^{4-}$ ion and the cryptand fragment and the refinement is clarified in the experimental section. The bond lengths around the U(IV) ion are listed in Table 2.1 (page 56) and some selected geometrical parameters are presented in Table 2.2 (page 57); instead the corresponding crystallographic data are shown in Appendix 1. The full list of bond lengths and angles of this compound is tabulated in Appendix 1.1, in the external CD source of this thesis.

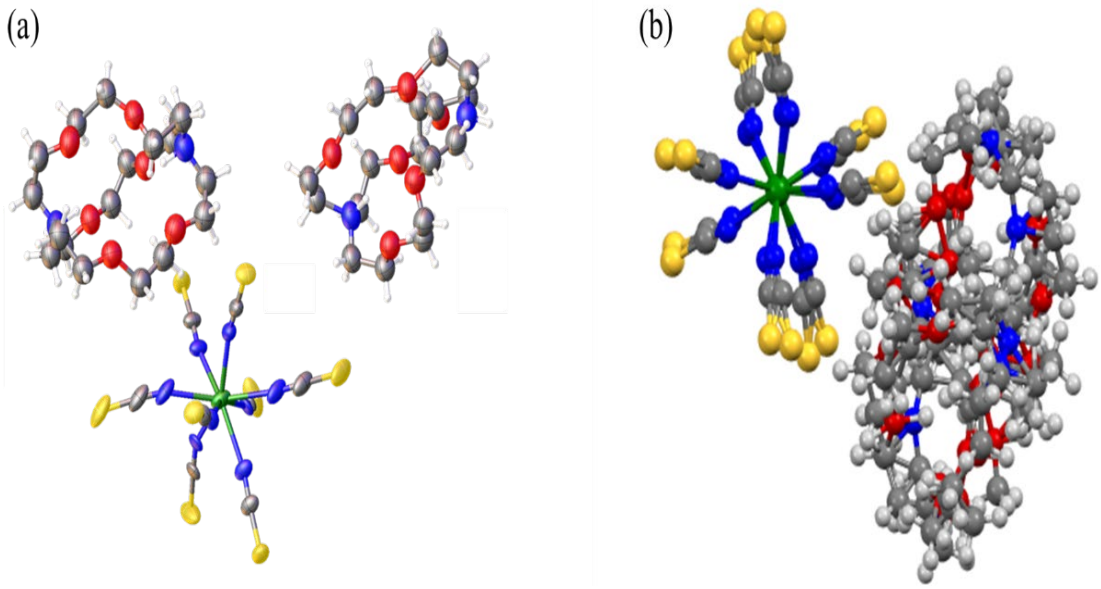

Figure 2.1. (a) Individual disordered moiety of $[H_2(2.2.2\text{-cryptand})]_2[U(NCS)_8]$ with coordinated $[NCS]^-$ groups all disordered in two sites with 50% occupancy for N1, N2, N4. N3 NCS 76 % occupancy and cryptand 59% occupancy. (b) Crystal structure of $[H_2(2.2.2\text{-cryptand})]_2[U(NCS)_8]$ evidencing the disorder in both the $[U(NCS)_8]^{4-}$ ion and in the cryptand fragment. Co-crystallized MeCN molecule omitted. Colour code: U – green, N – blue, C – grey, O – red, S – yellow, H – white.

This reaction was also repeated several times; in one case, two different crystalline products were produced and X-ray diffraction showed them to be compounds of formula

[Na(2.2.2-cryptand)][Na(H_2O)($NCS)_2$] and [Na(2.2.2-cryptand)]$_3$[UO_2($NCS)_5$]. The X-ray structure of [Na(2.2.2-cryptand)][Na(H_2O)($NCS)_2$] is shown in Appendix 1, Figure 7.1. The corresponding crystallographic data are listed in Appendix 1.1, in the external CD source of this thesis, with the list of bond lengths and angles. The uranyl(VI) compound [Na(2.2.2-cryptand)]$_3$[UO_2($NCS)_5$] will be discussed in Chapter 4.

The structure of [Na(2.2.2-cryptand)][Na(H_2O)($NCS)_2$] suffers disorder in the [Na(2.2.2-cryptand)]$^+$ cation and in one coordinated water molecule. There are two different Na^+ cations, Na1 is coordinated to the six oxygen and two nitrogen donor atoms of the 2.2.2-cryptand ligand, and Na2 is coordinated to the water molecule, whose refinement suffers of disorder, and to two $[NCS]^-$ ions, that have been presumably released by [Na]$_4$[U($NCS)_8$] during the reaction.

Subsequently, a number of organic salts were chosen and reacted with Na_4[U($NCS)_8$], as shown in Scheme 2.2, to allow the isolation of the $[U(NCS)_8]^{4-}$ ion in solid state from a non-aqueous media. Thus, it was possible to isolate and structurally characterize the complexes [Me_4N]$_4$[U($NCS)_8$] and [^{n}Pr$_4$N]$_4$[U($NCS)_8$]. The synthesis of [^{n}Pr$_4$N]$_4$[U($NCS)_8$], initially, afforded a green gelatinous product, but it was possible to grow single crystals by recrystallization from dried DCM. For [Me_4N]$_4$[U($NCS)_8$], instead, green single crystals were directly obtained by cooling down the corresponding MeCN solutions. The solid-state crystal structures of [Me_4N]$_4$[U($NCS)_8$] and [^{n}Pr$_4$N]$_4$[U($NCS)_8$] are collated in Figure 2.2 and in the structure of [Me_4N]$_4$[U($NCS)_8$] there are two independent $[U(NCS)_8]^{4-}$ fragments in the unit cell. For these compounds, selected bond lengths are listed in Table 2.1 (page 56) some useful geometrical parameters are compared in Table 2.2 (page 57) and the corresponding crystallographic data are tabulated in Appendix 1. The full list of bond lengths and angles are reported in Appendix 1.2, in the external CD source of this thesis.

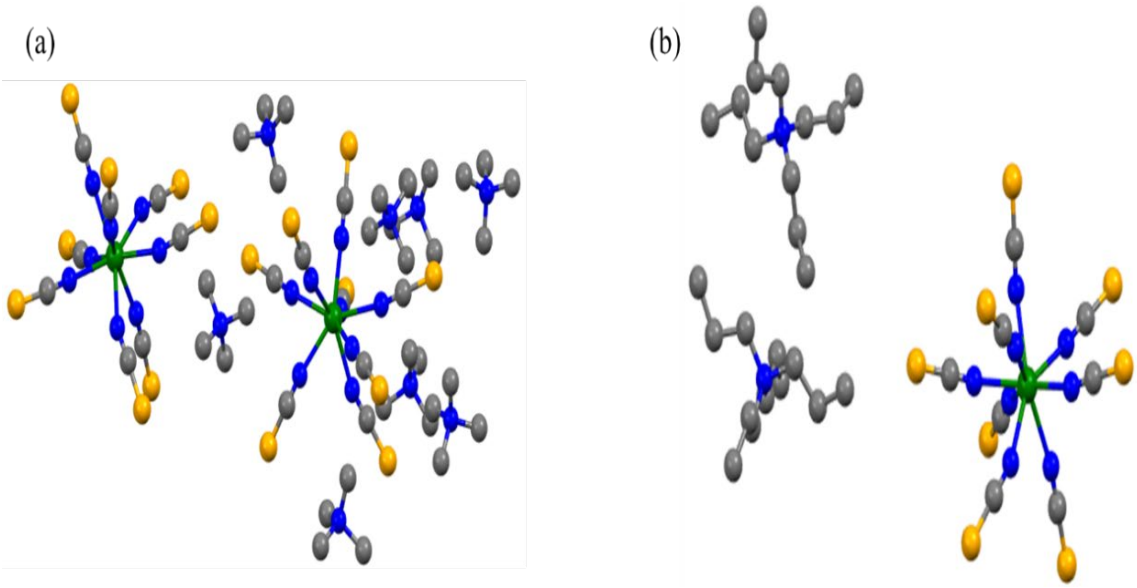

Figure 2.2. Solid-state crystal structures of (a) $[Me_4N]_4[U(NCS)_8]$ and (b) $[^nPr_4N]_4[U(NCS)_8]$, with atomic displacement shown at 50% probability. Hydrogen atoms and co-crystallized solvent molecules omitted for clarity. Colour code: U – green, N – blue, C – grey, S – yellow.

In the attempts to use other spherical cations, $Na_4[U(NCS)_8]$ was also reacted with $[Et_3BzN]Cl$, $[Me_3BzN]Cl$, Ph_3CCl and $[Ph_4P]Cl$. However, from these experiments the desired U(IV) complex was not obtained. In particular, while a green gel was the only material isolated with $[Et_3BzN]Cl$ and $[Me_3BzN]Cl$, colourless single crystals were formed using $[Ph_3C]Cl$ and X-ray diffraction revealed a compound of formula Ph_3CNCS. The formation of this molecule must be due to the loss of a coordinated $[NCS]^-$ ligand from $[U(NCS)_8]^-$, which led to the formation of a new C–N bond, perhaps reflecting the intrinsic ionicity of the U–N bond.[34] The crystal structure of Ph_3CNCS is shown Appendix 1 (Figure 7.2), along with the corresponding crystallographic data. The list of bond lengths and angles are given in Appendix 1.3, in the external CD source of this thesis.

In the [NCS] group of this molecule, the C=N (1.176(2) Å) and the C=S (1.5801(18) Å) bond lengths are, respectively, slightly longer and shorter compared to the corresponding average values found in the $A_4[U(NCS)_8]$ compounds (1.163(1) Å for C=N and 1.619(1) Å for C=S, Table 2.1). Moreover, the packing diagram of this molecule (Appendix 1, Figure 7.2), evidences the presence of two intermolecular C–H···S hydrogen bonding which involve the S atom of the [NCS] group and two different aromatic hydrogen atoms, one in *para* ($d_{C\cdots S}$ = 3.6251(17) Å) and one in *meta* ($d_{C\cdots S}$ = 3.8104(18) Å).

In order to ensure that any electronic effects on the structural distortions were taken into account, the analogous $5f^0$ Th(IV) compounds $[Me_4N]_4[Th(NCS)_8]$ and

[^{n}Pr$_4$N]$_4$[Th(NCS)$_8$] were synthesized and fully characterized. The preparation of these thorium compounds was achieved using ThCl$_4$(DME)$_2$ (DME = dimethoxyethane), as the source of Th(IV), and, as for the uranium complexes, the experimental procedure was not difficult; the synthesis is based on a two-step reaction only (Scheme 2.4). The reactions have been performed in dried MeCN and under an inert atmosphere, using standard Schlenk line and glove-box techniques; once isolated, the crystals proved to be stable in air.

$$[ThCl_4(DME)_2] + 8Na[NCS] \rightarrow Na_4[Th(NCS)_8] + 4NaCl$$

$$Na_4[Th(NCS)_8] + 4ACl \rightarrow A_4[Th(NCS)_8] + 4NaCl$$

Scheme 2.4. Schematic synthesis of A$_4$[Th(NCS)$_8$], with A = [Me$_4$N]$^+$, [^{n}Pr$_4$N]$^+$.

The solid-state crystal structures of [Me$_4$N]$_4$[Th(NCS)$_8$] and [^{n}Pr$_4$N]$_4$[Th(NCS)$_8$] are collated in Figure 2.3; interestingly, as observed for [Me$_4$N]$_4$[U(NCS)$_8$], in the unit cell of the structure of [Me$_4$N]$_4$[Th(NCS)$_8$] there are two independent [Th(NCS)$_8$]$^{4-}$ fragments. For these two thorium compounds, selected bond lengths are listed in Table 2.1 (page 56), some useful geometrical parameters are compared in Table 2.2 (page 57) and the corresponding crystallographic data are tabulated in Appendix 1. The full list of bond lengths and angles is shown in Appendix 1.4, in the external CD source of this thesis. The structure of [^{n}Pr$_4$N]$_4$[Th(NCS)$_8$] suffers of disorder in the [^{n}Pr$_4$N]$^+$ cation and the refinement is clarified in the experimental section.

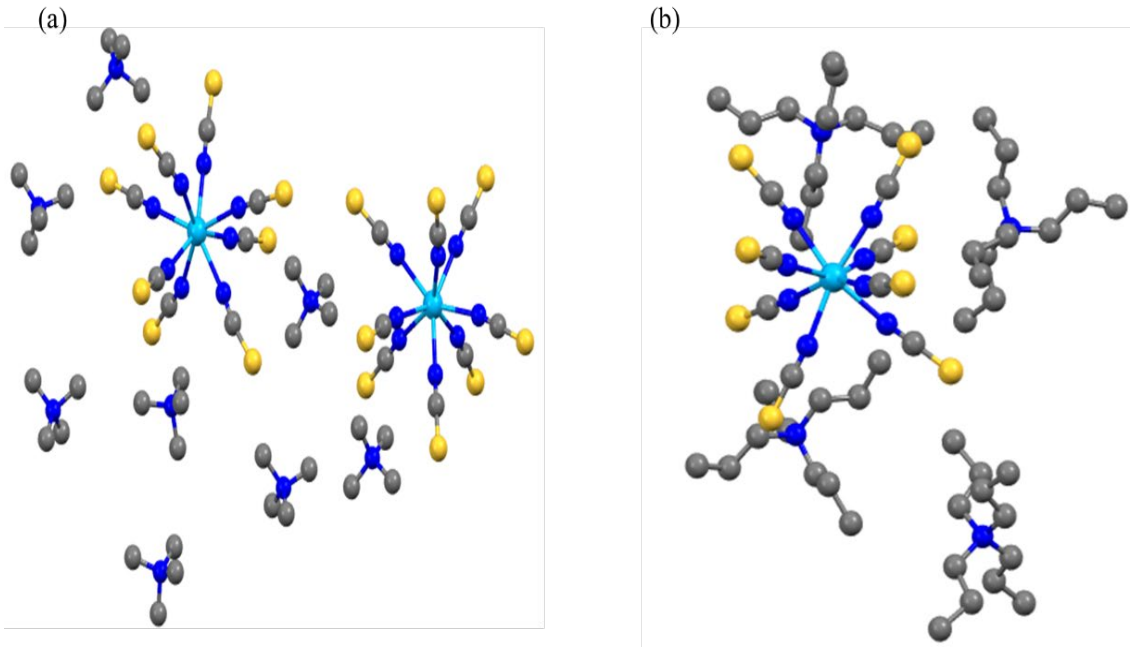

Figure 2.3. Solid-state crystal structures of (a) $[Me_4N]_4[Th(NCS)_8]$ and (b) $[^nPr_4N]_4[Th(NCS)_8]$, with atomic displacement shown at 50% probability. Hydrogen atoms and co-crystallized solvent molecules omitted for clarity. Colour code: Th – light blue, N – blue, C – grey, S – yellow.

In Table 2.1, the averages of selected bond lengths for all of the 8-coordinate U(IV) and Th(IV) thiocyanate complexes are shown. The reported data for $Cs_4[U(NCS)_8]$,[32] $[Et_4N]_4[U(NCS)_8]$,[33] $[^nBu_4N]_4[U(NCS)_8]$[34], $[Et_4N]_4[Th(NCS)_8]$[33], $[Me_4N]_4[Np(NCS)_8]$[36] and $[Et_4N]_4[Pu(NCS)_8]$[37] have been added for comparison. From this, there are no significant differences in the metric parameters for the coordinated $[NCS]^-$ ligands among the compounds. The average of the An–N bond lengths varies only with the nature of the An ion, in line with the actinide contraction (Th–N = 2.491(2) Å, U–N = 2.423(1) Å, Np–N 2.40(1) Å, Pu–N 2.372(2) Å).

Table 2.1. Selected average bond lengths (Å) for the structures of $A_4[An(NCS)_8]$ measured at 100 K, with An = Th, U, Np, Pu and A = $[Me_4N]^+$, $[Et_4N]^+$, $[^nPr_4N]^+$, $[^nBu_4N]^+$, Cs^+.

Compound	An–N	N=C	C=S
$[Me_4N]_4[Th(NCS)_8]$	2.489(3)	1.150(3)	1.631(3)
$[Et_4N]_4[Th(NCS)_8]$[(a)]	2.483(2)	1.154(3)	1.599(3)
$[^nPr_4N]_4[Th(NCS)_8]$	2.502(2)	1.159(2)	1.621(2)
$[Me_4N]_4[U(NCS)_8]$	2.430(2)	1.156(3)	1.622(3)
$[Et_4N]_4[U(NCS)_8]$[(a)]	2.391(1)	1.183(1)	1.594(1)
$[^nPr_4N]_4[U(NCS)_8]$	2.442(4)	1.170(2)	1.630(2)
$Cs_4[U(NCS)_8]$[(b)]	2.420(2)	1.140(2)	1.620(2)
$[^nBu_4N]_4[U(NCS)_8]$[(c)]	2.430(2)	1.167(3)	1.629(2)
$[H_2(2.2.2\text{-cryptand})]_2[U(NCS)_8]$	2.44(2)	1.162(5)	1.630(3)
$[Me_4N]_4[Np(NCS)_8]$[(d)]	2.40(1)	1.14(1)	1.61(1)
$[Et_4N]_4[Pu(NCS)_8]$[(e)]	2.372(2)	1.165(3)	1.606(2)

a - Data taken from Ref. 33; b - Data taken from Ref. 32; c - Data taken from Ref. 34; d - Data taken from Ref. 36; e - Data taken from Ref. 37.

In order to delineate the symmetry of the inner coordination sphere around the actinide ion in these compounds, specific geometrical parameters have been considered (Figure 2.4). The angle between the four-fold rotational axis and the An–N bond direction (compression angle, θ), provides a measurement for the axial distortion of the coordination environment and, in particular, a value of θ = 54.741° indicates an ideal non-distorted cubic environment while smaller or wider angles reflect axial elongation and compression, respectively.[38] The ratio between the interplanar distance (d_{pp}) and the shortest diagonal in the N_4 plane (d_{in}), gives indications of axial compressions.[38] Another useful geometrical parameter is the skew or twist angle (φ). It is defined as the angle between the diagonals of the two different N_4 planes and a value of $\varphi = 0°$ is expected for an ideal square prismatic or cubic symmetry, while a value of φ = 45° corresponds to a non-distorted square antiprismatic geometry.[38] Thus, these structural parameters have been measured for all the actinide compounds and the results are listed in Table 2.2.

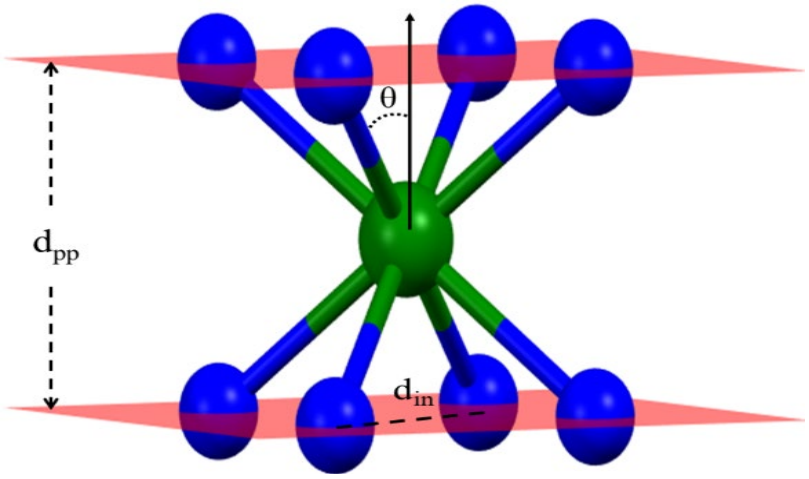

Figure 2.4. Key geometrical parameters analysed for the coordination environment of An–N_8 (An = Th, U, Np, Pu), with the image made using the structure of $[Et_4N]_4[U(NCS)_8]$; see text for details.

Table 2.2. Geometrical parameters in the An–N_8 (An = Th, U, Np, Pu) coordination sphere, measured from X-ray structures determined at 100 K.

Compound	d_{pp} (Å)	d_{in} (Å)	$\frac{d_{pp}}{d_{in}}$	θ (°) (average)	φ (°) (average)
$[Me_4N]_4[Th(NCS)_8]$ Th(1)	2.65454(10)	4.09264(18)	0.649	57.759(3)	45.037(3)
$[Me_4N]_4[Th(NCS)_8]$ Th(2)	2.69874(11)	4.07098(18)	0.663	57.137(3)	45.023(3)
$[Et_4N]_4[Th(NCS)_8]$	2.87531(8)	4.05102(8)	0.711	54.6339(9)	0.00
$[^nPr_4N]_4[Th(NCS)_8]$	2.79541(11)	3.70073(15)	0.755	55.775(3)	45.055(2)
$Cs_4[U(NCS)_8]$[a]	2.6663(5)	4.1097(5)	0.649	56.644(2)	45.000(3)
$[Me_4N]_4[U(NCS)_8]$ (U1)	2.676(9)	3.838(15)	0.697	56.4(2)	45.11(3)
$[Me_4N]_4[U(NCS)_8]$ (U2)	2.692(7)	3.991(6)	0.675	56.33(3)	45.02(3)
$[Et_4N]_4[U(NCS)_8]$	2.79304(7)	3.94870(7)	0.707	54.7270(9)	0.00
$[^nPr_4N]_4[U(NCS)_8]$	2.711(2)	3.868(4)	0.701	56.21(3)	45.03(3)
$[^nBu_4N]_4[U(NCS)_8]$[b]	2.679(3)	3.838(6)	0.698	56.49(4)	45.01(3)
$[H_2$(2.2.2-cryptand)$]_2[U(NCS)_8]$	2.56284(11)	4.17177(17)	0.614	58.135(3)	45.503(2)
$[Me_4N]_4[Np(NCS)_8]$[c]	2.610(12)	3.80(2)	0.687	57.0(2)	45.1(2)
$[Et_4N]_4[Pu(NCS)_8]$[d]	2.752(4)	3.863(5)	0.712	54.53(9)	0.00

a - Structure from Ref. 32; b - Structure from Ref. 34; c - Structure from Ref. 36; d - Structure from Ref. 37

From these data, it is evident that, in these complexes, the shape and the size of the counter cation determine changes in the coordination geometry of the actinide ion. However, to better quantify the distortions away from idealized polyhedral geometries (Figure 2.5), a continuous SHAPE measures approach[39] has been applied to all the compounds. The results of this analysis are summarized in Table 2.3.

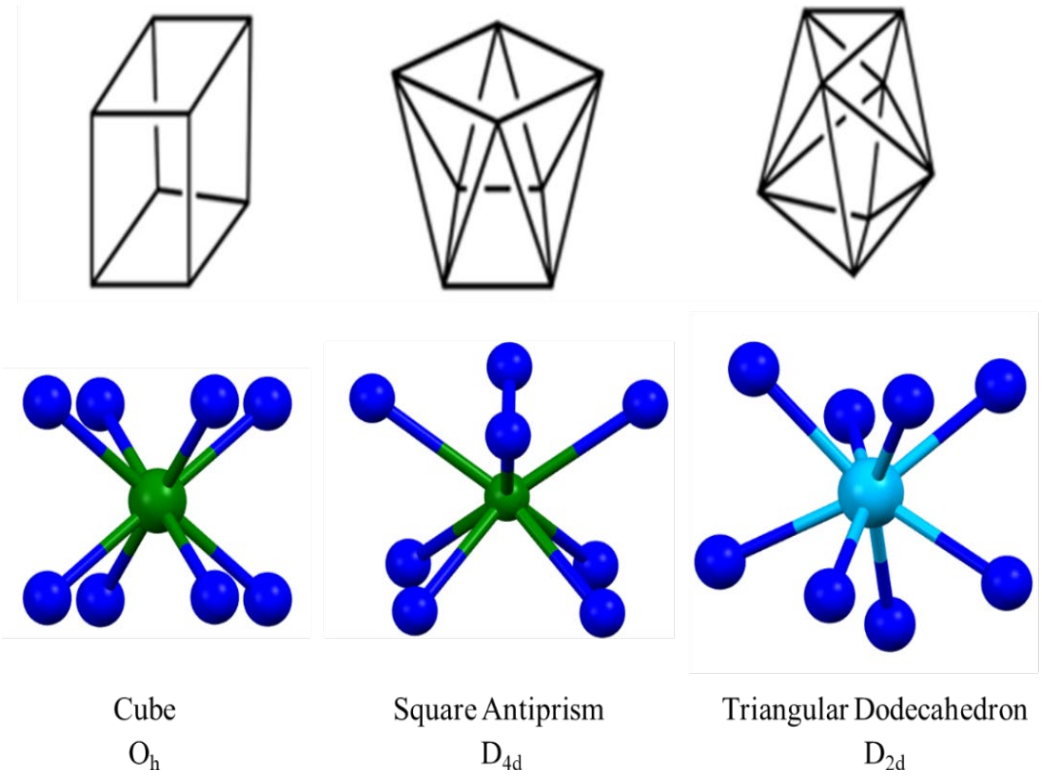

Figure 2.5. Structural depiction of the geometries observed in the $A_4[An(NCS)_8]$ (An = Th, U) series of compounds (colour code: U = green, Th = light blue; N = blue).

Table 2.3. Shape measures and path deviation functions for the An–N_8 (An = Th, U, Np, Pu) coordination sphere, with the best fit geometry in bold. (CU = cubic; SAP = square antiprismatic; TDD = triangular dodecahedron).

Compound	CU	SAP	TDD	Δ(SAP-CU)	Δ(SAP-TDD)
$[Me_4N]_4[Th(NCS)_8]$ Th(1)	10.70	**0.32**	1.68	15.3	9.9
$[Me_4N]_4[Th(NCS)_8]$ Th(2)	9.04	**0.27**	2.41	5.9	22.8
$[Et_4N]_4[Th(NCS)_8]$	**0.00**	10.99	7.95	0.5	-
$[^nPr_4N]_4[Th(NCS)_8]$	5.29	3.16	**0.42**	21.6	43.6
$Cs_4[U(NCS)_8]$[a]	9.25	**0.25**	2.42	6.4	21.9
$[Me_4N]_4[U(NCS)_8]$ (U1)	9.57	**0.51**	1.83	14.3	22.5
$[Me_4N]_4[U(NCS)_8]$ (U2)	9.81	**0.35**	2.05	11.9	19.8
$[Et_4N]_4[U(NCS)_8]$	**0.00**	10.98	7.95	0.0	-
$[^nPr_4N]_4[U(NCS)_8]$	8.46	**0.82**	0.88	14.2	9.0
$[^nBu_4N]_4[U(NCS)_8]$[b]	7.67	**0.68**	1.20	7.6	13.7
H_2(2.2.2-cryptand)]$_2$[$U(NCS)_8$]	6.86	**0.99**	2.44	7.9	51.2
$[Me_4N]_4[Np(NCS)_8]$[c]	9.50	0.97	**0.75**	21.9	9.4
$[Et_4N]_4[Pu(NCS)_8]$[d]	**0.00**	10.98	7.935	1.0	-

a - Structure from Ref. 32; b - Structure from Ref. 34; c - Structure from Ref. 36; d - Structure from Ref. 37

The combination between the data in Table 2.2 and Table 2.3 evidence clear trends for the An–N_8 coordination geometry. In particular:

1) with Et_4N^+ as the counter-cation, the An–N_8 coordination geometry is cubic (O_h) with all Th, U and Pu metals. This is in line with the values of φ: 0° for all three actinides.
2) changing the counter-cation from $[Et_4N]^+$, the An–N_8 coordination environment undergoes an axial compression (as indicated by an increasing of the angle θ and by a decreasing of the ratio d_{pp}/d_{in}) and the largest one is displayed by H_2(2.2.2-cryptand)]$_2$[$U(NCS)_8$] (d_{pp}/d_{in} = 0.614 and θ = 58.135(3)°).
3) when $[Me_4N]^+$ is the counter-cation, there are two unique ions in the unit cell for both Th and U complexes and one for Np. As the metal decreases in size from Th to Np, a geometrical distortion from square antiprismatic (SAP) towards triangular dodecahedron (TDD) increases. This distortion is in line with the axially elongation moving from the most compressed Th–N_8 (average d_{pp}/d_{in} = 0.656 and average θ =

57.448(2)° to the more elongated U–N_8 (average d_{pp}/d_{in} = 0.686 and average θ = 56.36(2)°) and Np–N_8 (d_{pp}/d_{in} = 0.687 and θ = 57.0(2)°) ions.

4) in the presence of $[^{n}Pr_4N]^+$, the An–N_8 coordination symmetry is clearly an intermediate between SAP and TDD for the smaller uranium compared to mostly TDD for the thorium analogue. Moreover, in this An–N_8 coordination geometry, there appear an axial elongation moving from the uranium (d_{pp}/d_{in} = 0.701 and θ = 56.21(3)°) to the thorium (d_{pp}/d_{in} = 0.755 and θ = 55.775(3)°) metal, which is in agreement with a distortion toward TDD for the thorium sample.
5) the size of the cation appears to have a structural directing influence so that with the smallest $[Me_4N]^+$ cation, there are numerous noncovalent intermolecular S···S interactions that are shorter than the van der Waals distance ($d_{S...S}$ = 3.49-3.55 Å for Th and $d_{S...S}$ = 3.24-3.54 Å for U). These interactions will be commented in detail in Chapter 4 with a discussion on uranyl(VI) thiocyanate and selenocyanate compounds.

In actinide complexes, in general, the coordination geometry is principally due to steric effects of the ligands and, for these compounds, the structural analysis suggests that the differences in energy between SAP and TDD are very small; therefore, it is possible to state that in these complexes the crystal packing forces are energetically more important than the CF splitting and, thus, determine the geometry adopted by the $[An(NCS)_8]^{4-}$ ion.

Further evidence for the importance of the size of the actinide ion comes from the isolated 9-coordinate $[Me_4N]_4[Th(NCS)_8(H_2O)]$, which was not accessible for the uranium analogue. The structure of this complex is shown in Figure 2.6, while the corresponding crystallographic data are listed in Appendix 1 and the full list of bond lengths and angles are tabulated in Appendix 1.5, in the external CD source of this thesis. There is some disorder and the refinement is further discussed in the experimental section.

This complex exhibits a mono-capped square antiprismatic (C_{4v}) geometry, with the water molecule as the capping ligand, and slightly longer Th–N bond lengths (average = 2.521(7) Å) compared to the 8-coordinate species (average = 2.496(7) Å).

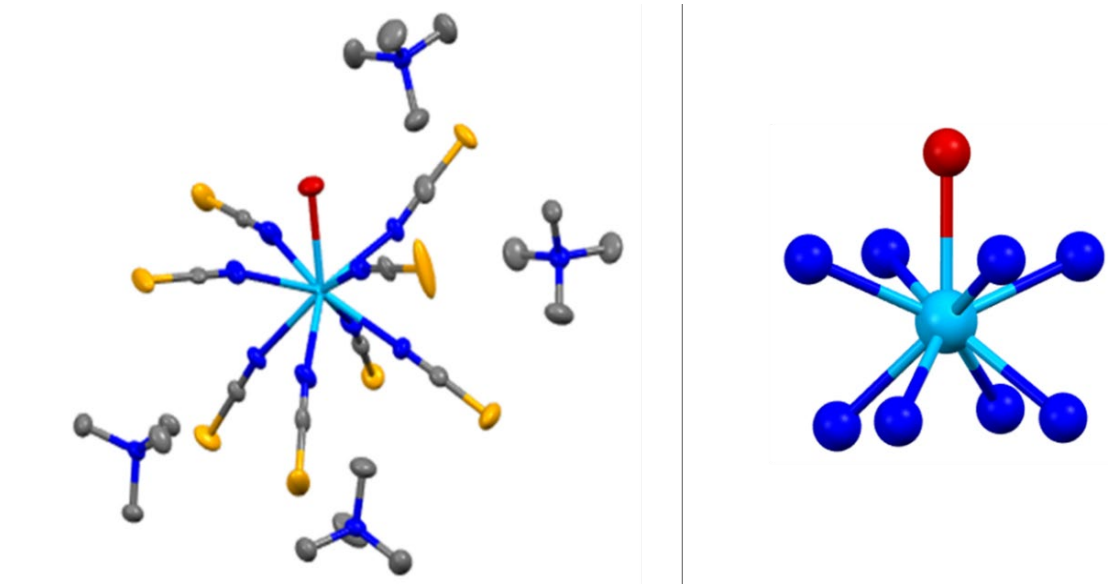

Figure 2.6. (Left) Molecular structure of $[Me_4N]_4[Th(NCS)_8(H_2O)]$, with hydrogen atoms omitted for clarity. Atomic displacement shown at 50% probability. (Right) Depiction of the Th(IV) coordination geometry. Colour code: Th – light blue, N – dark blue, C – grey, O – red, S – yellow.

The synthesis of the thorium complexes was initially attempted using $Th(NO_3)_4{\cdot}5H_2O$ as the source of Th(IV), but with this reagent the reaction worked well only for $[Et_4N]_4[Th(NCS)_8]$. For $[^nPr_4N]_4[Th(NCS)_8]$ a white gel was the only material isolated that was not possible to recrystallize; instead, with $[Me_4N]^+$ as counter-cation, the full substitution of the nitrate ions in $Th(NO_3)_4{\cdot}5H_2O$ was not achieved and the 9-coordinate mixed-ligand species $[Me_4N]_4[Th(NCS)_7(NO_3)].2MeCN$ was formed. Upon repeating the reaction, a different structure was also obtained that was disordered, but it was possible, with some restraints, to refine this to 95% of $[Me_4N]_4[Th(NCS)_7(NO_3)].4MeCN$ and 5% of a 10-coordinate $[Me_4N]_4[Th(NCS)_6(NO_3)_2]$. The solid-state crystal structures of $[Me_4N]_4[Th(NCS)_7(NO_3)].2MeCN$ and of the anion $[Th(NCS)_6(NO_3)_2]^{4-}$ are shown in Figure 2.7. The corresponding crystallographic data are listed in Appendix 1. Moreover, the full list of bond lengths and angles are tabulated in Appendix 1.6, in the external CD source of this thesis.

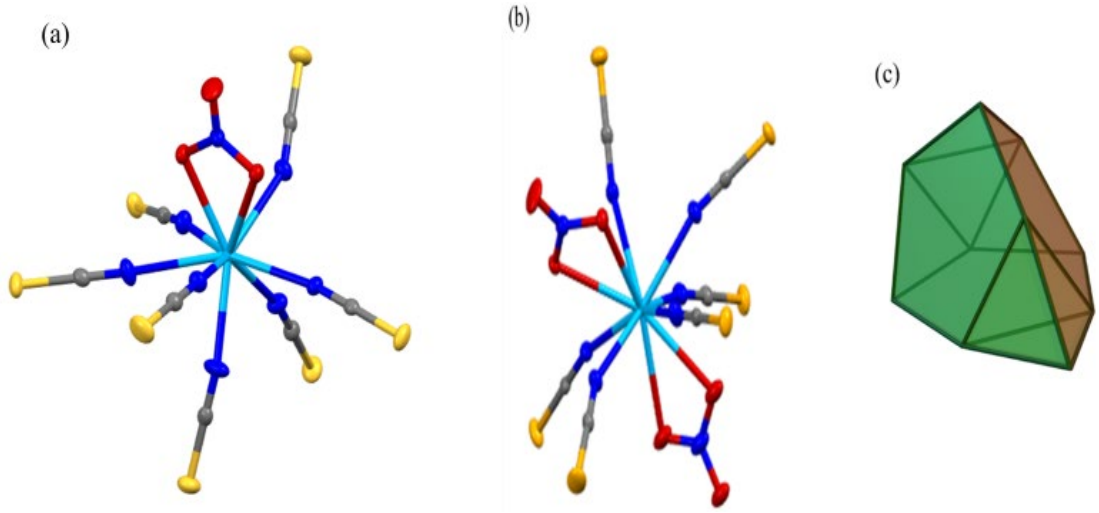

Figure 2.7. (a) Molecular structure of $[Th(NCS)_7(NO_3)]^{4-}$. (b) Disordered component of $[Th(NCS)_6(NO_3)_2]^{4-}$ (5% occupied). Atomic displacement shown at 50% probability and hydrogen atoms omitted for clarity. Colour code: Th – light blue, N – blue, C – grey, S – yellow, O – red. (c) Picture of the geometry in $[Th(NCS)_6(NO_3)_2]^{4-}$.

In $[Me_4N]_4[Th(NCS)_7(NO_3)]$, the Th(IV) ion is bound to seven thiocyanate ions, through Th–N bonds, and to one chelating nitrate ion, through two Th–O bonds, and the coordination geometry is mono-capped square antiprism (C_{4v}) from shape analysis[39] (CSAPR-9: 0.839). In turn, in $[Th(NCS)_6(NO_3)_2]^{4-}$, the Th(IV) ion is 10-coordinate, being bound to six thiocyanate ligands, through Th–N bonds, and two chelating nitrate ions, via two Th–O bonds. Moreover, from shape analysis,[39] the coordination geometry (Figure 2.7b) is distorted between augmented tridiminished icosahedron (C_{3v}, 18.693; Figure 2.7d) and bicapped cube (D_{4h}, 20.845), with a deviation path from the first to the second symmetry of 119.7. With caution, it is also possible to compare the structural parameters of these two complexes with those reported for $[^nBu_4N]_3[Th(NO_3)_3(NCS)_4]$.[40] The average Th–N and Th–O bond lengths are essentially invariant as are the N=C and C=S bond lengths, in line with the ionic nature of the bonding with these ligands.

2.2.2 Structural Distortion Study on $[Et_4N]_4[U(NCS)_8]$

The X-ray diffraction of single crystals of the cubic $[Et_4N]_4[An(NCS)_8]$ (An = Th, U) compounds revealed, at 100 K, structures (Figure 2.8) with a disorder in the position of the coordinated nitrogen atoms which was greater in the uranium complex. In Figure 2.8, the thermal ellipsoids at the coordinated nitrogen atoms are more oblate in the $5f^2$ uranium than in the $5f^0$ thorium complex. This comparison could signify that an electronic effect is

the cause for the unresolved disorder observed at the nitrogen atoms in the structure of $[U(NCS)_8]^{4-}$. Interestingly, in the structure of the Pu(IV) analogue $[Et_4N]_4[Pu(NCS)_8]$,[37] the nitrogen atoms were refined isotropically and no discussion was made on the thermal ellipsoids. However, in this compound, it could be very interesting to try to explain this disorder looking for an electronic effect, which indeed should also be more important than a possible one in the U(IV) equivalent, since Pu(IV) has four *f* unpaired electrons while U(IV) only two.

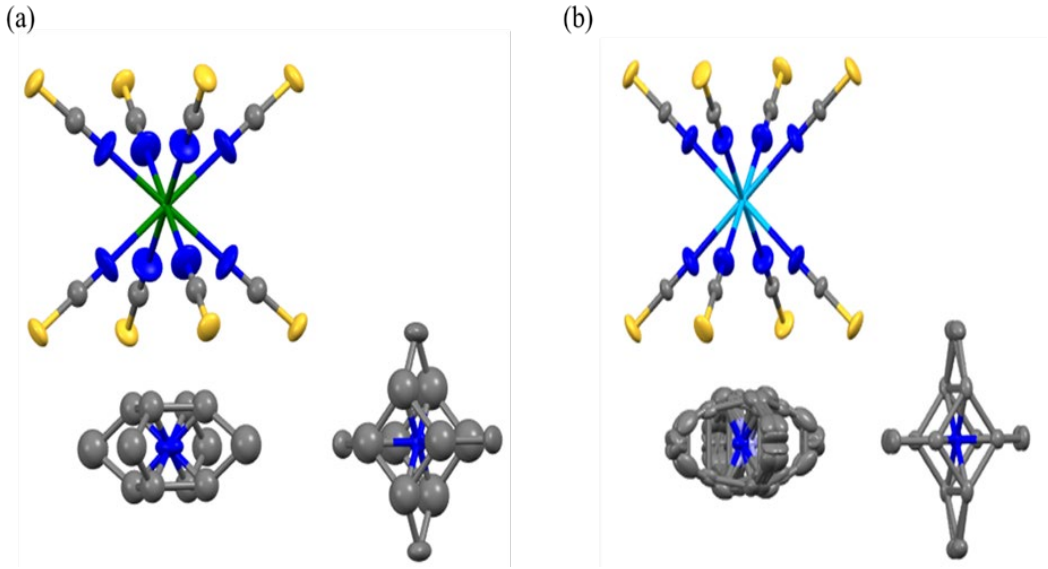

Figure 2.8. Molecular structure of (a) $[Et_4N]_4[U(NCS)_8]$ and (b) $[Et_4N]_4[Th(NCS)_8]$, measured at 100 K. Hydrogen atoms omitted for clarity and atomic displacement shown at 50% probability. Colour code: U – green, Th – light blue, N – blue, C – grey, S – yellow.

To further examine the structural disorder in $[Et_4N]_4[U(NCS)_8]$, in comparison to the thorium analogue, the crystal structure of these two complexes was measured by ultra-low temperature (4 K) X-ray and neutron single-crystal diffraction. In addition, variable temperature powder neutron diffraction measurements was performed for the uranium compound. For these measurements, the ultra-low temperatures were applied in order to reduce the vibrational motion of the atoms, to increase the atomic displacement probability.

The powder neutron diffraction measurements were carried out by Dr. D. Fortes, at the ISIS Neutron and Muon Facility in Harwell (UK), on the perdeuterated uranium compound $[d_{20}\text{-}Et_4N]_4[U(NCS)_8]$ (prepared reacting $Na_4[U(NCS)_8]$ with $d_{20}\text{-}Et_4NBr$) and the data (Figure 2.9) show no variation in the symmetry upon cooling from room temperature to 4 K. A tetragonal cell metric is retained at all temperatures and the refined

unit-cell parameters, from the measurements on HRPD, are listed in Table 2.4. Details on the diffractometer and sample preparation are described in the Appendix 1.

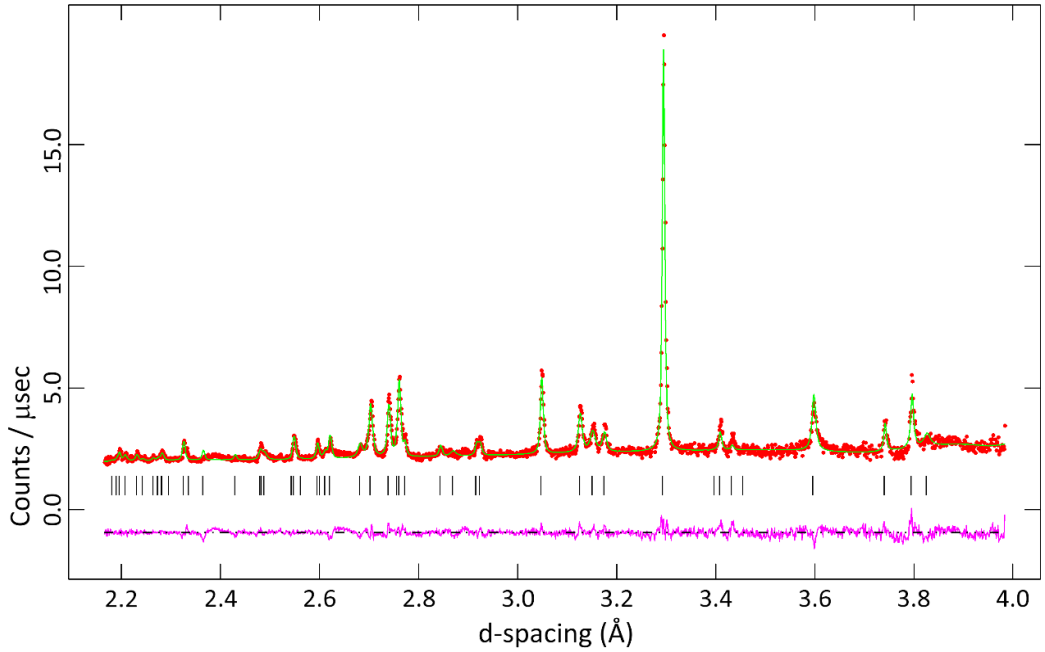

Figure 2.9. Neutron powder diffraction pattern of $[d_{20}\text{-}Et_4N]_4[U(NCS)_8]$ collected at 4.7 K on HRPD. Data are from the instrument's backscattering bank, measured in time-of flight window from 100-200 ms. Filled red circles are the measured data. Vertical tick marks underneath the diffraction pattern show the expected positions of Bragg reflections.

Table 2.4. Refined unit-cell parameters from measurement on HRPD.

Temperature (K)	a = b (Å)	c (Å)	V (Å^3)	c/a
200	11.52164(21)	22.9936(8)	3052.35(10)	1.9957
100	11.43675(19)	22.9704(7)	3004.51(10)	2.00085
4	11.37657(19)	22.9565(8)	2971.17(9)	2.0179

The X-ray diffraction measurements at 4 K have been performed with the aid of Dr. M. Probert at University of Newcastle and the corresponding structures of $[Et_4N]_4[U(NCS)_8]$ and $[Et_4N]_4[Th(NCS)_8]$ are shown in Figure 2.10.

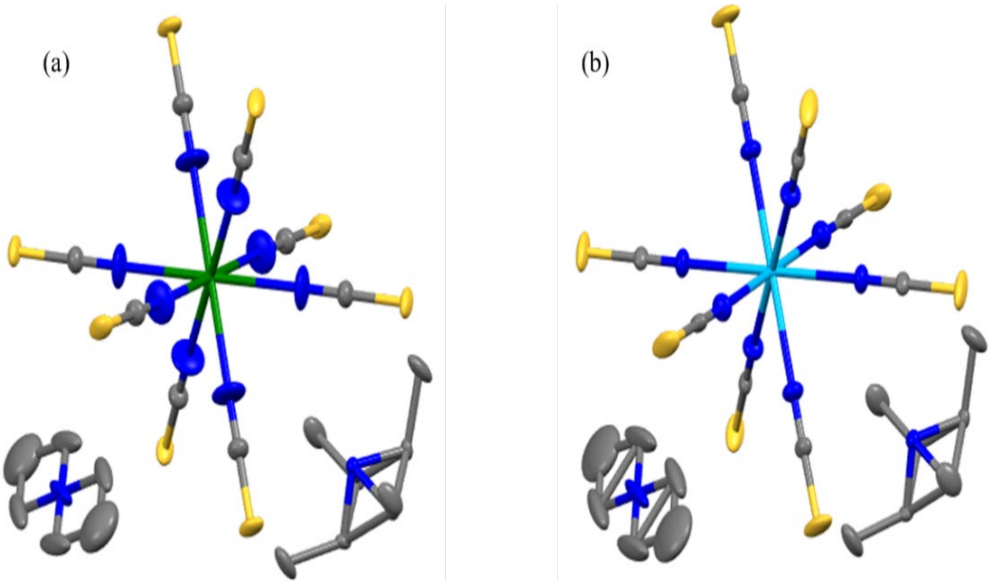

Figure 2.10. X-ray diffraction structures of (a) $[Et_4N]_4[U(NCS)_8]$ and (b) $[Et_4N]_4[Th(NCS)_8]$, measured at 4 K and showing the thermal ellipsoids of the atoms. Atomic displacement shown at 90% probability and H atoms omitted for clarity. Colour code: U – green, Th – light blue, N – blue, C – grey, S – yellow.

In these structures the atomic displacement is shown at 90% probability (Figure 2.10) and, in comparison with the structures measured at 100 K (Figure 2.8), it is even more evident that the disorder at the coordinated nitrogen atoms is greater in the $5f^2$ uranium than in the $5f^0$ thorium complex. The thermal ellipsoids at the nitrogen atoms are, indeed, significantly more oblate in the uranium than in the thorium compound; this reinforces the hypothesis that an electronic effect is the origin for the unresolved disorder in the position of the coordinated nitrogen atoms in $[Et_4N]_4[U(NCS)_8]$. This effect could also imply a small distortion of the cubic geometry around the U(IV) ion, which, however, is not evident. It is possible to say that, in this case, the high symmetry of the point group of this molecule forces the uranium coordination geometry toward a cubic symmetry (Figure 2.10, left).

Moreover, to further examine the differences in the $An–N_8$ coordination sphere between $[Et_4N]_4[U(NCS)_8]$ and $[Et_4N]_4[Th(NCS)_8]$, the structural parameters, d_{pp}, d_{in} and θ (illustrated in Figure 2.4) have been measured also for the X-ray structures measured at 4 K (Figure 2.10) and are listed in Table 2.5. The data relative to the structure of $[Et_4N]_4[Pu(NCS)_8]$, measured at 300 and 100 K,[37] and to the same structures of $[Et_4N]_4[An(NCS)_8]$ (An = Th, U), but measured at 300 and 100 K for Th,[37] and at 300,

200 and 100 K for U, have been added to investigate the influence of the temperature on the values of these geometrical parameters.

Table 2.5. Selected geometrical parameters for the An–N_8 coordination sphere at different temperatures, with An = Th, U and Pu.

Compound	d_{pp} (Å)	d_{in} (Å)	$\frac{d_{pp}}{d_{in}}$	θ (°) (average)	CU	SAP
$[Et_4N]_4[Th(NCS)_8]$ at 300 K[a]	2.854(7)	3.997(7)	0.714	54.47(16)	0.00	10.97
$[Et_4N]_4[Th(NCS)_8]$ at 100 K	2.87531(8)	4.05102(8)	0.710	54.6339(9)	0.00	10.99
$[Et_4N]_4[Th(NCS)_8]$ at 4 K	2.884(3)	4.067(5)	0.709	54.66(8)	0.00	10.98
$[Et_4N]_4[U(NCS)_8]$ at 300 K	2.827(4)	3.955(3)	0.715	54.45(4)	0.00	10.97
$[Et_4N]_4[U(NCS)_8]$ at 200 K	2.80147(15)	3.92958(14)	0.713	54.5142(17)	0.00	-
$[Et_4N]_4[U(NCS)_8]$ at 100 K	2.79304(7)	3.94870(7)	0.707	54.7270(9)	0.00	10.98
$[Et_4N]_4[U(NCS)_8]$ at 4 K	2.786(2)	3.946(6)	0.706	54.78(9)	0.00	10.98
$[Et_4N]_4[Pu(NCS)_8]$ at 300 K[a]	2.746(5)	3.849(7)	0.713	54.49(13)	-	-
$[Et_4N]_4[Pu(NCS)_8]$ at 100 K[a]	2.752(4)	3.863(5)	0.712	54.53(9)	0.00	-

a - Structure from Ref. 37

The data in Table 2.5 show that, as the temperature is lowered, the An–N_8 coordination geometry undergoes an axial compression toward a pure cubic symmetry in all the compounds. In fact, the ratio d_{pp}/d_{in} decreases from 0.714 (at 300 K) to 0.709 (at 4 K) for $[Th(NCS)_8]^{4-}$, from 0.715 (at 300 K) to 0.707 (at 4 K) for $[U(NCS)_8]^{4-}$ and from 0.713 (at 300 K) to 0.712 (at 100 K) for the plutonium derivative. Simultaneously the angle θ slightly increases from 54.470 (at 300 K) to 54.660 (at 4 K) in the case of $[Th(NCS)_8]^{4-}$, from 54.450 (at 300 K) to 54.730 (at 4 K) for $[U(NCS)_8]^{4-}$ and from 54.490 (at 300 K) to 54.839 (at 100 K) for $[Pu(NCS)_8]^{4-}$. Moreover, at 300 K, the cubic An–N_8 coordination sphere is slightly axially elongated for all the actinide complexes ($\theta < 54.74°$).

In these X-ray structures the diffraction pattern is dominated by the heavy actinide atoms, as expected. Therefore, to gain better information on the atomic positions, thermal vibrations and possible disorder of the lighter atoms in the structures of $[Et_4N]_4[Th(NCS)_8]$ and $[Et_4N]_4[U(NCS)_8]$, the crystal structures of these two actinide complexes were further determined by neutron diffraction experiments. Thus, over the course of two months and by diffusion of dried diisopropyl ether into MeCN solutions, single crystals of approximate dimensions of 5 mm x 5 mm x 2 mm were grown for both complexes (Figure 2.11) and analysed by single-crystal neutron diffraction at 4 K. These measurements were performed by Dr. S. Capelli on SXD at the ISIS Neutron and Muon Facility in Harwell (UK), the results are shown in Figure 2.12. Supplementary details on the sample preparation and on the experimental acquisition of the data are discussed in Appendix 1.

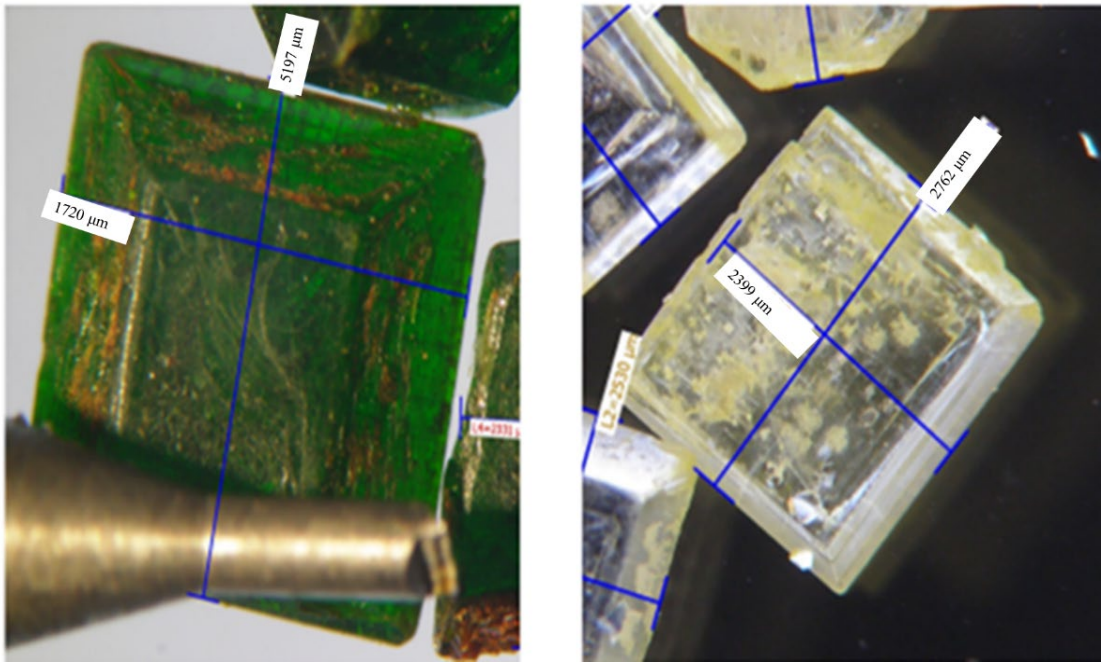

Figure 2.11. Single crystals of (left) $[Et_4N]_4[U(NCS)_8]$ and (right) $[Et_4N]_4[Th(NCS)_8]$, grown for neutron diffraction measurements. In the picture of the uranium sample is also shown the pin onto which the crystal has been mounted before the measurement. Photos taken using a digital camera and under an Olympus SZX16 microscope.

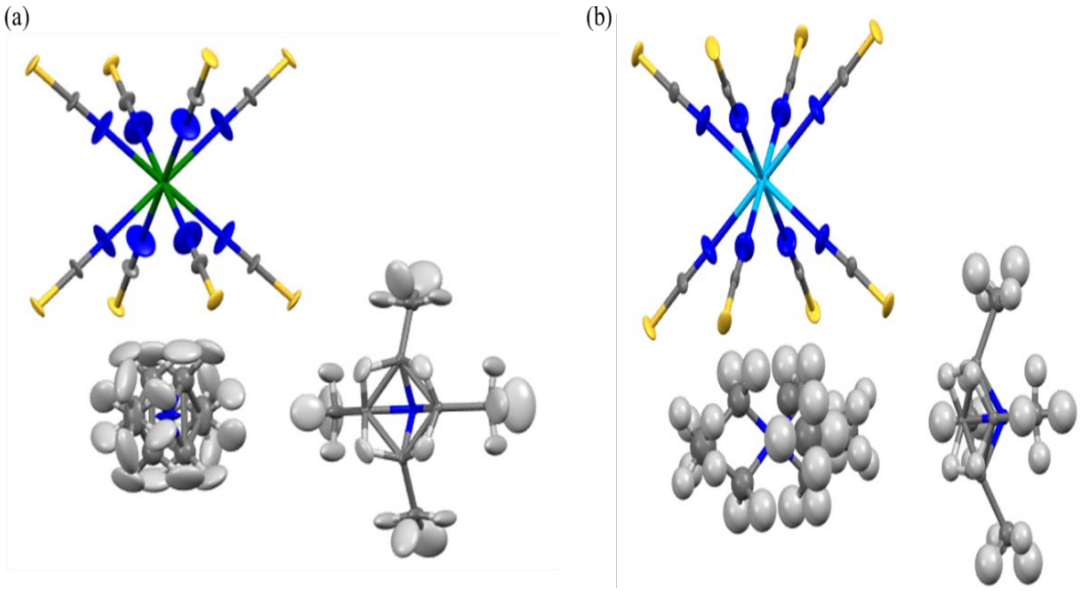

Figure 2.12. Neutron diffraction structures of (a) $[Et_4N]_4[U(NCS)_8]$ and (b) $[Et_4N]_4[Th(NCS)_8]$, measured at 4 K and showing the thermal ellipsoids of the atoms. Atomic displacement shown at 90% probability. The $[Et_4N]^+$ cation has been refined anisotropically only for the uranium complex. Colour code: U – green, Th – light blue, N – blue, C – grey, S – yellow, H – white.

In these neutron diffraction structures, the metric parameters of the ion $[An(NCS)_8]^{4-}$ (An = Th, U) are indistinguishable from the ones observed in the X-ray structures measured at the same temperature (Table 2.5). Moreover, the atomic displacement is shown at 90% probability (Figure 2.12) and, as already observed in the X-ray structures (Figure 2.10), the thermal ellipsoids at the coordinated nitrogen atoms are more oblate in the $5f^2$ uranium than in the $5f^0$ thorium complex. Thus, the neutron diffraction measurements validate the results from the X-ray diffraction study that the unresolved disorder in the position of the coordinated nitrogen atoms in $[Et_4N]_4[U(NCS)_8]$ is likely due to an electronic effect.

2.2.3 Vibrational Characterization

The vibrational data, most usefully the Raman spectra, can help to confirm the geometry adopted by the thorium and uranium complexes. Indeed, it has been reported that, when $[U(NCS)_8]^{4-}$ exhibits a cubic coordination symmetry (as in the case of $[Et_4N]_4[U(NCS)_8]$), the corresponding solid-state Raman spectrum shows two ν(C=N) stretches (A_{1g} and T_{2g}) at 2090 and 2040 cm^{-1}, while the IR spectrum displays one single absorption (T_{1u}) for the ν(C=N) stretching at 2047 cm^{-1}.[33] With a square antiprismatic coordination symmetry (as in the case of $Cs_4[U(NCS)_8]$), the solid-state Raman spectrum displays three ν(C=N)

stretches (A_1, E_2 and E_3) at 2090, 2055 and 2045 cm^{-1}, while, in the solid-state IR spectrum, two ν(C=N) stretches (B_2 and E_1) are observable at 2047 and 2090 cm^{-1}.[32]

Thus, Raman and IR spectra have been recorded for all the actinide thiocyanate complexes in solid state. The results are shown in Figure 2.13 for the uranium samples and in Figure 2.14 for the thorium equivalents. The measurements have been performed also in solution where, however, due to the loss of the crystal packing forces, the complexes exhibit the same ideal square antiprismatic symmetry and thus the same spectra; this is also in agreement with previous analysis.[34]

The absence of crystal packing forces in solution was also confirmed by ^{1}H DOSY NMR spectroscopic measurements performed on three solutions of $[Me_4N]_4[U(NCS)_8]$ in D-MeCN with different concentrations. No variation in the molecular size of the $[Me_4N]^+$ ions, determined using the Stokes-Einstein equation, was observed varying the concentration; this implies the loss of the weak C–H···S interactions in solution.

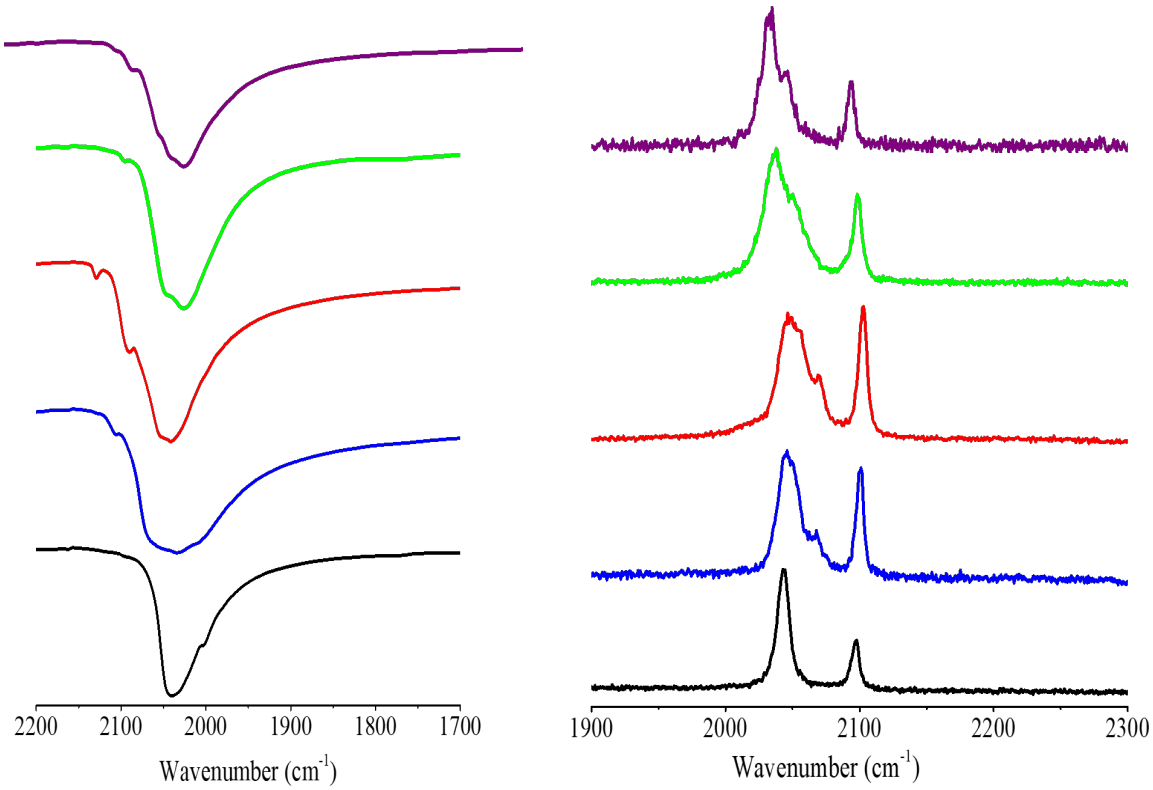

Figure 2.13. (Left) IR and (right) Raman spectra of $[Et_4N]_4[U(NCS)_8]$ (black), $Cs_4[U(NCS)_8]$ (blue), $[^nPr_4N]_4[U(NCS)_8]$ (red), $[Me_4N]_4[U(NCS)_8]$ (green) and $[H_2(2.2.2\text{-cryptand})]_2[U(NCS)_8]$ (purple), showing the regions for the ν(C=N) vibrational modes.

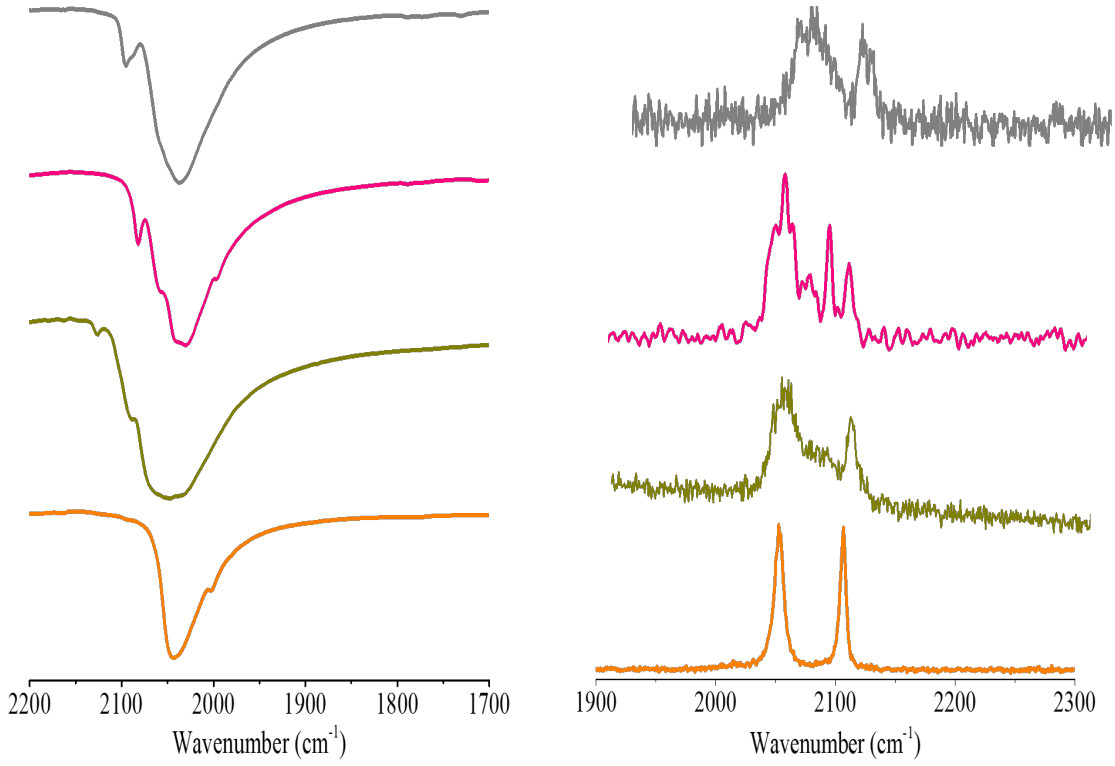

Figure 2.14. (Left) IR and (right) Raman spectra of $[Et_4N]_4[Th(NCS)_8]$ (orange), $Cs_4[Th(NCS)_8]$ (dark yellow), $[^nPr_4N]_4[Th(NCS)_8]$ (pink) and $[Me_4N]_4[Th(NCS)_8]$ (gray), showing the regions for the ν(C=N) vibrational modes.

In the vibrational spectra of Figure 2.13 and Figure 2.14, the ν(C=N) vibrational modes displayed by $A_4[An(NCS)_8]$ ($A = Cs^+$, $[Et_4N]^+$; An = U, Th) confirm the CU (O_h) and SAP (D_{4d}) symmetry for $[Et_4N]_4[An(NCS)_8]$ and $Cs_4[An(NCS)_8]$ (An = U, Th), respectively.

Regarding the other three uranium compounds of the series, $[^nPr_4N]_4[U(NCS)_8]$ displays two IR active ν(C=N) stretches at 2042 and 2091 cm^{-1} and three Raman active ν(C=N) stretches at 2046, 2069 and 2103 cm^{-1}, $[H_2(2.2.2\text{-cryptand})]_2[U(NCS)_8]$ shows two IR active ν(C=N) stretches at 2039 and 2026 cm^{-1} and three Raman active ν(C=N) stretches at 2093, 2045 and 2034 cm^{-1}, while $[Me_4N]_4[U(NCS)_8]$ exhibits two IR active ν(C=N) stretches at 2048 and 2027 cm^{-1} and three Raman active ν(C=N) stretches at 2039, 2050 and 2098 cm^{-1}. These data are in agreement with a distorted from SAP geometry (symmetry D_4) for the $[U(NCS)_8]^{4-}$ ion present in these three complexes at solid state.

Regarding the spectra of the other two thorium complexes (Figure 2.14), $[^nPr_4N]_4[Th(NCS)_8]$ displays two IR active ν(C=N) stretches (B_2 and E) at 2082 and 2030 cm^{-1} and four Raman active ν(C=N) stretches (A_1, B_1, B_2 and E) at 2047, 2069, 2085 and 2101 cm^{-1}, while $[Me_4N]_4[Th(NCS)_8]$ displays two IR active ν(C=N) stretches at 2096 and 2037 cm^{-1} and two poorly resolved Raman active ν(C=N) stretches at 2050 and 2092

cm^{-1}. These data confirm that, in solid state, the $[Th(NCS)_8]^{4-}$ ion adopts a TDD (D_{2d}) symmetry in $[^nPr_4N]_4[Th(NCS)_8]$ and a distorted geometry from square antiprismatic in $[Me_4N]_4[Th(NCS)_8]$.

Raman and IR spectra have been acquired also for $[Me_4N]_4[Th(NCS)_7(NO_3)]$ (Figure 2.15), in order to confirm the monocapped square antiprismatic coordination geometry shown by the corresponding $[Th(NCS)_7(NO_3)]^{4-}$ anion. This geometry falls into the C_{4v} point group and, therefore, $[Me_4N]_4[Th(NCS)_7(NO_3)]$ should display four Raman active ν(C=N) stretches (A_1, B_1, B_2, E) and two IR active ν(C=N) stretches (A_1, E).

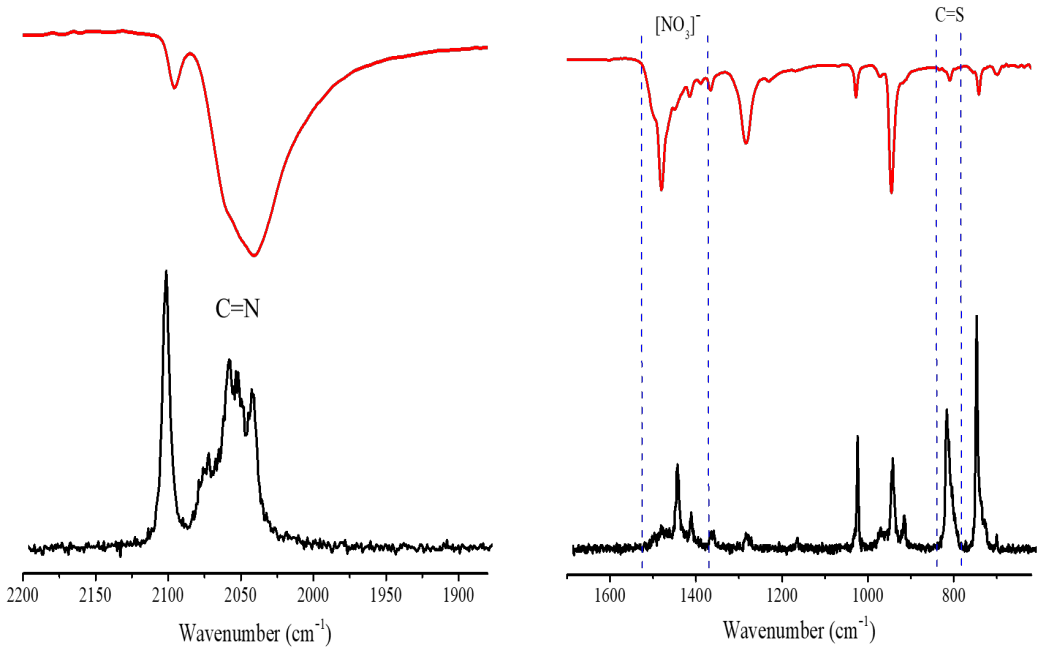

Figure 2.15. (Bottom) Raman and (top) IR spectrum of $[Me_4N]_4[Th(NCS)_7(NO_3)]$, measured in solid state.

The Raman spectrum of $[Me_4N]_4[Th(NCS)_7(NO_3)]$ (Figure 2.15, black line) shows five ν(C=N) stretches at 2045, 2056, 2062 and 2105 cm^{-1}, one ν(C=S) stretch at 828 cm^{-1} and bands associated with the $[NO_3]^-$ group at 1455 cm^{-1}. Thus, in contrast with the theory, there appear an additional fifth band for the ν(C=N) stretch. This is perhaps due to a coexistence between $[Me_4N]_4[Th(NCS)_7(NO_3)]$ and $[Me_4N]_4[Th(NCS)_6(NO_3)_2]$ whose $[Th(NCS)_6(NO_3)_2]^{4-}$ anion exhibits a different coordination geometry. Moreover, in the IR spectrum (Figure 2.15, red line), in line with the theory there are two bands for the ν(C=N) stretch at 2095 and 2041 cm^{-1}, while the IR active ν(C=S) stretch is observable at 809 cm^{-1} and the bands associated with the $[NO_3]^-$ group appear at 1480 cm^{-1}.

2.2.4 Magnetic Properties of $A_4[U(NCS)_8]$ Compounds

The focus of this study was to examine how the electronic ground state can change with different coordination geometries. To probe this, the magnetic properties have been measured by SQUID magnetometry on crushed X-ray quality single crystals. The results for the uranium samples are shown in Figure 2.16, and the data have been subsequently analysed using the CONDON approach.[41] The thorium compounds have also been analysed and they proved to be diamagnetic, as expected. The results for $[Et_4N]_4[Th(NCS)_8]$, as example for the thorium series, are reported in Appendix 1, Figure 7.3. The trend of the χT data is linear and negative with the temperature, in line with a diamagnetic nature. The calculated Pascal diamagnetism (red solid line) is in good agreement with the experimental data.

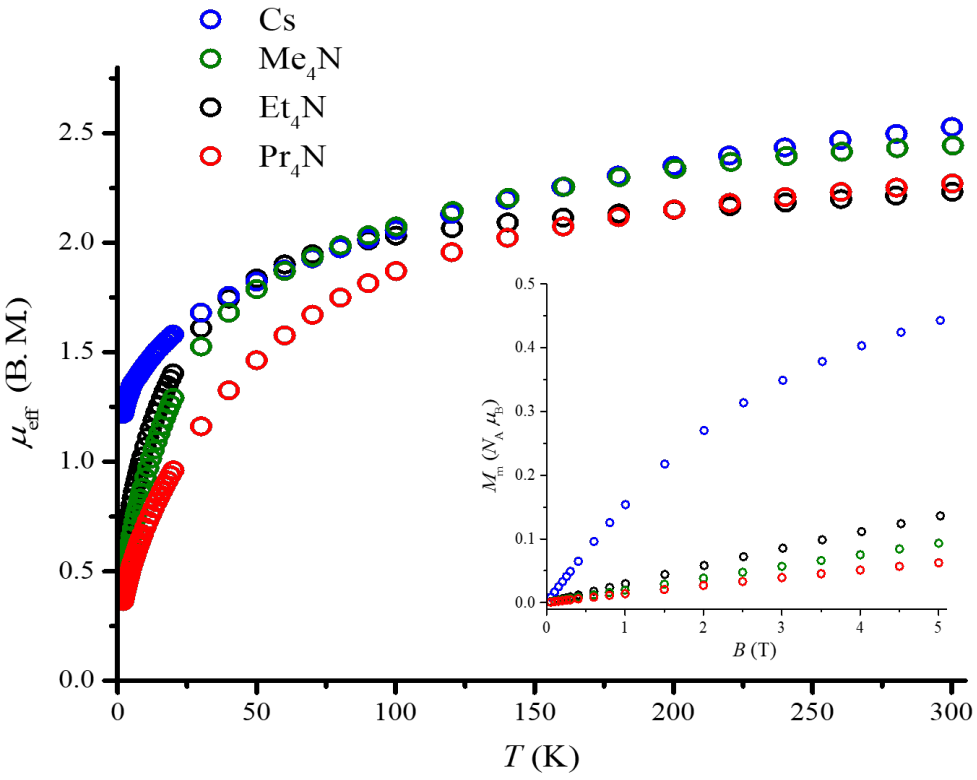

Figure 2.16. (Left) Experimental effective magnetic moments of $A_4[U(NCS)_8]$ {A = Cs (blue); Me_4N (green); Et_4N (black); $^nPr_4N$ (red)}, measured at B = 0.1 T. Inset: molar magnetization M_m vs applied magnetic field B of $A_4[U(NCS)_8]$ {A = Cs (blue); Me_4N (green); Et_4N (black); $^nPr_4N$ (red)} at 2.0 K (3.0 K for Me_4N)}. Experimental data for Cs and Et_4N taken from reference 34.

For the uranium compounds, at 300 K, the values of μ_{eff} are 2.53, 2.44, 2.23, and 2.27 B. M. for Cs, Me_4N, Et_4N, and $^nPr_4N$, respectively. On cooling the compounds, these

values continuously decrease reaching at 2.0 K values of: Cs = 1.22 B. M., Me_4N = 0.42 B. M., Et_4N = 0.52 B. M. and $^{n}Pr_4N$ = 0.36 B.M. It is clear from this analysis that the geometry does have an influence on the magnetic properties of the U(IV) ion and suggests that a different magnetic ground-state is observable. This is also observable in the field dependence of the molar magnetization M_m at low temperatures (Figure 2.16, inset). The molar magnetizations are roughly linear functions of the applied field for the alkylammonium derivates reaching a small value in the range 0.05 - 0.15 $N_A \mu_B$ at 5.0 T, while the magnetization curve of Cs shows a distinct curvature reaching a value of 0.44 $N_A \mu_B$ at 5.0 T. To further probe the difference in the magnetic behaviour, specific heat capacity measurements have been performed on the uranium complexes down to 0.3 K (Figure 2.17).

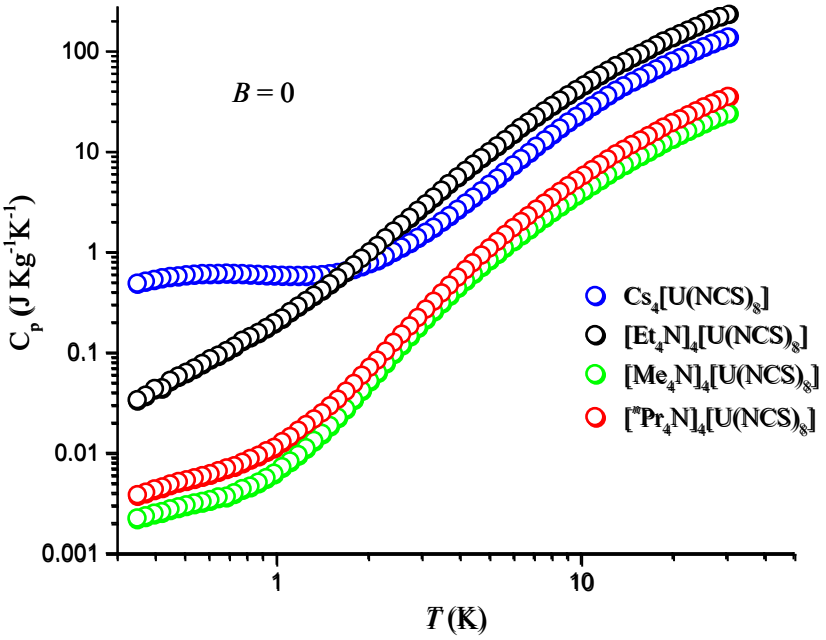

Figure 2.17. Low-temperature dependence of the experimental zero-field-applied heat capacity C_p for $A_4[U(NCS)_8]$ {A = Cs (blue); Me_4N (green); Et_4N (black); $^{n}Pr_4N$ (red)}, as labelled.

The heat capacity of each compound increases with temperatures higher than *ca.* 2 K. More importantly, below 1 K, the Me_4N and $^{n}Pr_4N$ compounds show similar values, but Et_4N and, more strikingly, Cs have higher values (Figure 2.17). At these low temperatures, the lattice contribution to the heat capacity is negligible and the measured heat capacity can be ascribed to magnetic degrees of freedom.[42] Therefore, these measurements probe the low-lying energy levels and they clearly corroborate, albeit qualitatively, the magnetization data.

2.2.5 CONDON Calculations on $A_4[U(NCS)_8]$

Since the contribution from interelectronic repulsion (≈ 10^4 cm^{-1}), spin-orbit coupling (≈ 10^3 cm^{-1}) and ligand field (≈ 10^3 cm^{-1}) are of the same energetic order, none of them should be treated in terms of perturbation theory. Therefore, the magnetic data of the uranium compounds have been fitted using the computational framework CONDON,[41] because it numerically solves a semi-empirical Schrödinger equation without using perturbation theory. These calculations have been performed by Prof. P. Kögeler from University of Aachen.

With actinide compounds, the corresponding data for the parametrization of interelectronic repulsion and spin-orbit coupling are scarce and may distinctly change with different coordination geometries, or with different ligands, in comparison to lanthanide or transition metal compounds. Nevertheless, it was possible to include in the magnetochemical analysis complementary data from other spectroscopic measurements; thus, the results from the far infrared (FIR) and inelastic neutron (INS) measurements (section 2.2.10) have been incorporated in the calculations. However, it is important to note that these were insufficient to derive a reliable set of Slater-Condon parameters and spin-orbit coupling constants; therefore, these parameters have been fixed for all compounds as mean values from analyses[43] of various U(IV) compounds: $F^2 \approx 45000$ cm^{-1}, $F^4 \approx 42000$ cm^{-1}, $F^6 \approx 23000$ cm^{-1}, and $\zeta_{5f^2} \approx 1750$ cm^{-1}. This approximation leads to larger uncertainties than expected for transition metals or lanthanide compounds and particularly affects the energies of the higher excited states (> 1000 cm^{-1}) and determining the degree of mixture of the energy states.

Nevertheless, assuming for the $[U(NCS)_8]^{4-}$ ion an approximate symmetry of C_{4v} and D_{4h} with Cs^+, Me_4N^+ and $^n Pr_4N^+$ and with Et_4N^+ as counter cation, respectively, based on the full U–NCS coordination geometry from the crystal structures, the simultaneous least-squares fits of the μ_{eff} vs T and M_m vs B data yield the ligand field parameters B_q^k (Wybourne notation) and relative root mean squared errors SQ given in Table 2.6. The corresponding fits are depicted as solid lines in Figure 2.18.

The qualities of the fits are moderate. However, taking into account the uncertainty introduced by the approximate values for F^n and ζ_{5f^2}, they are acceptable. The best solution found for $^n Pr_4N$ should be carefully regarded due to the rather large SQ of larger than 3%, since there are other solutions with slightly worse SQ (3.6 – 4.2 %) yielding a distinctly

different energy splitting that require large, and thus unlikely, ligand field parameters. The energy levels defined from this fitting are discussed in section 2.2.12.

Table 2.6. Parameters of the least-squares fit of $A_4[U(NCS)_8]$; assumed symmetry for A = Cs, Me_4N and $^nPr_4N$: C_{4v}, A = Et_4N: D_{4h}; F^n and ζ_{5f} derived from literature; errors are statistical only.

Compound	**Cs**	**Me_4N**	**Et_4N**	**$^nPr_4N$**
ζ_{5f^2} (cm^{-1})	1750			
F^2 (cm^{-1})	45000			
F^4 (cm^{-1})	42000			
F^6 (cm^{-1})	23000			
B_0^4 (cm^{-1})	–7397 ± 16	–9910 ± 14	–19777 ± 5	–7016 ± 11
B_4^4 (cm^{-1})	–7788 ± 13	–22068 ± 19	–13326 ± 7	–5485 ± 2
B_0^6 (cm^{-1})	16190 ± 4	5744 ± 20	18258 ± 6	7540 ± 6
B_4^6 (cm^{-1})	–14251 ± 11	–5525 ± 13	–24617 ± 11	–15703 ± 4
SQ	2.8 %	2.4 %	1.8 %	3.4 %

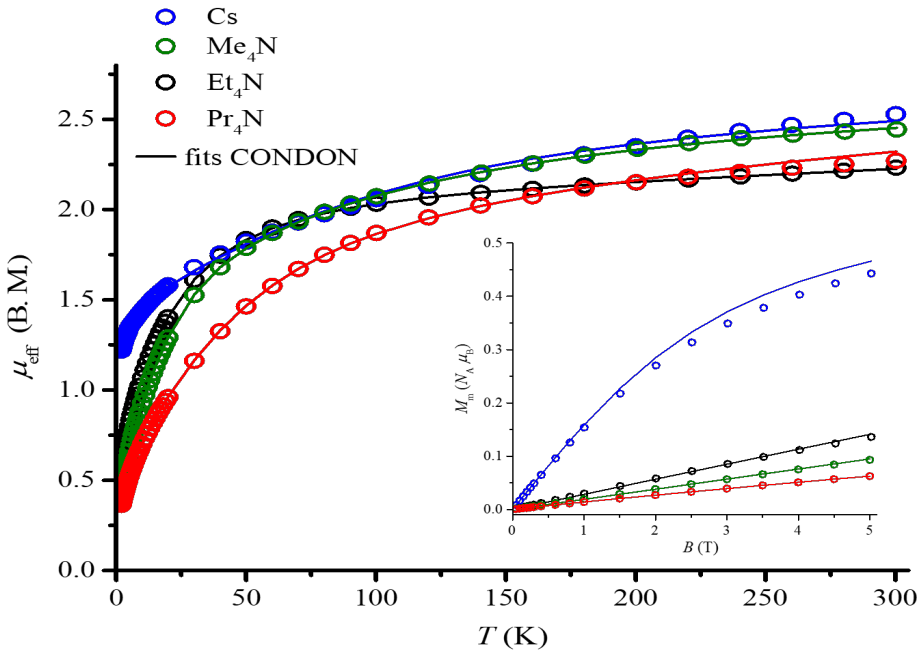

Figure 2.18. Experimental (symbols), fitted from CONDON calculations (solid lines) effective magnetic moments of $A_4[U(NCS)_8]$ {A = Cs (blue); Me_4N (green); Et_4N (black); $^nPr_4N$ (red)} at 0.1 T. Inset: molar magnetization M_m vs applied magnetic field B of $A_4[U(NCS)_8]$ {A = Cs (blue); Me_4N (green); Et_4N (black); $^nPr_4N$ (red)} at 2.0 K (3.0 K for Me_4N). Experimental data for A = Et_4N, Cs taken from reference 34.

2.2.6 EPR Spectroscopy on $A_4[U(NCS)_8]$

To further probe the ground state electronic structure of the uranium compounds, particularly to evidence the difference between a singlet and a triplet ground state, EPR spectroscopic measurements at low temperature have been performed. This analysis was carried out by Dr. D. M. Murphy from Cardiff University. With an integral J quantum number and even number of valence electrons, U(IV) ($5f^2$) is a non-Kramers ion; therefore its compounds are typically EPR silent, particularly in solution.[44] However, in the solid state, the local fields can distort the ion, and a paramagnetic signal can be detected.[44] In solution, the samples were found EPR silent, but in the solid-state $Cs_4[U(NCS)_8]$ produced a weak signal with a broad profile at 150 mT, which is indicative of a half-field transition (Figure 2.19), and therefore suggests the presence of a triplet electronic ground state (S = 1). The broadness of the signal precluded simulations to obtain g values, but this result is also in line with the higher low-temperature effective magnetic moment shown by this compound, compared with the other uranium(IV) samples with a different counter-cation (Figure 2.16). The other compounds were EPR silent also in the solid state.

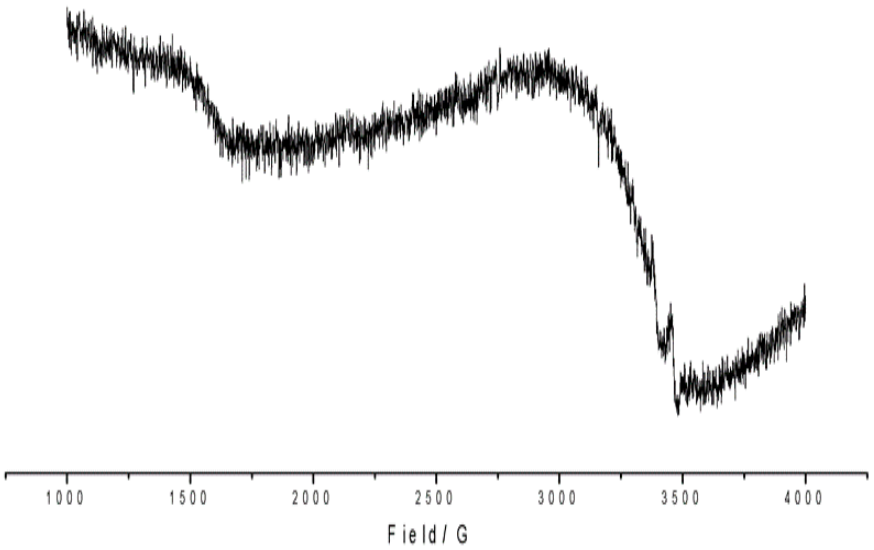

Figure 2.19. CW X-band (140 K) EPR spectrum of $Cs_4[U(NCS)_8]$, recorded as solid powder.

2.2.7 Spectroscopic Determination of Low-Lying Energy Level Structure

In lanthanide compounds, information on the crystal field (CF) splitting can be typically obtained from optical spectroscopies, such as electronic absorption, luminescence, or magnetic circular dichroism (MCD), which allow direct determination of CF splittings of ground and excited multiplets by direct observation of the splittings of peaks due to *f-f* transitions.[45] As an example, Figure 2.20 shows the energy levels for the electronic structure of a free Er^{3+} ion, along with a list of the different spectroscopic techniques required to measure specific energy levels.

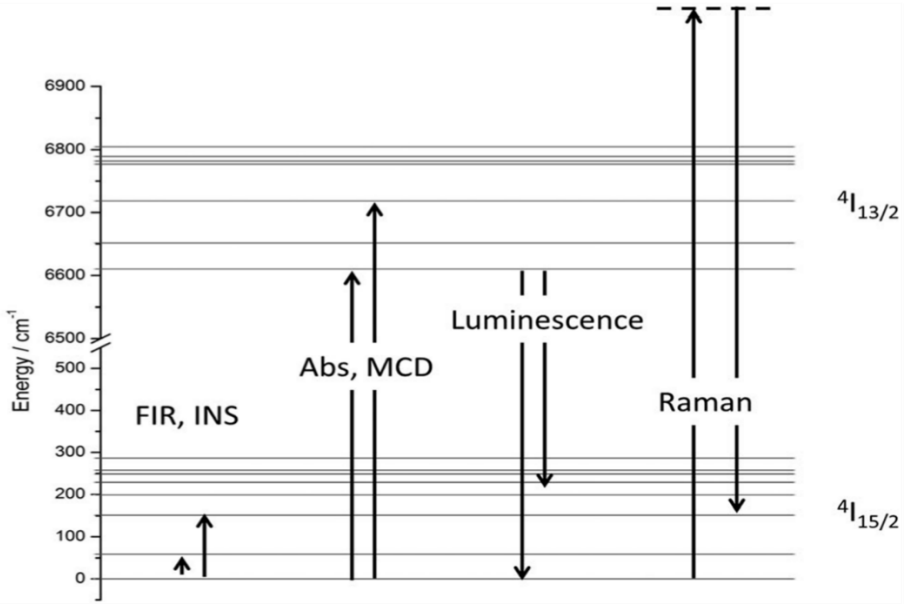

Figure 2.20. Crystal field levels of ground and excited multiplets and spectroscopic techniques to study the electronic structure (example Er^{3+}). Taken from Reference 46.

The situation is more complicated with the actinides. Due to the interplay between spin-orbit coupling, CF splitting and interelectronic repulsion effects, the electronic optical spectra of actinide compounds are much more challenging to understand and do not provide clear information to determine the energy gaps in the low-lying energy level structure. Nevertheless, the electronic structure of the above described $5f^2$ uranium(IV) compounds have been investigated using basic spectroscopic techniques, such as luminescence and UV-vis-NIR absorption spectroscopy, and more advanced ones, including Inelastic Neutron Scattering (INS) and Far Infrared (FIR) spectroscopy to probe the low-lying energy-level electronic structure. The results helped to validate the CONDON fitting of the magnetic profiles (section 2.2.5). Moreover, the spectroscopic measurements have been performed also on the analogues diamagnetic $5f^0$ thorium(IV) complexes, used as blank samples. Finally, to compare with the magnetochemical analysis, CASPT2 calculations have also been used.

2.2.8 Luminescence Spectroscopy

For lanthanide ions, photoluminescence spectroscopy has proved to be useful in probing the emissions to the ground state.[45a,b] Thus, a similar approach has been used for these uranium compounds in the solid state. The measurements have been performed on single crystals and, although these samples have proved to be emissive in solution,[34] in the solid

state it was possible to observe emission only from a uranyl(VI) contamination both at room temperature and at 77 K. Interestingly, the Raman spectra (Figure 2.13) showed no evidence of a uranyl(VI) contamination; this highlights the sensitivity of the emission spectroscopy. Nonetheless, this result is explainable considering the larger fluorescence quantum yield of a uranyl(VI) fragment compared to the U(IV) component.

2.2.9 UV-vis-NIR Spectroscopy

Classically, the CF splitting can be investigated by looking at the electronic transitions in absorption spectra measured in solution. However, due to the loss of the templating effect of the counter-cation, in solution these compounds exhibit the same square antiprismatic (D_{4d}) geometry and thus the same absorption spectrum. As example, the absorption spectrum of $[Et_4N]_4[U(NCS)_8]$ in the visible and NIR region, acquired in MeCN solution at room temperature, is shown in Appendix 1, Figure 7.4.

The spectrum displays the Laporte forbidden *f-f* electronic transitions typical of U(IV) complexes. Their intensity is relatively small (~ 80 - 300 M^{-1} cm^{-1}) suggesting the absence of any "intensity stealing mechanism" in which the *f-f* transitions could gain intensity by coupling to one or more fully allowed transitions, such as charge-transfer transitions within the complex.[47] The absence of this effect, however, is in line with the ionic nature of the U–NCS bonding in these complexes.[34]

To obtain more information on the differences in the CF splitting among these U(IV) complexes, the electronic absorption spectra have been measured on suspensions of these compounds in nujol mull, where this matrix does not influence the geometry as judged by IR spectroscopy. Figure 2.21 shows the bands for the near infrared (left) and visible (right) regions and these are assignable as Laporte forbidden *f-f* electronic transitions typical of U(IV) compounds, confirming the formal +4 oxidation state for the uranium ion in these compounds in solid state. Moreover, at low energy (between *ca.* 4500 and 7500 cm^{-1}), there appear some differences in the energy of these transitions in line with the different coordination geometry adopted by the U(IV) ion in these complexes in solid state.

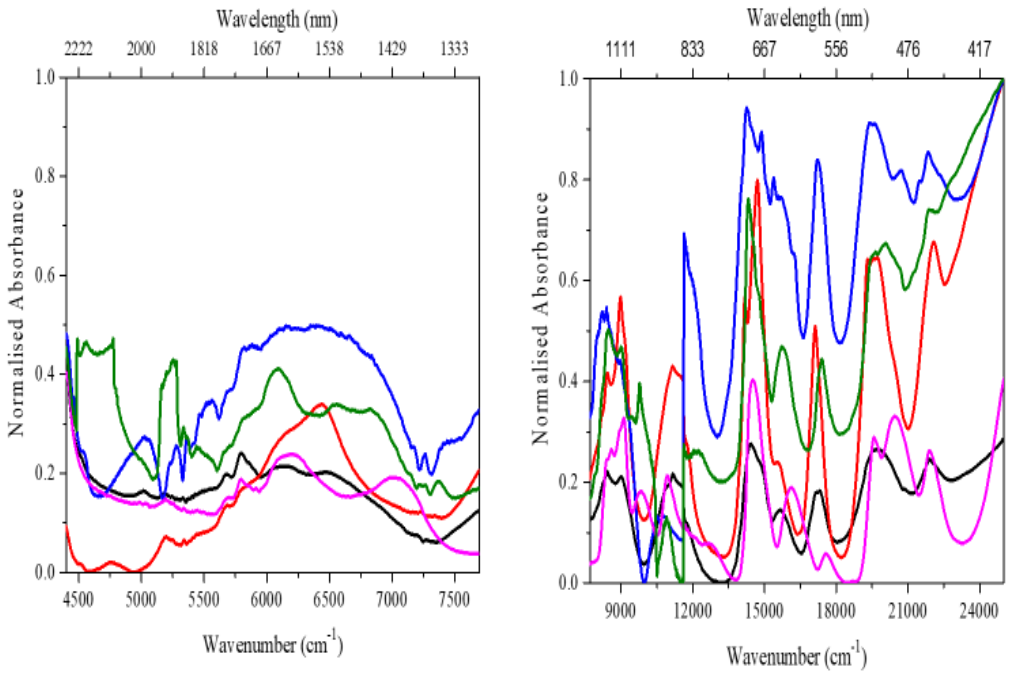

Figure 2.21. Absorption spectra of the $A_4[U(NCS)_8]$ compounds in a nujol mull, showing the *f-f* transitions between (left) 4400 and 7700 cm^{-1} and (right) 7700 and 25000 cm^{-1}. Colour code: $[^nPr_4N]_4[U(NCS)_8]$ (red), $Cs_4[U(NCS)_8]$ (blue), $[Me_4N]_4[U(NCS)_8]$ (black), $[Et_4N]_4[U(NCS)_8]$ (magenta) and $[H_2(2.2.2\text{-cryptand})]_2[U(NCS)_8]$ (green).

2.2.10 INS and FIR spectroscopic measurements

Inelastic Neutron Scattering (INS) and Far Infrared (FIR) measurements have been performed on $[Et_4N]_4[U(NCS)_8]$ and $[Cs]_4[U(NCS)_8]$, which can be considered as the two end members of the geometric distortion (Table 2.3). The combination of these two techniques can allow to directly measure crystal field transitions with energy levels up to *ca.* 500 cm^{-1} above the ground state.

The INS experiments have been performed by Dr. H. C. Walker and Dr M. D. Le at the ISIS Neutron and Muon Facility in Harwell (UK), using both the MARI and MERLIN spectrometers,[48] at three different temperatures: 150, 50 and 5 K. The $5f^0$ Th(IV) analogues, $[Et_4N]_4[Th(NCS)_8]$ and $[Cs]_4[Th(NCS)_8]$, have also been measured acting as isostructural phonon blanks. The results obtained for $[Cs]_4[U(NCS)_8]$ are shown in Figure 2.22, while the procedure for the sample preparation is discussed in the experimental section.

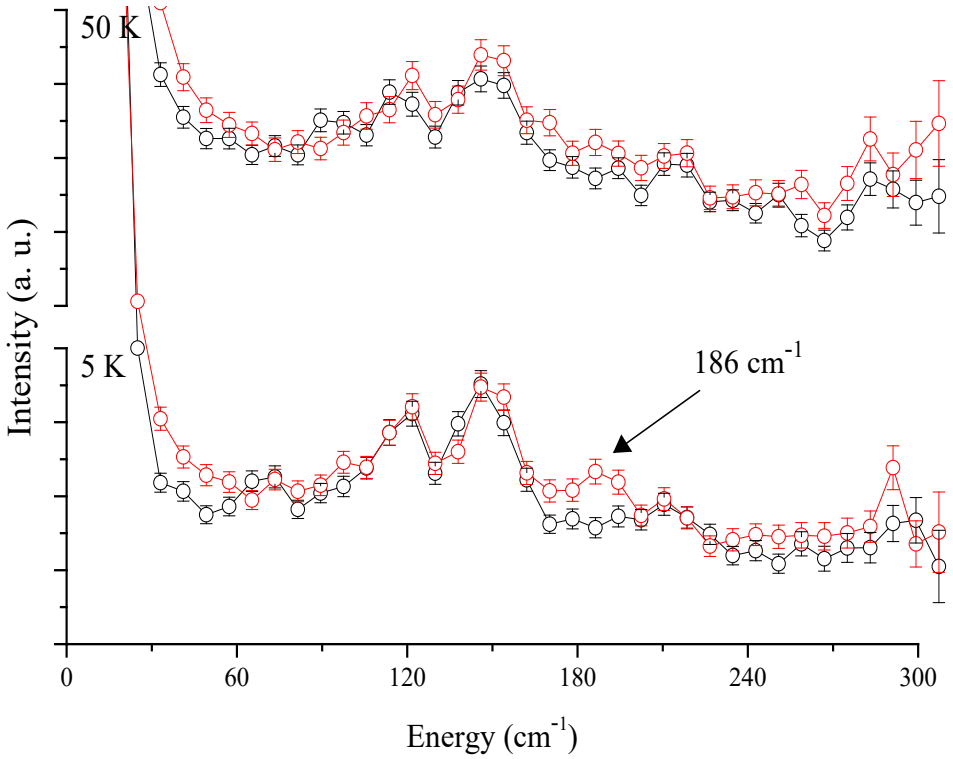

Figure 2.22. INS spectra of $Cs_4[An(NCS)_8]$, measured at (top) 50 K and (bottom) 5 K. (An = Th, black; An = U, red).

For the $[Et_4N]^+$ sample, it was not possible to observe any peaks in the INS spectrum and this could be explained as due to the very high symmetry of this complex or to the fact that incoherent scattering from the hydrogen atoms has screened the crystal field transitions (the measurement was conducted on a non-deuterated sample). However, for the Cs^+ compound, although the spectrum is dominated by phonon peaks, it was possible to observe a single peak at 186 cm^{-1} at 5 K which broadened significantly at 50 K and has a typical Q dependence for a magnetic form factor. This result is interesting since the use of INS spectroscopy for molecular uranium compounds is extremely rare,[49] although it has begun to be used in the investigation of the magnetic properties for molecular lanthanide complexes.[45e, 50]

The compounds $[Et_4N]_4[U(NCS)_8]$, $[Cs]_4[U(NCS)_8]$ and $[^nPr_4N]_4[U(NCS)_8]$ were further analysed by FIR spectroscopy and the measurements were performed by Dr. Milan Orlita, at the Laboratoire National des Champs Magnétiques Intenses in Grenoble. Thus, the samples were pressed into eicosane pellets and measured at variable fields and at 4.2 K. The FIR spectra, measured with $B = 0$ and at 4.2 K, are shown in Appendix 1, Figure 5. These show very strong absorption bands and, in particular, reveal the IR active ν(U–N) stretch, which appears as a strong transition at 186, 189 and 201 cm^{-1} for, respectively,

the Cs, the $^{n}Pr_4N$ and the Et_4N compound. When measured at room temperature, the IR active ν(U–N) vibrational mode gave only very broad bands for all the samples. Subsequently, upon the application of a magnetic field, a series of field dependent bands appeared in the spectra of $[Et_4N]_4[U(NCS)_8]$ and $Cs_4[U(NCS)_8]$ (Figure 2.23).

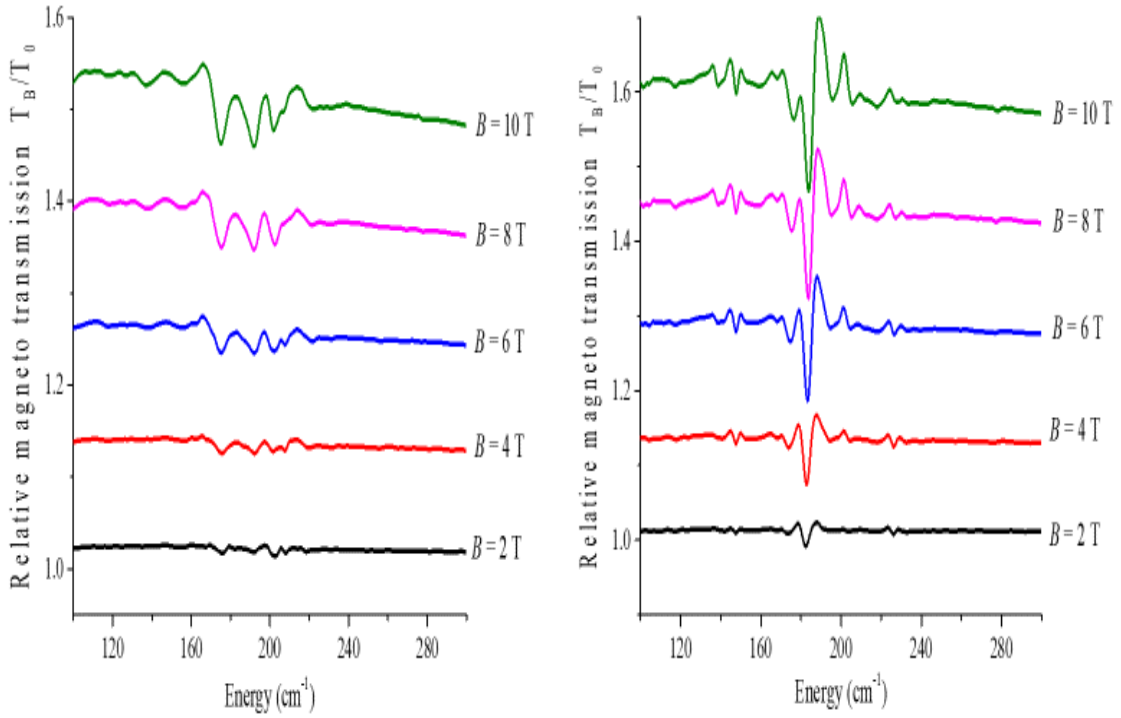

Figure 2.23. FIR spectra of (left) $[Et_4N]_4[U(NCS)_8]$ and (right) $[Cs]_4[U(NCS)_8]$, measured at fields of 2-10 T and at 4.2 K.

The results from this analysis further confirm that crystal packing forces, which give different coordination geometry, have a significant influence on the low-lying energy-level electronic structure of the $[U(NCS)_8]^-$ ion; indeed, the transitions observable for $[Et_4N]_4[U(NCS)_8]$ are different compared to those shown by $Cs_4[U(NCS)_8]$.

The spectra of $Cs_4[U(NCS)_8]$ reveal one strong band at 187 cm^{-1}, which is also in excellent agreement with the INS data (transition at 186 cm^{-1}). Regarding $[Et_4N]_4[U(NCS)_8]$, the corresponding FIR spectra display absorption bands at 175, 192 and 202 cm^{-1}, which were not observed in the INS spectrum. Among these, the one at 202 cm^{-1} is very close to the IR active ν(U–N) stretching, which appears at 201 cm^{-1} (Appendix 1, Figure 7.5), and, in addition, as the external magnetic field increases from 2 to 10 T, its intensity changes with an opposite profile compared to the other bands; therefore this transition could be thought as due to coupling to the U–N vibrational mode. Moreover, noticeably, there are no clear features at lower energy, although these may be

hidden in the noise. $[^{n}Pr_4N]_4[U(NCS)_8]$ was also measured at variable fields but no transitions were observed, possibly due to enhanced coupling to vibrational modes. Nevertheless, this study displays the power of combined INS/FIR spectroscopy to probe the first excited states in molecular uranium compounds. Finally, it is worth underlining that FIR spectroscopy has been recently used for studying lanthanide SMM complexes,[50b] but never for an actinide compound.

2.2.11 Computational Chemistry

Computational chemistry has been used to further probe these compounds. DFT is limited to investigate electronic structures for actinide compounds, therefore a CASPT2 approach was chosen, since it has been successfully used elsewhere to explain magnetic properties of lanthanides.[51] These calculations were performed by Dr. A. Kerridge at Lancaster University. The $5f^2$ singlet and triplet manifolds, corresponding to 28 singlet and 21 triplet states respectively, were calculated for three geometries: cubic (O_h), distorted (D_4) and square antiprismatic (D_{4d}). The resultant states were used as the basis of the spin-orbit coupled calculations. The $^3H_4$ ground state was calculated to be energetically well separated from the $^3F_2$ first excited state by 2840 cm^{-1}, 2580 cm^{-1} and 3222 cm^{-1} for the cubic, distorted, and square antiprismatic symmetry complexes, respectively. For comparison the solution experimental value is 5015 cm^{-1} for $[Et_4N]_4[U(NCS)_8]$ in a square antiprismatic geometry. The splitting of the $^3H_4$ state itself was calculated to be 1181 cm^{-1}, 1379 cm^{-1} and 966 cm^{-1} for the O_h, D_4, and D_{4d} symmetry complexes, respectively. The energies of the 9 components of the $^3H_4$ ground state are given Table 2.7. These calculations allow also the effective magnetic moments to be evaluated (Figure 2.24, dashed lines). These have been calculated in the presence of a 0.1 T magnetic field and qualitatively the data match the experimentally determined value: $[Et_4N]^+$ = 0.57, $[^{n}Pr_4N]^+$ = 0.38 and Cs^+ = 2.26 B.M at 2 K.

Moreover, it is worthy to underline that the limitations of CASSCF calculations on the magnetic properties have been taken into account.[41b] Notwithstanding this, the theoretical calculations are consistent with the spectroscopic data that the ground-states are different between the cubic and square antiprismatic geometries: the D_{4d} geometry has a doublet ground state while the others have a singlet ground state.

Table 2.7. Calculated relative energies of the $^3H_4$ components from CASPT2(2, 7) calculations.

Symmetry	Relative energy (cm^{-1})
O_h	0, 39, 203, 759, 860, 995, 1068, 1173, 1181
D_4	0, 140, 185, 949, 1119, 1128, 1195, 1344, 1379
D_{4d}	0, 0, 374, 380, 700, 718, 955, 957, 966

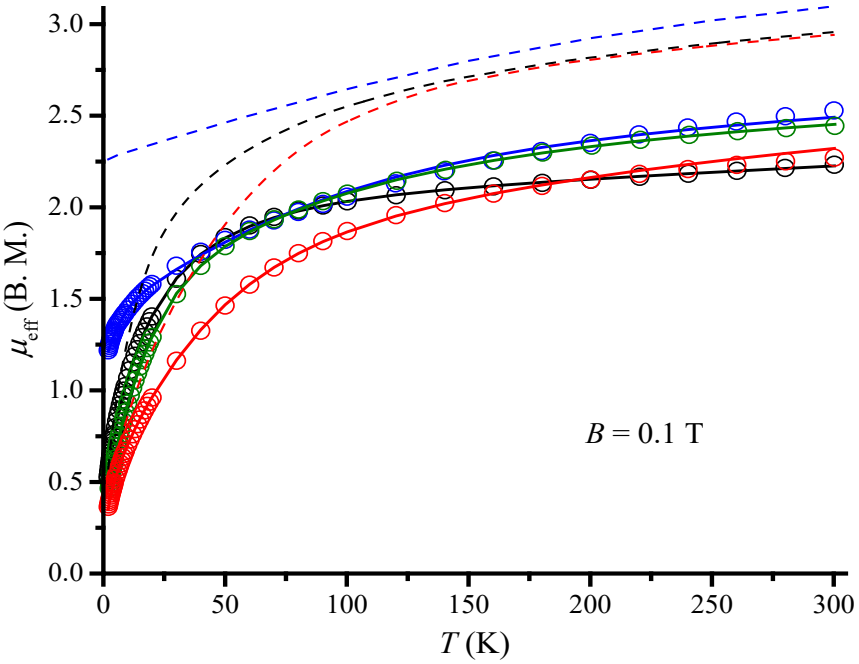

Figure 2.24. Experimental (circles), results from CONDON fitting (solid lines) and CASPT2(2, 7) calculated (dashed lines) effective magnetic moments of $A_4[U(NCS)_8]$ {A = Cs (blue); Me_4N (green); Et_4N (black); $^nPr_4N$ (red)} at B = 0.1 T.

2.2.12 Quantification of the Low-Lying Energy States from CONDON Calculation and Spectroscopy

CONDON calculations were performed by Dr. P. Kögerel, from Aachen University, in order to quantify the low-lying energy states of the uranium complexes. Thus, the calculated energy levels, below 1000 cm^{-1}, are shown in Figure 2.25, while a comparison with the results from the CASPT2(2, 7) approach and the experimental data, from both INS and FIR measurements, is presented in Figure 2.26.

It was possible to find for the Cs^+ compound a mixed doublet ground state ($m_J = \pm5, \pm3,$ and ±1), a first excited singlet state ($m_J = \pm4$ and 0) at 17 cm^{-1}, and another excited singlet at 188 cm^{-1} as mixed state composed of $m_J = \pm6$ and ±2 (Figure 2.26). These data are in good agreement with the INS and FIR measurements; thus, the bands observed in the INS (at 186 cm^{-1}) and FIR (at 187 cm^{-1}) spectra of $Cs_4[U(NCS)_8]$ (Figure 2.22 and Figure 2.23) can be considered as due to a transition from the ground ($m_J = \pm5, \pm3,$ and ±1) to the third excited state ($m_J = \pm6$ and ±2). This is also in line with the FIR spectroscopy selection rules ($\Delta j = \pm1$), while there are no selection rules for INS spectroscopy.

For the $[Et_4N]^+$ sample, a different ground state was observed (singlet, $m_J = \pm6$ and ±2), with the first excited state at only 12 cm^{-1} (singlet, $m_J = \pm4$ and 0), and two doublets at 52 cm^{-1} and 196 cm^{-1} (both $m_J = \pm5, \pm3,$ and ±1, but different mixture). As for the Cs^+ compound, these data agree well with the FIR results (Figure 2.23). Therefore, while a transition at *ca.* 52 cm^{-1} was not observed, the FIR band at 192 cm^{-1} can be thought as due to a transition from the ground ($m_J = \pm6$ and ±2) to the third excited state [$m_J = \pm5$ (5.5%), ±3 (25.2%), and ±1 (69.3%)], which is also allowed by the FIR spectroscopy selection rules ($\Delta j = \pm1$). Moreover, in line with the calculated energy levels, the other observed FIR transition at 175 cm^{-1} can be assigned as an "hot band", being due to a transition from the first ($m_J = \pm4$ and 0) to the third excited state [$m_J = \pm5$ (5.5%), ±3 (25.2%), and ±1 (69.3%)].

Regarding the $[Me_4N]^+$ complex, a singlet ground state was determined ($m_J = \pm4$ and 0), with an excited doublet at 66 cm^{-1} ($m_J = \pm5, \pm3,$ and ±1) and an excited singlet at 255 cm^{-1} ($m_J = \pm6$ and ±2). Finally, for the $[^n Pr_4N]^+$ equivalent, the CONDON method found a singlet ground state ($m_J = \pm6$ and ±2), a first singlet excited state ($m_J = \pm4$ and 0) at only 4 cm^{-1}, a doublet excited state ($m_J = \pm5, \pm3,$ and ±1) at 135 cm^{-1} and another singlet excited state ($m_J = \pm4$ and 0) at 307 cm^{-1}. It is important to note that, although the ground states of $[Et_4N]^+$ and $[^n Pr_4N]^+$ involve states characterized by the same m_J numbers, the mixture of the states and the energy splitting are distinctly different (Figure 2.25).

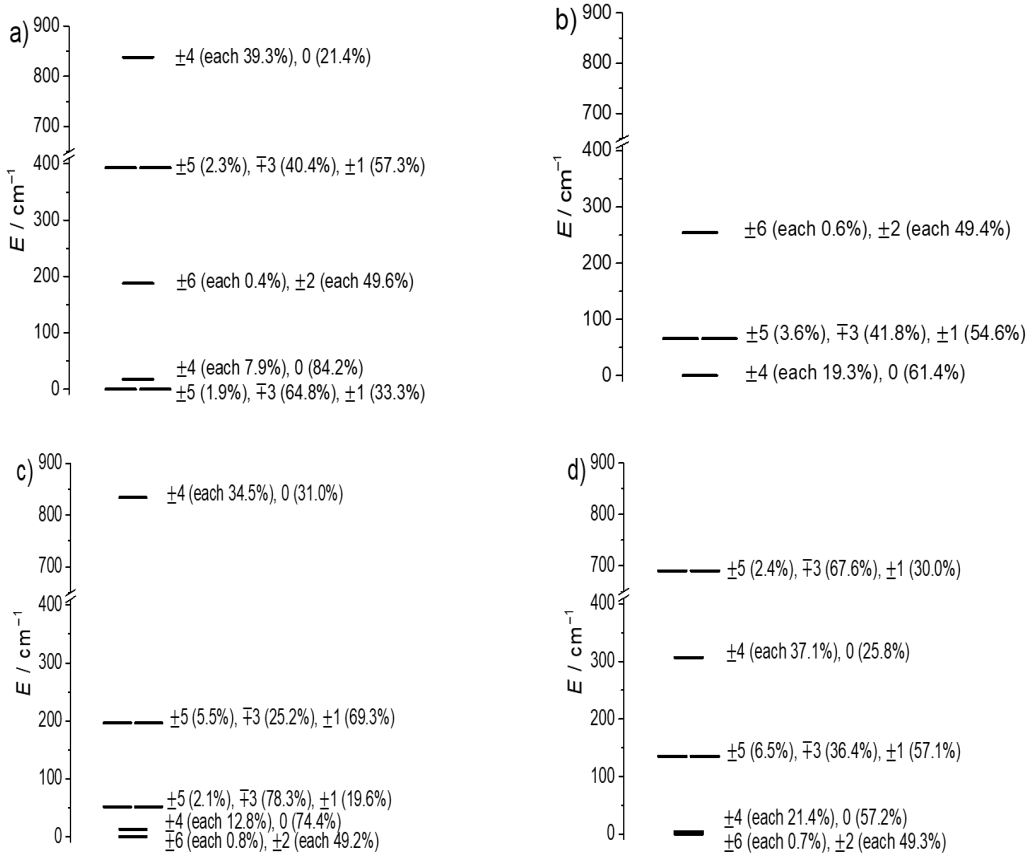

Figure 2.25. Energy splittings below 1000 cm^{-1} of (a) $Cs_4[U(NCS)_8]$, (b) $[Me_4N]_4[U(NCS)_8]$, (c) $[Et_4N]_4[U(NCS)_8]$ and (d) $[^nPr_4N]_4[U(NCS)_8]$, according to the least-squares fit by CONDON. A single line represents a singlet state, and double lines represent a doublet. The compositions of the states are given by the crystal quantum number m_J according to Hellwege.

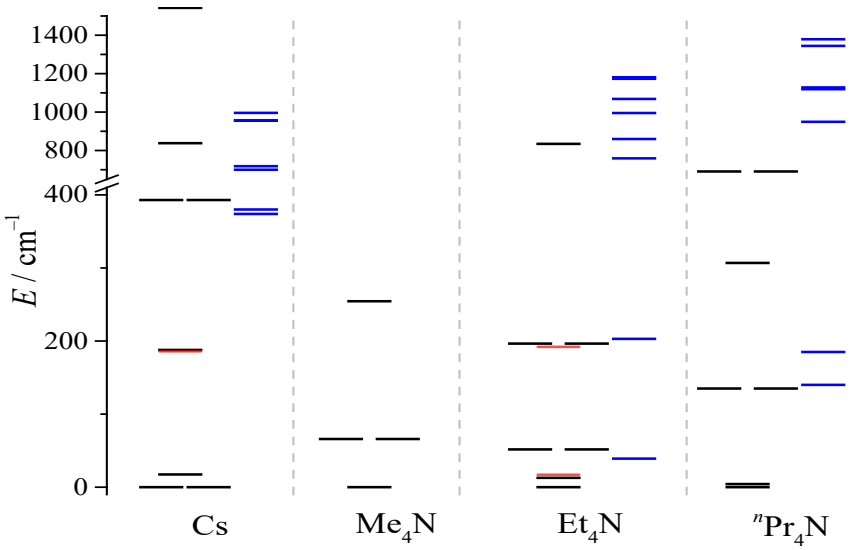

Figure 2.26. Summary of energy splitting of $A_4[U(NCS)_8]$ (A = Cs, Me_4N, Et_4N, $^nPr_4N$) for energies below 1500 cm^{-1} according to the least-squares fits using CONDON (black lines), CASPT2(2, 7) calculations (blue lines) and INS and FIR spectroscopic measurements (red lines).

From this analysis, it is clear that, the results from the CONDON fits are different to the ones from CASPT2(2, 7) calculations. The temperature dependences of μ_{eff} are, indeed, quantitatively not reproduced by the CASPT2(2, 7) calculations, but to some degree qualitatively (dashed lines in Figure 2.24); this can also be seen from the energy splitting diagram (Figure 2.26). In particular, the energy splittings of the fits from CONDON are denser at lower energies (< 400 cm^{-1}) and less dense at higher energies (> 700 cm^{-1}) than the corresponding levels from the CASPT2(2, 7) calculations. It is possible to conclude that, for actinide compounds, CASPT2 calculations cannot quantitatively replicate the energy splitting, although, in this study, the multiplicity of the ground state was correctly reproduced in all three geometries.

2.3 Investigation of Ligand Field Strength, $[U(NCSe)_8]^{4-}$ Complexes

2.3.1 Synthesis and Structural Characterization of $[Et_4N]_4[U(NCSe)_8]$

It was of interest to extend the analysis to different ligand systems, to understand if the influence of a specific coordination geometry on the electronic structure and magnetic behaviour of U(IV) can be considered as general for high symmetry U(IV) complexes. Therefore, the synthesis of a series of U(IV) selenocyanate complexes of the type $A_4[U(NCSe)_8]$ was attempted.

Following the same procedure for the thiocyanate equivalent, the compound $[Et_4N]_4[U(NCSe)_8]$ has been prepared and fully characterized. However, in comparison to $[Et_4N]_4[U(NCS)_8]$, this selenocyanate sample was found to be much more air and moisture sensitive, and also light sensitive; it often underwent a decomposition, changing colour from green to red and releasing a red precipitate of presumably elemental selenium. Nevertheless, it was possible to isolate this product, as a green powder and in relatively high yield and purity, by adopting a precipitation with dried Et_2O after one hour of stirring the solution in the dark; in addition, single crystals were also grown by recrystallization from MeCN solutions. These were stable at room temperature, under an inert atmosphere and in the dark. The synthesis of the Cs^+ and $[Me_4N]^+$ analogues was also attempted, however with these counter-cations, the compound $A_4[U(NCSe)_8]$ was found to be much more air and light sensitive. It rapidly decomposed, releasing a red precipitate and it was not possible to isolate and characterize any uranium containing compound.

The compound $[^nPr_4N]_4[U(NCSe)_8]$ has also been reported,[52] and shows a distorted square antiprismatic (D_4) symmetry for the uranium ion (from shape analysis:[39] SAPR-8),

similarly to the one observed in [^{n}Pr$_4$N]$_4$[U(NCS)$_8$] (Figure 2.2b). The solid-state crystal structure of [Et$_4$N]$_4$[U(NCSe)$_8$] is shown in Figure 2.27, exhibiting the thermal ellipsoids of the atoms. The corresponding crystallographic data are listed in Appendix 1, while the bond lengths and angles are tabulated in Appendix 1.7, in the external CD source of this thesis. This structure suffers of disorder in two positions for the [Et$_4$N]$^+$ cations and the refinement is clarified in the experimental section.

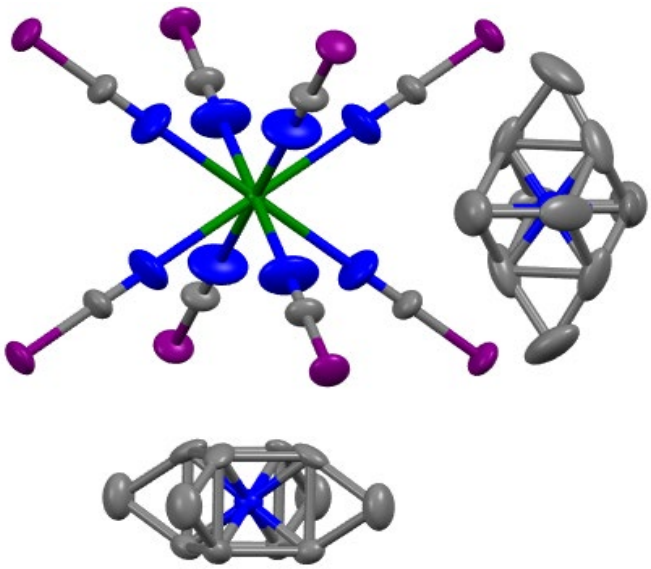

Figure 2.27. Molecular structure of [Et$_4$N]$_4$[U(NCSe)$_8$], with atomic displacement shown at 50% probability and hydrogen atoms omitted for clarity. Colour code: U – green, N – blue, C – grey, Se – violet.

In [Et$_4$N]$_4$[U(NCSe)$_8$] the U(IV) ion displays a cubic (O_h) geometry (Figure 2.27) with eight selenocyanate ligands coordinated to the U(IV) ion, via U–N bonds, similarly to the anion [U(NCS)$_8$]$^{4-}$ in [Et$_4$N]$_4$[U(NCS)$_8$]. The average of the U–N (2.405(4) Å) and N=C (1.139(5) Å) bond lengths are comparable with the corresponding value shown by the A$_4$[U(NCS)$_8$] compounds (2.423(1) Å for U–N and 1.163(1) Å for C=N), while the average of the C=Se bond lengths (1.764(3) Å) is comparable with the value observed in [^{n}Pr$_4$N]$_4$[U(NCSe)$_8$] (1.777(3) Å) and smaller in comparison with the C=Se bond length in K[NCSe] (1.829(25) Å).[53]

Moreover, a careful inspection of the X-ray structure of [Et$_4$N]$_4$[U(NCSe)$_8$] reveals some unresolved disorder in the position of the coordinated nitrogen atoms, indeed their thermal ellipsoids are more oblate than they should normally be (Figure 2.27). It is worthy to note that this structural feature is similar to the one observed in [Et$_4$N]$_4$[U(NCS)$_8$],

where the disorder has been attributed to an electronic effect (section 2.2.2). This structural similarity could also indicate a similar CF splitting in these uranium compounds, although the thiocyanate ligands are more electron donating than the selenocyanate equivalents, as explained in Table 2.9 and Figure 2.30.

2.3.2 Vibrational Characterization of $A_4[U(NCSe)_8]$ (A = Et_4N, $^nPr_4N$)

As discussed for the thiocyanate samples, vibrational spectroscopy is useful to confirm the geometry for the $[U(NCSe)_8]^{4-}$ ion. Thus, Raman and IR spectra of $[Et_4N]_4[U(NCSe)_8]$ have been measured in the solid state and are shown in Appendix 1 (Figure 7.6), while a comparison of the ν(C=N) stretching frequencies among the $A_4[U(NCE)_8]$ complexes (A = Et_4N, $^nPr_4N$; E = S, Se) is displayed in Table 2.8.

In the solid state, $[Et_4N]_4[U(NCSe)_8]$ shows one IR active ν(C=N) stretch at 2036 cm^{-1} and two Raman active ν(C=N) stretches at 2041 and 2092 cm^{-1}, confirming for the $[U(NCSe)_8]^{4-}$ ion of this complex the same solid-state cubic symmetry (O_h) as the thiocyanate analogue. In addition, $[Et_4N]_4[U(NCSe)_8]$ displays bands for the C=Se vibrational mode at 784 cm^{-1} in the IR and at 673 cm^{-1} in the Raman spectrum. Moreover, the trend of the vibrational data (Table 2.8) shows that only small differences are observable changing the ligands from $[NCS]^-$ to $[NCSe]^-$. This suggests that the structural parameters displayed by the $[U(NCS)_8]^{4-}$ ion are replicated in the $[U(NCSe)_8]^{4-}$ analogue.

Table 2.8. Comparison of the ν(C=N) stretching frequencies for the $A_4[U(NCE)_8]$ (A = Et_4N, $^nPr_4N$; E = S, Se) compounds in solid state.

Compound	Raman (cm^{-1})	IR (cm^{-1})
$[Et_4N]_4[U(NCSe)_8]$	2041, 2092	2036
$[Et_4N]_4[U(NCS)_8]$	2040, 2090	2047
$[^nPr_4N]_4[U(NCS_e)_8]$	2043, 2063, 2094	2054, 2093
$[^nPr_4N]_4[U(NCS)_8]$	2045, 2056, 2090	2047, 2090

2.3.3 UV-vis-NIR Characterization of $A_4[U(NCSe)_8]$ (A = Et_4N, $^nPr_4N$)

Differences in the ligand field strength between these uranium(IV) compounds could appear by comparing vis-NIR absorption spectra. Thus, vis-NIR spectra of $[Et_4N]_4[U(NCSe)_8]$ and $[^nPr_4N]_4[U(NCSe)_8]$ have been measured in the solid state and are displayed in Appendix 1 (Figure 7.7 and Figure 7.8) along with those of the analogue

thiocyanate complexes for comparison. In these spectra, the differences in energy of the *f-f* electronic transitions between the complexes with the same geometry are negligible, suggesting that the changes in the ligand field strength are very small.

2.3.4 Magnetic Properties of $A_4[U(NCSe)_8]$ (A = Et_4N, $^nPr_4N$)

It was of interest to examine if a small difference in the ligand field can influence the magnetic properties of the $[U(NCS(e))_8]^{4-}$ ion. Thus, the magnetic moments of $[Et_4N]_4[U(NCSe)_8]$ and $[^nPr_4N]_4[U(NCSe)_8]$ have been measured from 2 to 300 K using a SQUID magnetometer and compared with those of the equivalent thiocyanate compounds (Figure 2.28). For all of these $[U(NCS(e))_8]^{4-}$ compounds, as shown from the inset in Figure 2.28, there appear a small linear dependence of the molar magnetization upon the applied magnetic field.

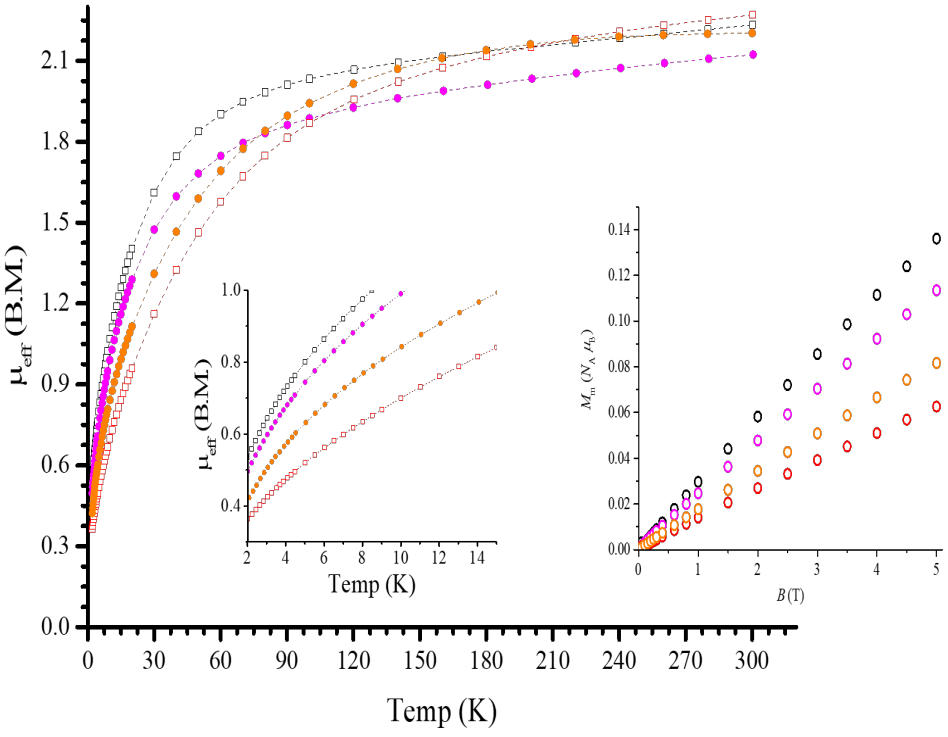

Figure 2.28. Temperature dependence of the experimental effective magnetic moments for $[Et_4N]_4[U(NCS)_8]$ (black), $[Et_4N]_4[U(NCSe)_8]$ (magenta), $[^nPr_4N]_4[U(NCS)_8]$ (red) and $[^nPr_4N]_4[U(NCSe)_8]$ (orange). Inset is a magnification of the low temperature magnetic moments and the profile of the molar magnetization M_m *vs* applied magnetic field B.

The two selenocyanate compounds show the typical magnetic profile for U(IV) samples, with a region of TIP until *ca.* 100 K followed by a precipitous drop at low

temperatures. At 300 K the values of μ_{eff} are 2.12 B.M. for $[Et_4N]_4[U(NCSe)_8]$ and 2.20 B.M. for $[^nPr_4N]_4[U(NCSe)_8]$; while, lowering the temperature, these values decrease until, at 2 K, reach the values of 0.50 B.M. for $[Et_4N]_4[U(NCSe)_8]$ and 0.42 B.M. for $[^nPr_4N]_4[U(NCSe)_8]$. In particular, by comparing the temperature dependence of the μ_{eff} values between the pairs of isostructural complexes, no noticeable differences emerge; therefore, it is possible to conclude that the small difference in the ligand field strength does not significantly change the magnetic properties of the $[U(NCS(e))_8]^{4-}$ ion.

2.4 $[U(NCTe)_8]^{4-}$ Complexes

2.4.1 Synthesis and Structural Characterization

Tellurium cyanate, $[NCTe]^-$, compounds are known to be rather unstable and undergo a rapid decomposition releasing elemental Te. For example, reactions of $[Et_4N][NCTe]$ with first row transition metal salts have been reported to afford immediate decomposition.[54] Nevertheless, the synthesis of a tellurium cyanate uranium(IV) compound, of formula $[Et_4N]_4[U(NCTe)_8]$, was attempted (Scheme 2.5).

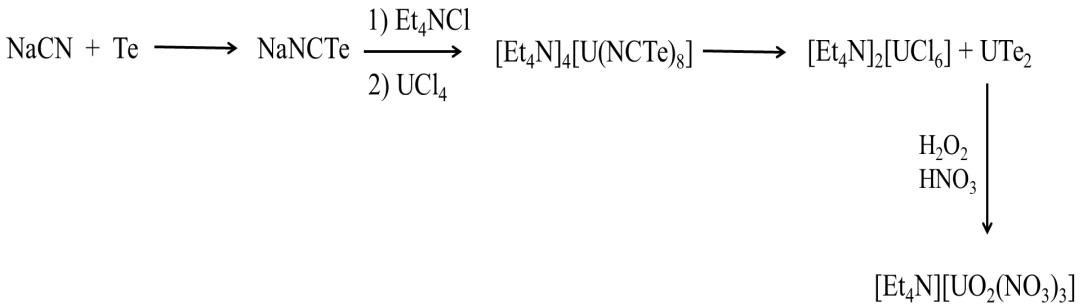

Scheme 2.5. Synthesis of $[Et_4N][UO_2(NO_3)_3]$.

A pale-white solution of $[Et_4N][NCTe]$, produced by reaction of Na[CN] with an excess of Te in dried MeCN and with the addition of $[Et_4N]Cl$,[54] was mixed with a green suspension of UCl_4 in dried MeCN; however, the formation of a black precipitate was immediately observed. From the very pale green acetonitrile solution, a small amount of crystalline material was isolated and X-ray diffraction showed this to be $[Et_4N]_2[UCl_6]$,[55] presumably formed by reaction of either UCl_4 with the $[Et_4N]Cl$ formed in the metathesis reaction or by reaction between the decomposed uranium sample and $[Et_4N]Cl$. The grey precipitate was amorphous by powder XRD, however oxidation

with H_2O_2 in dilute HNO_3 and subsequent extraction into MeOH afforded a yellow solution. From this, a few yellow single crystals were obtained and X-ray diffraction revealed them to be $[Et_4N][UO_2(NO_3)_3]$ (Scheme 2.5). The solid-state crystal structure of $[Et_4N][UO_2(NO_3)_3]$ is shown in Figure 2.29; the corresponding crystallographic data are listed in Appendix 1 and the full list of angles and bond lengths are tabulated in Appendix 1.7, in the external CD source of this thesis.

This is a rather uncommon product,[56] but the metric parameters are identical to those of $[Me_4N][UO_2(NO_3)_3]$.[56d] Due to the formation of $[Et_4N][UO_2(NO_3)_3]$, it is reasonable to state that in the black precipitate there was a mixed U-Te metal compound of possible formula of UTe_2 or $[Et_4N]U_2Te_6$.[57]

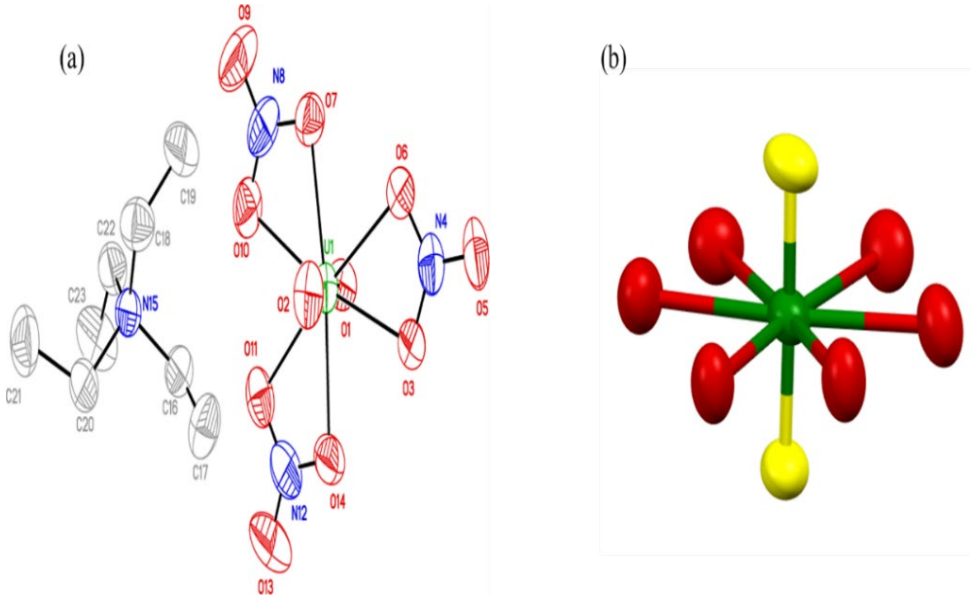

Figure 2.29. (a) Asymmetric unit of $[Et_4N][UO_2(NO_3)_3]$ with atomic displacement shown at 50% probability. H atoms omitted for clarity. (b) Depiction of the coordination geometry for the central uranium ion; colour code: uranium – green, yl-oxygens – yellow, oxygen – red.

Finally, the synthesis of a uranium(IV) cyanate complex, of the type $A_4[U(NCO)_8]$, was attempted, but no reaction was observed between UCl_4 and KNCO under the same experimental conditions adopted with Na[NCS] and K[NCSe].

2.4.2 DFT Calculations on $[U(NCE)_8]^{4-}$ (E = S, Se and Te)

To further probe the influence of the $[NCE]^-$ ligands (E = S, Se and Te) on the electronic structure of these uranium(IV) compounds, calculations at DFT level have been performed by Dr. J. A. Platts from Cardiff University. The results are summarised in Table 2.9, while

Figure 2.30 shows graphically the variation in energy of the ligand and *f*-orbitals as the chalcogenide is changed.

Table 2.9. DFT computed properties of $[U(NCE)_8]^{4-}$ (E = S, Se, Te).

BOND	S	Se	Te
U–N[(a)] (Å)	2.490 (2.423)	2.540 (2.405)	2.568
N=C[(a)] (Å)	1.194 (1.163)	1.191 (1.139)	1.189
C=E[(a)] (Å)	1.649 (1.619)	1.800 (1.764)	2.035
ν(N=C) (IR) (cm^{-1})	2072, 2076	2064, 2067	2062
ν(N=C) (Raman) (cm^{-1})	2101	2072	2071
% U/N	15/85	14/86	12/88
U-N bond order	0.61	0.54	0.51
N-C bond order	2.40	2.47	2.55
C-E bond order	1.56	1.45	1.27
ρ(U-N)	0.056	0.050	0.049
ρ(N-C)	0.427	0.429	0.432
ρ(C-E)	0.207	0.170	0.117

(a) Experimental bond lengths in parenthesis

The calculated bond distances are in relatively good agreement with the experimental data for $[NCS]^-$ and $[NCSe]^-$; for the tellurium sample the calculated bond lengths can be compared with the experimentally determined values of [K(18-crown-6)][TeCN][58] (Te=C = 2.031(5) Å, C=N = 1.148(6) Å) or [PNP][TeCN][59] (Te=C = 2.02(1) Å, C=N = 1.07(1) Å). The Raman and IR stretching frequencies (Table 2.9) are in good agreement with the experimental data; thus, we have benchmarked the values of the DFT calculated bond distances with the result of the comparison between the calculated and experimental stretching frequencies. In addition, in K[NCTe], the N=C vibrational stretching mode appears at 2079 cm^{-1} in the IR and at 2080 cm^{-1} in the Raman spectrum.[54]

Moreover, moving down along the chalcogenide group, the resonance form of the coordinated $[NCE]^-$ ligand tends towards a $[N{\equiv}C{-}E]^-$ structure, according to both the bond order from NBO analysis and the electron density at the bond critical point from AIM analysis (Table 2.9). This is also corroborated by a destabilization of the π C=E

orbital as the group is descended (Figure 2.30), in line with the "double bond rule", and may be a reason why the $[NCTe]^-$ complex is not stable.

The U−N bonding also changes upon varying the ligand so that, descending the group, the bond becomes more ionic, as shown by the variations of ρ from AIM calculations. NBO analysis reports that the U−N bond is made up of 14% U (12% *s*, 33% *p*, 31% *d* and 24% *f*) and 86% N (58% *s*, 42% *p*) with $[NCS]^-$, 13% U (13% *s*, 32% *p*, 36% *d* and 20% *f*) and 87% N (58% *s*, 42% *p*) with $[NCSe]^-$ and 12% U (12% *s*, 34% *p*, 42% *d*, 12% *f*) and 88% N (56% *s*, 44% *p*) with $[NCTe]^-$. Finally, in all compounds, the HOMO is ligand based since NBO analysis reports a lone pair on the chalcogenide ion (Figure 2.30).

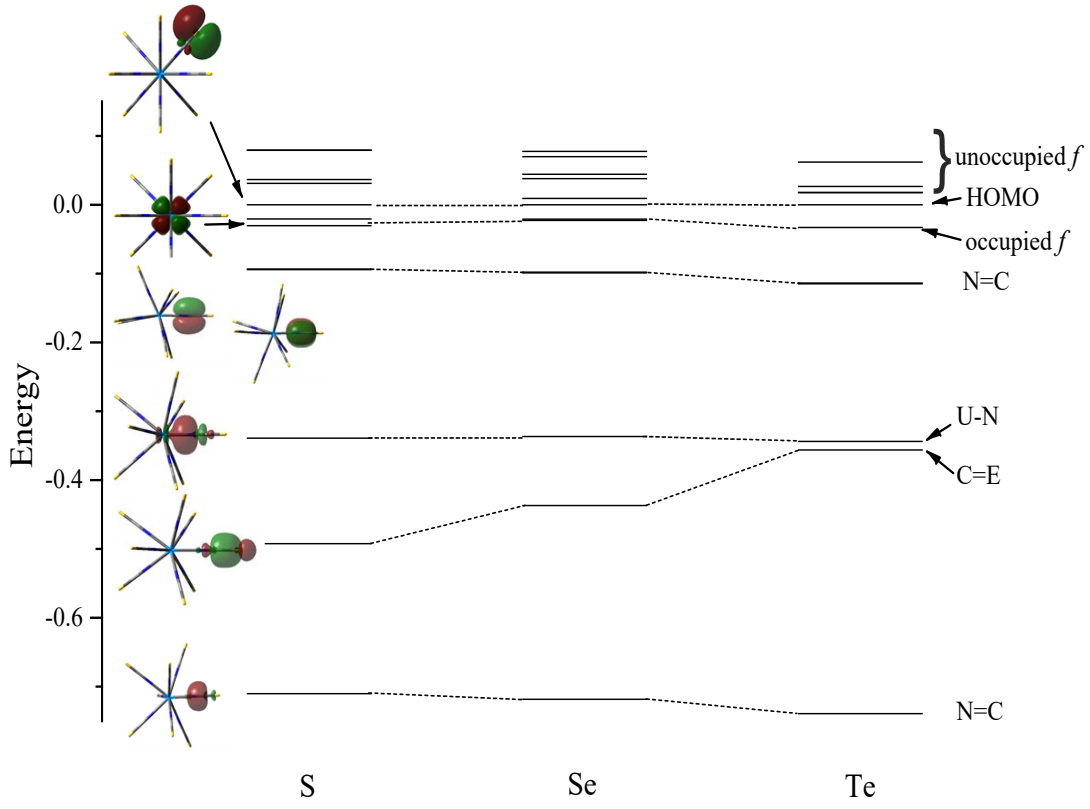

Figure 2.30. Energies of the ligand based and *f*-orbitals in the complex $[U(NCE)_8]^{4-}$ (E = S, Se, Te); plots are from NBO analysis.

2.5 Conclusions

It has been shown that in the compounds $A_4[An(NCS)_8]$ (A = Me_4N, Et_4N, $^nPr_4N$, Cs; An = U, Th) crystal packing forces determine the coordination geometry around the actinide ion. Interestingly, this effect has a significant influence on the magnetic properties of the $[U(NCS)_8]^{4-}$ ion, as measured by both SQUID and specific heat capacity measurements. In particular, the compound $Cs_4[U(NCS)_8]$, with a square antiprismatic

symmetry for the U(IV) coordination sphere, displays higher values of the effective magnetic moment and specific heat capacity at low temperatures, compared to the other compounds of different coordination geometry. These results, along with an EPR transition at 150 mT (although broad and weak), are indicative for a triplet electronic ground state for the U(IV) ion in this Cs complex, which is the first example of this type in U(IV) chemistry.

In order to investigate the disorder in the position of the coordinated nitrogen atoms in the structure of the $5f^2$ $[Et_4N]_4[U(NCS)_8]$, ultra-low temperature (4 K) X-ray and neutron single-crystals diffraction experiments have been performed on single crystals of this complex; the $5f^0$ thorium equivalent has also been analysed to account for any electronic effects on the structural distortions. The results showed the thermal ellipsoids of the coordinated nitrogen atoms significantly more oblate in the $5f^2$ U(IV) than in the $5f^0$ Th(IV) compound, suggesting that an electronic effect could be the cause of the disorder observed in $[Et_4N]_4[U(NCS)_8]$.

It has been demonstrated that the interplay between CONDON calculations (for the composition of the states) and advanced spectroscopic measurements (for accurate determination of the energy levels), such as INS and FIR spectroscopy, is a powerful approach to gain insight into the low-lying energy level electronic structure of molecular uranium compounds. In particular, the results from the CONDON framework are in line with the spectroscopic and magnetic data, predicting a triplet ground state for the Cs compound.

Subsequently, the structural, spectroscopic and magnetic properties of two U(IV) selenocyanate compounds {$[Et_4N]_4[U(NCSe)_8]$ (symmetry O_h) and $[^nPr_4N]_4[U(NCSe)_8]$ (symmetry D_4)} have been studied and compared with the ones belonging to the thiocyanate equivalents. No noticeable differences in the spectroscopic and magnetic properties have been observed between the compounds of the same symmetry, suggesting very small changes in the CF splitting.

Finally, the bonding in the family of compounds $[U(NCE)_8]^{4-}$ (E = S, Se and Te) has been explored by DFT calculations and it has been shown that, descending the group, the C=E π bonding orbital undergoes a destabilization and the U–N bonding becomes more ionic. These calculations could explain why it was not possible to isolate a U(IV) tellurium cyanate compound of the type $A_4[U(NCTe)_8]$.

2.6 Experimental Section

Caution! Natural uranium and thorium were used during the course of the experimental work. As well as the radiological hazards, both uranium and thorium are toxic metal ions and care should be taken with all manipulations. Experiments were carried out using pre–set radiological safety precautions in accordance with the local rules of Trinity College Dublin, University of Newcastle, Insitituto de Ciencia de Materiales de Aragòn, Laboratoire National des Champs Magnétiques Intenses in Grenoble and ISIS Neutron and Muon Facility in Harwell (UK).

All manipulations were carried out using standard Schlenk and glove box techniques under an atmosphere of a high purity dry argon or nitrogen. IR spectra were recorded on a Perkin Elmer Spectrum One spectrometer with attenuated total reflectance (ATR) accessory. Raman spectra were obtained using 785-nm excitation on a Renishaw 1000 micro-Raman system. FIR transmission spectra (30–600 cm^{-1}) were recorded by Dr. Milan Orlita at the Laboratoire National des Champs Magnétiques Intenses in Grenoble on samples diluted (1 : 20) in eicosane, using a Bruker IFS 66v/s FTIR spectrometer with globar source, where the sample was placed inside an 11 T solenoid magnet, with a composite bolometer detector element located inside the magnet. ^{1}H and $^{13}C\{^{1}H\}$ spectra were recorded on a Bruker AV400 spectrometer operating at 400.23 MHz and 155.54 MHz, respectively, and the chemical shifts were referenced to the residual ^{1}H and ^{13}C resonances of the solvent used. The measurement of the magnetic properties of both thorium and uranium compounds was performed by Dr. Marco Evangelisti Crespo and Dr. Giulia Lorusso at the Aragòn Material Science Insititute of University of Zaragoza, where thermal and field scans of DC and AC magnetization were carried out using a 5T Quantum Design MPMS XL SQUID magnetometer from 2 to 300 K. Powdered samples were fixed by eicosane and mounted in quartz sample holders of known susceptibility. Multiple measurements were also taken to ensure reproducibility. Diamagnetic corrections were made using Pascal's constants.[60] UV-vis-NIR measurements were made on a Perkin Elmer Lambda 1050 spectrophotometer over the range 230-2500 nm, using fused silica cells with a path length of 1 cm. For the acquisition of the vis-NIR spectra in nujol mull, the uranium samples were suspended in nujol mull and placed on filter paper strips, which were inserted into fused silica cells (path length of 1 cm) for the measurement. Steady-state photoluminescence spectra were recorded on a Horiba-Jobin-Yvon Fluorolog-3 spectrofluorimeter. X-ray crystallography data at 100 K were obtained on a Bruker Apex diffractometer and the structures were defined by Dr. Brendan Twamley at Trinity College Dublin, via direct methods, and refined by least squares method on F^2 using the SHELXTL

program package.[61] Crystal data and details of data collections are listed in Appendix 1. Powder X-ray Diffraction measurements were carried out on a Bruker D2 Phaser. MeCN and CD_3CN were distilled over CaH_2 and degassed immediately prior to use. Spectroscopic measurements used spectroscopic-grade solvents which were purchased from commercial sources, dried over molecular sieves and thoroughly degassed before use. For the preparation of the uranium samples, anhydrous UCl_4 was used as source of U(IV) and it was synthesised from U_3O_8 following a reported procedure.[62] $ThCl_4(DME)_2$ was synthesized from $Th(NO_3)_4{\cdot}5H_2O$, following a reported procedure.[63] $Cs_4[An(NCS)_8]$ (An = Th, U),[32] $[Et_4N]_4[An(NCS)_8]$ (An = Th, U)[33] and $[^nPr_4N]_4[U(NCSe)_8]$[52] were prepared via the literature procedures and $[d_{20}\text{-}Et_4N]_4[U(NCS)_8]$ was made from $d_{20}\text{-}Et_4NBr$, supplied by the deuteration facility of the ISIS Neutron and Muon Facility in Harwell (UK). The structure of these samples was verified by vibrational spectroscopic measurements and, for some of them, the bulk purity was checked by powder X-ray diffraction (Appendix 1, Figure 7.9 and Figure 7.10 and Figure 7.11). All other reagents were obtained from commercial sources and used as received.

2.6.1 Synthesis of $[R_4N]_4[U(NCS)_8]$

To a suspension of UCl_4 (200 mg, 0.526 mmol), in dried MeCN (20 cm^3), was added Na[NCS] (341 mg, 4.21 mmol) and R_4NCl (2.105 mmol) and the mixture was stirred at room temperature for *ca.* 30 min and in an inert Ar atmosphere. The resulting green solution was filtered, and the solvent was reduced in volume until *ca.* 5 cm^3. The solution was then stored at −20 °C and green crystals, suitable for X-ray diffraction, were isolated after *ca.* 48.

$[Me_4N]_4[U(NCS)_8]$. Yield: 21%, 112 mg, 0.112 mmol. IR (ATR, ν/cm^{-1}): 3021 (w), 2048 and 2027 (s, C=N), 1480 (m), 1410 (w), 944 (s, C=S), 742 (w). Raman (ν/cm^{-1}): 2098 and 2050 and 2039 (C=N), 1448, 942, 825, 752, 453.

$[^nPr_4N]_4[U(NCS)_8]$. Yield: 17%, 134 mg, 0.0927 mmol. IR (ATR, ν/cm^{-1}): 3384 (m), 2976 (w), 2091 and 2042 (s, C=N), 2875 (w), 1623 (w), 1482 (w), 967 (w), 924 (w), 755 (m C=S). Raman (ν/cm^{-1}): 2103 and 2069 and 2046 (C=N), 1467, 1316, 1032, 843 (C=S), 815, 344, 302.

$[H_2(2.2.2\text{-crytand})]_2[U(NCS)_8]$. Yield: 7.2%, 55 mg, 0.0377 mmol. IR (ATR, ν/cm^{-1}): 3145 (w), 2906 (w), 2026 (s, C=N), 1448 (m), 1379 (m), 1261 (w), 1095 (s), 922 (s), 806 (m). Raman (ν/cm^{-1}): 2093 and 2045 and 2034 (C=N), 1475, 1148, 110, 822 (C=S).

Refinement Note: Coordinated NCS groups all disordered in two sites with 50% occupancy for N1, N2, N4. The N3 NCS has a 76:24% occupancy. Restraints (DFIX, SADI, SIMU) used. Cryptand highly disordered, modelled in two positions only with 59:41% occupancy. Restraints (DFIX, SIMU) used. The acetonitrile group is half occupied and modelled with restraints (SIMU).

2.6.2 Synthesis of $[R_4N]_4[Th(NCS)_8]$

To a suspension of $ThCl_4(DME)_2$ (200 mg, 0.361 mmol), in dried MeCN (20 cm^3), was added Na[NCS] (234 mg, 2.89 mmol) and R_4NCl (1.44 mmol) and the mixture was stirred at room temperature for *ca.* 30 min in an inert Ar atmosphere. The resulting pale solution was filtered, and the solvent was reduced in volume until *ca.* 5 cm^3. The solution was then stored at −20 °C and colourless crystals, suitable for X-ray diffraction, were isolated after *ca.* 48.

$[Me_4N]_4[Th(NCS)_8(H_2O)]$. Yield: 25%, 92 mg, 0.091 mmol. IR (ATR, ν/cm^{-1}): 3370 (s, H_2O), 2048 (s, C=N), 1628 (m), 1478 (m), 1412 (w), 946 (s), 476 (s). Raman (ν/cm^{-1}): 2106 and 2067 (C=N), 1452, 949, 814 (C=S), 753, 454. UV-vis (ε, mol dm^{-3} cm^{-1}) (298 K, ~10^{-4} M in MeCN): 260 nm (11784).

Refinement Note: Two NCS groups were disordered. NCS (5 and 5a) were modelled in two positions with 84:16% occupancy with restraints (DFIX, SADI, SIMU and ISOR) and constraints (EADP). One other NCS group (7) was disordered with a water molecule with 60:40 % occupancy. Refined with restraints (ISOR) and constraints (EADP).

$[Me_4N]_4[Th(NCS)_8]$. Yield: 39%, 140 mg, 0.141 mmol. IR (ATR, ν/cm^{-1}): 2048 and 2027 (s, C=N), 1480 (s), 1415 (w), 1369 (w), 1282 (s), 1028 (w), 947 (m, C=S), 835 (w), 744 (m). Raman (ν/cm^{-1}): 2039 and 2050 and 2098 (C=N), 1444, 1065, 1023, 942, 816, 751. UV-vis (ε, mol dm^{-3} cm^{-1}) (298 K, ~10^{-4} M in MeCN): 260 nm (8071).

$[^n Pr_4N]_4[Th(NCS)_8]$. Yield: 57%, 180 mg, 0.204 mmol. IR (ATR, ν/cm^{-1}): 2972, 2935, 2879, 2082 and 2030 (s, C=N), 1602 (m), 1472 (m), 1383 (m), 969 (s, C=S), 755 (m). Raman (ν/cm^{-1}): 2047 and 2069 and 2085 and 2101 (C=N), 1464, 1321, 1067, 820, 756. UV-vis (ε, mol dm^{-3} cm^{-1}) (298 K, ~10^{-4} M in MeCN): 260 nm (8071), 313 nm (10559).

Refinement Note: Three $[^{n}Pr_4N]^+$ are disordered. N22/N22a and N35/N35a are fully disordered with 53:47 and 50:50% occupancy. The third cation N48 has one arm disordered C58-C60 60:40%. Restraints used to model the disorder (SADI, SIMU, ISOR). To prove bulk purity, powder X-ray diffraction was measured (Appendix 1, Figure 7.11).

2.6.3 Synthesis of $[Me_4N]_4[Th(NCS)_7(NO_3)]$

To a solution of $Th(NO_3)_4 \cdot 5H_2O$ (400 mg, 0.70 mmol) in acetonitrile (30 cm^3) were added Na[NCS] (455 mg, 5.6 mmol) and Me_4NCl (307 mg, 2.8 mmol). After 60 minutes of stirring at room temperature, the solution was filtered, and the solvent was left evaporate slowly in air. After 1 week at room temperature, the solution deposited colourless crystals suitable for X-ray diffraction. Yield: 53%, 34.7 mg, 0.037 mmol. ^{1}H NMR δ_H (400 MHz, CD_3CN/ppm): 3.17 (s, 12 H, CH_3). $^{13}C\{^1H\}$ NMR δ_C (100.64 MHz, CD_3CN/ppm): 55.30 (CH_3). IR (ATR, ν/cm^{-1}): 2957 (w, C-H), 2098 (w), 2041 (s, C=N), 1480 (m), 1414 (w), 1365 (w), 1284 (m, NO_3), 1027 (w), 945 (m, C=S), 809 (w), 744 (w). Raman (ν/cm^{-1}): 2928, 2257, 2105 and 2061 and 2045 (C=N), 1456, 1425, 1038, 957, 827, 758. UV-vis (ε, dm^3 mol^{-1} cm^{-1}), (298 K, ~10^{-4} M in MeCN): 344 nm (125).

2.6.4 Synthesis of Ph_3CNCS

To a suspension of UCl_4 (200 mg, 0.526 mmol) in dried MeCN (20 cm^3) was added Na[NCS] (341 mg, 4.21 mmol) and Ph_3CNCS (634 mg, 2.105 mmol). The mixture was stirred at room temperature for 30 min. The resulting green solution was filtered, and the solvent was reduced in volume until *ca.* 5 cm^3. Placement at −20 °C overnight yielded colourless single crystals of Ph_3PNCS. The fate of uranium was not determined. Yield: 35%, 55.4 mg, 0.184 mmol. ^{1}H NMR δ_H (CD_3CN/ppm): 7.364 (m, 6H), 7.3 (m, 6H), 7.2 (m, 6H); ^{13}C NMR δ_C (CD_3CN/ppm): 142.65 (NCS), 129.23, 127.89, 127.63, 127.30. IR (ATR, ν/cm^{-1}): 2112 and 2052 (s, C=N), 1490 (m), 1444 (m), 1032 (m), 896 (m), 826 (m), 738 (s, C=S), 692 (s), 694 (s), 518 (m). Raman (ν/cm^{-1}): 2116 and 2063 (C=N), 1598, 1184, 1157, 1033, 1001, 900, 680 (C=S), 619, 365. UV-vis (ε, mol dm^{-3} cm^{-1}) (298 K, ~10^{-5} M in MeCN): 441 nm (440), 326 nm (3350).

2.6.5 Synthesis of $[Et_4N]_4[U(NCSe)_8]$

To a suspension of UCl_4 (200 mg, 0.526 mmol) in dried MeCN (20 cm^3) was added K[NCSe] (606 mg, 4.21 mmol) and Et_4NCl (349 mg, 2.105 mmol). The mixture was stirred at room temperature for two hours in the dark and under inert Ar atmosphere. The resulting green solution was filtered, and the solvent was reduced in volume under vacuum until *ca.* 5 cm^3. A fine green powder was obtained by precipitation with the addition of *ca.* 30 cm^3 of dried Et_2O and dark green crystals, suitable for X-ray diffraction, were grown by recrystallization from dried MeCN.

$[Et_4N]_4[U(NCSe)_8]$. Yield: 58%, 487 mg, 0.305 mmol. IR (ATR, ν/cm^{-1}): 2984 and 2940 (w, C–H), 2036 (s, C=N), 1482 (m), 1450 (m), 1436 (m), 1418 (w), 1365 (m), 1173 (m), 999, 898 (w), 862 (w), 767 (s, C=Se). Raman (ν/cm^{-1}): 2092 and 2042 (C=N), 1120, 1005, 844, 673 (C=Se). **Refinement note**: $[Et_4N]^+$ cations modelled as disordered in two positions. Restraints (ISOR) used for two carbon atoms C6, C10.

2.6.6 Synthesis of $[Et_4N][UO_2(NO_3)_3]$

A pale-white solution of [Et4N][NCTe], obtained by reaction of Na[CN] (103 mg, 2.10 mmol) with an excess of Te in dried MeCN and with the addition of $[Et_4N]Cl$ (347 mg, 2.10 mmol), was added to a green suspension of UCl_4 (100 mg, 0.263 mmol) in MeCN at 77 K. The mixture was stirred, while the temperature was slowly increased. The green colour of the solution rapidly vanished, while a black precipitate was formed and removed by filtration. Oxidation with H_2O_2 in dilute HNO_3, followed by extraction into MeOH, afforded a yellow solution. This was concentrated, by slow evaporation of the solvent in air, and deposited yellow crystals suitable for X-ray diffraction.

2.7 References

[1] S. T. Liddle, *Angew. Chem. Int. Ed.*, 2015, **54**, 8604

[2] a) B. Kanellakopulos, T. J. Marks and R. D. E. Fischer, *Organometallics of the f-Elements*, Reidel: Dordrecht, 1979; b) B. Kanellakopulos, *Handbook of Inorganic Chemistry*, *Uranium Supplement,* 1983, Volume A6, Springer: Berlin; c) N. M. Edelstein and G. H. Lander, in *The Chemistry of the Actinide and Transactinide Elements*, 4th ed., L. R. Morss, N. M. Edelstein and J. Fuger, Eds.; Springer: The Netherlands, 2010; Vols. 1-6; p 2225; d) M. B. Jones and A. Gaunt, *J. Chem. Rev.*, 2013, **113**, 1137; e) E. A. Boudreaux and L. N. Mulay, *Theory and Applications of Molecular Paramagnetism*; Wiley: New York, 1976; f) B. N. Figgis, *Ligand field theory and its applications*; Wiley-VCH: New York, 2000; g) J. Lewis and R. G. Wilkins, *Modern Coordination Chemistry: Principles and Methods*; Interscience Publishers Inc.: New

York, 1960; h) R. L. Dutta and A. Syamal, *Elements of Magnetochemistry, Affiliated East-West Press Pvt Ltd.*: New Delhi, 2007; i) H. J. Emeleus and A. G. Sharpe, *Modern Aspects of Inorganic Chemistry*; Halsted Press: New York, 1973; m) R. L. Carlin and A. J. van Duyneveldt, *Magnetic Properties of Transition Metal Compounds*; Springer-Verlag: New York, 1977

[3] D. R. Kindra and W. J. Evans, *Chem. Rev.*, 2014, **114**, 8865

[4] J. Lewis and R. G. Wilkins, *Modern Coordination Chemistry: Principles and Methods*; Interscience Publishers Inc.: New York, 1960; b) R. L. Dutta and A. Syamal, *Elements of Magnetochemistry*; Affiliated East-West Press Pvt Ltd.: New Delhi, 2007; c) H. J. Emeleus, A. G. Sharpe, *Modern Aspects of Inorganic Chemistry*; Halsted Press: New York, 1973; d) R. L. Carlin, A. J. van Duyneveldt, *Magnetic Properties of Transition Metal Compounds*; Springer-Verlag: New York, 1977; e) W. J. Evans and M. A. Hozbor, *J. Organomet. Chem.*, 1987, **326**, 299

[5] L. S. Natrajan, *Coord. Chem. Rev.*, 2012, **256**, 1583

[6] C. Danilo, V. Vallet, J.-P. Flament and U. J. Wahlgren, *Chem. Phys.*, 2008, **128**, 154310

[7] a) L. C. J. Pereira, C. Camp, J. T. Coutinho, L. Chatelain, P. Maldivi, M. Almeida and M. Mazzanti, *Inorg. Chem.*, 2014, **53**, 11809; b) K. R. Meihaus and J. R. Long, *Dalton Trans.*, 2014; c) N. Magnani, *Int. J. Quantum Chem.*, 2014, **114**, 755

[8] M. L. Neidig, D. L. Clark and R. L. Martin, *Coord. Chem. Rev.*, 2013, **257**, 394

[9] R. K. Meihaus, G. S. Minasian, W. W. Lukens, S. A. Kozimor, K. D. Shuh, T. Tyliszczak R. J. Long, *J. Am. Chem. Soc.*, 2014, **136**, 6056

[10] H. W. Turner, R. A. Andersen and D. H. Templeton, *Inorg. Chem.*, 1979, **18**, 1221

[11] S. M. Mansell, B. F. Perandones and P. L. Arnold, *J. Organomet. Chem*., 2010, **695**, 2814

[12] a) J. L. Brown, C. C. Mokhtarzadeh, J. M. Lever, G. Wu and T. W. Hayton, *Inorg. Chem.*, 2011, **50**, 5105; b) B. M. Gardner, J. McMaster, W. Lewis and S. T. Liddle, *Chem. Commun.*, 2009, 2851

[13] a) D. M. King, F. Tuna, E. J. McInnes, J. McMaster, W. Lewis, A. J. Blake, S. T. Liddle, *Nat. Chem.*, 2013, **5**, 482; b) D. M. King, F. Tuna, E. J. McInnes, J. McMaster, W. Lewis, A. J. Blake and S. T. Liddle, *Science*, 2012, **337**, 717

[14] P. Roussel, N. W. Alcock, R. Boaretto, A. J. Kingsley, I. J. Munslow, C. J. Sanders and P. Scott, *Inorg. Chem.*, 1999, **38**, 3651

[15] S. Cotton, *Electronic and magnetic properties of actinides*, in: *Lanthanide and Actinide Chemistry*, John Wiley and Son Ltd, 2006

[16] D. M. King, J. McMaster, F. Tuna, E. J. McInnes, W. Lewis, A. J. Blake and S. T. Liddle, *J. Am. Chem. Soc.*, 2014, **136**, 5619

[17] B. M. Gardner, G. Balázs, M. Scheer, F. Tuna, E. J. McInnes, J. McMaster, W. Lewis, A. J. Blake and S. T. Liddle, *Angew. Chem. Int. Ed.*, 2014, **53**, 4484

[18] L.A. Seaman, S. Fortier, G. Wu and T.W. Hayton, *Inorg. Chem.*, 2011, **50**, 636

[19] S. Fortier, B.C. Melot, G. Wu and T.W. Hayton, *J. Am. Chem. Soc.*, 2009, **131**, 15512

[20] S. Fortier, J. R. Walensky, G. Wu and T. W. Hayton, *J. Am. Chem. Soc.*, 2011, **133**, 11732

[21] See for example: B. M. Gardner, J. C. Stewart, A. L. Davis, J. McMaster, W. Lewis, A. J. Blake, S. T. Liddle, *Proc. Natl. Acad. Sci. USA*, 2012, **109**, 9265

[22] S. Fortier, J. L. Brown, N. Kaltsoyannis, G. Wu and T.W. Hayton, *Inorg. Chem.*, 2012, **51**, 1625

[23] J. L. Brown, S. Fortier, R. A. Lewis, G. Wu and T. W. Hayton, *J. Am. Chem. Soc.*, 2012, **134**, 15468

[24] H.-D. Amberger, R. D. Fischer and B. Kanellakopulos, *Theoret. Chim. Acta*, 1975, **37**, 105

[25] F. M. Chadwick, A. Ashley, G. Wildgoose, J.M. Coicoechea, S.M. Randall and D. O'Hare, *Dalton Trans.*, 2010, **39**, 6789

[26] N. A. Siladke, K. R. Meihaus, L. W. Ziller, M. Fang, F. Furche, J. R. Long and W. J. Evans, *J. Am. Chem. Soc.*, 2012, **134**, 1243

[27] F. Gendron, B. Le Guennic and J. Autschbach, *Inorg. Chem.*, 2014, **53**, 13174

[28] J. J. Baldovì, S. Cardona-Serra, J. M. Clemente-Juan, E. Coronado and A. Gaita-Arino, *Chem. Sci.,* 2013, **4**, 938

[29] S. A. Pattenaude, K. C. Mullane, E. J. Schelter, M. G. Ferrier, B. W. Stein, S. E. Bone, J. S. Lezama Pacheco, S. A. Kozimor, P. E. Fanwick, M. Zeller and S. C. Bart, *Inorg. Chem.*, 2018, **57**, 6530

[30] a) S. G. McAdams, A.-M. Ariciu, A. K. Kostopoulos, J. P. S. Walsh and F. Tuna, *Coord. Chem. Rev.*, 2017, **346**, 216; b) J. D. Rinehart and J. R. Long, *Chem. Sci.*, 2011, **2**, 2078

[31] a) E. G. Arutyunyan and M. A. Porai-Koshits, *Zh. Struk. Khim.*, 1963, **4**, 110; b) K. W. Bagnall, D. Brown and R. Colton, *J. Chem. Soc.*, 1964, 2527

[32] G. Bombieri, P. T. Moseley and D. Brown, *J. Chem. Soc., Dalton Trans.*, 1975, 1520

[33] a) R. Countryman and W. S. McDonald, *J. Inorg. Nucl. Chem*., 1971, **33**, 2213; b) Z. M. S. Al-Kazzaz, K. W. Bagnall, D. Brown and B. Whittaker, *J. Chem. Soc., Dalton Trans.*, 1972, 2273

[34] E. Hashem, J. A. Platts, F. Hartl, G. Lorusso, M. Evangelisti, C. Schulzke and R. J. Baker, *Inorg. Chem.*, 2014, **53**, 8624

[35] a) W. Griffith and M. J. Mockford, *J. Chem. Soc., Dalton Trans*, 1986, 1057; b) G. Folcher, H. Marquet-Ellis, P. Rigny, E. Soulic and G. Goodman, *J. Inorg. Nucl. Chem.*, 1976, **38**, 757; c) I. E. Grey and P. W. Smith, *Australian J. Chem.*, 1969, **22**, 311

[36] N. A. Budantseva, G. B. Andreev, A. M. Fedoseev and M. Yu. Antipin, *Radiochemistry*, 2003, **45**, 335

[37] T. J. Carter and R. E. Wilson, *Chem. Eur. J.*, 2015, **21**, 15575

[38] a) L. Sorace, C. Benelli and D. Gatteschi*, Chem. Soc. Rev.*, 2011, **40**, 3092; b) J. J. Baldovì, S. Cardona-Serra, J. M. Clemente-Juan, E. Coronado, A. Gaita-Ariño and A. Palii, *Inorg. Chem.*, 2012, **51**, 12565; c) N. Koike, H. Uekusa, Y. Ohashi, C. Harnoode, F. Kitamura, T. Ohsaka and T. Tokuda, *Inorg. Chem.*, 1996, **35**, 5798; d) M. A. Sorensen, H. Weihe, M. G. Vinum, J. S. Mortensen, L. H. Doerrer and J. Bendix, *Chem. Sci.*, 2017, **8**, 3566

[39] SHAPE Program for the Stereochemical Analysis of Molecular Fragments by Means of Continuous Shape Measures and Associated Tools, 2013, Volume 2.1

[40] M. J. Lozano-Rodriguez, P. Thuery, S. Petit, R. Copping, J. Mustre de Leon and C. Den Auwer, *Acta Cryst.*, 2011, E**67**, m487

[41] a) M. Speldrich, H. Schilder, H. Lueken and P. Kögerler, *Isr. J. Chem.*, 2011, **51**, 215; b) J. van Leusen, M. Speldrich, H. Schilder and P. Kögerler, *Coord. Chem. Rev.*, 289-290, 2015, 137-148

[42] M. Evangelisti, F. Luis, L. J. de Jongh and M. Affronte, *J. Mater. Chem.*, 2006, **16**, 2534

[43] a) G. Folcher, H. Marquet-Ellis, P. Rigny, E. Soulié and G. Goodman, *J. Inorg. Nucl. Chem*., 1976, **38**, 747; b) H.-D. Amberger and G. R. Z. Sienel, *Naturforsch.*, 1976, **31**, 769; c) J. P. Desclaux and A. J. Freeman, in *Handbook on the Physics and Chemistry of the Actinides*, Vol.

1; Freeman, A. J.; Lander, G. H.; (Eds.); Elsevier, Amsterdam, 1984; d) W. T. Carnall, G. K. Liu, C. W. Williams and M. F. Reid, *J. Chem. Phys.*, 1991, **95**, 7194

[44] a) L. A. Boatner and M. M. Abraham, *Rep. Prog. Phys*, 1978, **41**, 87; b) E. Soulie, G. Folcher and B. Kanellakopulos, *Can. J. Chem.*, 1980, **58**, 2377

[45] a) M. E. Boulon, G. Cucinotta, J. Luzon, C. Degl'Innocenti, M. Perfetti, K. Bernot, G. Calvez, A. Caneschi and R. Sessoli, *Angew. Chem., Int. Ed.*, 2013, **52**, 350; b) P. S. Vila Nova, A. G. Pereira, A. Junior, F. Gilberto, H. Bazin, H. Autiero and G. Mathis, *Quìm. Nova*, 2004, **27**, 709; c) G. Cucinotta, M. Perfetti, J. Luzon, M. Etienne, P. E. Car, A. Caneschi, G. Calvez, K. Bernot and R. Sessoli, *Angew. Chem., Int. Ed.,* 2012, **51**, 1606; d) C. Görller-Walrand and K. Binnemans, *in Handbook on the Physics and Chemistry of Rare Earths*, ed. K. A. Gschneidner and L. Eyring, Elsevier, Amsterdam, 1996, vol. **23**; e) N. Magnani, R. Caciuffo, E. Colineau, F. Wastin, A. Baraldi, E. Buffagni, R. Capelletti, S. Carretta, M. Mazzera, D. T. Adroja, M. Watanabe and A. Nakamura, *Phys. Rev. B: Condens. Matter Mater. Phys.*, 2009, **79**, 104407

[46] S. T. Liddle and J. van Slageren, *Chem. Soc. Rev.*, 2015, **44**, 6655

[47] D. E. Morris, R. E. Da Re, K. C. Jantunen, I. Castro-Rodriguez and J. L. Kiplinger, *Organometallics*, 2004, **23**, 5142

[48] R. I. Bewley, T. Guidi and S. Bennington, *Notiziario Neutroni e Luce di Sincrotrone*, 2009, **14**, 22

[49] R. Caciuffo, P. Santini, S. Carretta, G. Amoretti, A. Hiess, N. Magnani, L.-P. Regnault and G. H. Lander, *Phys. Rev. B.*, 2011, **84**, 104409

[50] See for example: a) F. J. Kettles, V. A. Milway, F. Tuna, R. Valiente, L. H. Thomas, W. Wernsdorfer, S. T. Ochsenbein and M. Murrie, *Inorg. Chem.*, 2014, **53**, 8970; b) R. Marx, F. Moro, M. Doerfel, L. Ungur, M. Waters, S. D. Jiang, M. Orlita, J. Taylor, W. Frey, L. F. Chibotaru and J. van Slageren, *J. Chem. Sci.*, 2014, **5**, 3287; c) I. S. Klokishner, S. M. Ostrovsky, S. O. Reu, A. V. Palii, L. W. P. Tregenna-Piggott, T. Brock-Nannestad, J. Bendix and H. Mutka, *J. Phys. Chem.*, 2009, **113**, 8573; d) S. K. Pedersen, L. Ungur, M. Sigrist, A. Sundt, M. Schau-Magnussen, V. Vieru, H. Mutka, S. Rols, H. Weihe, O. Waldmann, F. L. Chibotaru, J. Bendix and J. Dreiser, *Chem. Sci.*, 2014, **5**, 1650; e) S. Tsukamoto, H. Mori, H. Tatewaki and E. Miyoshi, *Chem. Phys. Lett.*, 2009, **474**, 28; f) B. Vlaisavljevich, P. Mir, C. J. Cramer, L. Gagliardi, I. Infante and S. T. Liddle, *Chem. Eur. J.*, 2011, **17**, 8424

[51] a) D. Pàez-Hernàndez, A. Muñoz-Castro and R. Arratia-Perez, *Chem. Phys. Lett.*, 2017, **683**, 421; b) J. J. Baldovì, Y. Duan, R. Morales, A. Gaita-Ariño, E. Ruiz and E. Coronado, *Chem. Eur. J.*, 2016, **22**, 13532

[52] M.–J. Crawford, K. Karaghiosoff and P. Mayer, *Z. Anorg. Allg. Chem.,* 2010, **636**, 1903

[53] D. D. Swank and R. D. Willett, *Inorg. Chem.*, 1965, **4**, 499

[54] A. W. Down, *Chem. Commun.*, 1968, 1290

[55] D. Brown, *J. Chem. Soc. A*, 1966, 766

[56] There are 6 examples in the Cambridge Structural Database: a) I. A. Charushnikova and C. Den Auwer, *Koord. Khim*, 2004, **30**, 546; b) P. Thuery, *CrystEngComm*, 2013, **15**, 6533; c) J.-C. Berthet, P. Thuery, J.-P. Dognon, D. Guillaneux and M. Ephritikhine, *Inorg.Chem.*, 2008, **47**, 6850; d) K. M. Ok, M. B. Doran, D. O'Hare, *J. Mater. Chem.*, 2006, **16**, 3366; e) N. N. Rammo, K. R. Hamid and T. K. Ibrahim, *J. Alloys Compd.*, 1994, **210**, 319

[57] A. Mesbah and J. A. Ibers, *Acta Crystallogr.*, 2012, **68**, 76

[58] N. A. Semenov, A. V. Lonchakov, N. A. Pushkarevsky, E. A. Suturina, V. V. Korolev, E. Lork, V. G. Vasiliev, S. N. Konchenko, J. Beckmann, N. P. Gritsan and A. V. Zibarev, *Organometallics*, 2014, **33**, 4302

[59] A. S. Foust, *Chem. Commun.*, 1979, 414

[60] G. A. Bain and J. F. Berry, *J. Chem. Edu.*, 2008, **85**, 532

[61] SHELXTL 6.14 Bruker AXS Inc., Madison, WI, 2000-2003; Sheldrick, G.M. *Acta Crystallogr*, 2008, **A64**, 112

[62] J. L. Kiplinger, D. E. Morris, B. L. Scott and C. J. Burns, *Organometallics*, 2002, **21**, 5978

[63] T. Cantat, B. L. Scott and J. L. Kiplinger, *Chem. Commun.*, 2010, **46**, 919

Chapter 3

Reactivity Study of the $[U(NCS)_8]^{4-}$ Ions in Non-Aqueous Media

3.1 Introduction

Studies aimed at understanding the reactivity of actinide compounds can give insight into the electronic structure of these compounds and, therefore, into the degree of participation of the *5f* and *6d* orbitals in metal-ligand bonding.

Uranium chemistry has been attracting attention as some uranium compounds have proved to possess unusual magnetic behaviour. In particular, as discussed in Chapter 1 and Chapter 2, $5f^3$ U(III) compounds can exhibit unusual magnetization dynamics and are candidates for single-molecule (SMM) and single-ion (SIM) magnets.[1] $5f^1$ uranyl(V) compounds also have anisotropy and can show similar magnetic behaviour, on its own[2] or in combination with transition metals (TM)[3] or lanthanides (Ln).[4] These mixed-metal complexes are typically assembled via cation-cation interactions (CCIs), which often involve the $[UO_2]^+$ ion with another metal ion via a U=O_{yl} interaction, *i.e.* with the -yl oxygen acting as a Lewis base.[5] Although rather rare, these interactions between actinyl(V) units are attracting attention and they are also likely involved in the disproportionation[6] reaction of the $[UO_2]^+$ ion.

The first observation of a magnetic exchange coupling in an actinide-containing molecule was reported nearly 30 years ago for the dinuclear U(V) 1,4-diimido-benzene-bridged complex $[(MeC_5H_4)_3U]_2(\mu\text{-}1,4\text{-}N_2C_6H_4)$.[7] For this sample, the drop in the magnetic moment at very low temperature was attributed to an antiferromagnetic coupling between the two $5f^1$ U(V) centres. Subsequently, Arnold *et al.*[8] reported on a strong U(V)-U(V) coupling exhibited by a variety of dinuclear U(V) complexes characterised by an unusual core cluster [Si-OUO_2UO-Si], with a butterfly-shape (Figure 3.1, left). These complexes showed a short U−U separation (3.355(7) Å) and an antiferromagnetic exchange coupling between the two $5f^1$ centres via superexchange interactions.[8] More recently, an antiferromagnetically coupled dinuclear U(V) complex (Figure 3.1, right), characterized by a diamond-shaped [U(μ-O)$_2$U] structural motif (Figure 3.1, centre), has also been reported by Schmidt *et al.*[9]

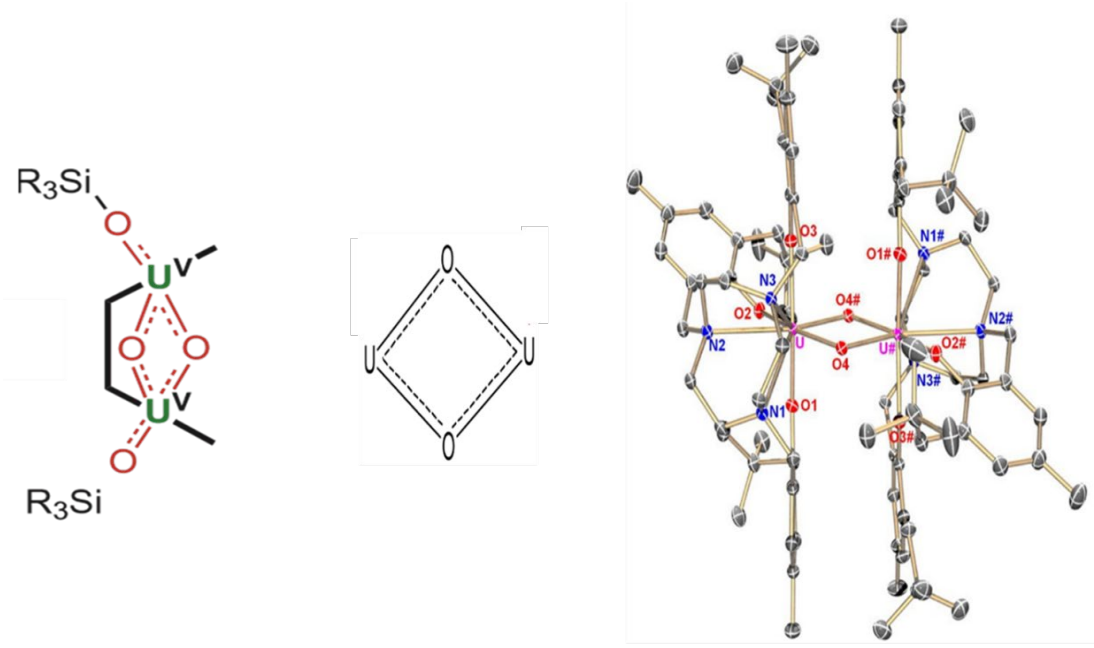

Figure 3.1. (Left) Dinuclear U(V) core cluster with a butterfly-shape, taken from reference 8. (Centre) diamond core [U(μ-O)$_2$U] structural motif. (Right) molecular structure of a dinuclear uranium oxo complex, featuring this diamond core and a strong antiferromagnetic exchange coupling between the two U(V) ions (taken from reference 9).

This chapter is focused on the exploration of the reactivity of the $[U(NCS)_8]^{4-}$ ion with different counter cations and in different media. Two mixed-valent uranium compounds will be fully described and, for one of them, exchange magnetic interactions between different paramagnetic uranium ions have also been investigated.

Next, a mixed-metal complex of formula $[Co(bipy)_3]_2[U(NCS)_8]_2$ will be presented; for this, structural, magnetic and spectroscopic data are indicative of a Co(III)-U(V) electronic configuration. In the subsequent section, the discussion will be centred on a 9-coordinate U(IV) complex of formula $Cs_5[U(NCS)_9][NCS]$. UV-vis-NIR and magnetic measurements have been performed on this system to unambiguously confirm the formal +4 oxidation state for the uranium ion, while the low-lying energy level electronic structure has been explored by specific heat capacity measurements and far-IR spectroscopy. Unsuccessful attempts to obtain a U(III) thiocyanate compound via chemical reduction of $[Et_4N]_4[U(NCS)_8]$ will be also examined. Finally, the results of spectroelectrochemistry measurements, performed on both $[Et_4N]_4[U(NCS)_8]$ and $Cs_5[U(NCS)_9][NCS]$, will be discussed.

3.2 Mixed-Valent Uranium Compounds from Oxidation of $[U(NCS)_8]^{4-}$

3.2.1 Structural and Vibrational Characterization

It has been proved that when isolated in solid state the $[U(NCS)_8]^{4-}$ ion is stable in air for months;[10] however, it can undergo slow oxidation in solution. The oxidation of $[U(NCS)_8]^{4-}$ was attempted in MeCN solutions using a number of inorganic- and organic-based one or two electron oxidation reagents, such as: 2-acetyl pyrazine, I_2, CuI and tetracyanoethylene (TCNE). However, a metal-based reactivity[11] was not observed, although it was predictable since previous electrochemistry measurements have shown a ligand-based oxidation for this thiocyanate U(IV) complex.[10] Nevertheless, a two metal-based electron oxidation occurred when $[Et_4N]_4[U(NCS)_8]$ was treated with nitrogen dioxide, $NO_{2(g)}$, or $NaNO_2$ in MeCN solutions, and the uranyl(VI) complex, $[Et_4N]_3[UO_2(NCS)_5]$, was isolated and identified by X-ray diffraction measurements. However, this reaction was too fast for an accurate spectroscopic monitoring. Previous studies also reported on the oxidation of U(IV) and U(V) complexes promoted by nitrite salts, where the uranium compound reductively cleaves an N–O bond, to selectively replace a U–X bond with an oxo ligand.[12] Subsequently, oxidation experiments on $[U(NCS)_8]^{4-}$ have been performed by simply dissolving $Cs_4[U(NCS)_8]$ in different solvents and leaving the vials in air. In this case, two different morphologies of dark green crystals were isolated and fully characterized. The recrystallization from MeCN formed, over a month, emerald green crystals, whose vibrational spectra show bands attributable to the $[UO_2]^{2+}$ ion at $\nu_1(U{=}O) = 844\ cm^{-1}$ and $\nu_3(U{=}O) = 922\ cm^{-1}$ (Figure 3.2). For clarity, this compound will be called **U-MeCN**.

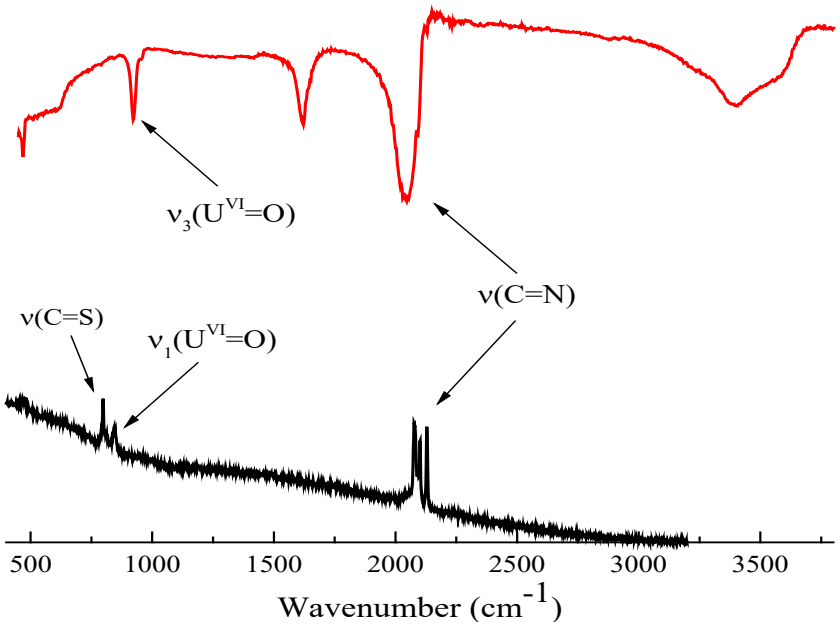

Figure 3.2. Raman (black line) and IR (red line) spectra of **U-MeCN**.

When the recrystallization was carried out in dimethylformamide (DMF), different dark green crystals were isolated and IR and Raman spectroscopy revealed bands assignable to the $[UO_2]^{2+}$ ion, at $\nu_1(U^{VI}{=}O)$ = 846 cm^{-1} and $\nu_3(U^{VI}{=}O)$ = 912 cm^{-1}, and bands characteristic of the $[UO_2]^{+}$ ion, at $\nu_1(U^{V}{=}O)$ = 815 cm^{-1} and $\nu_3(U^{V}{=}O)$ = 865 cm^{-1} (Figure 3.3).[3, 13] For clarity this compound will be called **U-DMF**.

Ordinarily, the oxidation in air of $Cs_4[U(NCS)_8]$ in the solid state yields dark yellow crystals of the uranyl(VI) thiocyanate $Cs_3[UO_2(NCS)_5]$,[10] therefore the formation of **U-DMF** and **U-MeCN** is, presumbaly, due to a solubility effect in different solvents.

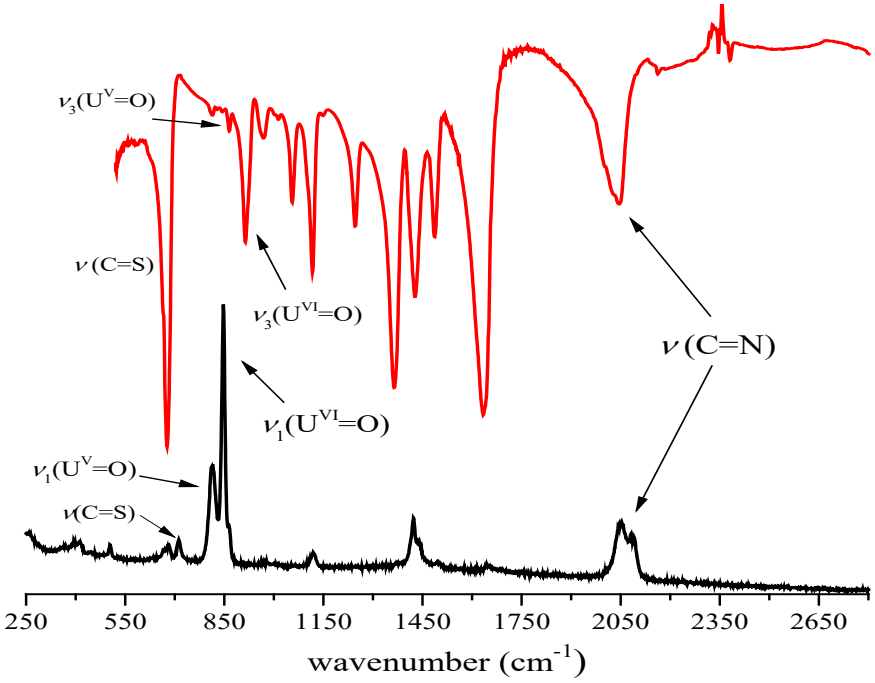

Figure 3.3. IR (red line) and Raman (black line) spectra of **U-DMF**.

The ν_1 and ν_3 stretching modes of the triatomic $[UO_2]^{n+}$ (n = 1, 2) system can be used to calculate the stretching force constants (k_1) and the interaction force constants (k_{12}) by the equations 1 and 2; where c is the speed of light (2.99776×10^{10} cm sec^{-1}), m_1 is the unified atomic mass unit (1.66×10^{-24} g) and m_x and m_y are the atomic masses of uranium and oxygen respectively.[14]

$$k_1 = \frac{4\pi^2 c^2 m_1 v_1^2 m_y + m_y \left(\frac{4\pi^2 c^2 m_1 v_3^2}{1 + \frac{2m_y}{m_x}} \right)}{2} \quad (1)$$

$$k_{12} = \frac{4\pi^2 c^2 m_1 v_1^2 m_y - m_y \left(\frac{4\pi^2 c^2 m_1 v_3^2}{1 + \frac{2m_y}{m_x}} \right)}{2} \quad (2)$$

For these systems, k_1 gives an indication of bond strength and k_{12} describes the interaction between the two -yl oxygen atoms. Selected vibrational data for **U-MeCN** and **U-DMF** are listed in Table 3.1, along with the corresponding calculated force constants k_1 and k_{12}. Notably, in this case, it is possible to ignore the interactions between the uranyl ion and the equatorial ligands (as they are principally ionic) and the O=U=O moiety can be treated as a linear triatomic molecule.[15]

Table 3.1. Vibrational data for **U-MeCN** and **U-DMF** in the solid state.

	U-MeCN	**U-DMF**	
	U(VI)	U(VI)	U(V)
ν_1(U=O) (cm^{-1})	844	846	815
ν_3(U=O) (cm^{-1})	922	912	865
k_1 (mdyn/Å)	6.88	6.83	6.24
k_{12} (mdyn/Å)	−0.17	−0.08	+0.03
Raman ν(N=C) (cm^{-1})	2128, 2101, 2078	2095, 2039	
IR ν(N=C) (cm^{-1})	2044	2050	
Raman ν(C=S) (cm^{-1})	796	743	
IR C=S (cm^{-1})	616	612	

For **U-DMF** the vibrational data show a decrease in the stretching force constant (k_1) for the U(V) compared to U(VI) ion. This signifies a weakening of the U=O bond, moving from U(VI) to U(V), and the reason might be the presence of one additional unpaired *f*-electron in the $[UO_2]^+$ ion, which is located in a δ_u nonbonding orbital.[16] For uranyl systems, Denning has shown that this δ_u nonbonding orbital mixes with a π_u^* antibonding orbital because of spin-orbit coupling, resulting in a configuration between $\sigma_u\pi_u^*$ and $\sigma_u\delta_u$.[17] Therefore, the presence of this additional *f*-electron in $[UO_2]^+$ could cause an increase in the antibonding character for the bonding in the uranyl moiety, moving from U(VI) to U(V), resulting in a reduced stretching force constant.

Moreover, the interaction force constant (k_{12}) for the $[UO_2]^{2+}$ ion, in both **U-MeCN** and **U-DMF**, was found to be negative, and this corresponds to a significant reduction of the force constant, and consequently of the energy, for the $\nu_1(U^{VI}{=}O)$ symmetric compared to the $\nu_3(U^{VI}{=}O)$ anti-symmetric stretching mode. Indeed, experimentally, in both **U-MeCN** and **U-DMF**, the $\nu_1(U^{VI}{=}O)$ symmetric stretching mode appears at lower energy compared to the equivalent anti-symmetric mode, determining a negative value for k_{12}. This result can be thought of as the two U=O bonds working in tandem due to an "inverse trans influence" effect,[18] which finally gives rise to a negative value for the interaction force constant. This "inverse trans influence" effect is often experienced by actinyl compounds, but interestingly in **U-DMF** the value of k_{12} for the $[UO_2]^+$ ion was found to be positive.

3.2.2 Photophysical Characterization of U-MeCN and U-DMF

To corroborate the results from IR and Raman spectroscopy for the oxidation of $[U(NCS)_8]^{4-}$, electronic absorption spectra of **U-DMF** and **U-MeCN** have been measured in MeCN solutions and compared with that of the parent $Cs_4[U(NCS)_8]$. Figure 3.4 shows the profiles in the UV region, while the bands in the vis-NIR region are presented in Figure 3.5. For **U-DMF**, the absorption spectrum has been acquired also in the solid state (Figure 3.6) and compared with that of $Cs_4[U(NCS)_8]$.

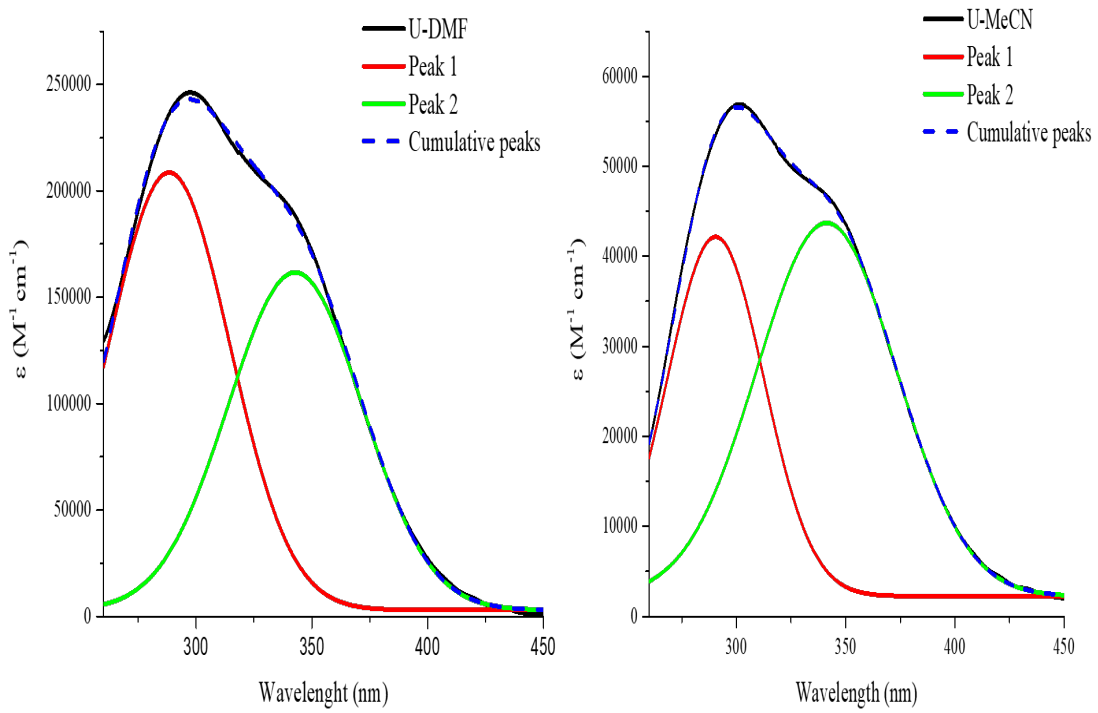

Figure 3.4. UV spectra of (left) **U-DMF** and (right) **U-MeCN** measured at 1.10 x 10^{-6} M in MeCN at room temperature.

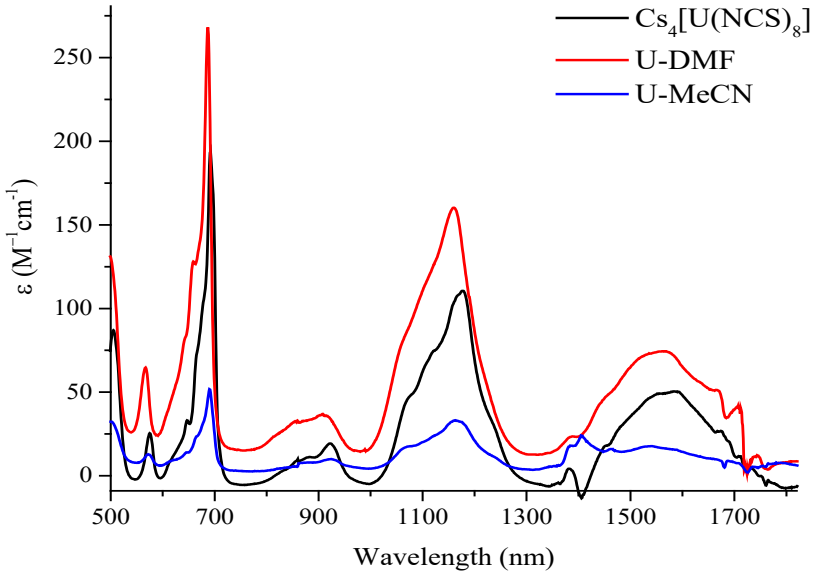

Figure 3.5. vis-NIR spectra of **U-DMF** (1.10 x 10^{-4} M), **U-MeCN** (1.10 x 10^{-3} M) and $Cs_4[U(NCS)_8]$ (1.69 x 10^{-4} M), measured in MeCN at room temperature.

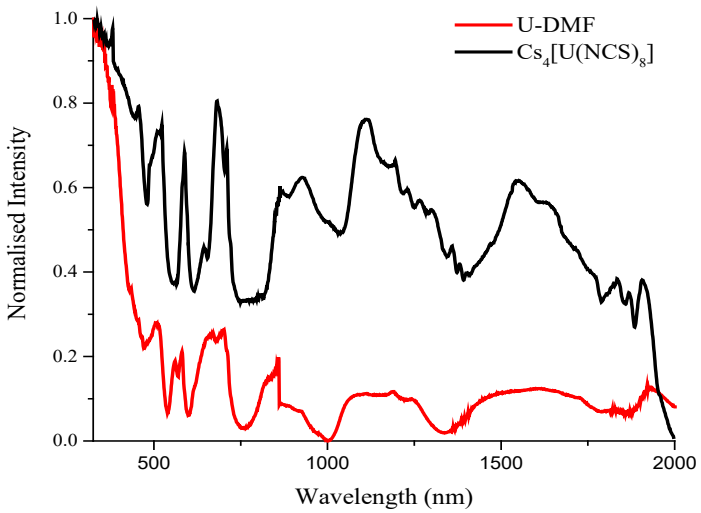

Figure 3.6. Solid state UV-vis-NIR spectrum of **U-DMF** and $Cs_4[U(NCS)_8$, measured at room temperature.

In the UV spectra (Figure 3.4) the intense band at 288 nm (peak 1) is due to thiocyanate-based $\pi \rightarrow \pi^*$ transitions, while the feature at 343 nm (peak 2) is assignable to $n \rightarrow \pi^*$ transitions, again thiocyanate-based. More significantly, the bands in the vis-NIR region (Figure 3.5 and Figure 3.6) are indicative of U(IV) species as they are due to the typical intra-configurational Laporte-forbidden *f-f* electronic transitions of a $5f^2$ U(IV) ion, which can be assigned to transitions from the Russell-Saunders coupled $^3H_4$ ground state to states of higher energy.[19] Moreover, in the vis-NIR region of the spectra of **U-DMF**, bands

attributable to the $[UO_2]^+$ ion have not been observed, but this is explainable as their extinction coefficients are known to be relatively very small ($\varepsilon \approx 10\ M^{-1}\ cm^{-1}$).[20] Table 3.2 lists the *f-f* transitions observed in the solution absorption spectra of **U-MeCN**, **U-DMF** and $Cs_4[U(NCS)_8]$ (Figure 3.5), along with the values of the corresponding molar extinction coefficients (ε) and oscillator strengths (*f*).

Table 3.2. *f-f* electronic transitions of **U-MeCN**, **U-DMF** and $Cs_4[U(NCS)_8]$ in MeCN solution.

Compound	Transition	λ (nm) [Energy (cm^{-1})]	ε ($M^{-1}\ cm^{-1}$)	Oscillator strength (f x 10^{-4})
$Cs_4[U(NCS)_8]$ (10^{-4} M)	$^3P_1$	573 [17452]	130	0.493
	$^3P_0/^1D_2/^1G_4$	691 [14471]	287	5.90
	$^3H_6$	918 [10893]	99	0.505
	$^3F_4$	1160 [8621]	192	4.38
	$^3F_3/^3H_5$	1539 [6498]	105	1.62
U-MeCN (10^{-3} M)	$^3P_2$	573 [17452]	13	5.27
	$^3P_0/^1D_2/^1G_4$	690 [14492]	52	2.23
	$^3H_6$	925 [10810]	10	0.712
	$^3F_4$	1074 [9311]	18	1.65
	$^3F_3/^3H_5$	1406 [12189]	24	0.956
U-DMF (10^{-3} M)	$^3P_1$	503 [19880]	250	8.25
	$^3P_0/^1D_2/^1G_4$	566 [17668]	128	2.85
	$^3H_6$	687 [14556]	536	11.5
	$^3F_4$	858 [11655]	65	3.14
	$^3F_3/^3H_5$	1159 [8628]	320	7.91

The intensity of these *f-f* electronic transitions is small ($\varepsilon \approx 10$ - $320\ M^{-1}\ cm^{-1}$) and this indicates the absence of any "intensity stealing mechanism"[21] by the *f-f* transitions from the fully allowed charge transfer transitions. This result is in line with an ionic nature for the U–N and U–O bonds in these systems.

The concept of oscillator strength derives from the classical theory that when an electron is bound to an atomic nucleus and possesses perfect oscillating properties, then its excitation probability has an oscillator strength of unity. The oscillator strength (*f*) is a dimensionless quantity and can have values between 0 and 1. Moreover, when a molecule is considered as a classical oscillating dipole, the oscillator strength can be calculated by the integrals over the absorption bands (Equation 3; ε = molar extinction coefficient, ν = wavenumber). From the data in Table 3.2, it is apparent that, within the calculation error,

there are no clear trends in the oscillator strengths for the observed *f-f* transitions among these uranium complexes.

$$f = 4.3\,x\,10^{-9} \int \varepsilon\, d\nu \qquad (3)$$

U-DMF allows for an interesting photophysical examination; indeed, all the three spectroscopically evidenced uranium species (U(IV), $[UO_2]^{+}$ and $[UO_2]^{2+}$) are amenable to study by photoluminescence spectroscopy, as discussed in Chapter 1. Thus, emission and excitation spectra of *ca.* 1 x 10^{-5} M solutions of **U-DMF** in MeCN were measured and are presented in Figure 3.7.

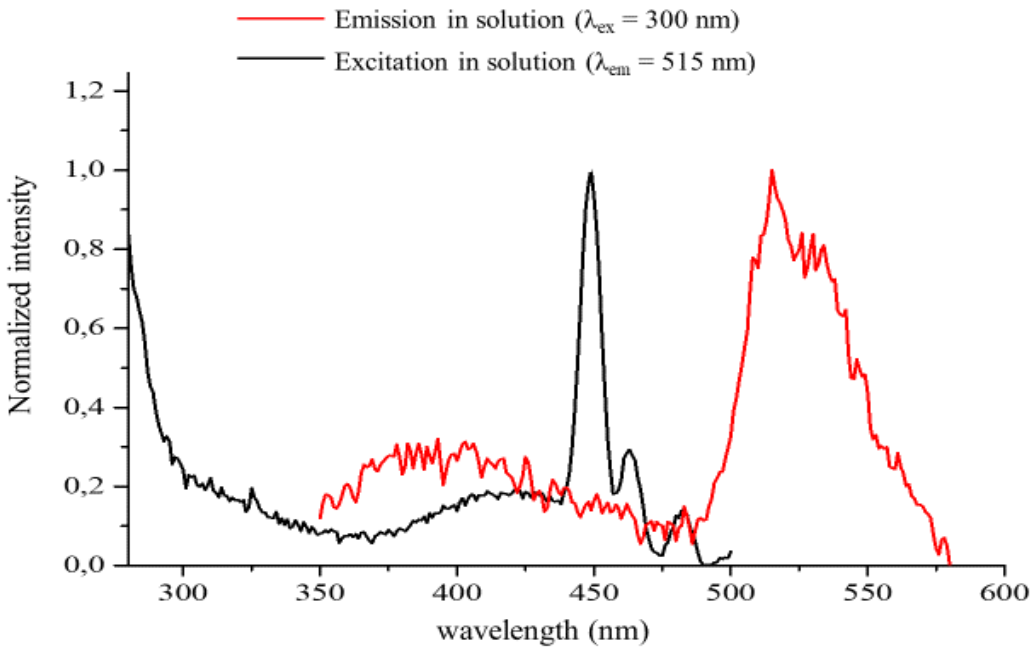

Figure 3.7. Emission (red line) and excitation (black line) spectrum of **U-DMF** (1 x 10^{-5} M) in MeCN.

The emission profile (Figure 3.7, red line) shows two features (between 350 and 470 nm and between 490 and 570 nm) that are broad and poorly resolved, while the corresponding excitation spectrum (Figure 3.7, black line) displays the characteristic vibronically coupled LMCT bands of the $[UO_2]^{2+}$ cation, between 440 and 480 nm. The emission spectrum for **U-DMF** was also measured in solid state at 77 K (Figure 3.8) and immediately apparent is the increase in the resolution.

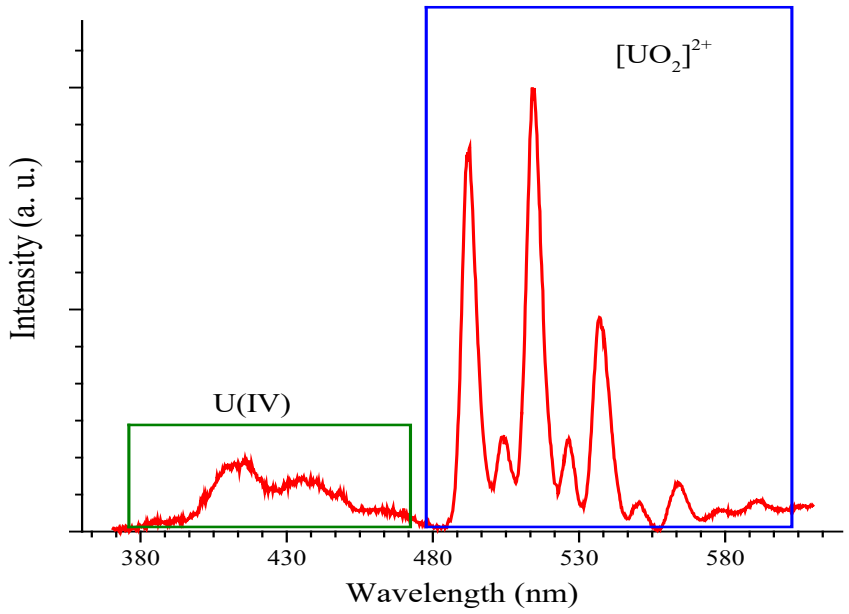

Figure 3.8. Solid state emission spectrum of **U-DMF** at 77 K (λ_{ex} = 330nm).

The relatively weak bands, from 400 to 470 nm, are assignable to a U^{IV} ion, while the transitions between 490 and 600 nm are characteristic of the $[UO_2]^{2+}$ ion. The vibronic coupling and peak positions of the uranyl(VI) bands are identical to those showed by the $[R_4N]_3[UO_2(NCS)_5]$ series (Chapter 4), while the emission profile of the U(IV) component is similar to those reported for $[Et_4N]_4[U(NCS)_8]$ (λ_{ex} = 280 - 350 nm, λ_{em}= 410 nm)[10] and $[Li(THF)_4[[UCl_5(THF)]$ (λ_{ex} = 278 - 331 nm, λ_{em} = 421 nm).[22]

Regarding **U-MeCN**, the excitation and emission spectra, recorded in solid state at 77 K, show the typical features of only the uranyl(VI) (Figure 3.9). The corresponding spectra measured in solution were broad and less informative.

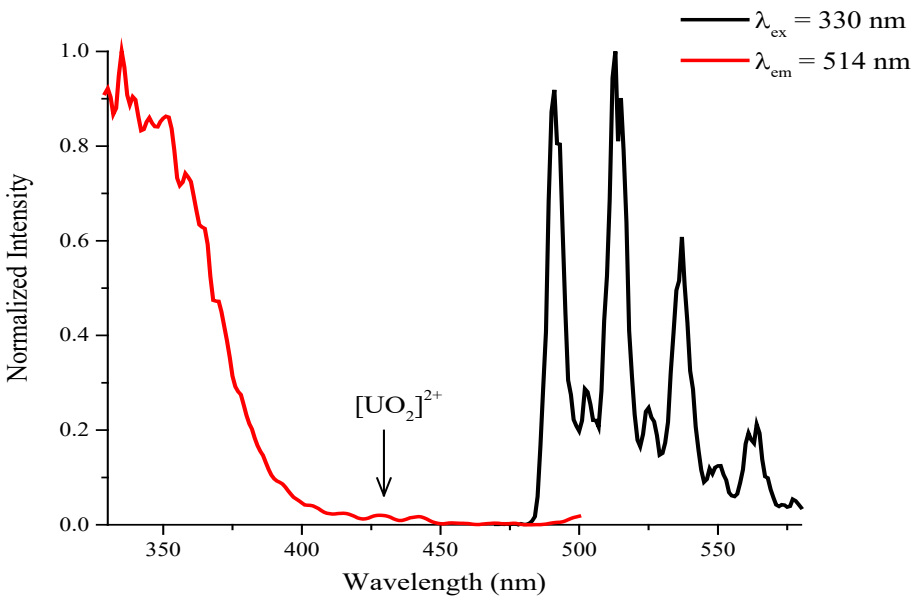

Figure 3.9. Solid-state excitation (red) and emission (black) spectra of **U-MeCN** at 77 K.

The lifetimes of the emission in solution, which is due to the uranyl(VI) ion, were 0.46 μs for **U-MeCN** and 0.40 μs for **U-DMF**, somewhat lower than the average of 1.5 μs showed by the $[R_4N]_3[UO_2(NCS)_5]$ series (Chapter 4).

Thus, taken together, the spectroscopic data suggest in these compounds the presence of uranium in different oxidation states: U(IV) and $[UO_2]^{2+}$ in **U-MeCN** and U(IV), $[UO_2]^{+}$ and $[UO_2]^{2+}$ in **U-DMF**. To confirm this, green single crystals of both compounds were studied by X-ray diffraction measurements.

3.2.3 X-ray Diffraction Studies of U-MeCN and U-DMF

X-ray diffraction measurements revealed a molecular composition of $Cs_{14}[\{U(NCS)_8\}_3\{UO_2(NCS)_4(H_2O)\}]\cdot 4.5H_2O$ for **U-MeCN** and of $[U(DMF)_8(\mu\text{-}O)U(NCS)_5(\mu\text{-}O)U(DMF)_7(NCS)][UO_2(NCS)_5]$ for **U-DMF**, confirming the results from the spectroscopic measurements.

The solid-state crystal structure of $[U(DMF)_8(\mu\text{-}O)U(NCS)_5(\mu\text{-}O)U(DMF)_8(NCS)][UO_2(NCS)_5]$ (**U-DMF**) is shown in Figure 3.10, along with a depiction of the coordination geometry around two selected uranium atoms; while the corresponding crystallographic data are in Appendix 2. The full list of angles and bond lengths of this compound have been tabulated in Appendix 2.1, in the external CD source of his thesis. Regarding **U-MeCN**, its solid-state crystal structure is presented in Figure 3.11 and a partial packing diagram, along the crystallographic *c*-axis, is shown in Figure

3.12. The corresponding crystallographic data are in Appendix 2, while the full list of angles and bond lengths is tabulated in Appendix 2.1, located in the external CD source of this thesis.

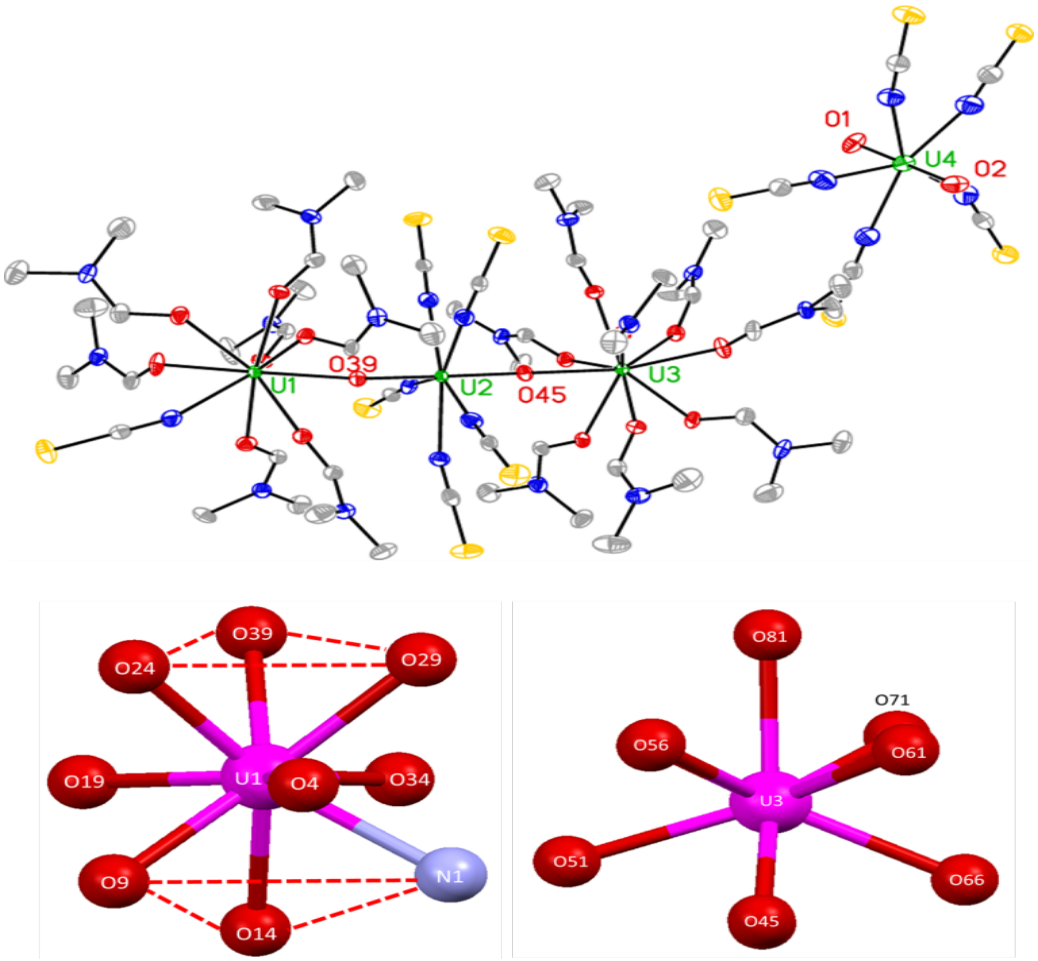

Figure 3.10. (Top) Thermal ellipsoid plot of $[U(DMF)_8(\mu\text{-}O)U(NCS)_5(\mu\text{-}O)U(DMF)_8(NCS)][UO_2(NCS)_5]$, with atomic displacement shown at 50% probability; colour code: U – green, O – red, N – blue, C – grey and S – yellow. Hydrogen atoms omitted, and only U and selected heteroatoms labelled for clarity. (Bottom) coordination geometry around U1 and U3.

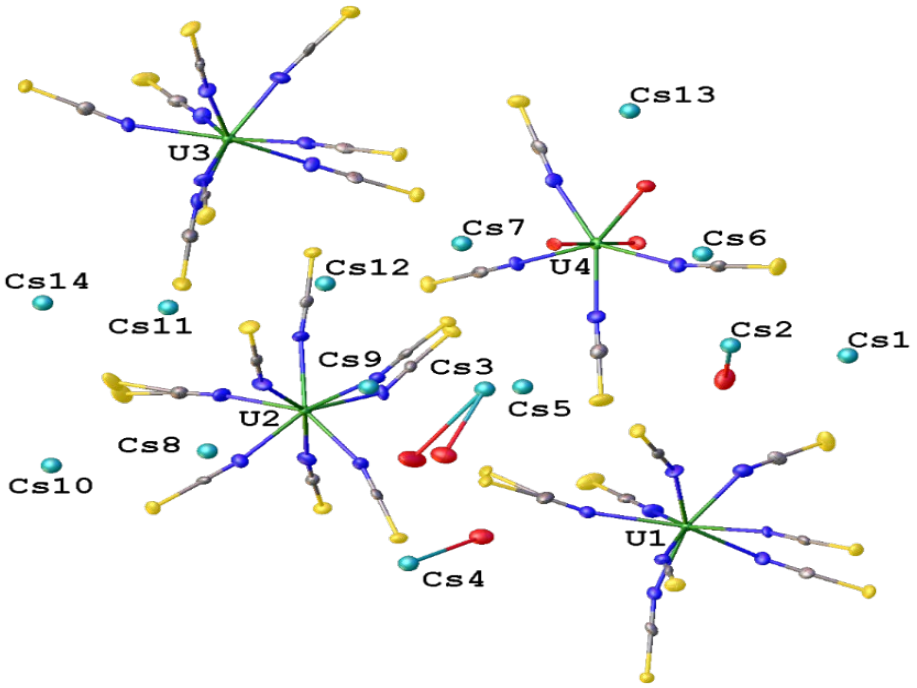

Figure 3.11. Thermal ellipsoid plot of **U-MeCN** with only metal atoms labelled and bonds to Cs atoms omitted (except coordinated water molecules) for clarity. Atomic displacement shown at 50% probability. Colour code: U – green, O – red, N – blue, C – grey, S – yellow and Cs – light blue.

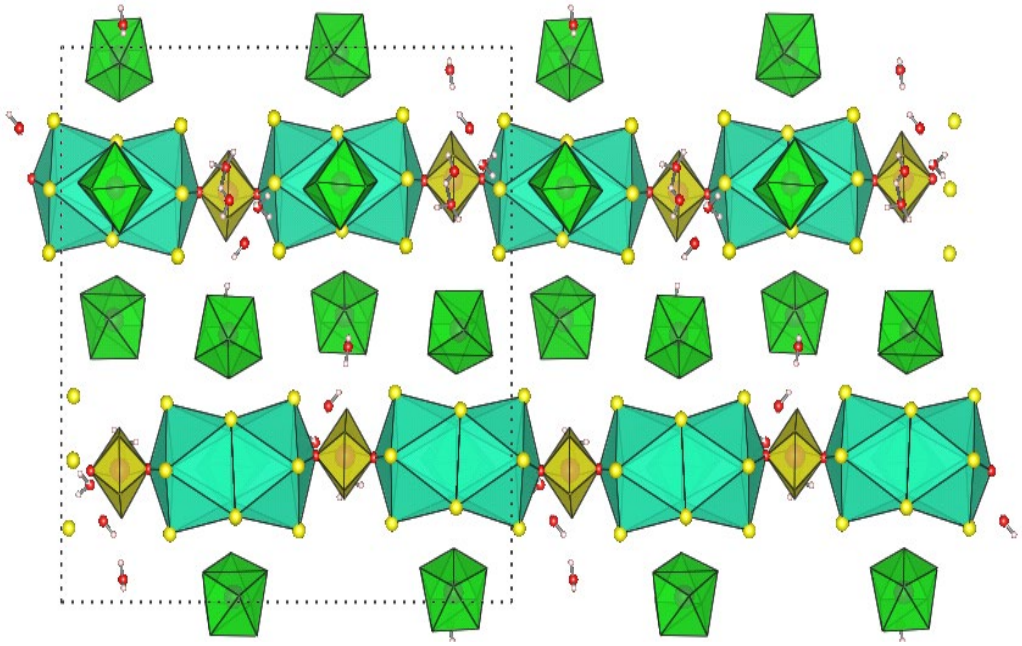

Figure 3.12. Partial packing of **U-MeCN** along the crystallographic *c*-axis showing the CCIs between the uranyl (yellow polyhedral) and Cs (blue polyhedral); S = yellow, O = red, green polyhedral = U(IV).

In both compounds, the N=C and C=S bond lengths are invariant irrespective of oxidation states and are consistent with previous examples on U(IV) thiocyanate complexes[10, 22, 23] and with the $[R_4N]_3[UO_2(NCS)_5]$ series (Chapter 4).

The structure of **U-MeCN** is a coordination polymer, whose monomeric unit (Figure 3.11) clearly shows three U(IV) and one uranyl(VI) ions. For the three U(IV) complexes, the average U(IV)–N (2.433(2) Å) bond length is very similar to that shown by previous examples.[10, 22] Regarding the uranyl(VI) ion, the average U–N (2.400(3) Å) bond length and the U=O (1.770(7) and 1.777(6) Å) bond lengths are unexceptional compared with the $[R_4N]_3[UO_2(NCS)_5]$ series (Chapter 4). The coordination geometry around U1, U2 and U3 are square antiprismatic from shape analysis[24] (U1: SAPR-8 0.364; U2: SAPR-8 1.180; U3: SAPR-8 0.384). There are numerous S…Cs short contacts and the uranyl(VI) ion forms a CCI with a Cs^+ ($d_{O\text{-}Cs}$ = 2.974(2) Å) that bridges to a second Cs^+ ion through Cs-S-Cs interactions (Figure 3.12); where the sulfur atoms are those from a U(IV)-NCS fragment. These CCIs are very weak; indeed, they do not perturb the –yl unit as can be judged by comparison with the vibrational spectra of the aforementioned $[R_4N]_3[UO_2(NCS)_5]$ compounds (Chapter 4). The water molecule coordinated to the uranyl ion is involved in hydrogen bonding to the water coordinated to the Cs^+ ion ($d_{O\cdots O}$ = 2.726(13) Å).

Moreover, after three months of exposure to air, **U-MeCN** lost its crystallinity and became a yellow gel. It was then redissolved in MeCN and a further 2-electron metal-based oxidation occurred slowly at the three U(IV)-NCS fragments; indeed, in air the new solution deposited yellow single crystals and X-ray diffraction showed them to be the known uranyl(VI) compound of formula $Cs_3[UO_2(NCS)_5]$.[25]

Regarding $[U(DMF)_8(\mu\text{-}O)U(NCS)_5(\mu\text{-}O)U(DMF)_8(NCS)][UO_2(NCS)_5]$ (**U-DMF**), in order to assign the oxidation states to the uranium centres, bond valence sum analysis[26] can be used and this gives values of U1 = 4.35, U2 = 4.79, U3 = 4.47, U4 = 5.61, indicating a [U(IV)-U(V)-U(IV)][U(VI)] configuration which also charge balances. The average U(VI)–N (2.460(3) Å), U(V)–N (2.458(2) Å) and U(IV)–N (2.471(6) Å) show the expected trend based on ionic radii,[27] but longer than in **U-MeCN**. The U(VI)=O bond lengths (1.783(6) and 1.769(6) Å) are very similar to the ones observable in $[R_4N]_3[UO_2(NCS)_5]$ series (average of 1.742(2), Chapter 4), while the U(V)=O bond lengths (1.915(5) and 1.922(5) Å) are more characteristic for uranyl(V) ions engaged in CCIs than for a U(IV)–O–U(IV) arrangement as the bond lengths are longer *e.g.* at 2.058(3) Å in the complex $[(UO_2I_4)\{UICl(py)_4\}_2]$.[4b] The U^{IV}–O_{DMF} bond lengths range from

2.379(5) - 2.474(5) Å and the –yl oxygen involved in the CCI shorter at U(1)–O(39) = 2.311(5) Å and U(3)–O(45) = 2.299(5) Å, with a linear O=U=O fragment (O(39)-U(2)-O(45) = 178.9(2)^{o}).

The geometry around U1 (Figure 3.10, bottom) is a distorted tricapped trigonal prism (D_{3h}), as described by continuous shape measures.[24] Support for this assignment comes from closer inspection of the bond lengths and angles. Thus, the longer U–O_{DMF} bonds are associated with the capping ligands (U(1)–O(4) = 2.474(5) Å; U(1)–O(19) = 2.472(5) Å; U(1)-O(34) = 2.440(5) Å) and the O-U-O angles are 114.07(17)^{o}, 117.29(17)^{o} and 128.34(17)^{o}, while the O-U-O angles in the trigonal prism are 70-80^{o}. The geometry around U3 is a mono-capped square antiprism, where O(81) is the capping oxygen and has the longest bond length (U(3)–O(81) = 2.461(5) Å). It is instructive to compare these U–O bond lengths to that of $[U(DMF)_9]^{n+}$ (n = 3,[28] 4)[29] which has the same geometry: the U–O bonds that define the square antiprism are 2.52(3) Å for U(III) and 2.37(1) Å for U(IV); in **U-DMF** this bond lengths average at 2.39(5) Å corroborates the assignment of U(IV) for U3.

Thus, the spectroscopic and structural analysis supports a [U(IV)-U(V)-U(IV)][U(VI)] configuration for **U-DMF**, with simultaneously three paramagnetic uranium ions (U1, U2 and U3). Therefore, it was of interest to investigate any relevant exchange interactions between these ions by measuring the magnetic behaviour of **U-DMF** at different temperatures.

3.2.4 Magnetic Properties of $U(DMF)_8(\mu\text{-}O)U(NCS)_5(\mu\text{-}O)U(DMF)_8(NCS)][UO_2(NCS)_5]$

The magnetic profile of $U(DMF)_8(\mu\text{-}O)U(NCS)_5(\mu\text{-}O)U(DMF)_8(NCS)][UO_2(NCS)_5]$ is shown in Figure 3.13, as μ_{eff} *vs* *T* plots, at 0.1 and 1.0 T, and as M_m *vs* *B* plot at 2.0 K (insert).

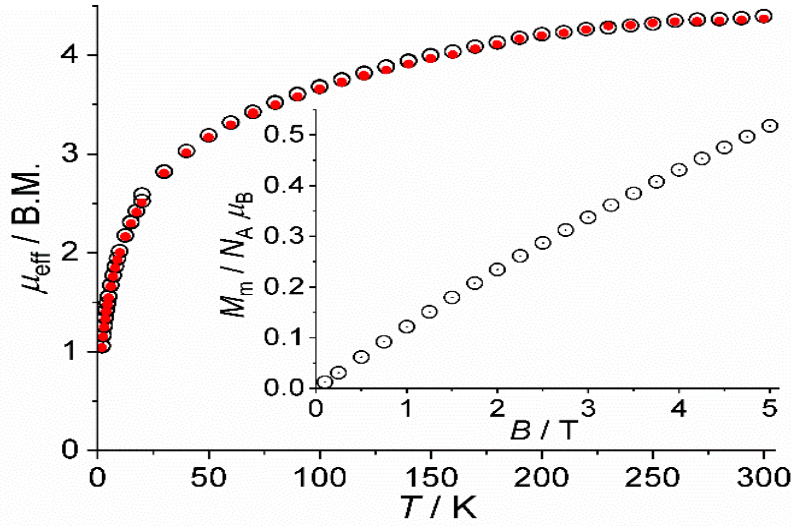

Figure 3.13. Effective magnetic moment *vs* *T* (K) of [U(DMF)$_8$(μ-O)U(NCS)$_5$(μ-O)U(DMF)$_8$(NCS)][UO_2(NCS)$_5$], measured at 0.1 T (open black circles) and 1.0 T (red full dots); inset: molar magnetization at 2.0 K.

At 300 K, the effective magnetic moment is 4.39 B.M. at 0.1 T and slightly less at 1.0 T (4.37 B.M.). Upon cooling, the effective moment gradually decreases with temperature, but there is a sharp drop below 50 K and, at 2.0 K, μ_{eff} has values of 1.05 and 1.04 B.M. at 0.1 and 1.0 T, respectively. This marginal difference is also reflected by the shape of the molar magnetization; indeed, at 2.0 K, M_m is an almost linear function of the applied field up to 5.0 T, indicating a virtually constant magnetic susceptibility in this field range, which yields a value of 0.5 N_A μ_B at the highest field (μ_B = B.M.).

As discussed in Chapter 1, determining the oxidation state of a uranium complex on the basis of the effective magnetic moment at room temperature is impossible with certainty, but the profile of the magnetic behaviour *vs* temperature can be more informative.[1d] For example, the sum of the room temperature mean values of the U(IV) and U(V) compounds reported in reference 1d gives $\mu_{eff} = (2\times2.77^2 + 2.07^2)^{1/2} = 4.43$ B.M., very close to the measured value for **U-DMF**. This very good agreement alone, however, cannot be used as proof for the postulated [U(IV)-U(V)-U(IV)][U(VI)] configuration; this is because the range of the room-temperature magnetic moments for each of the three paramagnetic uranium ions, discussed in reference 1d, is large and overlap is wide. In particular, the data range from 1.75 to 3.8, 1.36 to 3.79 and 1.24 to 3.77 B.M. for U(III), U(IV) and U(V), respectively. In other words, any room-temperature magnetic moment between 1.75 and 3.77 B.M. could be indicative at the same time of a U(III), U(IV) or U(V) species. Regarding the profile of μ_{eff} *vs* temperature, as explained in Chapter 1, U(IV) compounds

generally show a precipitous drop at temperatures below *ca.* 50 K, while U(V) {or U(III)} compounds tend to a more linear temperature dependence. From the data of **U-DMF**, a precipitous drop at 50 K is clearly evident, suggesting the presence of a U(IV) ion.

Moreover, the μ_{eff} mean value of the U(IV) compounds of reference 1d at 1.8 K is 1.67 B.M., *i.e.* higher than the observed value for **U-DMF** (1.0 B.M.). While this may be solely due to the aforementioned single-ion effects of each paramagnetic uranium site, this may also indicate the presence of relevant exchange interactions. However, considering the small values of the molar magnetization combined with an almost linear shape, these are most likely antiferromagnetic and weak. For comparison, the mixed-valent U(IV)/U(V) [K(2.2.2-crypt)][{((^{nP,Me}ArO)$_3$tacn)$U^{V/IV}$}$_2$(μ-O)$_2$] (tacn = 1,4,7-Triazacyclononane) exhibits magnetic moments of 2.26 B.M. at 300 K and 0.74 B.M. by extrapolation to 0 K, and no evidence of exchange coupling was observed.[9]

Thus, in addition to the spectroscopic and structural analysis, the magnetic data also corroborate the proposed [U(IV)-U(V)-U(IV)][U(VI)] configuration for **U-DMF**.

3.2.5 Theoretical Analysis on [U(DMF)$_8$(μ-O)U(NCS)$_5$(μ-O)U(DMF)$_8$(NCS)][UO$_2$(NCS)$_5$]

DFT calculations on **U-DMF** have been performed by Dr. J. A. Platts from Cardiff University, in order to further explore the bonding in this compound. A model of the cationic component of **U-DMF**, in which the DMF molecules are cut down to H_2NCO, was extracted from the crystal structure, with H-atoms placed at idealized bond lengths from neutron diffraction data and all other atoms fixed at crystallographic coordinates. Three possible spin states were tested, and a sextet revealed to be preferred by 0.37 and 0.56 eV over a doublet and quartet state, respectively; this state is consistent with a parallel alignment of spins for all U centres in the [U(IV)-U(V)-U(IV)] system. A plot of the DFT spin density from a sextet state is shown in Figure 3.14, and it lends further support to the description of the central U as U(V).

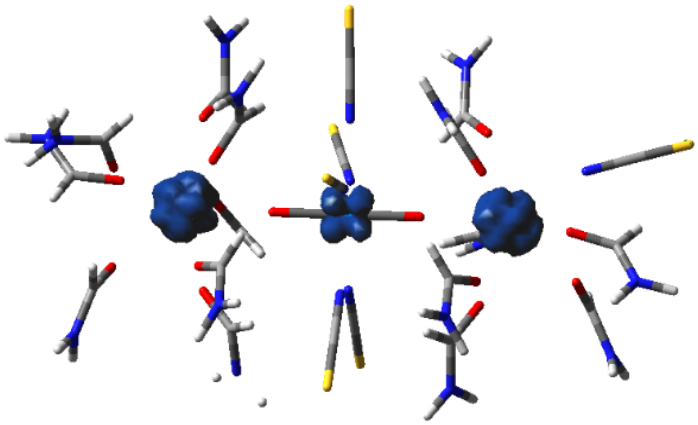

Figure 3.14. Plot of the DFT spin density from a sextet state of a model of $[U(DMF)_8(\mu\text{-}O)U(NCS)_5(\mu\text{-}O)U(DMF)_8(NCS)][UO_2(NCS)_5]$.

Mayer bond orders from the sextet calculation support the presence of CCIs in the central cation: orders of 1.44 and 1.45 are found for U2-O39 and U2-O45, respectively, compared to 0.47 for U1-O39 and U3-O45. For comparison, bond orders of *ca.* 0.38 and 0.48 are observed for $U–O_{DMF}$ and U–N, respectively. Atoms-in-Molecules (AIM) analysis supports this assignment: ρ_{BCP} is 0.20 au in U2–O39 and U2–O45, but just 0.07 au in U1–O39 and U3-O45. All U–O bonds are closed shell, with $\nabla^2\rho_{BCP}$ values of +0.33 au for U2–O39 and U2–O45 and +0.27 au for U1–O39 and U3–O45, although negative energy densities, *H*BCP, of −0.13 au for central U=O bonds indicate significant covalent character.

To summarize, two mixed-valent uranium compounds have been obtained from $Cs_4[U(NCS)_8]$, after oxidation processes in MeCN and DMF. In line with the crystallographic data, spectroscopic and magnetic measurements have been used for delineating the oxidation states of the uranium ions and for probing the electronic structure of these compounds. In particular, it has been proved that the $[UO_2]^+$ ion can be isolated using coordinating solvents, although the mechanism is not evident.

Mixed-valent uranium compounds are not rare in uranium chemistry;[30] nature itself has also provided examples of mixed-valent uranium minerals such as: ianthithite $[U_2^{4+}(UO_2)_4O_6(OH)_4(H_2O)_4](H_2O)_5]$, [31] uraninite or pitchblende, [32] whose chemical composition (mainly UO_2) contains variable proportions of U_3O_8, and wyartite $U^{5+}(UO_2)_2(CO_3)O_4(OH)\cdot 7H_2O$.[33] Moreover, among the variety of examples reported in the literature, interesting series of mixed-valent uranium compounds were studied by Chen *et al.*[34] and Chatelain *et al.*,[35] but, contrary to **U-DMF** and **U-MeCN**, these compounds

were mainly formed from hydrothemal synthesis and concomitant reduction of $[UO_2]^{2+}$ precursors. Two examples from these series are shown in Figure 3.15.

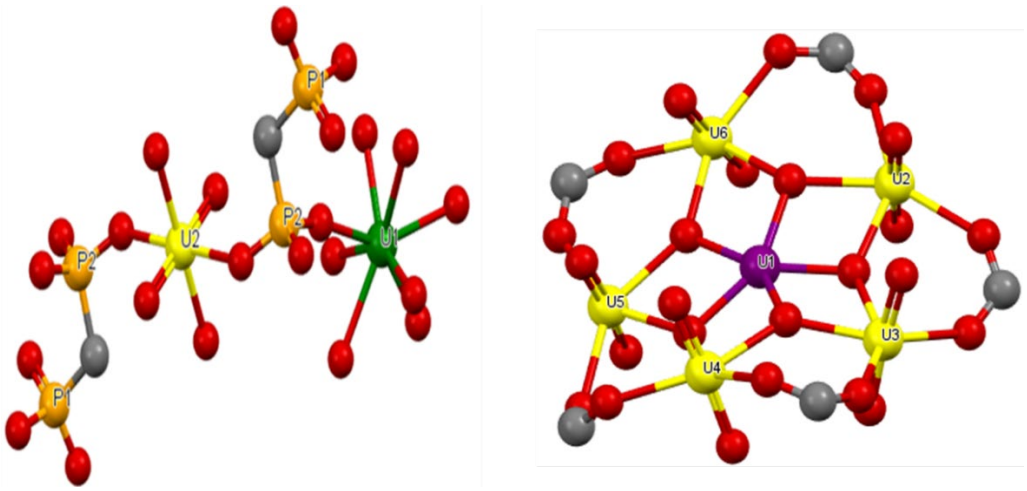

Figure 3.15. Ball and stick representation of, left, $(UO_2)U(H_2O)_2[CH_2(PO_3)(PO_3H)]_2$ (taken from reference 34) and, right, the core structure of $[U(UO_2)_5(\mu_3\text{-}O)_5(PhCOO)_5(Py)_7]$ (taken from reference 35). Only selected atoms labelled and H atoms omitted for clarity. Colour code: C – grey, O – red, P – orange, U(VI) – yellow, U(V) – violet, U(IV) – green.

3.3 Redox Reactions between $[U(NCS)_4]^{4-}$ and $[Co(bipy)_3]^{2+}$

3.3.1 Introduction

Compared to trivalent, tetravalent and hexavalent complexes, pentavalent uranium(V) complexes are more rare,[36] and, as consequence, very little is known about their chemistry. In the case of $[UO_2]^+$ systems, this paucity has been attributed to the instability toward redox disproportionation in aqueous solution, which leads to the more stable U(IV) and U(VI) oxidation states. Nevertheless, U(V) systems have been attracting attention since they can provide useful information to better understand actinide electronic structure, reactivity and bonding; in addition, as discussed in Chapter 1, uranyl(V) compounds are potential candidates for SMM behaviour. Systems with a single *5f*-electron (Pa^{4+}, U^{5+}, Np^{6+}) constitute the simplest examples to explore spin-orbit versus crystal-field effects since there are no electron-electron repulsion terms to consider and the *f*-orbital density of states is reduced to only two manifolds, a $^2F_{5/2}$ ground-state manifold and a $^2F_{7/2}$ excited-state manifold, whose individual multiplet levels will split in response to the symmetry and strength of the field induced by the ligands. Consequently, the analysis of spectroscopic and magnetic data, together with the performing of DFT calculations, result

easier with $5f^1$ actinide complexes than with systems bearing multiple unpaired electrons, such as U(III) $5f^3$ and U(IV) $5f^4$.[37]

In the previous section, it has been shown that it was not possible to obtain a one electron metal-based oxidation on $[U(NCS)_8]^{4-}$ using oxidation reagents; while uncontrolled oxidation processes in MeCN and DMF produced mixed-valent species. In this section it is discussed the reactivity of the $[U(NCS)_8]^{4-}$ anion towards the $[Co(bipy)_3]^{2+}$ cation.

3.3.2 Synthesis and Structural Analysis

With the purpose of synthesising a Co(II)-U(IV) compound of formula $[Co(bipy)_3]_2[U(NCS)_8]$, $Na_4[U(NCS)_8]$ was reacted with two equivalents of $[Co(bipy)_3][PF_6]_2$ in dried MeCN. A grey precipitate of $NaPF_6$ (verified by IR spectroscopy) was obtained and separated by filtration from the resulting green solution; however, when exposed to air, this solution slowly assumed a yellow colour and yellow crystals were isolated after *ca.* 1 week. They were analysed by single-crystal X-ray diffraction, which showed a compound of formulation $[Co(bipy)_3]_2[U(NCS)_8]_2$·bipy·MeCN (**Co-U**). The solid-state crystal structure of this compound is shown in Figure 3.16, along with a depiction of the coordination geometry around the uranium atoms; the corresponding crystallographic data are listed in Appendix 2; while the full list of bond lengths and angles are tabulated in Appendix 2.2, which is in the external CD source of this thesis. The refinement of this crystal structure suffers of significant disorder and it is clarified in the experimental section.

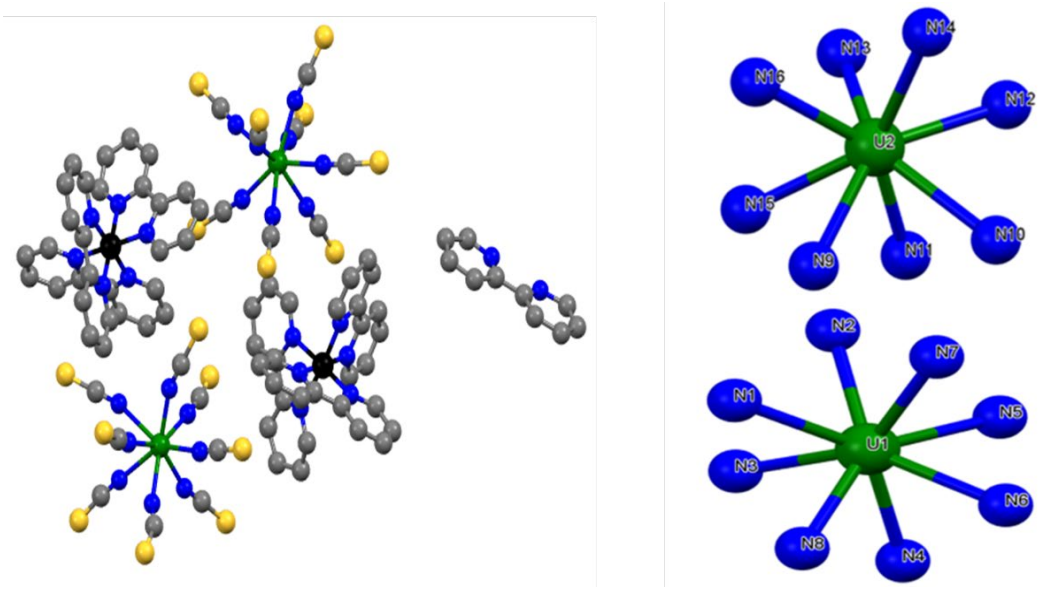

Figure 3.16. (Left) solid-state crystal structure of **Co-U**, with atomic displacement shown at 50% probability. Hydrogen atoms and a cocrystallized solvent molecules omitted, and only non metal atoms labelled for clarity. Colour code: U – green, Co – black, N – blue, C – grey and S – yellow. (Right) coordination geometry around U2 and U1.

In the unit cell there are two different $[Co(bipy)_3][U(NCS)_8]$ molecules, along with one free bipy and one MeCN molecule. A Co(III)-U(V) configuration can be assumed to balance the charge, but a closer inspection of the structural data is important to confirm assignments of formal oxidation states. There are eight thiocyanate ligands coordinated to each uranium ion, via the nitrogen atoms, and the coordination geometry around U1 and U2 is, respectively, square antiprismatic (D_{4d}) and triangular dodecahedron (D_{2d}) from shape analysis[24] (U1: SAPR8 = 0.663; U2: TDD8 = 0.601).

Moreover, to further evaluate the inner coordination sphere around U1 and U2, the geometrical parameters d_{pp}, d_{in}, θ, φ, discussed in Chapter 2 (Figure 2.6), have been measured. Thus, for U1, the analysis showed d_{pp} = 2.64153(10) Å, d_{in} = 3.83963(12) Å, d_{pp}/d_{in} = 0.688, θ = 56.893(2)° (average value) and φ = 45.00(4)° (average value); while for U2 the parameters were d_{pp} = 2.57137(9) Å, d_{in} = 3.34884(13) Å, d_{pp}/d_{in} = 0.768, θ = 57.4562(3)° (average value), and φ = 45.563(4)° (average value). These values confirm a D_{4d} symmetry for the coordination environment of U1 (φ = 45.00(4)°) with, however, an axial compression as evidenced by d_{pp}/d_{in} = 0.689 and θ = 56.893(2)°. Regarding U2, the angle φ = 45.563(4)° suggests a distorted geometry from D_{4d} but, at the same time, the angle θ = 57.4562(3)° and the ratio d_{pp}/d_{in} = 0.7678 are indicative of an axial compression from an ideal non-distorted cubic environment; thus, overall, the structural parameters d_{pp},

d_{in}, θ, φ of the coordination environment of U2 can be considered in line with the triangular dodecahedron symmetry, as determined by SHAPE analysis.

The U1−N bond distances range from 2.400(9) to 2.457(8) Å, while for the U2 system the U2−N bond lengths vary from 2.40(1) to 2.46(1) Å. Thus, considering both U1 and U2 fragments, the average U−N bond lengths is 2.43(2) Å, very similar to those observed in the U(IV) thiocyanate complexes $[Et_4N]_4[U(NCS)_8]$ (2.39(1) Å),[10] $Cs_4[U(NCS)_8]$ (2.42(2) Å),[38] $[^nPr_4N]_4[U(NCS)_8]$ (2.44(1) Å, Chapter 2) and $[Me_4N]_4[U(NCS)_8]$ (2.43(2) Å, Chapter 2), but also very close to that found for the uranyl(VI) complexes of the $[R_4N]_3[UO_2(NCS)_5]$ series (2.45(1) Å, Chapter 4). In turn, the average of the C=N and C=S bond lengths (1.16(1) and 1.62(1) Å, respectively), taking both U1 and U2 fragments, is very similar to the ones displayed by the U(IV) compounds $[Et_4N]_4[U(NCS)_8]$ (1.183(1) Å for N=C and 1.594(1) Å for C=S), $Cs_4[U(NCS)_8]$ (1.145(2) Å for N=C and 1.60(2) Å for C=S)[38] and $[^nPr_4N]_4[U(NCS)_8]$ (1.17(2) Å for N=C and 1.630(2) Å for C=S, Chapter 2), but also comparable to the ones shown by the uranyl(VI) complexes of the $[R_4N]_3[UO_2(NCS)_5]$ series (1.16(1) Å for N=C and 1.63(1) Å for C=S, Chapter 4). Thus, these structural data do not provide clear information to delineate the formal oxidation state of the uranium ions in **Co-U**.

Regarding the $[Co(bipy)_3]^{n+}$ (n = 3 or 2) ions, the metal coordination geometry is octahedral (O_h), with three bipy ligands coordinated to each Co ion via the nitrogen atoms, and, taking both $[Co(bipy)_3]^{n+}$ fragments, the Co−N bond distances range from 1.908(8) to 1.960(1) Å, with an average of 1.93(1) Å.

Before investigating on the formal oxidation state of the cobalt ion, it is important to unambiguously delineate the bipy oxidation level. Indeed, a bipy ligand can exist in three different redox levels, all of which are characterized by X-ray crystallography: neutral ($bipy^0$), the π-radical ($bipy^{\bullet-}$) monoanion and diamagnetic ($bipy^{2-}$) dianion (Scheme 3.1).[39]

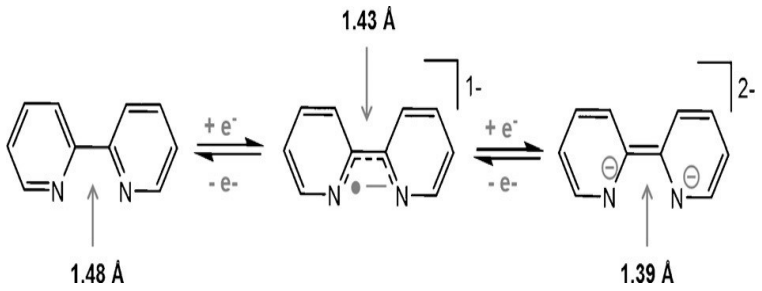

Scheme 3.1. C_{py}–C_{py} bond lengths as function of bipy redox levels.[39]

This redox non-innocence nature can complicate the assignments of formal oxidation states in organometallic complexes. Even with redox-limited metals, such as Ln, canonical oxidation state assignments can be non-trivial.[40] For instance, in the $[Lu(bipy)_4]$ complex, magnetic data support either $[Lu^0(bipy^0)_4]$ or $[Lu^{III}(bipy^{2-})(bipy^{\bullet-})(bipy^0)_2]$ configuration with an EPR value ($g = 2.0014$) indicative of the latter.[41] Perhaps more emblematic is also the example given by the compound $[Cp^*_2Yb(bipy)]$, which has proven to be multiconfigurational: it has a main configuration of f^{13}-$(bipy^{\bullet-})$, which consists of a $[Cp^*_2Yb]^+$ fragment coordinated by a bipy radical anion ($bipy^{\bullet-}$), and a minor configuration of f^{14}-$(bipy^0)$, which corresponds to a neutral $[Cp^*_2Yb]$ system coordinated by a neutral bipy ligand.[42]

However, as highlighted in Scheme 3.1, the C_{py}–C_{py} bond length of bipy is highly sensitive to the ligand charge-level, thus the bipy oxidation state can be discerned by bond metric analysis of X-ray determined structures. With this assumption and with the aid of magnetic measurements and theoretical calculation, for example, Fortier *et al.*[43] demonstrated that, contrary to the original description of a U(0) species with neutral bipy ligand, the $[U(bipy)_4]$ complex is composed by a U(IV) centre ligated by four radical bipy monoanions in the form of $[U^{IV}(bipy^{\bullet-})_4]$. In the $[Co(bipy)_3]^{n+}$ groups of **Co-U**, the C_{py}–C_{py} bond lengths range from 1.445(12) to 1.490(4) Å, with an average of 1.460(3) Å, which is slightly closer to 1.48 Å ($bipy^0$) than to 1.43 Å ($bipy^{\bullet-}$). For the free bipy, instead, the C_{py}–C_{py} distance of 1.475(14) Å confirms the neutral nature of this molecule.

At this point, to delineate the oxidation state for the cobalt ions in **Co-U**, it is useful to compare the Co−N bond lengths of **Co-U** with those displayed by the compounds $[Co(bipy)_3][PF_6]_2$ and $[Co(bipy)_3][PF_6]_3$. The crystal structure of $[Co(bipy)_3][PF_6]_2$ has been determined[44] and shows an average for the Co−N bond lengths equals to 2.141(2) Å. However, the crystal structure of $[Co(bipy)_3][PF_6]_3$ has not been reported. This compound was synthesized according to a previously reported procedure[45] and it was possible to grow yellow single crystals from MeCN solutions. They have been analysed by X-ray diffraction and revealed to be a compound of formula $[Co(bipy)_3][PF_6]_3 \cdot MeCN$. The solid-state crystal structure of $[Co(bipy)_3][PF_6]_3 \cdot MeCN$ is shown in Figure 3.17; the corresponding crystallographic data are listed in Appendix 2, while the full list of bond lengths and angles is tabulated in Appendix 2.2, in the external CD source of this thesis. This structure suffers of significant disorder in the three $[PF_6]^+$ cations and the refinement is clarified in the experimental section.

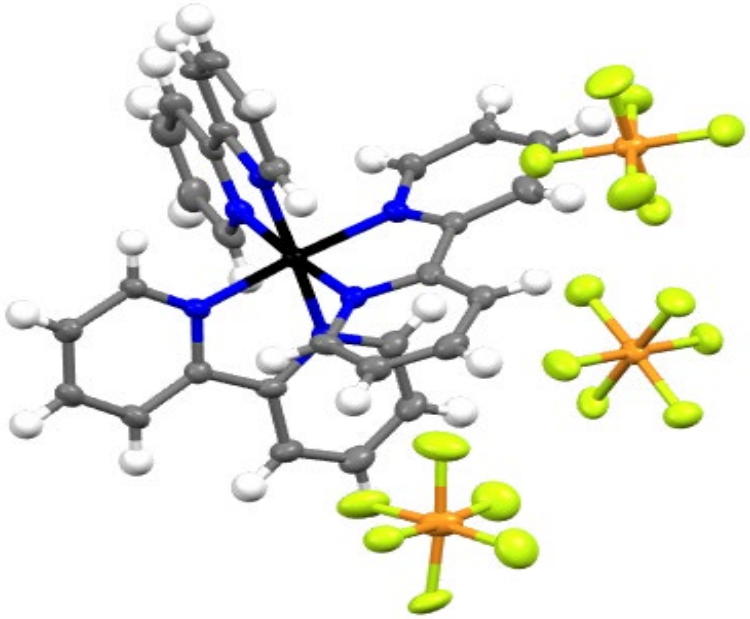

Figure 3.17. Solid-state crystal structure of $[Co(bipy)_3][PF_6]_3$, with atomic displacement shown at 50% probability and co-crystalizzed MeCN molecule omitted for clarity. Colour code: Co – black, N – blue, C – grey, P – orange, F – yellow and H white.

In $[Co(bipy)_3][PF_6]_3$, a d^6 Co(III) cation is coordinated to three bipy ligands, through six Co−N bonds, forming an octahedral (O_h) complex and the +3 charge of the $[Co(bipy)_3]^{3+}$ cation is balanced by three $[PF_6]^-$ anions. In this compound, the average of the Co−N bond lengths is 1.932(1) Å, which is almost identical to that shown by **Co-U** (1.93(1) Å), and different to the value displayed by $[Co(bipy)_3][PF_6]_2$ (2.141(2) Å).[44] This structural similarity suggests a d^6 Co(III) configuration for the two cobalt ions in **Co-U**.

To corroborate this result, the synthesis of an analogue Th(IV)-Co(III) complex was attempted. Thus, under Ar atmosphere, two equivalents of $[Co(bipy)_3][PF_6]_2$ were added to a colourless solution of $Na_4[Th(NCS)_8]$ in dried MeCN, obtained mixing $[ThCl_4(DME)_2]$ with eight equivalents of Na[NCS] and removing by filtration a grey precipitate of NaCl. The resulting white solution was filtered in air and, after 1 week, colourless single crystals were isolated. X-ray diffraction revealed them to be a compound of formula $[bipyH][Co(bipy)_3]_2[Th(NCS)_7(H_2O)][Th(NCS)_8(H_2O)]\cdot MeCN\cdot 2H_2O$ (**Co-Th**). The solid-state crystal structure of **Co-Th** is shown in Figure 3.18, a depiction of the coordination geometry around the thorium atoms is presented in Figure 3.19. The corresponding crystallographic data are tabulated in Appendix 2, while the full list of bond lengths and angles are collated in Appendix 2.3, in the external CD source of this thesis.

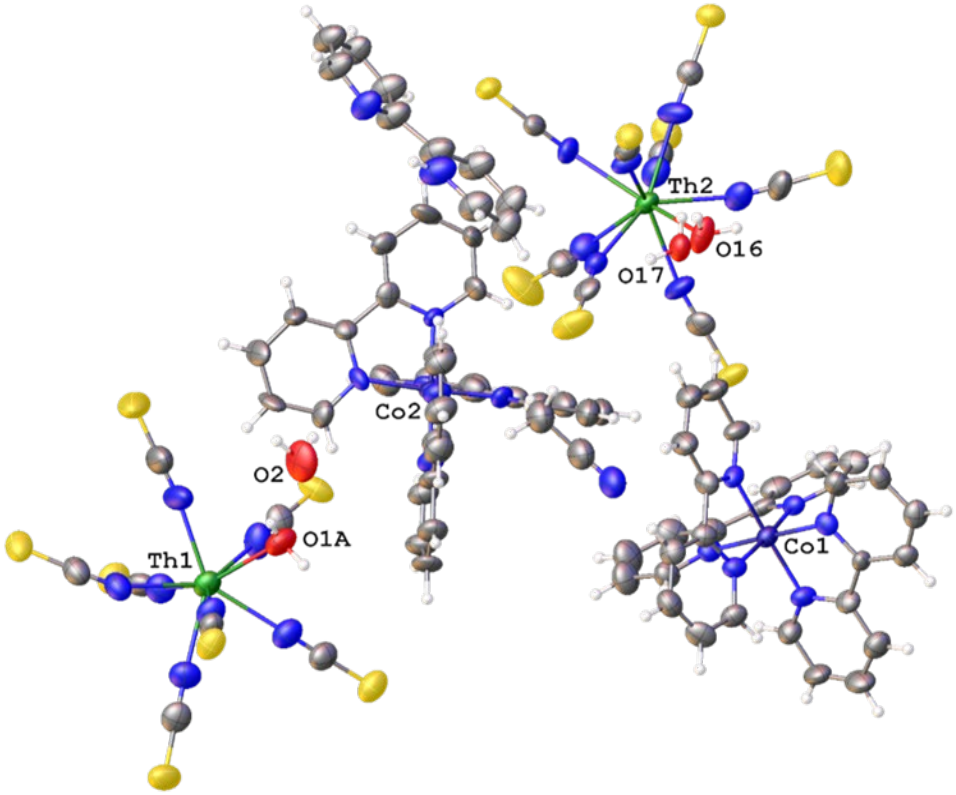

Figure 3.18. Solid-state crystal structure of **Co-Th**, with NCS 58 and 57% and water O1 73% occupied. $Co(bipy)_3$ 73% and lattice MeCN 58%. Displacement parameters shown at 50% probability and only selected atoms labelled for clarity. Colour code: Th – green, Co – violet, N – blue, C – grey, O – red, S – yellow and H – white.

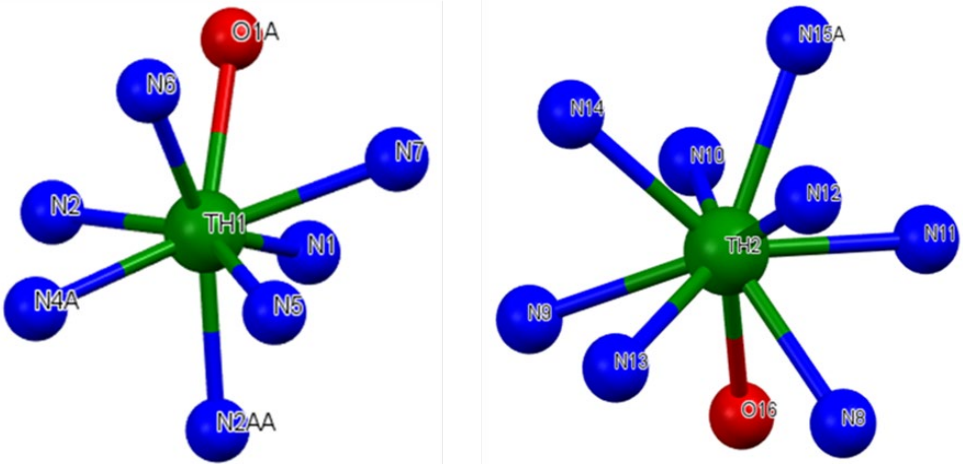

Figure 3.19. Coordination geometry around the throrium atoms in Co-Th.

In the unit cell of **Co-Th** there are two different Th(IV) ions, two $[Co(bipy)_3]^{n+}$ groups, two uncoordinated water molecules, one bipyridinium cation and one free MeCN molecule. Regarding the two Th(IV) ions, Th1 is coordinated to seven $[NCS]^-$ ions,

through Th–N bonds, and one water molecule, while Th2 is linked to eight $[NCS]^-$ ions, through Th–N bonds, and one water molecule. The Th1−N bond distances range from 2.440(12) to 2.515(12) Å, while for Th2 the Th2−N bond lengths vary from 2.491(13) to 2.533(11) Å. Thus, considering both Th1 and Th2, the average of the Th−N bond lengths is 2.501(3) Å, which is similar to that observed for the Th(IV) thiocyanate complexes discussed in Chapter 2 (2.406(3) Å) and longer than the one shown by **Co-U** (2.43(2) Å), as expected due to the actinide contraction. This corroborates the assignment of the formal +4 oxidation state for both thorium ions in **Co-Th**, as predicted. Moreover, in this compound, considering both Th1 and Th2, the averages of the C=N (1.147(4) Å) and C=S (1.632(4) Å) bond lengths are very similar to those shown by the Th(IV) compounds discussed in Chapter 2 (C=N, 1.154(2) Å; C=S, 1.617(2) Å).

Regarding the coordination geometry, a continuous SHAPE measures approach[24] suggests a square antiprismatic (D_{4d}) geometry (SAPR-8: 1.069) for the 8-coordinate Th1 and a monocapped square antiprism (C_{4v}) symmetry (CSAPR-9: 0.325) for the 9-coordinate Th2. For Th2, the Th(2)–N(9) corresponds to the longest Th–N bond ($d_{Th–N}$ = 2.5745(5) Å) and it is also longer than Th–O ($d_{Th–O}$ = 2.5125(5)Å), therefore represents to the capping nitrogen.

To corroborate the results from SHAPE analysis,[24] the geometrical parameters d_{pp}, d_{in}, θ, φ, discussed in Chapter 2 (Figure 2.6), have been measured for both Th1 and Th2. For Th2 the measurements have been performed for the polyhedron formed by the bonds of Th(2) with N(8), N(10), N(11), N(12), N(13), N(14), N(15), O(16), which possesses the Th(2)–N(9) bond as the central rotational axis. Thus, it was found d_{pp} = 2.6789(5) Å, d_{in} = 3.7619(7) Å, d_{pp}/d_{in} = 0.712, θ = 57.183(4)° (average value) and φ = 45.047(3)° (average value) for Th1 and d_{pp} = 2.4066(5) Å, d_{in} = 3.5582(7) Å, d_{pp}/d_{in} = 0.676, θ = 60.875(4)° (average value), φ = 45.092(3) (average value) for Th2. These values confirm for Th1 a slightly distorted D_{4d} coordination symmetry (φ = 45.047(3)°), with an axial compression from a non-distorted cubic environment (θ = 57.183(4)°, d_{pp}/d_{in} = 0.712). In turn, in the case of Th2, these geometrical parameters are indicative of a distorted square antiprismatic symmetry (φ = 45.092(3)°) for the selected polyhedron, with a large axial compression from a non-distorted cubic environment (θ = 60.875(4)°, d_{pp}/d_{in} = 0.676); however, this compression is in comprehensible considering the presence of the capping Th(2)–N(9) bond.

In the two $[Co(bipy)_3]^{n+}$ (n = +3 or +2) ions, the metal coordination geometry is octahedral (O_h), with three bipy ligands coordinated to each Co ion via the nitrogen atoms.

Considering both $[Co(bipy)_3]^{n+}$ fragments, the Co−N bond distances range from 1.911(6) to 1.957(7) Å, with an average of 1.933(3) Å which is almost identical to the one shown by **Co-U** (1.93(1) Å) and $[Co(bipy)_3][PF_6]_3$ (1.932(1) Å). This corroborates the assignment of +3 for the formal oxidation state for both cobalt ions in **Co-Th**. Moreover, in these two $[Co(bipy)_3]^{n+}$ groups, the average of the C_{py}–C_{py} bond lengths is 1.470(4) Å, suggesting that the coordinated bipy ligands are neutral.[39] For the bipyridinium cation, instead, the C_{py}–C_{py} bond length is equal to 1.53(2) Å. This value is somewhat higher compared to the average of the C_{py}–C_{py} bond lengths for the reported crystal structures of compounds containing a bipyridinium cation (1.477 Å), although there are some examples where this bond length is longer.[46]

Thus, the structural data indicate a Co(III)-Th(IV) configuration for **Co-Th**, which also charge balances including the bipyridinium cation. Noticeable, in the structure, there are hydrogen bonds[47] of the type: O–H···O ($d_{O\cdots O}$ 2.69(3), 2.755(3) and 2.97(3) Å), among the water molecules, N–H···S ($d_{N\cdots S}$ 3.247(14) Å), involving the bipyridinium cation and one $[NCS]^-$ ligand, and O–H···S ($d_{O\cdots S}$ 3.291(9), 2.98(3) and 3.293(18) Å), connecting water molecules and $[NCS]^-$ ligands.

Subsequently, in order to further explore the reactivity between $[U(NCS)_8]^{4-}$ and $[Co(bipy)_3]^{2+}$ and to give insight into the apparent U(IV)→U(V) oxidation, $Na_4[U(NCS)_8]$ was reacted with the Co(III) complex $[Co(bipy)_3][PF_6]_3$ under inert conditions. The resulting green mixture was stirred for 24 hours, the grey precipitate of $NaPF_6$ was removed by filtration and the green solution was exposed to air; however, in this case, it kept the same green colour. After 1 week, green single crystals were isolated and X-ray diffraction revealed them to be a Co(II) compound of formula $[Na(H_2O)_4]_2[Co(NCS)_4]$, while the fate of uranium was not determined. The solid-state crystal structure of $[Na(H_2O)_4]_2[Co(NCS)_4]$ is shown in Figure 3.20; the corresponding crystallographic data are listed in Appendix 2, while the full list of bond lengths and angles are tabulated in Appendix 2.3, in the external CD source of this thesis.

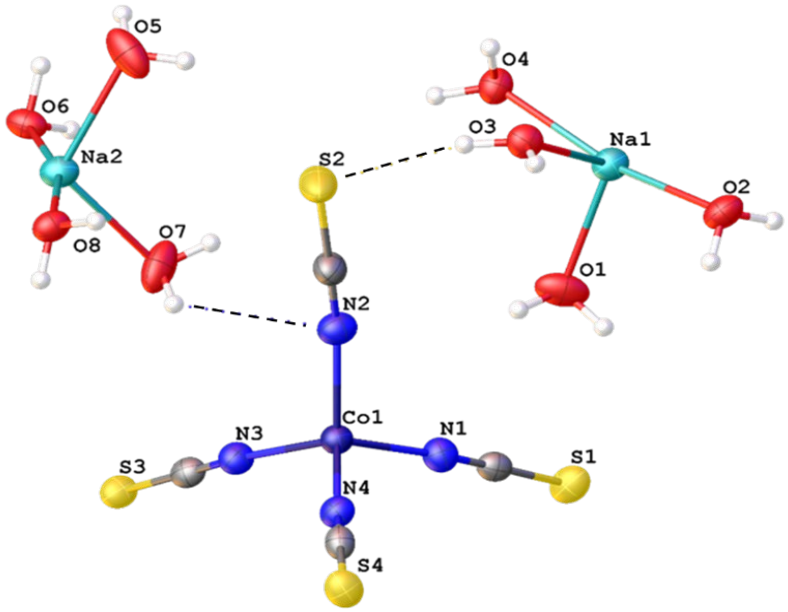

Figure 3.20. (Left) Solid-state crystal structure of $[Na(H_2O)_4]_2[Co(NCS)_4]$, showing the unique coordination of the Na and Co ions. Atomic displacement shown at 50% probability and hydrogen bonding indicated by dotted lines.

In this compound a d^7 Co(II) ion is coordinated to four $[NCS]^-$ ions, through Co–N bonds, forming an almost perfect tetrahedron (T_d) (the N-Co-N angle varies from 105.57(17) to 113.02(16)°). The average of the Co–N bond lengths (1.1965(2) Å) is comparable with the corresponding one displayed by the compound $[Co(bipy)_2(NCS)_2]$ (2.070(1) Å) (section 3.3.4). Moroever, the averages of the N=C (1.165(3) Å) and C=S (1.634(2) Å) bond lengths are similar to the ones shown by the U(IV) (C=N, (1.163(1) Å; C=S, (1.621(1) Å) and Th(IV) (C=N, 1.154(2) Å; C=S, 1.617(2) Å) thiocyanate compounds described in Chapter 2, but also to those from **Co-U** (C=N, 1.16(1) Å; C=S, 1.62(1) Å).

Moreover, during one attempt at the synthesis of **Co-U**, the uranium(IV) ion underwent a 2-electron oxidation and yellow single crystals of $[bipyH]_3[UO_2(NCS)_5][bipy]$ were isolated. The solid-state crystal structure of this uranyl(VI) complex is shown in Figure 3.21. The corresponding crystallographic data are listed in Appendix 2, while the full list of bond lengths and angles are tabulated in Appendix 2.4, in the external CD source of this thesis. The X-ray crystal structure of this compound suffers of significant disorder and the refinement is clarified in the experimental section.

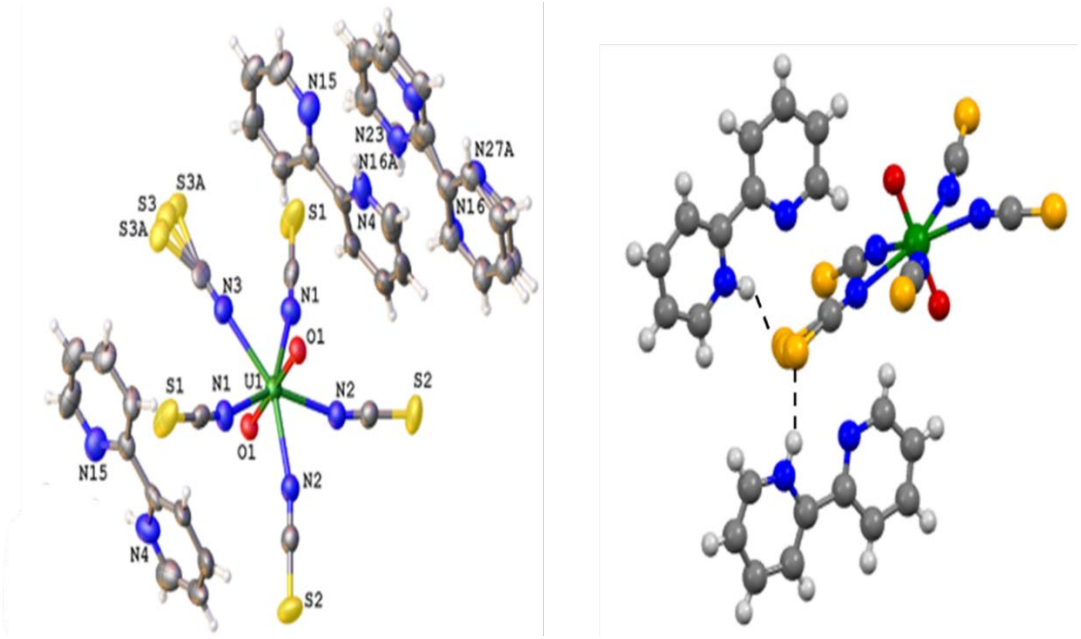

Figure 3.21. (Left) Solid-state crystal structure of $[bipyH]_3[UO_2(NCS)_5]$ with only heteroatoms labelled for clarity; (right) ball and stick representation of $[bipyH]_3[UO_2(NCS)_5]$, with hydrogen bonding highlighted with dotted black lines. Colour code: U – green, N – blue, C – grey, S – yellow, O – red, H – light grey.

In this complex, as expected, the uranyl(VI) ion exhibits a pentagonal bipyramidal coordination geometry (D_{5h}). There are five $[NCS]^-$ ligands, located on the plane and coordinated to the uranium via the N atoms, while the two O atoms are located axially to form the linear (179.7(2)°) O=U=O moiety. The −3 charge of $[UO_2(NCS)_5]^{3-}$ is balanced by three bipyridinium cations. The average of the U=O (1.777(3) Å), U–N (2.432(2) Å), N=C (1.141(3) Å) and C=S (1.559(3) Å) bond lengths are comparable with the corresponding values shown by the $[R_4N]_3[UO_2(NCS)_5]$ series in Chapter 4 (1.741(5) Å for U=O, 2.44(2) Å for U–N, 1.155(2) Å for N=C and 1.63(2) Å for C=S). Moreover, the average of the C_{py}–C_{py} bond lengths is 1.486(8) Å, very close to the corresponding value for the reported crystal structures of compounds presenting a bipyridinium cation (1.477 Å). In this compound, there are no intermolecular S···S close contacts (which will be discussed in detail in Chapter 4 for the $[R_4N]_3[UO_2(NCS)_5]$ series), but noticeable are S···H—N hydrogen bonds[47] ($d_{S\ldots C}$ = 3.218(3) Å) between one bipyridinium cation and the disordered sulfur atom of one $[NCS]^-$ ligand.

Finally, Table 3.3 lists the averages of the Co–N, N=C, C=S and C_{py}–C_{py} bond lengths for **Co-U**, **Co-Th**, $[Co(bipy)_3][PF_6]_2$ and $[Co(bipy)_3][PF_6]_3$, providing a comparison of the main structural parameters among these $[Co(bipy)_3]^{n+}$ (n = 2 or 3) compounds.

Table 3.3. Averages of selected bond lengths (Å) for **Co-U**, **Co-Th**, $[Co(bipy)_3][PF_6]_2$ and $[Co(bipy)_3][PF_6]_3$.

Compound	An–N (An = U or Th)	Co–N	N=C	C=S	C_{py}–C_{py}
Co-U	2.43(2)	1.93(1)	1.16(1)	1.62(1)	1.46(3)
Co-Th	2.501(3)	1.933(3)	1.152(15)	1.60(4)	1.470(4)
$[Co(bipy)_3][PF_6]_2$	-	2.141(2)	-	-	1.487(1)
$[Co(bipy)_3][PF_6]_3$	-	1.932(1)	-	-	1.458(3)

Thus, the crystallographic data of both **Co-U** and **Co-Th** suggest that a Co(II)→Co(III) oxidation occurred when $[Co(bipy)_3][PF_6]_2$ was reacted with $Na_4[An(NCS)_8]$ (An = Th, U) in dried MeCN solutions; moreover, the C_{py}–C_{py} bond lengths are indicative of the presence of neutral bipy ligands. However, regarding the two actinide thiocyanate groups, while in **Co-Th** it is reasonable to assign a formal +4 oxidation state to both thorium ions (considering its high stability, as discussed in Chapter 1), for **Co-U** these structural data does not provide conclusive proof to unambiguously delineate the oxidation state for the uranium ions.

Therefore, in order to corroborate the conclusions drawn from the X-ray analysis and to give more insight into the electronic structure of **Co-U**, all of the samples have been characterised by Raman and IR spectroscopy and, in addition, the magnetic properties of **Co-U** have been probed by SQUID magnetometry at different temperatures and by EPR spectroscopy at low temperature. Finally, the luminescence properties of **Co-U** have been investigated with the aim of identifying features indicative of a U(V) species.

3.3.3 Spectroscopic Determination of Oxidation State in Co-Th and Co-U

3.3.3.1 Vibrational Characterization of Co-Th and Co-U

The complexes **Co-U** and **Co-Th** have been characterized by Raman and IR spectroscopy, to principally confirm the redox level of the bipy ligand. In an IR spectrum of a complex containing bipy ligands, intense absorption bands between 900 and 1000 cm^{-1} are indicative of $bipy^{\bullet-}$ radical ion, while bands of medium intensity between 1620 and 1680 cm^{-1} are typical of neutral bipy.[48]

The Raman and IR spectra of **Co-U** and **Co-Th** in solid-state, showing the regions for the *ν*(C=N) and *ν*(C=S) vibrational stretches only, are reported in Appendix 2 (Figure 7.14 and Figure 7.15); while a comparison between the complete IR and Raman spectra of **Co-U**, **Co-Th**, $[Co(bipy)_3][PF_6]_2$, $[Co(bipy)_3][PF_6]_3$ and uncoordinated bipy is shown in Appendix 2 (Figure 7.16).

The vibrational spectra of **Co-U** and **Co-Th** display bands attributable to the $[NCS]^-$ ligand. For **Co-U** the *ν*(C=N) stretch is observable at 2073 and 2082 cm^{-1}, in the Raman, and at 2052 cm^{-1} in the IR spectrum, while the *ν*(C=S) stretch is visible at 757 cm^{-1} in the Raman spectrum. For **Co-Th** these stretching vibrational frequencies do not change significantly, indeed the *ν*(C=N) appears at 2072 and 2081 cm^{-1} in the Raman and at 2048 cm^{-1} in the IR spectrum, and the *ν*(C=S) is observable in the Raman spectrum at 756 cm^{-1}. In addition, for **Co-U**, in both IR and Raman spectra there are no strong absorption bands between 820 and 940 cm^{-1} which are usually diagnostic of the $[UO_2]^{2+}$ cation, as discussed in Chapter 1 and Chapter 4.

Moreover, in the IR spectra of both **Co-U** and **Co-Th** there are no intense absorptions between 900 and 1000 cm^{-1} that could suggest the presence of a $bipy^{\bullet-}$ radical ion. Instead, there appear bands of medium intensity at *ca.* 1640 cm^{-1}, which can be attributed to a neutral bipy. This is also clear from the comparison with the IR spectrum of uncoordinated bipy (Appendix 2, Figure 7.16). Finally, in the Raman spectra of **Co-U** and **Co-Th** (Appendix 2, Figure 7.16), the bands of the *ν*(C=N) the *ν*(C=C) bonds of the bipy ligand do not significantly change in position when compared to uncoordinated bipy.

3.3.3.2 Magnetic Properties of Co-U

As discussed in Chapter 1, magnetic susceptibility measurements can be used to support assignments of oxidation states in uranium compounds. Thus, the magnetic behaviour of **Co-U** was probed by SQUID magnetometry on crushed X-ray quality single-crystals. The results of this investigation are shown in Figure 3.22 and compared with the temperature-dependent magnetic profile of the U(IV) complex $[Et_4N]_4[U(NCS)_8]$, taken from Chapter 2.

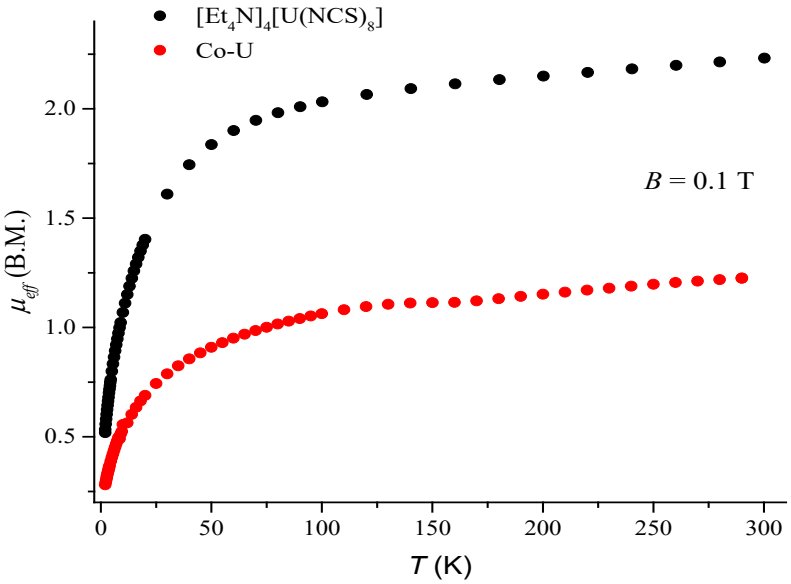

Figure 3.22. Effective magnetic moment *vs* *T* (K) of $[Et_4N]_4[U(NCS)_8]$ (black dotted line) and **Co-U** (red dotted line), measured at $B = 0.1$ T.

At 290 K the μ_{eff} of **Co-U** is 1.23 B.M. with $B = 0.1$ T. By cooling the sample, the values of μ_{eff} decrease until reaching a value of 0.27 B.M. at 2.0 K. The data at room temperature are indicative of a diamagnetic low-spin d^6 Co(III) octahedral complex linked with a, most likely, $5f^1$ U(V) species; with a Co(III)-U(IV), Co(III)-U(V), Co(II)-U(IV) or Co(II)-U(V) configuration, μ_{eff} at 290 K would be much larger. Indeed, with the "spin only formula" (which works well for TM complexes), the calculated room-temperature μ_{eff} for a low-spin Co(II) ion in an octahedral complex is 1.73 B.M., already higher than the value found for **Co-U**. This observation clearly suggests the presence of a low-spin diamagnetic d^6 Co(III) ion in **Co-U**. Moreover, the average of the room-temperature μ_{eff} of the U(V) and U(IV) compounds, reported in reference 1d, is, respectively, 2.07 and 2.77 B.M.; therefore, the μ_{eff} at 290 K of **Co-U** would probably be slightly higher than the measured value of 1.23 B.M., if there was a U(IV) ion. The indication for a U(V) ion comes also from the shape of the magnetic profile *vs* the temperature: from 290 to *ca.* 70 K, the magnetic profile of **Co-U** appears slightly flatter than that of the U(IV) complex $[Et_4N]_4[U(NCS)_8]$.

Thus, the analysis of the magnetic behaviour of **Co-U** suggests a Co(III)-U(V) configuration. Additionally, no slow relaxation was observed and this further corroborates the evidence that (as discussed in Chapter 1) $5f^1$ uranyl(V), and not uranium(V), compounds can show unusual magnetic behaviour.[49]

Co-U was also analysed by EPR spectroscopy in solution at 77 K and it was found to be EPR silent. With a $5f^1$ configuration, paramagnetic U(V) compounds are in principle

EPR active;[50] however the exact EPR response is dependent upon the nature of the ground state. In fact, it has been reported that, in a U(V) system with a C_{3v} symmetry, the J = 5/2 ground state splits into three magnetic doublets, two EPR active $\mu = \pm 1/2$ and one EPR inactive $\mu = \pm 3/2$, where μ is the crystal quantum number.[5d, 51] Thus, for **Co-U**, the ground state should be the EPR inactive $\mu = \pm 3/2$. Nevertheless, the absence of any signals in the EPR spectrum of **Co-U** clearly confirms the presence of a diamagnetic $3d^6$ Co(III) ion.

3.3.3.3 UV-Vis-NIR Spectroscopic Characterization of Co-U

In an $5f^1$ octahedral complex, the *5f* orbitals are split by interactions with the ligand orbitals into a nonbonding a_{2u} orbital, a π^* antibonding t_{2u} orbital, and a σ^* and π^* antibonding t_{1u} orbitals.[52] In Figure 3.23, the difference in energy between the a_{2u} and t_{2u} orbitals is defined as Δ and the one between the t_{2u} and t_{1u} orbitals is indicated as θ.[52] Moreover, when these orbitals (lower case) are singly occupied, the resulting states (upper case) are, respectively, A_{2u}, T_{1u}, and T_{2u}. However, in actinide complexes, the spin-orbit coupling is almost as strong as the ligand field and, therefore, splits further these states, producing a new set of Γ_7, Γ_8, Γ_7', Γ_8' and Γ_6 states (Figure 3.23, right).[52]

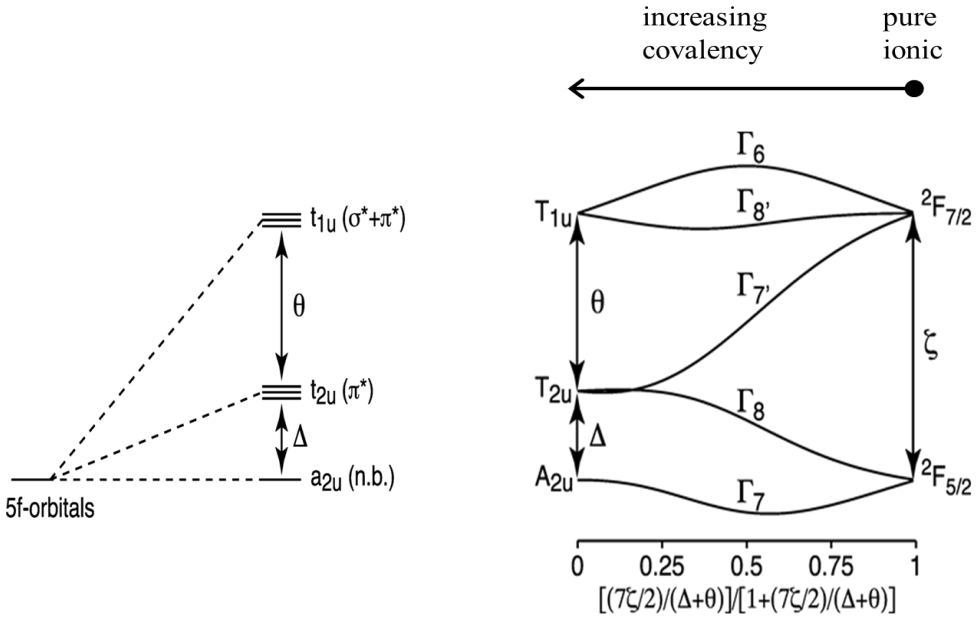

Figure 3.23. (Left) Splitting of the *5f* orbitals in an octahedral complex showing the relationship of θ and Δ to the relative energies of the orbitals. (Right) Relationship between the low-lying states of an octahedral $5f^1$ complex as a function of the strength of the crystal field (θ and Δ) relative to spin-orbit coupling (ζ). The diagram is drawn for $\theta/\Delta = 2$ and with the barycenter of the *f* orbitals equal to zero.[52]

For U(V) complexes with an octahedral CFS, transitions between these states occur in the infrared (IR) and near-infrared (NIR) regions, although the exact position is dependent upon the strength of the ligand field, as expressed in terms of Δ, θ, and the strength of the spin-orbit coupling, ζ.[52] Therefore, assuming an O_h coordination geometry for both U1 and U2 of **Co-U**, four *f-f* electronic transitions should appear in the NIR region of its absorption spectrum. To confirm this, a UV-vis-NIR absorption spectrum of **Co-U** was acquired in dried MeCN and at room temperature (Figure 3.24).

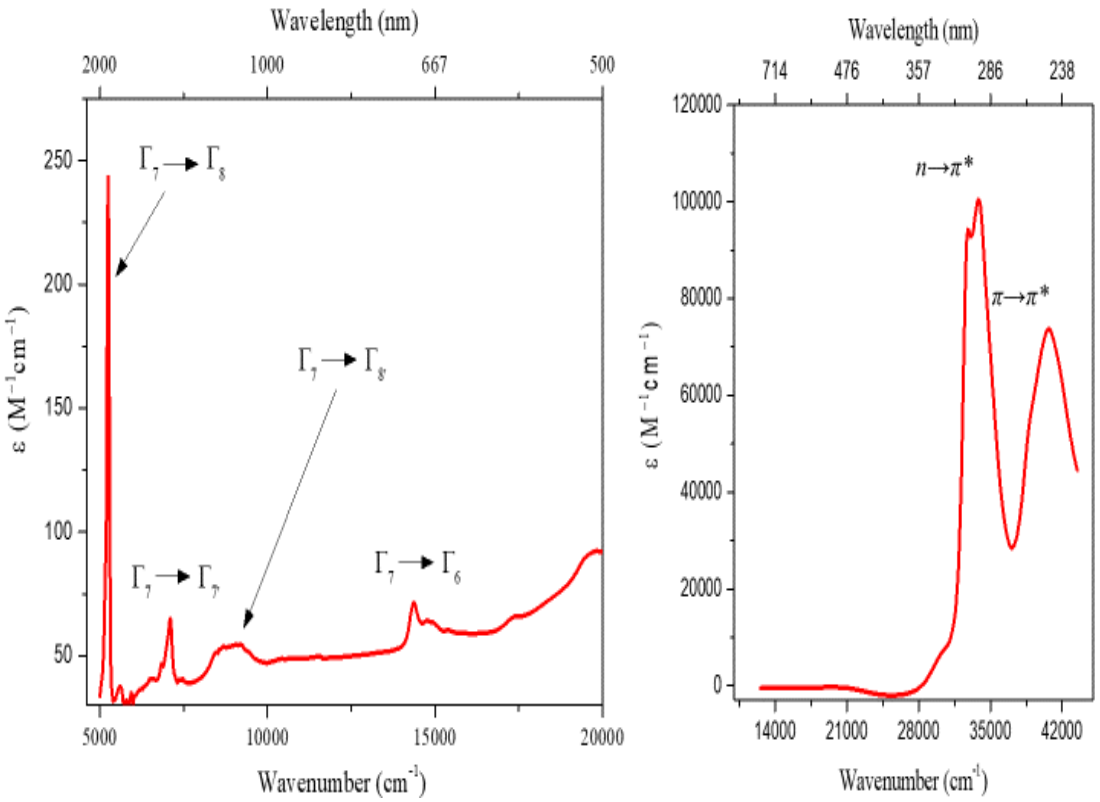

Figure 3.24. Absorption spectrum of **Co-U**, showing (left) the vis-NIR region measured at 3 x 10^{-4} M and (right) the UV region measured at 1.1 x 10^{-4} M. Measurements performed in MeCN solutions and at room temperature.

Four *f-f* electronic transitions are observable in the NIR region (Figure 3.24, left) and, in accordance with the energy level diagram in Figure 3.23, have been assigned as arising from the Γ_7 ground state to the excited states Γ_8 (5247 cm^{-1}), $\Gamma_{7'}$ (7102 cm^{-1}), $\Gamma_{8'}$ (9124 cm^{-1}) and Γ_6 (14367 cm^{-1}). Regarding the UV region (Figure 3.24, right), the bands at 32787, 33784 cm^{-1} can be assigned as due to $n \rightarrow \pi^*$ transitions of both the bipy and thiocyanate ligands, and the band at 40651 cm^{-1} is, most likely, due to $\pi \rightarrow \pi^*$ transitions of the bipy ligands. Moreover, in the spectrum of Figure 3.24, the absence of strong

transitions in the vis-NIR region confirms the oxidation level as $(bipy)^0$ for both the coordinated and uncoordinated bipy molecules of **Co-U**. In fact, an uncoordinated bipy radical monoanion, $bipy^{\bullet-}$, displays intense ($\varepsilon \sim 10^4$ M^{-1} cm^{-1}) bands at ~ 820, 530 and 385 nm, while two intense ($\varepsilon \sim 10^5$ M^{-1} cm^{-1}) bands at ~ 610 and 373 nm should be observable in the presence of a $bipy^{2-}$ dianion.[48]

3.3.3.4 Luminescence Spectroscopic Study of Co-U

In the literature there are only few examples of luminescence spectroscopy studies on $5f^1$ $[UO_2]^+$ compounds,[53] showing a fluorescence emission profile in the wavelength range of 415 - 475 nm, but none on pentavalent U(V) samples. Nevertheless, the luminescence properties of **Co-U** have been probed in solid-state, both at room temperature and at 77 K (Figure 3.25), with the aim of identifying features attributable to a U(V) ion. It was possible to observe photophysical features of only a uranyl(VI) contamination, but this is explainable considering the much higher quantum yield of a uranyl(VI) ion compared to the putative U(V) component. Indeed, the emission spectrum (Figure 3.25, red line) displays the characteristic vibrational fine structure with four well resolved "hot bands" centred at 520 nm and corresponding to LMCT emission bands of a uranyl(VI) moiety. These uranyl(VI) LMCT bands are also observable in the excitation spectrum (Figure 3.25, black line), as a group of well resolved bands centred at 430 nm.

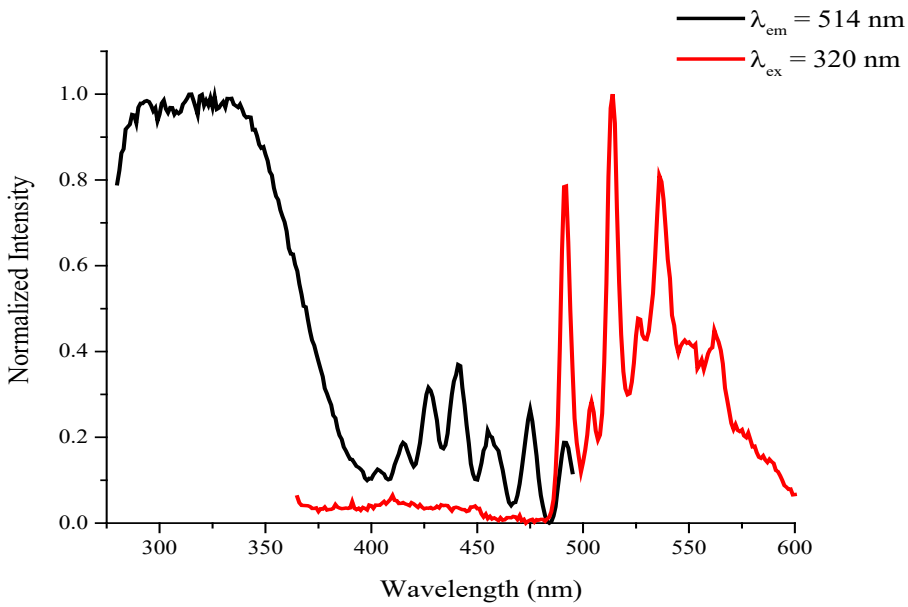

Figure 3.25. Solid-state excitation (black line) and emission (red line) spectrum of **Co-U** measured at 77 K.

3.3.4 Study of the Mechanism for the Formation of Co-U

To explore the mechanism for the formation of **Co-U**, the synthesis was repeated, and the resulting solution was analysed by UV-vis-NIR spectroscopy before, during and after a UV irradiation, which was applied to catalyse the Co(II)→Co(III) oxidation. The first spectrum of the starting green solution was indicative for the presence of a U(IV) species by the typical intraconfigurational $5f^2$ U(IV) Laporte-forbidden *f-f* transitions. The solution was then irradiated under a UV lamp (λ_{max} = 254 nm) for *ca.* 8 hours, in order to ultimately catalyse the Co(II)→Co(III) oxidation, and absorption spectra were acquired at intervals of *ca.* 60 minutes (Figure 3.26) with the aim of observing a change in the energy of the transitions. However, no change in the position of the *f-f* transitions was observed during the UV irradiation and the only noticeable variation was a lowering in the absorption intensity. Nevertheless, when exposed to air, the green solution slowly assumed a yellow colour and the vis-NIR absorption spectrum revealed a clear variation in the *f-f* transitions; this spectrum, in particular, was indistinguishable from the one of pure Co-U (Figure 3.24). In addition, after *ca.* 1 week, yellow single crystals of **Co-U** were also isolated.

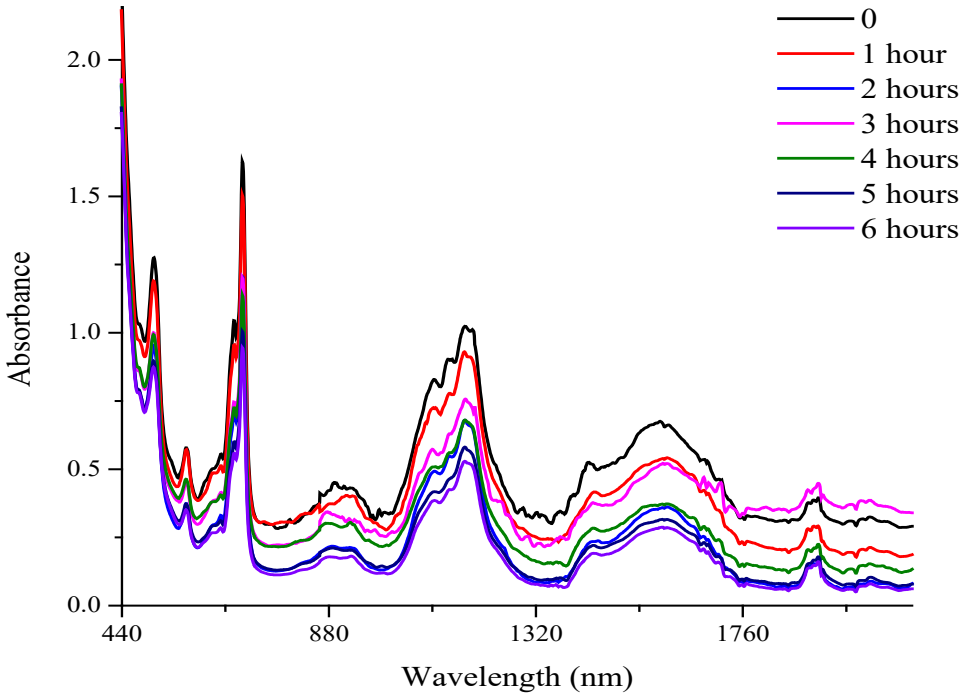

Figure 3.26. Monitoring over time, during a UV (λ_{max} = 254 nm) irradiation, of the vis-NIR absorption profile of the green solution, obtained mixing $[Co(bipy)_3][PF_6]_2$ and $Na_4[U(NCS)_8]$. Spectra recorded keeping the solution under Ar pressure.

Along with **Co-U**, moreover, a different crystalline product was obtained from the yellow solution after the UV irradiation and the X-ray diffraction showed a Co(II) complex of formula $[Co(bipy)_2(NCS)_2]$. Thus, presumably, the UV light catalyses the liberation and exchange of the $[NCS]^-$ and bipy ligands between the $[Co(bipy)_3]^{2+}$ and $[U(NCS)_8]^{4-}$ ions. For comparison, Barbour *et al.* reported on the dissociation of coordinated bipy ligands from a $[Cr(bipy)_3]^{3+}$ complex during a UV irradiation process.[54] This result could also explain why **Co-U** co-crystallized with a free bipy molecule, which presumably is easily released by an excess of $[Co(bipy)_3][PF_6]_2$. In addition, $[Co(bipy)_2(NCS)_2]$ was also isolated during a second attempt at the synthesis of **Co-Th**. A rational synthesis for $[Co(bipy)_2(NCS)_2]$ was also developed; indeed, this compound was prepared by reacting $[Co(bipy)_3][PF_6]_2$ with two equivalents of Na[NCS] in MeCN. In contrast, no reaction was observed between Na[NCS] and $[Co(bipy)_3][PF_6]_3$ and this difference is explainable considering that the low-spin $3d^6$ configuration of Co(III) in $[Co(bipy)_3]^{3+}$ makes this system less labile compared to $[Co(bipy)_3]^{2+}$, where the Co(II) ion is in a low-spin $3d^7$ configuration. The solid-state crystal structure of $[Co(bipy)_2(NCS)_2]$ is reported in Figure 3.27 and the corresponding crystallographic data are listed in Appendix 2; the full list of bond lengths and angles are tabulated in Appendix 2.4 in the external CD source of this thesis. In $[Co(bipy)_2(NCS)_2]$, the cobalt ion is coordinated by two bipy and two $[NCS]^-$ ligands, through Co−N bonds, forming a complex of octahedral symmetry (O_h). Considering the bipy ligands, the average of the Co−N bond lengths is 2.163(3) Å, similar to that observed for $[Co(bipy)_3][PF_6]_2$ (2.141(2) Å)[44], while, with the $[NCS]^-$ ligands, the average of the Co−N bond lengths (2.070(1) Å) is similar to that shown by $[Na(H_2O)]_2[Co(NCS)_4]$ (1.965(2) Å). These values corroborate the assignment of +2 to the formal oxidation state of the cobalt ion in this compound. Moreover, the averages of the N=C (1.161(2) Å) and C=S (1.631(2) Å) bond lengths are comparable with the corresponding values shown by **Co-U** (N=C, 1.16(1) Å; C=S, 1.62(1) Å) and **Co-Th** (C=N, 1.147(4) Å and C=S 1.632(4) Å).

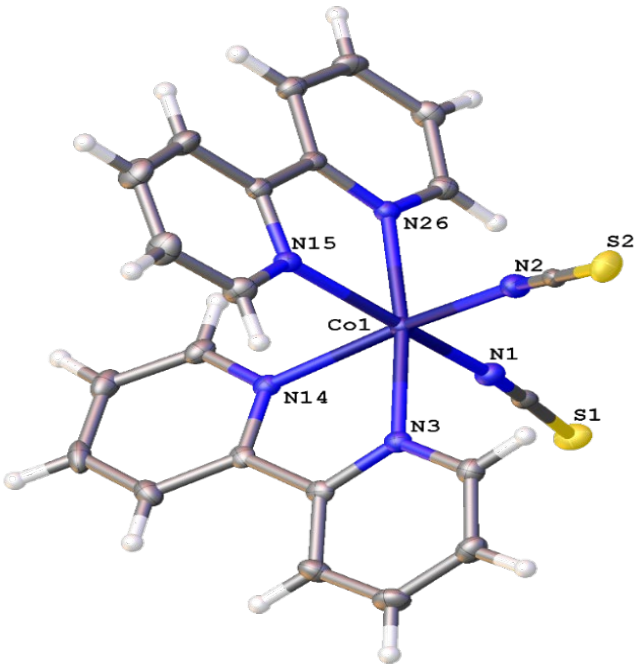

Figure 3.27. Solid-state crystal structure of $[Co(bipy)_2(NCS)_2]$, with atomic displacement shown at 50% probability. Only heteroatoms labelled for clarity. Colour code: Co – dark blue, N – blue, S – yellow, C – grey, H – white.

At this point, in line with the structural, magnetic and spectroscopic data and considering the results from a UV-vis-NIR monitoring during the UV irradiation, it is possible to hypothesize on the redox processes behind the formation of both **Co-U** and **Co-Th**. Thus, for both compounds, the Co(II)→Co(III) oxidation occurred, presumably, in solution and also under inert atmosphere. Then, for the formation of **Co-Th**, it is reasonable to state that the Th(IV) ion was not involved in any redox processes, given its high redox stability; instead, for the synthesis of **Co-U**, a U(IV)→U(V) oxidation occured, most likely, when the initial green solution was exposed to air, as evidenced by the UV-vis-NIR monitoring during the UV irradiation. However, further studies are required to better understand these redox processes; for clarity, they have been summarised in Scheme 3.2.

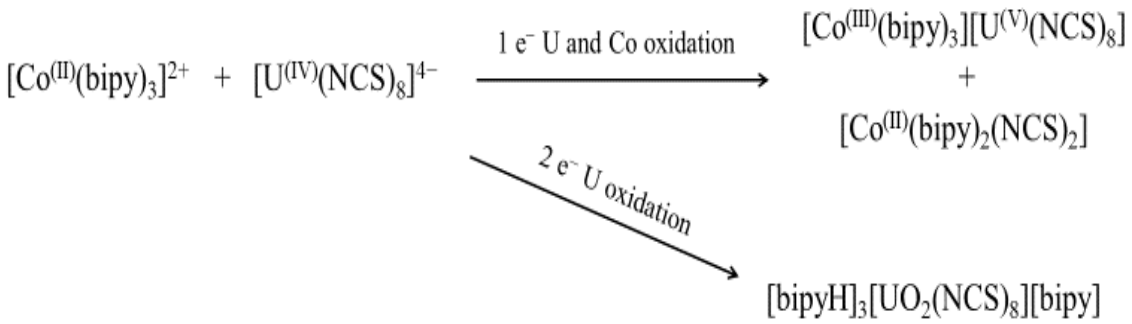

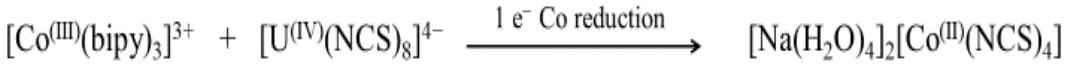

Scheme 3.2. Redox processes occurred when $[U(NCS)_8]^{4-}$ reacted with $[Co(bipy)_3]^{2+}$ and $[Co(bipy)_3]^{3+}$ ions in MeCN solutions.

3.3.5 Density Functional Theory Calculations on Co-U

To corroborate the spectroscopic assignment for a Co(III)-U(V) configuration in **Co-U**, DFT calculations have been carried out with the aid of Dr. James A. Platts from Cardiff University. A calculated spin-density plot is shown in Figure 3.28.

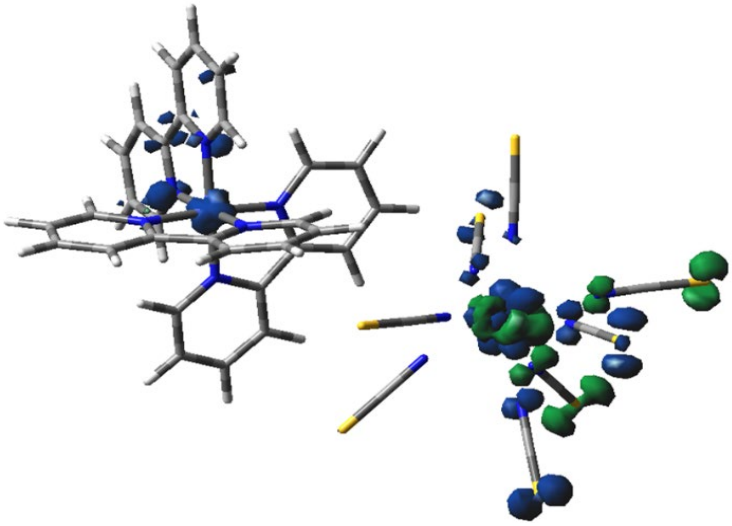

Figure 3.28. DFT calculated spin density of **Co-U**.

This figure reveals for **Co-U** a spin density located mostly on the uranium and sulfur atoms of the $[U(NCS)_8]^{3-}$ fragment, and only slightly on the $[Co(bipy)_3]^{3+}$ ion, in line with a Co(III)-U(V) configuration.

3.4 Reduction Experiments and Electrochemistry Measurements on $[Et_4N]_4[U(NCS)_8]$

3.4.1 Chemical Reduction Experiments on $[Et_4N]_4[U(NCS)_8]$

In light of the peculiar magnetic behaviour of U(III) compounds,[1] the synthesis of a U(III) thiocyanate complex has been attempted through reduction of the U(IV) complex $[Et_4N]_4[U(NCS)_8]$ with a variety of reducing reagents such as Na, K and $KC_{10}H_8$.

These experiments were performed in dried MeCN, where the colour of the solution can provide an indication of the formal uranium oxidation state: solutions with a U(III) compound usually exhibit a reddish colour, while the presence of a U(IV) complex causes the predominance of a bright green colour. Upon adding the reducing reagent, however, the initial green solution of $[Et_4N]_4[U(NCS)_8]$ in dried MeCN rapidly became colourless and the formation of a grey precipitate was observed. The reaction was also repeated at −78 °C, but the same result was observed. The resulting colourless solution was then filtered and analysed by UV-vis-NIR spectroscopy, but no bands attributable to *f-f* transitions were noted. The grey powder was also isolated and characterized by Raman and IR spectroscopy, but no bands assignable to C=N or C=S bonds of the thiocyanate ligands were detected and, finally, attempts of recrystallization with a number of solvents of different polarity such as toluene, hexane, ether, dichloromethane, tetrahydrofuran, ethyl acetate, ethanol, methanol and water, did not succeed.

A further attempt was performed using SmI_2 in THF. SmI_2 is a one-electron reducing agent that is often used in organic and inorganic redox reactions.[55] One equivalent of SmI_2 in THF was added to a green solution of $[Et_4N]_4[U(NCS)_8]$ in dried MeCN, and the resulting solution assumed a red colour. A few red single crystals were also grown by vapor diffusion of diisopropyl ether into the MeCN solution, but the X-ray diffraction showed a compound of formula $[Et_4N]I_3$ whose crystal structure has been previously reported.[56] The red solution was also analysed by UV-vis-NIR absorption and photoluminescence spectroscopy. In the absorption spectrum no bands due to *f-f* transitions were noticed and it was not possible to finally verify the fate of uranium. The corresponding emission spectrum (Figure 3.29) revealed three bands which are indicative of a Sm(III) species, confirming the successful Sm(II)→Sm(III) oxidation, as expected. These bands are centred at 561, 596 and 642 nm and are due to the transitions $^4G_{5/2}\rightarrow{}^6H_J$, where the $^6H_{5/2}$ corresponds to the ground level of the $4f^5$ Sm(III) ion.[57] It is worthy to underline that, to date, there are no examples in the literature of emission spectra for a

U(III) compound, while absorption spectroscopy is often used to identify this oxidation state.

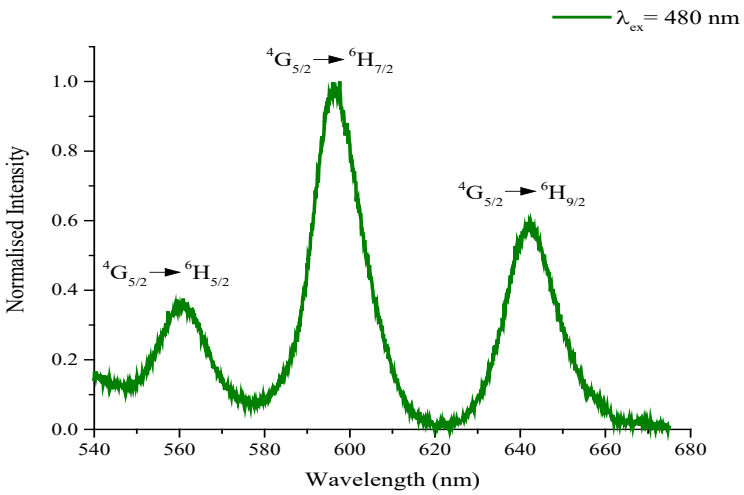

Figure 3.29. Emission spectrum of the red solution obtained mixing $[Et_4N]_4[U(NCS)_8]$ and SmI_2.

3.4.2 Spectroelectrochemistry Measurements on $[Et_4N]_4[U(NCS)_8]$

Given the unsuccessful attempts to isolate any chemically reduced U(III) compounds, it was of interest to investigate the cathodic behaviour of $[Et_4N]_4[U(NCS)_8]$ using IR spectroelectrochemistry. This study was performed by the group of Professor Frantisek Hartl from University of Reading. Previous conventional Cyclic Voltammetry (CV) measurements determined an irreversible cathodic wave at $E_{p,c} = -1.80$ V *vs* Fc/Fc^+, but this was rather broad and poorly resolved.[10] Thus, to obtain a more accurate result, the electrochemistry measurements were performed using a combination of Thin-Layer Cyclic Voltammetry (TLCV) and IR spectroscopy; in this way, the cathodic potentials read from TLCV are more reliable, as the electron transfer can be directly identified by the corresponding infrared spectral changes observed during the electrolyses. The reduction process was monitored by in situ IR spectroscopy in the region of the ν(C=N) stretching, whose energy gives an indication of the formal oxidation state for the uranium ion in the $[U(NCS)_8]$ system. The thin-layer cyclic voltammogram of $[Et_4N]_4[U(NCS)_8]$ is shown in Figure 3.30 and, for this measurement, decamethyl ferrocene (Fc*) was conveniently used as the internal standard ($Fc^*/Fc^{*+} = -0.48$ V *vs* Fc/Fc^+).[58]

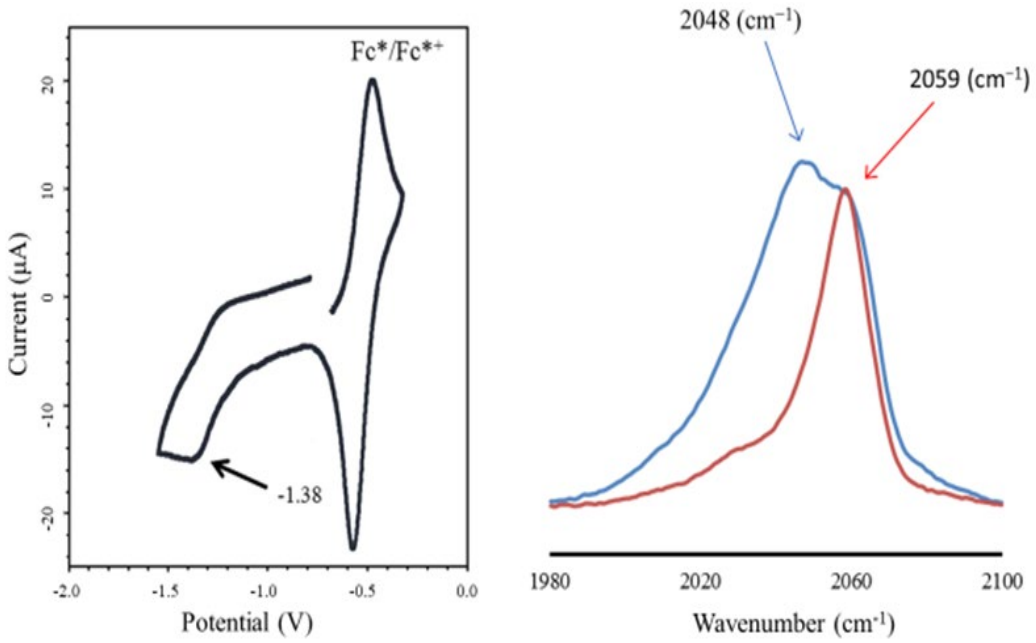

Figure 3.30. (Left) Thin-layer cyclic voltammogram of $[Et_4N]_4[U(NCS)_8]$ against Fc/Fc^+ determined in MeCN at 293 K, with ~0.1 M $^n Bu_4NPF_6$ as the supporting electrolyte, at v = 2 mV s^{-1}. (The depicted scan shows oxidation of decamethylferrocene, Fc^*/Fc^{*+}, used as the internal standard; two cycles were applied to exclude any potential drift). (Right) IR spectral changes in the ν(C=N) region accompanying the one-electron reduction of $[Et_4N]_4[U(NCS)_8]$ in MeCN/$^n Bu_4NPF_6$ at 293 K within an OTTLE cell. Blue spectrum, before the reduction at −1.38 V vs Fc/Fc^+; red spectrum, after the reduction.

The reduction potential was found at $E_{p,c}$ = −1.38 V *vs* Fc/Fc^+. The value determined from conventional CV measurements was much more negative ($E_{p,c}$ = −1.80 V) and, in light of the greater accuracy of the TLCV experiment, must be erroneous.

Moreover, during the reduction process, the IR monitoring (Figure 3.30, right) shows that the broad ν(C=N) band at 2048 cm^{-1} of $[U(NCS)_8]^{4-}$ decreases in intensity and a new signal rises at 2059 cm^{-1}, which can be assigned to free $[NCS]^-$.[10] A U(III)-NCS compound could also show a band coincident with the free $[NCS]^-$ ion, but with a different line shape. Apparently, the addition of one electron triggers dissociation of all the thiocyanate ligands from $[U(NCS)_8]^{4-}$ and decomposition of the compound. In line with this result, the chemical reduction of $[Et_4N]_4[U(NCS)_8]$ was repeated in the presence of excess of Na[NCS], but again no isolable U-NCS containing product was formed. It is clear that, alone, the strong π-donor $[NCS]^-$ ligands are not able to stabilize a U(III) ion efficiently. In addition, $[Et_4N]_4[U(NCS)_8]$ also displayed a reversible oxidation wave at

0.24 V (*vs* Fc/Fc^+) which, in line with previous conventional CV measurements (0.22 V *vs* Fc/Fc^+),[10] must be ligand-based and not due to the redox couple U(IV)/U(V).

3.4.3 DFT Calculations on $[U(NCS)_8]^{n-}$ (n = 3, 4)

In order to finally understand the change in reactivity between U(III) and U(IV), DFT calculations have been performed. This analysis was carried out by Dr. James A. Platts from University of Cardiff. In a previous work conducted in our group, the hybrid and pure DFT methods have been benchmarked to the vibrational data of the U(IV) compound and it was found that the BP86 functional gave a satisfactory fit to the experimental data.[10] Therefore, this has been chosen to compare the bonding in $[M(NCS)_8]^{5-}$, where M = Ce and U; QTAIM analysis has also been used to further probe the results. It is worthy to underline that the 8-coordinate Ce(III) compound is not known experimentally, but it has been used strictly as a comparison to the putative U(III) species. Natural Bond Order (NBO) analysis find a single bonding orbital for each M–N bond and indicates a charge on U of just +0.96 and Ce of +0.90, much less than the formal charge of +3. Inspection of the spin densities (Figure 3.31) reveals that there is a small amount of electronic delocalization onto the $[NCS]^-$ ligands in the U(III) compound, which is not observed in the Ce(III) species.

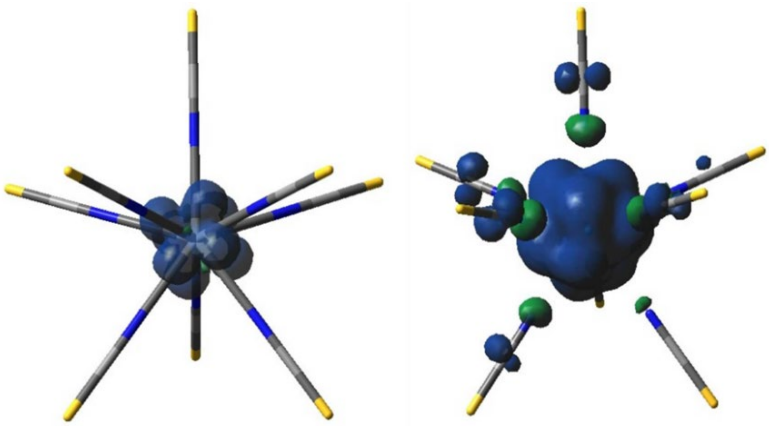

Figure 3.31. Calculated spin densities on $[Ce(NCS)_8]^{5-}$ (left) and $[U(NCS)_8]^{5-}$ (right).

Significantly, QTAIM analysis show that both $U^{(III)}$–N and $Ce^{(III)}$–N bonds are more ionic than the $U^{(IV)}$–N bond, with a low ρ associated with the M–N bond and a decrease in the bond order (Table 3.4); this result could explain the observed decomposition during both the chemical and electrochemical reduction experiments. Literature precedent has

also reported on An–Cl bond showing enhanced covalency in the U(IV)–Cl bond versus the U(III)–Cl bond.[59] Using QTAIM,[60] indeed, the ρBCP for the U–Cl bond in $[UCl_6]^{n-}$ at the B3LYP functional is 0.064 for U(IV) and 0.037 for U(III), which follows the trend of the data herein obtained. This result has been partly ascribed to an increase in the localization of the *5f*-orbitals with decreased oxidation state, which may cause a decrease in the covalency for the U(III)–NCS bond versus the U(IV)–NCS . This can be considered as an example of an energy mismatch between the metal and the ligand orbitals in lower oxidation states. NBO analysis of $[U(NCS)_8]^{n-}$ gives some evidence for this; in fact, there is a decrease in the *f*-orbital contribution to the bonding in the lower oxidation state: {U(III) 11% U: made up of *s* (12%), *p* (34%), d (39%), and *f* (15%); U(IV) 14% U: made up of *s* (12%), *p* (33%), *d* (31%), and *f* (24%)}.

Table 3.4. DFT Geometry and Vibrational Modes Using BP86 Functional, selected QTAIM properties for $[U(NCS)_8]^{4-}$ and the putative $[M(NCS)_8]^{5-}$ compounds and experimental (exp) data of the $[U(NCS)_8]^{4-}$ species.

Property	**U(IV) exp[b]**	**U(IV) BP86[b]**	**U(III) BP86**	**Ce(III) BP86**
M–N (Å)	2.38(3) 2.46 (3)	2.469	2.615	2.672
N=C (Å)	1.15(4) 1.14(4)	1.185	1.183	1.182
C=S (Å)	1.63 (4) 1.61(3)	1.644	1.663	1.663
ν(C=N) (cm^{-1})[a]	2047 2090	2067 (b_2) 2071 (e_1)	2078	2081
ν(C=S) (cm^{-1})[a]	783	797	748	749
ρ_{M-N} (au)	-	0.056	0.034	0.031
$\rho_{N=C}$ (au)	-	0.450	0.452	0.441
$\rho_{C=S}$ (au)	-	0.212	0.207	0.208
M–N bond order	-	0.336	0.235	0.188

[a] IR active bands; [b] data taken from reference 10

3.5 Structural and Spectroscopic Study on two 9-Coordinate Uranium and Thorium Thiocyanate Complexes

In comparison to Ln, structurally characterized An thiocyanate complexes are scarce; but, as discussed in Chapter 1, the study of their properties is necessary to improve the liquid-liquid Ln/An separation from spent nuclear fuels.[61] Lanthanide thiocyanate complexes exhibit a rich coordination chemistry,[62] while, for the actinides, complexes with high coordination numbers are favourable. This has been evidenced in Chapter 2 with the structures of the 9-coordinate $[Me_4N]_4[Th(NCS)_7(NO_3)]$ and 10-coordinate $[Me_4N]_4[Th(NCS)_6(NO_3)_2]$ compounds and it is also witnessed by the reported 10-coordinate $[^nBu_4N]_3[Th(NCS)_4(NO_3)_3]$.[63] Herein, a comprehensive structural and spectroscopic study on two isostructural 9-coordinate U(IV) and Th(IV) thiocyanate complexes is discussed.

3.5.1 $Cs_5[U(NCS)_9][NCS]$

3.5.1.1 Synthesis and Structural Characterization of $Cs_5[U(NCS)_9][NCS]$

During one attempt at the synthesis of $[Cs]_4[U(NCS)_8]$, bright green crystals were grown from an MeCN solution and X-ray diffraction showed them to be a 9-coordinate uranium complex of the formula $Cs_5[U(NCS)_9][NCS]$. The reaction was also repeated, again under the experimental conditions reported for $[Cs]_4[U(NCS)_8]$,[38] but the same 9-coordinate compound was the only crystalline product formed, which also proved to be stable in air, keeping the same green colour and crystallinity. It was also possible to increase the yield, using correct stoichiometry for $Cs_5[U(NCS)_9][NCS]$. Nevertheless, it is important to point out that $[Cs]_4[U(NCS)_8]$ was always the first product formed during the reactions; indeed, it was isolated several times, as a green powder, with the structure verified by vibrational spectroscopy. However, during the recrystallization processes, it converted into $Cs_5[U(NCS)_9][NCS]$.

$[Cs]_4[U(NCS)_8]$ should possess a slightly less polar character with respect to the equivalent 9-coordinate derivative. Thus, driven by this consideration, the reaction was repeated in solvents of higher polarity than MeCN (DCM, EtOAc and MeOH), from where the less polar $[Cs]_4[U(NCS)_8]$ should selectively crystallize. However, $Cs_5[U(NCS)_9][NCS]$ was once more the only crystalline product obtained.

The solid-state crystal structure of $Cs_5[U(NCS)_9][NCS]$ is shown in Figure 3.32 and the corresponding bond lengths are listed in Table 3.5. The crystallographic data of this compound are listed in Appendix 2, while the full list of bond lengths and angles are tabulated in Appendix 2.5 in the external CD source of this thesis.

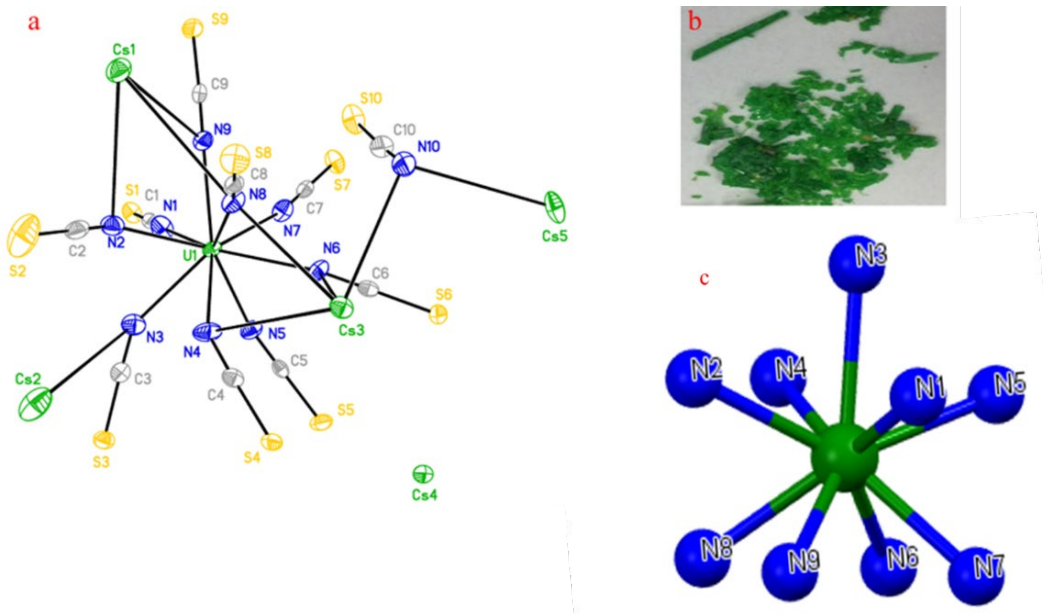

Figure 3.32. (a) Asymmetric unit of $Cs_5[U(NCS)_9][NCS]$ with atomic displacement shown at 50% probability; contacts from Cs atoms to C, S as well as H atoms are omitted for clarity. (b) Picture of some $Cs_5[U(NCS)_9][NCS]$ crystals. (c) Depiction of the monocapped square antiprismatic coordination geometry of the uranium ion in $Cs_5[U(NCS)_9][NCS]$.

Table 3.5. Bond lengths (Å) in $Cs_5[U(NCS)_9][NCS]$.

U(1)-N(1)	2.418(6)	N(1)-C(1)	1.160(9)	S(1)-C(1)	1.619(6)
U(1)-N(2)	2.475(6)	N(2)-C(2)	1.157(9)	S(2)-C(2)	1.628(8)
U(1)-N(3)	2.548(6)	N(3)-C(3)	1.158(9)	S(3)-C(3)	1.639(7)
U(1)-N(4)	2.477(6)	N(4)-C(4)	1.166(9)	S(4)-C(4)	1.631(7)
U(1)-N(5)	2.459(5)	N(5)-C(5)	1.161(8)	S(5)-C(5)	1.631(7)
U(1)-N(6)	2.502(6)	N(6)-C(6)	1.175(9)	S(6)-C(6)	1.632(7)
U(1)-N(7)	2.456(6)	N(7)-C(7)	1.170(9)	S(7)-C(7)	1.631(7)
U(1)-N(8)	2.471(6)	N(8)-C(8)	1.152(9)	S(8)-C(8)	1.635(7)
U(1)-N(9)	2.474(6)	N(9)-C(9)	1.167(9)	S(9)-C(9)	1.634(7)
		N(10)-C(10)	1.186(10)	S(10)-C(10)	1.606(8)

The $[U(NCS)_9]$ fragment in $Cs_5[U(NCS)_9][NCS]$ exhibits a monocapped square anti-prismatic symmetry (C_{4v}), with nine thiocyanate ligands coordinated to the uranium metal centre via the nitrogen atoms (Figure 3.32c), and a N-U-N angle from 67.7 to 142.3°. The

U−N bond distance ranges from 2.418(6) to 2.548(6) Å, with an average of 2.49(2) Å similar to those observed in the parent 8-coordinate $Cs_4[U(NCS)_8]$ (2.42(2) Å)[38] and in the U(IV) thiocyanate complexes $[Et_4N]_4[U(NCS)_8]$ (2.39(1) Å), $[^nPr_4N]_4[U(NCS)_8]$ (2.44(1) Å) and $[Me_4N]_4[U(NCS)_8]$ (2.43(2) Å) (Chapter 2). This similarity, as evidenced for **Co-U**, cannot be used as proof to unequivocally assign a formal +4 oxidation state to the uranium ion in $Cs_5[U(NCS)_9][NCS]$. The crystal structure (Figure 3.32) also shows the U(1)−N(3) bond as the longest (d_{U-N} = 2.548(6) Å), therefore the capping nitrogen. Moreover, the average of the bond lengths for the coordinated N=C and C=S are 1.163(3) and 1.631(3) Å, respectively, similarly observed in $[Cs]_4[U(NCS)_8]$ (N=C 1.14(2) Å and C=S 1.62(2) Å)[38] and in the uncoordinated $[NCS]^-$ fragment, the N=C bond is slightly lengthened (1.186(10) Å) and the C=S is shorter (1.606(8) Å) than in the coordinated $[NCS]^-$ ligands.

To further delineate the coordination geometry around the uranium ion, the geometrical parameters d_{pp}, d_{in}, θ, φ, (Chapter 2, Figure 2.6) have been measured for the polyhedron formed by the coordination bonds of U with N1, N2, N4, N5, N6, N7, N8 and N9, which possesses the U–N3 bond as the central rotational axis (Figure 3.32c). The results are: d_{pp} = 2.397(4) Å, d_{in} = 3.978(8) Å d_{pp}/d_{in} = 0.603, θ = 60.66(3)° (average) and φ = 45.00(4)° (average). These values are indicative of a square antiprismatic symmetry (φ = 45.00(4)°) for this polyhedron with a strong axial compression (θ = 60.66(3)°). The large compression, however, is explainable as due to the presence of the additional capping $[NCS]^-$ ligand.

3.5.1.2 Vibrational Characterization of $Cs_5[U(NCS)_9][NCS]$

The vibrational data can help to confirm the coordination geometry, indeed, the square antiprismatic (D_{4d}) $Cs_4[U(NCS)_8]$ possess three Raman active ν(C=N) stretches (A_1, E_2, E_3) and two IR active ν(C=N) stretches ($B_2 + E_1$).[38] The monocapped square antiprismatic symmetry falls into the C_{4v} point group and, therefore, $Cs_5[U(NCS)_9][NCS]$ should have four Raman active ν(C=N) stretches (A_1, B_1, B_2, E) and two IR active ν(C=N) stretches (A_1, E). Thus, to confirm this, Raman and IR spectra of $Cs_5[U(NCS)_9][NCS]$ have been measured in solid-state and are shown in Figure 3.33 and Figure 3.34, respectively, along with the analogue spectra of $Cs_4[U(NCS)_8]$ for comparison.

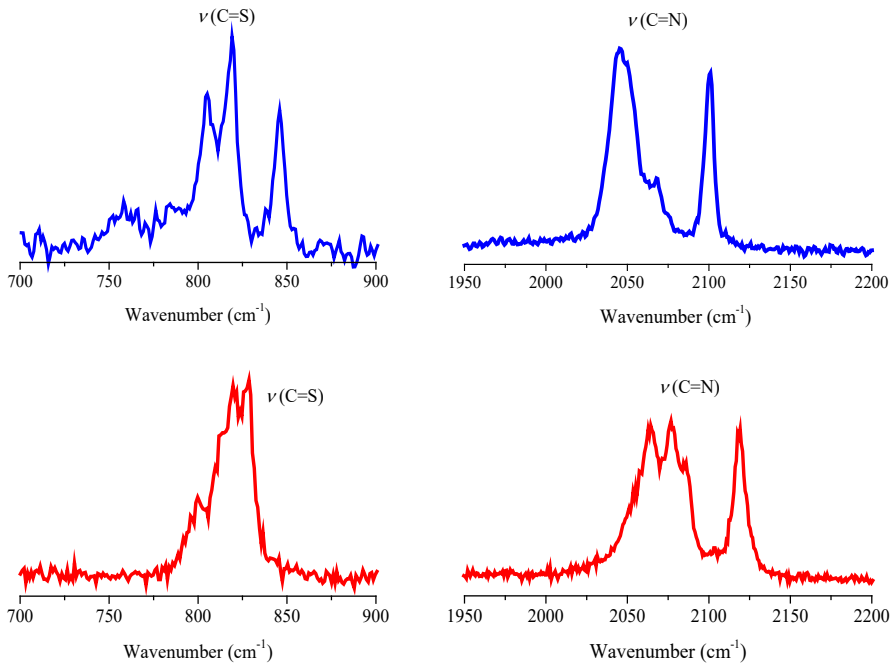

Figure 3.33. Raman spectra of (top) $Cs_4[U(NCS)_8]$ and (bottom) $Cs_5[U(NCS)_9][NCS]$ in solid-state, showing (left) the *ν*(C=S) and (right) the *ν*(C=N) Raman active stretches.

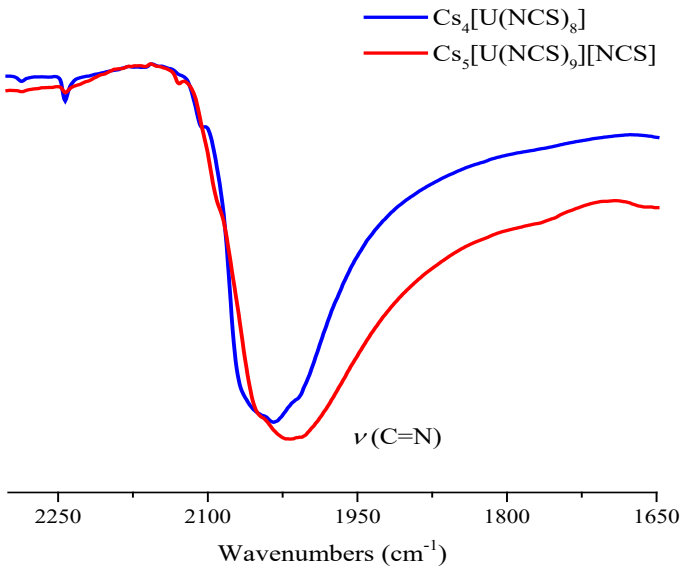

Figure 3.34. IR spectra of $C_4[U(NCS)_8]$ (blue line) and $Cs_5[U(NCS)_9][NCS]$ (red line) in solid-state, showing the region for the *ν*(C=N) IR active stretching mode.

The Raman spectrum of $Cs_5[U(NCS)_9][NCS]$ (Figure 3.33) shows four *ν*(C=N) stretches at 2064, 2076, 2086 and 2118 cm^{-1} (in line with the theory), and two *ν*(C=S) stretches at 820 and 828 cm^{-1}. In the IR spectrum (Figure 3.34), the IR active *ν*(C=N) stretch of $Cs_5[U(NCS)_9][NCS]$ appears at 2018 cm^{-1}, slightly red-shifted compared to the

analogue signal in $Cs_4[U(NCS)_8]$ (2035 cm^{-1}); this is in agreement with the structural data showing the coordinated C=N bond being, in average, slightly longer in $Cs_5[U(NCS)_9][NCS]$. Thus, the vibrational data confirm for $Cs_5[U(NCS)_9][NCS]$ a different structure compared to the parent $Cs_4[U(NCS)_8]$.

The $Cs_5[U(NCS)_9][NCS]$ molecular formula is indicative of a U(V) ion, as this also charge balances. Moreover, as already observed, the average of the U–N bond lengths (2.49(2) Å) can be only an indication of a U(IV) species. Thus, to unequivocally confirm the oxidation state of the uranium ion, $Cs_5[U(NCS)_9][NCS]$ has been fully characterized through magnetic and spectroscopic measurements.

3.5.1.3 Spectroscopic determination of the Low-Lying Energy Level Structure of $Cs_5[U(NCS)_9][NCS]$

The magnetic behaviour of $Cs_5[U(NCS)_9][NCS]$ was probed at different temperatures by SQUID magnetometry on crushed X-ray quality single crystals. The measured magnetic profile is shown in Figure 3.35; the data of $Cs_4[U(NCS)_8]$ and $[Et_4N]_4[U(NCS)_8]$, taken from Chapter 2, have also been added for comparison. At 300 K $Cs_5[U(NCS)_9][NCS]$ displays a μ_{eff} of 2.53 B.M.; upon cooling the sample, the values of μ_{eff} decrease until reaching a value of 0.74 B.M. at 2.0 K. For comparison, the 8-coordinate U(IV) $Cs_4[U(NCS)_8]$ and $[Et_4N]_4[U(NCS)_8]$ show, at 300 K, a μ_{eff} of 2.53 and 2.23 B. M., respectively, and at 2.0 K a μ_{eff} of 1.22 and 0.52 B. M., respectively.

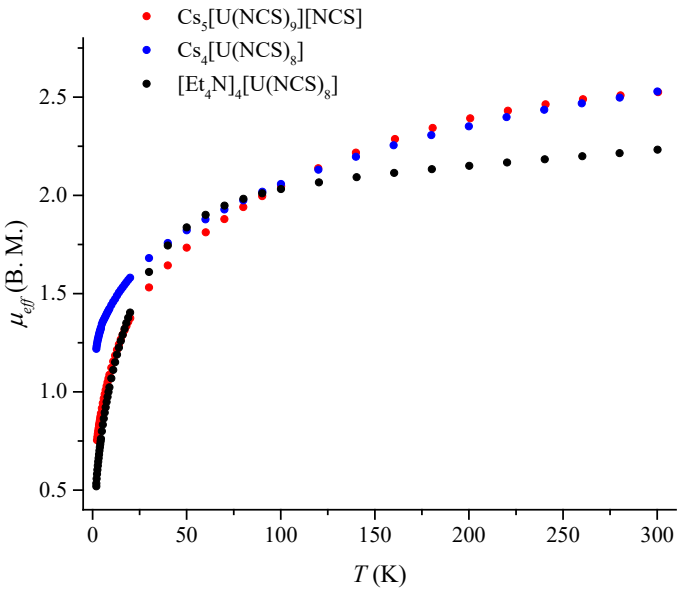

Figure 3.35. Effective magnetic moment *vs T* (K) of $Cs_5[U(NCS)_9][NCS]$ (dotted red line), $Cs_4[U(NCS)_8]$ (dotted blue line) and $[Et_4N]_4[U(NCS)_8]$ (dotted black line), collected at $B = 0.1$ T.

Regarding the shape of the temperature dependence of μ_{eff} for $Cs_5[U(NCS)_9][NCS]$, the data in Figure 3.35 show a region of temperature independent paramagnetism (TIP) from 300 to *ca.* 100 K, followed by a precipitous drop in the magnetic moment at low temperatures and, as explained in Chapter 1, this magnetic profile is typical of a U(IV) species. A U(V) ion, usually, displays a flatter line with small variation from room temperature to *ca.* 50 K (Figure 3.22), followed by a rapid drop at low temperatures, but, even at 2.0 K, an appreciable value (*ca.* 1.1 B. M.) tends to remain because a $5f^1$ U(V) ion is always a doublet electronic state (S = 1).

Therefore, the SQUID data suggest the presence of a U(IV) ion in $Cs_5[U(NCS)_9][NCS]$. Herein, it is worthy to underline the difference in the low-temperature magnetic moments between $Cs_5[U(NCS)_9][NCS]$ and $Cs_4[U(NCS)_8]$, which suggests that a different magnetic ground state should be observable. To further investigate this effect, specific heat capacity measurements, down to 0.3 K, have been performed on $Cs_5[U(NCS)_9][NCS]$. The results of this analysis are shown in Figure 3.36 where the data of $[Et_4N]_4[U(NCS)_8]$ and $Cs_4[U(NCS)_8]$, taken from Chapter 2, have been added for comparison. At 0.3 K the specific heat capacity of $Cs_5[U(NCS)_9][NCS]$ is similar to that of $[Et_4N]_4[U(NCS)_8]$, but clearly different compared to $Cs_4[U(NCS)_8]$. This latter gives rise to higher values below 4 K. Therefore, in line with the low-temperature magnetic data (Figure 3.35), qualitatively at least, $Cs_5[U(NCS)_9][NCS]$ and $[Et_4N]_4[U(NCS)_8]$ have approximately the same low-lying energy level structure, but different compared to $Cs_4[U(NCS)_8]$.

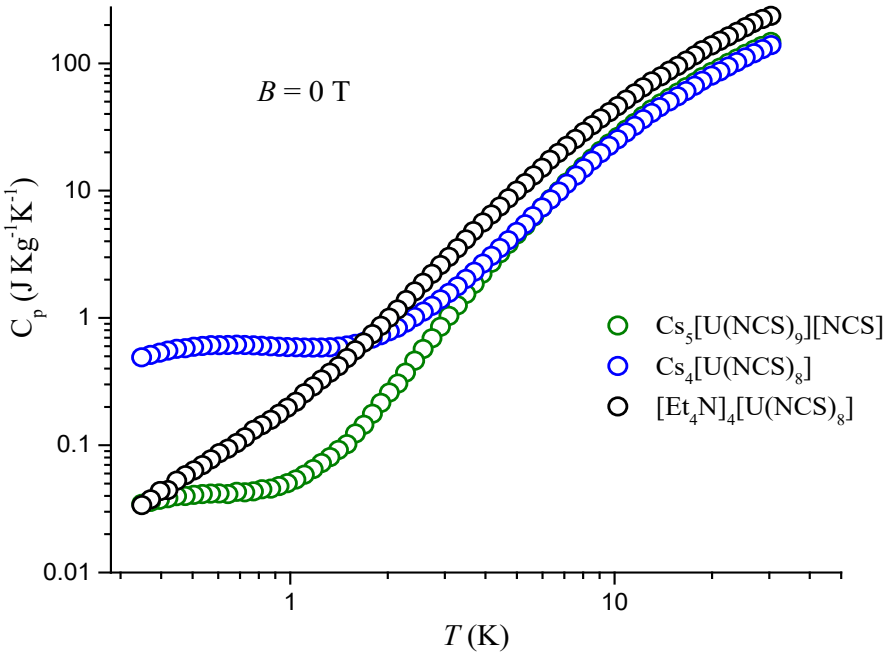

Figure 3.36. Low-temperature dendence of the experimental zero-field-applied heat capacity C_p for $Cs_5[U(NCS)_9][NCS]$ (green), $Cs_4[U(NCS)_8]$ (blue) and $[Et_4N]_4[U(NCS)_8]$ (black), as labelled.

In order to quantify the energy gaps from the ground electronic state, the low-lying energy level structure of $Cs[U(NCS)_9][NCS]$ has been investigated by far-IR magneto-transmission spectroscopy; indeed, as evidenced in Chapter 2, this technique is very powerful in probing the first excited states of actinide compounds. These measurements were performed by Dr. Milan Orlita, at the Laboratoire National des Champs Magnétiques Intenses in Grenoble. Thus, $Cs_5[U(NCS)_9][NCS]$ was pressed into an eicosane pellet (dilution 1 : 20) and measured at variable fields and at 4.2 K (Figure 3.37). The FIR spectrum acquired at zero field is shown in Appendix 2 (Figure 17).

This transmission spectrum is much less resolved than the one of $Cs_4[U(NCS)_8]$ (Appendix 1, Figure 5). In particular, it appears very broad between 250 and 150 cm^{-1}, where the U–N vibrational stretching mode should appear, as observed in Chapter 2 for the compounds $A_4[U(NCS)_8]$; thus it is not informative. However, upon the application of a magnetic field, a number of field-dependent bands appear (Figure 3.37).

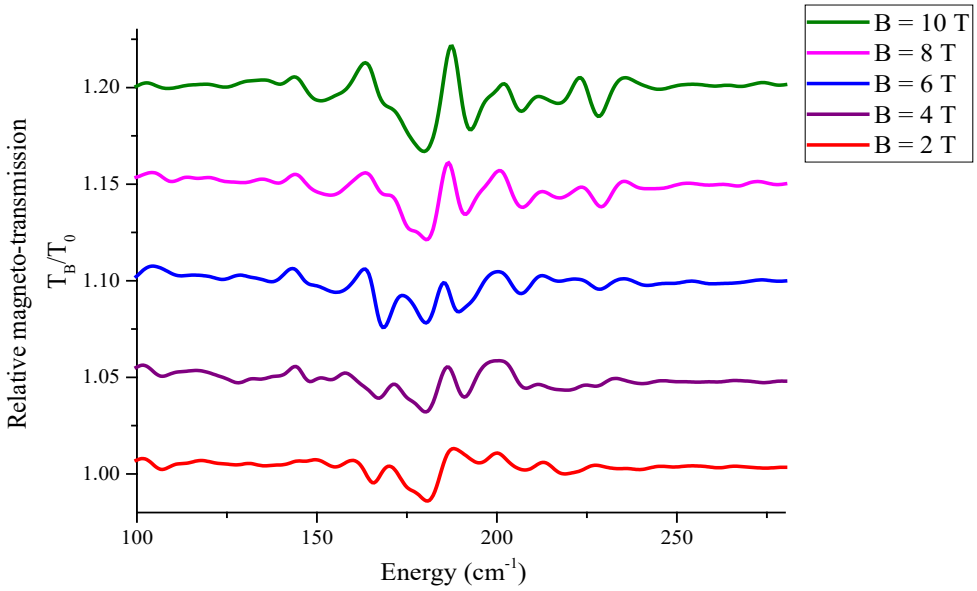

Figure 3.37. FIR spectra of $Cs_5[U(NCS)_9][NCS]$, dispersed in eicosane and measured at fields 2-10 T at 4.2 K.

In Figure 3.37, permitted by the $\Delta J = \pm 1$ selection rule, there appear six electronic transitions between 150 and 250 cm^{-1}. They are at 151, 179, 193, 207, 217 and 228 cm^{-1} and their intensity increases as the external magnetic field is amplified. These transitions could be used to delineate the crystal field splitting for this compound. As already mentioned, results from specific heat capacity (Figure 3.36) and magnetic moments (Figure 3.35) measurements at low temperature (T < 3 K) indicate that $Cs_5[U(NCS)_9][NCS]$ and $[Et_4N]_4[U(NCS)_8]$ should have a similar low-lying energy level electronic structure.

Thus, with this consideration and using the electronic transitions revealed by the far-IR measurements, it is possible to build an approximate low-lying energy level diagram for $Cs_5[U(NCS)_9][NCS]$ (Figure 3.38).

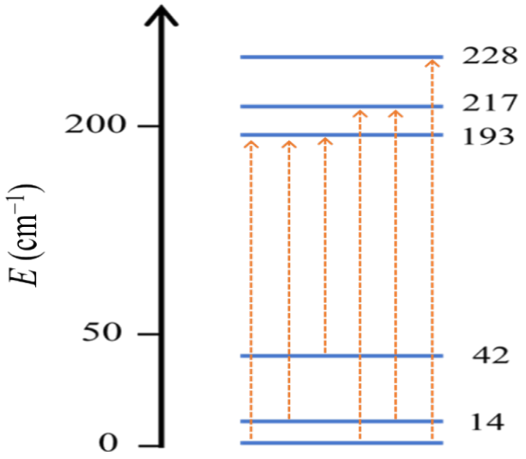

Figure 3.38. Approximate energy splitting of $Cs_5[U(NCS)_9][NCS]$, with electronic transitions observed through far-IR spectroscopy.

Thus, the FIR band at 193 cm^{-1} can be assigned as due to an electronic transition from the ground to the third excited state (~ 193 cm^{-1}), while the signals at 179 and 151 cm^{-1} can be considered as "hot bands" as due to transitions from, respectively, the first (~ 14 cm^{-1}) and the second (~ 42 cm^{-1}) to the third excited state (~ 193 cm^{-1}). Moreover, considering the FIR band at 217 cm^{-1} as due to a transition from the ground to the fourth excited state, the transition at 207 cm^{-1} can be defined as an "hot band" being due to a transition from the first (~ 14 cm^{-1}) to the fourth (217 cm^{-1}) excited state. Finally, the FIR band at 228 cm^{-1} can be assigned as arising from an electronic transition from the ground to the fifth excited state (~ 228 cm^{-1}). In order to quantify these low-lying energy states, CONDON calculations will be performed on $Cs_5[U(NCS)_9][NCS]$, as observed in Chapter 2 for the complexes $A_4[U(NCS)_8]$ (A = Me_4N, Et_4N, $^nPr_4N$, Cs).

3.5.1.4 Photophysical Characterization of $Cs_5[U(NCS)_9][NCS]$

The electronic absorption spectrum of $Cs_5[U(NCS)_9][NCS]$ has been acquired in MeCN solution. It is shown in Figure 3.39, along with the spectrum of the parent $Cs_4[U(NCS)_8]$, for comparison.

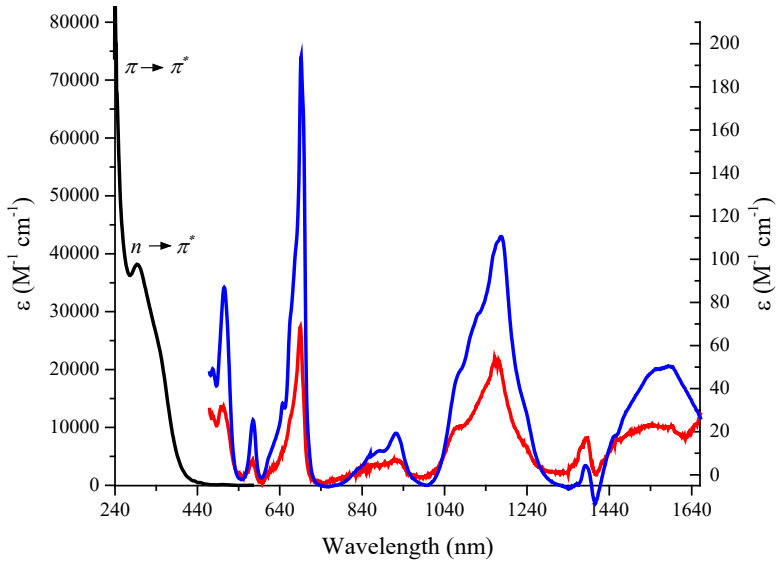

Figure 3.39. UV-vis-NIR spectrum of $Cs_5[U(NCS)_9][NCS]$ in MeCN; UV region (black line) measured at 2.5 x 10^{-6} M and vis-NIR region (red line) measured at 2.5 x 10^{-3} M. (Blue line) absorption spectrum of $Cs_4[U(NCS)_8]$ (1.69 x 10^{-4} M), showing the *f-f* transitions.

In the UV region (Figure 3.39, black line), the band at *ca.* 250 nm can be assigned to thiocyanate-based $\pi \rightarrow \pi^*$ transitions, as these are also observable in absorption spectra of solutions of Na[NCS] in MeCN, and the less intense feature at *ca.* 300 nm is due to $n \rightarrow \pi^*$ transitions, again based on the thiocyanate ligands. In Figure 3.39, the absorption profile in the vis-NIR region (red line) is very similar to that of the parent $Cs_4[U(NCS)_8]$ (blue line) and clearly indicative, in MeCN solutions, of a U(IV) species, showing the typical Laporte-forbidden *f-f* electronic transitions of a $5f^2$ U(IV) ion. As discussed for **U-DMF** and **U-MeCN**, these transitions can be assigned to transitions from the Russell-Saunders coupled $^3H_4$ ground state to states of higher energy.[19] They are listed in Table 3.6,along with the values of the corresponding molar extinction coefficients and oscillator strengths.

Table 3.6. *f-f* electronic transitions of $Cs_4[U(NCS)_8]$ and $Cs_5[U(NCS)_9][NCS]$.

Compound	Transition	λ (nm) [Energy (cm^{-1})]	ε (M^{-1} cm^{-1})	Oscillator strength (f x 10^{-4})
$Cs_4[U(NCS)_8]$ (10^{-4} M)	$^1I_6$	505 [15381]	87.0	3.96
	$^3P_1$	573 [17452]	130	0.493
	$^3P_0/^1D_2/^1G_4$	691 [14471]	287	5.90
	$^3H_6$	918 [10893]	99.0	0.505
	$^3F_4$	1160 [8621]	192	4.38
	$^3F_3/^3H_5$	1539 [6498]	105	1.62
$Cs_4[U(NCS)_9][NCS]$	$^1I_6$	503 [19880]	31.6	1.64
	$^3P_1$	575 [17391]	6.32	0.113
	$^3P_0/^1D_2/^1G_4$	690 [14492]	68.7	1.94
	$^3H_6$	923 [10834]	7.17	0.204
	$^3F_4$	8598 [1163]	54.0	2.08
	$^3F_3/^3H_5$	1533 [6466]	17.3	0.733

From the data in Table 3.6, within the errors from the experimental measurements and from the equation 3, the oscillator strengths of the observed *f-f* transitions for $Cs_5[U(NCS)_9][NCS]$ are slightly lower than the ones for $Cs_4[U(NCS)_8]$, perhaps in line with an overall higher polarity for the 9-coordinate compound.

The absorption spectrum of $Cs_5[U(NCS)_9][NCS]$ has also been measured in solid-state. It is shown in Figure 3.40, along with the spectrum of $Cs_4[U(NCS)_8]$. Despite the difference in the symmetry, there are no clear differences in the energy of the *f-f* transitions between these two complexes; nevertheless, this supports the assignment of the formal +4 oxidation state for the uranium ion in $Cs_5[U(NCS)_9][NCS]$ also in solid state.

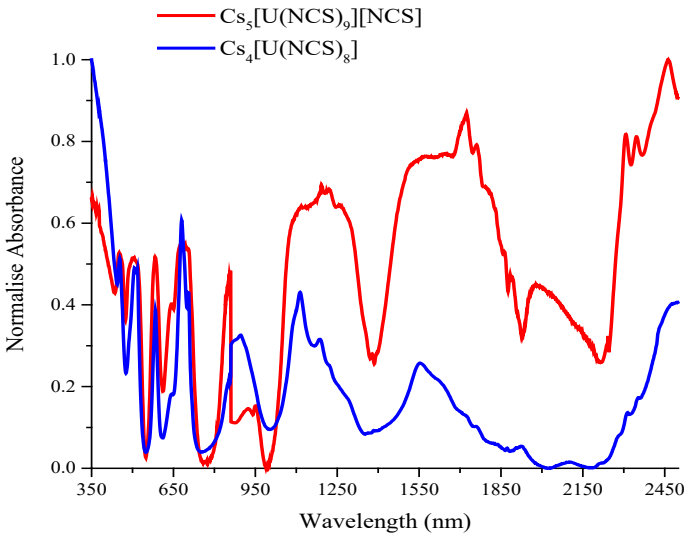

Figure 3.40. Solid-state absorption spectra of $Cs_5[U(NCS)_9][NCS]$ (red line) and $Cs_4[U(NCS)_8]$ (blue line).

The absorption spectra of $Cs_5[U(NCS)_9][NCS]$ did not show any ligand-based charge transfer bands encroaching into the visible region; therefore, as recently demonstrated,[22] emission spectroscopy could be used to corroborate the assignment of +4 as the formal oxidation state of the uranium ion in this complex. Thus, photoluminescence measurements have been recorded on solutions of $Cs_5[U(NCS)_8][NCS]$ and the results are shown in Figure 3.41.

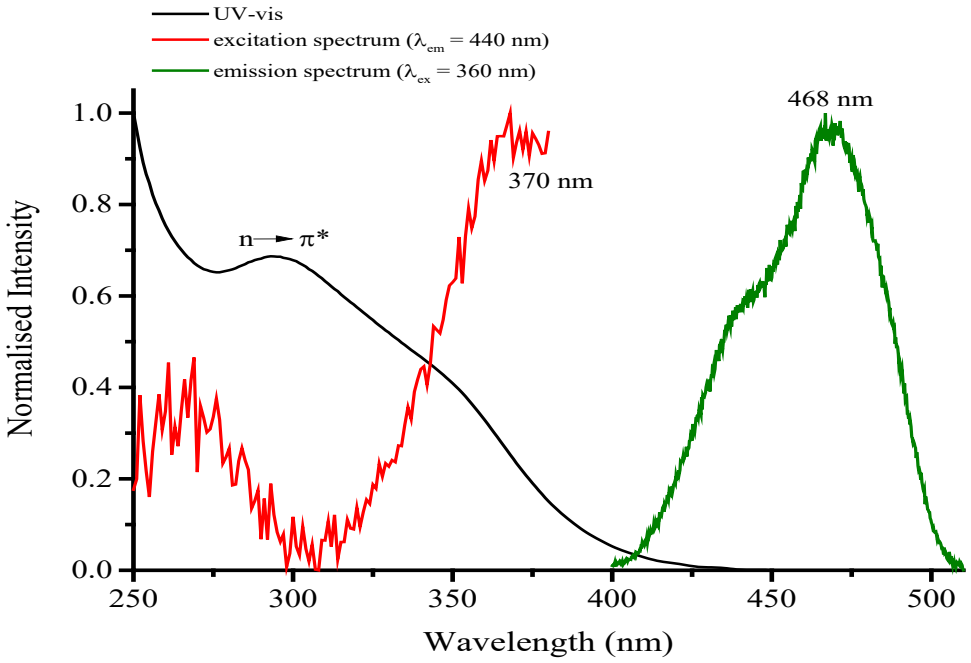

Figure 3.41. UV-vis spectrum (black line), excitation spectrum (red line) and emission spectrum (green line) of $Cs_5[U(NCS)_9][NCS]$, measured at 2.5 x 10^{-6} M in MeCN.

Excitation into the thiocyanate-based absorption bands, between 280 and 380 nm, produced an emission spectrum (Figure 3.41, green line) assignable to a U(IV) species,[22] with a maximum emission at λ_{em} = 468 nm. Direct excitation into any of the *f-f* transitions showed no emission as the absorption extinction coefficients were relatively weak. It can be postulated that excitation into ligand chromophore bands is followed by inefficient electron transfer and subsequent de-excitation through the *f*-orbital manifold. In effect, an "antenna" effect is used to sensitize the emission of U(IV) complexes, which is reminiscent of lanthanide emission spectroscopy.[64]

To date, there are very few examples reported of photoluminescence spectroscopy studies on uranium(IV) compounds in non-aqueous solutions, but the emission profile of $Cs_5[U(NCS)_9][NCS]$ can be compared with that of **U-DMF (**Figure 3.8**)** and those for the compounds $[Li(THF)_4][UCl_5(THF)]$ (λ_{ex} = 303 nm; λ_{em} = 420 nm)[22] and $[Et_4N]_4[U(NCS)_8]$ (λ_{ex} = 280 – 350 nm; λ_{em} = 410 nm).[10]

3.5.2 $Cs_5[Th(NCS)_9][NCS]$

3.5.2.1 Synthesis and Structural Characterization of $Cs_5[Th(NCS)_9][HNCS]$

The synthesis of the 9-coordinate Th(IV) complex of formula $Cs_5[Th(NCS)_9][NCS]$ has been achieved and the product fully characterized providing a comparison with $Cs_5[U(NCS)_9][NCS]$. During one attempt at the synthesis of $Cs_4[Th(NCS)_8]$, which would have provided a structural comparison for $Cs_4[U(NCS)_8]$, colourless single crystals were isolated and X-ray diffraction revealed a 9-coordinate Th(IV) complex, of formula $Cs_5[Th(NCS)_9][NCS]$. Although the synthesis required strictly anaerobic conditions, this compound proved to be stable in air, keeping the same crystallinity. The reaction was also repeated, using correct stoichiometry for $Cs_5[Th(NCS)_9][NCS]$, and the same complex isolated with a higher yield. Herein, it is worth noting that, to date, the crystal structure of the parent eight coordinated $Cs_4[Th(NCS)_8]$ has not been reported. The solid-state crystal structure of $Cs_5[Th(NCS)_9][NCS]$ is shown in Figure 3.42; the corresponding crystallographic data are listed in Appendix 2 and the full list of bond lengths and angles are tabulated in Appendix 2.5, in the external CD source of this thesis.

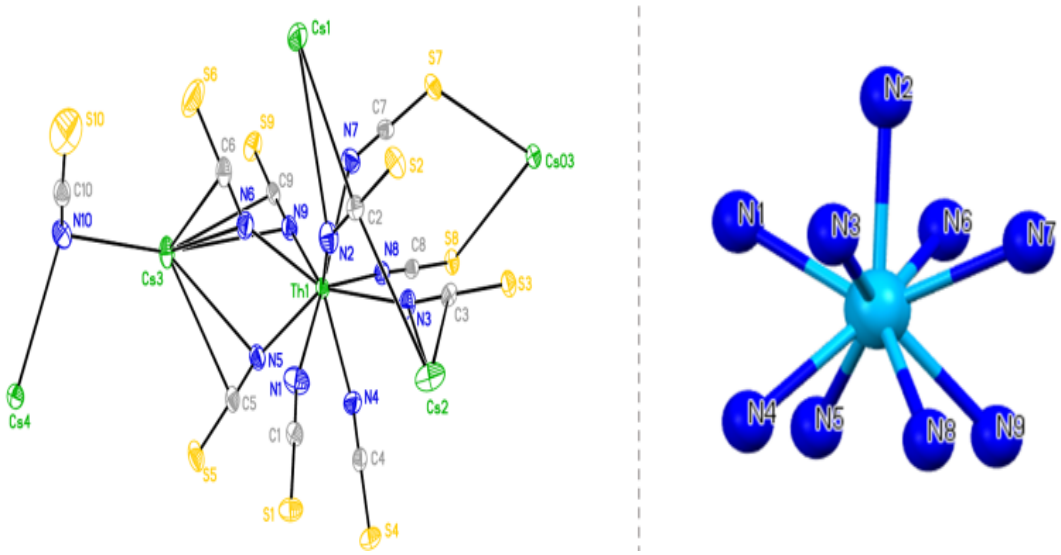

Figure 3.42. (Left) Asymmetric unit of $Cs_5[Th(NCS)_9][NCS]$, with atomic displacement shown at 50% probability. (Right) Depiction of the coordination geometry around the thorium ion. Colour code: Thorium – pale blue, Nitrogen – dark blue.

The $[Th(NCS)_9]$ fragment of $Cs_5[Th(NCS)_9][NCS]$ exhibits the same monocapped square anti-prismatic symmetry (C_{4v}) (Figure 3.42, right) as $[U(NCS)_9]$ (Figure 3.32c) with nine thiocyanate ligands coordinated to the thorium ion via the nitrogen atoms and an N-Th-N angle from 67.62(16) to 141.82(15)°. The Th–N bond distance ranges from 2.476(5) to 2.600(5) Å, with an average of 2.53(2) Å very close to the one displayed by the compound $[Et_4N]_4[Th(NCS)_8]$ (2.48(4) Å) (Chapter 2). The N(2) atom corresponds to the capping nitrogen in the structure, where the Th(1)–N(2) bond shows the longest Th–N distance (2.600(5) Å), also longer compared to U(1)–N(3) (2.548(6) Å) in $Cs_5[U(NCS)_9][NCS]$, as expected due to the actinide contraction. The average bond lengths for the coordinated N=C and C=S is 1.16(3) and 1.63(2) Å, respectively, and these values are similar to the ones found in $Cs_5[U(NCS)_9][NCS]$ (N=C 1.163(3) Å and C=S 1.631(3) Å). In the uncoordinated $[NCS]^-$ fragment, both the N=C and C=S bonds are slightly shorter (1.153(7) and 1.591(6) Å, respectively) in comparison to the ones in the coordinated $[NCS]^-$ ligands.

Moreover, to further evaluate the coordination symmetry around the thorium ion, the geometrical parameters d_{pp}, d_{in}, θ and φ have been measured for the polyhedron formed by the coordination bonds of Th with N1, N3, N4, N5, N6, N7, N8 and N9, which possesses the Th–N2 bond as the central rotational axis (Figure 3.42, right). The results are: d_{pp} = 2.560(5) Å, d_{in} = 4.067(6) Å, d_{pp}/d_{in} = 0.629, θ = 60.592(4)° (average) and φ = 45.00(3)° (average). These values are in line with a square antiprismatic symmetry (φ =

45.00(3)°) for the selected polyhedron with a strong axial compression (θ = 60.64°). The large compression, however, is in line with the presence of the additional capping $[NCS]^-$ ligand.

The highest oxidation state of thorium is +4, consequently, in the crystal structure of $Cs_5[Th(NCS)_9][NCS]$, the non coordinated $[NCS]^-$ fragment must be [HNCS] (isothiocyanic acid), although it was not possible to crystallographically locate the H atom. Moreover, considering the several structural similarities between $Cs_5[U(NCS)_9][NCS]$ and $Cs_5[Th(NCS)_9][NCS]$, the existence of the uncoordinated $[NCS]^-$ fragment as [HNCS] can also be postulated in $Cs_5[U(NCS)_9][NCS]$, corroborating the assignment of the formal +4 oxidation state for the uranium centre in this complex.

3.5.2.2 Spectroscopic Characterization of $Cs_5[Th(NCS)_9][NCS]$

As for $Cs_5[U(NCS)_9][NCS]$, vibrational spectra of $Cs_5[Th(NCS)_9][NCS]$ can help to confirm the coordination symmetry. Indeed, the cubic (O_h) $[Et_4N]_4[Th(NCS)_8]$ possess two Raman active ν(C=N) stretches, at 2054 and 2107 cm^{-1}, and one sharp IR active ν(C=N) stretch at 2043 cm^{-1}.[65] Thus, Raman and IR spectra of $Cs_5[Th(NCS)_9][NCS]$ have been measured in solid state and are shown in Figure 3.43.

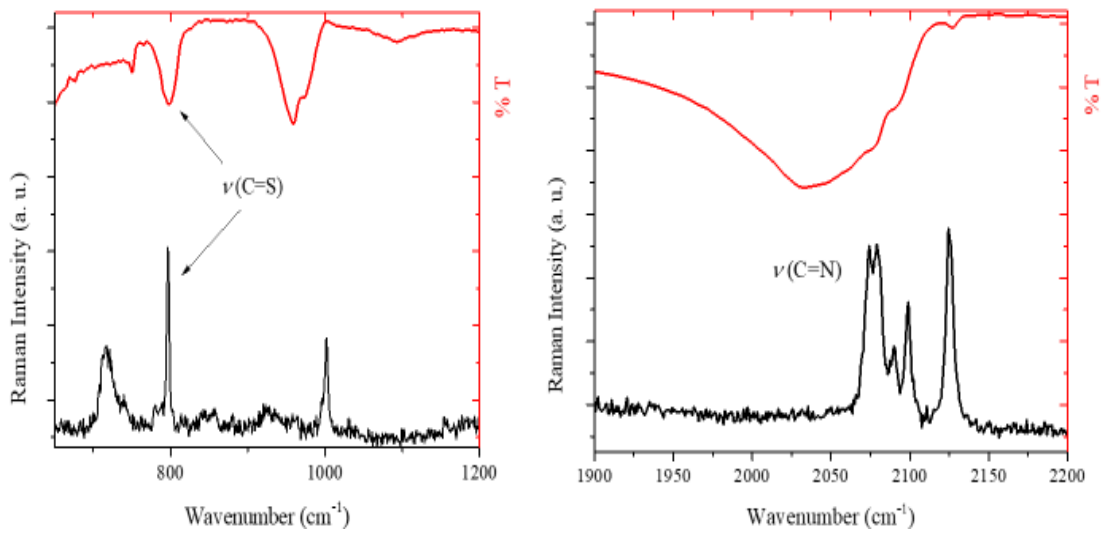

Figure 3.43. Raman (black line) and IR (red line) spectra of $Cs_5[Th(NCS)_9][NCS]$ measured in solid state, showing (left) the ν(C=S) and (right) the ν(C=N) vibrational modes.

The Raman spectrum of $Cs_5[Th(NCS)_9][NCS]$ (Figure 3.43) shows five Raman active ν(C=N) stretches at 2124, 2099, 2090, 2079 and 2074 cm^{-1}, and one narrow Raman active ν(C=S) stretch at 796 cm^{-1}. With the coordination symmetry belonging to the C_{4v} point

group, $Cs_5[Th(NCS)_9][NCS]$ should possess only four Raman active ν(C=N) stretches (A_1, B_1, B_2, E), similarly to $Cs_5[U(NCS)_9][NCS]$; in this case, perhaps, the additional fifth ν(C=N) transition is assignable to the uncoordinated $[NCS]^-$. In the IR spectrum (Figure 3.43), the IR active ν(C=N) stretch appears at 2033 cm^{-1}, slightly blue shifted compared to the analogue signal in $Cs_5[U(NCS)_9][NCS]$ (2018 cm^{-1}), perhaps due to the shorter N=C bond in the uncoordinated $[NCS]^-$ ion (1.153(6) Å in the thorium and 1.186(1) Å in the uranium compound). Moreover, the IR active ν(C=S) stretch is observable at 797 cm^{-1}, as a broad band of low intensity (Figure 3.43).

$Cs_5[Th(NCS)_9][NCS]$ has also been characterized by UV-vis spectroscopy. Its electronic absorption spectrum, measured in MeCN solution (Appendix 2, Figure 18), shows an intense band at *ca.* 265 nm, assignable to thiocyanate-based $\pi \rightarrow \pi^*$ transitions, and a smaller feature at *ca.* 320 nm, which is due to thiocyanate-based $n \rightarrow \pi^*$ transitions.

Finally, to unequivocally confirm the diamagnetic nature, $Cs_5[Th(NCS)_9][NCS]$ has been analysed by SQUID magnetometry (Appendix 2, Figure 19). The trend of the χT data is linear and negative with the temperature, in line with a closed-shell $5f^0$ configuration and with a diamagnetic $^1S_0$ ground state.

3.6 Structural Determination of the Isothiocyanic Acid, [HNCS]

3.6.1 Introduction

In both $Cs_5[U(NCS)_9][NCS]$ and $Cs_5[Th(NCS)_9][NCS]$ it was not possible to crystallographically locate the H atom in the non coordinated $[NCS]^-$ ion and its presence was only hypothesised. Therefore, the structural determination of [HNCS] (isothiocyanic acid) was subsequently attempted, with the aim of comparing the structural parameters with the ones shown by $Cs_5[U(NCS)_9][NCS]$ and $Cs_5[Th(NCS)_9][NCS]$.

Isothiocyanic acid is a well-established interstellar molecule that was first detected by microwave spectroscopy in the gas cloud Sagittarius B2 (*Sgr B2*), close to the centre of the Milky Way.[66] Several spectroscopic studies on this molecule have been reported including IR spectroscopy in the gas phase,[67] organic solvents and water,[68] and in a low temperature matrix,[69] and the shift of the N=C bond stretch was found negligible compared to the anion $[NCS]^-$. The structure of [HNCS] was initially elucidated through the analysis of microwave spectroscopy and the first assumption was of a linear molecule,[70] although more accurate spectra showed a bending of the [HNC] group.[71] Nevertheless, since [HNCS] is a gas that rapidly decomposes at room temperature,[72] there

has been no crystallographic evidence presented for any of its possible isomers: [HNCS], [HSCN], [HSNC] and [HCNS].

However, thanks to the formation of a hydrogen bonding between [HNCS] and $[NCS]^-$, it was possible to isolate and structurally characterize a molecule of isothiocyanic acid. Hydrogen bonding is, indeed, an interesting aspect of the chemistry of [HNCS], which has been observed in matrix isolation studies in low temperature argon matrices of CO,[73] N_2 and Xe,[74] and as hydrogen bonded dimers in an N_2 matrix.[75]

3.6.2 Structural Characterization of $[Ph_4P][NCS][HNCS]$

The structural determination of [HNCS] was achieved in the compound $[Ph_4P][NCS][HNCS]$, which was isolated as a red crystalline product from the reaction between $[Ph_4P][NCS]$, synthesised by mixing $[Ph_4P][Cl]$ and Na[NCS], and gaseous [HNCS] in MeCN solution. Alternatively, passing gaseous [HNCS] over single crystals of $[Ph_4P][NCS]$ also produced $[Ph_4P][NCS][HNCS]$, albeit much more slowly and with loss of crystallinity; nevertheless, the identity was confirmed by IR and UV-vis spectroscopy and powder XRD.

The solid-state crystal structure of $[Ph_4P][NCS][HNCS]$ is shown in Figure 3.44 and the bond lengths for the [HNCS] fragment are listed in Table 3.7, along with those from theory and microwave spectroscopy. The crystallographic data of $[Ph_4P][NCS][HNCS]$ are listed in Appendix 2 and the full list of bond lengths and angles is tabulated in Appendix 2.6 (external CD source). Notably the hydrogen atom was located on the difference map as the highest remaining density peak and was allowed to refine without constraints. $[Ph_4P][NCS][HNCS]$ represents the first determination of [HNCS] in a crystal structure; a coordination complex to a copper macrocycle is also reported, but the hydrogen was not crystallographically located and the assignment corroborated only on the basis of IR spectroscopy.[76]

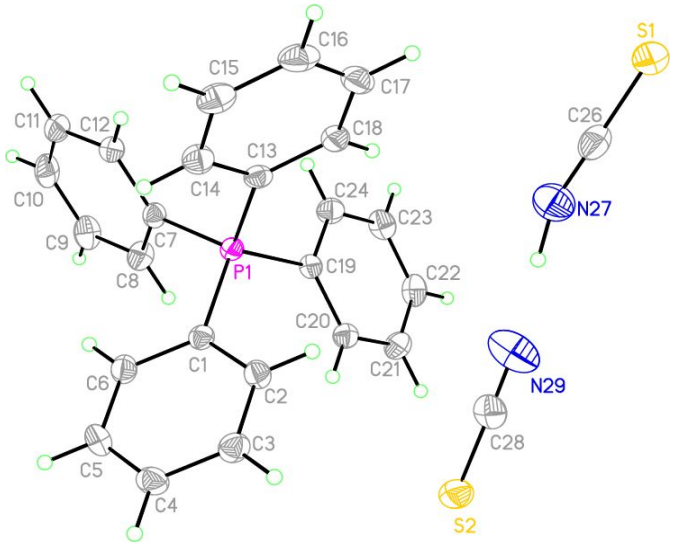

Figure 3.44. Solid-state crystal structure of [Ph_4P][NCS][HNCS], with atomic displacement shown at 50% probability.

Table 3.7. Comparison of bond lengths (Å) and angles (°) for [HNCS] in [Ph_4P][NCS][HNCS] from experiment, theory and microwave spectroscopy.

	Structure	**DFT**	**CASSCF of [HNCS][77]**	**Microwave of [HNCS][71b]**
N–H	0.98(3)	1.099	1.009	0.993(6)
N–C	1.162(2)	1.173	1.206	1.207(3)
C–S	1.6033(19)	1.618	1.591	1.567(1)
H–N–C	160(2)	164.8	134	131.7(19)
N–C–S	178.93(19)	179.0	173.6	173.8(23)
H···N	1.60(3)	1.488	—	—
N···N	2.577(2)	2.585	—	—

The bond lengths and angles in the anionic component of [Ph_4P][NCS][HNCS] can be compared with the ones possessed by [Ph_4P][NCS], whose reported crystal structure[78] has been remeasured.

The bond lengths in the anionic component of [Ph_4P][NCS][HNCS] [N(29)–C(28) = 1.147(3) Å; C(28)–S(2) = 1.623(2) Å], are typical for anionic, uncoordinated $[NCS]^-$ ions,[79] and in [Ph_4P][NCS] the corresponding bond lengths are 1.128(4) Å for N=C and 1.675(3) Å for C=S bond. The structure of [Ph_4P][NCS][HNCS] also shows a very short hydrogen bond of 1.60(3) Å (Table 3.12), shorter than those calculated in $(HNCS)_2$ dimer (H···N 2.034 Å).[80] From the solid-state structures it is apparent that, compared to the

uncoordinated $[NCS]^-$ ions, in the isothiocyanic acid fragment the N=C bond length is only slightly lengthened, but surprisingly the C=S bond is shorter.

Moreover, the structure of [HNCS] is not linear, with the H–N–C group bent to 160(2)° (Table 3.7). This angle is in good agreement with the DFT calculation (164.8°), while the large difference with the microwave spectroscopy (131.7(19)°) can be attributed to the hydrogen bonding.

In order to unequivocally confirm the presence of the [HNCS] group, given the uncertainty in refining a structure with a hydrogen atom next to a much heavier atom, $[Ph_4P][NCS][HNCS]$ has been spectroscopically characterized.

3.6.3 Spectroscopic Charaterization of $[Ph_4P][NCS][HNCS]$

The IR and Raman spectra of $[Ph_4P][NCS][HNCS]$ have been measured in solid state and are shown in Figure 3.45, along with those of Na[NCS] and $[Ph_4P][NCS]$ for comparison.

In the IR spectrum, the N=C band is broad and distinctly asymmetric with a maximum at 2054 cm^{-1} and a shoulder at 2018 cm^{-1}; the C=S stretch at 750 cm^{-1} is almost identical to the one in $[Ph_4P][NCS]$ and Na[NCS]. Interestingly, a peak assignable to the N–H stretch is not observable, possibly due to the very strong hydrogen bond; this has been further studied by DFT methods (section 3.6.4).

The Raman spectrum of $[Ph_4P][NCS][HNCS]$, is more clear. It shows two broad peaks for the N=C group (between 2050 and 2150 cm^{-1}) and the C=S stretch slightly blue-shifted compared to the one in $[Ph_4P][NCS]$ and Na[NCS], corroborating the structural data.

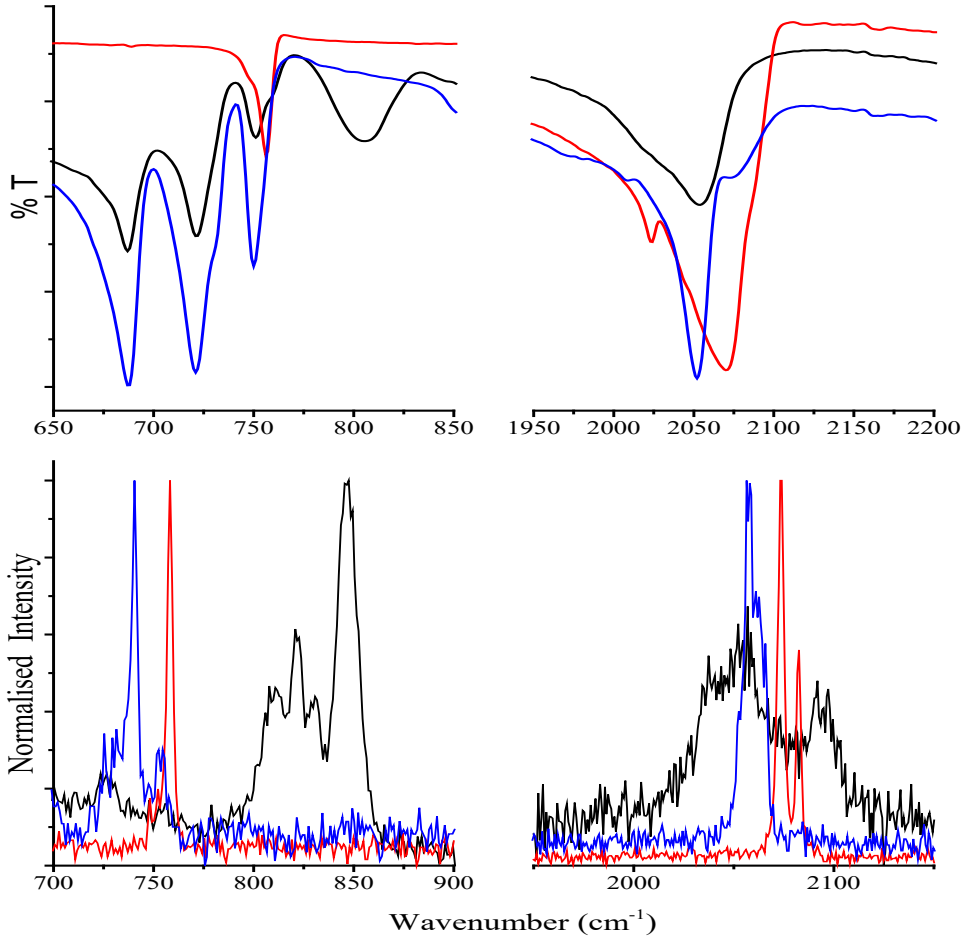

Figure 3.45. Infrared (top) and Raman (bottom) spectra of $[Ph_4P][NCS][HNCS]$ (black line), Na[NCS] (red line) and $[Ph_4P][NCS]$ (blue line) in the solid-state, showing the regions with (left) the *ν*(C=S) stretch and (right) the *ν*(N=C) stretch.

To obtain spectroscopic evidence of the presence of [HNCS] fragment in $[Ph_4P][NCS][HNCS]$, the deuterated compound $[Ph_4P][NCS][DNCS]$ was prepared and characterized. This was synthesized by reaction between [DNCS], produced mixing DCl and Na[NCS], and $[Ph_4P][NCS]$. The IR spectrum of $[Ph_4P][NCS][DNCS]$ (Appendix 2, Figure 20) shows a N=C band narrower compared to the one in $[Ph_4P][NCS][HNCS]$, suggesting that this band in $[Ph_4P][NCS][HNCS]$ is due to both N=C and N–H stretches. It is worth noting that, on the basis of reduced masses, the N–D stretch is predicted to be at 1428 cm^{-1}, but in this case it was obscured by bands belonging to the $[Ph_4P]^+$ cation.

$[Ph_4P][NCS][HNCS]$ was also analysed by NMR spectroscopy and the ^1H NMR spectrum (Appendix 2, Figure 21, blue spectrum) displays a broad resonance at 8.82 ppm, assignable to the [HNCS] fragment, in addition to the aromatic protons of the $[Ph_4P]^+$ cation. This is a large shift in comparison to the resonance showed by $[HNCS]_{(g)}$ dissolved

in $CDCl_3$ (Appendix 2, Figure 21, red spectrum), which appears at 5.47 ppm as a triplet presumably due to coupling to ^{14}N.[81]

Moreover, in the ^2H NMR spectrum of $[DNCS]_{(g)}$ dissolved in CH_3Cl (Appendix 2, Figure 22, red spectrum), there is a resonance at 0.94 ppm and no resonances in the ^1H NMR spectrum, confirming the above assignment for $[HNCS]_{(g)}$. $[Ph_4P][NCS][DNCS]$ was also examined by both ^1H and ^2H NMR spectroscopy and the ^2H NMR spectrum (Appendix 2, Figure 22, blue spectrum) shows a resonance at $\delta_{(D)}$ = 7.28 ppm, which is very close to the broad [HNCS] resonance of $[Ph_4P][NCS][HNCS]$ at 8.82 ppm (Appendix 2, Figure 21, blue line). This confirms the hydrogen bonding interaction. Finally, the thiocyanate carbons are not visible in the $^{13}C\{^1H\}$ NMR spectra, which is a common observation.[82]

The UV-vis spectra of $[Ph_4P][NCS][HNCS]$ and $[Ph_4P][NCS]$ have also been measured and are shown in Figure 3.46.

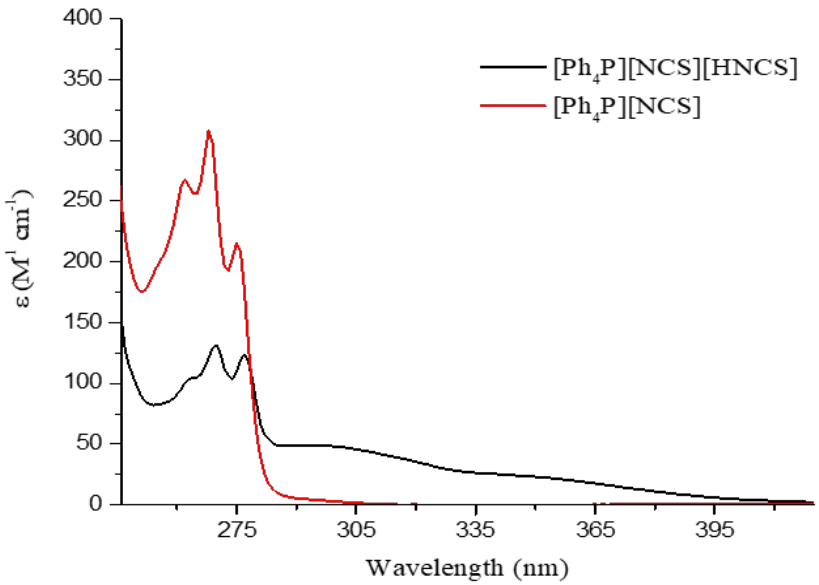

Figure 3.46. UV-vis spectrum of $[Ph_4P][NCS][HNCS]$ (black line) and $[Ph_4P][NCS]$ (red line), both 1.10^{-7} M in MeCN.

$[Ph_4P][NCS]$ shows two absorption bands at 262 (236 M^{-1} cm^{-1}) and 268 nm (278 M^{-1} cm^{-1}), most likely due to $\pi \rightarrow \pi^*$ transitions within the $[Ph_4P]^+$ cation, and a less intense feature at 280 nm (215 M^{-1} cm^{-1}), which is probably due to thiocyanate-based $\pi \rightarrow \pi^*$ transitions, as it also appears in the absorption spectra of solutions of Na[NCS] in MeCN. In the absorption spectrum of $[Ph_4P][NCS][HNCS]$, these bands are less intense and slightly red shifted and, additionally, there are two broad bands at 302 nm (ε = 49 M^{-1}

cm^{-1}) and 351 nm (ε = 24 M^{-1} cm^{-1}), which can be attributed to thiocyanate-based $n \rightarrow \pi^*$ transitions. In $[Ph_4P][NCS][HNCS]$, perhaps, the hydrogen bonding between $[NCS]^-$ and [HNCS] determines an increase in the extension of the π-conjugated system over the molecule and this might explain the lowering in energy of the $\pi \rightarrow \pi^*$ transitions in $[Ph_4P][NCS][HNCS]$ compared to $[Ph_4P][NCS]$.

In order to further identify the presence of [HNCS], TGA-IR measurements have been conducted on $[Ph_4P][NCS][HNCS]$ (Figure 3.47). Thus, during the heating process (Figure 3.47, left), several IR spectra have been recorded. In particular, the spectrum acquired after 10 minutes, when the temperature was 125 °C, corresponds to the IR spectrum of gaseous [HNCS] (Figure 3.47, right). This analysis indicates also that, although stable, the hydrogen bonded complex decomposes at relatively low temperatures (125 °C); nevertheless, at room temperature, $[Ph_4P][NCS][HNCS]$ has proven to retain stability as a red crystalline solid for at least six months.

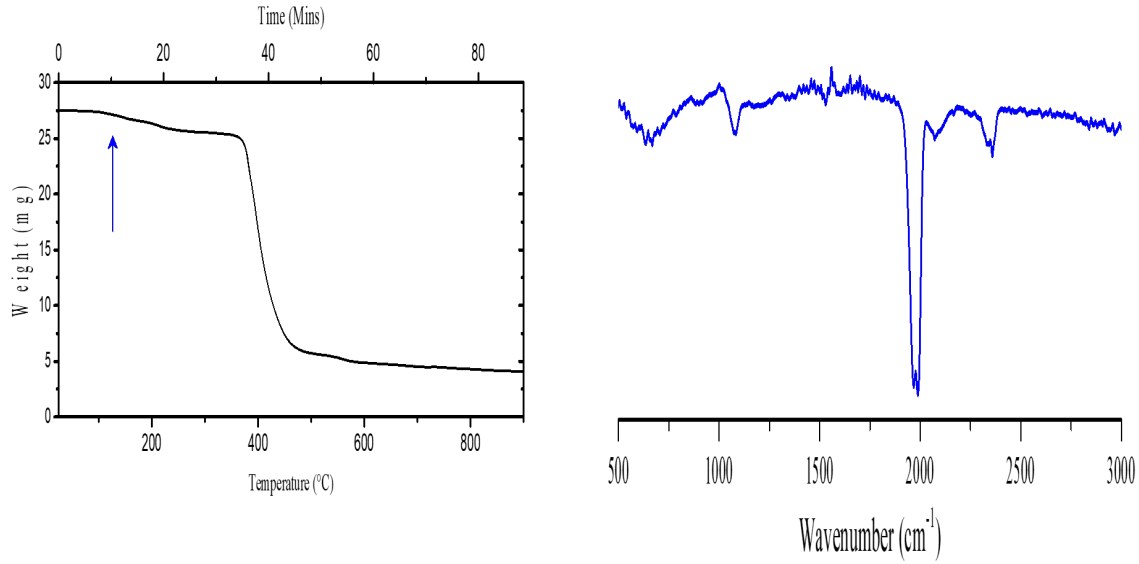

Figure 3.47. (Left) TGA of $[Ph_4P][NCS][HNCS]$. (Right) IR spectrum recorded after 10 minutes.

Finally, Table 3.8 lists the C=N and C=S bond lengths of the [HNCS] group from $[Ph_4P][NCS][HNCS]$ and of the $[NCS]^-$ ions from $Cs_5[U(NCS)_9][NCS]$, $Cs_5[Th(NCS)_9][NCS]$ and $[Ph_4P][NCS]$.

Table 3.8. Comparison of C=N and C=S bond lengths of [HNCS] from $[Ph_4P][NCS][HNCS]$ and of $[NCS]^-$ from $Cs_5[U(NCS)_9][NCS]$, $Cs_5[Th(NCS)_9][NCS]$ and $[Ph_4P][NCS]$.

Compound	**C=N** (Å)	**C=S** (Å)
[HNCS]	1.162(2)	1.6033(19)
$[NCS]^-$ from $Cs_5[U(NCS)_9][NCS]$	1.186(10)	1.606(8)
$[NCS]^-$ from $Cs_5[Th(NCS)_9][NCS]$	1.153(7)	1.591(6)
$[Ph_4P][NCS]$	1.128(4)	1.675(3)

The differences in the C=N and, especially, C=S bond lengths between [HNCS] from $[Ph_4P][NCS][HNCS]$ and $[NCS]^-$ from the two $Cs_5[An(NCS)_9][NCS]$ (An = Th and U) complexes are negligible, suggesting that this $[NCS]^-$ fragment in the structures of the actinide compounds is more likely to be [HNCS]. Finally, a comparison of the Raman and IR active ν(C=N) and ν(C=S) stretches among $Cs_5[U(NCS)_9][NCS]$, $Cs_5[Th(NCS)_9][NCS]$ and $[Ph_4P][NCS][HNCS]$ does not give clear information to further confirm the structure of the uncoordinated $[NCS]^-$ as [HNCS] in the actinide compounds.

3.6.4 Theoretical Analysis of [HNCS]

The structural parameters of the [HNCS] group in $[Ph_4P][NCS][HNCS]$ have also been explored by dispersion-corrected DFT (Table 3.7). The optimized geometry reflects well the experimentally determined metric parameters, confirming the stability of the trimolecular complex and the assignment of hydrogen positions. A strong N–H···N hydrogen bond is indicated by H···N and N···N distances, the latter in excellent agreement with the crystallographic data. The DFT data also support the bending of the H–N–C linkage in $[Ph_4P][NCS][HNCS]$. It appears that the non-linear symmetry of [HNCS] is influenced strongly by the crystalline environment, since the tetraatomic [HNCS] optimized at the same level of theory exhibits an angle of 134.4° (in agreement with experiment and high-level *ab initio* prediction) while the hydrogen bonded dimer $[SCN\cdots HNCS]^-$ is linear (H–N–C = 179.6°).

To examine hydrogen bond strength in more detail, Binding Energy and Atoms in Molecules (AIM) analysis have been carried out on $[Ph_4P][NCS][HNCS]$. The counterpoise corrected binding energy of the $[SCN\cdots HNCS]^{-1}$ dimer extracted from $[Ph_4P][NCS][HNCS]$ is predicted to be −104.9 kJ mol^{-1}, *i.e.* within the range of ‘‘very strong hydrogen bonding’’. The value of the electron density at the critical point, ρ_{bcp},

often taken as a proxy for bond strength, for the H···N bond in [Ph_4P][NCS][HNCS] is 0.082 e Bohr^{-3}, very large compared, for example, with the value of 0.027 e Bohr^{-3} for the O···H bond in a water dimer, optimised with the same method and basis set. In contrast, the weakening of the donor N–H bond in [Ph_4P][NCS][HNCS] is evident from the ρ_{bcp} of 0.243 e Bohr^{-3}, compared to a value of 0.334 e Bohr^{-3} in isolated [HNCS].

3.7 Synthesis and Structural Characterization of [Ph_4P][NCSe]

Since the structural determination of the isothiocyanic acid was achieved successfully, it was of interest to try to synthesize and characterize the analogue selenium compound, [HNCSe], known as isoselenocyanic acid. The synthesis of gaseous [HNCSe] has been reported as a gas-solid phase reaction between Ag[NCSe] and HBr, and this product has been characterized by microwave and millimetre wave spectroscopy in the gas phase and by IR spectroscopy both in the gas phase and Ar matrix.[83] Thus, following a literature procedure, the inclusion of [HNCSe] was attempted on [Ph_4P][NCSe], taking advantage of a SeCN···HNCSe hydrogen bonding. [Ph_4P][NCSe], in turn, was synthesized by reaction between [Ph_4P][Cl] and K[NCSe] in MeCN; its solid-state crystal structure is shown in Figure 3.48. The corresponding crystallographic parameters are listed in Appendix 2, while full list of bond lengths and angles is tabulated in Appendix 2.6 in the external CD source of this thesis.

Thus, white single crystals of [Ph_4P][NCSe] were dissolved in MeCN and, under an inert pressure of Ar, reacted with an excess of gaseous [HNCSe], prepared in situ by mixing Ag[NCSe] with HBr in excess.[84] This produced a colour change from colourless to red over a period of ten minutes; however it was not possible to structurally or spectroscopically identify the presence of [HNCSe] and [Ph_4P][NCSe] was the only product reclaimed. Gaseous [HNCSe] is notoriously very unstable.[83]

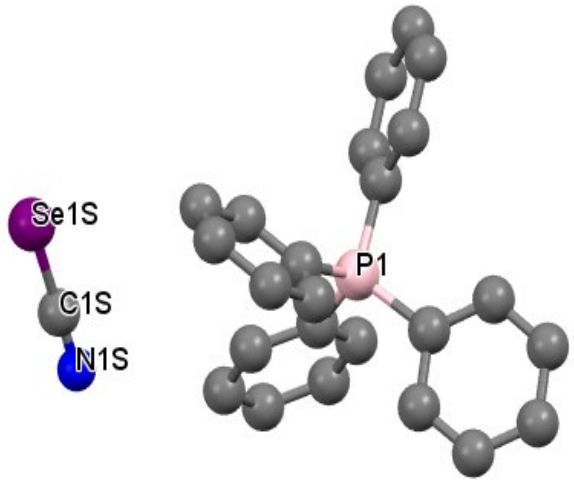

Figure 3.48. Solid-state crystal structure of $[Ph_4P][NCSe]$. Atomic displacement shown at 50% probability. Only selected atoms labelled, and hydrogens atoms omitted for clarity.

The synthesis of tetraphenyl phosphonium cyanide, $[Ph_4P][NC]$, was also attempted via removal of "Se" from $[Ph_4P][NCSe]$. Thus, single crystals of $[Ph_4P][NCSe]$ were dissolved in MeCN and reacted with an excess of triphenylphosphine, Ph_3P, acting as extracting reagent for the Se atoms. A grey precipitate was formed and the removal of "Se" in the solution phase, as Ph_3PSe, was proved by $^{31}P\{^1H\}$ NMR spectroscopy (δ_P 35.81 ppm, Ph_3PSe). White single crystals of Ph_3PSe were also obtained from the solution phase after *ca.* one week, however attempts to recrystallize the precipitate were not successful and further spectroscopic analysis gave no informative data. Finally, the synthesis of the tellurium cyanide equivalent, $[Ph_4P][NCTe]$, was also attempted, but unsuccessfully. Indeed, reaction between tellurium cyanide $[NCTe]^-$ ion, prepared in situ by mixing NaCN and Te in MeCN, and $[Ph_4P]Cl$ afforded immediate decomposition to a grey precipitate of presumably tellurium metal. After *ca.* one week, from the MeCN soluble fraction, a colourless powder was deposited and spectroscopically characterized. However, no clear information was obtained. $[NCTe]^-$ chemistry is dominated by this decomposition.[85]

3.8 Spectroelectrochemistry Study on $[Cs]_5[U(NCS)_9][NCS]$

In section 3.4.2, TLCV measurements performed on the 8-coordinate U(IV) $[Et_4N]_4[U(NCS)_8]$ have shown for this complex a metal-based irreversible cathodic wave at −1.38 V (*vs* Fc/Fc^+) and a reversible ligand-based anodic wave at 0.24 V (*vs* Fc/Fc^+). Moreover, IR spectroscopic measurements, revealed that during the cathodic electrolytic

step (Figure 3.35) the addition of one electron causes dissociation of all the π-donor thiocyanate ligands and decomposition of the compound.

The 9-coordinate $[U(NCS)_9]^{5-}$ ion of $Cs_5[U(NCS)_9][NCS]$ has an overall different polarity compared to $[U(NCS)_8]^{4-}$, therefore it was of interest to perform spectroelectrochemistry analysis on $Cs_5[U(NCS)_9][NCS]$ and compare the results with those obtained for $[Et_4N]_4[U(NCS)_8]$. Thus, in collaboration with Prof. Frantisek Hartl from the University of Reading, spectroelectrochemistry measurements have been carried out on $Cs_5[U(NCS)_9][NCS]$, using the same experimental conditions as the measurements performed on $[Et_4N]_4[U(NCS)_8]$. Figure 3.49 shows the anodic thin-layer cyclic voltammogram of $Cs_5[U(NCS)_9][NCS]$, along with IR spectral changes in the ν(C=N) region accompanying the oxidation process.

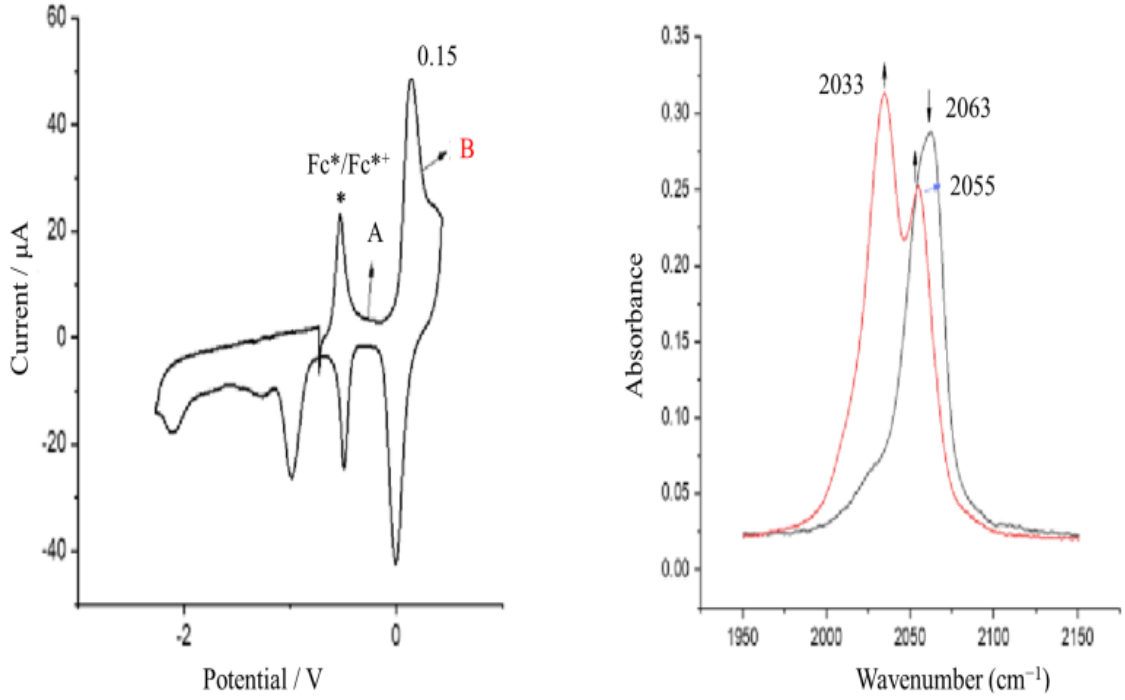

Figure 3.49. (Left) Anodic thin-layer cyclic voltammogram of $Cs_5[U(NCS)_9][NCS]$ (2 mM) in PrCN, with $[^nBu_4N][PF_6]$ (0.1 M) as supporting electrolyte (scan rate = 2 $mV \cdot s^{-1}$); the letters A and B indicate the potentials at which the corresponding IR spectra have been recorded. (Right) IR spectral changes in the ν(C=N) region accompanying the oxidation of $Cs_5[U(NCS)_9][NCS]$ within the same cell; black spectrum – before the oxidation, red spectrum – after the oxidation.

$Cs_5[U(NCS)_9][NCS]$, dissolved in PrCN, exhibits a reversible oxidation potential at 0.15 V (*vs* Fc/Fc^+), which is less positive compared to 0.25 V (*vs* Fc/Fc^+) of $[Et_4N]_4[U(NCS)_8]$, in line with the presence of an additional π-donor $[NCS]^-$ ligand in the

uranium coordination sphere. IR spectroelectrochemical monitoring (Figure 3.49, right) shows that, at the potential of 0.15 V (*vs* Fc/Fc^+), the $[U(NCS)_9]^{5-}$ ion becomes the equivalent 8-coordinated $[U(NCS)_8]^{4-}$, losing one $[NCS]^-$ ligand. Indeed, the ν(C=N) band of $[U(NCS)_9]^{5-}$ at 2063 cm^{-1} is replaced by a new ν(C=N) band at 2033 cm^{-1}, which belongs to the $[U(NCS)_8]^{4-}$ ion. Moreover, an additional ν(C=N) band appears at 2055 cm^{-1}, which is due to free $[NCS]^-$, as independently confirmed by the IR spectrum of Na[NCS] in the same solution.

However, as confirmed by IR spectroscopy, this process is reversible. Indeed, as summarized in Scheme 3.3, the $[U(NCS)_8]^{4-}$ ion can re-coordinate the additional $[NCS]^-$ ligand, restoring the parent complex for *ca.* 90%.

$$[U(NCS)_9]^{5-} \rightleftharpoons [U(NCS)_8]^{4-} + [NCS]^-$$

ν(C=N) = 2063 cm^{-1} ν(C=N) = 2033 cm^{-1} ν(C=N) = 2055 cm^{-1}

Scheme 3.3. Spectroelectrochemical process of $[U(NCS)_9]^{5-}$.

A further second oxidation from $[U(NCS)_8]^{4-}$ could irreversibly form a dithiolate species NCS–SCN which has a characteristic ν(C=N) band at 2060 cm^{-1},[86] but this has not been explored. Therefore, similarly to $[Et_4N]_4[U(NCS)_8]$, the anodic wave supported by $Cs_5[U(NCS)_9][NCS]$ was found to be ligand-based. Figure 3.50 shows the cathodic thin-layer cyclic voltammogram of $Cs_5[U(NCS)_9][NCS]$, along with the IR spectral changes in the ν(C=N) region accompanying the reduction process.

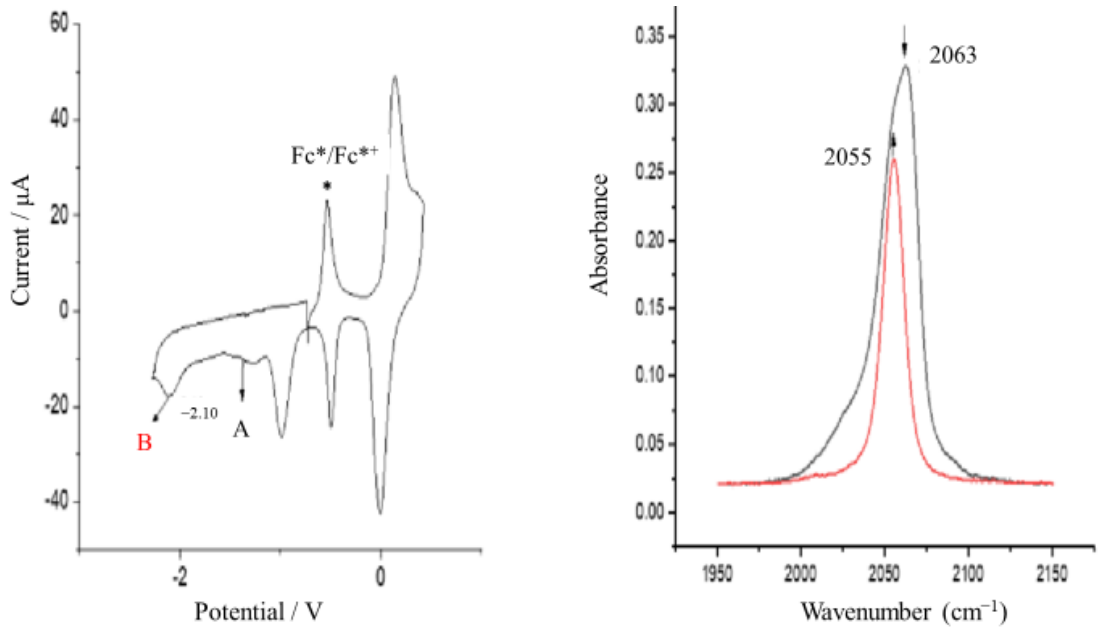

Figure 3.50. (Left) Cathodic thin-layer cyclic voltammogram of $Cs_5[U(NCS)_9][NCS]$ (2 mM) in PrCN, with $[Bu_4N][PF_6]$ (0.1 M) as supporting electrolyte (scan rate = 2 $mV \cdot s^{-1}$); the letters A and B indicate the potentials at which the corresponding IR spectra have been recorded. (Right) IR spectral changes in the ν(C=N) region accompanying the one-electron reduction of $Cs_5[U(NCS)_9][NCS]$, within the same cell; black spectrum – before the reduction, red spectrum – after the reduction.

This cathodic voltammogram shows an irreversible reduction at −2.10 V (*vs* Fc/Fc^+), ascribed to the U(IV)/U(III) redox couple, more negative compared to −1.38 V (*vs* Fc/Fc^+) displayed by $[Et_4N]_4[U(NCS)_8]$. This is explainable considering that the additional π-donor $[NCS]^-$ ligand determines an increase of the electronic density on the uranium centre, resulting in a more negative reduction potential for the U(IV)/U(III) couple. Moreover, IR spectroelectrochemical monitoring (Figure 3.50, right) shows that, at the potential of −2.10 V (*vs* Fc/Fc^+), the ν(N=C) band of $[U(NCS)_9]^{5-}$ at 2063 cm^{-1} is replaced by a new band of free $[NCS]^-$ at 2055 cm^{-1}. Therefore, similarly to what observed for $[Et_4N]_4[U(NCS)_8]$, the addition of one electron to the U(IV) ion leads to the dissociation of all the nine π-donors $[NCS]^-$ ligands and decomposition of the complex.

To summarize, the oxidation and reduction potentials of $Cs_5[U(NCS)_9][NCS]$, measured by TLCV, have been listed in Table 3.9, along with those of $[Et_4N]_4[U(NCS)_8]$ under the same experimental conditions.

Table 3.9. Formal redox half potentials (*vs.* Fc/Fc^+) for the U(IV)/U(III) and (IV)/(V) couples of $Cs_5[U(NCS)_9][NCS]$ and $[Et_4N]_4[U(NCS)_8]$.

Complex	E/V *vs* Fc/Fc^+	
	U(IV)/U(III)	ligand based oxidation
$Cs_5[U(NCS)_9][NCS]$	−2.10	0.15
$[Et_4N]_4[U(NCS)_8]$	−1.8	0.25

An attempt to obtain the eight coordinate complex $[Cs]_4[U(NCS)_8]$ from $[Cs]_5[U(NCS)_9][HNCS]$ has also been tried via reaction with NaH, according to the Equation 4.

$$[Cs]_5[U(NCS)_9][HNCS] + NaH \rightarrow H_2 + Na[NCS] + [Cs]_5[U(NCS)_9] \rightarrow [Cs]_4[U(NCS)_8] \quad (4)$$

NaH should act as reducing reagent towards the [HNCS] fragment, inducing liberation of H_2. Subsequently, $[Cs]_5[U(NCS)_9]$ species could lose one $[NCS]^-$ ligand, to become the eight coordinated equivalent complex. Thus, green crystals of $[Cs]_5[U(NCS)_9][NCS]$ were dissolved in dried MeCN and, under an inert atmosphere of Ar, reacted with one equivalent of NaH; however, after *ca.* 10 minutes the green colour vanished and a grey precipitate was formed. Attempts to recrystallize this precipitate failed and the corresponding IR spectrum did not show any bands attributable to N=C or C=S bond stretches; presumably the reduction (Equation 4) afforded decomposition with liberation of all the $[NCS]^-$ ligands.

3.9 Conclusion

From oxidation processes of $Cs_4[U(NCS)_8]$ in different solvents, two mixed-valent uranium species were isolated and structurally characterized. The presence of uranium in different oxidation states has been confirmed by spectroscopic and magnetic measurements. A photophysical study showed emission from both U(IV) and U(VI) centres and the results are corroborated by theoretical analysis. Interesting oxo-bonding interactions have also been noted and their strength and influence on the electronic structure of these compounds has been probed. Figure 3.51 summaries the results obtained from oxidation processes of $Cs_4[U(NCS)_8]$, performed in different conditions.

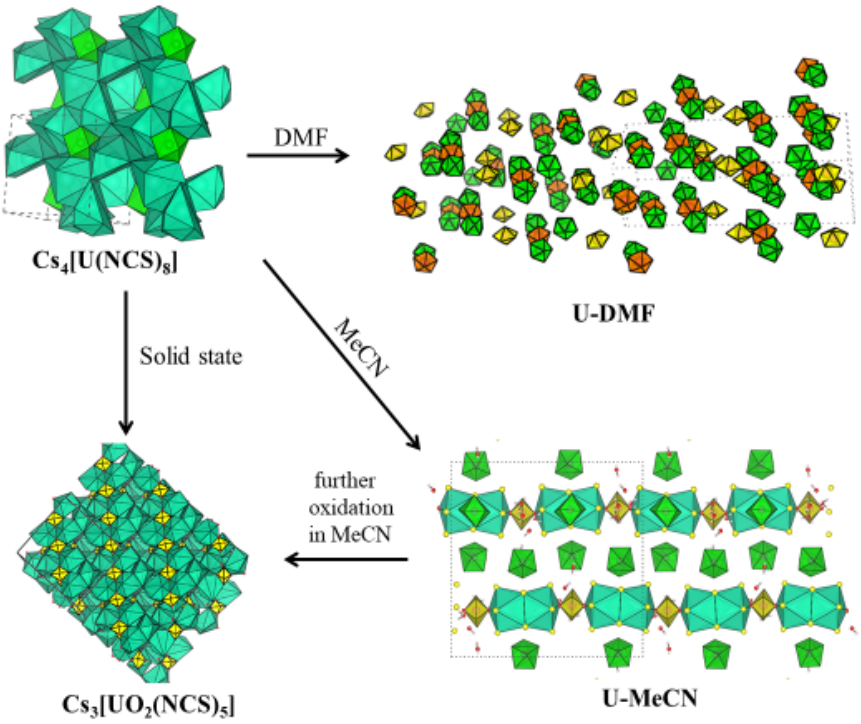

Figure 3.51. Oxidation diagram for $Cs_4[U(NCS)_4]$, showing the species obtained with different experimental conditions.

The reaction between the U(IV) species $Na_4[U(NCS)_8]$ and $[Co(bipy)_3][PF_6]_2$ led to the formation of a compound of formula $[Co(bipy)_3][U(NCS)_8]$, for which spectroscopic and magnetic analysis are in agreement with a Co(III)-U(V) configuration. A one-electron Co(II)→Co(III) oxidation also occurred when $[Co(bipy)_3][PF_6]_2$ was reacted with $Na_4[Th(NCS)_8]$ under the same experimental condition. Moreover, in one case, the $[U(NCS)_8]^{4-}$ ion underwent a 2-electron metal-based oxidation and a uranyl(VI) thiocyanate compound was isolated. Clearly, further spectroscopic analysis, along with an accurate electrochemistry study, are necessary to understand these redox reactions.

The synthesis of homoleptic U(III) thiocyanate complexes, from reductions of U(IV) precursors, did not succeed; however a spectroelectrochemistry study on $[Et_4N]_4[U(NCS)_8]$ has shown that the addition of one electron to the metal ion causes the dissociation of all the π-donor $[NCS]^-$ ligands and decomposition of the sample. Theoretical approaches have also revealed an enhanced ionicity for the U(III)–N compared to the U(IV)–N bond, which can explain the observed decomposition.

In the last section, a study on a 9-coordinate uranium thiocyanate complex, of formula $[Cs]_5[U(NCS)_9][NCS]$, has been discussed. Spectroscopic and magnetic measurements have been used to confirm the +4 oxidation state for the uranium ion. Spectroelectrochemistry measurements have also been conducted on this sample and the

results are comparable with the ones of $[Et_4N]_4[U(NCS)_8]$. Finally, the solid-state crystal structure of the isothiocyanic acid, [HNCS], (which has never been previously reported) has been discussed in detail along with an accurate spectroscopic and theoretical analysis.

3.10 Experimental Section

Caution! Natural uranium ans thorium were used during the course of the experimental work. As well as the radiological hazards, uranium and thorium are toxic metals and care must be taken with all manipulations. Experiments with uranium and thorium compounds were carried out using pre-set radiological safety precautions in accordance with the local rules of Trinity College Dublin, University of Reading and Aachen University.

Description of the Raman, IR and UV-vis-NIR spectrophotometers and of the spectrophotofluorimeter is as discussed in the experimental section of Chapter 2. TGA spectra were recorded on a Perkin Elmer Pyris 1 TGA and TGA-IR, using a 10 cm flow cell, Perkin Elmer FTIR-Spectrum 100. Nitrogen gas-flow was 15 mL/min through the FTIR. Luminescence lifetime data were recorded following 372 nm excitation, using time-correlated single-photon counting (a PCS900 plug-in PC card for fast photon counting). Lifetime values were obtained by tail fit on the data obtained, and the quality of the fit was judged by minimization of the reduced chi-squared and residuals squared. ^{1}H, $^{13}C\{^{1}H\}$, $^{31}P\{^{1}H\}$ and $^{77}Se\{^{1}H\}$ spectra were recorded on a Bruker AV400 spectrometer operating at 400.23 MHz, 155.54 MHz, 161.98 MHz and 76.33 MHz, respectively, and the chemical shifts were referenced to the residual ^{1}H and ^{13}C resonances of the solvent used or external H_3PO_4 or Me_2Se. Description of the X-ray diffractometer and of the methods used to analyse the crystallographic data is as discussed in the experimental section of Chapter 2. The structures were refined by Dr. Brendan Twamley (Trinity College Dublin) and the crystallographic data are collated in Appendix 2. Structural figures were prepared using VESTA[87] or mercury. Powder X-ray Diffraction was carried out on a Bruker D2 Phaser, while microanalysis on $[Ph_4P][NCS]$ and $[Ph_4P][NCS][HNCS]$ were carried out at University College Dublin.

CV measurements were conducted with a Metrohm Autolab PGSTAT302N potentiostat in an airtight three electrode cell connected to a Schlenk line with a Pt microdisc (0.14 mm^2) working electrode, Pt coil counter electrode, and Ag coil pseudoreference electrode; the $[^{n}Bu_4N][PF_6]$ electrolyte was recrystallized twice from absolute ethanol and dried under vacuum at 80 °C overnight. Controlled-potential electrolyses within the room-temperature OTTLE cell[88] were carried out using an EmStat3 (PalmSens) potentiostat. IR

spectral monitoring of the redox reactions was carried out with a Bruker Vertex 70v FT-IR spectrometer. The different redox steps were localized with the aid of contemporarily recorded thin-layer cyclic voltammograms. Ferrocene and decamethylferrocene (Fc*) were used as multiple internal potential standards in the experiments. For cyclic voltammetry and IR spectroelectrochemistry analysis, the compounds were first characterized by IR spectroscopy; then, the uranium complexes were dissolved in dry acetonitrile containing the supporting electrolyte and checked for decomposition.

UCl_4,[89] $ThCl_4(DME)_2$,[90] $Cs_4[U(NCS)_8]$,[38] $[Co(bipy)_3][PF_6]_2$ and $[Co(bipy)_3[PF_6]_3$,[45] were synthesized following reported procedures. MeCN was dried over CaH_2, while Na was used to dry diethyl and diisopropyl ether; the solvents were also distilled under N_2 before using. Na[NCS], K[NCSe], CsCl, $NaPF_6$ and all other reagents were obtained from commercial sources and used as received.

3.10.1 Synthesis of $[U(DMF)_8(\mu\text{-}O)U(NCS)_5(\mu\text{-}O)U(DMF)_8(NCS)][UO_2(NCS)_5]$ (U-DMF)

$Cs_4[U(NCS)_8]$ (100 mg, 0.081 mmol) was dissolved in DMF (10 cm^3) in air and the sample-vial covered with parafilm. The solution was left for *ca.* one month by which time emerald green crystals, suitable for X-ray diffraction, were deposited and isolated (55 mg, 0.02 mmol). IR (ATR, ν/cm^{-1}): 2933 (w), 2870 (w), 2385 (w), 2046 (s, C=N), 1634 (s), 1485 (m), 1428 (m), 1382 (s), 1245 (m), 1114 (m), 1055 (m), 968 (w), 912 (s, U^{VI}=O), 865 (w, U^{V}=O), 674 (m, C=S). Raman (ν/cm^{-1}): 2558 and 2528 and 2450 (C=N), 1293, 1441, 1423, 1120, 846 (U^{VI}=O), 815 (U^{V}=O), 710, 671, 503, 404. UV (ε, $dm^3\ mol^{-1}\ cm^{-1}$), (298 K, ~ 10^{-5} M in MeCN): 302 nm (17121), 344 nm (13381). Vis-NIR (ε, $dm^3\ mol^{-1}\ cm^{-1}$), (298 K, ~ 10^{-3} M in MeCN): 503 nm (250), 566 nm (128), 687 nm (536), 858 nm (65), 1159 (320), 1708 (81).

3.10.2 Synthesis of $Cs_{15}[\{U(NCS)_8\}_4\{UO_2(NCS)_5\}].H_2O$ (U-MeCN)

$Cs_4[U(NCS)_8]$ (70 mg, 0.057 mmol) was dissolved in MeCN (10 cm^3) in air and the sample vial covered with parafilm. The solution was left for *ca.* one month by which time emerald green crystals, suitable for X-ray diffraction, were deposited and isolated (30 mg, 5.58 x 10^{-3} mmol). IR (ATR, ν/cm^{-1}): 3406 (m, H_2O), 2046 (s, C=N), 1622 (m), 922 (m, U=O), 626 (w, C=S). Raman (ν/cm^{-1}): 2129 and 2101 and 2092 and 2076 (C=N), 844 (U=O), 798, 478, 227, 176, 139. UV (ε, $dm^3\ mol^{-1}\ cm^{-1}$), (~ 10^{-6} M in MeCN): 230 nm

(74325), 300 (56850). Vis-NIR (ε, $dm^3\ mol^{-1}\ cm^{-1}$), (298 K, ~ 10^{-3} M in MeCN): 573 nm (12), 690 nm (52), 925 nm (10), 1074 nm (18), 1406 (24), 1904 nm (115).

3.10.3 Synthesis of $[Co(bipy)_3]_2[U(NCS)_8]_2 \cdot bipy \cdot MeCN$ (Co-U)

Under an inert atmosphere of Ar, to a green suspension of UCl_4 (200 mg, 0.53 mmol) in dried MeCN (20 cm^3) were added eight equivalents of Na[NCS]. A grey precipitate, of presumably NaCl, was formed and, after 30 minutes of stirring, filtered off. Two equivalents of $[Co(bipy)_3][PF_6]_2$ were added and the mixture was stirred for 48 hours under an inert atmosphere. A grey precipitate of $NaPF_6$ (whose identity confirmed by IR spectroscopy), was formed and removed by filtration in air. The resulting green solution was slowly concentrated in air and, after one week, yellow single crystals of **Co-U** were isolated. Yield: 45%, 0.63 g. IR (ATR, ν/cm^{-1}): 3445 (w), 2359 (w), 2050 (s, C=N), 1622 (w), 1440 (w), 1314 (w), 816 (s), 556 (s), 480 (s). Raman (ν/cm^{-1}): 2081 and 2072 and 2030 (C=N), 1599, 1568, 1493, 1316, 1264, 1248, 1158, 1067, 1044, 1025, 1015, 851, 768. UV (298 K, ~ 1.1 x 10^{-7} M in MeCN) vis-NIR (298 K, ~ 3 x 10^{-4} M in MeCN) (ε, $dm^3\ mol^{-1}\ cm^{-1}$): 246 nm (73680), 296 nm (100467), 695 nm (71.3), 1096 nm (54.3), 1408 nm (65), 1685 nm (35.1), 1906 nm (243.5).

Refinement Note: One $U(NCS)_8$ disordered over two positions (50:50% occupancy) and was refined with restraints (DFIX, SADI, SIMU, ISOR). One coordinated bipy was disordered over two positions (65:35%) and was modelled with restraints (SIMU). Solvents were located in the void. There are one bipy and one MeCN. The remainder electron density in the void could not be modelled and was dealt with using the SQUEEZE algorithm (Spek, 2009) yielding a Solvent Accessible Volume = 586 with Electrons Found in S.A.V. = 234.

3.10.4 Synthesis of $[Co(bipy)_3][PF_6]_3$

$[Co(bipy)_3][PF_6]_3$ was synthetized following the procedure reported in reference 45 and yellow crystals, suitable for X-ray diffraction, were grown through recrystallization from MeCN. Yield: 62%. IR (ATR, ν/cm^{-1}): 1606 (w), 1506 (w), 1469 (w), 1450 (m), 1320 (w), 1244 (w), 1168 (w), 1039 (w), 828 (s), 761 (s), 725 (m), 559 (s), 473 (w), 422 (m). Raman (ν/cm^{-1}): 1610, 1574, 1503, 1337, 1076, 1048, 771, 744, 673, 644, 379, 262. UV-vis (ε, $dm^3\ mol^{-1}\ cm^{-1}$), (298 K, ~ 10^{-6} M in MeCN): 319 nm (27503), 307 nm (30265), 222 nm (79547).

Refinement Note: Three PF_6 moieties over 4 main sites. P1 and P2 are fully occupied and P3 is 1/3 occupied. P4 is 2/3 occupied but disordered over two locations with P4 45% and P4a 21% occupied. Rigid group used to model P3 and P4a and restraints and constraints used (P3, ISOR, EADP and SIMU for P4a). Two solvent acetonitrile groups present with N37 split over two locations with 54:46% occupancy with restraints and constraints (DFIX, SADI, EADP). N40 (on a special position) modelled at 25% occupancy with restraints (DFIX, SIMU, ISOR).

3.10.5 Synthesis of $[Co(bipy)_3]_2[Th(NCS)_7(H_2O)][Th(NCS)_8(H_2O)]\cdot bipyH\cdot MeCN\cdot 2H_2O$ (Co-Th)

Under an inert atmosphere of Ar, to a colourless solution of $ThCl_4(DME)_2$ (230 mg, 0.497 mmol) in dried MeCN (30 cm^3) were added eight equivalents of Na[NCS]. A grey precipitate, of presumably NaCl, was formed and, after 30 minutes of stirring, filtered off. Two equivalents of $[Co(bipy)_3][PF_6]_2$ were added and the mixture stirred for 48 hours under inert atmosphere. A grey precipitate of $NaPF_6$, whose identity confirmed by IR spectroscopy, was formed and filtered off in air. After one week at room temperature, the solution deposited colourless single crystals of **Co-Th** (0.60 g). IR (ATR, ν/cm^{-1}): 3414 (m, H_2O), 2050 (s C=N), 1642 (m), 1440 (w), 1376 (w), 814 (C=S, s), 554 (s), 388 (w). Raman (ν/cm^{-1}): 2081 and 2073 (C=N), 1601, 1569, 1493, 1317, 1026, 756 (C=S). UV-vis (ε, $dm^3\ mol^{-1}\ cm^{-1}$), (298 K, ~ 1 x 10^{-5} M in MeCN): 232 nm (12987), 302 nm (3336).
Refinement Note: One $[NCS]^-$ ligand per Th centre is disordered. In each case the N atom was refined with the same x, y and z parameters (EXYZ). For the Th1 centre, the NCS moiety was refined with restraints and constraints (DFIX, SADI, SIMU, ISOR, EADP) with 58:42% occupancy. For Th2, the disordered NCS was modelled with restraints and constraints (DFIX, SADI, SIMU, ISOR, EADP and EXYZ) with 57:43% occupancy. The coordinated water molecule on Th1 was modelled in two positions with restraints (SADI, SIMU) with 73:27% occupancy. The lattice water molecule O2 associated with O1 was modelled as 50% occupied. The lattice acetonitrile molecule was also modelled in two positions 58:42% occupied with restraints (SADI, SIMU). The central $[Co(bipy)_3]^{3+}$ cation was modelled in two positions as a rigid group (modelled on Co1) with occupancies 73:27% with restraints (SIMU).

3.10.6 Synthesis of $[Co(bipy)_2(NCS)_2]$

To a yellow solution of $[Co(bipy)_3][PF_6]_2$ (50 mg, 0.061 mmol) in MeCN (30 cm^3) was added Na[NCS] (9.9 mg, 0.122 mmol) and the mixture was stirred at room temperature for 30 minutes. A grey precipitate of $NaPF_6$ (whose identity verified by IR spectroscopy) was removed by filtration and purple crystals of $[Co(bipy)_2(NCS)_2]$, suitable for X-ray diffraction, were grown by vapour diffusion of diisopropyl ether in MeCN solutions. Yield: 70 %, 17.6 mg. IR (ATR, ν/cm^{-1}): 2062 (s, C=N), 1596 (s), 1564 (s), 1470 (s), 1436 (m), 1310 (m), 1248 (m), 1218 (m), 1170 (m), 1152 (m), 1104, 1056, 1016 (m), 958 (w), 898 (w). Raman (ν/cm^{-1}): 2082, 2068 (C=N), 1601, 1571, 1495, 1321, 1268, 1163, 1061, 1023, 803, 770 (C=S), 652, 633. UV-vis (ε, dm^3 mol^{-1} cm^{-1}), (298 K, ~ 10^{-6} M in MeCN): 343 nm (152), 282 nm (2984).

3.10.7 Synthesis of $[Na(H_2O)_4]_2[Co(NCS)_4]$

Under an inert atmosphere of Ar, to a green suspension of UCl_4 (200 mg, 0.53 mmol) in dried MeCN (20 cm^3) were added eight equivalents of Na[NCS]. A grey precipitate, of presumably NaCl, was formed and, after 30 minutes of stirring, removed by filtration. Two equivalents of $[Co(bipy)_3][PF_6]_3$ were added and the mixture was stirred for 48 hours under an inert atmosphere. A grey precipitate of $NaPF_6$ (whose identity confirmed by IR spectroscopy), was formed and removed by filtration in air. The resulting green solution was slowly concentrated in air and, after two weeks, green crystals, suitable for X-ray diffraction, were isolated (92 mg). IR (ATR, ν/cm^{-1}): 3415 (s, H_2O), 2062 (s, C=N), 1626 (m), 838 (s). Raman (ν/cm^{-1}): 2113 and 2095 (C=N), 819 (C=S), 807, 300, 160. UV-vis (ε, dm^3 mol^{-1} cm^{-1}) (298 K, ~ 10^{-5} M in MeCN): 305 nm (4016), 232 (17234).

Refinement Note: Water hydrogen atoms treated as a mixture of located (O3, O4, O6, O8) and geometrically placed (O1, O2, O5, O7) atoms. Located hydrogen atoms modelled with restraints (AFIX 3) and allowed to refine.

3.10.8 Synthesis of $[bipyH]_3[UO_2(NCS)_5]$

The procedure for the synthesis of this compound was analogue to the one followed for **Co-U**, but a 2-electron oxidation occurred and a uranyl(VI) complex was isolated. Yield: 58%, 317 mg. IR (ATR, ν/cm^{-1}): 3416 (m), 2926 (w), 2854 (w), 2058 (s, C=N), 1620 (m), 920 (w, U=O) 844 (s). Raman (ν/cm^{-1}): 2077 (C=N), 848 (U=O), 811, 754 (C=S).

Refinement Note: Half occupied bipy is disordered over 2 locations with 25% occupancy each and refined as rigid groups with restraints (SIMU). One sulfur is disordered by symmetry over the 2-fold axis and modelled with 0.3333 occupancy with constraints (EADP). The NC group bonded to this disordered sulfur was modelled with restraints (SIMU).

3.10.9 Synthesis of $Cs_5[U(NCS)_9][NCS]$

To a green suspension of UCl_4 (75 mg, 0.20 mmol), in dried and degassed MeCN (25 cm^3) and under a flow of high purity Ar, were added Na[NCS] (162 mg, 2.0 mmol) and CsCl (168 mg, 1.0 mmol). The solution was stirred at room temperature for 2 hours, filtered to remove the NaCl precipitate and reduced in volume. Dark green crystals of $Cs_5[U(NCS)_9][NCS]$, suitable for X-ray diffraction, were grown by vapor diffusion of diisopropyl ether into an MeCN solution. Yield: 55%, 163 mg. IR (ATR, ν/cm^{-1}): 2857 (w), 2243, 2030 (s, C=N), 1615 (w), 1366 (w), 960 (w), 920 (w), 797 (m, C=S), 751 (w). Raman (ν/cm^{-1}): 2119 and 2086 and 2077 and 2065 (C=N), 868 and 820 (C=S). UV (ε, dm^3 mol^{-1} cm^{-1}), (~ 2.5 x 10^{-6} M in MeCN): 242 nm (76824), 296 nm (38126); vis-NIR (ε, dm^3 mol^{-1} cm^{-1}), (~ 2.5 x 10^{-3} M in MeCN): 503 nm (31.61), 573 nm (6.74), 690 nm (68.72), 920 nm (7.167), 1163 nm (53.96), 1386 nm (17.28), 1535 nm (23.19).

3.10.10 Synthesis of $Cs_5[Th(NCS)_9][NCS]$

To a colourless solution of $ThCl_4(DME)_2$ (75 mg, 1.52 mmol), in dried and degassed MeCN (25 cm^3) and under a flow of high purity Ar, were added Na[NCS] (1.10 g, 13.7 mmol) and CsCl (1.28 g, 7.61 mmol). The solution was stirred at room temperature for 2 hours, filtered to remove the NaCl precipitate and reduced in volume. Colourless crystals of $Cs_5[Th(NCS)_9][NCS]$, suitable for X-ray diffraction, were grown by vapor diffusion of diisopropyl ether into an MeCN solution. Yield: 36%, 0.81 g. IR (ATR, ν/cm^{-1}): 3398 (w), 2033 (s, C=N), 1612 (w), 954 (w), 797 (w, C=S). Raman (ν/cm^{-1}): 2124, 2099, 2090 and 2074 (C=N), 1603, 1442, 1289, 1001, 796 (C=S), 716, 477. UV-vis (ε, dm^3 mol^{-1} cm^{-1}), (2.1 x 10^{-6} M in MeCN): 263 nm (559084), 316 nm (52700).

3.10.11 Synthesis of $[Ph_4P][NCS][HNCS]$

Freshly prepared $HNCS_{(g)}$ was added, via syringe, into a colourless solution of $[Ph_4P][NCS]$ (80 mg, 0.20 mmol) in MeCN (20 cm^3). After *ca*. 2 minutes, the solution

assumed a red colour and it was stirred for 1 hour at room temperature. The red solution was filtered, and the solvent was left slowly evaporate at room temperature. After 48 hours dark red single crystals, suitable for X-ray diffraction, were formed and washed twice with Et_2O. Yield: 60%, 55mg. ^{1}H NMR δ_H (400 MHz, CD_3CN/ppm): 7.64 (m, 8H, m-CH), 7.81 (m, 8H, o-CH), 7.92 (m, 4H, p-CH). $^{13}C\{^{1}H\}$ NMR δ_C (155 MHz, CD_3CN/ppm): 117.5 (d, $^{1}J_{P-C}$ = 90.0 Hz, ipso-C), 134.5 (d, $^{3}J_{P-C}$ = 13.0 Hz, m-C), 134.3 (d, $^{2}J_{P-C}$ = 9.4 Hz, o-C), 135.8 (d, $^{4}J_{P-C}$ = 3.6 Hz, p-C). $^{31}P\{^{1}H\}$ NMR δ_P (162 MHz, $CDCl_3$/ppm): 23.3 ppm (s). IR (ATR, ν/cm^{-1}): 2960 (w), 2054 (s, C=N), 1586 (m), 1483 (w), 1432 (w), 1260 (m), 1106 (w), 1030 (m), 994 (s), 914 (s), 807 (m), 750 (s, C=S), 725 (w), 692. Raman (ν/cm^{-1}): 2055 (C=N), 1580, 1188, 1154, 1092, 1025, 995, 846 (C=S), 676, 608, 245. Despite numerous attempts on multiple single crystals and powders, acceptable elemental analysis was not obtained. To prove the bulk purity, powder X-ray diffraction was measured (Appendix 2, Figure 23).

3.10.12 Synthesis of [Ph_4P][NCS]

[Ph_4P]Cl (250 mg, 0.667 mmol) and Na[NCS] (54 mg, 0.663 mmol) were mixed together in dried and degassed MeCN (30 cm^3) and stirred at room temperature for 30 minutes. The solution was filtered in air to remove the NaCl precipitate and after 24 hours colourless crystals of [Ph_4P][NCS], suitable for X-ray diffraction, were isolated (222 mg, 84%). ^{1}H NMR δ_H (400 MHz, $CDCl_3$/ppm): 7.66 (m, 8H, $^{3}J_{H-H}$ = 7.08 Hz, m-CH), 7.80 (m, 8H, $^{3}J_{H-H}$ = 7.81 Hz, o-CH), 7.93 (m, 4H, $^{3}J_{H-H}$ = 7.55 Hz, p-CH). $^{13}C\{^{1}H\}$ NMR δ_C (155 MHz, CD_3CN/ppm): 117.5 (d, $^{1}J_{P-C}$ = 89.3 Hz, ipso-C), 130.8 (d, $^{3}J_{P-C}$ = 13.3 Hz, m-C), 134.5 (d, $^{2}J_{P-C}$ = 9.2 Hz, o-C), 135.8 (d, $^{4}J_{P-C}$ = 3.0 Hz, p-C). $^{31}P\{^{1}H\}$ NMR δ_P (162 MHz, $CDCl_3$/ppm): 23.8 (s). IR (ATR, ν/cm^{-1}): 3418 (m), 3055 (w), 2055 (s, C=N), 1585 (m), 1485(w), 1435 (s), 1310 (w), 1110 (s), 997 (w), 748 (s, C=S), 723 (m), 690 (m). Raman (ν/cm^{-1}): 2058 (C=N), 1591, 1193, 1167, 1103, 1032, 1001, 740 (C=S), 682, 618, 257. Calcd for $C_{25}H_{20}NPS$: C 75.54 %, H 5.07 %, N 3.52 %; found C 75.45, H 5.04, N 3.49.

3.10.13 Synthesis of [HNCS][69]

In a Schlenk flask and under static Ar condition, 25 cm^3 of HCl (12 M) was added to Na[NCS] (6.0 g, 62 mmol) and vigorously stirred for 30 minutes at room temperature, during which time the mixture turned yellow. Colourless $HNCS_{(g)}$ was produced and

transferred via a gas-tight syringe. A ^{1}H NMR spectrum in CD_3Cl was immediately acquired. δ_H ($CDCl_3$): 5.45 ppm (t, $^{1}J_{N\text{-}H}$ = 75.18 Hz, [HNCS]). The ^{1}H NMR spectrum of [HNCS] has not been reported, but calculations on HNC suggest that the triplet is due $^{1}J_{N\text{-}H}$ coupling.[81a]

3.10.14 Synthesis of [DNCS]

This was prepared analogously to [HNCS] but using DCl in D_2O. δ_D ($CHCl_3$): 0.94 ppm.

3.10.15 Synthesis of [Ph$_4$P][NCSe]

Ph_4PCl (250 mg, 0.667 mmol) and KNCSe (96 mg, 0.665 mmol) were mixed together in dried and degassed MeCN (30 cm^3) and stirred at room temperature for 30 minutes. The solution was filtered in air to remove the NaCl precipitate and after 24 hours colourless crystals of [Ph$_4$P][NCSe], suitable for X-ray diffraction, were isolated. Yield: 79%, 233 mg. ^{1}H NMR δ_H (400 MHz, $CDCl_3$/ppm): 7.70 (m, 8H, $^{3}J_{H-H}$ = 4.18 Hz, m-CH), 7.77 (m, 8H, $^{3}J_{H-H}$ = 7.69 Hz, o-CH), 7.95 (m, 4H, $^{3}J_{H-H}$ = 7.50 Hz, p-CH). ^{13}C{^{1}H} NMR δ_C (155 MHz, CD_3CN/ppm): 118.4 (d, 104.8 Hz, ipso-C); 130.34 (d, 12.64 Hz, m-C), 134.7 (d, $^{2}J_{P-C}$ = 10.64 Hz, o-C), 135.4 (d, $^{4}J_{P-C}$ = 3.02 Hz, p-C). ^{31}P{^{1}H} NMR δ_P (162 MHz, $CDCl_3$/ppm): 23.0 (s). ^{77}Se{^{1}H} NMR (76 MHz, CD_3Cl_3): −308 (s). IR (ATR, ν/cm^{-1}): 3053 (w), 2064 (s, C=N), 1585 (m), 1479 (m), 1432 (s), 1313 (m), 994 (s), 854 (C=Se), 751 (s), 724 (s), 690 (s). Raman (ν/cm^{-1}): 2079 and 2075 (C=N), 1595, 1199, 1171, 1108, 1037, 1009, 690 (C=Se), 624, 569, 302, 272, 258, 204.

3.10.16 Computational details

All the DFT calculations were performed by Dr. James A. Platts, from Cardiff University.

On **U-DMF** the analysis was carried out with the ORCA package v 4.0.0.2,[91] using the BP86 functional[92] and a basis set consisting of 78-electron Lanl2DZ ECP/basis on U and def2-TZVP(-f) on all remaining atoms.[93] Efforts to use small-core 60-electron ECP failed due to SCF convergence issues. All such calculations made use of the resolution of identity method, using ORCA's automatically generated auxiliary basis. Expectation values of the S^2 operator were 3.71, 5.62 and 9.85 for doublet, quartet and sextet states, indicating that some spin contamination is present in these data. AIM analysis used the AIMAll suite,[94] with MultiWfn used as to convert ORCA files to .wfx format.[95]

Single point DFT calculations on the $[U(NCS)_8]^{n-}$ (n = 3, 4) have been performed in Gaussian0958 using the BP86 and B3LYP59 functionals. The (27s 24p 18d 14f 6g)/[8s 7p 5d 3f 1g] all-electron ANO-RCC basis sets of DZP quality were used for uranium,[96] with 6-31+G(d,p) on C, N, and S.[97] Scalar relativistic effects were included via the second-order Douglas− Kroll−Hess Hamiltonian.[98] Natural bond orbital (NBO) analysis[99] was performed using Gaussian09; Atoms-in-Molecules (AIM) analysis used AIMAll.[90] Topological analysis of the electronic density (ρ) is based upon those points where the gradient of the density, $\nabla\rho$, vanishes.[100]

Regarding the theoretical analysis of the structure of $[Ph_4P][NCS][HNCS]$, the coordinates of this trimolecular complex were extracted from the corresponding X-ray structure and optimised without symmetry constraints at the ωB97x-D/6-31+G(d,p) DFT level,[101] and the resulting geometry confirmed as a true minimum by harmonic frequency calculation. Coordinates of isolated [HNCS] and $[SCN\cdots HNCS]^-$ were also extracted and treated in the same manner. Binding energies were corrected for BSSE using the counterpoise procedure. AIM data was evaluated with the AIMA11 package.[94]

3.11 References

[1] a) S. G. McAdams, A. -M. Ariciu, A. K. Kostopoulos, J. P. S. Walsh and F. Tuna, *Coord. Chem. Rev*., 2017, **346**, 216; b) K. R. Meihaus and J. D. Long, *Dalton Trans*., 2015, **44**, 2517; c) S. T. Liddle and J. van Slageren, *Chem. Soc. Rev*., 2015, **44**, 6655; d) D. R. Kindra and W. J. Evans, *Chem. Rev.*, 2014, **114**, 8865

[2] a) D. M. King, P. A. Cleaves, A. J. Wooles, B. M. Gardner, N. F. Chilton, F. Tuna, W. Lewis, E. J. L. McInnes and S. T. Liddle, *Nat. Commun*., 2016, **7**, 13773; b) D. M. King, F. Tuna, J. McMaster, W. Lewis, A. J. Blake, E. J. L. McInnes and S. T. Liddle, *Angew. Chem. Int. Ed*., 2013, **52**, 4921

[3] Recent examples: a) V. Mougel, L. Chatelain, J. Pécaut, R. Caciuffo, E.Colineau, J.-C. Griveau and M. Mazzanti, *Nat. Chem.*, 2012, **4**, 1011; b) L. Chatelain, V. Mougel, J. Pécaut and M. Mazzanti, *Chem. Sci.*, 2012, **3**, 1075; c) L. Chatelain, F. Tuna, J. Pecaut and M. Mazzanti, *Chem. Commun*., 2015, **51**, 11309

[4] See e.g.: a) P. L. Arnold, E. Hollis, G. S. Nichol, J. B. Love, J.-C. Griveau, R. Caciuffo, N. Magnani, L. Maron, L. Castro, A. Yahia, S. O. Odoh and G. Schreckenbach, *J. Am. Chem. Soc.*, 2013, **135**, 3841; b) P. L. Arnold, B. E. Cowie, M. Suvova, M. Zegke, N. Magnani, E. Colineau, J.-C. Griveau, R. Caciuffo and J. B. Love, *Angew. Chem. Int. Ed*., 2017, **56**, 10775

[5] B. Vlaisavljevich, P. Miró, D. Ma, G. E. Sigmon, P. C. Burns, C. J. Cramer and L. Gagliardi, *Chem. Eur. J*., 2013, **19**, 2937

[6] H. Steele and R. J. Taylor, *Inorg. Chem.,* 2007, **46**, 6311

[7] R. K. Rosen, R. A. Andersen and N. M. Edelstein, *J. Am. Chem. Soc.*, 1990, **112**, 4588

[8] P. L. Arnold, G. M. Jones, S. O. Odoh, G. Schreckenbach, N. Magnani and J. B. Love, *Nat. Chem.*, 2012, **4**, 221

[9] A.-C. Schmidt, F. W. Heinemann, W. W. Lukens Jr. and K. Meyer, *J. Am. Chem. Soc.*, 2014, **136**, 11980

[10] E. Hashem, J. A. Platts, F. Hartl, G. Lorusso, M. Evangelisti, C. Schulzke and R. J. Baker, *Inorg. Chem.*, 2014, **53**, 8624

[11] Example of $1e^-$ oxidation of U(IV) are known: S. Fortier, G. Wu and T. W. Hayton, *J. Am. Chem. Soc.*, 2010, **132**, 6888

[12] a) F. Dulong, J. Pouessel, P. Thuéry, J.-C. Berthet, M. Ephritikhine and T. Cantat, *Chem. Commun*., 2013, **49**, 2412; b) A. J. Lewis, P. J. Carroll and E. J. Schelter, *J. Am. Chem. Soc.*, 2013, **135**, 511; c) T. W. Hayton, *Dalton Trans.*, 2010, **39**, 1145; d) B. Kosog, H. S. La Pierre, F. W. Heinemann, S. T. Liddle and K. Meyer, *J. Am. Chem. Soc.*, 2012, **134**, 5284

[13] Recent examples: a) P. L. Arnold, E. Hollis, G. S. Nichol, J. B. Love, J. -C. Griveau, R. Caiuffo, N. Magnani, L. Maron, L. Castro, A. Yahia, S. O. Odoh and G. Schreckenbach, *J. Am. Chem Soc.*, 2013, **135**, 3841; b) P. L. Arnold, B. E. Cowie, M. Suvova, M. Zegke, N. Magnani, E. Colineau, J. -C Griveau, R. Caciuffo and J. B. Love, *Angew. Chem. Int. Ed.*, 2017, **56**, 10775

[14] a) D. D. Schnaars and R. E. Wilson, *Inorg. Chem.*, 2013, **52**, 14138; b) J. I. Bullock, *J. Chem. Soc. A.*, 1969, 781; c) G. Herzberg, *Infrared and Raman Spectra of Polyatomic Molecules*, D. Van Nostrand Company, Inc.: New York, 1946

[15] L. H. Jones, *Spectrochim. Acta*, 1958, **10**, 395

[16] L. R. Morss, N. M. Edelstein, J. Fuger and J. J. Katz, *The Chemistry of the Actinide and Transactinide Elements*, Volume 1, 3rd ed.; Springer: Dordrecht, 2006.

[17] R. G. Denning, *J. Phys. Chem. A*, 2007, **111**, 4125

[18] R. G. Denning, In: *Structure and Bonding: Complexes, Clusters and Crystal Chemistry*; M.J. Clarke, J. B. Goodenough, J. A. Ibers, C. K. Jørgensen, D. M. P. Mingos, J. B. Neilands, G. A. Palmer, D. Reinen, P. J. Sadler, R. Weiss and J. P. Williams, Eds.; Springer-Verlag: New York, 1992, Vol. 79, pp 215-276

[19] G. Folcher, H. Marquet-Ellis, P. Rigny, E. Soulic and G. Goodman, *J. Inorg. Nucl. Chem.*, 1976, **38**, 757

[20] K. Mizuoka, S. Tsushima, M. Hasegawa, T. Hoshi and Y. Ikeda, *Inorg. Chem.*, 2005, **44**, 6211

[21] D. E. Morris, R. E. Da Re, K. C. Jantunen, I. Castro-Rodriguez and J. L. Kiplinger, *Organometallics*, 2004, **23**, 5142

[22] E. Hashem, A. N. Swinburne, C. Schulzke, R. C. Evans, J. A. Platts, A. Kerridge, L. S. Natrajan and R. J. Baker, *RSC Adv.*, 2013, **3**, 4350

[23] E. Hashem, G. Lorusso, M. Evangelisti, T. McCabe, C. Schulzke, J. A. Platts and R. J. Baker, *Dalton Trans.*, 2013,**42**, 14677

[24] SHAPE Program for the Stereochemical Analysis of Molecular Fragments by Means of Continuous Shape Measures and Associated Tools V 2.1 2013

[25] V. N. Serezhkina, E. V. Peresypkinab, M. O. Karaseva, A. V. Virovetsb and L. B. Serezhkina, *Crystallography reports*, 2014, **59**, 196

[26] M. Nyman and M. A. Rodriguez, *Inorg. Chem.*, 2010, **49**, 7748

[27] R. D. Shannon**,** *Acta Cryst.*, 1976, **A32**, Pages 751

[28] J. -C. Berthet, P. Thuéry and M. Ephritikhine, *Polyhedron*, **25**, 2006, 1700

[29] J.-C. Berthet, P. Thuéry and M. Ephritikhine, *Inorg. Chem.*, 2005, **44**, 1142

[30] a) C. H. Lin and K. H. Lii, *Angew. Chem., Int. Ed.*, 2008, **47**, 8711; b) C. M. Wang, C. H. Liao, H. M. Lin and K. H. Lii, *Inorg. Chem.*, 2004, **43**, 8239; c) C. S. Lee, C. H. Lin, S. L. Wang and K. H. Lii, *Angew. Chem., Int. Ed.*, 2010, **49**, 4254; d) C. S. Lee, S. L. Wang and K. H. Lii, *J. Am. Chem. Soc.*, 2009, **131**, 15116; e) E. M. Villa, C. J. Marr, L. J. Jouffret, E. V. Alekseev, W. Depmeier and T. E. Albrecht-Schmitt, *Inorg. Chem.*, 2012, **51**, 6548

[31] P. C. Burns, R. J. Finch, F. C. Hawthorne, M. L. Miller and R. C. Ewing, *J. Nucl. Mater.* 1997, **249**, 199

[32] M. H. Klaproth, *Chem. Ann. Freunde. Naturlehre*. 1789, **2**, 387

[33] F. C. Hawthorne and R. J. Finch, *The Canadian Mineralogist*, 2006, **44**, 1379

[34] L. Chen, J. Diwu, D. Gui, Y. Wang, Z. Weng, Z. Chai, T. E. Albrecht-Schmitt and S. Wang, *Inorg. Chem.*, 2017, **56**, 6952

[35] L. Chatelain, S. White, R. Scopelliti and M. Mazzanti, *Angew. Chem., Int. Ed.*, 2016, **55**, 14325

[36] *The Chemistry of the Actinide and Transactinide Elements*, ed. L. R. Morss, N. M. Edelstein and J. Fuger, Springer, Berlin, 3rd edn, 2006, vol. 3, Chapter 5

[37] a) G. Liu and J. V. Beitz, Optical Spectra and Electronic Structure, in *The Chemistry of the Actinide and Transactinide Elements*, ed. L. R. Morss, N. Edelstein and J. Fuger, Springer, Berlin, 3rd edn, 2006, vol. 3, pp. 2013-2111; b) N. M. Edelstein and G. H. Lander, Magnetic Properties, in *The Chemistry of the Actinide and Transactinide Elements*, ed. L. R. Morss, N. M. Edelstein and J. Fuger, Springer, Berlin, 3rd edn, 2006, vol. 4, pp. 2225-2306; c) N. Kaltsoyannis, P. J. Hay, J. Li, J. P. Blaudeau and B. E. Bursten, *Theoretical Studies of the Electronic Structure of Compounds of the Actinide Elements*, in The Chemistry of the Actinide and Transactinide Elements, ed. L. R. Morss, N. M. Edelstein and J. Fuger, Springer, Berlin, 3rd edn, 2006, vol. 3, pp. 1893–2012

[38] G. Bombieri, P. T. Moseley and D. Brown, *J. Chem. Soc., Dalton Trans.,* 1975, 1520

[39] C. C. Scarborough and K. Wieghardt, *Inorg. Chem.*, 2011, **50**, 9773

[40] C. H. Booth, M. D. Walter, D. Kazhdan, Y.-J. Hu, W. W. Lukens, E. D. Bauer, L. Maron, O. Eisenstein and R. A. Andersen, *J. Am. Chem. Soc.*, 2009, **131**, 6480

[41] I. L. Fedushkin, T. V. Petrovskaya, F. Girgsdies, V. I. Nevodchikov, R. Weimann, H. Schumann and M. N. Bochkarev, *Russ. Chem. Bull.*, 2000, **49**, 1869

[42] a) C. H. Booth, M. D. Walter, D. Kazhdan, Y. J. Hu, W. W. Lukens, E. D. Bauer, L. Maron, O. Eisenstein and R. A. Andersen, *J. Am. Chem. Soc.*, 2009, **131**, 6480; b) N. A. G. Bandeira, C. Daniel, A. Trifonov and M. Calhorda, *J. Organometallics*, 2012, **31**, 4693

[43] S. Fortier, J. Veleta, A. Pialat, J. Le Roy, K. B. Ghiassi, M. M. Olmstead, A. J. Metta-Magaña, M. Murugesu and D. Villagran, *Chem. Eur. J.*, 2016, **22**, 1931

[44] P. M. Björemark, J. Jönsson and M. Håkansson, *Chem. Eur. J.*, 2015, **21**, 10630

[45] F. Qu, T. Q. Nguyen and A. F. Janzen, *J. Fluor. Chem.*, 1999, **94**, 15

[46] a) C.-J. Zhang, H.-J. Pang, D.-P. Wang and Y.-G. Chen, *J. Coord. Chem.*, 2010, **63**, 568; b) C. Pichon, A. Dolbecq, P. Mialane, J. Marrot, E. Riviere, M. Goral, M. Zynek, T. McCormac, S. A. Borshch, E. Zueva and F. Secheresse, *Chem.-Eur. J.*, 2008, **14**, 3189; c) N. Veiga, J. Torres, C. Bazzicalupi, A. Bianchi and C. Kremer, *Chem. Comm.*, 2014, **50**, 14971

[47] a) R. Reddi, K. K. Singarapu, D. Pal and A. Addlagatta, *Mol. BioSyst.*, 2016, **12**, 2408; b) K. J. Wei, J. Ni, Y. S. Xie and Q. L. Liu, *Inorg. Chem. Commun.*, 2007, **10**, 279; c) H. P. Zhou, Y. M. Zhu, J. J. Chen, Z. J. Hu, J. Y. Wu, Y. Wie, M. H. Jiang, X. T. Tao and Y. P. Tian, *Inorg. Chem. Commun.*, 2006, **9**, 90; d) F. H. Allen, C. M. Bird, R. S. Rowland and P. R. Raithby,

Acta Crystallogr. Sect. B Struct. Sci., 1997, **53**, 696; e) G. R. Desiraju and T. Steiner, *The Weak Hydrogen Bond in Structural Chemistry and Biology*, Oxford University Press, 1999

[48] E. König and S. Kremer, *Chem. Phys. Lett.*, 1970, **5**, 87

[49] a) L. C. J. Pereira, C. Camp, J. T. Coutinho, L. Chatelain, P. Maldivi, M. Almeida and M. Mazzanti, *Inorg. Chem.* 2014, **53**, 11809; b) K. R. Meihaus and J. R. Long, *Dalton Trans.*, 2014; c) N. Magnani, *Int. J. Quantum Chem.*, 2014, **114**, 755

[50] a) C. R. Graves, P. Yang, S. A. Kozimor, A. E. Vaughn, A. L. Clark, S. D. Conradson, E. J. Schelter, B. L. Scott, J. D. Thompson, P. J. Hay, D. E. Morris and J. L. Kiplinger, *J. Am. Chem. Soc.*, 2008, **130**, 5272; b) Q. B. Nguyen, C.-L. Chen, Y.-W. Chiang and K.-H. Lii, *Inorg. Chem.*, 2012, **51**, 3879; c) C. Miyake, Y. Yamana, S. Imoto and H. Ohya-Nishiguchi, *Inorg. Chim. Acta*, 1984, **95**, 17

[51] a) S. C. Bart, C. Anthon, F. W. Heinemann, E. Bill, N. M. Edelsteinand and K. Meyer, *J. Am. Chem. Soc.*, 2013, **135**, 10742; b) D. M. King, P. A. Cleaves, A. J. Wooles, B. M. Gardner, N. F. Chilton, F. Tuna, W. Lewis, Eric J. L. Mclnnes and S. T. Liddle, *Nat. Commun.*, 2016, **7**, 13773; c) D. M. King, F. Tuna, Eric J. L. Mclnnes, J. McMaster, W. Lewis, A. J. Blake and S. T. Liddle, *Science*, 2012, **337**, 717

[52] W. W. Lukens, N. M. Edelstein, N. Magnani, T. W. Hayton, S. Fortier and L. A. Seaman, *J. Am. Chem. Soc.*, 2013, **135**, 10742

[53] a) L. S. Natrajan, *Coord. Chem. Rev.*, 2012, **256**, 1583; b) R. Steudner, T. Arnold, K. Grobmanвmann, G. Giepel and V. Brendler, *Inorg. Chem. Commun*., 2006, **9**, 939; c) K. Grossman, T. Arnold, R. Steudtner, S. Weills and G. Bernhard, *Naturwissenschaften.*, 2009, **96**, 963; d) T. Arnold, K. Grossmann and N. Baumann, *Anal. Bioanal. Chem.,* 2010, **396**, 1641

[54] J. C. Barbour, A. J. I. Kim, E. DeVries, S. E. Shaner and B. M. Lovaase, *Inorg. Chem.*, 2017, **56**, 8212

[55] a) G. A. Molander, C. R. Harris and A. B. Charette, *Encyclopedia of Reagents for Organic Synthesis*, 2005; b) P. Girard, J. L. Namy and H. B. Kagan, *J. Am. Chem. Soc.*, 1980, **102**, 2693; W. J. Evans, T. S. Gummersheimer and J. W. Ziller; *J. Am. Chem. Soc.*, 1995, **117**, 8999

[56] T. S. Bailey, T. J. Woods and T. B. Rauchfuss, *CSD Communication*, 2016

[57] J. Yang, J. Dong, R. Wu, H. Wu, H. Song, S. Gan and L. Zou, *Dalton Trans.*, 2018, **47**, 9795

[58] N. G. Connelly and W. E. Geiger, *Chem. Rev.*, 1996, **96**, 877

[59] a) J. Jung, Atanasov, M.; Neese, F. *Inorg. Chem.* 2017, 56, 8802; b) A. Kerridge, *Chem. Commun.* 2017, **53**, 6685; c) J.-P Dognon, *Coord. Chem. Rev.*, 2017, **344**, 150

[60] R. Beekmeyer and A. Kerridge, *Inorganics*, 2015, **3**, 482

[61] a) R. Chiarizia, P. R. Danesi, G. Scibona and L. Magon, *J. Inorg. Nucl. Chem.*, 1973, **35**, 3595; b) P. K. Khopkar and P. Narayanankutty, *J. Inorg. Nucl. Chem.* 1971, **33**, 495; c) F. L. Moore, *Anal. Chem.* 1964, **36**, 2158

[62] S. P. Petrosyants, *Russ. J. Coord. Chem.*, 2015, **41**, 715

[63] M. J. Lozano-Rodriguez, P. Thuery, S. Petit, R. Copping, J. Mustre de Leon and C. Den Auwer, *Acta Crystallogr., Sect. E: Struct. Rep. Online*, 2011, **67**, 487

[64] D. F. de Sà, O. L. Malta, C. De Mello Donegà, A. M. Simas, R. L. Longo, P. A. Santa Cruz and E. F. Silva, *Coord. Chem. Rev.*, 2000, **196**, 165

[65] R. Countryman and W. S. McDonald, *J. Inorg. Nucl. Chem.*, 1971, **33**, 2213; b) Z. M. S. Al-Kazzaz, K. W. Bagnal, D. Brown and B. Whittaker, *J. Chem. Soc. Dalton. Trans.*, 1972, 2273

[66] M. A. Frerking, R. A. Linke and P. Thaddeus, *Astrophys. J.*, 1979, **234**, L143

[67] G. R. Draper and R. L. Werner, *J. Mol. Spectrosc.*, 1974, **50**, 369

[68] C. Houchins, D. Weidinger and J. C. Owrutsky, *J. Phys. Chem. A*, 2010, **114**, 6569

[69] M. Wierzejewska and Z. Mielke, *Chem. Phys. Lett.*, 2001, **349**, 227

[70] C. I. Beard and B. P. Dailey, *J. Chem. Phys.*, 1947, **15**, 762

[71] a) M. Niedenhoff, K. M. T. Yamada and G. Winnewisser, J. *Mol. Spectroc.*, 1997, **183**, 176; b) M. Rodler, S. Jans-Bürli, M. Oldani and A. Bauder, *Chem. Phys. Lett.*, 1987, **142**, 10; c) K. Yamada, M. Winnewisser, G. Winnewisser, L. B. Szalanski and M. C. L. Gerry, *J. Mol. Spectrosc.*, 1980, **79**, 295; d) K. Yamada, M. Winnewisser, G. Winnewisser, L. B. Szalanski and M. C. L. Gerry, *J. Mol. Spectrosc.*, 1979, **78**, 189; e) R. Kewley, K. V. L. N. Sastry and M. Winnewisser, *J. Mol. Spectrosc.*, 1963, **10**, 418; f) C. I. Beard and B. P. Dailey, *J. Chem. Phys.*, 1950, **18**, 1437

[72] N. N. Greenwod and A. Earnshaw, The Chemistry of the Elements, Elsevier Butterworth-Heinemann, 2nd edn, 2005, ch. 8

[73] M.Wierzejewska and A. Olbert-Majkut, *J. Phys. Chem. A*, 2003, **107**, 1928

[74] M. Wierzejewska and R. Wieczorek, *Chem. Phys.*, 2003, **287**, 169

[75] J. Krupa and M. Wierzejewska, *Chem. Phys. Lett.*, 2016, **652**, 46

[76] M. G. B. Drew, B. P. Murphy, J. Nelson and S. M. Nelson, *J. Chem. Soc.*, *Dalton Trans.*, 1987, **873**, 3227

[77] T. Liu, Z.-X. Zhao, M.-X. Song, H.-X. Zhang and C.-C. Sun, *Theor. Chem. Acc.*, 2011, **128**, 215

[78] M. Köckerling and J.B. Willems, *Zeitschrift fur Kristallographie - New Crystal Structures*, 1999, **214**, 460

[79] Average value from the Cambridge Structural database (version 5.37 and updates to November 2016) N=C = 1.151, C=S = 1.639 Å

[80] J. Krupa and M. Wierzejewska, *Chem. Phys. Lett.*, 2016, **652**, 46

[81] a) P. F. Provasi, G. A. Aucar, M. Sanchez, I. Alkorta, J. Elguero and S. P. A. Sauer, *J. Phys. Chem. B*, 2005, **109**, 18189; b) J. M. Lehn and R. Sehe, *Chem. Commun.*, 1966, **847**, c) J. P. Kintzinger and J. M. Lehn, *Molecular Physics*, 1968, **14**, 133

[82] R. Glaser, R. Hillebrand, W. Wycoff, C. Camasta and K. S. Gates, *J. Org. Chem.*, 2015, **80**, 4360

[83] a) B. M. Landsberg, *Chem. Phys. Lett.*, 1979, **60**, 265; b) J. Vogt and M. Winnewisser, *Ber. Bunsen-Ges.*, 1984, **88**, 439; c) J. Vogt and M. Winnewisser, *Ber. Bunsen-Ges.*, 1984, **88**, 444

[84] T. Vörös, G. Bazsó and G. Tarczay, *J. Phys. Chem. A*, 2013, **117**, 13616

[85] A. W. Down, *Chem. Commun.*, 1968, 1290

[86] L. P. Eremin, O. Kh. Poleshchuk, V. A. Poluboyarov, L. V. Babovskaya and A. E. Lapin*., J. Struct. Chem.*, 2003, **44**, 404

[87] K. Momma and F. Izumi, *J. Appl. Crystallogr*., 2011, **44**, 1272

[88] M. Krejčík, M. Daněk and F. Hartl, *Electroanal. Chem. Interfacial Electrochem.*, 1991, **317**, 179

[89] J. L. Kiplinger, D. E. Morris, B. L. Scott and Carol J. Burns, *Organometallics*, 2002, **21**, 5978

[90] T. Cantat, B. L. Scott and J. L. Kiplinger, *Chem. Commun.*, 2010, **46**, 919

[91] The ORCA program system F. Neese, Wiley interdisciplinary Reviews - Computational Molecular Science, 2012, **2**, 73

[92] a) A. D. Becke, *Phys. Rev. A*, 1988, **38**, 3098; b) J. P. Perdew, *Phys. Rev. B*, 1986, **33**, 8822

[93] a) P. J. Hay and W. R. Wadt, *J. Chem. Phys*., 1985, **82**, 299; b) F. Weigend and R. Ahlrichs, *Phys. Chem. Chem. Phys*. 2005, **7**, 3297

[94] AIMAll (Version 12.06.03), T. A. Keith, TK Gristmill Software, Overland Park KS, USA, 2012

[95] T. Lu and F. Chen, *J. Comput. Chem.*, 2012, **33**, 580

[96] B. O. Roos, R. Lindh, P.-A. Malmqvist, V. Veryazov, P.-O. Widmark and A. C. Borin, *J. Phys. Chem. A*, 2008, **112**, 11431

[97] a) W. J. Hehre, R. Ditchfield, J. A. Pople, *J. Chem. Phys.*, 1972, **56**, 2257; b) T. Clark, J. Chandrasekhar, G. W. Spitznagel and P. V. R. Schleyer, *Comput. Chem.*, 1983, **4**, 294; c) P. C. Hariharan and J. A. Pople, *Theoret. Chimica Acta*, 1973, **28**, 213

[98] G. Jansen and B. A. Hess, *Phys. Rev. A*, 1989, **39**, 6016

[99] A. E. Reed and F. Weinhold, *J. Chem. Phys.*, 1985, **83**, 1736

[100] R. F. W. Bader, *Atoms in Molecules A Quantum Theory*, Oxford University Press, Oxford, UK, 1990

[101] a) J.-D. Chai and M. Head-Gordon, *Phys. Chem. Chem. Phys.*, 2008, **10**, 6615; b) R. Ditchfield, W. J. Hehre and J. A. Pople, *J. Chem. Phys.*, 1971, **54**, 724; c) P. C. Hariharan and J. A. Pople, *Theor. Chem. Acc.*, 1973, **28**, 213; d) T. Clark, J. Chandrasekhar, G. W. Spitznagel and P. v. R. Schleyer*, J. Comp. Chem.*, 1983, **4**, 294

Chapter 4

Pseudohalide Tectons within the Coordination Sphere of the Uranyl Ion: Experimental and Theoretical Study of C–H···O, C–H···S and Chalcogenide Noncovalent Interactions

4.1 Introduction

4.1.1 Noncovalent Interactions: the σ-Hole Concept

An understanding of the plethora of noncovalent interactions is of importance, not just in structural chemistry but also materials and biological chemistry. While the hydrogen bond is the most well studied,[1] over the past few years other non-conventional noncovalent interactions have garnered significant amount of attention, such as halogen bonding,[2] pnictogen bonding,[3] and even aerogen bonding.[4] Chalcogen bonding[5] is a relatively recent addition to the toolbox of crystal engineering and follows the same type of bonding scheme as halogen bonding, namely a σ-hole.[6] This bonding scheme can be viewed comparably to hydrogen bonding as X—D···A, where X is any atom, D is the donor atom and A is the acceptor atom. The σ-hole is visualized as a region of positive electrostatic potential located on an empty σ* orbital and is dependent upon two parameters: the σ-hole becomes more positive (and hence stronger interactions) when (1) D is more polarizable and (2) when the X atom is more electron withdrawing. Therefore, as the polarizability increases descending the group, stronger halogen bonds should occur moving from F to At and, indeed, Guo *et al.*[7] have recently demonstrated that astatine, the heaviest halogen, possesses the highest halogen-bond donating ability owing to its much more electrophilic σ-hole.

Figure 4.1 shows examples of molecular surface electrostatic potentials, with the σ-hole highlighted in red, for (from left to right): halogen, chalcogen, pnictogen and tetrel bonding.

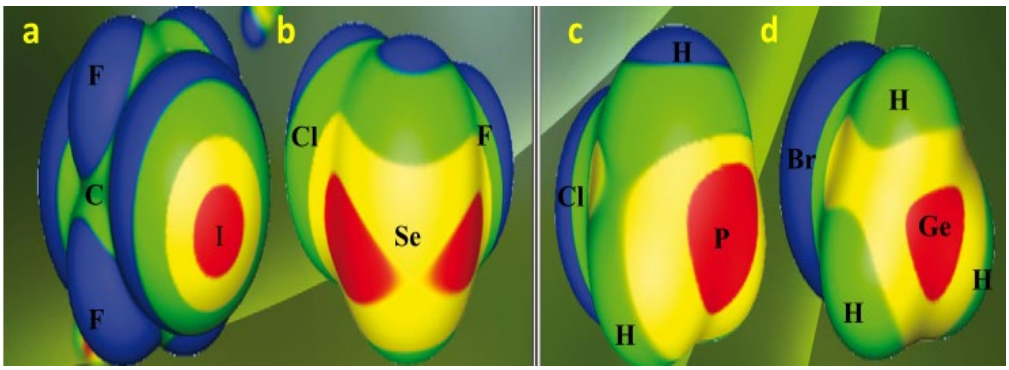

Figure 4.1. Molecular surface electrostatic potential, computed on the 0.001 au contour of the electronic density, of: (a) 1,2-diiodoperfluoroethane (ICF_2CF_2I), (b) SeFCl, (c) PH_2Cl and (d) GeH_3Br. Colour ranges, in kcal mol^{-1}, are: red, greater than 25; yellow, between 15 and 25; green, between 0 and 15; blue, less than 0 (negative). Computational level: M06-2X/6-311G(d).[8]

The majority of chalcogenide bonds features attractive interactions between S or Se and an electronegative N or O donor. Computational studies on $X_2Se\cdots O$ or $X_2S\cdots N$ interactions have recently been conducted and shown them to be dependent on the substituents on the chalcogenide atom and the interactions described as a charge transfer from the N or O lone pair to the σ^* S(e)—X orbital (Figure 4.2).[5j,9] Synthetic molecular balances based on formamide and thioformamide units have confirmed this, and shown that chalcogenide$\cdots$H—C interactions can also be described in this manner.[5b] The atomic polarizability increases descending the group so that S = 19.3 a.u. and Se 25.4 a.u. (a.u. = atomic units); thus a stronger interaction should occur moving from S to Se.[10] Moreover, as the atomic radius increases, steric effects become less pronounced when the group is descended. These interactions can be comparable in strength to hydrogen and halogen bonding. For example, the computed interaction energy of $FHS\cdots NH_3$ is −8.4 kcal mol^{-1} compared to −11.3 kcal mol^{-1} for $FHSe\cdots NH_3$ and −10.3 kcal mol^{-1} for the halogen bonded $F—Cl\cdots NH_3$.[6d] Perhaps more informative is the low temperature structure of the $F_4S\cdots NEt_3$ adduct which displays an S—N bond length of 2.384(2) Å, typical for a dative covalent bond;[11] theory supports this hypothesis[12] and reports a binding energy of −14.4 kcal mol^{-1}.

Halogen interactions have been further delineated by the geometric parameters shown in Figure 4.2. $0^o \leq |\theta_1-\theta_2| \leq 15^o$ are classified as type I, $15^o \leq |\theta_1-\theta_2| \leq 30^o$ are quasi-type I/type II and $|\theta_1-\theta_2| \geq 30^o$ are type II.[13] Type I are generally considered as due to crystal packing, while type II are stabilizing interactions. A recent examination of the Cambridge database showed that the majority of S$\cdots$S interactions between sp^2 hybridized sulfur atoms are type I ($\theta_1 \approx \theta_2$).[14] It is also apparent that S$\cdots$O interactions are prevalent in molecular recognition and host-guest interactions in biological systems.[15] However only few examples of chalcogenide interactions exist where a metal ion is included.[16] Indeed, even the more mature field of halogen bonding features rare examples, notably iodoform adducts of *trans*-$[PtX_2(NCNR_2)_2]$[17] or in a uranyl organic framework based on halogen substituted isonicotinic acids.[18]

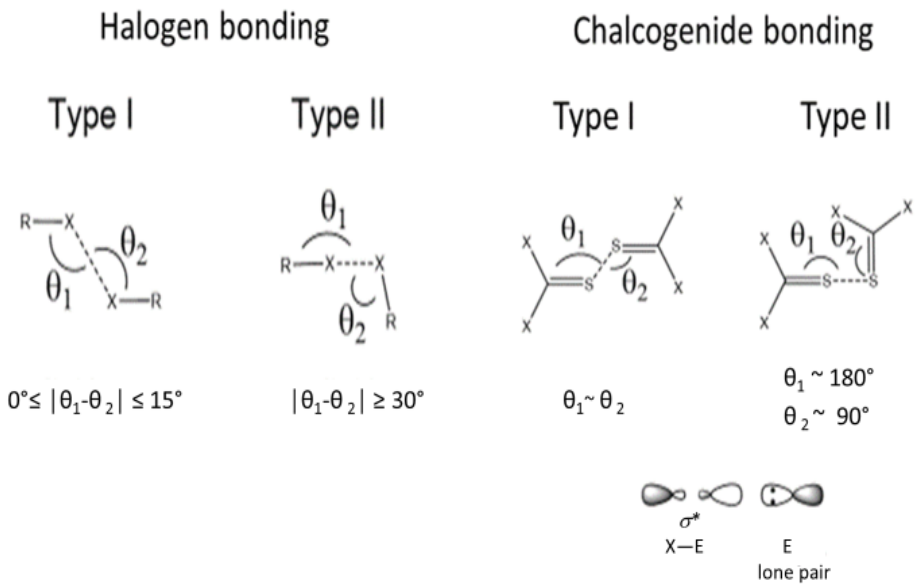

Figure 4.2. Types of halogen and chalcogen bonds.

4.1.2 Supramolecular Interactions Within the Uranyl Coordination Sphere

The uranyl ion has a number of features that make it suitable for a study on noncovalent interactions. The coordination geometry is generally limited by the O=U=O (-yl) fragment, which infrequently deviates from linearity (180°), so that all coordination is constrained to the equatorial plane.[19] However, multiple approaches have shown ability for influencing uranyl coordination geometry and reactivity, including: -yl oxygens functionalization,[20] distorting equatorial planarity[21] and breaking the linearity of the -yl unit.[22] Recently, the possibility of bending the uranyl cation via a crystal engineering approach has been studied in three uranyl(VI) complexes featuring 2,4,6-trihalobenzoic acids (where halo = F, Cl, Br) and 1,10-phenanthroline (phen) ligands.[23] Moreover, specific ligands can also induce the formation of uranyl coordination polymers.[24]

Over the last few years, the -yl moiety has proved to act as a secondary directing influence in supramolecular assembly to form 3-dimensional structures. However, since the -yl groups are generally considered as weak Lewis bases, these interactions have been somewhat neglected. Interactions with metal cations can elongate the U=O bond length to a degree that is perceptible crystallographically.[20b, 25] Some evidence suggests that this weakening of the U=O bond is due to an increase in electron density around the uranyl cation and to an amplified electrostatic repulsion within the U=O group.[26] Moreover, weaker interactions such as hydrogen bonding acceptor via C—H···O=U interactions,[27] sometimes via charge assisted hydrogen bonding,[28] can be used to recognize or separate

the uranyl ion selectively from complex mixtures[29] and, in addition, the uranyl ion has also recently been observed as a halogen bond acceptor.[30]

A useful method to probe noncovalent interactions in uranyl complexes is by examining the optical properties of the uranyl group, since they are sensitive to the nature of the coordination environment; these properties have been fully described in Chapter 1 (section 1.4.1). Moreover, recently the influence of the tecton in $[UO_2Cl_4]^{2-}$ has been interrogated using luminescence spectroscopy[31] and it appeared that those ligands that have vibrational modes that can couple with the U=O vibrations could directly influence the luminescence properties.

Additional supramolecular interactions utilizing the equatorial ligands as tectons have also been considered; for example, the elegant studies focused on uranyl thiocyanate to explore noncovalent bonding in halogenated pyridinium cations showed some evidence for S···S close contacts.[32] Moreover, noncovalent interactions in uranyl thiocyanate compounds have recently been examined by Surbella *et al.,*[33] where terminal sulfur atoms can accept hydrogen bonds and/or engage in S···S and S···O_{yl} interactions, and this work has been reported a few weeks earlier than the publication of the main results herein. A series of $[R_4N]_3[UO_2(NCS)_5]$ (R = Me, Et, ^{n}Pr)[34] have also been structurally characterized as examples of species present in spent nuclear fuel reprocessing. Finally, the uranyl thiocyanate ion has shown to have a reversible thermochromic behaviour in ionic liquids and this phenomenon is ascribed to changes in the local environment of the uranyl ion, including the coordination number, as well as to cation-anion interactions.[35]

4.2 Structural and Spectroscopic Characterization of $[R_4N]_3[UO_2(NCS)_5]$ and $[R_4N]_3[UO_2(NCSe)_5]$, a Systematic Investigation of Noncovalent Interactions

4.2.1 Synthesis of $[R_4N]_3[UO_2(NCS)_5]$ and $[R_4N]_3[UO_2(NCSe)_5]$

This chapter contains a detailed structural and spectroscopic study on a series of uranyl(VI) thiocyanate $[NCS]^-$ and selenocyanate $[NCSe]^-$ complexes, of the type $[R_4N]_3[UO_2(NCS)_5]$ and $[R_4N]_3[UO_2(NCSe)_5]$. X-ray crystallography, NMR, vibrational and photoluminescence spectroscopy and theoretical methods have been used to explore the noncovalent interactions present in these compounds, namely: charge assisted C—

H···O=U and C—H···S(e) hydrogen bonding, and Se···Se or S···S chalcogenide interactions.

When the reaction with the cyanate $[NCO]^-$ ion was examined (Equation 1), hydrolysis of $[NCO]^-$ was consistently observed and $K_4[UO_2(CO_3)_3]$ the only product obtained, as determined by X-ray diffraction.[36]

The synthesis of the uranyl(VI) compounds with $[NCS]^-$ and $[NCSe]^-$ ligands are trivial (Equations 2, 3) and X-ray quality crystals were grown for all. In order to distinguish these compounds, the nomenclature RE will be adopted, where R is the alkyl group of the ammonium cation and E is S or Se. Thus, a small library of compounds is reported and structural parameters and packing motifs can be compared (1) within the $[NCS]^-$ series, (2) within the $[NCSe]^-$ series and (3) with the same cations. In one case, a small amount of a decomposition product, presumably from $[NCS]^-$ oxidation, was obtained and this has been structurally characterized. In contrast, the reaction between the tellurium cyanide $[NCTe]^-$ ion, made in situ by mixing Na[CN] and Te in MeCN, uranyl nitrate and $[Et_4N]Cl$ (Equation 4) afforded immediate decomposition to a grey precipitate of presumably tellurium metal and, from the MeCN soluble fraction, single crystals of $[Et_4N]_2[UO_2Cl_4]$ were deposited. $[NCTe]^-$ chemistry is dominated by this decomposition.[37]

$$[UO_2(NO_3)_2].6H_2O + 5KNCO + 3Et_4NCl \rightarrow K_4[UO_2(CO_3)_3] \quad (1)$$

$$[UO_2(NO_3)_2].6H_2O + 5NaNCS + 3R_4NCl \rightarrow [R_4N]_3[UO_2(NCS)_5] \quad (2)$$
(R = Me, Et, ^{n}Pr, ^{n}Bu, Me_3NBz, Et_3NBz)

$$[UO_2(NO_3)_2].6H_2O + 5KNCSe + 3R_4NCl \rightarrow [R_4N]_3[UO_2(NCSe)_5] \quad (3)$$
(R = Me, Et, ^{n}Pr, Et_3NBz)

$$[UO_2(NO_3)_2].6H_2O + 5NaNCTe + 3Et_4NCl \rightarrow [Et_4N]_2[UO_2Cl_4] + Te \quad (4)$$

4.2.2 Structural Characterization of the $[R_4N]_3[UO_2(NCS)_5]$ series

In the RS series, the compounds MeS, EtS and ^{n}PrS have been already reported,[34] but the focus of that work was not on the supramolecular structures, while ^{n}BuS, Me_3NBzS and Et_3NBzS are new species. In addition, as described in Chapter 2 (section 2.2), during the attempts of encapsulating the Na^+ cation of the green U(IV) complex $[Na]_4[U(NCS)_8]$,

by adding four equivalents of 2.2.2-cryptand and 18-crown-6, a serendipitous oxidation of U(IV) to uranyl(VI) occurred in both experiments and yellow single crystals of the respective $[(2.2.2\text{-crypt})Na]_3[UO_2(NCS)_5]$ and $[(18\text{-C-6})Na]_3[UO_2(NCS)_5]$ complexes were isolated. These have been fully characterized and included in the study of the RS series, with the corresponding labels: (2.2.2-crypt)NaS and (18-C-6)NaS.

The solid-state crystal structures of ^{n}BuS, Me_3NBzS and Et_3NBzS are collated in Figure 4.3, along with a picture of crystals of Et_3NBzS as example for the RS series. The structures of (2.2.2-crypt)NaS and, more substantially, (18-C-6)NaS suffer significant disorder in the encapsulating ligand and are shown in Figure 4.4; for (18-C-6)NaS, in particular, the structure refinement has been further explained in the experimental section.

Selected metric parameters for the whole RS series are listed in Table 4.1, while the crystallographic data of the structures are listed in Appendix 3. The full list of bond lengths and angles for these compounds have been tabulated in Appendix 3.1-3.2-3.3, which have been added in the external CD source of this thesis.

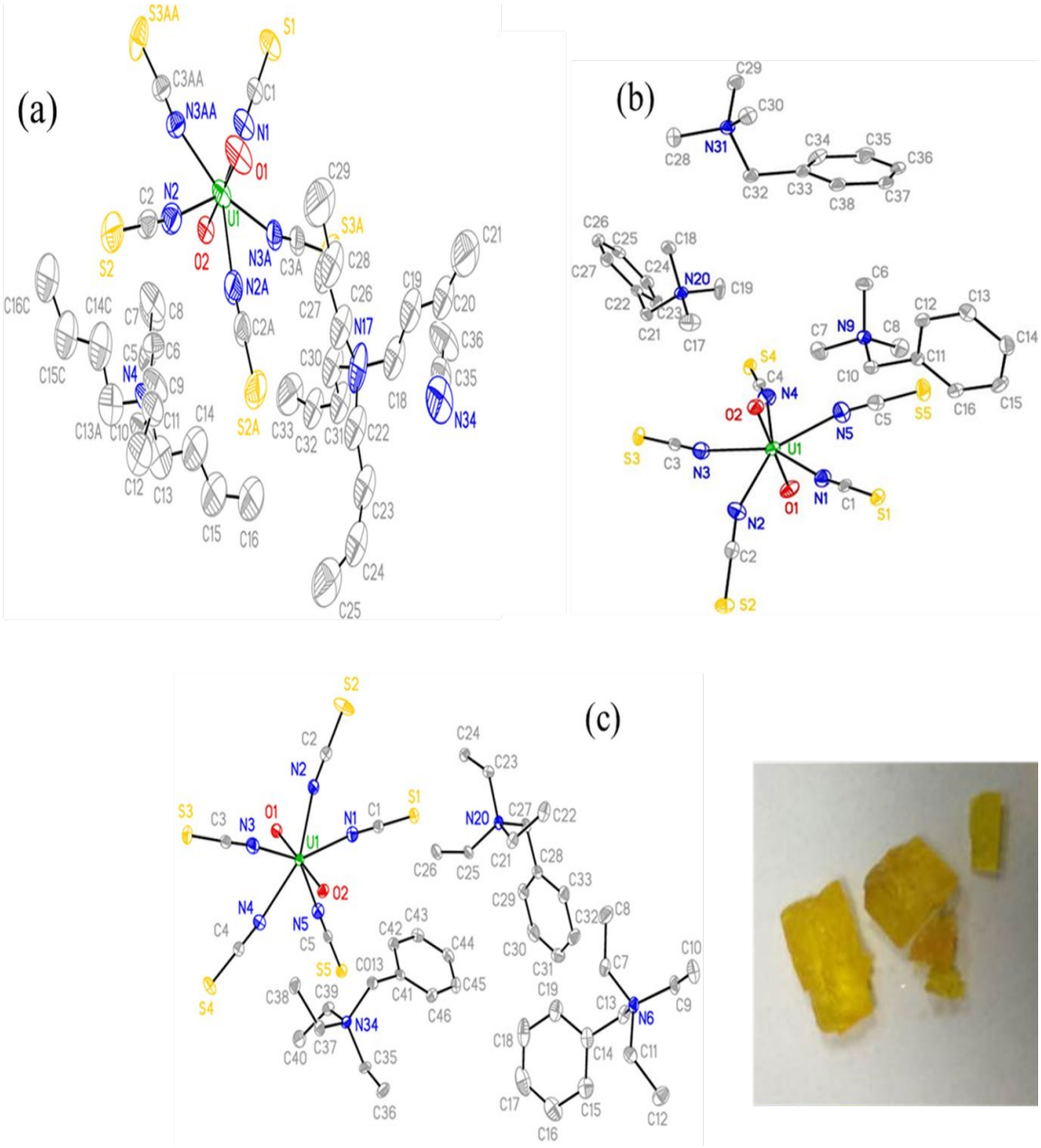

Figure 4.3. Asymmetric unit of: (a) ^{n}BuS, (b) Me_3NBzS and (c) Et_3NBzS, along with a picture of yellow crystals of Et_3NBzS. Atomic displacement parameters shown at 50% probability, hydrogen atoms and co-crystallized solvent molecules omitted for clarity.

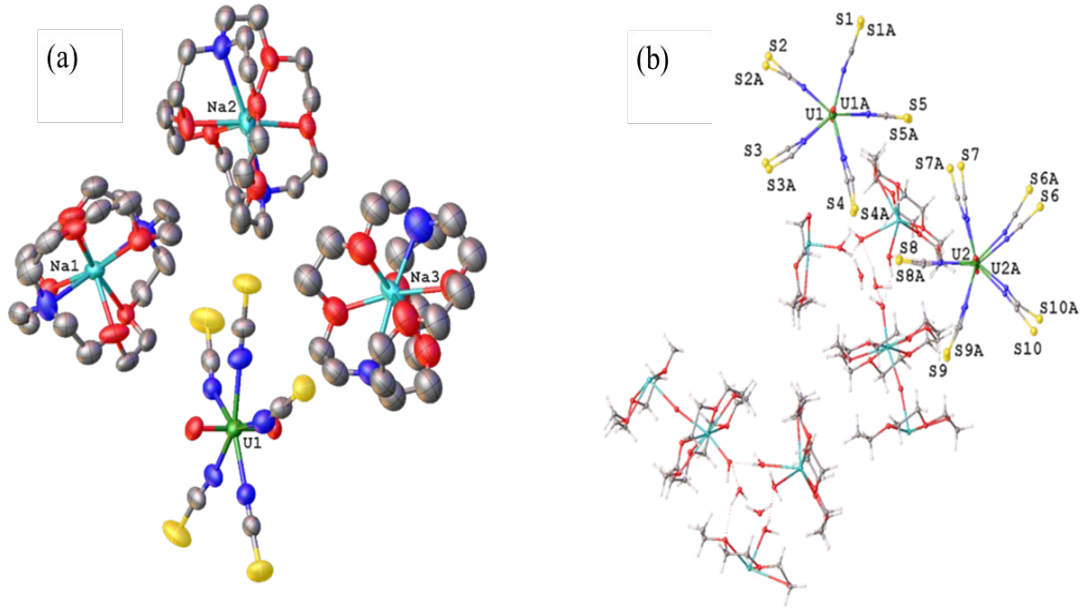

Figure 4.4. (a) Asymmetric unit of $[(2.2.2\text{-crypt})Na]_3[UO_2(NCS)_5]$, with the occupancy being: NCS 67%; cryptand Na1 60%, Na2 50% and Na3 66% occupied. (b) Illustration of the asymmetric unit of $[(18\text{-C-}6)Na]_3[UO_2(NCS)_5]$, with the structure refinement clarified in the experimental section. Hydrogens atoms omitted, and only selected heteroatoms labelled for clarity.

For all the compounds, the X-ray structure analysis has revealed the expected D_{5h} pentagonal bipyramidal coordination geometry around the uranyl ion of the five $[NCS]^-$ anions, coordinated via the N atom, and the O atoms of the linear O=U=O moiety located axially. The U—N, N=C and C=S bond lengths are also statistically identical. The only differences are in the orientation of how the $[NCS]^-$ ions coordinate to the uranium; in particular the U—N=C angle and the deviation of the S atoms out of the UN_5 plane, which is significant in some cases.

Table 4.1. Selected average bond lengths (Å) and angles (°) for the RS series.

Compound	U=O	U—N	N=C	C=S	O=U=O	U—N=C	S o.o.p (Å)[a]
MeS[b]	1.770(4)	2.45(2)	1.15(2)	1.62(1)	179.7(1)	154.1(4) to 176.2(4)	S1 −0.343 S2 +1.100 S3 −0.910 S4 +0.394 S5 +0.181
EtS[b]	1.763(6)	2.45(2)	1.16(1)	1.62(3)	177.4(3) 178.3(4)	155.3(7) to 176.4(7)	S1 +0.260 S2 +0.072 S3 −0.625 S4 −1.042 S5 −0.702
^{n}PrS[b]	1.749(4)	2.44(2)	1.14(1)	1.62(3)	178.9(3)	158.4(6) to 179.6(8)	S1 −0.286 S2 −0.475 S3 −0.683 S4 +0.574 S5 +0.103
^{n}BuS	1.769(10) 1.759(9)	2.45(1)	1.16(1)	1.63(1)	179.4(9)	168.6(2) to 172.3(2)	S1 −0.479 S2 −0.364 S2A −0.364 S3A −0.474
Me_3NBzS	1.778(3) 1.774(3)	2.45(1)	1.16(1)	1.62(1)	179.21(13)	153.2(3) to 167.2(3)	S1 −0.797 S2 −1.404 S3 −0.087 S4 −0.760 S5 −0.708
Et_3NBzS	1.772(2) 1.773(2)	2.45(1)	1.16(1)	1.63(1)	179.4(9)	168.9(3) to 172.6(3)	S1 +0.466 S2 +0.307 S3 −0.219 S4 −0.342 S5 +0.296
(18-C-6)NaS	1.344(4) 1.799(6)	2.418(1) 2.441(4)	1.16(3)	1.65(3)	178.7(3) 179.05(5)	168.0(3) to 178.0(3)	S1 −0.1537 S2 −0.0663 S3 +0.1460 S4 +0.0268 S5 +0.0528
(2.2.2-crypt)NaS	1.800(5) 1.797(5)	2.45(3)	1.15(3)	1.63(3)	179.1(3)	154.0(7) to 176.8(7)	S1 +0.1833 S2 +0.3347 S3 −0.5540 S4 +0.5813 S5 −0.4325

[a]Distance out of the UN_5 plane. [b]From Reference 34

Apparent in the structures of MeS and EtS are S···S close contacts within the van der Waals radii for two S atoms (3.78 Å).[38] In MeS these are type I interactions ($d_{S\ldots S}$ = 3.587 Å, θ_2-θ_1 = 0°). In contrast, EtS forms chains along the crystallographic *b*-axis and the angles θ_1 and θ_2 suggest these are not crystal packing (Figure 4.5a), in accord with the conventional description for halogen bonding (Figure 4.2). This theory should be applicable here as both interactions are of a σ-hole type. In EtS, the S···S distances and angles are: $d_{S\ldots S}$ = 3.470 Å, θ_2-θ_1 = 38.3° and $d_{S\ldots S}$ = 3.591 Å, θ_2-θ_1 = 20.8°. There are

also S···H—C weak hydrogen bonds[39] ($d_{S\ldots C}$ = 3.540(8) to 3.895(7) Å) where the alkylammonium cation links two chains and it appears that this S···H—C interaction is responsible for the movement of the sulfur atom out of the UN_5 plane.

However, as the size of the R group increases, the close contacts between two S centres disappear and in ^{n}PrS, for example, S···H—C interactions are prevalent (Figure 4.5b) ($d_{S\ldots C}$ = 3.74 – 3.84 Å) along with bifurcated hydrogen bonding to the uranyl ion ($d_{O\ldots C}$ = 3.40 and 3.49 Å). Moreover, ^{n}BuS does not present any S···S close contacts. Thus, it appears that there is a steric effect of the cation in the nature of these noncovalent interactions, whereby the conformationally non-rigid arms of the *n*-propyl chain are large enough to 'turn-off' the S···S close contacts, while the S···H—C interactions dominate in all the structures (Figure 4.5b). Support for this hypothesis comes from the supramolecular interactions present in $[Me_3NBz]_3[UO_2(NCS)_5]$ (Figure 4.6) and $[Et_3NBz]_3[UO_2(NCS)_5]$, where there are short contacts between two sulfur atoms, but the angles suggest a type I interaction, *i.e.* due simply to packing (Me_3NBzS: $d_{S\ldots S}$ = 3.350 Å, θ_2-θ_1 = 0°; Et_3NBzS: $d_{S\ldots S}$ = 3.540 Å, θ_2-θ_1 = 14.0°). However, these systems exhibit also C—H···S interactions (Me_3NBzS: $d_{S\ldots C}$ = 3.690(3) to 3.824(3) Å; Et_3NBzS: $d_{S\ldots C}$ = 3.711(4) to 3.849(5) Å) and allowed a deeper analysis of this hydrogen bonding. Computational studies reported that the strength of this weak hydrogen bond is dependent upon the hybridization of the C—H donor and this decreases as hybridization increases,[40] but in the structures of Me_3NBzS and Et_3NBzS there is no direct correlation.

From this description, it is clear that the supramolecular structures are subtly influenced by the steric effects of the cation.

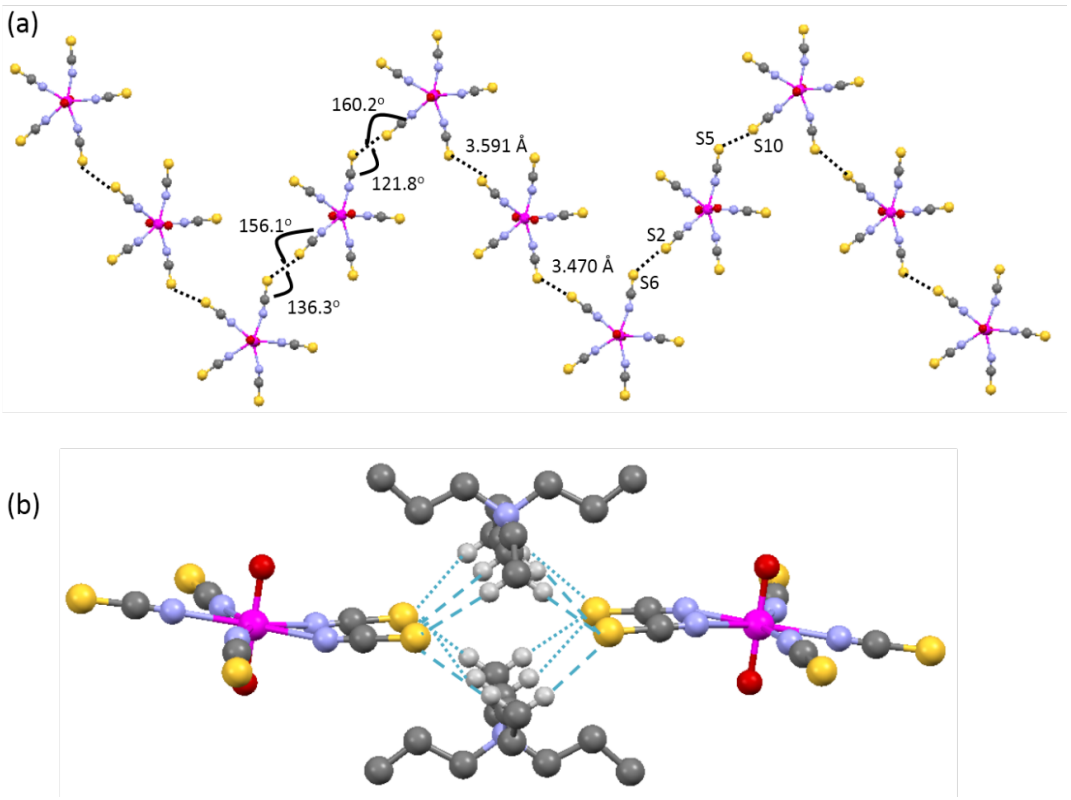

Figure 4.5. (a) Supramolecular structure of EtS highlighting the noncovalent S···S interactions (dotted black lines); (b) the S···H—C hydrogen bonding in ^{n}PrS (dotted blue lines). Colour code: U – pink; O – red; N – light blue; C – grey; S – yellow; H – light grey.

A further secondary interaction occurs between the C—H of the cation and the uranyl group, in line with the -yl groups acting as weak Lewis bases. In all the compounds of this series, except for ^{n}BuS, (2.2.2-crypt)NaS and (18-C-6)NaS, there are numerous short contacts with $d_{C\cdots O}$ between 3.0 and 3.5 Å; Figure 4.6 shows a specific example. These hydrogen bonding interactions are rather weak and do not perturb the U=O bond lengths. Indeed, in all the compounds, the U=O bond lengths are essentially identical to that in ^{n}BuS where there are no U=O···H—C close contacts (Table 4.1).

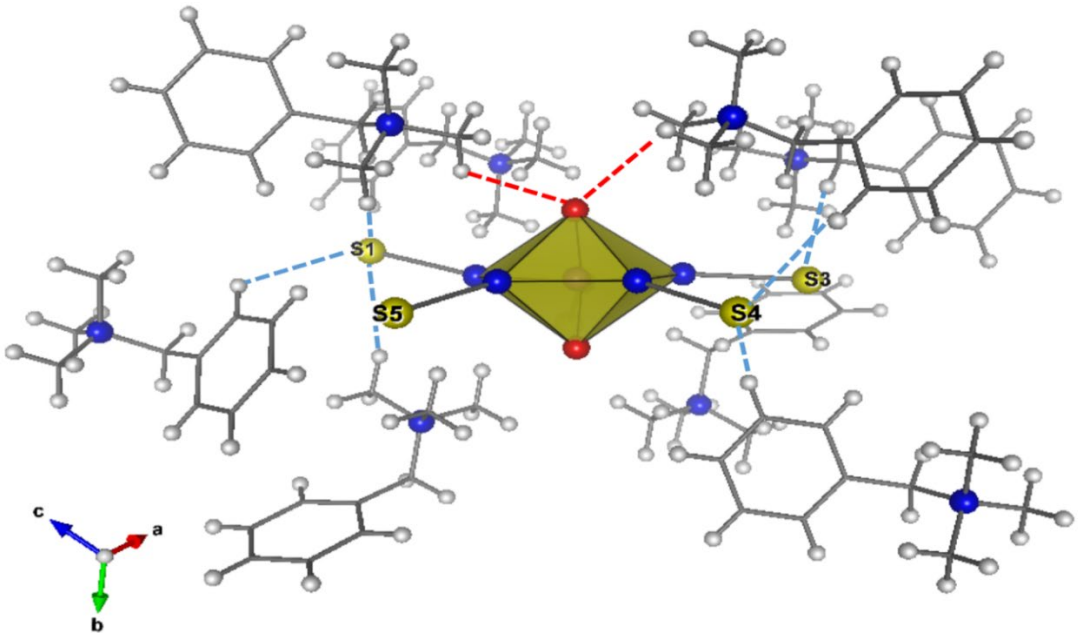

Figure 4.6. Supramolecular interactions in Me_3NBzS: dashed red lines U=O···H—C and dashed blue lines S···H—C interactions. Colour code: O – red; N – blue; S – yellow; H – light grey.

In the supramolecular structure of (2.2.2-crypt)NaS there are no S···S interactions, and this is most likely due to the steric effect of the three $[(2.2.2\text{-crypt})Na]^+$ ions that completely shield the uranyl complex, as clearly evidenced in the space-filling structure of Figure 4.7. The X-ray structure of $[(18\text{-C-6})Na]_3[UO_2(NCS)_5]$ is not of sufficient quality to comment upon metric parameters, but no S···S interactions are present.

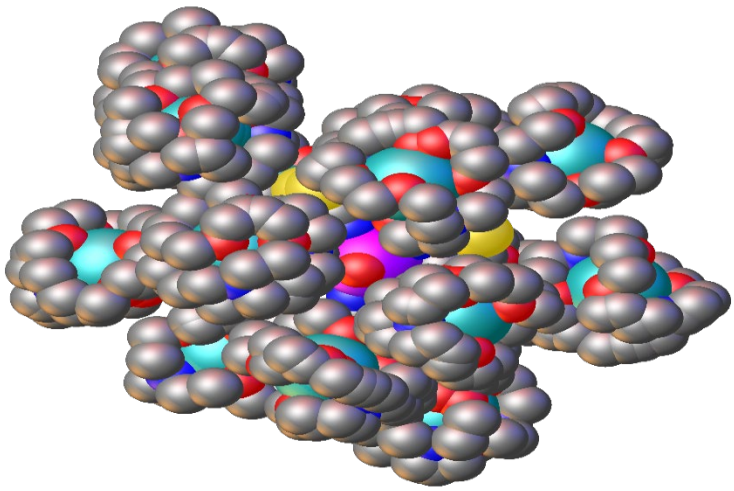

Figure 4.7. Space-filling view of $[(2.2.2\text{-crypt})Na]_3[UO_2(NCS)_5]$. Colour code: Na – light blue, S – yellow, N – blue, C – grey, O – red and U – purple. Uranyl axis is perpendicular to the page.

During one attempt for the synthesis of $[Ph_4P]_3[UO_2(NCS)_5]$ a few single crystals were obtained; however, X-ray diffraction showed them to be $[Ph_4P]_2[UO_2(NCS)_3(NO_3)]$. It was possible to increase the yield using the correct stoichiometry, albeit as a polymorph; but all syntheses towards the homoleptic thiocyanate complex were unsuccessful with the $[Ph_4P]^+$ cation. The molecular crystal structure of $[Ph_4P]_2[UO_2(NCS)_3(NO_3)]$ is shown in Figure 4.8, along with a packing diagram. The corresponding crystallographic data are listed in Appendix 3; while full list of bond lengths and angle is tabulated in Appendix 3.3 in the external CD source of this thesis.

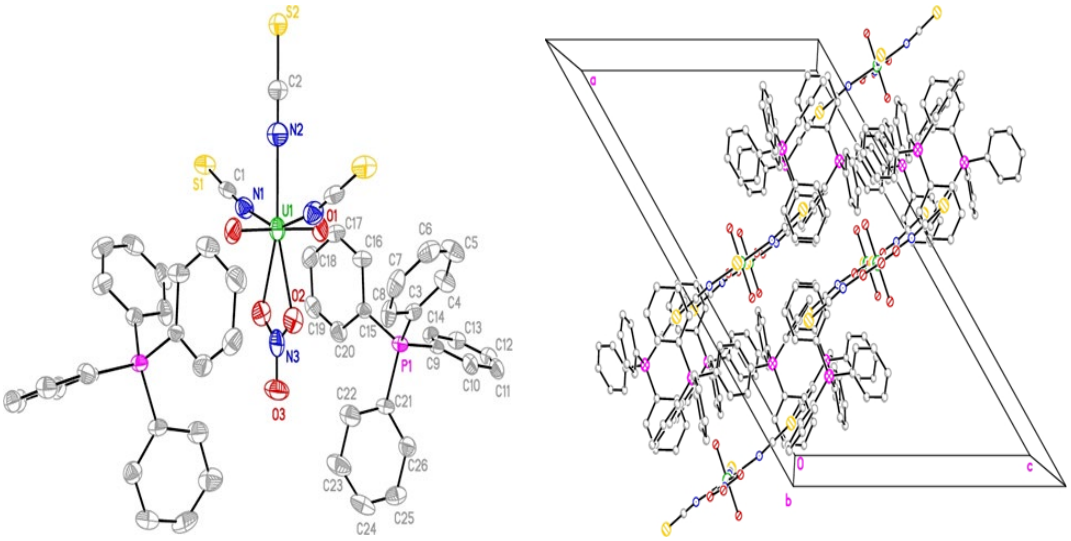

Figure 4.8. (a) Asymmetric unit of $[Ph_4P]_2[UO_2(NCS)_3(NO_3)]$, with atomic displacement parameters shown at 50% probability. (b) Packing diagram viewed down the crystallographic *b*-axis. Hydrogen atoms omitted for clarity.

In this compound, the bond lengths are similar to the homoleptic series described above (U=O 1.772(4) Å), with the exception that the U—N bond lengths are slightly shorter (U(1)—N(1) 2.412(8) and U(1)—N(2) 2.402(11) Å). The U—O bond length (2.503(7) Å) is typical for a nitrate ion coordinated in a bidentate fashion. There are no S···S close contacts in this compound and the dominant interactions are C—H···O hydrogen bonding to the nitrate ion ($d_{C\ldots O}$ = 3.237(10) Å) and longer C—H···S ($d_{C\ldots S}$ = 3.736(9) Å); the $[NCS]^-$ ion involved in this interaction is bent out of the UN_5 plane (0.307 Å; C(1)-N(1)-U(1) = 166.2(7)º) in comparison to the $[NCS]^-$ ion that does not show close contacts which is in the plane (C(2)-N(2)-U(1) = 180.0º), adding weight to the thesis that this weak hydrogen bonding is responsible for the disruption in the U—NCS coordination environment.

In an attempted reaction between uranyl nitrate, sodium thiocyanate and Me_3SnCl, the expected $[Me_3Sn]_3[UO_2(NCS)_5]$ species was not isolated, but instead a few single crystals of $[(UO_2)_2(SO_4)_2(H_2O)_4]\cdot 3H_2O$ were collected and characterized. The mechanism of the oxidation of $[NCS]^-$ to SO_4^{2-} is not completely clear, but there is some literature for oxidation of coordinated thiocyanate to sulfate.[41] Nevertheless the structure is α-uranyl sulfate, first determined in 1978,[42] and similar to the mineral Shumwayite,[43] $[(UO_2)_2(SO_4)_2]\cdot 5H_2O$. Here the previous refinement has been improved and so the crystal structure and a packing diagram are shown in Appendix 3 (Figure 7.24). There are no significant differences in the structural parameters from the previous report.

4.2.3 Structural Characterization of the $[R_4N]_3[UO_2(NCSe)_5]$ series

Following the same synthetic procedure for the RS series, four new uranyl selenocyanate complexes, corresponding to $[Me_4N]_3[UO_2(NCSe)_5].H_2O$ (MeSe), $[Et_4N]_4[UO_2(NCSe)_5][NCSe]$ (EtSe), $[^nPr_4N]_3[UO_2(NCSe)_5]$ (^{n}PrSe) and $[Et_3NBz]_4[UO_2(NCSe)_5]$ (Et_3NBzSe), have been synthesized. To date, the only other structurally characterized uranyl selenocyanate compound has been described by Walensky *et al.,*[44] when they reported on a tridentate salicylaldiminate uranyl complex of the $[NCSe]^-$ ion.

For these compounds, X-ray diffraction analysis showed the expected D_{5h} pentagonal bipyramidal coordination geometry around the uranyl ion, with five $[NCSe]^-$ anions coordinated via the N atom. The gross solid-state structures are the same as for the RS series and the crystal structures are collated in Figure 4.9, along with a picture of crystals of ^{n}PrSe. Pertinent metric parameters are listed in Table 4.2 and there are no significant differences in the series. The crystallographic data are listed in Appendix 3; while the full lists of bond lengths and angles are tabulated in Appendix 3.4-3.5 in the external CD source of this thesis.

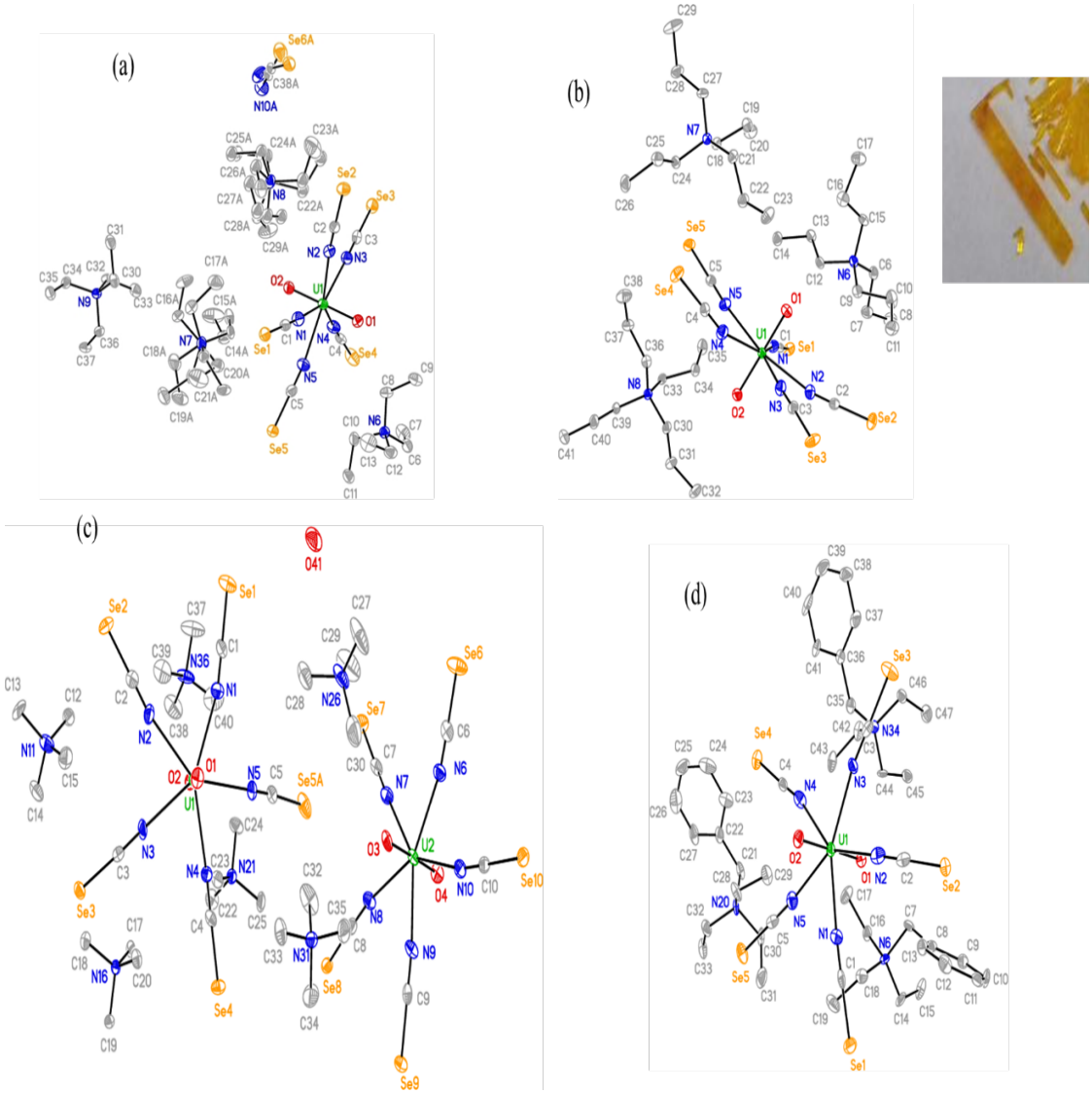

Figure 4.9. Asymmetric unit of (a) EtSe, (b) ^{n}PrSe (along with a picture of crystals), (c) MeSe, (d) Et_3NBzSe. Atomic displacement parameters are shown at 50% probability and hydrogen atoms are omitted for clarity.

Table 4.2. Selected average bond lengths (Å) and angles (°) for the RSe series.

Compound	U=O	U—N	N=C	C=Se	O=U=O	U—N=C	Se o.o.p[a]
MeSe	1.769(5) 1.763(5) 1.768(5) 1.764(5)	2.46(2)	1.15(3)	1.80(3)	179.0(3) 178.7(3)	162.0(6) to 179.0(7)	Se1 +0.609 Se2 +0.710 Se3 +0.114 Se4 +0.227 Se5A +1.552 Se5B +1.879 Se6 −1.145 Se7 +0.135 Se8 +0.249 Se9 −0.073 Se10 +0.018
EtSe	1.771(2)	2.46(1)	1.15(1)	1.79(1)	179.57(9)	171.0(2) to 177.6(3)	Se1 −0.164 Se2 +0.482 Se3 −0.258 Se4 +0.496 Se5 −0.481
^{n}PrSe	1.7632(19) 1.7690(19)	2.46(1)	1.15(1)	1.78(1)	179.48(10)	157.1(2) to 173.8(2)	Se1 +0.329 Se2 −0.673 Se3 −0.035 Se4 −0.638 Se5 −0.498
Et_3NBzSe	1.765(5) 1.756(5)	2.45(3)	1.14(3)	1.79(3)	179.5(3)	167.3(7) to 174.9(7)	Se1 +0.232 Se2 +0.499 Se3 +0.203 Se4 −0.158 Se5 −0.267

[a]Distance out of the UN_5 plane.

The supramolecular interactions in the RSe series are greater and more complex than in the RS series; in particular Se···Se interactions closer than the sum of the van der Waals

radii (3.64 Å)[38] are preponderant, as expected if the bonding is via a σ-hole scheme. Se···H—C interactions[45] and U=O···H—C weak hydrogen bonds are also prevalent.

The packing of MeSe is shown in Figure 4.10. There are a number of Se···Se distances which are all slightly longer than the van der Waals radii ($d_{Se\ldots Se}$ = 3.671(2) - 3.755(3) Å), but theory shows that these are stabilizing interactions (section 4.5). Interestingly Se(1)···Se(7), Se(4)···Se(8) and Se(3)···Se(9) form 1D sheets along the *c*-direction (Figure 4.10b), with C—H···Se weak hydrogen bonds ($d_{C\ldots Se}$ = 3.75 – 4.07 Å) linking the layers. C—H···O=U hydrogen bonding ($d_{C\ldots O}$ = 3.35 and 3.57 Å) interactions are also present, along with hydrogen bonding from the free water to U=O ($d_{O\ldots O}$ = 3.13 Å) and Se ($d_{O\ldots Se}$ = 3.79 Å). The water presumably comes adventitiously from the recrystallization process; notably all of these compounds have been prepared and recrystallized in air, so it may be that the smaller $[Me_4N]^+$ cation allows for the inclusion of water in this case. Irrespective of its source, the water molecule clearly engages in hydrogen bonding to the preference of C—H···O=U hydrogen bonding and possibly chalcogenide bonding.

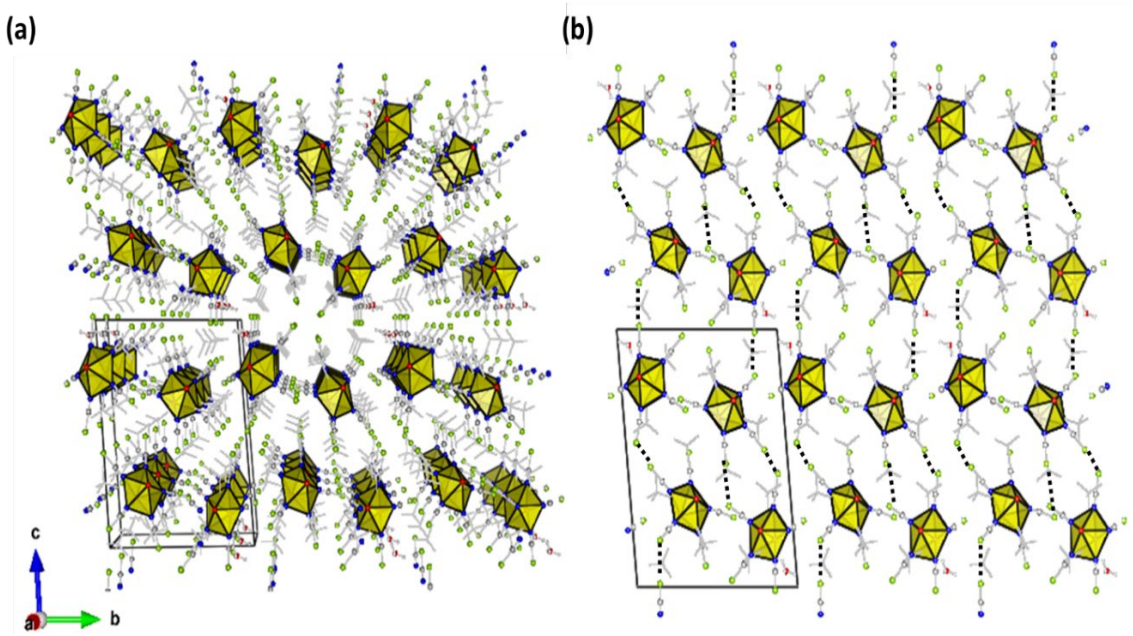

Figure 4.10. Packing of MeSe along the crystallographic *a*-axis. (a) A perspective view and (b) a view highlighting the Se···Se interactions (black dashed lines).

The packing of $[Et_4N]_4[UO_2(NCSe)_5][NCSe]$ (Figure 4.11) shows that the structure is a layer type where the cationic components sit between layers of uranyl ions, similarly to MeSe. There are a number of C—H···O=U hydrogen bonds ($d_{C\ldots O}$ = 3.175 - 3.300 Å) linking the layers, along with Se···H—C short contacts between a C—H of an ethyl group

and a Se atom of the coordinated and non-coordinated $[NCSe]^-$ anion ($d_{C\ldots Se}$ = 3.687(16) - 3.856(10); C–H…Se = 142 - 155°).[45] Present in the structure are also Se···Se close contacts (3.427(1) Å), between a selenium of a coordinated $[NCSe]^-$ ligand and the selenium of the free $[NCSe]^-$ fragment, that are shorter than the van der Waals radii (3.64 Å).[38]

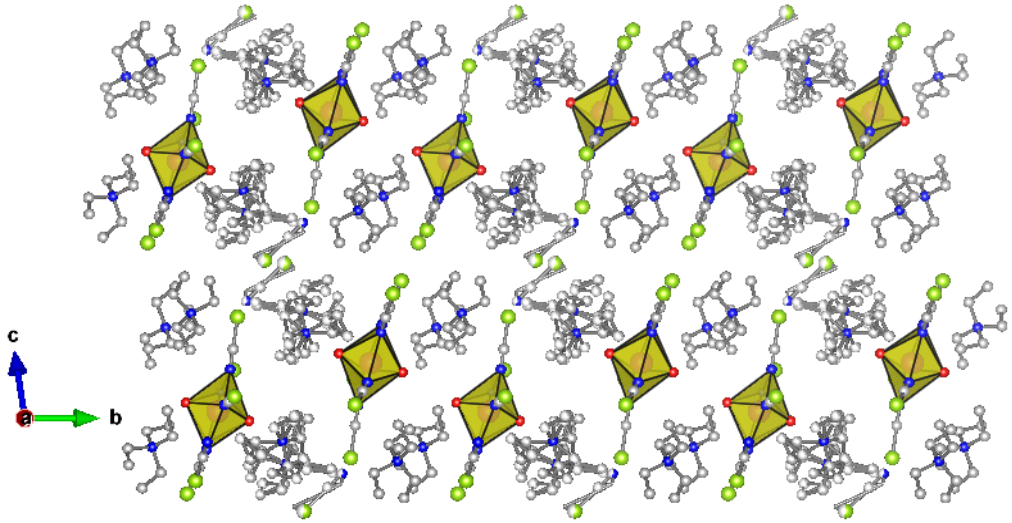

Figure 4.11. Packing diagram of EtSe viewed down the crystallographic *a*-axis.

^{n}PrSe shows no Se···Se interactions, probably due to the steric effect of the longer *n*-propyl arms that completely shield the uranyl complex, as illustrated in the space-filling structure of Figure 4.12. There are several Se···H—C ($d_{C\ldots Se}$ = 3.64 to 4.00 Å) and C—H···O=U ($d_{C\ldots U}$ = 3.175(3), 3.271(3) and 3.387(3) Å) close contacts that link the uranyl ions in layers. As in the previous series, it appears that the Se···H—C interactions bend the Se atom out of the UN_5 plane.

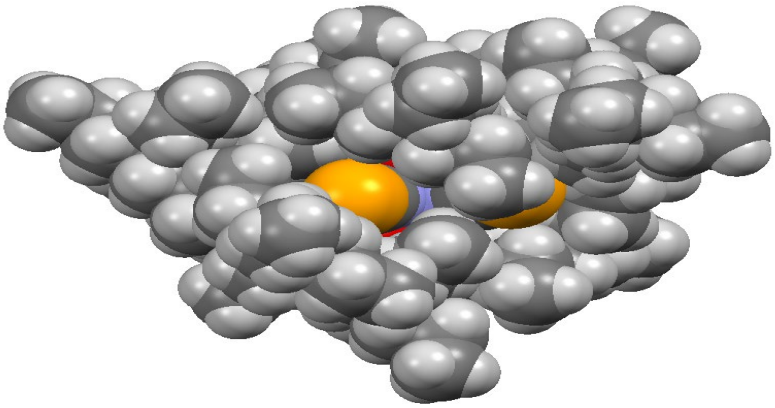

Figure 4.12. Space-filling view of ^{n}PrSe. Colour code: orange – Se; blue – N, dark grey – C; light gray – H; red – O. Uranyl axis is parallel to the page.

In Et_3NBzSe (Figure 4.13) there are a number of Se···Se close contacts ($d_{Se…Se}$ = 3.565(2) Å, θ_2-θ_1 = 20.7°; $d_{Se…Se}$ = 3.665(2) Å, θ_2-θ_1 = 66.1°). There are also multiple Se···H—C ($d_{C…Se}$ = 3.790(8) - 3.913(8) Å) and U=O···H—C ($d_{C…O}$ = 3.175(3), 3.271(3) and 3.387(3) Å) interactions.

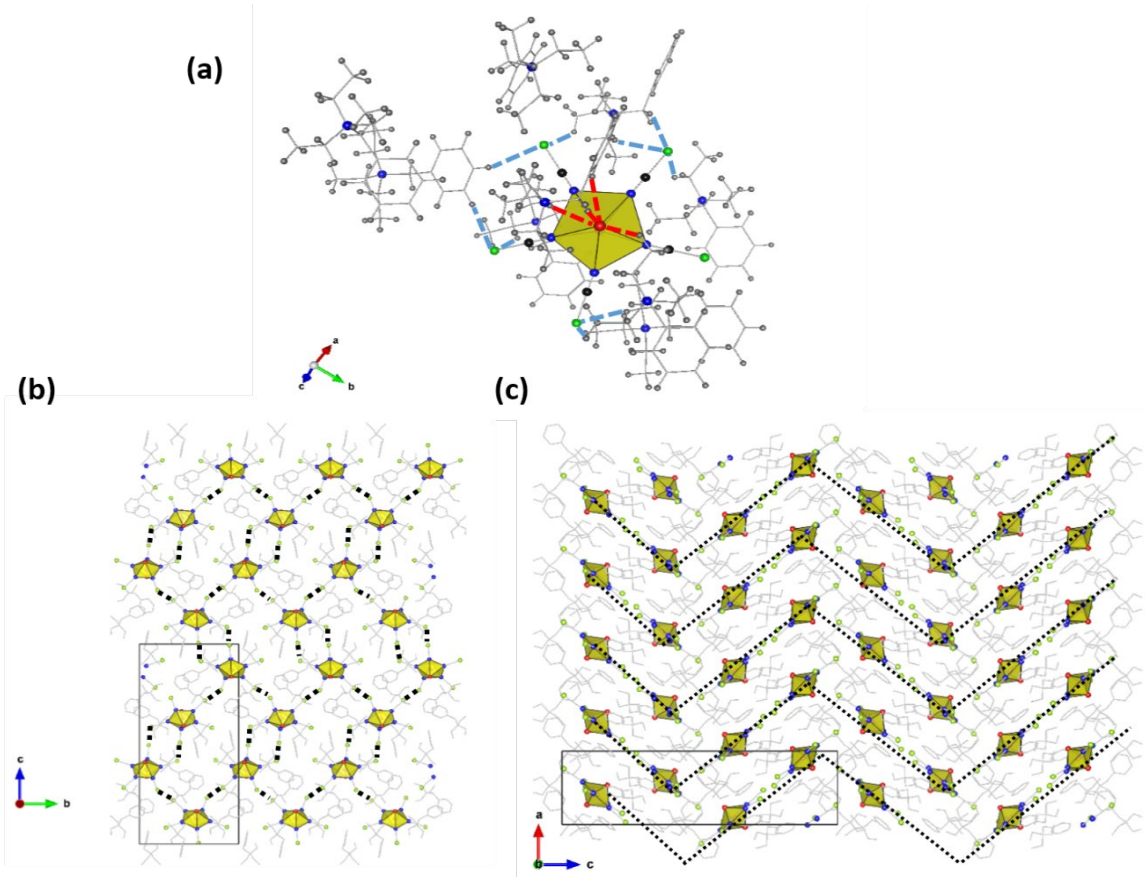

Figure 4.13. Supramolecular interactions in Et_3NBzSe: (a) a view of the C—H···O and C—H···Se interactions; (b) the packing along the crystallographic *a*-axis and (c) along the crystallographic *b*-axis highlighting the chalcogenide interactions (dashed black line Se···Se, dashed red line U=O···H—C and dashed blue line Se···H—C interactions).

4.2.4 Structural Comparisons Within the RS and RSe Series – ^{n}PrS/^{n}PrSe and Et_3NBzS/Et_3NBzSe

A summary of the types of interactions in these compounds is shown in Table 4.3 where there is a comparison of structural parameters between the two series with the same cation.

For the ^{n}Pr compounds, the immediate conclusion is that the chalcogenide···chalcogenide interactions are not present. Perhaps this is due to the non-

rigid nature of the *n*-propyl arms, such that S(e)···H—C and U=O···H—C interactions are more favoured over S(e)···S(e) interactions. The charge assisted hydrogen bonds to the uranyl ion are about the same length. Interestingly, the Et_3NBz couple shows that, as the polarizability of the chalcogenide atom increases, the type II interactions become preferred, even though these are isostructural pairs. The charge assisted hydrogen bond distances do not significantly change, indicating that perhaps these weak interactions are purely electrostatic in origin. A similar trend is observed for the S(e)···H—C interactions.

Table 4.3. Structural comparison between the $[UO_2(NCS)_5]^{3-}$ and $[UO_2(NCSe)_5]^{3-}$ compounds.

Compound	S···S	S···H—C	O···H—C	Compound	Se···Se	Se···H—C	O···H—C
MeS	type I	multiple	multiple	MeSe	type I type II	multiple	multiple
EtS	type II	multiple	multiple	EtSe	type II	multiple	multiple
^{n}PrS	no	multiple	multiple	^{n}PrSe	no	multiple	multiple
^{n}BuS	no	one	no	-			
Me_3BzNS	type I	multiple	multiple	-			
Et_3BzNS	type I	multiple	multiple	Et_3BzNSe	type II	multiple	multiple
(2.2.2-crypt)Na	no	no	no	-			
(18-C-6)Na	no	no	no	-			

A useful method for comparing solid state structures is via the Hirschfeld surfaces.[46] Thus this method has been employed to examine the noncovalent interactions present in the RS and RSe series, along with another example of homoleptic uranyl thiocyanate complex.[35] A quantitative analysis is shown in Figure 4.14. The chalcogenide···chalcogenide interactions decrease as the R group increases in size, but those with the R_3NBz group are type I for S and type II for Se. However, it is clear that the S(e)···H—C interactions are the largest noncovalent interactions present but also decrease in the same order. The structures of ^{n}BuS, (18-C-6)NaS and (2.2.2-crypt)NaS suffer of significant disorder and this has precluded the application of this method on these compounds.

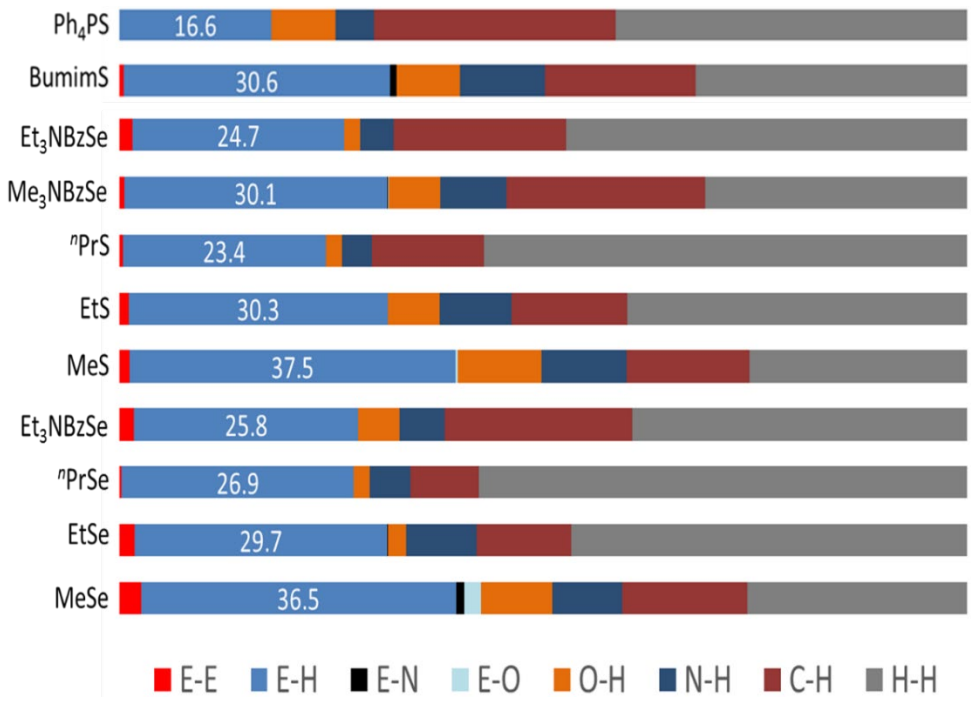

Figure 4.14. Quantitative Hirschfield analysis of RS and RSe series. BumimS (Bumim:1-butyl-3-methylimidazolium) from Ref. 35.

4.3 Spectroscopic Characterization

4.3.1 NMR Spectroscopy

^{1}H and ^{13}C{^{1}H} NMR spectra have been acquired for all the compounds but are not particularly informative; they clearly show the presence of the cations but not the quaternary carbon of the [NCS(e)]$^{-}$ ion, which is notoriously difficult[47] to observe by NMR spectroscopy. ^{77}Se{^{1}H} NMR spectra have been recorded for all the [NCSe]$^{-}$ complexes and are essentially identical in solution ($\delta_{Se} \approx -340$ ppm). For comparison, the Schiff's base complex of a uranyl selenocyanate shows a resonance at −357.3 ppm (in d_8-THF)[44] and the K[NCSe] salt, used to prepare the selenocyanate complexes, resonates at −314.2 ppm (in CD_3CN). Moreover, to investigate the strength of the Se···Se interactions in solution, ^{77}Se{^{1}H} NMR spectra have been acquired on solutions of Et_3NBzSe in MeCN at three different concentrations (4.02 mM, 10.3 mM and 25.3 mM). No variations in the ^{77}Se chemical shift have been observed, indicating the absence of Se···Se interactions and the existence of monomeric species in solution. It is worth noting that recently ^{125}Te NMR spectroscopy has been proved to be useful in studying the autoassociation of organo-ditelluride samples in solution, as consequence of tellurium-centered supramolecular interactions.[48]

Solid-state MAS ^{77}Se NMR spectra have also been recorded and are shown in Figure 4.15. None of the resonances are due to spinning side bands (as judged by variable spin rate measurements) so numerous δ_{iso} values indicate that there are different selenium environments in the solid. To date, solid state ^{77}Se NMR spectroscopy has not been extensively used for the characterization of chalcogenide interactions[49] and so it is difficult to quantify these Se···Se interactions, although there are changes from the starting K[NCSe] and ^{n}PrSe, which is the species that in the crystal structure does not show any Se···Se close contacts.

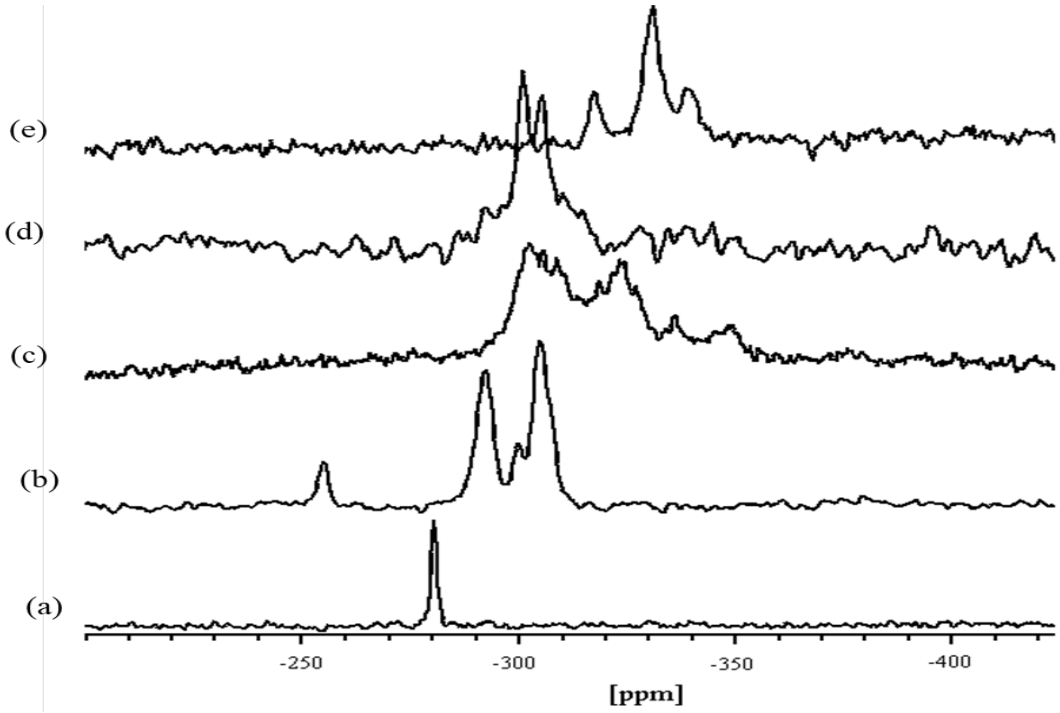

Figure 4.15. MAS ^{77}Se NMR spectra of (a) KNCSe; (b) MeSe; (c) EtSe; (d) ^{n}PrSe; (e) Et_3NBzSe at 20 kHz spin rate (except (c) at 17 kHz).

4.3.2 Vibrational Spectroscopy

Raman and IR spectra have been acquired on crushed single crystals for all of the new compounds and are shown in Figure 4.16. The principal vibrational modes, including the ones for MeS, EtS and ^{n}PrS,[34] are listed in Table 4.4.

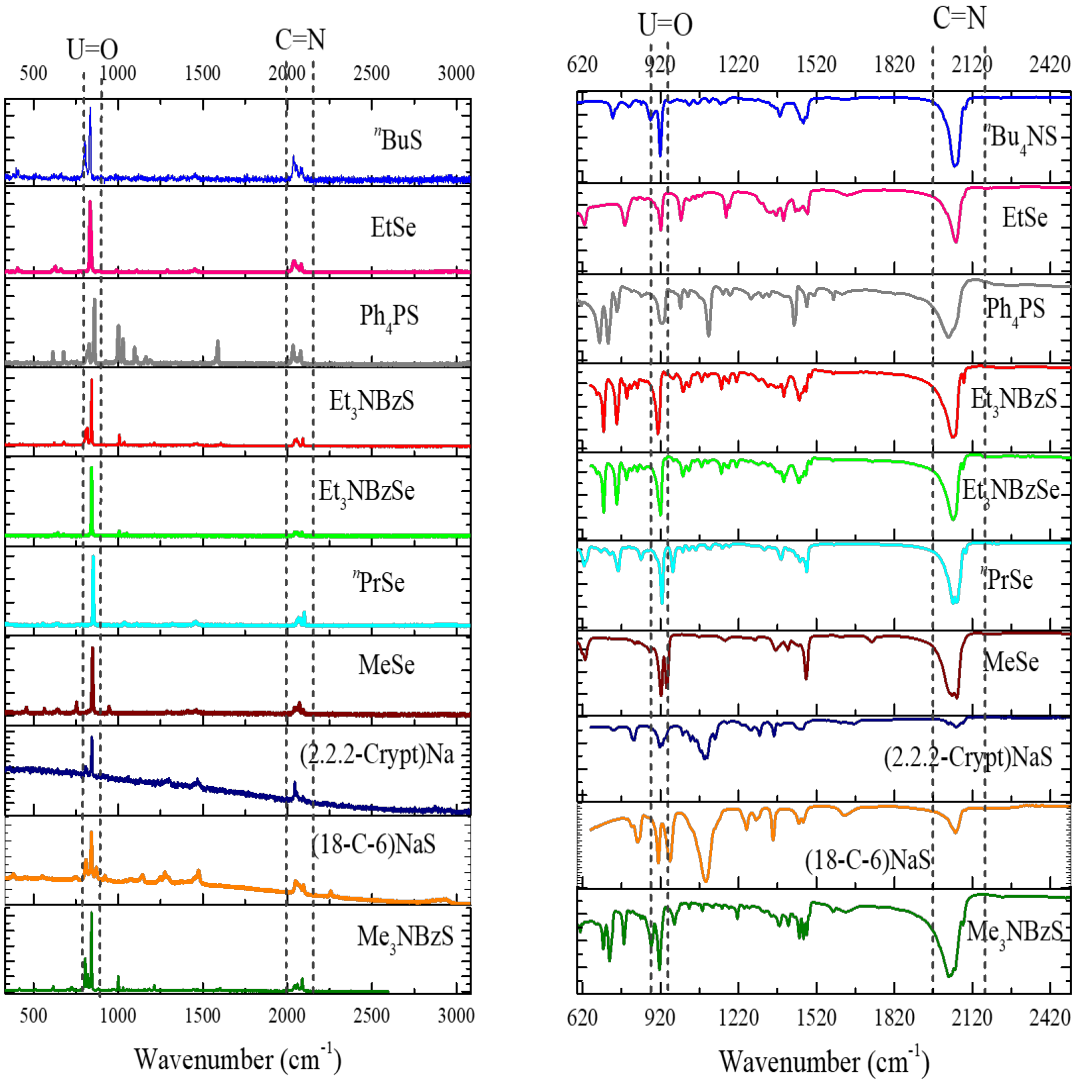

Figure 4.16. (left) IR spectra, (right) Raman spectra of all the new complexes. Black dashed lines highlight the bands due to the vibrational modes of the C=N and U=O groups.

The spectra clearly show the uranyl stretch and the N=C and C=S(e) bond stretches and in the series the bands attributable to these modes do not change significantly; the Raman active ν_1(U=O) symmetric stretching mode lies in a narrow range between 842 and 860 cm^{-1}, while the IR active ν_3(U=O) asymmetric stretching mode appears between 910 and 940 cm^{-1}. For comparison, the $[UO_2(H_2O)_5]^{2+}$ ion shows these bands at *ca.* 860-880 cm^{-1} and 930-960 cm^{-1} for the ν_1 and ν_3 modes respectively;[50] thus the presence of the donor atoms in the equatorial plane causes a red shift, as expected.

Table 4.4. Selected vibrational modes of the compounds of the RS and RSe series.

	U=O		N=C		C=S(e)	
Compound	ν_1 (cm^{-1})	ν_3 (cm^{-1})	IR (cm^{-1})	Raman (cm^{-1})	IR (cm^{-1})	Raman (cm^{-1})
MeS[a]	843	916	2042	2051, 2069, 2092	745	808, 816
EtS[a]	847	922	2063	2090, 2054, 2043	784	807
^{n}PrS[a]	848	922	2062, 2043	2050, 2061, 2100	759	813, 804
^{n}BuS	850	919	2052	2059, 2070,2099	736	808
Ph_4PS	860	928	2030	2041, 2048, 2062, 2090	779	823, 808
MeBzS	845	916	2042	2042, 2089	752	804, 812, 816
EtBzS	842	910	2029	2034, 2079	754	826, 819
(2.2.2-crypt)NaS	845	917	2055	2045, 2058, 2093	740	810
(18-C-6)NaS	842	911	2055	2047, 2096	832	808
MeSe	848	920	2060, 2042	2071, 2091	632	753
EtSe.NCSe	844	921	2056	2051, 2060, 2091	785	635, 672
^{n}PrSe	852	926	2060, 2046	2065, 2079, 2100	756	640
EtBzSe	842	920	2050	2056, 2087	736	631

[a] data taken from Ref. 34

As discussed in Chapter 3 for the compounds **U-MeCN** and **U-DMF** (section 3.2.1, equation 1-2), the ν_1 and ν_3 stretches modes of the triatomic $[UO_2]^{2+}$ system can be used to calculate the stretching force constants (k_1) and the interaction force constants (k_{12}),[51] where k_1 gives an indication of bond strength and k_{12} describes the interaction between the two –yl oxygen atoms. The values for all the samples are listed in Table 4.5, along

with the U=O bond lengths and the donor…acceptor bond lengths of the hydrogen bonding from the X-ray structures.

Table 4.5. Force constants, k_1, interaction force constants, k_{12}, U=O bond lengths and donor…acceptor bond lengths of the hydrogen bonding.

Compound	k_1 (mdyn/Å)	k_{12} (mdyn/Å)	$d_{U=O}$ (Å)	D…A (Å)
MeS[a]	6.84	−0.13	1.770(4)	3.21, 3.47
EtS[a]	6.91	−0.15	1.765(6)	3.00, 3.43, 3.51
^{n}PrS[a]	6.91	−0.14	1.747(5)	3.40, 3.49
^{n}BuS	6.92	−0.10	1.769(10) 1.759(9)	-
Ph_4PS	7.06	−0.09	1.767(6)	3.12, 3.35
MeNBzS	6.00	−0.12	1.778(3) 1.774(3)	3.20, 3.31
EtNBzS	6.78	−0.10	1.772(2) 1.773(2)	3.29, 3.36, 3.38, 3.44, 3.47, 3.57
(2.2.2-crypt)NaS	6.83	−0.11	1.799(2)	-
(18-C-6)NaS	6.74	−0.11	1.571(2)	-
MeSe	6.90	−0.13	1.763(5) 1.765(3)	3.13, 3.36, 3.57
EtSe.NCSe	6.88	−0.16	1.771(2)	3.17, 3.19, 3.29, 3.30
^{n}PrSe	6.98	−0.14	1.763(2) 1.769(2)	3.17, 3.27, 3.38, 3.52
EtNBzSe	6.86	−0.17	1.756(6) 1.765(5)	3.30, 3.31, 3.45, 3.50, 3.59

[a]structural data taken from Reference 34

Any changes in the values of k_1 and k_{12} must be due to differences in C—H···O=U hydrogen bonding, and it is possible to benchmark the data to the unperturbed U=O bond of ^{n}BuS compound, whose solid-state structure does not exhibit any hydrogen bonding. The force constants do not change significantly from the value in ^{n}BuS (k_1 = 6.92 mdyn/Å; range between 6.84 and 7.06 mdyn/Å) and there is no correlation to the donor…acceptor bond distances (Table 4.5), so the hydrogen bonding does not influence these parameters, as also observed by others.[28] There is however an increase in values of k_1 and k_{12} associated with the $[NCSe]^-$ compounds compared to the $[NCS]^-$ analogues, as shown by

the ^{n}PrS/^{n}PrSe (S: k_1 = 6.91 mdyn/Å, k_{12} = −0.14 mdyn/Å; Se: k_1 = 6.98 mdyn/Å, k_{12} = −0.14 mdyn/Å) and Et_3NBzS/Et_3NBzSe (S: k_1 = 6.78 mdyn/Å, k_{12} = −0.10 mdyn/Å; Se: k_1 = 6.86 mdyn/Å, k_{12} = −0.17 mdyn/Å) couples. The structural information (Table 4.5) showed no significant changes in donor…acceptor bond lengths, so this could be a manifestation of the different donor abilities of the coordinating ligands.[26a] It is noticeable that, to date, there are no other examples where these structural parameters have been used to study ligand equatorial bonding in the $[UO_2]^{2+}$ system.

4.3.3 Photoluminescence Spectroscopy

The electronic absorption spectra of the RS and RSe compounds have been acquired in MeCN solutions (Figure 4.17), where all noncovalent interactions break up and mononuclear species dominate, as already proved by ^{77}Se-NMR spectroscopy (section 4.3.1).

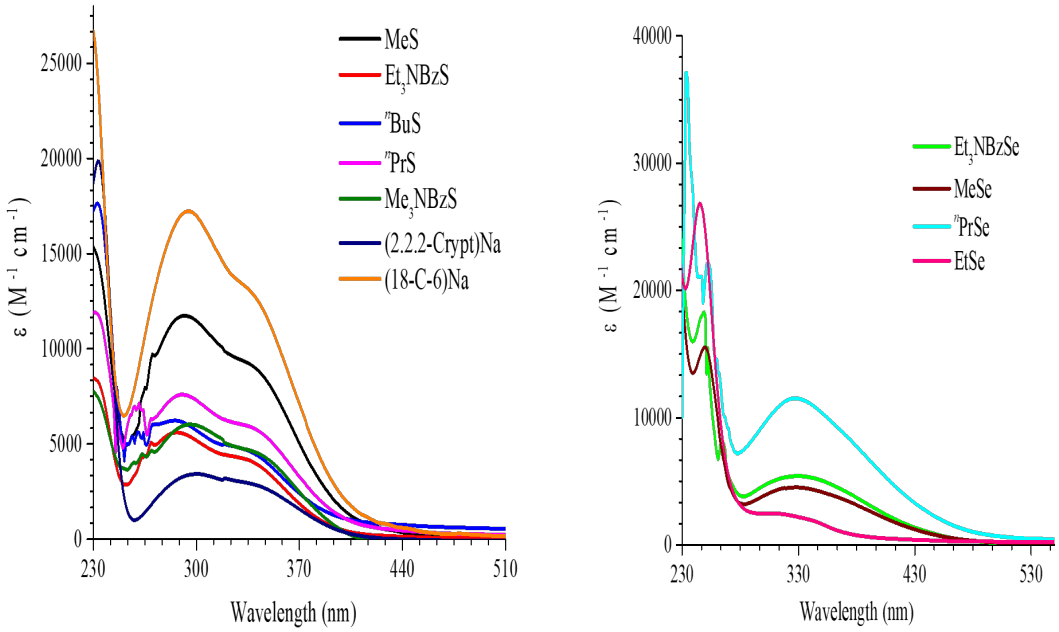

Figure 4.17. UV-vis absorption spectra of (left) the RS and (right) RSe complexes, measured at room temperature and at *ca.* 0.01 mM in MeCN.

These spectra display an intense band in the UV region ($\lambda_{max} \approx 230$ nm) assignable to a spin allowed ligand centred $\pi \rightarrow \pi^*$ transition within the thiocyanate or selenocyanate chromophore, as also observable in absorption spectra of solutions of Na[NCS] and K[NCSe] in MeCN. The broader bands at ≈ 290 and 340 nm can be attributed to $n \rightarrow \pi^*$ transitions based on the thiocyanate and selenocyanate chromophore, and their tails cover

the less intense vibronically coupled LMCT uranyl band, expected between 400 and 460 nm. However, this uranyl-based transition is observable in the solid-state excitation spectra of these compounds measured at low temperature (77 K). Selected examples, from the RS and RSe series, are shown in Figure 4.18, while the data for all the samples are listed in Table 4.6.

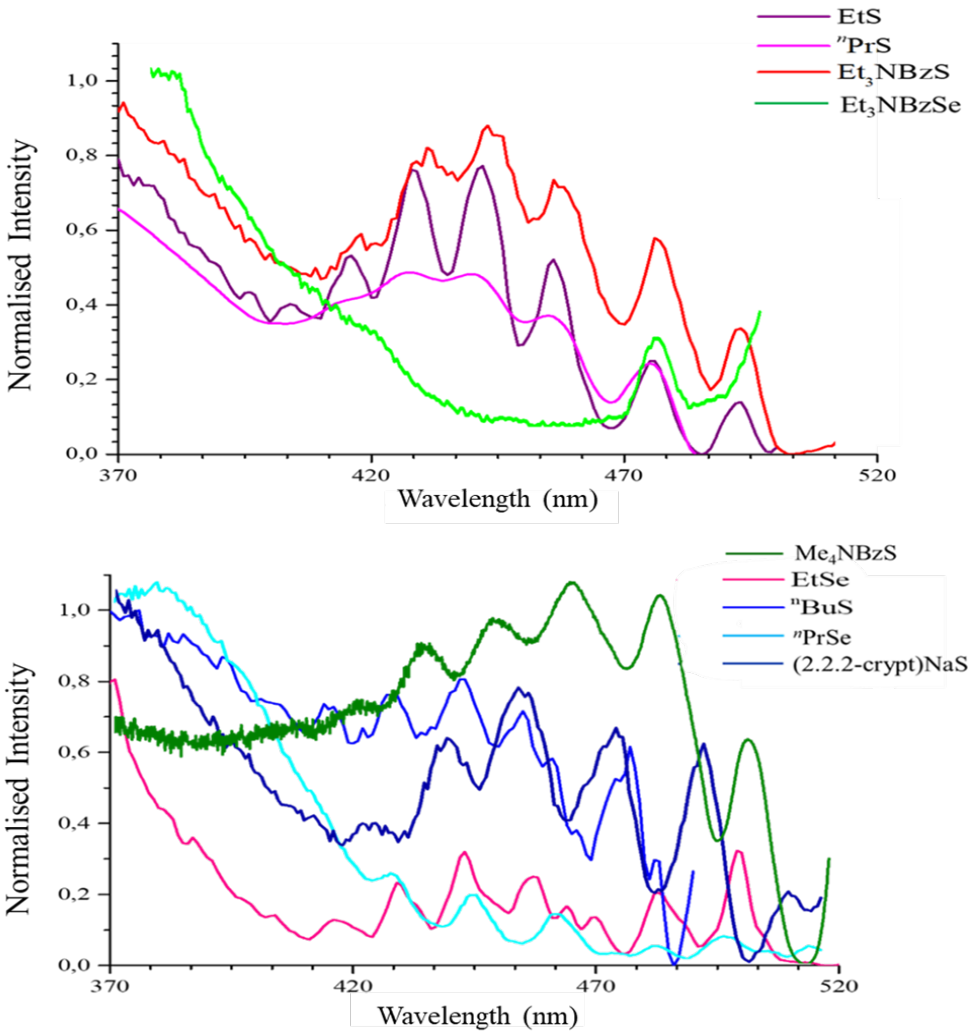

Figure 4.18. Solid-state excitation spectra of selected samples from the RS and RSe series. Spectra measured at 77 K (λ_{em} = 515 nm).

The emission and excitation spectra of the RS and RSe compounds have been recorded also at room temperature and both in solid state and solution, where mononuclear species dominate, and selected data are shown in Table 4.6. In the solution emission spectra (Figure 4.19) there are clear differences between the RS and RSe families; the $[NCS]^-$ ion is more electron donating than $[NCSe]^-$ and on par with the nitrate ion, thus the emission bands relative to the $[UO_2]^{2+}$ cation are at lower energy in the thiocyanate

samples than in the selenocyanate equivalents. The differences within each family are small and mainly due to changes in the vibronic coupling, and this is also observed in the room temperature solid state emission spectra (Figure 4.20). The room temperature emission spectra of (18-C-6)NaS and (2.2.2-crypt)NaS, both in solution and solid state, were much less intense and poorly resolved and for this reason have not been shown.

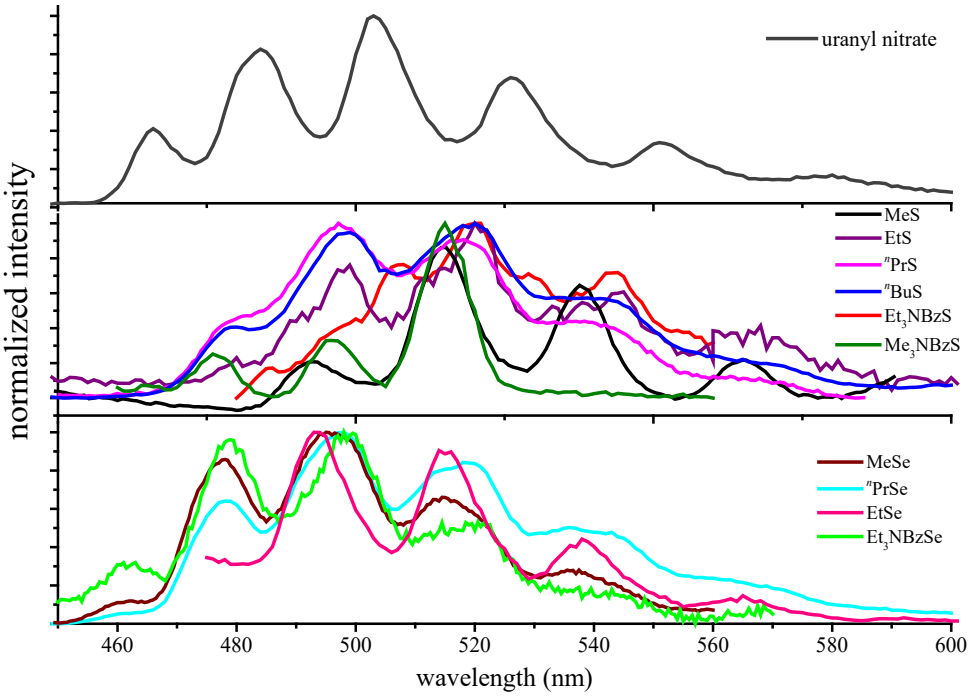

Figure 4.19. Room temperature emission spectra of RS and RSe compounds in MeCN solution, along with uranyl nitrate (λ_{ex} = 300 nm).

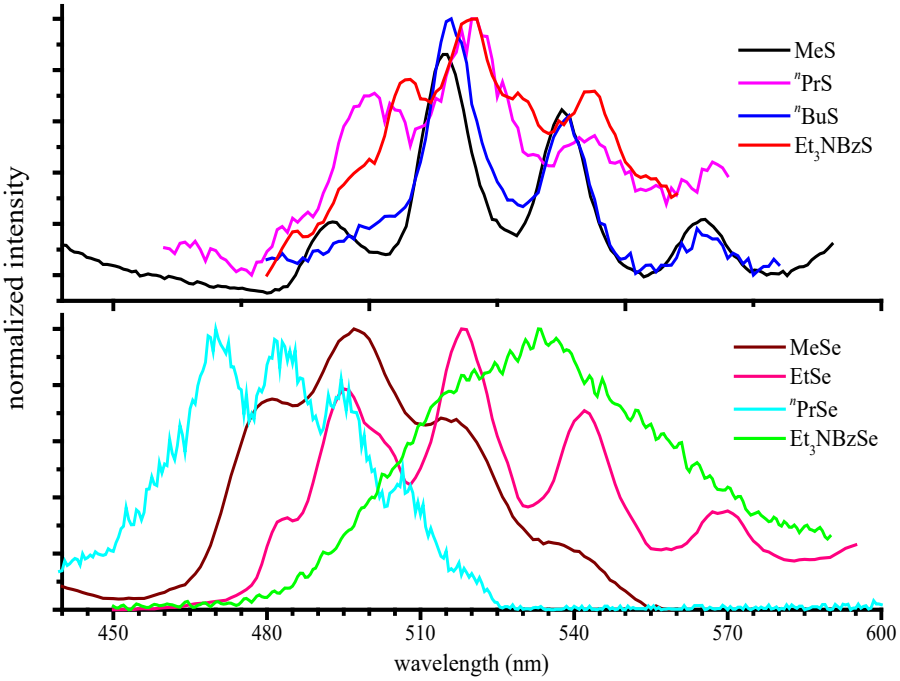

Figure 4.20. Room temperature emission spectra of RS and RSe in solid state (λ_{ex} = 300 nm).

In the room temperature emission spectra in solid state (Figure 4.20), there is a wider variation between the two families and again the thiocyanate complexes exhibit emission bands at lower energy compared to the selenocyanate equivalents.

Given the poor resolution of these spectra, photoluminescent properties of these compounds in the solid state have been subsequently examined at low temperature (77 K) and the results, including the measurements for (18-C-6)NaS and (2.2.2-crypt)NaS, are shown in Figure 4.21. For comparison the spectrum of uranyl nitrate was also acquired, and it is shown along with the other samples, while MeSe was the only compound that did not show any resolution enhancement.

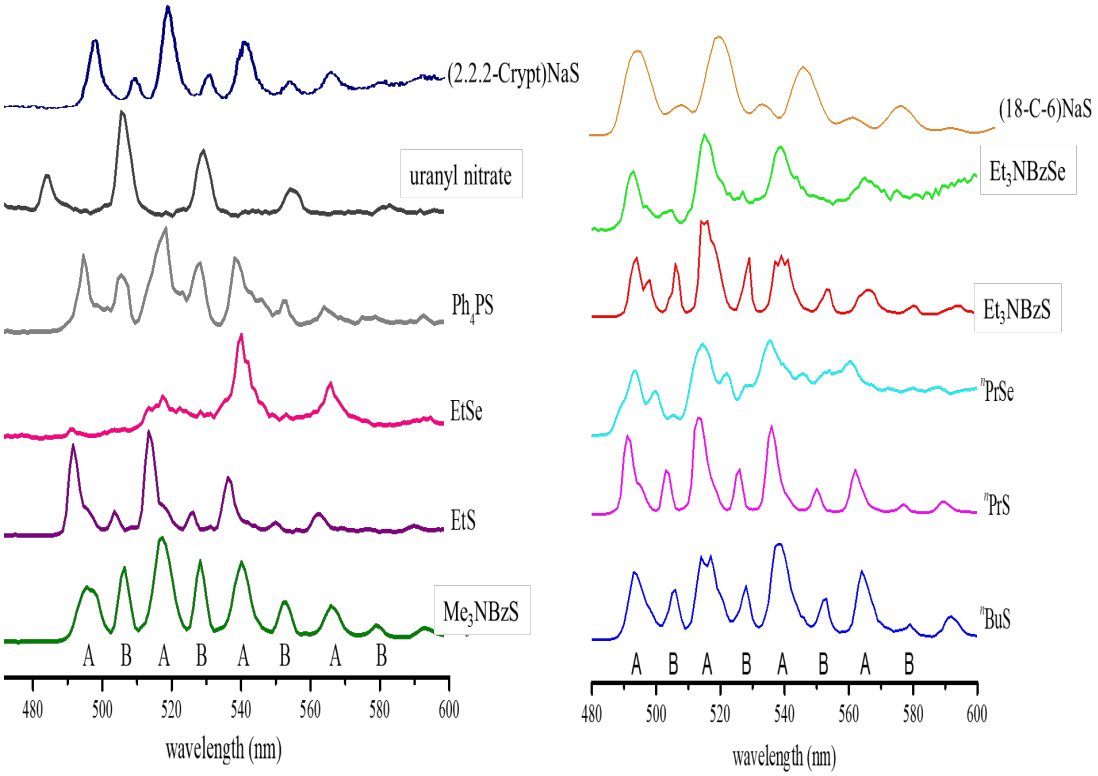

Figure 4.21. Emission spectra of RS and RSe samples, along with uranyl nitrate, in the solid state at 77 K (λ_{ex} = 340 nm).

Immediately apparent is the increase in resolution, to the point that additional weaker bands appear, and are labelled as set A and B. The weak bands of set B are separated from each other by a vibrational progression of *ca.* 850 cm^{-1} which is due to strong coupling to the ν_1(U=O) mode (as illustrated in Chapter 1, section 1.4.1), but the differences between set A and B are *ca.* 490 cm^{-1}. It is noteworthy that these additional bands were observed in the room temperature emission spectra of $[UO_2(NCS)_5]^{3-}$ in ionic liquids and ascribed to changes in the coordination environment. However, a close examination of the Raman spectra of the RS compounds shows a number of rather weak bands at 500 and 544 cm^{-1} due to the δ(NCS) mode,[52] so it appears that this can couple with the uranyl vibrational mode. Supporting this hypothesis is the smaller and weaker coupling at *ca.* 450 cm^{-1} in the RSe family which corresponds to the very weak δ(NCSe) vibrational bend at *ca.* 430 cm^{-1} in the Raman spectra (Figure 4.22).

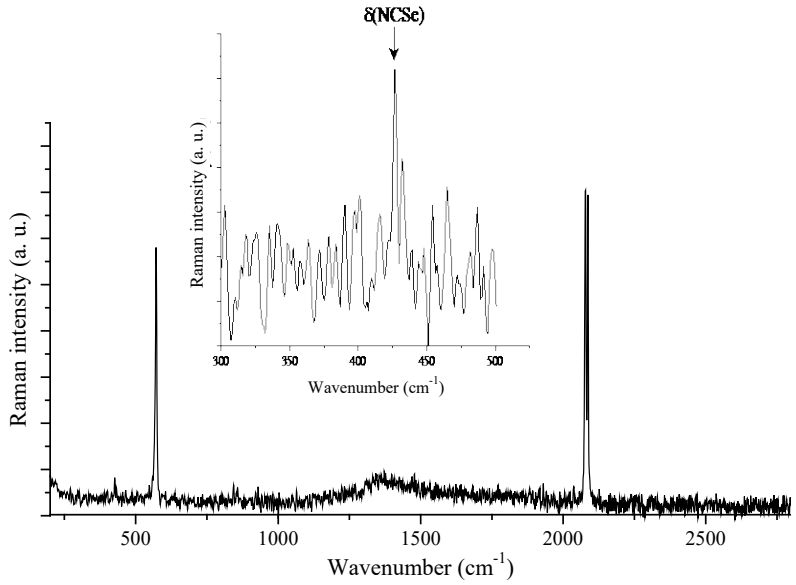

Figure 4.22. Raman spectrum of KNCSe. Insert shows the (NCSe) bending mode.

The only other mode that could couple is the U—N bend, but in U(IV) thiocyanates this comes at *ca.* 200 cm^{-1}, as seen in Chapter 2, section 2.2.10.[53] The differences between the RS and RSe families are not marked at low temperature.

Finally, the lifetimes of the emissions, both in the solid state and solution, have been measured for all the samples and are listed in Table 4.6. They vary substantially across the series and so no definitive conclusions can be drawn.

In summary, the spectroscopic data show small differences between the $[R_4N]_3[UO_2(NCS)_5]$ and $[R_4N]_3[UO_2(NCSe)_5]$ families, but they suggest that the C–H···O interactions are not sufficiently strong to perturb the electronic structure of the uranyl ion, while the consequences from chalcogenide interactions are not clearly observable.

Table 4.6. Photophysical properties of RS and RSe compounds at room temperature in MeCN and solid state; λ_{em} - emission wavelength of the most intense band; $E_{0\text{-}0}$ - energy of the first emission band; λ_{ex} - excitation wavelength of the most intense band, measured at 77 K.

Compound	solution				solid state			solid state (77 k)
	λ_{em} (nm)	$E_{0\text{-}0}$ (cm^{-1})	Vibronic progression (cm^{-1})	τ (μs) (χ^2)	λ_{em} (nm)	$E_{0\text{-}0}$ (cm^{-1})	τ (μs) (χ^2)	λ_{ex} (nm)
MeS	497	20,155	869	1.13 (0.94)	515	19,420	84.4 (1.17)	460
EtS	520	20,072	846	1.40 (1.02)	524	19,086	20.7 (1.28)	441
^{n}PrS	497	20,155	805	0.644 (1.88)	520	19,244	83.0 (1.66)	441
^{n}BuS	520	19,244	814	1.46 (1.11)	526	19,013	30.5 (1.36)	443
Me_3BzS	527	18,988	-	1.15 (1.37)	510	19,610	84.3 (1.14)	460
Et_3BzS	520	19,244	814	1.22 (1.01)	521	19,196	30.4 (1.36)	476
Ph_4PS	496	20,175	810	1.50 (1.22)	521	19,196	82.4 (1.13)	446
MeSe	496	20,175	749	3.47 (1.88)	497	20,155	83.0 (1.07)	428
EtSe	514	20,267	872	1.30 (1.40)	518	19,318	26.0 (1.23)	443
^{n}PrSe	498	20,082	836	1.50 (1.85)	515	19,420	38.0 (1.18)	429
Et_3BzSe	499	20,042	808	1.55 (1,09)	533	18,775	44.7 (1.41)	465
(18-C-6)NaS	-	-	-	-	515	20,284		429
(2.2.2-crypt)NaS	-	-	-	-	514	20,244		444

4.4 Electrochemistry Study on EtS and EtSe

4.4.1 Spectroelectrochemical Measurements on EtS

To accurately investigate the redox properties of the uranyl thiocyanate ion, spectroelectrochemistry (SEC) measurements have been conducted. It has been previously reported that the redox behaviour of this ion is rather difficult to study by conventional cyclic voltammetry (CV);[54] however, SEC[55] has proven to be more useful for thiocyanate systems as the *ν*(C=N) and *ν*(C=S) frequencies in the IR spectrum and the intraligand π-π^* and n-π^* transitions in the electronic absorption spectrum are sensitive parameters. In addition, the redox system U(VI)/U(V)/U(IV) can be examined

monitoring the vis-NIR region of the electronic absorption spectrum, where the energy of the *f-f* transitions is diagnostic of the oxidation state of the uranium ion, as discussed in Chapter 1 (section 1.4).

Thus, in collaboration with Prof. Frantisek Hartl from the University of Reading, a SEC study on EtS, as example of the RS series, has been carried out using a combination of Thin-Layer Cyclic Voltammetry (TLCV) and FTIR spectroscopy. The measurements were performed at 293 K, with controlled potential electrolysis and in anhydrous MeCN solutions, containing [^{n}Bu$_4$N][PF$_6$] (TBAH) (~ 0.1 M) as supporting electrolyte. Moreover, the characteristics of the cell were the same as for the electrochemistry measurements performed on [Et$_4$N]$_4$[U(NCS)$_8$] and Cs$_5$[U(NCS)$_9$][NCS], which have been discussed in Chapter 3 (experimental section).

For the determination of $E_{p,c}$ of $[UO_2(NCS)_5]^{3-}$, decamethyl ferrocene (Fc^*) was used as internal standard, along with ferrocene; indeed, it has a standard redox potential not particularly negative (−0.48 V *vs* Fc/Fc^+) and so it does not cover the cathodic wave of $[UO_2(NCS)_5]^{3-}$, which is −1.45 V (*vs* Fc/Fc^+) from conventional CV.[54] In this way, the reduction potential of $[UO_2(NCS)_5]^{3-}$ was determined to be −1.43 V (*vs* Fc/Fc^+) (yellow curve in Figure 4.23, left). Subsequently, using only ferrocene as internal standard, the anodic wave of $[UO_2(NCS)_5]^{3-}$ was found at 0.21 V (*vs* Fc/Fc^+) (blue curve in Figure 4.23, left).

The changes in the vibrational frequencies of ν(C=N) and ν(C=S) were monitored during the redox processes and the one of ν(C=N), accompanying the reduction step, is shown in Figure 4.23 (right).

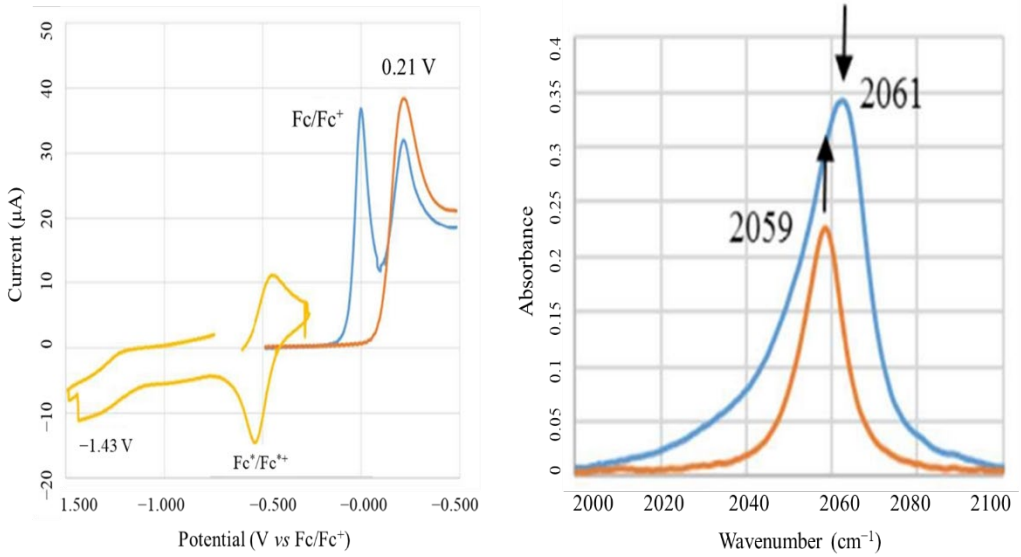

Figure 4.23. (left) Thin-layer cyclic voltammogram of complex $[Et_4N]_3[UO_2(NCS)_5]$ (*vs* Fc/Fc^+) determined in MeCN at 293 K, with ~0.1 M [^{n}Bu$_4$N][PF$_6$] as supporting electrolyte (scan rate = 2 mV s^{-1}). (right) IR spectral changes in the ν(C=N) region accompanying the one-electron reduction of $[Et_4N]_3[UO_2(NCS)_5]$ in MeCN/TBAH at 293 K within an OTTLE cell. Blue spectrum: before the reduction; orange spectrum: after the reduction.

The irreversible cathodic wave at $E_{p,c} = -1.43$ V (*vs* Fc/Fc^+) is ascribed to the unstable $[UO_2]^{2+}/[UO_2]^+$ redox couple. In turn, IR spectroelectrochemical monitoring (Figure 4.23, right) displays that, during the reduction process, the ν(N=C) band of the uranyl thiocyanate complex is replaced by a new band at 2059 cm^{-1} which belongs to free $[NCS]^-$, as independently confirmed by the IR spectrum of Na[NCS] in MeCN. Therefore, the addition of one electron to the uranyl cation causes the dissociation of all the π-donors $[NCS]^-$ ligands and decomposition of the complex. The putative $1e^-$ reduced uranyl(V) species $[Et_4N]_4[UO_2(NCS)_5]$ would be predicted to be quite unstable as it is well established that good π-donors and/or sterically bulky groups in the equatorial plane are required to stabilize this unusual oxidation state;[56,57] although, there is evidence for a kinetic stabilization of the $[UO_2]^+$ ion in ionic liquids.[58]

In the voltammogram (Figure 4.23, blue line), the irreversible oxidation at $E_{p,a} = +0.21$ V (*vs* Fc/Fc^+) must be $[NCS]^-$ based, since the metal is in its highest oxidation state. Therefore, also during the oxidation process, the complex $[UO_2(NCS)_5]^{3-}$ rapidly decomposes losing $[NCS]_x$; moreover, a yellow precipitate was found at the bottom of the electrochemistry cell after the oxidation process.

These electrochemistry results suggest that, in this system, the HOMO is based on the $[NCS]^-$ ligands and the LUMO is principally placed on the metal; this has also been previously confirmed by DFT calculations.[54]

Subsequently, under the same SEC conditions, the oxidation behaviour of EtS has been examined in the presence of three equivalents of the π-acceptor bipy ligand and the changes in the vibrational frequencies of ν(C=N) and ν(C=S) have been monitored (Figure 4.24).

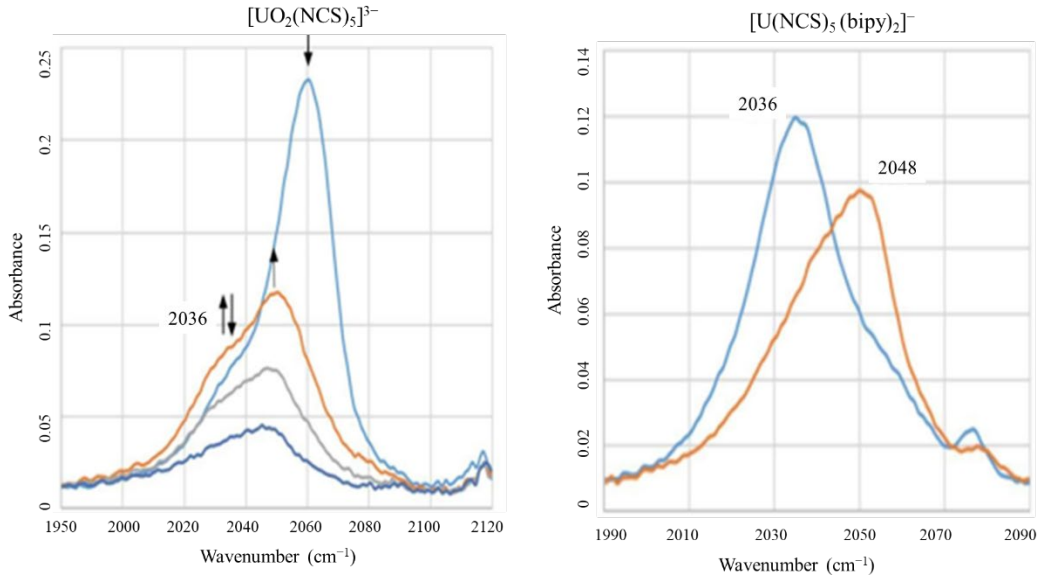

Figure 4.24. (Left) IR spectral changes in the ν(C=N) region accompanying the oxidation of $[Et_4N]_3[UO_2(NCS)_5]$ in MeCN/TBAH with three equivalents of bipy added to the electrolyte, at 293 K and within an OTTLE cell. Blue spectrum: before the oxidation; orange spectrum: after the oxidation. (Right) IR spectral changes in the ν(C=N) region accompanying the oxidation of $[U(NCS)_5(bipy)_2]^-$ in MeCN/TBAH, at 293 K and within an OTTLE cell. Blue spectrum: before the oxidation; orange spectrum: after the oxidation. The band at 2048 cm^{-1} corresponds to $[U(NCS)_8]^{4-}$.

In the presence of bipy, a new species with a ν(C=N) band at 2036 cm^{-1} is initially generated (Figure 4.24, left), which belongs to the uranium(IV) complex $[U(NCS)_5(bipy)_2]^-$.[59] Under further oxidation, this intermediate band decays and is replaced by the ν(C=N) band of $[U(NCS)_8]^{4-}$ at 2048 cm^{-1} (Figure 4.24, right), indicating that the bipy ligands dissociate completely. As expected, the coordination of the π-acceptor bipy ligand weakens significantly upon the oxidation, which is again ligand-based with the metal in its highest oxidation state. It is very interesting that a ligand-based

oxidation triggers a metal-based reduction, U(VI) → U(IV). It is well-known[60] that the transient one-electron oxidized $[U(V)O_2]^+$ species undergo a disproportionation reaction to form $[U(IV)O_2]$ and $[U(VI)O_2]^{2+}$. It is also possible that the $[UO_2]^{2+}$ cation releases molecular oxygen (gas bubbles were also observed at the Pt minigrid electrode in the OTTLE cell), and the U(IV) ion can be stabilized by the bipy/$[NCS]^-$ and ultimately only by $[NCS]^-$ ligands. Equation 7 summarizes the oxidation steps of the ion $[UO_2(NCS)_5]^{3-}$, with 3 equivalents of bipy added to the supporting electrolyte.

$$[UO_2(NCS)_5]^{3-} \xrightarrow[+\,bipy]{-\,e^-} [UO_2(NCS)_5(bipy)_2]^- \xrightarrow{-\,e^-} [U(NCS)_8]^{4-} + O_2 \qquad (7)$$

ν(C=N) at 2061 cm^{-1} | ν(C=N) at 2036 cm^{-1} | ν(C=N) at 2048 cm^{-1}

4.4.2 Cyclic Voltammetry Measurements on EtSe

In order to determine the redox potentials of the uranyl selenocyanate ion, $[UO_2(NCSe)_5]^{3-}$, EtSe has been studied by electrochemistry. Conventional CV of a solution of EtSe in MeCN (Figure 4.25), containing $[^nBu_4N][BPh_4]$ (0.1 M) as supporting electrolyte, shows an irreversible cathodic wave at $E_{p,c} = -0.95$ V (*vs* Fc/Fc^+) ascribed to the unstable $[UO_2]^{2+}/[UO_2]^+$ redox couple, in line with some known formal reduction potentials of the U(VI)/U(V) semicouple listed in Table 4.7. As observed for the thiocyanate equivalent (section 4.3.1), the production of the unstable $[UO_2]^+$ species would manifest itself in an irreversible reduction, which was indeed observed. Observable in this voltammogram is also an irreversible oxidation at $E_{p,a} = +0.09$ V (*vs* Fc/Fc^+) which, given that the metal is in its highest oxidation state, must be $[NCSe]^-$ based.

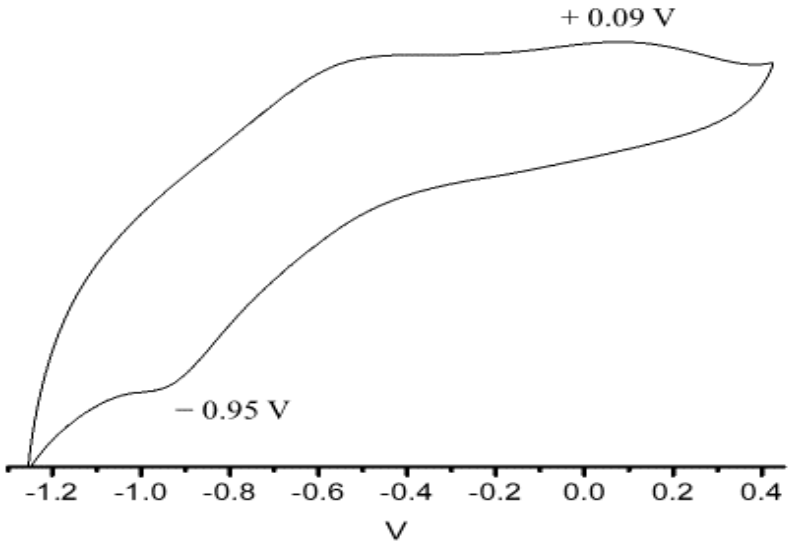

Figure 4.25. Cyclic voltammogram of EtSe *vs* Fc/Fc^+ in MeCN at 293 K, with 0.1 M $[^nBu_4N][BPh_4]$ as supporting electrolyte (scan rate = 0.1 V s^{-1}).

Table 4.7 lists formal reduction potentials for the U(VI)/U(V) semicouple of selected uranyl complexes, measured against ferrocene/ferrocenium.

Table 4.7. Formal redox half potentials (*vs* Fc/Fc^+) for the U(VI)/U(V) couple of selected uranyl complexes; $salmnt^{(Et2N)2}$ = 2,3-bis[(4-diethylamino-2-hydroxobenzylidene)amino]but-2-enedinitrile, salen = *N,N′*-disalicylidene-1,2-ethylenediaminate and salophen = *N,N′*-disalicylidene-1,2-phenylenediaminate.

Complex	E/V *vs* $[(C_5H_5)_2Fe]/Fe^+$	Ref
	$[UO_2]^{2+}/[UO_2]^+$	
$[UO_2(NCSe)_5]^{3-}$	−0.95	This work
$[UO_2(NCS)_5]^{3-}$	−1.45	54
$[UO_2(OH)_5]^{3-}$	−1.11	61
$[UO_2Cl_4]^{2-}$	−0.24	61
$[UO_2(salmnt^{(Et2N)2}(py))]$	−1.81	56
$[UO_2(salen(py))]$	−1.67	62
$[UO_2(salophen)(py)]$	−1.63	62

Conventional CV of a solution of $[UO_2(NCS)_5]^{3-}$ in MeCN gives a formal reduction potential of −1.45 V (*vs* Fc/Fc^+),[54] which is more negative compared to −0.95 V (*vs*

Fc/Fc^+) of $[UO_2(NCSe)_5]^{3-}$. This is reasonable considering that $[NCS]^-$ is more electron donating than $[NCSe]^-$ and so the $[UO_2]^{2+}$ cation is more difficult to reduce in $[UO_2(NCS)_5]^{3-}$ than in $[UO_2(NCSe)_5]^{3-}$. Instead, the less negative reduction potential of $[UO_2Cl_4]^{2-}$, compared to the other examples, is explainable given the presence of strong π donors chloride ligands, which are necessary to stabilize the $[UO_2]^+$ species.

4.5 DFT calculations

To deepen the understanding of the noncovalent interactions in these species, DFT calculations have been performed by Dr. James A. Platts from Cardiff University. Molecular Electrostatic Potential (MEP), Atoms-in-Molecules (AIM) and Natural Bond Orbital (NBO) derived properties have been chosen to characterize U=O···H—C, Se···H—C and chalcogenide interactions in molecules and dimers selected from the crystal structures of the complexes belonging to the RS and RSe families. Supramolecular calculations of energy would be dominated by charge-charge interactions and therefore they have not been tested.

4.5.1 Chalcogenide Interactions

In order to study the Se···Se interactions in $[Et_4N]_4[UO_2(NCSe)_5][NCSe]$, where the Se···Se distances are substantially shorter than the van der Waals radii, the presence of a σ-hole on Se has been hypothesized. Figure 4.26 shows the molecular electrostatic potential projected onto the 0.001 au isodensity surface for $[UO_2(NCS)_5]^{3-}$ (top) and $[UO_2(NCSe)_5]^{3-}$ (bottom).

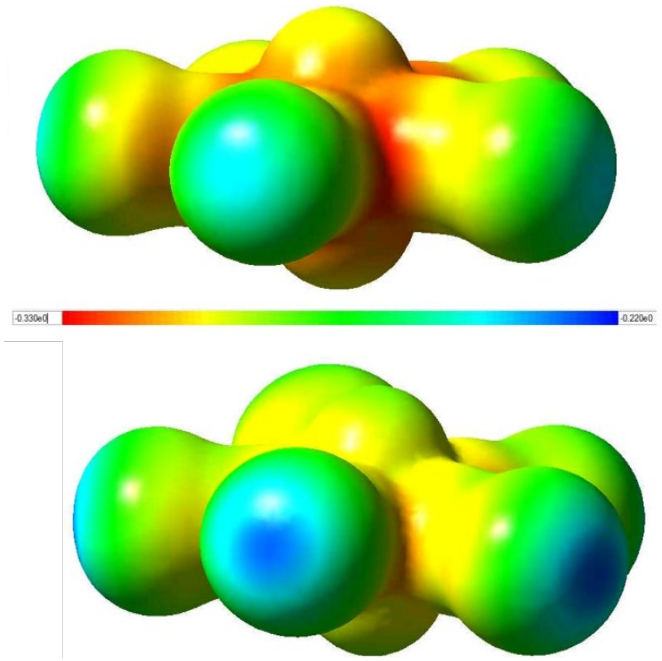

Figure 4.26. Molecular electrostatic potential projected onto the 0.001 au isodensity surface for $[UO_2(NCS)_5]^{3-}$ (top) and $[UO_2(NCSe)_5]^{3-}$ (bottom).

The overall negative charge of each complex means that the MEP is negative across the entire surface, although the plots show regions of relative electron depletion (*i.e.* a σ-hole) on both S and Se, with the hole more pronounced on Se (−0.231 au) than on S (−0.246 au). There are also small differences on the –yl oxygens and this is in line with the different electron donating strength of the ligands, as already seen from the photoluminescence spectroscopic measurements and force constant values.

DFT calculations have been performed on the dimers of $[UO_2(NCSe)_5]^{3-}$ from MeSe and on the complex $[UO_2(NCSe)_5]^{3-}$ with a free $[NCSe]^-$ fragment extracted from EtSe, as these give representative examples of the weak Se···Se interactions present in the RSe series. NBO analysis indicates that, in the dimers extracted from MeSe, the major interactions are donations from a Se lone pair of a coordinated $[NCSe]^-$ to a C=Se σ^* orbital on another $[NCSe]^-$ moiety (1.94 kcal/mol and 0.58 kcal/mol); instead, in the dimer extracted from EtSe, donations occur from a Se lone pair of the coordinated $[NCSe]^-$ to the C=Se σ^* orbital of the free $[NCSe]^-$ (2.94 kcal/mol) and from the Se lone pair of the free $[NCSe]^-$ to the C=Se σ^* orbital of a coordinated $[NCSe]^-$ (2.20 kcal/mol). Figure 4.27 shows the orbitals involved for the chalcogenide interactions in EtSe.

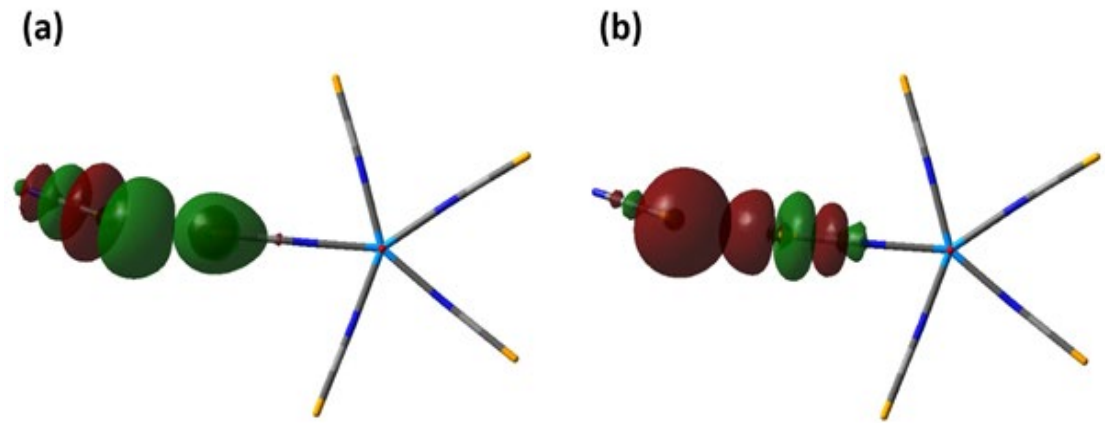

Figure 4.27. Theoretical analysis of Se···Se interactions in $[Et_4N]_4[UO_2(NCSe)_5][NCSe]$; NBO orbitals involved in (a) the coordinated $[NCSe]^-$ to free $[NCSe]^-$, (b) free $[NCSe]^-$ to σ* orbitals of coordinated $[NCSe]^-$.

The energies in the MeSe dimers are lower than those in EtSe[NCSe] and in keeping with the longer Se…Se distances in the structures. Finally, the interaction energies in model compounds $Me_2Se{\cdots}SeMe_2$ (−2.82 kcal/mol) and $Me_2Se{\cdots}Se(Me)CN$ (−4.62 kcal/mol)[63] are comparable to these uranyl systems.

The value of the electron density at the bond critical point, ρ_{bcp}, is often taken as an indication for bond strength. Here the Se···Se contact exhibits a bond critical point with ρ_{bcp} = 0.009 au for both dimers, corroborating the NBO analysis that a weak but stabilizing interaction is present. This is noteworthy as, in MeSe, the Se···Se contacts were slightly greater than the sum of the van der Waals radii. There are few reports of Se···E examples characterized via this methodology to compare, but in $XRSe{\cdots}OH_2$ and $XRSe{\cdots}NH_3$ (R = H and Me; X = H, F, Me, CF_3, Cl, OH, OMe, NH_2, NHMe and CN) ρ_{bcp} ranges between 0.053 - 0.270 au for the Se···O/N interaction, or in $F_2C{=}Se{\cdots}NX$ (X = CH, H_3, HCH_2, CLi and Me_3) ρ_{bcp} ranges between 0.0089 - 0.0197 au and in $F_2C{=}Se{\cdots}XY$ (XY = BrCl, ClF and BrF) ρ_{bcp} is between 0.0276 - 0.0440 au.[64] In the optimized dimers of $(X_2C{=}S)_2$, ρ_{bcp} range from 0.039 and 0.050 au with the sum of the charge transfer 1.52 to 3.12 kcal/mol (X = H, NH_2, OH, F and Cl).[14] These data can be put into a broader context by comparing to other non-conventional bonding that has been reported. While it is clear that substitution effects are important, these chalcogenide interactions are on par with the weak fluorine bonding (e.g., ρ_{bcp} = 0.0073 au for the interaction in H—F···F—F[65]), or halogen lone pair···π interactions,[66] and weaker than, for example, F—Br···I—F (ρ_{bcp} = 0.0320 au)[67] as anticipated from the σ-hole mechanism of bonding which depends on the polarizability of the atom.

4.5.2 Weak Hydrogen Bonding

Dimers bound by Se···H—C and U=O···H—C hydrogen bonding, taken from MeSe and ^{n}PrSe, have been characterized using an AIM approach. A dimer taken from MeSe contains three C—H···O=U bond critical points with ρ_{bcp} = 0.007, 0.006 and 0.005 au, while the H-bonds from ^{n}PrSe displays 6 x C—H···Se = 0.008, 0.006, 0.005, 0.005, 0.004 and 0.003 au. Thus, individual C—H···Se are weak but rather numerous, lending support to the hypothesis that these dominate in samples such as ^{n}PrSe with many such donors. C—H···O=U interactions seem even weaker, supporting the above observation that the terminal oxygens in the uranyl species are relatively weak Lewis bases. Intramolecular C—H···O=U hydrogen bonding has also recently been theoretically analysed and, in this case, ρ_{bcp} = 0.002-0.0243 a.u., indicating that intramolecular hydrogen bonding can be stronger than intermolecular hydrogen bonding.

4.6 Reactivity Studies

4.6.1 Chemical Oxidation of $[Et_4N]_3[UO_2(NCS)_5]$

Given the interesting result from the electrochemical deoxygenation of $[Et_4N]_3[UO_2(NCS)_5]$ (section 4.4.1), attempts to induce a similar effect through a chemical oxidation were then performed. Reaction with organic oxidants, such as tetracyanoethylene and I_2 gave no reaction, as judged by IR and UV-vis spectroscopy. In contrast, reaction with $CuCl_2$ (Equation 8) in MeCN produced a brown solution, but there were no bands in the UV-vis-NIR spectral region attributable to *f-f* electronic transitions. Recrystallization afforded three different morphologies of single crystals and X-ray crystallography showed them to be copper sulfate, $[Et_4N]_2[UO_2Cl_4]$ and $[Et_4N]_4[UO_2Cl_4][CuCl_4]$.

$$[Et_4N]_3[UO_2(NCS)_5] + CuCl_2 \rightarrow Cu(SO_4) + [Et_4N]_2[UO_2Cl_4] + [Et_4N]_4[UO_2Cl_4][CuCl_4] \quad (8)$$

Copper sulfate must have been formed from the oxidation of $[NCS]^-$ to $[SO_4]^{2-}$,[68] as $CuCl_2$ was sulfate-free (judged with IR spectroscopy); notably, this oxidation was also seen in the attempted preparation of $[Me_3Sn]_3[UO_2(NCS)_5]$. The formation of uranyl halides corroborates the results of computational investigations showing the U−Cl bond to be more covalent than U−NCS.[54] The X-ray crystal structure of $[Et_4N]_4[UO_2Cl_4][CuCl_4]$ is shown in Figure 4.28; it suffers of disorder in the uranyl

coordination environment and the refinement is clarified in the experimental section. The corresponding crystallographic data are listed in Appendix 3, while full list of bond lengths and angles is tabulated in Appendix 3.6, in the external CD source of this thesis. In this compound, the U=O (1.772(3) Å) and U–Cl (average 2.637(3) Å) bond lengths are comparable with the analogues bond lengths present in $Cs_2UO_2Cl_4$ (U=O, 1.774(4) Å; U–Cl, average 2.671(1) Å).[69]

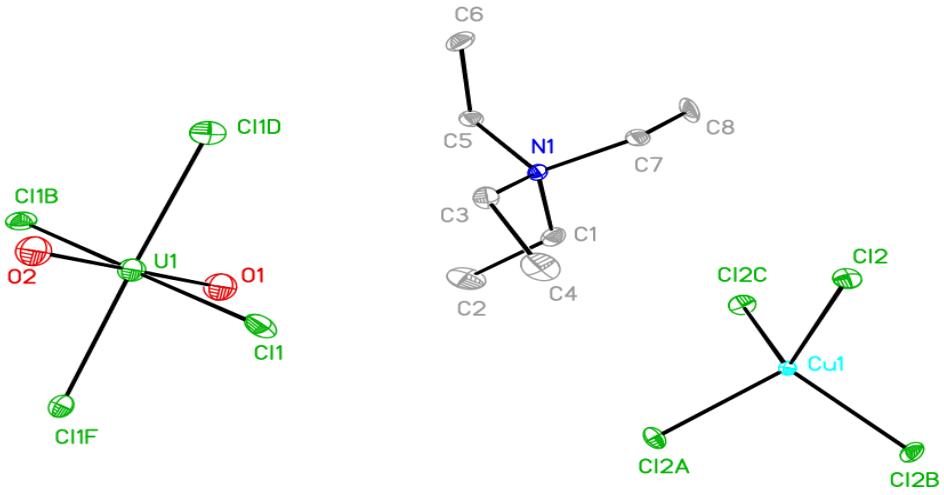

Figure 4.28. Asymmetric unit of $[Et_4N]_4[UO_2Cl_4][CuCl_4]$, with atomic displacement parameters shown at 50% probability. Hydrogen atoms omitted for clarity.

The photophysical properties have been measured in MeCN solution at room temperature and are presented in Figure 4.29. The UV-vis absorption spectrum of a ~10^{-6} M solution of $[Et_4N]_4[UO_2Cl_4][CuCl_4]$ in MeCN (Figure 4.29, black line) displays four features. The bands at 256 and 313 nm are attributable to ligand-to-metal charge transfer (LMCT) transitions from the equatorial coordinated Cl^- ligands to the uranyl cation;[59] the broad and less intense signal at 460 nm is assignable to the vibronically coupled LMCT transition of the uranyl moiety and this transition is also perceptible in the excitation spectrum at 420 nm (Figure 4.29, blue line). In the NIR region of the absorption spectrum, between 830 and 1100 nm (Figure 4.29, inset), is also observable a broad and very weak band due to the Laporte forbidden *d-d* transitions from the Cu^{2+} cation of the $[CuCl_4]^{2-}$ fragment. Moreover, excitation between 280 and 430 nm produces a luminescence spectrum which is dominated by the LMCT emission bands characteristic of the uranyl moiety centered at *ca.* 520 nm. The vibrationally resolved fine structure of this emission profile is due to coupling with the Raman active ν_1(U=O) symmetric

vibrational mode. This appears at 832 cm^{-1} in the Raman spectrum (Appendix 3, Figure 7.25).

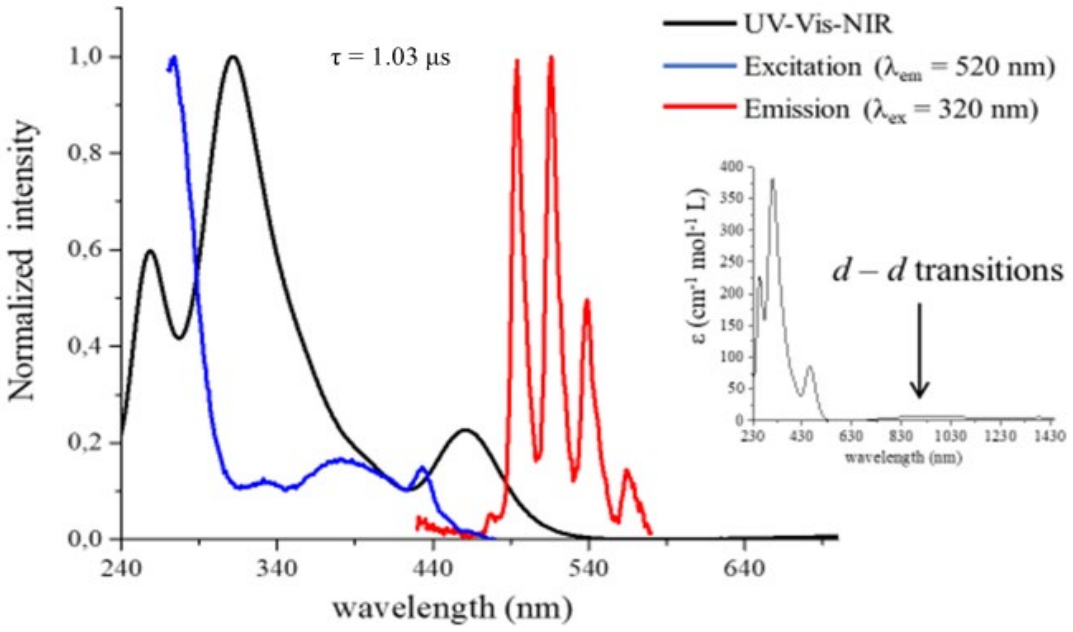

Figure 4.29. (black) UV-vis-NIR absorption, (red) emission and (blue) excitation spectrum of $[Et_4N]_4[UO_2Cl_4][CuCl_4]$ in MeCN, τ = 1.03 μs. (Inset) Expanded UV-vis-NIR absorption spectrum, emphasizing the *d-d* transitions of $[CuCl_4]^{2-}$.

4.6.2 Attempted Synthesis of Uranyl(VI) pentaisocyanide complexes, $[R_4N]_3[UO_2(NC)_5]$

The stability of uranyl(VI) cyano complexes has been the subject of recent theoretical debates and the coordination mode of the $[CN]^-$ group to the $[UO_2]^{2+}$ ion, via cyanide U–CN or isocyanide U–NC bonding, has been questioned. [70] In the gas phase, DFT calculations on $[UO_2(CN)_2]$ and $[UO_2(NC)_2]$ found the isocyanide U–NC interaction being about 40 kJ mol^{-1} more stable.[70b] However, in solution, these calculations state that, in a complex with five coordinated ligands, the more stable structure is with U–CN bonds, while a change in stability, from cyanide to the isocyanide isomer, is observable when there are four ligands bond to the metal center.[70c] It is always desirable to meet the theoretical analyses results with experimental data. Therefore, a few experiments have been attempted with the aim of sequestering S or Se atoms from the above described $[R_4N]_3[UO_2(NCS)_5]$ and $[R_4N]_3[UO_2(NCSe)_5]$ compounds, in order to obtain single crystals of uranyl(VI) pentaisocyanide complexes, of the type $[R_4N]_3[UO_2(NC)_5]$.

Thus, Et_3BzNS and Et_3BzNSe were separately dissolved in MeCN, producing yellow solutions, and reacted with five equivalents of triphenylphosphine (Ph_3P), acting as extracting reagent for the chalcogenide atoms. While no reaction was observed with Et_3BzNS, when Ph_3P was mixed with Et_3BzNSe, a grey precipitate was formed and the initial yellow solution of Et_3BzNSe became colourless. More importantly, in this colourless solution, the successfully removal of "Se" from Et_3BzNSe, as Ph_3PSe, was verified by $^{31}P\{^1H\}$ NMR spectroscopy (δ35.81 ppm, Ph_3PSe). Moreover, after one week, white single crystals of Ph_3PSe (as verified by X-ray diffraction) were also obtained from this solution. The grey precipitate was then analysed by IR and Raman spectroscopy. The results of this analysis (Figure 4.30) revealed the absence of N=C groups in this product. Several efforts have then been made to recrystallize this grey powder; however, even using solvents of different polarity such as hexane, dimethyl sulfoxide, dichloromethane, tetrahydrofuran, ethanol, methanol and water, all the attempts failed. In addition, further spectroscopic analysis gave no informative data.

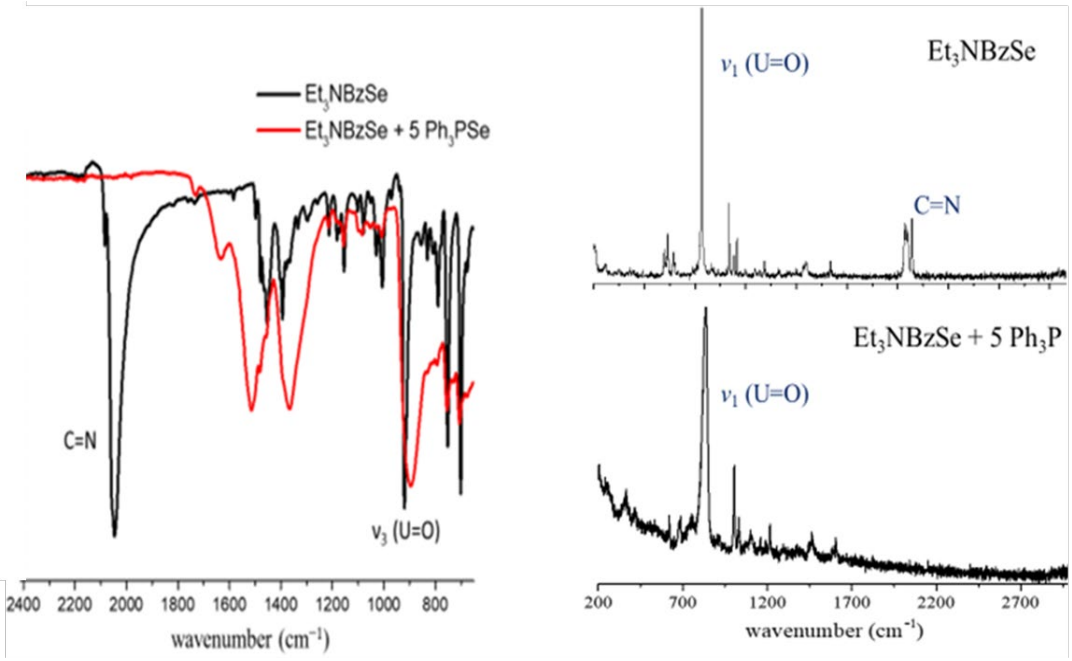

Figure 4.30. (left) IR spectra of (black) Et_3BzNSe and (red) Et_3BzNSe reacted with 5 equivalents of Ph_3P; (right) Raman spectra of Et_3BzNSe, at upper side, and Et_3BzNSe reacted with 5 equivalents of Ph_3P, at the bottom.

Subsequently, the removal of "S" from the $[UO_2(NCS)_3(NO_3)]^{2-}$ ion was attempted adding an excess of Hg into an MeCN solution of $[Ph_4P]_2[UO_2(NCS)_3(NO_3)]$. From this experiment, white single crystals were isolated; however, X-ray diffraction revealed

crystals of $[Ph_4P][NCS]$, indicating that the interaction with Hg has led to a decomposition of $[Ph_4P]_2[UO_2(NCS)_3(NO_3)]$.

Some efforts to engineer chalcogenide interactions of the type S···O, S···S and S···Se have also been performed. The complex $[Et_4N]_3[UO_2(NCS)_5]$ was dissolved in MeCN and, in six different reaction vessels, treated with an excess of K[NCO], Na[NCS], K[NCSe], $[Et_4N][NCS]$, $[Et_4N][NCSe]$ and $[Et_4N][NCO]$; however, in all cases, the recrystallization afforded the starting homoleptic thiocyanate complex.

4.6.3 Attempt of Engineering Halogen Bonding on the Uranyl Ion

An attempt of engineering a halogen bond on the uranyl ion was tried using iodine monochloride, ICl, as halogen source. Indeed, as the polarizability increases descending the group, the σ hole on the iodine atom of ICl is significantly pronounced and this has been proved to be a crucial condition to build a halogen bond interaction.[30a] Thus, at room temperature and under air, yellow crystals of Me_3NBzS were dissolved in MeCN and reacted with one equivalent of ICl. The solution assumed a red colour and a yellow precipitate was formed and isolated by filtration. After *ca.* 1 week, yellow single crystals were isolated and X-ray diffraction analysis revealed a compound of formula $[Me_3NBz]_2[UO_2Cl_4]$.

The molecular crystal structure of $[Me_3NBz]_2[UO_2Cl_4]$ is shown in Figure 4.31; the structure suffers of disorder and the refinement is clarified in the experimental section. The corresponding crystallographic data are listed in Appendix 3, while the list of bond lengths and angles is tabulated in Appendix 3.6 (external CD source of this thesis). In this compound, the U=O (1.767(7) Å) and the U–Cl (average 2.637(3) Å) bond lengths are comparable with the corresponding values exhibited by $Cs_2UO_2Cl_4$ (U=O, 1.774(4) Å; U–Cl, average 2.682(3) Å)[69] and $[Et_4N]_4[UO_2Cl_4][CuCl_4]$ (U=O, 1.772(3) Å; U–Cl, average 2.682(3) Å) (section 4.6.1).

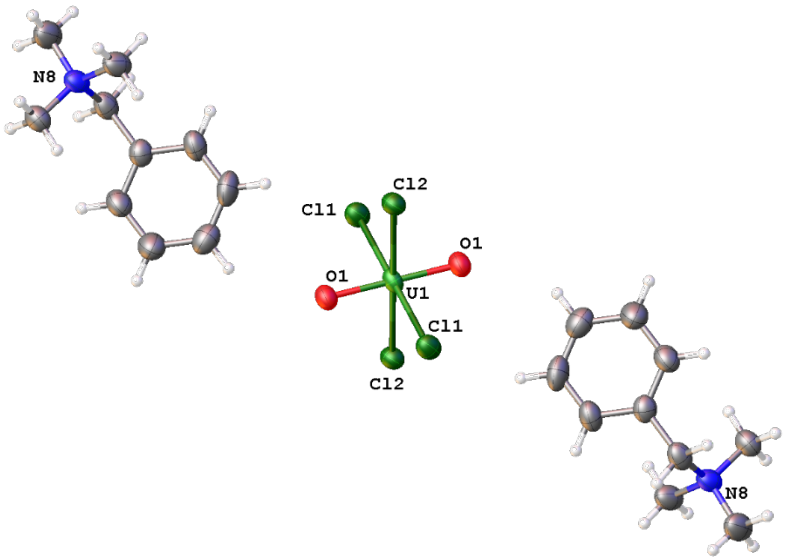

Figure 4.31. Asymmetric unit of $[Me_3NBz]_2[UO_2Cl_4]$, showing the major occupied moiety. Atomic displacement parameters shown at 50% probability. Only heteroatoms labelled for clarity. Carbon and hydrogen atoms marked with, respectively, grey and white colours.

The photophysical properties of this sample, measured in solution and at room temperature, are presented in Figure 4.32. The UV-vis absorption spectrum of a ~10^{-6} M solution in MeCN (Figure 4.32, purple line) displays two bands at 290 and 360 nm. They are attributable to LMCT transitions from the equatorial bound Cl^- ligands to the uranium cation,[59] similarly to $[Et_4N]_4[UO_2Cl_4][CuCl_4]$ (Figure 4.29). The band at 360 nm is also broad and covers the less intense vibronically coupled LMCT uranyl band, expected between 400 and 460 nm. This uranyl-based band is however observable in the excitation spectrum at *ca.* 450 nm (Figure 4.32, red line). Excitation into either of the absorption bands produces a luminescence spectrum (Figure 4.32, blue line), which is dominated by the characteristic LMCT emission bands of the uranyl moiety centred at 520 nm.

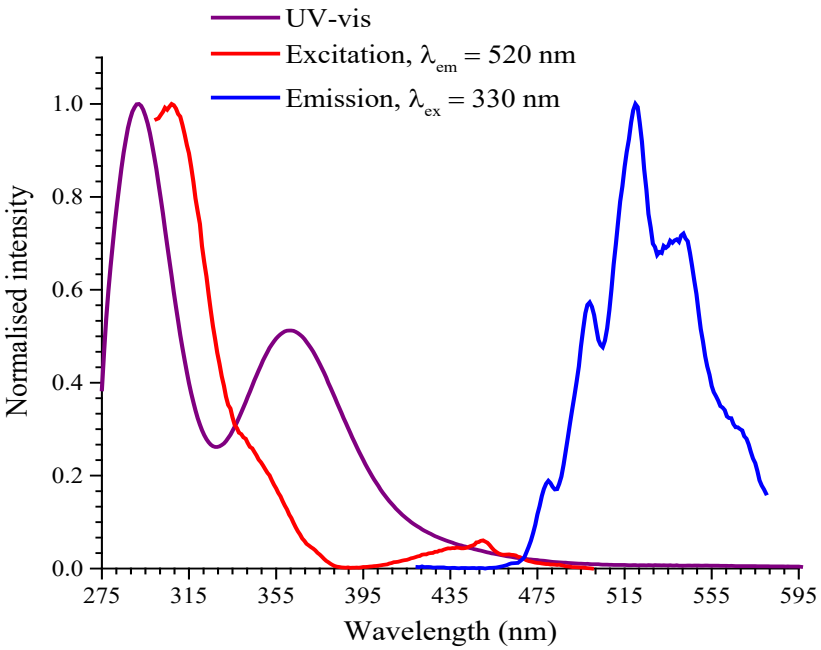

Figure 4.32. UV-vis absorption (purple line), excitation (red line) and emission (blue line) spectrum of $[Me_3NBz]_2[UO_2Cl_4]$ in MeCN, ~10^{-6} M, at room temperature, $\tau = 0.34$ μs ($\chi^2 = 1.34$).

The photophysical properties of this compound have been measured also in solid state at 77 K. The results are shown in Figure 4.33 and immediately apparent is the increase in the resolution. The vibronically coupled LMCT uranyl bands are very well resolved in both the excitation (Figure 4.33, red line) and emission (Figure 4.33, blue line) spectra. The fine vibrationally resolved structure of the emission profile is due to coupling of the $^3\Pi_u$ electronic triplet excited state with the Raman active ν_1(U=O) symmetric vibrational mode and, perhaps, also with the U–Cl vibrational stretching mode.[31, 33] The Raman and IR spectra have also been acquired and are reported in Appendix 3 (Figure 7.26). In particular, the Raman active ν_1(U=O) symmetric vibrational mode appears at 846 cm^{-1} and the IR active ν_3(U=O) asymmetric vibrational mode is observable at 934 cm^{-1}.

The formation of this uranyl chloride system validates further the results of computational investigations showing the U−Cl bond to be more covalent than U−NCS.[54]

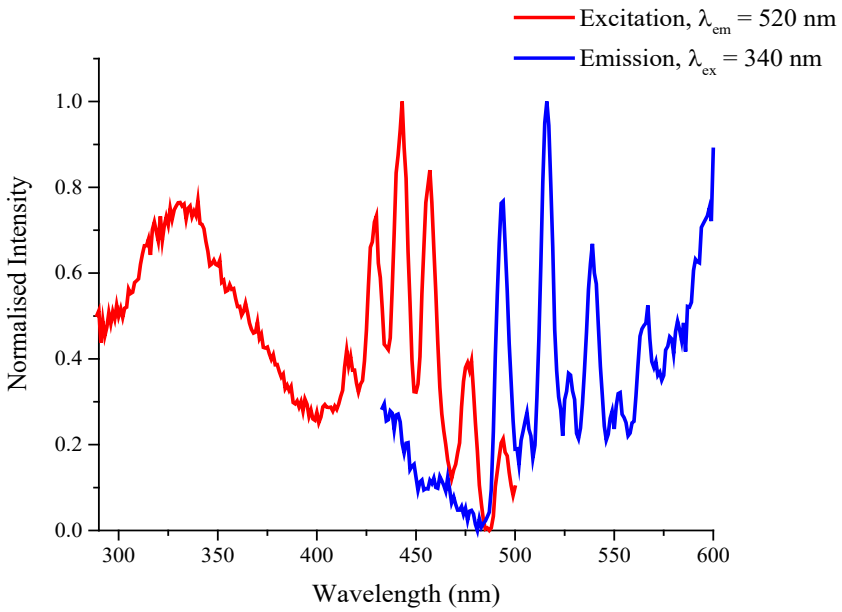

Figure 4.33. Excitation (red line) and emission (blue line) spectrum of $[Me_3NBz]_2[UO_2Cl_4]$, measured in solid state at 77 K.

Finally, previous NBO analysis performed on uranium thiocyanate compounds located one σ and two π bonding orbitals on N−C and a single σ bonding orbital on C−S, suggesting that the most appropriate resonance form for the coordinated thiocyanate ligand is $^{-}N{\equiv}C{-}S$, with lone pairs of electrons on the sulfur that may be accessible for bonding to soft transitional metals.[54] Considering this type of reactivity, $[UO_2(NO_3)_2]{\cdot}6H_2O$ has been reacted with five equivalents of Na[NCS] and $[(Ph_3P)Au]Cl$ in MeCN, to investigate a possible $[Ph_3PAu]^{+}\cdots S{-}C{\equiv}N^{-}$ interaction; however, this experiment did not lead to any product suitable for X-ray diffraction and further spectroscopic measurements gave ambiguous results.

4.7 Conclusions

A series of uranyl thiocyanate and selenocyanate compounds have been synthesized and structurally characterized. Chalcogenide, C—H···O=U and C—H···S(e) interactions have been observed in the solid state, although they depend on the nature of the alkyl ammonium group.

Chalcogenide interactions have been observed in some of the structures and were more prevalent in the $[NCSe]^{-}$ series than in the $[NCS]^{-}$, in line with the increased polarizability of Se which renders a σ-hole on Se (−0.231 au from MEP) more pronounced than on S (−0.246 au from MEP). The molecular orbitals responsible for this

were identified and correspond with the known ideas of $n \rightarrow \sigma^*$ charge transfer in these non-classical interactions, albeit in this example the non-bonded pair of electrons resides in a σ orbital. Comparison with other weak σ-hole type bonds puts these chalcogenide interactions similar to interactions involving fluorine or, more commonly used in synthetic chemistry, lone pair$\cdots\pi$ interactions.[71] C—H$\cdots$S(e) interactions are individually weak from an AIM analysis but numerous and account for their preponderance in the solid-state structures. The vibrational data suggest that the charge assisted hydrogen bonding to the –yl oxygens does not influence the spectroscopic properties of the uranyl moiety and DFT studies show that these interactions are the weakest of the three studied. Unusually, the coupling between the δ(NCS) and δ(NCSe) vibrational modes and the uranyl mode manifests itself in the photophysical properties of these species in the solid state measured at 77 K. Taken together, these results show that collectively non-classical interactions can have an important influence of the solid-state structures, but in these cases are not observable by conventional spectroscopic techniques. Nonetheless, these add to the growing field of chalcogenide interactions in the coordination sphere of metals.

The electrochemical study on both $[UO_2(NCS)_5]^{3-}$, by TLCV, and $[UO_2(NCSe)_5]^{3-}$, by CV, confirmed that the putative uranyl(V) compound is unstable with respect to disproportionation, and the $[NCSe]^-$ ligands are less electron donating than $[NCS]^-$ towards the uranyl(VI) cation, as also seen by photoluminescence spectroscopy. In addition, the electrochemical oxidation of $[UO_2(NCS)_5]^{3-}$ in the presence of bipy afforded $[U(NCS)_8]^{4-}$ via $[U(NCS)_5(bipy)_2]^-$; however, chemical oxidation with $CuCl_2$ produced only uranyl chlorides.

Finally, attempts to obtain uranyl(VI) pentaisocyanide complexes of the type $[R_4N]_3[UO_2(NC)_5]$, via removal of S or Se from the RS or RSe compounds, were not successful.

4.8 Experimental Section

Caution! Natural uranium was used during the course of the experimental work. As well as the radiological hazards, uranium is a toxic metal and care should be taken with all manipulations. Experiments with uranium compounds were carried out using pre–set radiological safety precautions in accordance with the local rules of Trinity College Dublin and University of Reading.

^{1}H, $^{13}C\{^{1}H\}$, $^{31}P\{^{1}H\}$ and $^{77}Se\{^{1}H\}$ spectra were recorded on a Bruker AV400 spectrometer operating at 400.23 MHz, 155.54 MHz, 161.98 MHz and 76.33 MHz respectively, and were referenced to the residual ^{1}H and ^{13}C resonances of the solvent used or external H_3PO_4 or Me_2Se. Solid state ^{77}Se NMR spectra were recorded on a Bruker 400 HD at 76.3 MHz.

For the acquisition of the FTIR, Raman, UV-vis-NIR and photoluminescence spectra, the experimental conditions and the characteristics of the spectrophotometers were the same as for the analysis of the U(IV) compounds discussed in Chapter 2. For the luminescence lifetime measurements, the experimental procedure for the acquisition and the mathematical fitting on the data obtained were the same as for the analysis performed on the uranyl compounds discussed in Chapter 3.

Description of the X-ray diffractometer and of the methods used to analyse the crystallographic data is as discussed in the experimental section of Chapter 2. The structures were refined by Dr. Brendan Twamley (Trinity College Dublin) and the crystallographic data are collated in Appendix 3. Structural figures were prepared using VESTA[72] or mercury.

Regarding the SEC measurements on EtS, the experimental conditions and the characteristics of the electrochemistry cell were the same as described in the experimental section of Chapter 3 for the experiments performed on $[Et_4N]_4[U(NCS)_8]$. Regarding the CV measurements on EtSe, they have been conducted in a standard three-electrode cell using a high performance digital potentiostat (CH model 1760 D Bi-potentiostat system monitored using CH1760D electrochemical workstation beta software). All solutions were degassed for 15 minutes before commencing analysis. A platinum electrode with a diameter of 2 mm was employed as working electrode, a platinum rod (together with internal referencing *vs* Fc/Fc^{+}) was used as a reference electrode and a platinum wire electrode as counter electrode. The supporting electrolyte, $[^{n}Bu_4N][PF_6]$, was recrystallized twice from absolute ethanol, dried under vacuum at 80 °C overnight and used as solution of 0.1 M in MeCN.

DFT calculations were carried out using the meta-hybrid M06-2X[73] DFT method Gaussian09,[74] without symmetry constraints. Monomer or dimer coordinates were extracted from relevant crystal structures, and where necessary C—H bond lengths normalized to values from neutron diffraction (1.082 Å), with all heavy atom positions frozen at crystalline values. Scalar relativistic effects in uranium were included through the use of effective core potentials as defined in Preuss et al's ECP/basis set on U,[75] while

for lighter atoms 6-31+G(d,p) was used. Natural bond orbital (NBO) analysis was performed using Gaussian09; Atoms-in-Molecules (AIM) analysis used AIMAll.[76] Topological analysis of the electronic density (ρ) is based upon those points where the gradient of the density, $\nabla\rho$, vanishes. In this work, points, where one curvature (in the inter-nuclear direction) is positive and two (perpendicular to the bond direction) are negative, have been considered and termed (3, -1) or bond critical points. Properties evaluated at such points characterize the bonding interactions present.

MeCN was dried over CaH_2 before using, while the ammonium chloride salts were obtained commercially and used as received. $[R_4N]_3[UO_2(NCS)_5]$ (R = Me, Et, ^{n}Pr) were synthesized via a slight modification of a literature procedure,[34] whereby the reactants were mixed in MeCN rather than H_2O.

4.8.1 Synthesis of Uranyl Thiocyanate Complexes, $[R_4N]_4[UO_2(NCS)_5]$

To a solution of $[UO_2(NO_3)_2]\cdot 6H_2O$ (0.300 g, 0.6 mmol) in MeCN (30 cm^3) were added Na[NCS] (5 equivalents) and the appropriate cation (3 equivalents). The solution mixture was stirred at room temperature for 60 minutes. The resulting yellow solution was filtered, and the solvent reduced in volume. Crystals suitable for X-ray diffraction were obtained by vapor diffusion of ^{i}Pr$_2$O into MeCN solutions of the products and yellow crystals obtained after *ca.* one week.

$[^n Bu_4N]_3[UO_2(NCS)_5]$. Yield: 57%, 0.44 g. ^{1}H NMR δ_H (400 MHz, CD_3CN/ppm): 1.00 (t, 36H, $J_{H\text{-}H}$ = 7.36 Hz, CH_3), 1.38 (m, 24H, $J_{H\text{-}H}$ = 7.43 Hz, CH_2), 1.63 (m, 24H, $J_{H\text{-}H}$ = 8.55 Hz, CH_2), 3.11 (m, 24H, $J_{H\text{-}H}$ = 8.62 Hz, CH_2). $^{13}C\{^1H\}$ NMR δ_C (155 MHz, CD_3CN/ppm): 12.89 (CH_3), 19.39 (CH_2), 23.36 (CH_2), 58.33 (CH_2). IR (ATR, ν/cm^{-1}): 2960 (m), 2872 (w), 2052 (s, C=N), 1467 (m), 1380 (w), 1152 (w), 1108 (w), 1067 (w), 1026 (w), 919 (s, U=O), 882 (m), 736 (m, C=S). Raman (ν/cm^{-1}): 2099 and 2059 (C=N), 1456, 1324, 909, 850 (U=O), 736 (C=S). UV-vis (ε, $dm^3\ mol^{-1}\ cm^{-1}$), (298 K, ~10^{-5} M in MeCN): 330.4 nm (4868), 284 nm (6240.5), 232 nm (17618).

$[Me_3NBz]_3[UO_2(NCS)_5]$. Yield: 55%, 0.29 g. ^{1}H NMR δ_H (400 MHz, CD_3CN/ppm): 3.05 (s, 27H, CH_3), 4.43 (s, 6H, CH_2), 7.52 (m, 6H, o-CH), 7.53 (m, 3H, p-CH), 7.56 (m, 6H, m-CH). $^{13}C\{^1H\}$ NMR δ_C (155 MHz, CD_3CN/ppm): 52.4 (CH_3), 69.3 (CH_2), 127.6 (ipso-C), 129.2 (m-CH), 130.7 (p-CH), 132.9 (o-CH). IR (ATR, ν/cm^{-1}): 3420 (m), 3025 (w), 2030 (s, C=N), 1634 (w), 1581 (w), 1475 (m), 1408 (m), 1375 (m), 1211 (m), 1076 (w),

1036 (w), 970 (m), 916 (s, U=O), 885 (m), 779 (m, C=S), 725 (s), 700 (s). Raman (ν/cm^{-1}): 2090 and 2062 and 2048 and 2041 (C=N), 1065, 1584, 1471, 1446, 1216, 1184, 1157, 1033, 1003, 845 (U=O), 823, 808 (C=S), 725, 621. UV-vis (ε, dm^3 mol^{-1} cm^{-1}), (298 K, ~10^{-5} M in MeCN): 342 nm (14461), 300 nm (17597).

[Et$_3$NBz]$_3$[UO$_2$(NCS)$_5$]. Yield: 62%, 0.41 g. ^{1}H NMR δ_H (400 MHz, CD$_3$CN/ppm)): 1.37 (t, 27H, $J_{H\text{-}H}$ = 7.11 Hz, CH$_3$), 3.18 (q, 18H, $J_{H\text{-}H}$ = 7.18 Hz, CH$_2$), 4.35 (s, 6H, CH$_2$), 7.51 (m, 3H, p-CH), 7.53 (m, 6H, m-CH), 7.55 (m, 6H, o-CH). ^{13}C{^{1}H} NMR δ_C (155 MHz, CD$_3$CN/ppm): 8.13 (CH$_3$), 53.5 (CH$_2$), 61.1 (CH$_2$), 128.1 (ipso-C), 130.2 (m-CH), 131.5 (p-CH), 133.4 (o-CH). IR (ATR, ν/cm^{-1}): 3437 (w), 2994 (w), 2086 (m), 2042 (s, C=N), 1455 (m), 1399 (m), 1330 (w), 1214 (w), 1182 (w), 1150 (m), 1086 (m), 1033 (m), 1005 (m), 910 (s, U=O), 788 (m) 752 (s, C=S), 693 (s). Raman (ν/cm^{-1}): 2089 and 2042 (C=N), 1005, 842 (U=O), 816 and 812 and 804 (C=S), 679. UV-vis (ε, dm^3 mol^{-1} cm^{-1}), (298 K, ~10^{-5} M in MeCN): 333 nm (4268) nm, 286 nm (5610), 230 nm (8503).

[Ph$_4$P]$_2$[UO$_2$(NCS)$_3$(NO$_3$)]. Yield: 51%, 0.36 g. ^{1}H NMR δ_H (400 MHz, CD$_3$CN/ppm): 7.71 (m, 8H, $J_{H\text{-}H}$ = 8.43 Hz, m-CH), 7.78 (m, 8H, $J_{H\text{-}H}$ = 7.93 Hz, o-CH), 7.95 (m, 4H, $J_{H\text{-}H}$ = 7.53 Hz, p-CH). ^{13}C{^{1}H} NMR δ_C (155 MHz, CD$_3$CN/ppm): 118.4 (d, $^1J_{P\text{–}C}$ = 89.60 Hz, ipso-C), 130.3 (d, $^3J_{P\text{–}C}$ = 12.8 Hz, m-CH), 134.7 (d, $^2J_{P\text{–}C}$ = 10.3 Hz, o-CH), 135.4 (d, $^4J_{P\text{–}C}$ = 2.94 Hz, p-CH). ^{31}P{^{1}H} NMR (162 MHz, CD$_3$CN): δ 22.7 ppm; IR (ATR, ν/cm^{-1}): 3054 (w), 2029 (s, N=C), 1584 (w), 1481 (w), 1433 (m), 1341 (w), 1312 (w), 1269 (w), 1189 (w), 1163 (w), 1104 (s), 1025 (w), 996 (m), 928 (s, U=O), 754 (m, C=S), 720 (s), 678 (s), 616 (w), 523 (s). Raman (ν/cm^{-1}): 2079 and 2034 (C=N), 1586, 1575, 1187, 1165, 1111, 1095, 1037, 1001, 860 (U=O), 826 and 819 (C=S), 677, 615, 278, 257, 244. UV-vis (ε, dm^3 mol^{-1} cm^{-1}), (298 K, ~10^{-5} M in MeCN): 330 nm (4727), 275 nm (11131), 232 (49865).

4.8.2 Synthesis of [(2.2.2-crypt)Na]$_3$[UO$_2$(NCS)$_5$] and [(18-C-6)Na]$_3$[UO$_2$(NCS)$_5$]

Under a flow of Ar, to a green solution of UCl$_4$ (0.020 g, 0.053 mmol) in dried MeCN (20 cm^3), were added 8 equivalents of Na[NCS] and 4 equivalents of 2.2.2-cryptand. The solution mixture was stirred at room temperature for 60 minutes. A precipitate was formed and isolated by filtration, the solvent was then reduced in volume until *ca.* 5 cm^3. The solution changed colour from green to yellow, indicating an unexpected oxidation of

uranium from U(IV) to Uranyl(VI). Finally, yellow crystals suitable for X-Ray diffractions were obtained by vapor diffusion of $^{i}Pr_2O$ into MeCN solutions of the product.

[(2.2.2-crypt)Na]$_3$[$UO_2(NCS)_5$]. Yield: 22%, 0.02 g. ^{1}H NMR δ_H (400 MHz, D-Acetone/ppm): 2.73 (t, 12H, J_{H-H} = 4.91 Hz, CH_2), 3.67 (t, 12H, J_{H-H} = 4.91 Hz, CH_2), 3.70 (s, 12H, CH_2). $^{13}C\{^1H\}$ NMR (155 MHz, D-Acetone): 52.7 (CH_2), 67.5 (CH_2), 68.3 (CH_2). IR (ATR, ν/cm^{-1}): 2966 (w), 2867 (w), 2815 (w), 2055 (m, C=N), 1666 (w), 1461 (m), 1382 (w), 1356 (m), 1302 (m), 1269 (w), 1130 (w), 1088 (s), 917 (s, U=O), 817 (m), 740 (m, C=S). Raman (ν/cm^{-1}): 2093, 2058 and 2045 (C=N), 1468, 1299, 845 (U=O), 810 (C=S). UV-vis (ε, dm^3 mol^{-1} cm^{-1}), (298 K, ∼10^{-5} M in MeCN): 319 nm (3201), 300 nm (3444), 233 nm (19996).

[(18-C-6)Na]$_3$[$UO_2(NCS)_5$]. Yield: 25%, 0.015 g; ^{1}H NMR δ_H (400 MHz, D-Acetone/ppm): 3.66 (s, CH_2); $^{13}C\{^1H\}$ NMR δ_C (155 MHz, D-Acetone/ppm): 69.5 (CH_2); IR (ATR, ν/cm^{-1}): 2915 (w), 2054 (m, C=N), 1628 (w), 1470 (w), 1453 (w), 1353 (m), 1290 (w), 1249 (w), 1091 (s), 956 (s), 911 (s, U=O), 832 (m, C=S); Raman (ν/cm^{-1}): 2924, 2255, 2096 and 2047 (C=N), 1475, 1277, 1246, 1142, 1071, 920, 871, 842 (U=O), 808 (C=S), 750, 550, 380; UV-vis (ε, dm^3 mol^{-1} cm^{-1}), (298 K, ∼10^{-5} M in MeCN): 339 nm (13192), 299 nm (17137), 232 nm (27158).

Refinement note for [(18-C-6)Na]$_3$[$UO_2(NCS)_5$]

The structure was resolved as a rotational twin with a refined twin fraction (BASF) of 0.185(4). Rotational twin around the 2-axis (0 0 1) [0 0 1], Angle = 1.95° with a twin matrix of (-1.000, 0.000, 0.000, 0.000, -1.000, 0.000, -0.140, -0.038, 1.000). Poorly diffracting sample. Each uranyl center was modelled as disordered in two positions with U1 83, 17% and U2 92, 8% occupied. Many restraints (DFIX, SADI, SIMU, RIGU, ISOR) and constraints (EADP). Crown ethers were not modelled as disordered, but were modelled with many restraints (DFIX, SADI, SIMU, ISOR). Hydrogen placement on the half occupied waters was calculated and modelled as riding on the carrier atom. Hydrogen atoms for the bridging water molecules between Na(crown) were not located or added. The molecular formula $C_{82}H_{161}N_{10}Na_6O_{49.50}S_{10}U_2$ does include these missing atoms.

4.8.3 Synthesis of Uranyl Selenocyanate Complexes $[R_4N]_4[UO_2(NCSe)_5]$

To a solution of $[UO_2(NO_3)_2]\cdot 6H_2O$ (0.300 g, 0.6 mmol) in MeCN (30 cm^3) were added a solution of K[NCSe] (5 equivalents) in 10 cm^3 MeCN and the appropriate cation (3 equivalents) in 10 cm^3 MeCN. The solution was stirred at room temperature for 60 minutes in the dark. The resulting orange solution was filtered, and the solvent reduced in volume. Orange crystals suitable for X-ray diffraction were obtained by vapor diffusion of $^{i}Pr_2O$ into MeCN solutions of the products in *ca.* 1 week. Finally, they were stored in dark to avoid any decompositions by light absorption.

$[Me_4N]_3[UO_2(NCSe)_5].H_2O$. Yield: 39%, 0.20 g. ^{1}H NMR δ_H (400 MHz, CD_3CN/ppm): 3.14 (s, 12H, CH_3), 2.25 (s, 2H, H_2O). $^{13}C\{^1H\}$ NMR δ_C (155 MHz, CD_3CN/ppm): 54.9 (CH_3). $^{77}Se\{^1H\}$ NMR δ_{Se} (76 MHz, CD_3CN/ppm): −340.5 (NCSe). IR (ATR, ν/cm^{-1}): 3027 (w), 2956 (w), 2060 and 2042 (s, C=N), 1738 (w), 1480(m), 1410 (w), 1365 (w), 944 (s), 920 (s, U=O), 632 (m, C=Se). Raman (ν/cm^{-1}): 2071 and 2091 (C=N), 1460, 948, 848 (U=O), 753 (C=Se), 637, 564, 457, 250. UV-vis (ε, dm^3 mol^{-1} cm^{-1}), (298 K, ∼10^{-5} M in MeCN): 329 nm (7311), 250 nm (25068).

$[Et_4N]_4[UO_2(NCSe)_5][NCSe]$. Yield: 43%, 0.56 g. ^{1}H NMR δ_H (400 MHz, CD_3CN/ppm): 3.21 (q, 2H, $^3J_{H\text{-}H}$ = 7.28 Hz, CH_2), 1.25 (t, 3H, $^3J_{H\text{-}H}$ = 7.32 Hz, CH_3). $^{13}C\{^1H\}$ NMR δ_C (155 MHz, CD_3CN/ppm): 29.9 (CH_2), 6.8 (CH_3). $^{77}Se\{^1H\}$ NMR δ_{Se} (76 MHz, D-Acetone/ppm): −342.2 (NCSe). IR (ATR, ν/cm^{-1}): 2991 (w), 2056 (s, C=N), 1642 (w), 1494 (m), 1394 (m), 1166 (m), 1001 (m), 921 (s, U=O), 782 (m, C=Se), 627 (m). Raman (ν/cm^{-1}): 2091 and 2060 and 2051 (C=N), 1461, 1297, 1116, 1071, 1043, 1000, 845 (U=O), 672 and 635 (C=Se). UV-vis (ε, dm^3 mol^{-1} cm^{-1}), (298 K, ∼10^{-5} M in Acetone): 322 nm (4638), 491 nm (278), 475 nm (323), 459 (388).

$[^{n}Pr_4N]_3[UO_2(NCSe)_5]$. Yield: 45%, 0.36 g; ^{1}H NMR δ_H (400 MHz, CD_3CN/ppm): 0.977 (t, 36H, $J_{H\text{-}H}$ = 7.27 Hz, CH_3), 1.69 (m, 18H, $J_{H\text{-}H}$ = 9.27 Hz, CH_2) 3.10 (m, 18H, $J_{H\text{-}H}$ = 5.20 Hz, CH_2). $^{13}C\{^1H\}$ NMR (155 MHz, CD_3CN/ppm): 10.8 (CH_3), 16.0 (CH_2), 61.0 (CH_2). $^{77}Se\{^1H\}$ NMR δ_{Se} (76 MHz, D-Acetone/ppm): −305 (NCSe). IR (ATR, ν/cm^{-1}): 2968 (m), 2937 (w), 2877 (w), 2094 (w), 2060 and 2046 (s, C=N), 1482 (m), 1455 (m), 1385 (m), 968 (m), 926 (s, U=O), 842 (w), 756 (m, C=Se), 627 (m). Raman (ν/cm^{-1}): 2100 and 2079 and 2065 (C=N), 1459, 1316, 1140, 1110, 1037, 852 (U=O), 783, 757,

640 (C=Se), 557, 333, 313, 210; UV-vis (ε, $dm^3\ mol^{-1}\ cm^{-1}$), (298 K, ~10^{-5} M in MeCN): 330 nm (9696).

$[Et_3NBz]_3[UO_2(NCSe)_5]$. Yield: 54%, 0.44 g; ^1H NMR δ_H (400 MHz, D-Acetone): 1.55 (t, 27H, J_{H-H} = 7.31 Hz, CH_3), 3.47 (q, 18H, J_{H-H} = 7.33 Hz, CH_2), 4.70 (s, 6H, CH_2), 7.55 (m, 3H, p-CH), 7.57 (m, 6H, m-CH), 7.66 (m, 6H, o-CH). $^{13}C\{^1H\}$ NMR δ_C (155 MHz, D-Acetone/ppm): 7.35 (CH_3), 52.7 (CH_2), 60.3 (CH_2), 128 (ipso-C), 129 (m-CH), 131 (p-CH), 133 (o-CH). $^{77}Se\{^1H\}$ NMR δ_{Se} (76 MHz, D-Acetone/ppm): −342 (NCSe); IR (ATR, ν/cm^{-1}): 2984 (w), 2086 (w), 2047 (s, C=N), 1451 (m), 1395 (m) 1210 (w), 1186 (w), 1154 (m), 1078 (w), 1030 (m), 969 (w), 920 (s, U=O), 831 (w), 806 (w), 791 (m), 751 (s, C=Se), 701 (s). Raman (ν/cm^{-1}): 2087 and 2056 and 2043 (C=N), 1604, 1460, 1212, 1051, 1033, 1003, 842 (U=O), 677, 643 (C=Se), 624. UV-vis (ε, $dm^3\ mol^{-1}\ cm^{-1}$), (298 K, ~10^{-5} M in MeCN): 329 nm (5383), 264 nm (8167), 248 nm (18259).

4.8.4 Attempted Synthesis of $[Et_4N]_3[UO_2(NCTe)_5]$

To a yellow solution of $[UO_2(NO_3)_2]\cdot 6H_2O$ (200 mg, 0.4 mmol) in MeCN (30 cm^3) were added 5 equivalents of Na[NCTe], prepared in situ mixing Te and Na[CN] in 10 cm^3 of MeCN, and 3 equivalents of $[Et_4N]Cl$ dissolved in 10 cm^3 of MeCN. The resulting solution immediately assumed a pale-yellow colour and was stirred at room temperature for 60 minutes in the dark. A grey precipitate was formed and isolated by filtration. The MeCN solvent was then left to evaporate slowly and, after *ca.* 1 week at room temperature, yellow crystals of $[Et_4N]_2[UO_2Cl_4]$ suitable for X-ray diffraction were isolated (0.2 mg, yield: 33%).

4.8.5 Synthesis of $[Et_4N]_4[UO_2Cl_4][CuCl_4]$

To a yellow solution of $[Et_4N]_3[UO_2(NCS)_5]$ (200 mg, 0.21 mmol) in MeCN (20 cm^3), was added anhydrous $CuCl_2$ (56.5 mg, 0.46 mmol). After 2h of stirring at room temperature, a clear brown solution was formed and filtered twice. The solvent was left to evaporate slowly and, after 48 h at room temperature, the solution deposited yellow crystals suitable for X-ray diffraction. Yield: 62%, 148 mg. IR (ATR, ν/cm^{-1}): 2989 and 2950 (w, C-H), 1460 (m), 1392 (m), 1308 (w), 1184 (m), 1030 (m), 1006 (m), 916 (s, U=O), 789 (m), 637 (w), 603 (w). Raman (ν/cm^{-1}): 1459, 1060, 887, 832 (U=O), 658,

389, 255, 200. UV-vis (ε, $dm^3\ mol^{-1}\ cm^{-1}$), (298 K, 2.78 mM in MeCN): 1381 nm (7.94), 914 nm (7.00), 460 nm (86.4), 310 nm (381), 256 nm (229).

Refinement note: refined as a merohedral twin with twin law (0 1 0 1 0 0 0 0 -1) with BASF 0.469(3). Large residual of ca. 4 electrons 0.88 Angstroms from O2 is a twinning/absorption artefact and could not be modelled or eliminated. Cl1 was disordered over two positions with 70/30% occupancy and modelled with constraints (EADP). The uranyl moiety was modelled with restraints (SADI) and constraints (EADP). The NEt4 group was modelled with restraints (SIMU, ISOR) and constraints (EADP).

4.8.6 Attempted Synthesis of $[R_4N]_3[UO_2(NC)_5]$ via Extraction of S or Se

To an orange solution of Et_3BzNSe (0.030 g, 0.022 mmol) in MeCN (20 cm^3) were added 5 equivalents of Ph_3P. The solution was stirred at room temperature for 30 minutes. A grey precipitate was formed and isolated by filtration. The solution became colourless and was reduced in volume by slow evaporation of the solvent at room temperature. Single crystals of Ph_3PSe, suitable for X-ray diffraction, were formed after *ca*. 1 week. No reaction was observed between Et_3BzNS and Ph_3P, under the same experimental conditions.

4.8.7 Synthesis of $[Me_3NBz]_2[UO_2Cl_4]$

To a yellow solution of Me_3NBzS (0.030 g, 0.030 mmol) in MeCN (20 cm^3) were added ICl (1 equivalent). The solution assumed a red colour and was stirred at room temperature for 24h. An orange precipitate was formed and isolated by filtration. Finally, after *ca.* 1 week, the solution deposited yellow single crystals of $[Me_3NBz]_2[UO_2Cl_4]$ suitable for X-ray diffraction (47%, 0.008 g). ^{1}H NMR δ_H (400 MHz, CD_3CN/ppm): 2.95 (s, 27H, CH_3), 4.02 (s, 6H, CH_2), 7.35 (m, 6H, o-CH), 7.41 (m, 3H, p-CH), 7.58 (m, 6H, m-CH). $^{13}C\{^1H\}$ NMR δ_C (155 MHz, CD_3CN/ppm): 48.4 (CH_3), 63.3 (CH_2), 123.6 (ipso-C), 125.2 (m-CH), 128.7 (p-CH), 130.9 (o-CH). IR (ATR, ν/cm^{-1}): 3375 (m), 2153 (w), 2028 (w), 1639 (m), 1460 (m), 1045 (m), 930 (s, U=O), 733 (s), 639 (m). Raman (ν/cm^{-1}): 1219, 999, 841 (U=O), 661, 632, 443, 282

Refinement note: cation disordered over two positions (54:46%) and modelled with restraints (SIMU). UO_2Cl_4 anion is disordered over three positions with occupancies 55; 30 and 15%; modelled with restraints (SIMU, ISOR) and constraints (EADP for O1, O1A, O1B).

4.9 References

[1] a) L. Sobczyk, D. Chudoba, P. M. Tolstoy and A. Filarowski, *Molecules*, 2016, **21**, 1657; b) R. C. Johnston and P. Ha-Yeon Cheong, *Org. Biomol. Chem.*, 2013, **11**, 5057; c) Y. E. Khoury and P. Hellwig, *Chem. Commun.*, 2017, **53**, 8389; d) G. N. Pairas and P. G. Tsoungas, *Chemistry Select*, 2016, **1**, 4520

[2] For recent reviews see: a) G. Cavallo, P. Metrangolo, R. Milani, T. Pilati, A. Priimagi, G. Resnati and G. Terraneo, *Chem. Rev.*, 2016, **116**, 2478-2601; b) L. C. Gilday, S. W. Robinson, T. A. Barendt, M. J. Langton, B. R. Mullaney and P. D. Beer, *Chem. Rev*., 2015, **115**, 7118-7195; c) R. Bishop, *CrystEngComm*., 2015, **17**, 7448; d) R. W. Troff, T. Makela, F. Topic, A. Valkonen, K. Raatikainen and K. Rissanen, *Eur. J. Org. Chem.*, 2013, 1617-1637

[3] a) J. E. Del Bene, I. Alkorta and J. Elguero, *Noncovalent Forces: Challenges and Advances in Computational Chemistry and Physics*, S. Ed. Scheiner, Springer: New York, 2015, **19**, 191; b) D. Setiawan, E. Kraka and D. Cremer, *J. Phys. Chem. A*, 2015, **119**, 1642; c) S. Sarkar, M. S. Pavan and T. N. Guru Row, *Phys. Chem. Chem. Phys.*, 2015, **17**, 2330; d) L. Guan and Y. Mo, *J. Phys. Chem. A*, 2014, **118**, 8911; e) J. E. Del Bene, I. Alkorta and J. Elguero, *J. Phys. Chem. A*, 2014, **118**, 3386; f) P. Politzer, J. S. Murray, G. V. Janjić and S. D. Zarić, *Crystals*, 2014, **4**, 12; g) S. Scheiner, *Acc. Chem. Res.*, 2013, **46**, 280; h) S. Scheiner, *Int. J. Quantum Chem.*, 2013, **113**, 1609; i) K. Eskandri and N. Mahmoodabadi, *J. Phys. Chem. A*, 2013, **117**, 13018; j) U. Adhikary and S. Scheiner, *J. Chem. Phys.*, 2011, **135**, 184306; k) S. Zahn, R. Frank, E. Hey-Hawkins and B. Kirchner, *Chem. – Eur. J.*, 2011, **17**, 6034; l) P. Kilian, A. M. Z. Slawin and J. D. Woollins, *Chem. – Eur. J.*, 2003, **9**, 215

[4] A. Bauzá and A. Frontera, *Angew. Chem. Int. Ed.*, 2015**, 54**, 7340

[5] a) R. Gleiter, G. Haberhauer, D. B. Werz, F. Rominger and C. Bleiholder, *Chem. Rev.*, 2018, **118**, 2010; b) D. J. Pascoe, K. B. Ling and S. L. Cockroft, *J. Am. Chem. Soc.*, 2017, **139**, 15160; c) H. -T. Huynh, O. Jeannin and M. Fourmigué, *Chem. Commun*., 2017, **53**, 8467; d) V. Oliveira, D. Cremer and E. Kraka, *J. Phys. Chem. A*, 2017, **121**, 6845; e) R. Shukla and D. Chopra, *Phys. Chem. Chem. Phys.*, 2016, **18**, 13820; f) X. Pang and W. J. Jin, *New J. Chem.*, 2015, **39**, 5477; g) L. M. Azofra, I. Alkorta and S. Scheiner, *J. Phys. Chem. A*, 2015, **119**, 535; h) M. K. Si, R. Lo and B. Ganguly, *Chem. Phys. Lett.*, 2015, **6**, 631; i) M. Esrafili and F. Mohammadian-Sabet, *Struct. Chem*., 2015, **26**, 199; j) V. d. P. N. Nziko and S. Scheiner, *J. Org. Chem.*, 2015, **80**, 2356; k) G. E. Garrett, G. L. Gibson, R. N. Straus, D. S. Seferos and M. S. Taylor, *J. Am. Chem. Soc.*, 2015, **137**, 4126; l) S. P. Thomas, K. Satheeshkumar, G. Mugesh and T. N. Guru Row, *Chem. Eur. J.*, 2015, **21**, 6793; m) R. Shukla and D. Chopra, *J. Phys. Chem. B*, 2015, **119**, 14857; n) U. Adhikari and S. Scheiner, *J. Phys. Chem. A*, 2014, **118**, 3183; o) S. Tsuzuki and N. Sato, *J. Phys. Chem. B*, 2013, **117**, 6849; p) W. Wang, B. Ji and Y. Zhang, *J. Phys. Chem. A*, 2009, **113**, 8132; q) J. S. Murray, P. Lane and P. Politzer, *Int. J. Quantum Chem.*, 2008, **108**, 2770; r) R. E. Rosenfield, R. Parthasarathy and J. D. Dunitz, *J. Am. Chem. Soc.*, 1977, **99**, 4860

[6] a) S. J. Grabowski and W. A. Sokalski, *ChemPhysChem*, 2017, **18**, 1569–1577; b) V. Oliveira and E. Kraka, *J. Phys. Chem. A*, 2017, **121**, 9544; c) H. Wang, W. Wang and W. J. Jin, *Chem. Rev.*, 2016*,* **116***,* 5072-5104; d) M. H. Kolář and P. Hobza, *Chem. Rev.*, 2016**, 116**, 5155; e) P. Politzer, J. S. Murray and T. Clark, *Phys. Chem. Chem. Phys*., 2013, **15**, 11178; f) P. Politzer and J. S. Murray, *ChemPhysChem*, 2013, **14**, 278; g) P. Politzer, J. S. Murray and T. Clark, *Phys. Chem. Chem. Phys.*, 2010, **12**, 7748

[7] N. Guo, R. Maurice, D. Teze, J. Graton, J. Champion, G. Montavon and N. Galland, *Nat. Chem.*, 2018, **10**, 428

[8] P. Politzer, J. S. Murray and T. Clark, *Phys.Chem.Chem.Phys*., 2013, **15**, 11178

[9] S. Scheiner, *J. Phys. Chem. A*, 2015, **119**, 9189

[10] A. Bauzá, T. J. Mooibroek and A. Frontera, *ChemPhysChem*, 2015, **16**, 2496

[11] J. T. Goettel, P. Chaudhary, P. Hazendonk, H. P. A. Mercier and M. Gerken, *Chem. Commun.*, 2012, **48**, 9120

[12] V. d. P. N. Nziko and S. Scheiner, *J. Phys. Chem. A*, 2014, **118**, 10849

[13] a) A. Mukherjee, G. R. Desiraju, *IUCrJ*, 2014, **1**, 49; b) S. Tothadi, S. Joseph and G. R. Desiraju, *Cryst. Growth Des.*, 2013, **13**, 3242

[14] R. Shukla and D. Chopra, *Cryst. Growth Des.*, 2016, **16**, 6734

[15] a) H. Peacock, J. Luo, T. Yamashita, J. Luccarelli, S. Thompson and A. D. Hamilton, *Chem. Sci.*, 2016, **7**, 6435; b) M. E. Brezgunova, J. Lierig, E. Aubert, S. Dahaoui, P. Fertey, S. Lebègue, J. G. Ángyán, M. Fourmigué and E. Espinosa, *Cryst. Growth Des*., 2013, **13**, 3283; c) M. Iwaoka and N. Isozumi, *Molecules*, 2012, **17**, 7266; d) E. A. Meyer, R. K. Castellano and F. Diederich, *Angew. Chem. Int. Ed.*, 2003, **42**, 1210; e) M. Iwaoka, S. Takemoto and S. Tomoda, *J. Am. Chem. Soc.*, 2002, **124**, 10613

[16] a) K. T. Mahmudova, M. N. Kopylovich, M. F. C. Guedes da Silva and A. J. L. Pombeiro, *Coord. Chem. Rev.*, 2017, **345**, 54; b) E. R. T. Tiekink, *Chem. Rev.*, 2017, **345**, 209

[17] D. M. Ivanov, A. S. Novikov, I. V. Ananyev, Y. V. Kirina and V. Y. Kukushkin, *Chem. Commun*., 2016, **52**, 5565

[18] L. Mei, C.-Z. Wang, L. Wang, Y.-L. Zhao, Z.-F. Chai and W.-Q. Shi, *Cryst. Growth Des.*, 2015, **15**, 1395

[19] R. J. Baker, *Chem. Eur. J.*, 2012, **18**, 16258

[20] a) S. Fortier and T. W. Hayton, *Coord. Chem. Rev.*, 2010, **254**, 197; b) P. L. Arnold, A.-F. Pecharman, E. Hollis, A. Yahia, L. Maron, S. Parsons and J. B. Love, *Nat. Chem.*, 2010, **2**, 1056; c) P. L. Arnold, A.-F Pecharman, R. M. Lord, G. M. Jones, E. Hollis, G. S. Nichol, L. Maron, J. Fang, T. Davin and J. B. Love, *Inorg. Chem.*, 2015, **54**, 3702; d) L. A. Seaman, E. A. Pedrick, G. Wu and T. W. Hayton, *J. Organomet. Chem.*, 2017, **857**, 34

[21] a) J. L. Sessler, D. Seidel, A. E. Vivian, V. Lynch, B. L. Scott and D. W. Keogh, *Angew. Chem.*, *Int. Ed.*, 2001, **40**, 591; b) J. -C. Berthet, M. Nierlich and M. Ephritikhine, *Chem Commun.*, 2003, **14**, 1660; c) R. Copping, B. Jeon, C. D. Pemmaraju, S. Wang, S. J. Teat, M. Janousch, T. Tyliszczak, A. Canning, N. Grønbech-Jensen, D. Prendergast and D. K. Shuh, *Inorg. Chem.*, 2014, **53**, 2506; d) C. D. Pemmaraju, R. Copping, D. E. Smiles, D. K. Shuh, N. Grønbech-Jensen, D. Prendergast and A. Canning, *ACS Omega*, 2017, **2**, 1055

[22] a) M. P. Wilkerson, C. J. Burns, D. E. Morris, R. T. Paine and B. L. Scott, *Inorg. Chem*., 2002, **41**, 3110; b) J. Maynadie, J.-C. Berthet, P. Thuery and M. Ephritikhine, *Chem. Commun.*, 2007, **5**, 486; c) J. -C. Berthet, P. Thuery, J.-P. Dognon, D. Guillaneux and M. Ephritikhine, *Inorg. Chem*., 2008, **47**, 6850; d) G. Szigethy and K. Raymond, *J. Am. Chem. Soc.*, 2011, **133**, 7942; e) E. A. Pedrick, J. W. Schultz, G. Wu, L. M. Mirica and T. W. Hayton, *Inorg. Chem*., 2016, **55**, 5693

[23] K. P. Carter, M. Kalaj, A. Kerridge, J. A. Ridenour and C. L. Cahill, *Inorg. Chem.*, 2018, **57**, 2714

[24] a) P. Thuéry and J. Harrowfield, *Dalton Trans*., 2017, **46**, 13660; b) M. B. Andrews, and C. L. Cahill, *Chem. Rev.*, 2013, **113**, 1121

[25] See for example: a) M. Kalaj, K. P. Carter, A. V. Savchenkov, M. M. Pyrch and C. L. Cahill, *Inorg. Chem*., 2017, **56**, 9156; b) M. J. Sarsfield, M. Helliwell and J. Raftery, *Inorg. Chem.*, 2004, **43**, 3170; c) P. L. Arnold, D. Patel, A. J. Blake, C. Wilson and J. B. Love, *J. Am. Chem. Soc.*, 2006, **128**, 9610

[26] See for example: a) P. Di Pietro and A. Kerridge, *Inorg. Chem*., 2016, **55**, 573; b) V. Vallet, U. Wahlgren and I. Grenthe, *J. Phys. Chem. A*, 2012, **116**, 12373

[27] a) T. Terencio, J. Roithová, S. Brandès, Y. Rousselin, M. –J. Penouilh and M. Meyer, *Inorg. Chem.*, 2018, **57**, 1125; b) S. Kannan, M. Kumar, B. Sadhu, M. Jaccob and M. Sundararajan, *Dalton. Trans.*, 2017, **46**, 16939; c) L. A. Watson and B. P. Hay, *Inorg. Chem.*, 2011, **50**, 2599; d) S. Fortier and T. W. Hayton, *Coord. Chem. Rev.*, 2010, **254**, 197

[28] J. de Groot, B. Cassell, M. Basile, T. Fetrow and T. Z. Forbes, *Eur. J. Inorg. Chem.*, 2017, 1938

[29] See for example a) A. C. Sather, O. B. Berryman and J. Jr. Rebek, *Chem. Sci.*, 2013, **4**, 3601; b) B. F. Parker, A. S. Knight, S. Vukovic, J. Arnold and M. B. Francis, *Ind. Eng. Chem. Res.*, 2016, **55**, 4187; c) A. C. Sather, O. B. Berryman and J. Jr. Rebek, *J. Am. Chem. Soc.*, 2010, **132**, 13572; d) T. S. Franczyk, K. R. Czerwinski and K. N. Raymond, *J. Am. Chem. Soc.*, 1992, **114**, 8138

[30] a) M. Kalaj, K. P. Carter and C. L. Cahill, *Eur. J. Inorg. Chem.*, 2017, 4702; b) K. P. Carter, M. Kalaj, R. G. Surbella III, L. C. Ducati, J. Autschbach and C. L. Cahill, *Chem. Eur. J.*, 2017, **23**, 15355; c) R. G. Surbella, L. C. Ducati, K. L. Pellegrini, B. K. McNamara, J. Autschbach, J. M. Schwantes and C. L. Cahill, *J. Am. Chem. Soc*., 2017, **139**, 10843; d) M. Kalaj, K. P. Carter, C. L. Cahill, *Acta Crystallogr., Sect. B: Struct. Sci*, 2017, **73**, 234; e) K. P. Carter, M. Kalaj and C. L. Cahill, *Inorg. Chem. Front.*, 2017, **4**, 65; f) K. P. Carter and C. L. Cahill, *Inorg. Chem. Front.*, 2015, **2**, 141; g) N. P. Deifela and C. L. Cahill, *Chem. Commun*., 2011, **47**, 6114

[31] R. G. Surbella III, M. B. Andrews and C. L. Cahill, *J. Solid State Chem*., 2016, **236**, 257

[32] R. G. Surbella III and C. L. Cahill, *CrystEngComm*, 2014, **16**, 2352

[33] R. G. Surbella III, L. C. Ducati, J. Autschbach, N. P. Deifel and C. L. Cahill, *Inorg. Chem.*, 2018, **57**, 2455

[34] C. E. Rowland, M. G. Kanatzidis and L. Soderholm, *Inorg. Chem.*, 2012, **51**, 11798

[35] a) F. Qu, Q. –Q. Zhu and C. –L. Liu, *Cryst. Growth Des.*, 2014, **14**, 6421; b) N. Aoyagi, K. Shimojo, N. R. Brooks, R. Nagaishi, H. Naganawa, K. Van Hecke, L. Van Meervelt, K. Binnemans and T. Kimura, *Chem. Commun.*, 2011, **47**, 4490

[36] a) J. C. Han, S. B. Rong, Q. M. Chen and X. R. Wu, *Chin. J. Chem.*, 1990, **4**, 313; b) R. Skala, P. Ondrus, F. Veselovsky, I. Cisarova and J. Hlousek, *Mineral. Petrol.*, 2011, **103**, 169

[37] A. W. Down, *Chem. Commun.*, 1968, 1290

[38] van der Waals radii taken from: S. Alvarez, *Dalton Trans.*, 2013, **42**, 8617

[39] a) R. Reddi, K. K. Singarapu, D. Pal and A. Addlagatta, *Mol. BioSyst.*, 2016, **12**, 2408; b) K. J. Wei, J. Ni, Y. S. Xie and Q. L. Liu, *Inorg. Chem. Commun.*, 2007, **10**, 279; c) H. P. Zhou, Y. M. Zhu, J. J. Chen, Z. J. Hu, J. Y. Wu, Y. Wie, M. H. Jiang, X. T. Tao and Y. P. Tian, *Inorg. Chem. Commun.*, 2006, **9**, 90; d) F. H. Allen, C. M. Bird, R. S. Rowland and P. R. Raithby, *Acta Crystallogr. Sect. B Struct. Sci.*, 1997, **53**, 696; e) G. R. Desiraju and T. Steiner, *The Weak Hydrogen Bond in Structural Chemistry and Biology*, Oxford University Press, 1999

[40] a) M. Domagała and S. J. Grabowski, *Chemical Physics*, 2010, **367**, 1; b) M. Domagała and S. J. Grabowski, *J. Phys. Chem. A*, 2005, **109**, 5683; c) S. Scheiner, S. J. Grabowski and T. Kar, *J. Phys. Chem. A*, 2001**, 105**, 10607

[41] a) S. Collado, A. Laca and M. Díaz, *J. Hazard. Mater*., 2010, **177**, 183; b) N. Kitanovski, A. Golobič and B. Čeh, *Acta Chim. Slov*., 2008, **55**, 767; c) L. J. Kirschenbaum and Y. Sun, *Inorg. Chem.*, 1991, **30**, 2360

[42] A. Zalkin, H. Ruben and D. H. Templeton, *Inorg. Chem.*, 1978, **17**, 3701

[43] A. R. Kampf, J. Plášil, A. V. Kasatkin, J. Marty, J. Čejka and L. Lapčák, *Mineral. Mag.*, 2017, **81**, 273

[44] A. L. Tamasi, P. Rungthanapathsophon, A. N. Dame, M. A. Moody, C. L. Barnes, M. P. Wilkerson and J. R. Walensky, *J. Coord. Chem.*, 2016, **69**, 1904

[45] See for example: R. Michalczyk, J. G. Schmidt, E. Moody, Z. Li, R. Wu, R. B. Dunlap, J. D. Odom and L. A. Silks III, *Angew. Chem. Int. Ed.*, 2000, **39**, 3067

[46] a) J. J. McKinnon, M. A. Spackman and A. S. Mitchell, *Acta Crystallogr. Sect. B: Struct. Sci.*, 2004, **60**, 627; b) M. A. Spackman and J. J. McKinnon, *CrystEngComm,* 2002, **4**, 378; c) S. K. Wolff, D. J. Grimwood, J. J. McKinnon, M. J. Turner, D. Jayatilaka and M. A. Spackman, *CrystalExplorer* (Version 3.1); University of Western Australia, 2012

[47] R. Glaser, R. Hillebrand, W. Wycoff, C. Camasta and K. S. Gates, *J. Org. Chem.*, 2015, **80**, 4360

[48] P. J. W. Elder and I. Vargas-Baca, *Phys. Chem. Chem. Phys.*, 2016, **18**, 30740

[49] J. Viger-Gravel, I. Korobkov and D. L. Bryce, *Cryst. Growth Des*., 2011, **11**, 4984

[50] L. H. Jones and R. A. Penneman, *J. Chem. Phys.*, 1953, **21**, 542

[51] a) D. D. Schnaars and R. E. Wilson, *Inorg. Chem.*, 2014, **53**, 11036; b) D. D. Schnaars and R. E. Wilson, *Inorg. Chem.*, 2013, **52**, 14138; c) G. Herzberg, *Infrared and Raman Spectra of Polyatomic Molecules*, D. Van Nostrand Company, Inc.: New York, 1946

[52] K. Nakamoto, *Infrared and Raman Spectra of Inorganic and Coordination Compounds*, 4th Edn John Wiley & Sons, 2006

[53] T. J. Carter and R. E. Wilson, *Chem. Eur. J.*, 2015, **21**, 15575

[54] E. Hashem, J. A. Platts, F. Hartl, G. Lorusso, M. Evangelisti, C. Schulzke and R. J. Baker, *Inorg. Chem.*, 2014, **53**, 8624

[55] W. Kaim and J. Fiedler, *Chem. Soc. Rev.*, 2009, **38**, 3373

[56] H. C. Hardwick, D. S. Royal, M. Helliwell, S. J. A. Pope, L. Ashton, R. Goodacre and C. A. Sharrad, *Dalton Trans.*, 2011, **40**, 5939

[57] D. L. Clark, S. D. Conradson, R. J. Donohoe, D. W. Keogh, D. E. Morris, P. D. Palmer, R. D. Rogers and C. D. Tait, *Inorg. Chem.*, 1999, **38**, 1456

[58] For recent examples see: a) D. Yaprak, E. T. Spielberg, T. Bäcker, M. Richter, B. Mallick, A. Klein and A. -V. Mudring, *Chem. Eur. J.*, 2014, **20**, 6482; b) T. Ogura, K. Takao, K. Sasaki, T. Arai and Y. Ikeda, *Inorg. Chem.*, 2011, **50**, 10525; c) Y. Ikeda, K. Hiroe, N. Asanuma and A. Shirai, *J. Nucl. Sci. Technol.*, 2009, **46**, 158

[59] E. Hashem, G. Lorusso, M. Evangelisti, T. McCabe, C. Schulzke, J. A. Platts and R. J. Baker, *Dalton Trans.*, 2013, **42**, 14677

[60] a) I. Grenthe, J. Drożdżyński, T. Fujino, E. C. Buck, T. A. Albrecht-Schmitt and S. F. Wolf, *The Chemistry of the Actinides and Transactinides,* 4th ed.; L. R. Morss, N. M. Edelstein and J. Fuger, Springer: Dordrect, The Netherlands, 2010, Chapter 5

[61] D. E. Morris, *Inorg. Chem.,* 2002, **41**, 3542

[62] S. -Y. Kim, H. Tomiyasu and Y. Ikeda, *J. Nul. Sci. Technol.*, 2002, **39**, 160

[63] a) C. Bleiholder, D. B. Werz, H. Köppel and R. Gleiter, *J. Am. Chem. Soc.*, 2006, **128**, 2666; b) C. Bleiholder, R. Gleiter, D. B. Werz and H. Köppel, *Inorg. Chem.*, 2007, **46**, 2249

[64] X. Guo, X. An and Q. Li, *J. Phys. Chem. A*, 2015, **119**, 3518

[65] I. Alkorta, I. Rozaz and J. Elguero, *J. Phys. Chem. A*, 1998, **102**, 9278

[66] See for example: A. Mandal, B. K. Patel, R. Shuklaand and D. Chopra, *CrystEngComm*, 2017, **19**, 1607

[67] D. J. R. Duarte, G. L. Sosa, N. M. Peruchenaa and I. Alkort, *Phys. Chem. Chem. Phys.*, 2016, **18**, 7300

[68] a) S. Collado, A. Laca and M. Díaz, *J. Hazard. Mater*., 2010, **177**, 183; b) L. J. Kirschenbaum and Y. Sun, *Inorg. Chem.*, 1991, **30**, 2360

[69] D. J. Watkin, R. G. Denning and K. Prout, *Acta Crystallogr., Sect. C: Cryst. Struct. Commun.*, 1991, **47**, 2517

[70] a) C. Clavaguèra-Sarrio, S. Hoyau, N. Ismail and C. J. Marsden, *J. Phys. Chem. A*, 2003, **107**, 4515; b) M. Straka, M. Patzschke and P. Pyykkö, *Theor. Chem. Acc.*, 2003, **109**, 332; c) J. L. Sonnenberg, P. J. Hay, R. L. Martin and B. E. Bursten, *Inorg. Chem.*, 2005, **44**, 2255; d) N. Iché-Tarrat, N. Barros, C. J. Marsden and L. Maron, *Chem. Eur. J.*, 2008, **14**, 2093

[71] See for example: A. J. Neel, M. J. Hilton, M. S. Sigman and F. D. Toste, *Nature*, 2017, **543**, 637

[72] K. Momma and F. Izumi, *J. Appl. Crystallogr*., 2011, **44**, 1272

[73] Y. Zhao and D. G. Truhlar, *Theor. Chem. Acc.,* 2008, **120**, 215

[74] Gaussian 09, Revision C.01, M. J. Frisch, G. W. Trucks, H. B. Schlegel, G. E. Scuseria, M. A. Robb, J. R. Cheeseman, G. Scalmani, V. Barone, B. Mennucci, G. A. Petersson, H. Nakatsuji, M. Caricato, X. Li, H. P. Hratchian, A. F. Izmaylov, J. Bloino, G. Zheng, J. L. Sonnenberg, M. Hada, M. Ehara, K. Toyota, R. Fukuda, J. Hasegawa, M. Ishida, T. Nakajima, Y. Honda, O. Kitao, H. Nakai, T. Vreven, J. A. Montgomery, Jr., J. E. Peralta, F. Ogliaro, M. Bearpark, J. J. Heyd, E. Brothers, K. N. Kudin, V. N. Staroverov, T. Keith, R. Kobayashi, J. Normand, K. Raghavachari, A. Rendell, J. C. Burant, S. S. Iyengar, J. Tomasi, M. Cossi, N. Rega, J. M. Millam, M. Klene, J. E. Knox, J. B. Cross, V. Bakken, C. Adamo, J. Jaramillo, R. Gomperts, R. E. Stratmann, O. Yazyev, A. J. Austin, R. Cammi, C. Pomelli, J. W. Ochterski, R. L. Martin, K. Morokuma, V. G. Zakrzewski, G. A. Voth, P. Salvador, J. J. Dannenberg, S. Dapprich, A. D. Daniels, O. Farkas, J. B. Foresman, J. V. Ortiz, J. Cioslowski, and D. J. Fox, Gaussian, Inc., Wallingford CT, **2010**

[75] W. Küchle, M. Dolg, H. Stoll and H. Preuss, *J. Chem. Phys.*, 1994, **100**, 7535

[76] AIMAll (Version 12.06.03), Todd A. Keith, TK Gristmill Software, Overland Park KS, USA, 2012

Chapter 5

Noncovalent Interactions in *N*-Aryl-9,10-iminophenanthrenequinones and Reactions between Iminoalkoxy Semiquinone Radical Anions and UCl_4

5.1 Introduction

5.1.1 Magnetic Coupling Interactions Between Radical-Ligands and Metal Ions

The possibility of modifying the magnetic properties of a metal by coupling interactions with an organic radical has been attracting the attention of the scientific community and several research groups are currently studying new strategies for synthesising novel organometallic complexes bearing organic radicals.[1]

A strong spin-spin magnetic coupling has been clearly observed in many radical-containing transition metal (TM) complexes, where the coupling principally arises from direct orbital overlap between the TM and the radical. The radical-ligands most successfully used for this purpose range among different type of molecules: from the more established nitronyl nitroxide and benzosemiquinonoid ligands,[2] to the more recently developed verdazyl, thiazyl, and carbene ligands,[3] including tetracyanoethylene, 7,7,8,8-tetracyanoquinodimethane, *N,N′*-dicyanoquinonediimine and perchlorotriphenylmethyl radicals.[4] Some examples of these are shown in Figure 5.1.

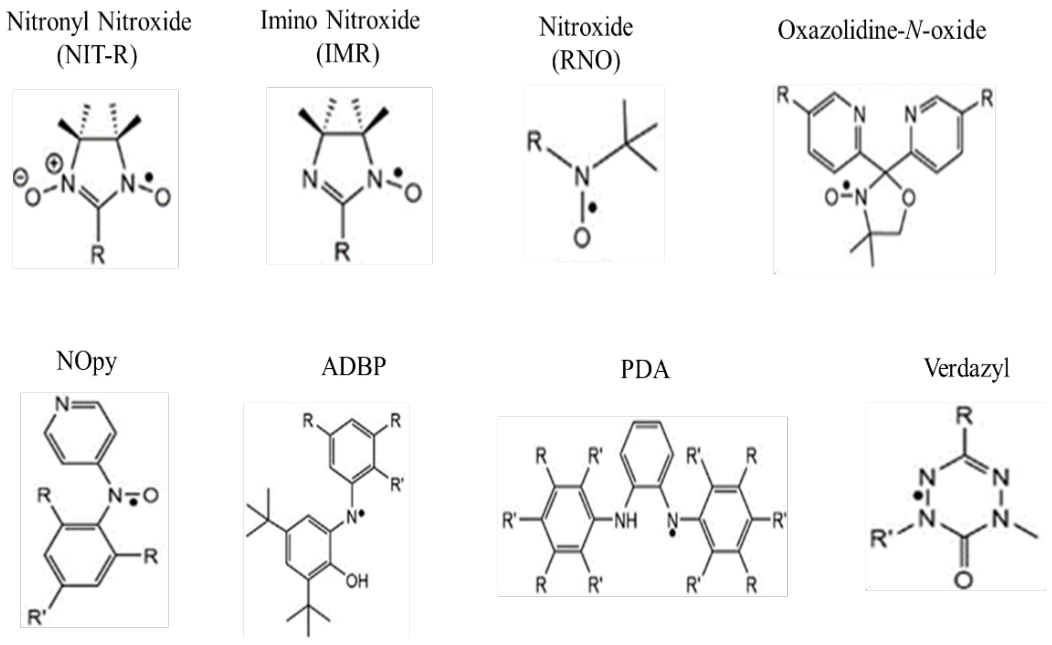

Figure 5.1. Examples of radical-ligands which show magnetic coupling with transition metals, from top-to bottom, left-to-right: nitronyl nitroxide, imino nitroxide, nitroxide, oxazolidine-*N*-oxide, NOpy, ADBP, DPA, verdazyl.

In contrast to TM chemistry, the synthesis of lanthanide-radical compounds showing strong magnetic coupling interactions is more challenging, mainly considering the contracted valence *4f* orbitals of the lanthanide ions. This aspect, indeed, represents an obstacle for building extended magnetically coupled structures. Nevertheless, extraordinary efforts have been undertaken to synthesize lanthanide complexes bearing radical-ligands and several examples have been reported.[5] In this field, the lanthanides have been attracting attention because they possess greater spin-orbit coupling and, therefore, larger magnetic anisotropy (*D*). With these features, their complexes could display unusual interesting magnetic properties. Additionally, although their chemistry is mainly restricted on the +3 oxidation state, the ability of lanthanides to accommodate high coordination numbers offer possibilities of extended Ln^{III}-radical networks.

Compared to TM and lanthanides, actinides are particularly attractive for synthesising complexes featuring magnetic coupling between a metal centre and a radical-ligand. In fact, spin-orbit coupling for the actinides is approximatively twice that of the lanthanides, giving rise to much larger single-ion anisotropies (*D*) compared to both TM and lanthanides. Furthermore, the greater radial extension of the actinide *5f* valence orbitals can better facilitate magnetic exchange through enhanced overlap with radical-ligands orbitals. Moreover, actinides (especially the early An) possess a wide range of accessible oxidation states,[6] which makes the usage of oxidising and reducing organic radicals more conceivable. However, in comparison with TM and lanthanides, examples of radical-containing actinide complexes are more rare and mainly restricted to uranium compounds. Figure 5.2 lists six selected examples for U(IV) complexes. These U(IV) complexes are composed with (a) ketyl,[7] (b) diphenyldiazomethane,[8] (c) ($CO_2^{\bullet-}$),[9] (d) azobenzene,[10] (e) iminoquinone[11] and (f) bridging quinoid radical-ligands.[12] Moreover, while for the last compound (Figure 5.2f) the variable temperature magnetic profile has not been reported, the other complexes exhibit a low temperature (5 K) effective magnetic moment higher compared to common U(IV) complexes[13] and this effect has been assigned as due to an additional contribution from the radical-ligand. For example, for [((*t*-BuArO)$_3$tacn)U^{IV}(OC•*t*-BuPh$_2$)] (Figure 5.2a), four resonance structures constitute the whole molecular structure (Figure 5.3) which have also been confirmed by DFT calculations.[14]

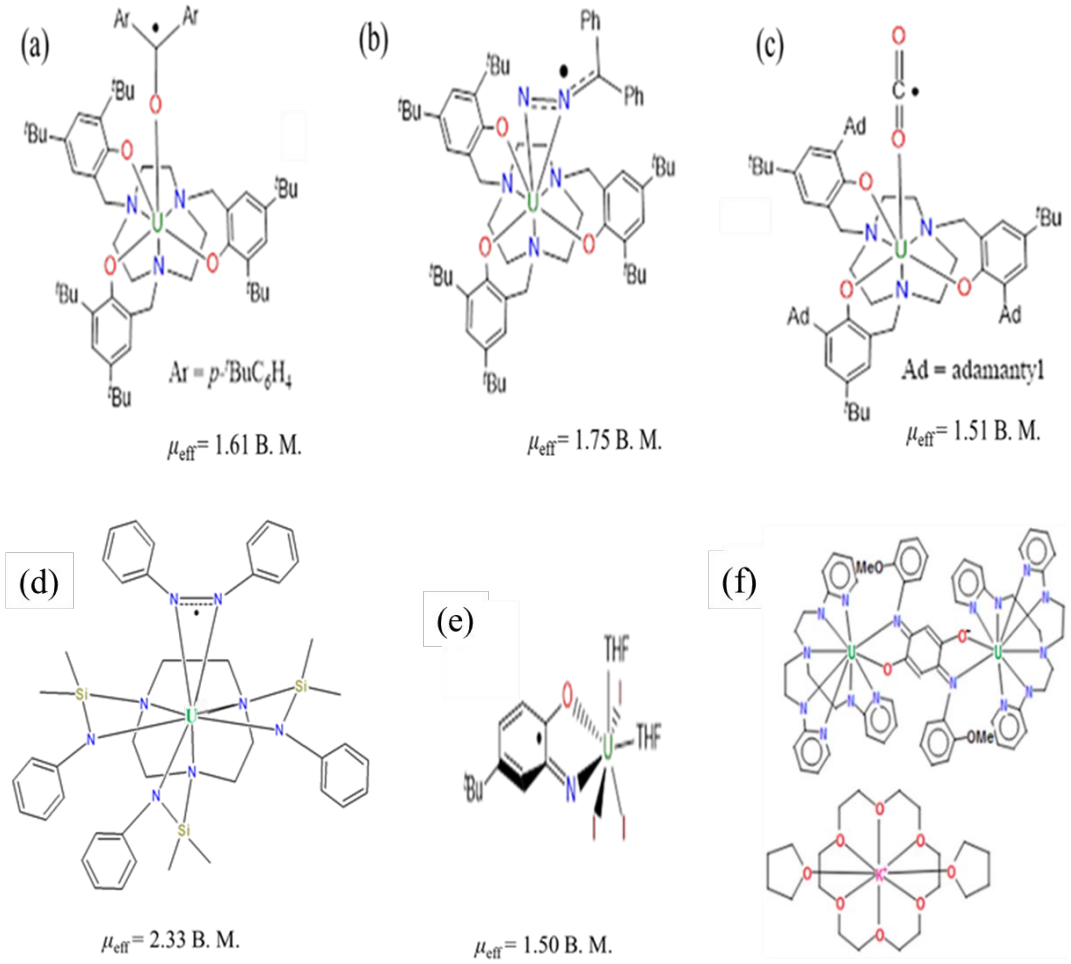

Figure 5.2. Radical-ligand containing U(IV) complexes, that have unusual high magnetic susceptibility (> 1.0 B. M.) at low temperatures (< 5 K).

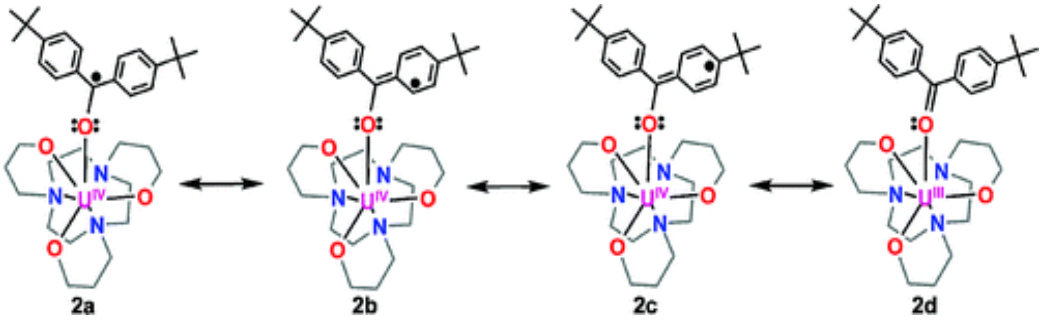

Figure 5.3. Resonance structures of [((*t*-BuArO)$_3$tacn)U^{IV}(OC•*t*-BuPh$_2$)].[12]

Among these resonance structures, one displays a U(III) ion formed by delocalization of the unpaired electron on the uranium ion. Thus, this compound cannot be considered as an ordinary $5f^2$ U(IV) complex and its low-temperature magnetic moment (5 K, μ_{eff} =1.61 B. M.), unusually high for a U(IV) complex,[13] is likely due to magnetic

contributions from both the disubstituted benzophenone radical-ligand and the resonance structure possessing a U(III) ion.

On this line, remarkable are also the attempts performed by Walter *et al.* [15] where they tried to isolate a Th(III) complex by coordination with a 2,2′-bipyridyl ligand. The 2,2′-bipyridyl is, indeed, a redox non-innocent ligand and, as shown in Chapter 3, can also behave as a radical monoanion. Thus, they synthesized thorium metallocene complexes containing a 2,2′-bipyridyl ligand: $[\eta^5\text{-}1,2,4\text{-}(Me_3C)_3C_5H_2]_2Th(bipy)$ and $[\eta^5\text{-}1,3\text{-}(Me_3C)_2C_5H_3]_2Th(bipy)$. However, experimental and computational data are consistent with a diamagnetic Th(IV)($bipy^{2-}$) ($f^0d^0\ \pi^{*2}$, $S = 0$) configuration for both complexes. Nevertheless, as clearly shown by the ytterbium complex $Cp^*_2Yb(bipy)$, whose configuration would be best described as a mixture between f^{13}-($bipy^{\bullet-}$) and f^{14}-($bipy^0$),[16] the assignment of formal oxidation states in organometallic complexes bearing a bipy ligand is very complicated.

Interestingly, it is also possible that there is no magnetic coupling between coordinated radical-ligands and a uranium central ion. In fact, Bart *et al.*[17] reported a study on U(IV) complexes bearing redox-active diazabutadiene ligands, namely $(^{Mes}DAB^{Me})_2U(THF)$ and $Cp_2U(^{Mes}DAB^{Me})$ ($^{Mes}DAB^{Me}$ = [ArN=C(Me)C(Me)=NAr]; Ar = 2,4,6-trimethylphenyl), for which the magnetic data are consistent with singlet ground states at low temperature and variable-temperature dependencies that are typical of simple U(IV) species.

5.1.2 SMM Based on Lanthanide and Actinide Complexes

Single-molecule magnets (SMM) are molecules that exhibit an energy barrier (U) to magnetic relaxation that enables them to retain their magnetization orientation after removal of an applied field.[1] Remarkably, these molecules exhibit magnetic hysteresis loops reminiscent of classical magnets[18] and their molecular nature also leads to unusual quantum phenomena such as quantum tunnelling of the magnetization. Due to these properties, single-molecule magnets could be potentially used for fabrication of molecular spintronics, quantum information storage and processing devices.[19]

The energy barrier for the magnetic relaxation can be considered as the energy level that the spins must overcome to switch from parallel to antiparallel alignment with respect to the applied field. It is defined as $U = S^2 \left| D \right|$, for integer-spin molecules, and as $U = (S^2 - ¼) \left| D \right|$, for half-integer spin molecules, where: S is the dimensionless total spin

state and *D* is the axial zero-field splitting parameter (magnetic anisotropy), measured in cm^{-1}.[1] The energy barrier is typically reported in cm^{-1} or K and the higher is the value, the longer a material can remain magnetized.

From this definition, it is clear that a high energy barrier (SMM behaviour) can be obtained with many unpaired electrons and with a large value of *D*. The lanthanides, which possess larger spin-orbit coupling compared to TM, have proved to be good candidates for this purpose and a considerable number of lanthanide-based compounds exhibiting SMM behaviour have been reported.[20] However, the actinides exhibit stronger spin-orbit coupling, larger magnetic anisotropy and, due to the larger radial extension of the *5f* orbitals, enhanced exchange interactions. Thus, they can be considered as better candidates than lanthanides to provide SMM behaviour.[21]

The most feasible *5f* element to be employed in SMM research appears to be uranium, which has Russell-Saunders ground states of $^4I_{9/2}$, $^3H_4$ and $^2F_{5/2}$ in its +3, +4 and +5 oxidations states, respectively. Some examples of SMM systems based on U(III) ($5f^3$, J = 9/2)[22] and uranyl(V) ($5f^1$, J = 5/2) have been reported.[23] Both U(III) and U(V) are Kramers ions (S = half integer) and possess large values of angular momentum *J*. These properties guarantee the presence of a doubly-degenerate $\pm mJ$ ground state, which is an important requisition for SMM behaviour. The U(IV) ion, instead, with a valence $5f^2$ configuration and a Russel-Saunders $^3H_4$ ground state, is a non-Kramers ion, and thus no SMM behaviour should be expected for a U(IV) complex, as it tends to exhibit a non-degenerate singlet ground state at low temperature.[24] In this regard, however, the only exception seems to be represented by the compound $Cs_4[U(NCS)_8]$, in which, as discussed in Chapter 2, the U(IV) ion shows a triplet electronic ground state even at low temperature. In addition, Coronado *et al.*[10] have proved that an appropriate choice of ligand environment at U(IV) and the presence of a radical can drastically change the magnetic behaviour. In fact, in the complex $[\{(SiMe_2NPh)_3tacn\}U^{IV}(\eta^2\text{-}N_2Ph_2\bullet)]$ (tacn = 1, 4, 7 - triazacyclononane) (Figure 5.2d), a strong magnetic coupling between an azobenzene radical ligand and the U(IV) ion centre switched the parity of the U(IV) ion from non-Kramers to Kramers, allowing magnetic relaxation to occur. This represents the first example of a formally U(IV) complex with SMM behaviour.

5.1.3 *N*-(mono-substituted)-9,10-iminoalkoxy Semiquinone Radical Ions

In this chapter, attempted reactions between *N*-(mono-substituted)-9,10-iminoalkoxy semiquinone radical ions and UCl_4, as source of a paramagnetic U(IV) compound, will be described. The main goal was to synthesize a complex between an iminoalkoxy semiquinone radical ion and uranium(IV), to finally investigate magnetic coupling interactions between the $5f^2$ U(IV) ion and the radical spin system.

N-aryl-9,10-iminoalkoxy semiquinone radical ions can be obtained by reduction of neutral *N*-aryl-9,10-iminophenanthrenequinone ligands. *N*-aryl-9,10-iminophenanthrenequione ligands, indeed, can behave as redox non-innocent ligands: they can readily undergo a one-electron reduction to form iminoalkoxy semiquinone radical ions, but also a two-electron reduction to form aminophenolate derivatives, as shown in Scheme 5.1.

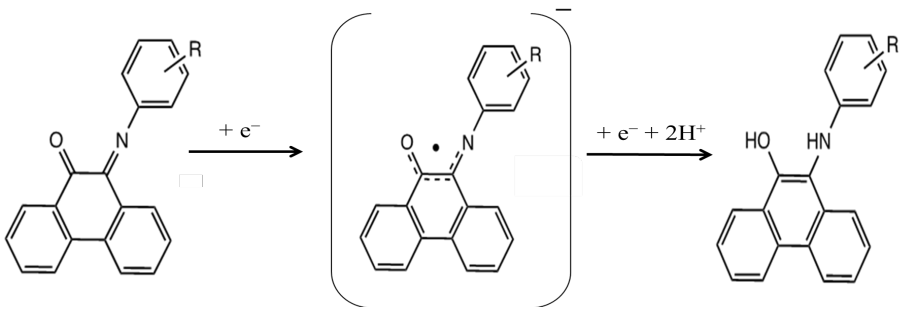

Scheme 5.1. Redox states of *N*-aryl(mono-alkylsubstituted)-9,10-iminophenanthrenequinone ligands.

In the intermediate radical, the unpaired electron can be considered as delocalized over the O–C–C–N system. In addition, several resonance structures can be drawn for this radical, where both the *N*-aryl ring and the phenanthrene system can contribute to stabilize the intermediate radical.

Moreover, recently, B. Gao *et al.* [25] demonstrated that *N*-Aryl-9,10-iminophenanthrenequinones can be successfully reduced by $CrCl_2$ affording corresponding monoanionic Cr(III) complexes (Scheme 5.2), for which the magnetic data are indicative of a Cr(III) ion ($S = 3/2$) antiferromagnetically coupled to a ligand centered radical ($S = 1/2$).[26] B. Gao *et al.*[27] also reported on the reduction of *N*-Aryl-9,10-iminophenanthrenequinones mediated by magnesium in THF solution (Scheme 5.2); in particular, using 0.5 equiv. of Mg, a 1-electron reduction occurred and paramagnetic mononuclear magnesium complexes bearing radical ligands were isolated, but with an

excess of Mg a 2-electron reduction was observed and a diamagnetic dinuclear magnesium complex was obtained. In this regard, B. Xu *et al.*[28] showed that *N*-aryl-9,10-iminophenanthrenequinone ligands can be successfully reduced also by direct reaction with iron powder in THF solution (Scheme 5.2). The crystallographic and magnetic data of the resulting compounds, indeed, were indicative of a Fe(III) complex with two radical anionic ligands in an η^2 fashion and one amine-phenolate ligand in an η^1 manner. Moreover, they also proved that the redox reaction of these ligands with $FeCl_2$ in THF produces Fe(III) chloride complexes with two chelating iminoalkoxy semiquinone radical anions.

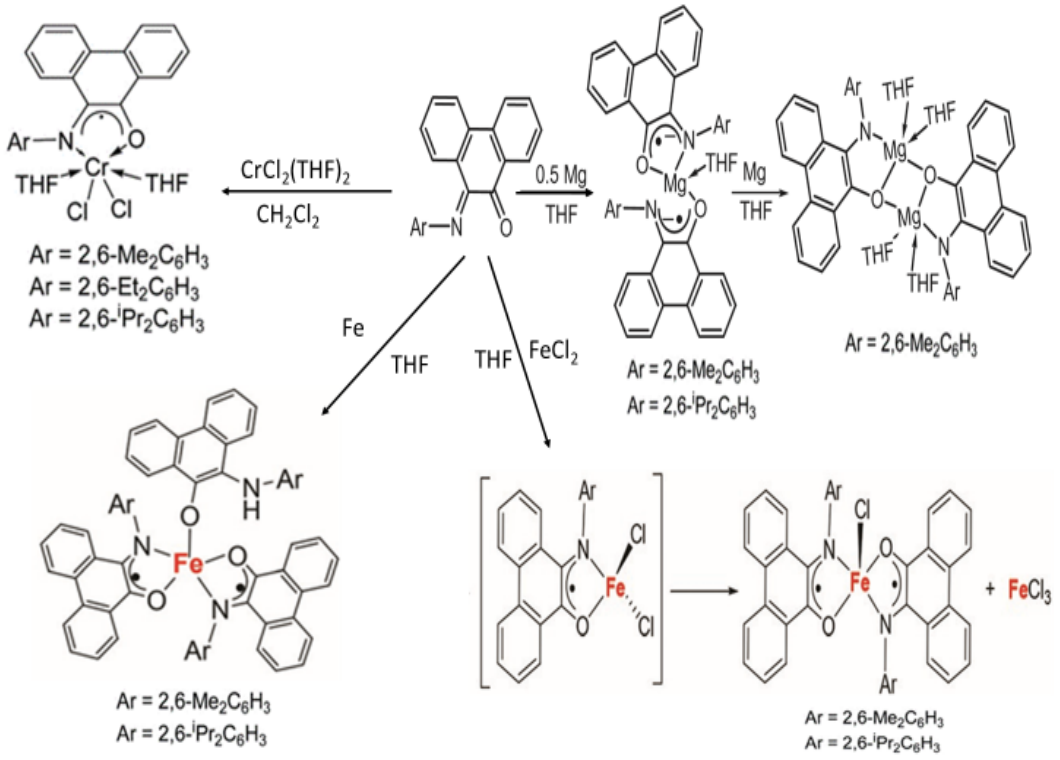

Scheme 5.2. Reduction of *N*-aryl(mono-alkylsubstituted)-9,10-iminophenanthrenequinone ligands mediated by $CrCl_2$, Mg, Fe and $FeCl_2$.

When coordinate via nitrogen or oxygen donor atoms, these radicals behave also as "hard" ligands; thus, they could readily coordinate "hard" metals, such as Ln or Ac. For example, recently, Farnaby *et al.*[51] have successfully isolated and spectroscopically characterized a novel Yb(III) complex bearing a semiquinone radical of 1,10-phenanthroline-5,6-dione, where the radical is coordinated to the Yb^{3+} cation through Yb–N bonds.

There are few reported structures containing the phenanthrene moiety, thus this Chapter contains a structural and spectroscopic study on a series of *N*-Aryl-9,10-iminophenanthrenequinone compounds, with particular attention reserved to explore the supramolecular noncovalent interactions.

Of the multitude of noncovalent interactions reported in the literature, aromatic interactions such as C–H···π interactions[29] or π-stacking are important, especially in π-conjugated organic molecules. Several studies have been ongoing for the past two decades to understand the origin of substitution effects on the strength of the π-stacking interactions. The popular model proposed by Hunter and Sanders, [30] namely π-polarisation, has now been called into question and the model elaborated by Wheeler and Houk[31] is consistent with most of the literature. This involves the direct interactions between the C–H/X dipoles of substituted aromatic interactions, which may be attractive or repulsive. According to this model, electron-withdrawing substituents enhance π-stacking interactions by withdrawing π-electron density from the substituted benzene, reducing the electrostatic repulsion with the other benzene, while electron-donating substituents reduce π-stacking interactions by the opposite mechanism. A number of recent reviews summarise the current thinking,[32] but it is clear that more experimental data is required. Halogen bonding is another noncovalent interaction which has become increasingly recognised, [33] particularly in supramolecular chemistry and crystal engineering.[34]

Thus in this Chapter a number of *N*-Aryl-9,10-iminophenanthrenequinone compounds have been used as scaffolds for exploring noncovalent interactions such as "π–π stacking" via the Wheeler and Houk mechanism,[31] C–H···π, C–X lone pair···π, C–X···H–C and C–X···X–C, where it is possible to also control the steric demand of the ligand systems. Particular attention has been reserved on two types of interactions: (1) those arising from the introduction of a halogen, and (2) those due to the steric demands of the ligands. DFT and AIM analysis have been used to compare the strength of these interactions. Reduction reactions of these ligands have also been attempted and the resulting radical anions have been spectroscopically characterized. Finally, these radicals have been reacted with UCl_4 and the resulting products are described.

5.2 Synthesis and Structural Investigation of Mono Substituted Iminophenanthrenequinones

5.2.1 Structural Characterization

The phenanthrene ligands were synthesized according to Scheme 5.3.

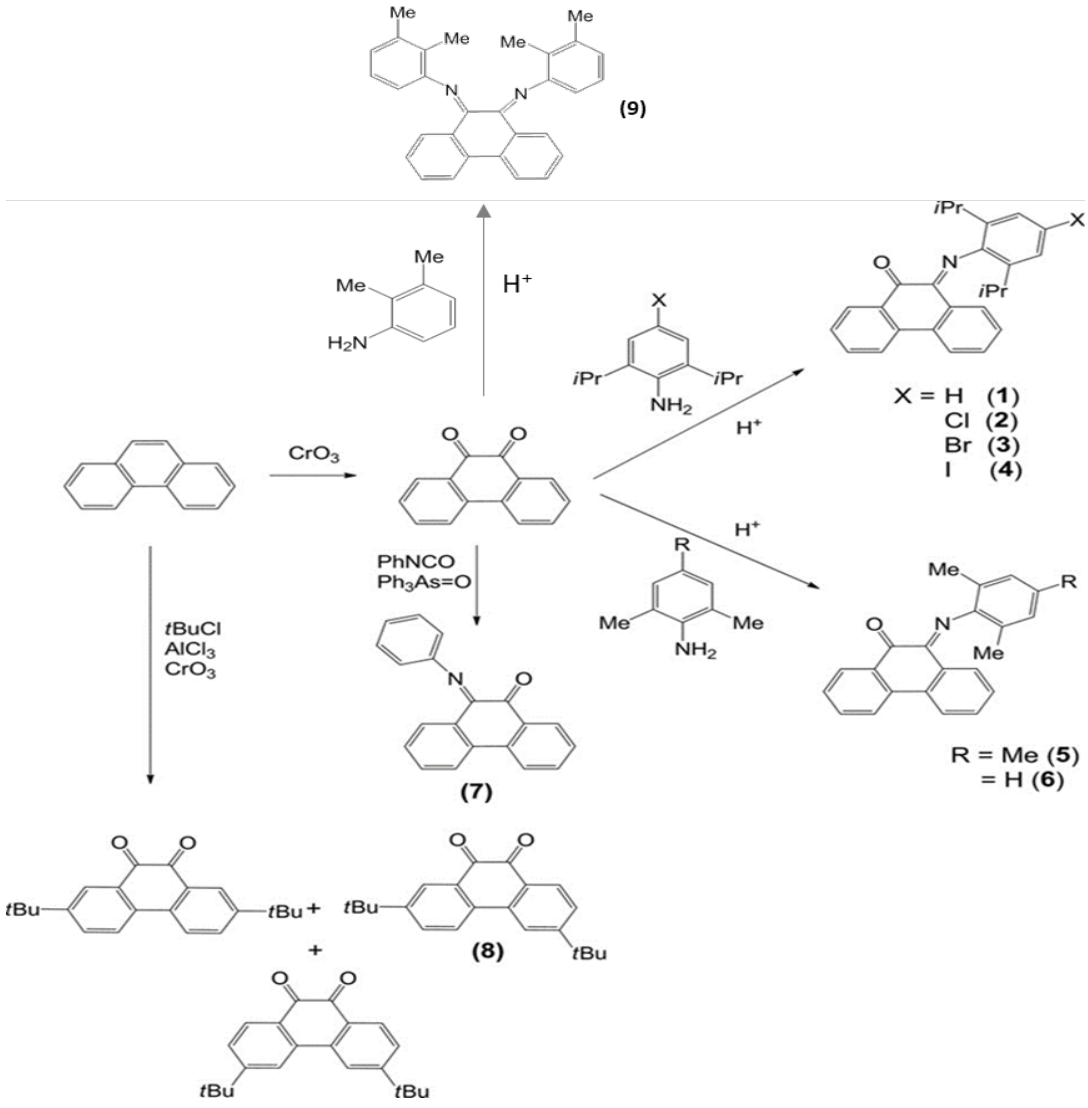

Scheme 5.3. Synthesis of the different phenanthrene ligands from **1** to **9**.

The phenanthrene-9,10-dione was obtained from commercial sources or prepared from phenanthrene via a Jones oxidation. The compounds from **1** to **6** were then obtained by condensation reaction between the appropriate substituted aniline and phenanthrene-9,10-dione in MeCN solutions, in the presence of a catalytic amount of formic acid. This method did not work for the aniline (compound **7**), probably because of the absence in

ortho positions of alkyl electron-donating groups stabilizing the carbocation intermediate of the reaction. Thus, for the preparation of **7**, an alternative strategy was used, whereby phenanthrene-9,10-dione was reacted with phenyl isocyanate in the presence of a catalytic amount of $Ph_3As{=}O$.[35] After the synthesis, the crude products were purified by column chromatography to obtain the desired compounds. The 2,7-di-*tert*-butylphenanthrene-9,10-dione (**8**) was prepared via Friedel-Craft alkylation and the three isomers separated by careful column chromatography; however, it was not possible to grow single crystals for the other two isomers, so these will be not discussed. Moreover, when the same condensation reaction was performed with 2,3-dimethylaniline (as the substituted aniline), a diimino compound, namely *N,N′*-(2,3-dimethylphenyl)-9,10-diiminophenanthrene (**9**), was obtained. The presence of a strong Lewis acid, such as $TiCl_4$/Dabco (Dabco = 1,4-diazabicyclo[2.2.2]octane),[36] is necessary to catalyse the condensation reaction on both carbonyl functions, therefore the mechanism that led to the formation of this molecule is not clear.

Finally, no reaction occurred with the very bulky 2,4,6-tri-*tert*-butylaniline, even after prolonged reflux. Crystals of the compounds **1**-**4**, **6**, **8, 9** were grown by slow evaporation of solutions of chloroform. For **5** and **7**, however, a further recrystallisation from Bu_2O and hexane was found necessary. The discussion will firstly focus on the molecular structures, followed by the packing arrangements and the description of the noncovalent interactions. The molecular structure of **1**, reported in Appendix 4 (Figure 27), suffers disorder from whole molecule and therefore the corresponding metric parameters will not be described. Its crystallographic data are listed in Appendix 4, while the full list of bond lengths and angles are tabulated in Appendix 4.1.

The molecular structures of the ligands **2**, **3**, **4**, **5**, **6**, **7** and **8** are collated in Figure 5.4; the corresponding crystallographic data are listed in Appendix 4, while the full list of bond lengths and angles are tabulated in Appendix 4.2-4.5 in the external CD source of this thesis.

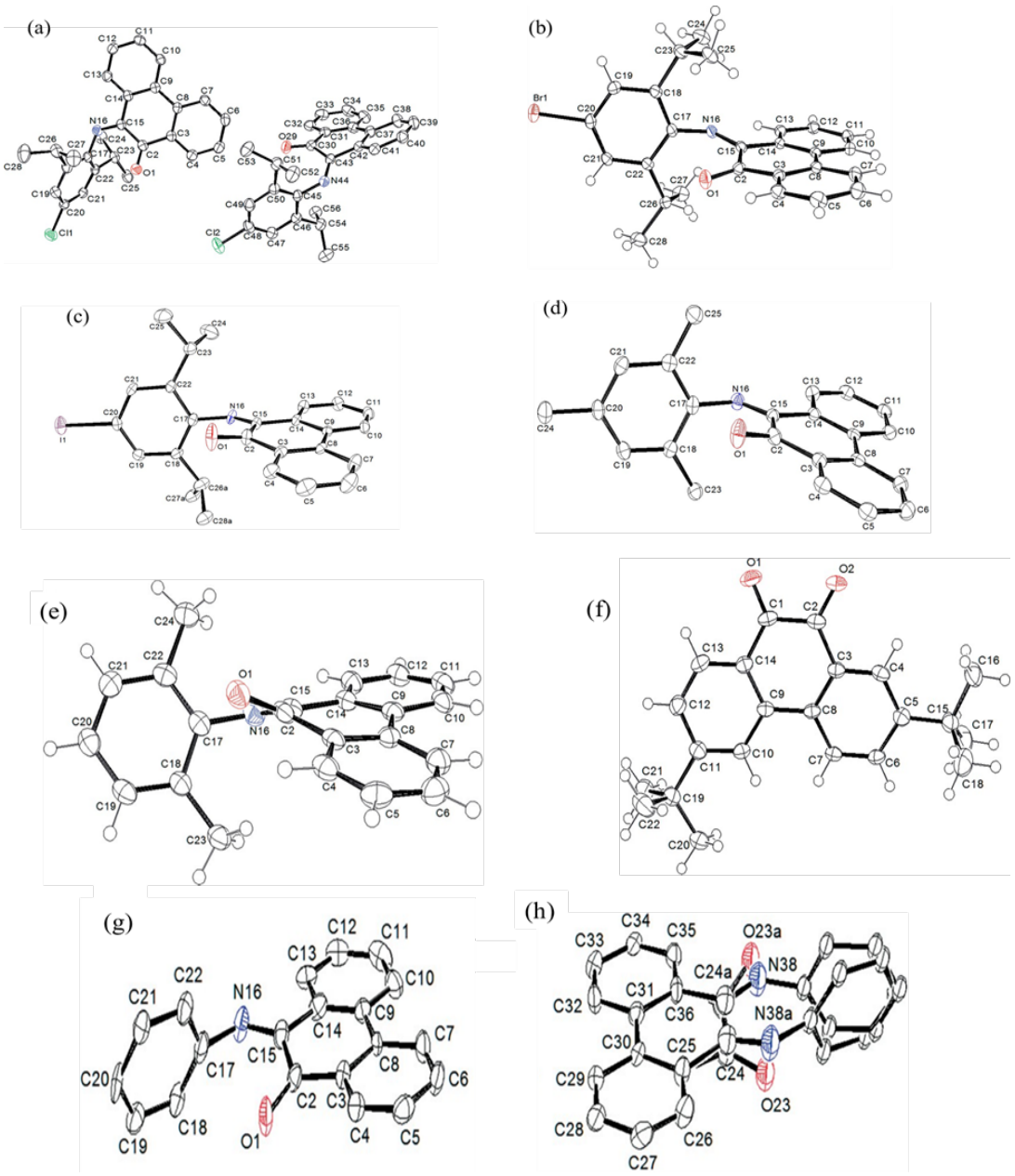

Figure 5.4. Molecular structure of (a) **2**, (b) **3**, (c) **4**, (d) **5**, (e) **6** and (f) **8**; (g) major 82% and (h) minor 18% disordered moiety of **7**, that will be labelled as, respectively, **7g** and **7h** in the text. Atomic displacement shown at 50% probability and hydrogen atoms omitted for clarity in the structures of **2**, **4**, **5** and **7**. For compound **2**, there were two molecules in the asymmetric unit and are labelled as **2a** and **2b** in the text.

The metric parameters of the phenanthrene backbone in the series **2-8** are listed in Table 5.1. In the series **2-7**, they do not change significantly and the C–C, C=N and C=O bond lengths are also essentially identical. The molecular structure of compound **9** will be discussed separately.

Table 5.1. Selected structural parameters in the structures of **2-9** (in Å and °).

	C=O	C=N	C–C	C–C–C–C	N–C–C–O	C=N oop[(a)]	C=O oop[(a)]	α[(b)]	β[(b)]
2a	1.216(3)	1.282(3)	1.526(3)	6.6(4)	16.2(4)	−0.429	0.375	-	-
2b	1.220(3)	1.275(3)	1.520(3)	11.5(4)	29.6(4)	−1.013	0.375	70	112
3	1.216(2)	1.279(2)	1.519(2)	5.2(2)	15.2(2)	−0.320	0.226	82	85
4	1.208(5)	1.280(5)	1.519(6)	2.3(6)	8.8(6)	−0.179	0.142	89	79
5	1.218(3)	1.280(3)	1.520(2)	2.1(3)	8.6(3)	−0.193	0.123	-	-
6	1.218(3)	1.278(4)	1.517(4)	9.11(4)	29.1(4)	−0.546	0.787	-	-
7g[(c)]	1.215(7)	1.273(8)	1.506(9)	3.3(9)	13.7(10)	−0.170	0.464	-	-
8	1.215(2), 1.220(2)	-	1.541(2)	7.1(2)	6.3(2)	-	0	-	-
9	-	1.417(2) 1.4154(19)	1.514(2)	12.3(2)	N–C–C–N 51.8(2)		-	-	-

(a) o.o.p. = distance out of the plane of the phenanthrene backbone (Å). (b) Intermolecular contacts α is the angle between the plane of the ring, centroid and X,[37] while β = C–X···centroid angle. (c) = There are two molecules in the asymmetric unit of which one is disordered. Only dimensions from the ordered molecule (**7g**) are reported.

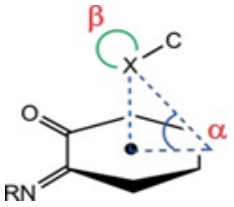

Figure 5.5. Representation of the angles α, formed between the plane of the ring, its centroid and X;[37] β, formed from the intersection between C–X bond and X···centroid distance.

The most noticeable difference is in the planarity of the phenanthrene backbones which is disrupted in **2** and **6** and to a much lesser extent in **3**; while **4**, **5** and **7** are flat. Compound **2** has two molecules in the asymmetric unit; the bond lengths in **2a** and **2b** are identical, but interesting the planarity of the phenanthrene backbones is different. In molecule **2a** the torsion angles C(7)–(C8)–C(9)–C(10) = 6.6(4)° and O(1)–C(2)– C(15)–N(16) = 16.2(4)°, while in molecule **2b** the torsion angles C(35)–C(36)–C(37)–C(38) = 11.5(4)° and O(29)–C(30)–C(43)–N(44) = 29.6(4)°. A search of the Cambridge Structural Database (CSD version 5.37 and updates to November 2016), on the fragment shown below (Figure 5.6), generated 195 hits and shows that the median of the C–C–C–C torsion angle (in red bold in the fragment below) is of 2.999° and the one of the X–C–C–X is equals to 2.882° (X = any atom).

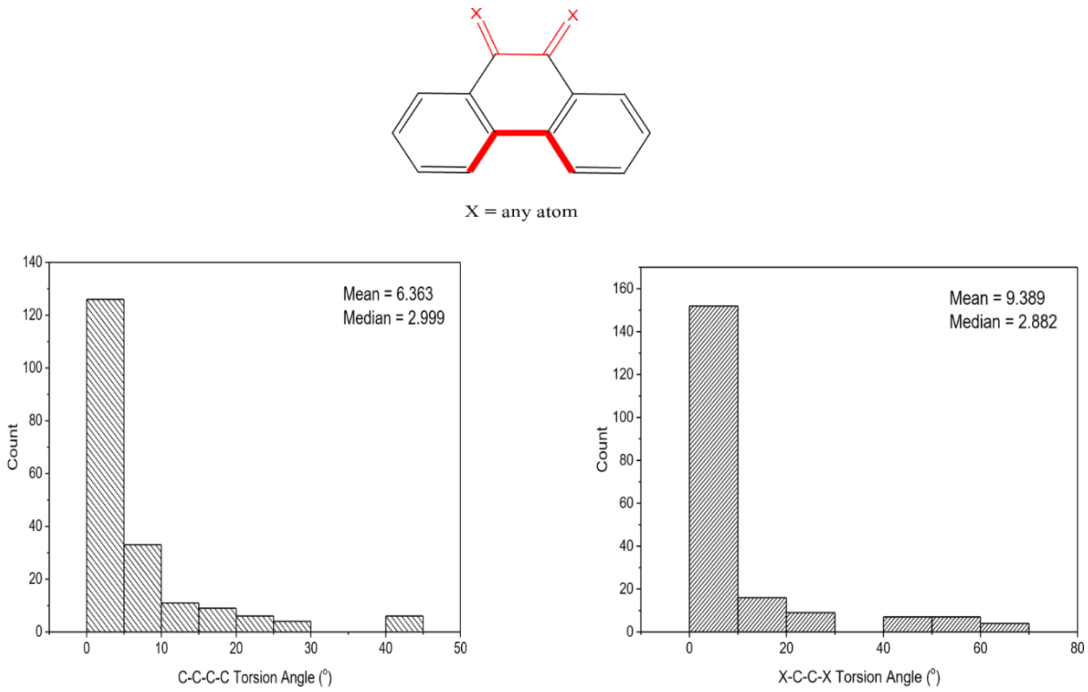

Figure 5.6. Histograms of the C-C-C-C (left) and X-C-C-X (right) torsion angles obtained from a CCDC search.

Compound **7** (Figure 5.4g and Figure 5.4h) has two molecules in the unit cell, one of which (**7h**) is disordered, but the metric parameters are identical. Moreover, in this molecule, the C=O and the C=N bonds are significantly out of the plane of the phenanthrene unit. In the structure of **8** (Figure 5.4f), the C(1)–C(2) bond length of 1.541(2) Å and the C=O bond lengths of 1.220(2) and 1.215(2) Å are typical of phenanthrene-9,10-diones, e.g. 1.52(3) to 1.524(5) Å for the C–C and 1.207(6)-1.25(2) Å for the C=O in the different polymorphs of phenanthrene-9,10-dione.[38]

5.2.2 Packing and Intermolecular Interactions in 2-4

In the structures of the halogenated compounds, **2**-**4**, there are no C–X···O=C or X···X interactions, but some identical interactions are observed (Figure 5.7). In **2** there are a number of C–H···O interactions [39] between H(5) and H(6) [hydrogens are in the calculated positions in all structures; $d_{C\cdots O}$ = 3.293(3) and 3.279(3) Å] and C–H···N interactions involving N(44) and H(7) and H(10) [$d_{C\cdots N}$ = 3.633(11) and 3.618(8) Å] (Figure 5.7a); if **2** is recrystallized from DMF, the same structure is formed, indicating that the crystal packing interactions are reproducible in different solvents. In contrast, in **3** and **4** the C–H···O are from H(10) and H(11) [**3**: $d_{C\cdots O}$ = 3.123(4) and 3.081(4) Å; **4**: $d_{C\cdots O}$ = 3.108(5) and 3.117(6) Å] and no C–H···N interactions are present (Figure 5.7c

for **3**; **4** is identical). A C–H···π interaction from a phenanthrene H to the X-substituted aryl group ($d_{C–H\cdots cent}$ = 2.564 Å) is present in 2 (Figure 5.7a), while in 3 and 4 there is also longer one from an isopropyl hydrogen to the phenanthrene (3: $d_{C–H\cdots cent}$ = 2.576 and 3.160 Å; 4: $d_{C–H\cdots cent}$ = 2.552 and 3.126 Å; Figure 5.7b). In **2a**, there are phenanthrene groups not involved in a lone pair···π interactions[40] but are close to another Cl atom and inspection of the angles show that this is a type I interaction[41] (the two types of halogen bonding have been described in the introduction of Chapter 4). There is a short contact of 3.238 Å between the C–Cl and the centroid of an adjacent phenanthrene ring which has the larger deviation from planarity (**2b**) and shown in Figure 5.7b. This lone pair···π interaction is of a semi-localized type according to the scheme developed by Shishkin,[42] and within the sum of van der Waals radii (C···Cl = 3.45 Å). In **3** and **4** this lone pair···π interaction [**3**: 3.396(8) Å; **4**: 3.569(7) Å; Figure 5.7d] is a delocalized interaction[42] where an inspection of the α and β angles shows that the heavier halogens move close to the centre of the ring (Table 5.1). Both are within the van der Waals radii (3.55 Å for C···Br and 3.68 Å for C···I). However, a recent high level theoretical study has shown that in R–Br··π interactions with benzene (R = H, HC≡C and NC), it is only the distance that influences the strength of the interactions and not the angles.[43] The closest Br···Br and I···I distances are 4.370(6) and 4.125(6) Å respectively and thus outside the sum of the van der Waals radii. The second form of weak hydrogen bonds are X···H–C_{sp2} [**2**: $d_{C\cdots Cl}$ = 3.781(3) Å; **3**: $d_{C\cdots Br}$ = 3. 800(4) Å] from a phenanthrene hydrogen in **2** and an isopropyl hydrogen in **3**; in **4** there are no C–H···I contacts within the sum of the van der Waals radii. There are no obvious π–π stacking interactions in **2**–**4**, presumably due to the increased steric demand of the halogen substituents.

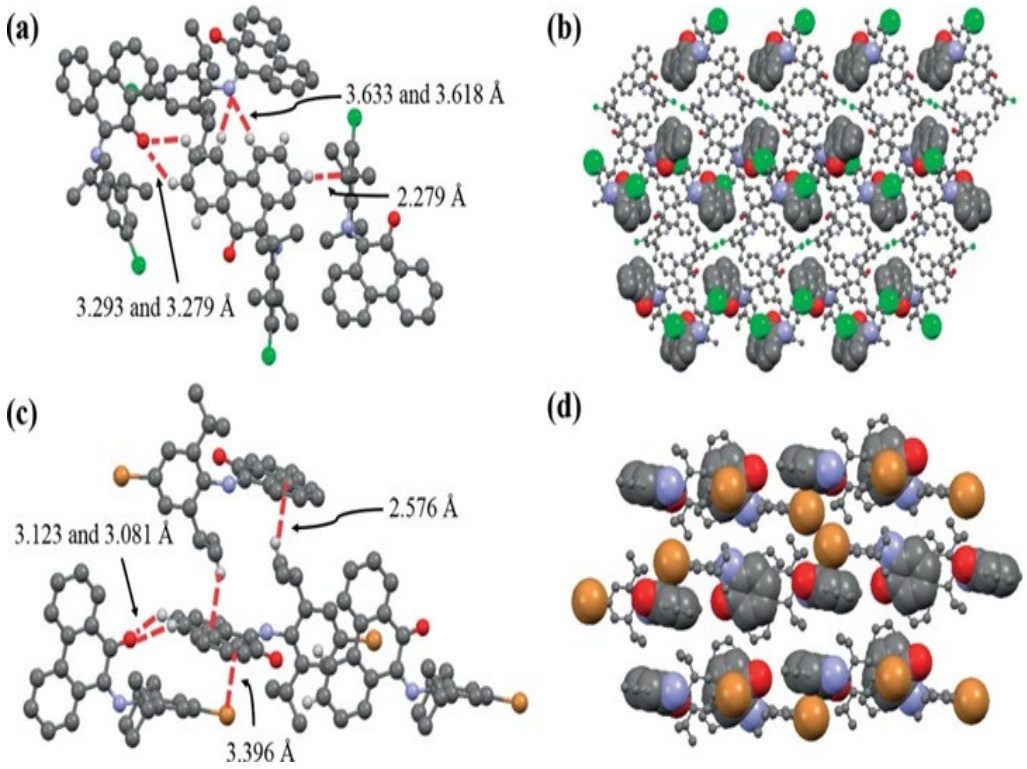

Figure 5.7 (a) View of **2** highlighting the noncovalent interactions; (b) packing of **2** as viewed along the crystallographic *c*-axis; (c) view of **3** highlighting the noncovalent interactions; (d) packing of **3** as viewed along the crystallographic *b*-axis. Colour code: Cl – green; Br – brown N – blue, C – grey and H – light grey; only hydrogen atoms involved in hydrogen bonds are shown, others are omitted for clarity.

5.2.3 Packing and Intermolecular Interactions in 1, 5-8

The relative stability of the noncovalent interactions has been investigated in compounds **1**, **5**, **6** and **7**, in which the steric demand of the *ortho*-groups is different. The packing of **1** is shown in Appendix 4 (Figure 28) and there appear only C–H···π interactions between a phenanthrene hydrogen and the centroid of the aryl ring ($d_{C\cdots cent}$ = 2.570 Å).

The packing of **5** (Figure 5.8a) does not show C–H···π interactions, but two C–H···O interactions [$d_{C\cdots O}$ = 3.370(3) and 3.493(3) Å] which create chains. Observable are also "π–π stacking" between two phenanthrene rings ($d_{cent\cdots cent}$ = 3.622 Å) that stack in a head-to-tail fashion. However, in **6** (Figure 5.8b), where only the methyl group in *para*-position has been removed, the C–H···O hydrogen bond is no longer present. Instead, in this compound, the dominant interaction is "π–π stacking" between two phenanthrene rings ($d_{cent\cdots cent}$ = 3.929 Å), which is longer than that found in **5**. Observable are also weak C–

H···N hydrogen bonds [$d_{C\cdots N}$ = 3.606(14) Å], comparable to those observed in **2a**. Compound **7** (Figure 5.8c) possesses a different packing, where C–H···π interactions are prevalent, involving hydrogens (H(12) and H(5)) of the phenanthrene backbone and the phenyl ring of the disordered imine, and extend along the crystallographic *b*-axis. π-π stacking, between two phenanthrene rings ($d_{cent\cdots cent}$ = 3.803 Å), and C–H···O interactions ($d_{C\cdots O}$ = 3.218(8) Å) are also present, but the latter involves the hydrogens of C(13) and not the same as observed in **2-4**. Therefore, the reducing of the steric bulk at the *ortho*-positions, from *i*Pr to Me to H, leads to an increasing of the propensity for "π–π stacking", as might be expected. Surprisingly, however, there is a difference between the mesityl and xylyl substituents and the origin for this is not clear.

To further investigate the influence of the steric bulk of the ligand on the noncovalent interactions, the packing of **8** (Figure 5.8d) is suitable as in this molecule the steric bulk is large enough to apparently allow only C–H···O interactions. The packing of **8** is formed by chains of phenanthrene-9,10-diones hydrogen bonded [$d_{C\ldots O}$ = 3.243(2) and 3.392(2) Å] along the *c*-axis and by head-to-tail "π-π stacking" between the two central rings ($d_{cent\cdots cent}$ = 3.759 Å) and in the outer rings ($d_{cent\cdots cent}$ = 3.772 Å), along with C–H···π interactions.

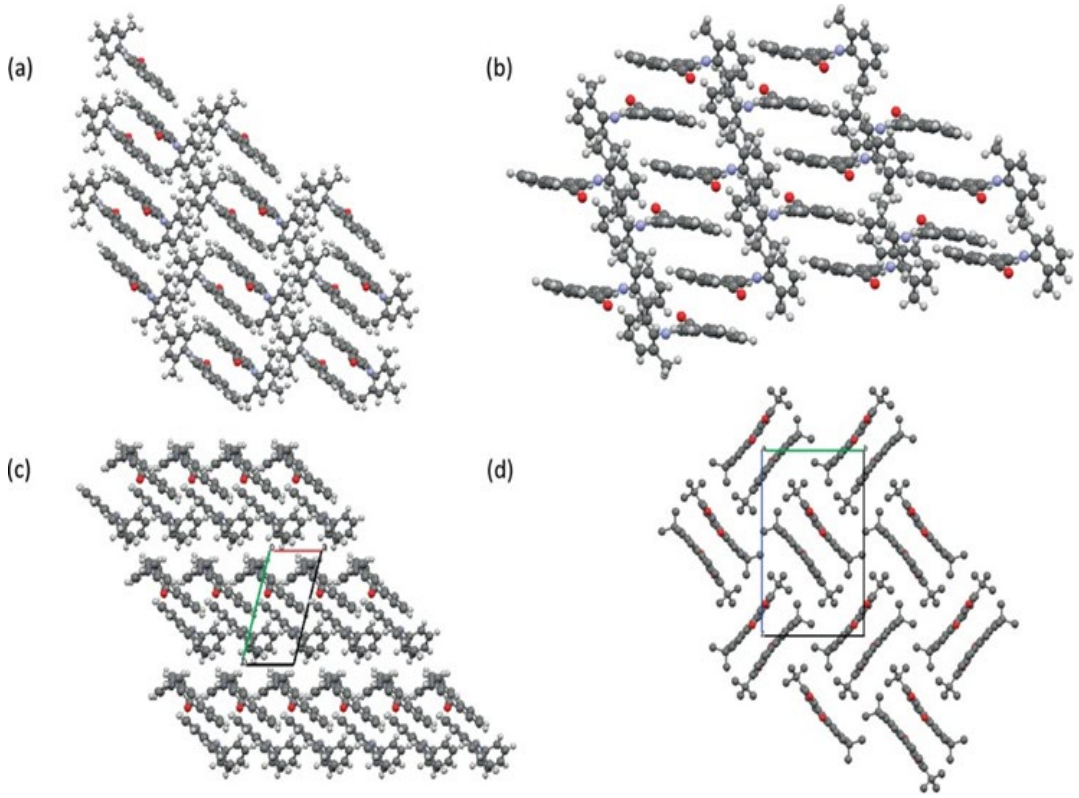

Figure 5.8. Packing diagram of (a) **5** and (b) **6**, viewed along the crystallographic *b*-axis, (c) **7**, viewed along the crystallographic *c*-axis, (d) **8**, viewed along the crystallographic *a*-axis.

5.2.4 *N,N*-(2,3-dimethylphenyl)-9,10-diiminophenanthrene (9)

The crystal structure of **9** is shown in Figure 5.9. The crystallographic data of this compound are listed in Appendix 4, while the full list of bond lengths and angles is tabulated in Appendix 4.4 in the external CD source of this thesis. The principal structural parameters of this molecule are listed in Table 5.1, along with the values from the other samples. The C–C bond length (1.514(2) Å) and the average of the C=N bond lengths (1.279(1) Å) are comparable to the corresponding values displayed by the phenanthrene mono-imine ligands (C–C, average 1.518(2) Å; C=N, average 1.278(2) Å). The C(15)-C(16)-C(17)-C(18) torsion angle (12.3(2)°) is, instead, relatively large if compared to those shown by the phenanthrene mono-imine ligands (values from 2.1(3)° to 11.5(4)°); in addition, the N(9)-C(10)-C(23)-N(24) torsion angle was also found very large (51.8(2)°), but this is explainable considering the steric requirements of the two aryl-imine systems.

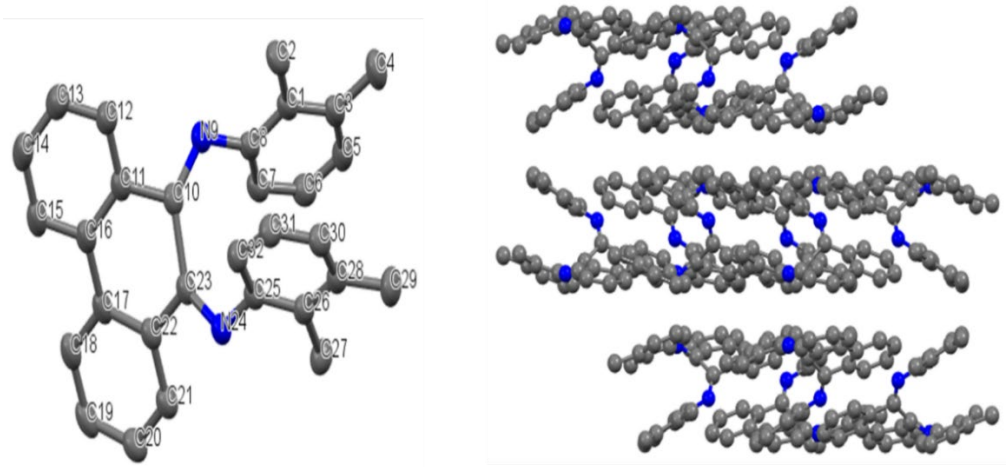

Figure 5.9. (Left) Asymmetric unit of **9**, with atomic displacement shown at 50% probability; (right) packing diagram of **9** viewed along the crystallographic *c*-axis. Hydrogen atoms omitted for clarity.

This molecule does not show any hydrogen bonds and the dominant interaction is a "π–π stacking" (Figure 5.9) between the phenanthrene rings ($d_{cent\cdots cent}$ = 3.303 Å), which is shorter than those found in **5**, **6** and **8**. This interaction is, most probably, responsible for the large value of the C(15)-C(16)-C(17)-C(18) torsion angle (12.3(2)°) in comparison with the other compounds.

5.2.5 DFT and AIM Calculations on Lone Pair···π Interactions

In order to establish whether the lone pair···π interaction is simply due to crystal packing, DFT and AIM analysis have been performed by Dr. J. A. Platts from Cardiff University. Dimers exhibiting a range of intermolecular interactions were extracted from the crystal structure of **4**, and counterpoise-corrected binding energies calculated with M06-2X and with both Def2TZVP and Def2SVP basis sets. The dimers are bound by –43.9 and –43.6 kJ mol^{-1}, respectively. A dispersion-corrected functional (B97D), which gives a binding energy of –58 kJ mol^{-1}, has also been included. Given the excellent agreement between the basis sets, the computationally smaller Def2SVP basis can be used to give qualitative data for comparison between this small library of compounds.

While the dimers may not entirely reproduce the overall crystal environment, this approach permits to interrogate individual types of interaction, and also to compare observed and hypothetical interaction modes on an equal footing.

The isostructural dimers of **3**, containing X···π contacts, are bound by –45.5 kJ mol^{-1}. A hypothetical dimer of **2**, built by replacement of Br with Cl followed by optimization of the position of Cl, is bound by –42.2 kJ mol^{-1} and so almost identical to those for **3** and **4**. In contrast, the real dimers of **2** extracted from the crystal structure are much more weakly bound: the dimer containing Cl···π contacts is bound by –22.3 kJ mol^{-1}, while that containing Cl···Cl contact is predicted to be unbound (binding energy = +2.1 kJ mol^{-1} after counterpoise correction), in agreement with the assignment of a type I interaction.[41] It is important to underline that this is the total energy of the interactions between the dimers, and not of individual components, but lone pair···π interactions are energetically significant in cooperation with other noncovalent interactions; this has been noted in previous examples.[44]

The molecular electrostatic potentials have been calculated for the monomeric units in **2**–**4**. Figure 5.10 shows the results for **4**. The results for **2**, **3**, **6** and **7** are collated in Figure 5.11 and all the plots are very similar to the one for **4**.

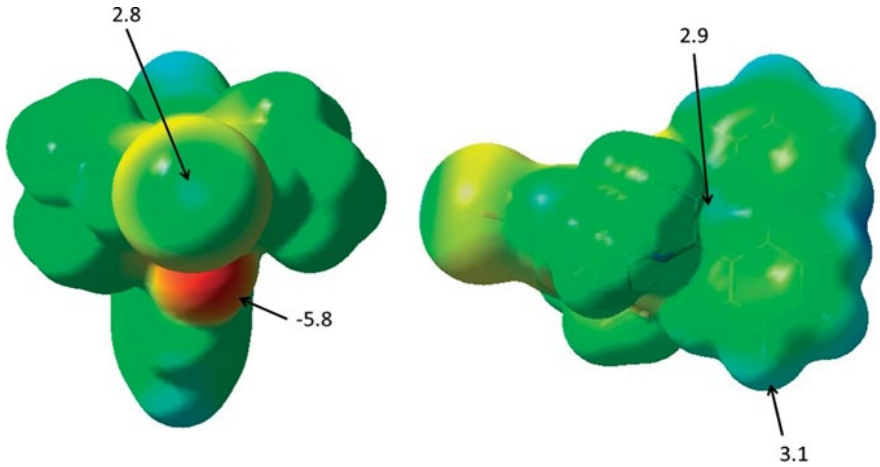

Figure 5.10. Molecular electrostatic potential of **4** (numerical values are x 10^{-2} a.u.; colour: blue = 6.0 x 10^{-2} to red = −6.0 x 10^{-2} a.u.).

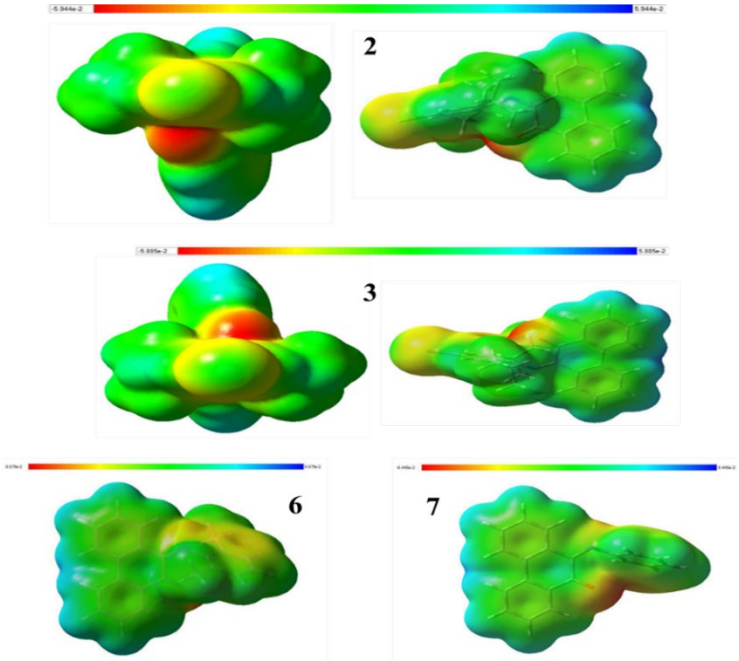

Figure 5.11. Molecular electrostatic plot of (top) **2**, (middle) **3**, (bottom left) **6** and (bottom right) **7**.

There is a σ-hole on the iodine atom, although quite small; for **2** and **3** this is not observed, and this is likely due to the differences in electronegativity between the halogen atoms. A small π-hole, defined as a positive region, is evident on the central phenanthrene ring (**3** = 2.2 × 10^{-2} a.u.; **4** = 2.9 × 10^{-2} a.u.) and corresponds to the lone pair···π interaction; in the plot of **2** this is absent and corroborates the differences in binding energies. The aromatic hydrogens are slightly δ^+, possibly due to the polarizing effect of the carbonyl group and could explain the prevalence of the C–H···O hydrogen bonds.[45]

AIM analysis have been performed and showed multiple bond paths corresponding to intermolecular interactions, as illustrated in Figure 5.12 and Table 5.2.

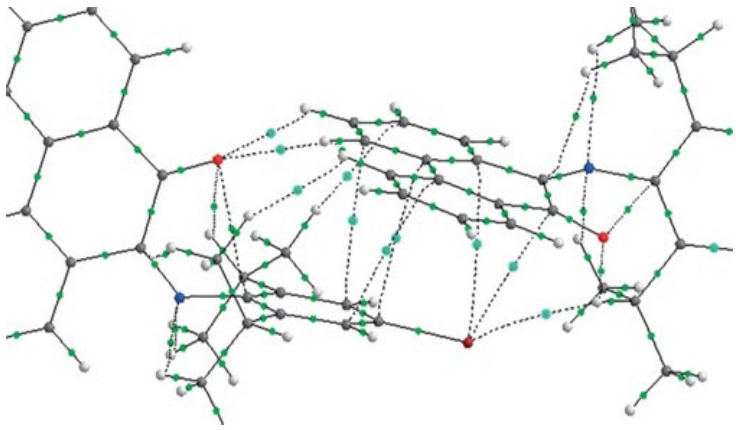

Figure 5.12. AIM analysis of **3** displaying intermolecular bond paths as dotted lines.

Two X···π bond paths are present, along with one C–H···X path. A further three π···π contacts and one C–H···π are predicted, along with two C–H···O contacts. The value of the electron density at the bond critical point, ρ_{bcp}, is widely used as an estimate of the strength of contacts: largest values are observed for C–H···O, followed by X···π and with C–H···π and π···π contacts predicted to be the weakest. In the literature there are many computational studies on lone pair···π interactions, and the electron density at the bcp is similar to that calculated for a variety of electron rich or electron poor arenes and lone pairs originating from oxygen or nitrogen donors.[46]

Table 5.2. Calculated electron density (in a.u.) at bcps in the dimers extracted from **2-4**.

Compound	C–H···O	π	C–H···X	C–H···π	π···π	X···X
2 hypothetical	0.008	0.006	0.006	0.006	0.005 = x2	
	0.010	0.007			0.006	
2 X···X						0.008
2 X···π	-	0.010	0.005	0.003 0.004 × 2	-	
3	0.008	0.007 × 2	0.009	0.006 × 2	0.005 × 2	
	0.009				0.006	
4	0.009	0.006 × 2	0.007	0.004	0.004	
	0.010				0.005 × 2	

5.2.6 DFT and AIM Calculations on 5-8

In order to probe the π-interactions in the compounds from **5** to **8**, the computational approach described above (M06-2x/Def2SVP level) has been used, which has also been adopted in previous works.[47] The binding energies of the dimers extracted from the crystal structures are –52.94 kJ mol^{-1} for **5**, –48.54 kJ mol^{-1} for **6**, –36.53 kJ mol^{-1} for **7** and –74.45 kJ mol^{-1} for **8**. A possible explanation for the interactions comes from the molecular electrostatic potentials shown in Figure 5.13 for **5** and **8** (**6** and **7** are similar and are shown in Figure 5.11). From this analysis, the hydrogen atoms on the phenanthrene are polarized due to the C=O and C=N (for **5-7**) electron withdrawing groups, but since the prevalent interaction is a head to tail stacking, it follows that the positively polarized hydrogens are preferentially interacting with the negatively polarised carbonyl function. This is in line with the Wheeler and Houk theory for noncovalent π-stacking interactions.[31]

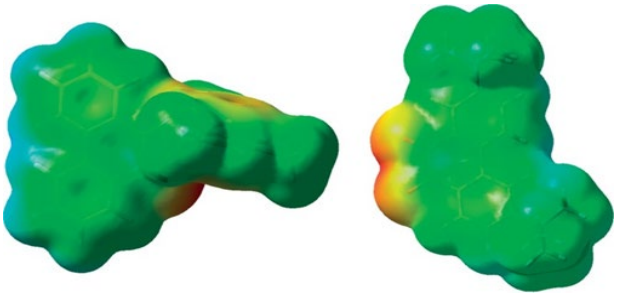

Figure 5.13. Molecular electrostatic potential of (left) **5** and (right) **8** (colour: blue = 8.0 x 10^{-2} to red = −8.0 x 10^{-2} a.u.).

AIM analysis of **5**–**8** showed multiple bond paths corresponding to intermolecular interactions, as illustrated in Figure 5.14 and Table 5.3. There are several π···π, C–H···π and C–H···O contacts in this series. Inspection of the electron density at the bond critical point, ρ_{bcp}, shows a trend in which the π···π contacts are stronger than the C–H···π. Moreover **7** appears to display the weakest binding, in line with the binding energies; **8**, instead, has the most stabilization from π···π contacts.

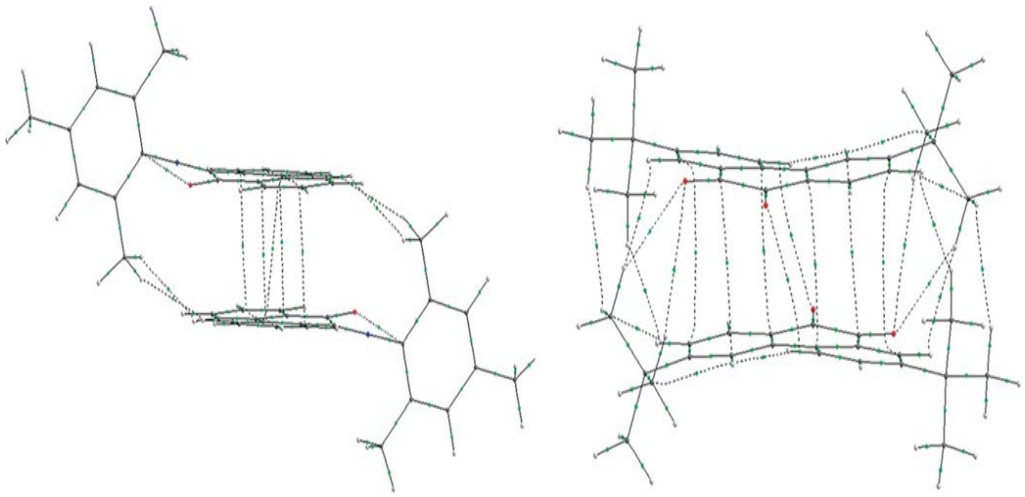

Figure 5.14. AIM analysis of **5** (left) and **8** (right), displaying intermolecular bond paths as dotted lines.

Table 5.3. Calculated electron density (in a.u.) at bcps in the dimers extracted from **5-8**.

Compound	C–H···O	O···π	C–H···π	π···π
5			0.006 × 2	0.007 × 2
			0.005 × 2	0.006 × 3
6			0.002 × 2	0.006 × 2 0.005 0.004 × 2
7	0.007 × 2			0.006 × 2
8		0.004 × 2	0.002 × 4	0.007 × 2 0.004 × 4

5.2.7 Hirshfeld Analysis on 1-8

To expand the study on the different packing arrangements, Hirshfeld analysis have been used for the compounds **1-8**.[48] The results of the fingerprint analysis for the lone pair···π interactions in **2**–**4** are shown in Figure 5.15.

From this analysis, it is evident that the dominant interaction is H···H, but C···H (i.e. C–H···π) are also important. X···lone pair interactions are small but clearly observable, particularly in the plot of the shape index. The C–H···π interaction is the largest for **7** according to this analysis.

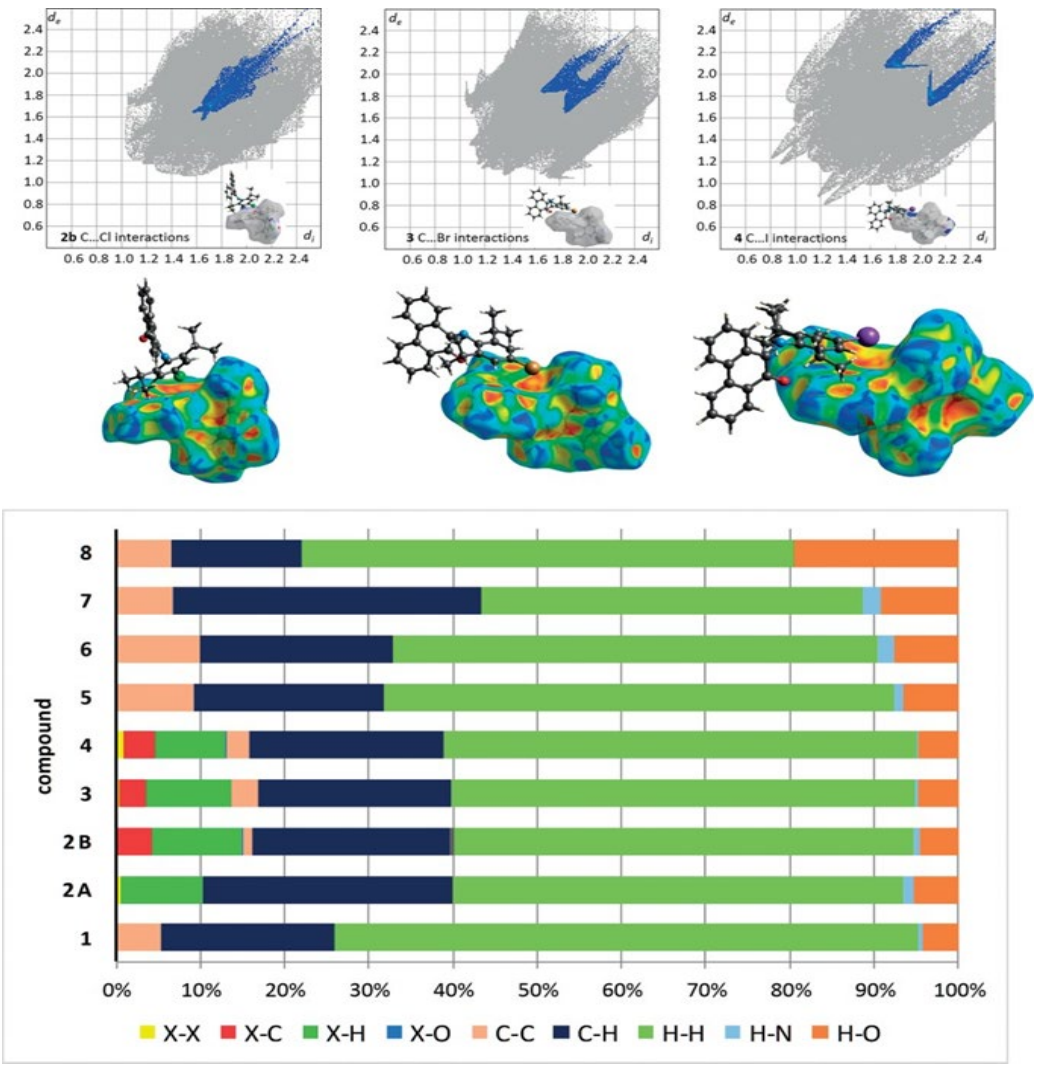

Figure 5.15. (top) Fingerprint plots of **2b**, **3**, and **4** displaying the X···C interactions (d_{norm} plotted at −0.161 to 1.605), (middle) the shape index (plotted at −1 to +1) and (bottom) the quantitative analysis of the Hirshfeld surfaces for **1**-**8**.

5.2.8 Spectroscopic Characterization of the Phenanthrene Ligands

Infrared and UV-vis spectroscopic measurements have been performed to characterize these compounds and the pertinent parameters are recorded in Table 5.4.

Table 5.4. Selected spectroscopic properties of the ligands **1-8** and phenanthrene-9,10-dione.

Compound	ν(C=O) (cm^{-1})	ν(C=N) (cm^{-1})	λ_{max} (nm) (ε, M^{-1} cm^{-1})		
			π – π*	π – π*	*n* – π*
Phenanthrene-9,10-dione	1674	-	319 (3805)	-	412 (1453)
1	1679	1589	315 (1488)	390 (530)	587 (96)
2	1677	1592	314 (2367)	380 (733)	583 (160)
3	1681	1592	318 (3253)	389 (869)	574 (199)
4	1679	1591	313 (3557)	385 (1389)	581 (285)
5	1675	1590	313 (2150)	378 (800)	599 (162)
6	1677	1591	314 (4954)	388 (1604)	575 (302)
7	1647	1591	312 (4497)	-	540 (530)
8	1675	-	325 (2034)	-	426 (522)

The C=O and C=N bond stretching frequencies in the IR spectra of crushed single crystals are scarcely perturbed, suggesting that the electronic influence of the *para*-substituent is not particularly strong, and the hydrogen bond interactions discussed above are weak. The UV-vis spectra of the compounds **1**-**8**, recorded at room temperature and in MeCN solution, are shown in Figure 5.16. In the series **1**-**8**, a very broad and weak band at *ca.* 600 nm appears upon substitution on the aryl ring. This has been assigned to C=O and C=N *n*-π* transitions, and the intensity variation is likely due to deviations from non-planarity of these carbonyl and imino groups.[49] Moreover, the absorption bands at 390 nm and 315 nm, which arise from π–π* transitions within the phenanthrene ring, undergo a small hyperchromic effect upon halogen substitution from **1** to **4**. In addition, there is a hypochromic effect in the spectrum of **8** compared to the unsubstituted phenanthrene-9,10-dione and it is likely due to the structural variability caused by the increasing steric bulk and the deviations from planarity of the carbonyl groups. Therefore, overall, the UV-vis data indicate small perturbations of the electronic structure due to structural differences for the ligands from **1** to **8**. Compound **9** was isolated as only few single crystals and no spectroscopic measurements were possible.

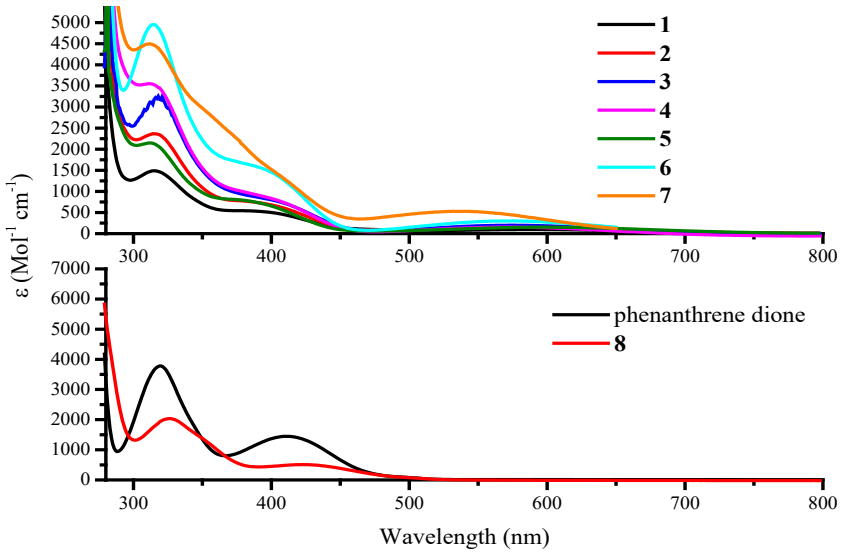

Figure 5.16. Electronic absorption spectra of the compounds **1**-**8**, measured at 298 K and in MeCN solution (concentration ≈ 1 × 10^{-5} M).

5.3 Iminoalkoxy Phenanthrene Semiquinone Radicals

5.3.1 Synthesis

As already mentioned, the main object of this part of the project was to synthesize a molecular U(IV) complex containing an iminoalkoxy semiquinone radical, to study the possible magnetic coupling interactions. Thus, the anionic radical of each mono-substituted iminophenanthrenequinone ligand was prepared by a one-electron reduction with potassium metal. The reaction was carried out in dried toluene, under Ar and at reflux (Scheme 5.4), and a colour change from green to brown was observed after *ca.* eight hours. The solution was then filtered, and the solvent reduced in volume under vacuum. Finally, by adding an excess of dried hexane, a fine brown powder was formed and it kept the same colour indefinitely under Ar. Once isolated, the radical have been characterized.

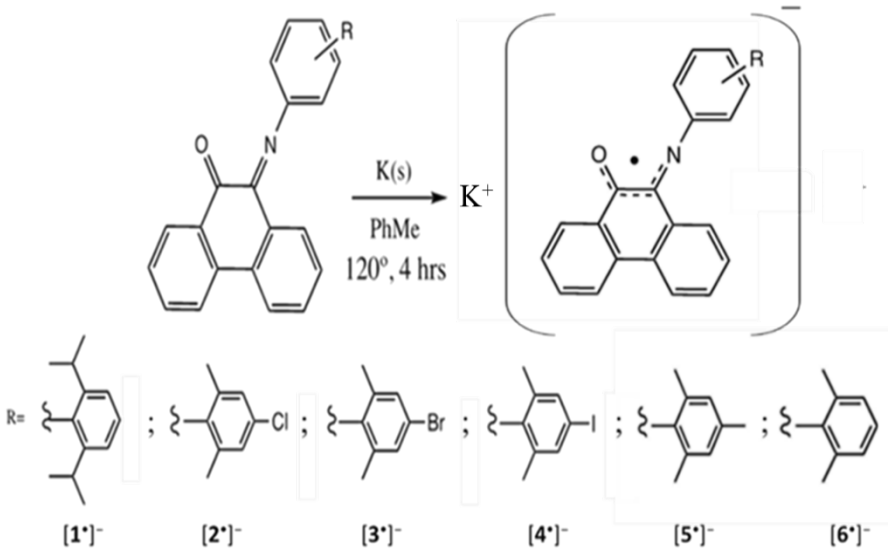

Scheme 5.4. Synthesis of iminoalkoxy semiquinone radical anions.

5.3.2 EPR Spectroscopic Measurements

EPR spectroscopic measurements have been performed at room temperature on the isolated radical [**4**•]⁻ dissolved in dried toluene solutions (Figure 5.17).

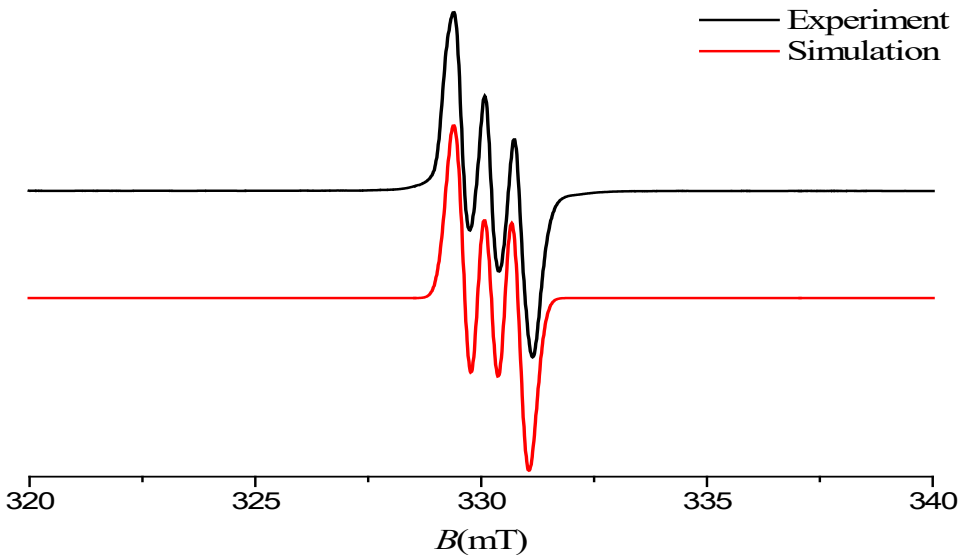

Figure 5.17. X-band EPR spectrum of the radical [**4**•]⁻. Experimental conditions: frequency, 9.2305 GHz; power, 20 dc; modulation amplitude, 0.2 G; 10 scans. Spectrum acquired at 298 K in dried PhMe solution. Experimental data are represented by the black line and the simulation depicted by the red trace.

With a frequency of 9.2305 GHz the fitting gives a *g* value of 1.997, which is consistent with a free organic radical (very close to 2.0023). Moreover, the spectrum has a hyperfine

structure which is due to the coupling to the ^{14}N (I = 1) nuclei, with a coupling constant of a_N = 17 MHz. This coupling suggests that the unpaired electron is delocalised principally on the O–C–C–N system.[51, 50]

5.3.3 UV-vis and IR Spectroscopic Characterization of the Iminoalkoxy Phenanthrene Semiquinone Radicals

The UV-vis spectra of the iminoalkoxy semiquinone radicals have been measured at room temperature and in dried toluene solution (Figure 5.18) and compared with the ones of the neutral ligands.

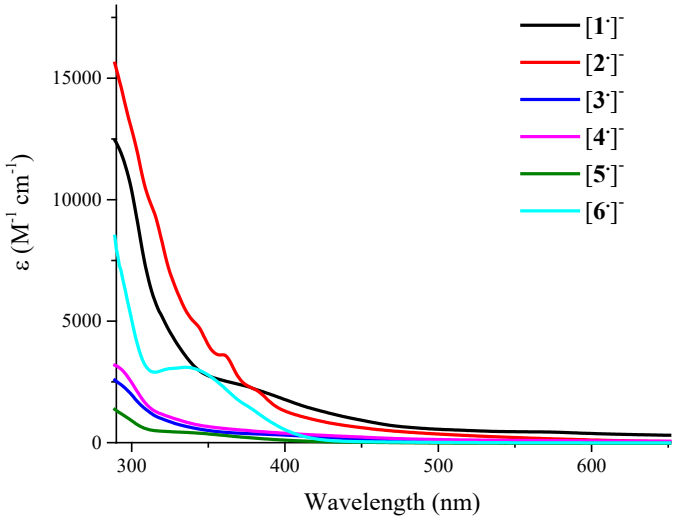

Figure 5.18. UV-vis absorption spectra of the iminoalkoxy semiquinone radicals, measured at room temperature and in dried PhMe solutions (1 x 10^{-5} M).

The spectra of the radicals display two broad bands at *ca.* 350 and 280 nm, which can be assigned to π–π* transitions within the phenanthrene ring. These two bands were noted also for the neutral ligands (Figure 5.16), but an hypsochromic shift is observable in the spectra of the radicals. Moreover, the weak and broad bands observed in the spectra of the neutral ligands at *ca.* 600 nm, which are due to C=O and C=N n-π* transitions, are absent in the spectra of the radicals; this result might suggest that, in contrast with the neutral ligands, the O–C–C–N group has assumed a planar conformation in the radicals, which could also be expected.

The frequencies of the IR active C=O and C=N vibrational modes of the radicals are listed in Table 5.5 and have been compared with the analogue values shown by the

corresponding neutral ligands. In particular, they decrease significantly moving from the neutral ligands to the radicals; this implies a weakening of these double bonds during the reduction process.

Table 5.5. Comparison of the IR active C=O and C=N vibrational modes between the neutral phenanthrene imine ligands and the corresponding radicals.

Compound	Neutral ligand[(a)]		Radical species[(b)]	
	ν(C=O)	*ν*(C=N)	*ν*(C=O)	*ν*(C=N)
[**1**]	1679	1589	1532	1479
[**2**]	1677	1592	1566	1481
[**3**]	1681	1592	1592	1478
[**4**]	1679	1591	1476	1441
[**5**]	1675	1590	1586	1478
[**6**]	1677	1591	1477	1439

a) ATR; b) Nujol mull

Therefore, the UV-vis and IR spectroscopic data of the radicals, in comparison with the corresponding neutral ligands, are consistent with the presence of an unpaired electron most likely delocalized within the $p\pi$ orbital system of the O=C–C=N pocket.

5.3.4 Structural Studies

Several strategies have been adopted to grow single crystals of the radicals; however, under all the conditions, only decomposition products have been obtained. In some cases, colourless single crystals were also isolated, and X-ray diffraction revealed them to be neutral amides; the mechanism for the formation of these amides is not clear. In Figure 5.19 is shown the molecular structure of the *N*-(2,6-dimethylphenyl)formamide that was obtained from the solution containing the radical [**6**$^{\bullet}$]$^{-}$. The corresponding crystallographic data are reported in Appendix 4 and the full list of bond lengths and angles is reported in Appendix 4.56 in the external CD source of this thesis.

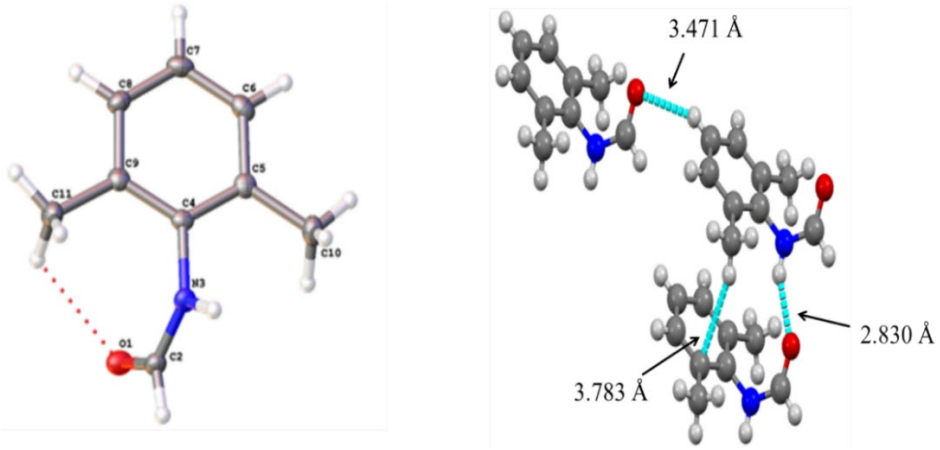

Figure 5.19. (left) Asymmetric unit of *N*-(2,6-dimethylphenyl)formamide, with atomic displacement shown at 50% probability and the hydrogen bond indicated by a red dotted line. (right) View of *N*-(2,6-dimethylphenyl)formamide, with the intermolecular hydrogen bonds highlighted as light blue lines. Colour code: N – blue, C – grey, O – red, H – white.

The crystal structure of this compound has been previously determined and the metric parameters are comparable.[51] Moreover, in this molecule the amide moiety is out of the plane of the phenyl ring (C(2)-N(3)-C(4): 123.77(14)°) and adopts a *trans* conformation in which the hydrogen bonded to the N atom is *trans* to the O atom. There is an intramolecular C–H···O hydrogen bonding ($d_{Csp3\ldots O}$ = 3.173(2) Å), between the carbonyl oxygen and the hydrogen atom of one methyl group in *ortho* position (dotted red line in Figure 5.19). In addition, there are intermolecular hydrogen bonds of the type: N–H···O ($d_{N\ldots O}$ = 2.830 Å), between the amide functions from two adjacent molecules; C–H···O ($d_{Csp2\ldots O}$ = 3.471 Å), between the aromatic hydrogen in *para* position and the carbonyl function from the adjacent molecule; C–H···π ($d_{Csp3\ldots cent}$ = 3.783 Å), involving the methyl group and the carbonyl function from the adjacent molecule.

5.4 Reactions between UCl_4 and radicals

Although it was not possible to isolate single crystals of the radicals, powders of $[\mathbf{1}^{\bullet}]^-$, $[\mathbf{2}^{\bullet}]^-$, $[\mathbf{4}^{\bullet}]^-$ and $[\mathbf{6}^{\bullet}]^-$ have been reacted with uranium containing compounds in dried PhMe. Thus, reactions have been attempted between UCl_4 or $[UO_2Cl_2(THF)_2]_2$ and two equivalents of an iminoalkoxy semi-quinone radical, where an expected co-precipitation of KCl could drive forward the process. While no reaction was observed mixing $[UO_2Cl_2(THF)_2]_2$ with all the radicals, the formation of a grey precipitate, of probably KCl, was observed when UCl_4 was reacted with two equivalents of the radical $[\mathbf{1}^{\bullet}]^-$.

However, the desired U(IV) complex was not isolated; brown single crystals were obtained from the resulting solution, but X-ray diffraction showed them to be a uranyl(VI) compound of formula $[K(H_2O)]_2[UO_2Cl_4]$. The molecular crystal structure of $[K(H_2O)]_2[UO_2Cl_4]$ is shown in Figure 5.20; while bond lengths, angles and other structural parameters are listed in Appendix 4.6 (located in the external CD source of this thesis).

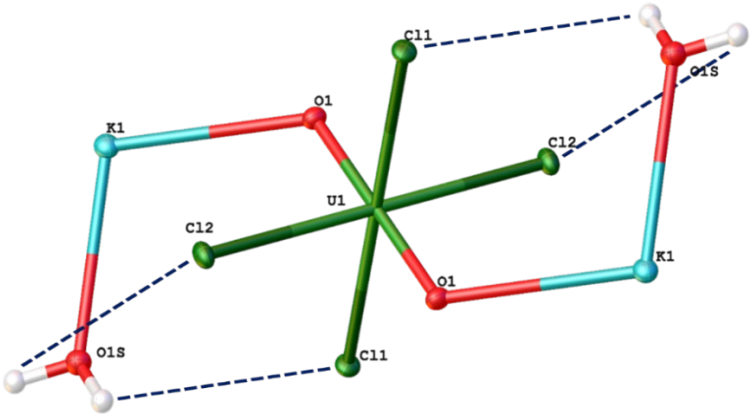

Figure 5.20. Symmetry generated structure of $[K(H_2O)]_2[UO_2Cl_4]$, with atomic displacement shown at 50% probability. Colour code: U – green, Cl – dark green, O – red, K – light blue, H – white. Hydrogen bonds indicated by dotted blue lines.

The U=O (1.778(2) Å) and U–Cl (average 2.6619(3) Å) bond lengths of this compound are comparable with the corresponding bond lengths displayed by $Cs_2UO_2Cl_4$ (U=O, 1.774(4) Å; U–Cl, average 2.671(1) Å).[52] Other comparisons can also be made with $[Me_3NBz]_2[UO_2Cl_4]$ (U=O, 1.767(7) Å; U–Cl, average 2.637(3) Å) and $[Et_4N]_4[UO_2Cl_4][CuCl_4]$ (U=O, 1.772(3) Å; U–Cl, average 2.682(3) Å) described in Chapter 4. Moreover, the triatomic uranyl(VI) unit is perfectly linear (O–U–O 180°), as expected due to symmetry. This structure displays also O–H···Cl hydrogen bonding (Figure 5.20, red dotted lines) between the water molecules and two coordinated Cl atoms ($d_{O\cdots Cl(1)}$ = 3.290(3) Å and $d_{O\cdots Cl(2)}$ = 3.342(3) Å).

Another different reaction occurred when, during a second attempt, UCl_4 was mixed with two equivalents of the radical $[\mathbf{1}^{\bullet}]^{-}$. A grey precipitate was again formed and isolated by filtration, while, from the resulting brown solution, colourless single crystals were isolated. However, X-ray diffraction revealed them to be a neutral amide, *N*-(2,6-diisopropylphenyl)formamide, and it was not possible to determine the fate of the U(IV)

ion. The molecular structure of this amide is shown in Figure 5.21. The corresponding crystallographic data are listed in Appendix 4.

In this structure, each amide displays an intramolecular C–H···O hydrogen bonding ($d_{Csp3...O}$ = 3.313(6) Å), between the carbonyl oxygen and the hydrogen atom of a CH group from one isopropyl substituent in *ortho* position, and an intermolecular C–H···O hydrogen bonding ($d_{Csp2...O}$ = 3.352(6) Å) involving the same carbonyl oxygen and the hydrogen atom of the aromatic ring in *para* position. Interestingly, these hydrogen bonds have led to the formation of a chiral spiral and, thanks to several hydrophobic interactions, an oil molecule was found trapped in the central void. Reasonably, it is possible to believe that this oil molecule comes from the high-density mineral oil that, before the X-ray diffraction measurements, was added on top of the single crystals to avoid oxidation by exposition to air. Nevertheless, considering a single *N*-(2,6-diisopropylphenyl)formamide molecule out from the whole structure, the metric parameters of this amide are comparable to the ones previously reported.[51] Moreover, similarly to *N*-(2,6-dimethylphenyl)formamide (Figure 5.19), the amide moiety is again out of the plane of the phenyl ring (C(003)-N(002)-C(005): 125.5(3)°) and adopts a *trans* conformation in which the hydrogen bonded to the N atom is *trans* to the O atom.

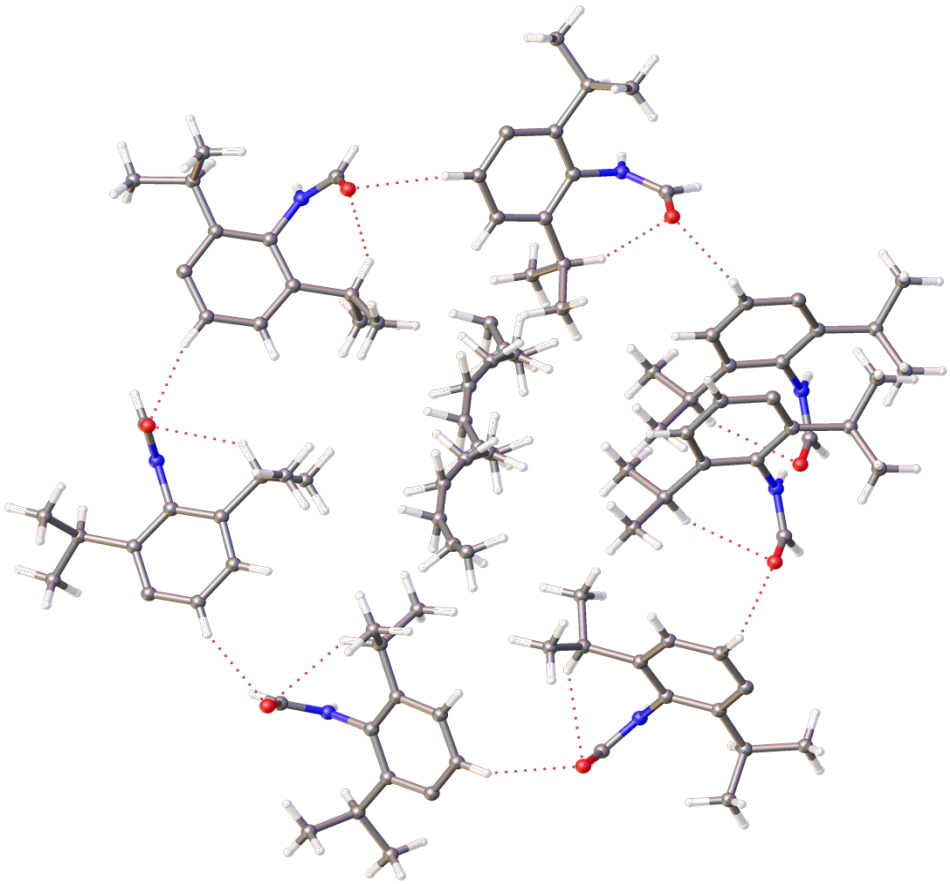

Figure 5.21. Symmetry generated chiral spiral of *N*-(2,6-diisopropylphenyl)formamide, with half occupied oil in the central void. Atomic displacement shown at 50% probability and hydrogen bonding indicated by red dotted lines.

5.5 Conclusion

In summary, a number of ligands based on a phenanthrene core have been structurally characterized and the noncovalent interactions shown by the solid-state structures of these molecules have been fully investigated. The lone pair···π interactions have been found as the dominant halogen type interaction; however, among all the interactions, the most important one appeared to be a weak C–H···O hydrogen bond between a C–H of a phenanthrene and the carbonyl oxygen. Inspection of the molecular electrostatic potential shows that the aromatic hydrogen atoms are polarized, probably due to the C=O and C=N functional groups on the opposite side of the ring, which can account for this interaction. The steric bulk of the imino aryl group has also been evaluated and, if reduced, then "π–π stacking" and eventually C–H···π interactions become the dominating interactions.

From these ligands, a series of iminoalkoxy semiquinone radical anions have been synthesized via reduction with potassium metal. These systems have been

spectroscopically characterized and the results confirm the presence of a single unpaired electron, most probably delocalized over the O–C–C–N group. However, all the attempts to isolate single crystals of these radicals did not succeed and only decomposition products have been obtained. In some cases, single crystals of neutral amides have also been formed, but the reaction mechanism is not clear.

Complexation reactions between a uranium compound (UCl_4 or $[UO_2Cl_2(THF)_2]_2$) and these iminoalkoxy semiquinone radicals (isolated in a powder form) have been attempted in dried toluene, but the desired complexes have not been formed. It is clear that the experimental conditions of these reactions have to be changed and, perhaps, the nature of the solvent plays a crucial role.[53]

5.6 Experimental section

Caution! Natural uranium was used during the course of the experimental work. As well as the radiological hazards, uranium is a toxic metal and care should be taken with all manipulations. Experiments with uranium compounds were carried out using pre–set radiological safety precautions in accordance with the local rules of Trinity College Dublin and University of Reading.

4-X-2,6-diisopropylaniline (X = Cl, [54] Br, [55] I [56]), N-(phenyl)-9,10-iminophenanthrenequinone[35] and 2,6-di-tert-butyl-9,10-phenanthrenequinone [57] were prepared according to literature procedures.

^1H, and $^{13}C\{^1H\}$ spectra were recorded on a Bruker AV400 spectrometer operating at 400.23 MHz and 155.54 MHz, respectively, and were referenced to the residual ^1H and ^{13}C resonances of the solvent used. Mass spectra were measured on MALDI-QTOF Premier MS system. For the acquisition of the FTIR and UV-vis spectra, the spectrophotometers have been described in the experimental section of Chapter 2. The X-ray diffractometer and the methods used to analyse the crystallographic data is as discussed in the experimental section of Chapter 2. The crystallographic data are collated in Appendix 4. Structural figures were prepared using VESTA[58] or mercury.

DFT calculations were carried out in Gaussian09[59] with the metahybrid M06-2X functional[60] and def2-SVP basis set.[61] All calculations of interaction energy used the counterpoise method to account for basis set superposition error,[62] and positions of hydrogen nuclei normalised to optimal positions by partial geometry optimisation with all heavy-atom positions fixed. Converged molecular orbitals were obtained from these

calculations and used for topological analysis of the resulting electron density using the AIMAll package.[63]

5.6.1 General Synthesis of the Iminophenanthrenequinone Ligands

9,10-phenanthrenequinone (1 equiv.) and the appropriate aniline (*ca.* 1.2 equiv.) were dissolved in MeOH or MeCN. A catalytic amount of formic acid was added and the mixture was refluxed for 12 h. The reaction was diluted in hexane and the solvent evaporated. The crude sample was eluted from silica gel with an ethyl acetate/hexane solution (25% ethyl acetate in hexane). The desired fractions were concentrated to yield the pure products. The numbering schemes for the NMR spectroscopic assignments are shown in Figure 5.22.

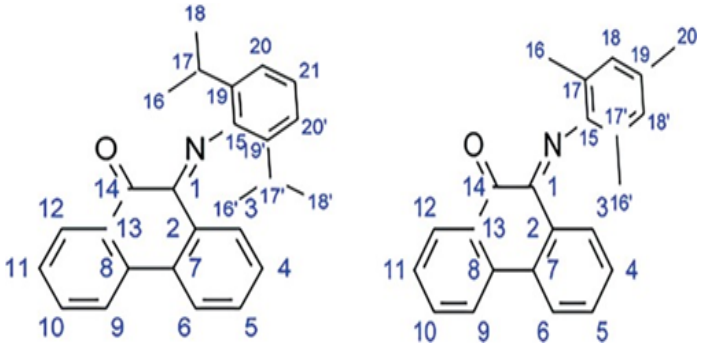

Figure 5.22. Numbering scheme for NMR spectroscopic data.

5.6.2 *N*-(2,6-Diisopropylphenyl)-9,10-iminophenanthrenequinone (1)

Phenanthrenequinone (0.4172 g, 2.00 mmol) and 2,6-diisopropylaniline (0.75 cm^3, 3.98 mmol) were reacted according to the method to yield **1** as a dark green solid (0.4965 g, 68 %). M.p. 142– 145 °C. IR (ATR, ν/cm^{-1}): 3072 (w), 2960 (s), 2864 (m), 1679 (s, C=O), 1589 (s, C=N), 1478 (w), 1461 (w), 1450 (s), 1434 (m), 1294 (s), 1281 (s), 1254 (s), 1232 (s), 963 (w), 937 (m), 882 (w), 868 (w), 830 (w), 807 (w), 797 (m), 782 (m), 773 (m), 754 (s), 721 (s), 704 (w). ^{1}H NMR δ_H (400 MHz, $CDCl_3$/ppm): 1.13 (d, J = 6.4 Hz, 6 H, 16 and 16′-CH_3), 1.24 (d, J = 6.4 Hz, 6 H, 18 and 18′-CH_3), 2.74 (m, 2 H, 17 and 17′-CH), 7.20 (m, 1 H, 21CH), 7.27 (d, J = 7.6 Hz, 2 H, 20 and 20′-CH), 7.48 (m, 1 H, 4-CH), 7.60 (t, J = 7.2 Hz, 1 H, 5-CH), 7.72 (t, J = 7.6 Hz, 1 H, 11-CH), 7.78 (t, J = 7.6 Hz, 1 H, 10-CH), 8.06 (d, J = 7.2 Hz, 1 H, 3-CH), 8.14 (d, J = 8.0 Hz, 2 H, 6 and 9-CH), 8.48 (d, J = 7.2 Hz, 1 H, 12-CH). ^{13}C{^{1}H} NMR δ_C (155 MHz, $CDCl_3$/ppm): 23.1 (C-16 and 16′), 23.1 (C-18 and 18′), 28.7 (C-17 and 17′), 123.0 (C-21), 123.5 (C-6 or 9), 123.6 (C-

20 and 20′), 123.7 (C-6 or 9), 128.4 (C-12), 129.0 (C-4), 129.5 (C-5), 129.7 (C3), 131.5 (C-2), 132.3 (C-11), 132.5 (C-7), 132.8 (C-8), 133.0 (C-13), 135.3 (C-10), 136.8 (C-19 and 19′), 148.2 (C-15), 154.0 (C-1), 179.8 (C14). UV-vis (ε, mol dm^{-3} cm^{-1}) (298 K, ~10^{-5} M in MeCN): 586 nm (96.33), 385 nm (539), 315 nm (1488). HRMS (ESI^+): *m/z* calc. for $C_{26}H_{25}NO$: 368.2014, found 368.2015.

5.6.3 *N*-(4-Chloro-2,6-diisopropylphenyl)-9,10-iminophenanthrenequinone (2)

Phenanthrenequinone (1.0286 g, 4.94 mmol) and aniline (1.30 cm^3, 5.79 mmol) were reacted according to the method to yield **2** as a green crystalline solid (0.6967 g, 35 %). M.p. 164–168 °C. IR (ATR, *v*/cm^{-1}): 3065 (w), 2961 (s), 2926 (m), 2867 (m), 1677 (m, C=O), 1614 (m), 1592 (s, C=N), 1451 (s), 1430 (m), 1295 (s), 1285 (s), 1259 (s), 1233 (s), 759 (s) (C – Cl), 794 (s), 773 (s), 744 (s), 723 (s), 706 (m). ^{1}H NMR δ_H (400 MHz, $CDCl_3$/ppm): 1.01 (d, *J* = 6.4 Hz, 12 H, 16 and 16′-CH_3), 1.13 (d, *J* = 6.4 Hz, 6 H, 18 and 18′-CH_3), 2.60 (m, 2 H, 17 and 17′-CH), 7.12 (s, 2 H, 20 and 20′-CH), 7.42 (t, *J* = 7.2 Hz, 1 H, 4-CH), 7.51 (t, *J* = 7.2 Hz, 1 H, 5-CH), 7.65 (t, *J* = 7.6 Hz, 1 H, 11-CH), 7.70 (*J* = 7.6 Hz, 1 H, 10-CH), 7.97 (d, *J* = 7.2 Hz, 1 H, 3-CH), 8.05 (d, *J* = 8.0 Hz, 2 H, 6 and 9-CH), 8.36 (d, *J* = 7.6 Hz, 1 H, 12-CH) ppm. $^{13}C\{^1H\}$ NMR δ_C (155 MHz, $CDCl_3$/ppm): 22.8 (C-16 and 16′), 23.0 (C-18 and 18′), 28.8 (C-17 and 17′), 122.9 (C-7), 123.2 (C-20 and 20′), 123.6 (C-6 or 9), 123.7 (C-9 or 6), 128.4 (C-12), 128.9 (C-8), 129.0 (C-4), 129.5 (C5), 129.6 (C-3), 132.2 (C-2), 132.5 (C-11), 135.2 (C-13), 135.4 (C-10). UV-vis (ε, mol dm^{-3} cm^{-1}) (298 K, ~10^{-5} M in MeCN): 588 nm (159), 393 nm (733), 316 nm (2400). HRMS (ESI^+): *m/z* calc. for $C_{26}H_{24}ClNO$: 402.1625, found 402.1621.

5.6.4 *N*-(4-Bromo-2,6-diisopropylphenyl)-9,10-iminophenanthrenequinone (3)

Phenanthrenequinone (1.3849 g, 6.65 mmol) and aniline (1.60 cm^3, 7.49 mmol) were reacted according to the method to yield **3** as a black crystalline solid (2.5278 g, 85 %). M.p. 180–183 °C. IR (ATR, *v*/cm^{-1}): 2959 (s), 2930 (m), 2869 (m), 1681 (m, C=O), 1614 (m), 1592 (s, C=N), 1462 (m), 1450 (s), 1439 (m), 1423 (m), 1297 (m), 1283 (m), 1275 (m), 1258 (w), 1229 (w), 760 (s), 721 (s) cm^{-1}. ^{1}H NMR δ_H (400 MHz, $CDCl_3$/ppm): 1.07 (d, *J* = 6.8 Hz, 6 H, 16 and 16′-CH_3), 1.17 (d, *J* = 6.4 Hz, 6 H, 18 and 18′-CH_3), 2.65 (m, 2 H, 17 and 17′-CH), 7.31 (s, 2 H, 20 and 20′-CH), 7.44 (m, 1 H, 4-CH), 7.55 (m, 1 H, 5-CH), 7.69 (m, 1 H, 11-CH), 7.74 (m, 1 H, 10-CH), 8.02 (d, *J* = 7.6 Hz, 1 H, 3-CH), 8.10

(d, J = 7.6 Hz, 2 H, 6 and 9-CH), 8.41 (d, J = 7.6 Hz, 1 H, 12-CH). $^{13}C\{^{1}H\}$ NMR δ_C (155 MHz, $CDCl_3$/ppm): 22.7 (16 and 16′-CH_3), 22.9 (18 and 18′-CH_3), 28.7 (C-17 and 17′), 116.6 (C-21), 123.6 (C-6 or 9), 123.7 (C-6 or 9), 126.1 (C-20 and 20′), 128.4 (C-12), 129.0 (C-4), 129.5 (C-3), 129.6 (C-5), 132.5 (C-11), 135.5 (C-10), 136.7 (C-15), 154.4 (C-1), 190.0 (C-14). UV-vis (ε, mol dm^{-3} cm^{-1}) (298 K, ~10^{-5} M in MeCN): 578 nm (207), 388 nm (875), 320 nm (3209). HRMS (ESI^+): *m/z* calc. for $C_{26}H_{24}BrNO$: 446.1120, found 446.1128.

5.6.5 *N*-(4-Iodo-2,6-diisopropylphenyl)-9,10-iminophenanthrenequinone (4)

Phenanthrenequinone (1.0245 g, 4.94 mmol) and aniline (2.0 cm^3, 9.26 mmol) were reacted according to the method to yield **4** as a blue crystalline solid. Yield: 84%, 2.0420 g. M.p. 160-165 °C. IR (ATR, ν/cm^{-1}): 3069 (w), 2957 (s), 2926 (m), 2867 (m), 1679 (m, C=O), 1612 (m), 1591 (s, C=N), 1462 (m), 1450 (s), 1297 (s), 1282 (s), 1256 (s), 1228 (m), 761 (s), 721 (s) cm^{-1}. ^{1}H NMR δ_H (400 MHz, $CDCl_3$/ppm): 1.10 (d, J = 6.8 Hz, 6 H, 16 and 16′-CH_3), 1.21 (d, J = 6.4 Hz, 6 H, 18 and 18′-CH_3), 2.65 (m, 2 H, 17 and 17′-CH), 7.50 (m, 1 H, 4-CH), 7.52 (s, 2 H, 20 and 20′-CH), 7.60 (t, J = 6.8 Hz, 1 H, 5-CH), 7.74 (t, J = 7.6 Hz, 1 H, 11-CH), 7.80 (t, J = 7.2 Hz, 1 H, 10-CH), 8.07 (d, J = 7.6 Hz, 1 H, 3-CH), 8.15 (d, J = 7.6 Hz, 2 H, 6 and 9-CH), 8.45 (d, J = 7.6 Hz, 1 H, 12-CH). $^{13}C\{^{1}H\}$ NMR δ_C (155 MHz, $CDCl_3$/ppm): 22.8 (16 and 16′-CH_3), 23.0 (18 and 18′-CH_3), 28.7 (17 and 7′-CH), 87.7 (C-21), 123.0 (C-20 and 20′), 123.7 (C-6 or 9), 123.8 (C-7), 128.5 (C-8), 129.1 (C-12), 129.6 (C2), 129.7 (C-4), 131.2 (C-5), 132.2 (C-3), 132.6 (C-11), 135.3 (C-13), 135.5 (C-10), 135.7 (C-19 and 19′), 136.7 (C-15), 148.1 (C-1), 179.1 (C-14). UV-vis (ε, mol dm^{-3} cm^{-1}) (298 K, ~10^{-5} M in MeCN): 579 nm (165), 399 (875), 313 nm (3566). HRMS (ESI^+): *m/z* calc. for $C_{26}H_{24}INO$: 494.0981, found 494.0982.

5.6.6 *N*-(2,4,6-Trimethylphenyl)-9,10-iminophenanthrenequinone (5)

Phenanthrenequinone (1.0013 g, 4.80 mmol) and 2,4,6-trimethylaniline (1.00 cm^3, 7.12 mmol) were reacted according to the method to yield **5** as a green crystalline solid. Yield: 14%, 0.2136 g. M.p. 132-135 °C. IR (ATR, ν/cm^{-1}): 2916 (m), 2849 (m), 1675 (m, C=O), 1601 (m), 1590 (s, C=N), 1473 (m), 1450 (s), 1369 (w), 1293 (s), 1277 (s), 1247 (s), 1224 (m), 850 (s), 805 (w), 781 (w), 757 (s), 730 (m), 716 (s), 659 (w). ^{1}H NMR δ_H (400 MHz, $CDCl_3$/ppm): 1.97 (s, 6 H, 16 and 16′-CH_3), 2.08 (s, 3 H, 20-CH_3), 6.89 (s, 2 H, 18 and 18′-CH), 7.39 (t, J = 7.6 Hz, 1 H, 4CH), 7.49 (t, J = 7.6 Hz, 1 H, 5-CH), 7.62 (m, 1 H,

11-CH), 7.69 (m, 1 H, 10-CH), 8.02 (m, 3 H, 3, 6 and 9-CH), 8.42 (d, J = 7.6 Hz, 1 H, 12CH). $^{13}C\{^{1}H\}$ NMR δ_C (155 MHz, $CDCl_3$/ppm): 18.2 (C-16 and 16′), 21.0 (C-20), 122.7 (C-17 and 17′), 123.6 (C-6), 123.7 (C-9), 128.1 (C-8), 128.3 (C12), 128.6 (C-18 and 18′), 128.9 (C-4), 129.4 (C-5), 129.7 (C-3), 131.1 (C-7), 132.0 (C-2), 132.3 (C-11), 132.7 (C-13), 135.3 (C-10), 136.9 (C15), 147.9 (C-1), 180.0 (C-14). UV-vis (ε, mol dm^{-3} cm^{-1}) (298 K, ∼10^{-5} M in MeCN): 585 nm (142), 383 nm (761), 313 nm (2127). HRMS (ESI^+): m/z calc. for $C_{23}H_{19}NO$: 326.1545, found 326.1546.

5.6.7 *N*-(2,6-Dimethylphenyl)-9,10-iminophenanthrenequinone (6)

Phenanthrenequinone (0.6004 g, 2.88 mmol) and 2,6-dimethylaniline (0.68 cm^3, 5.76 mmol) were reacted according to the method to yield **6** as a blue crystalline solid. Yield: 60%, 535 mg. M.p. 75-81 °C. IR (ATR, ν/cm^{-1}): 3072 (w, Aryl C–H) , 2936 (w, CH_3), 1677 (m, C=O) , 1610 (w), 1591 (s, C=N) , 1465 (m), 1450 (s, C–H def), 1326 (w), 1293 (m), 1186 (w), 1091 (m), 1023 (m), 939 (m), 835 (w), 754 (s, Aromatic oop), 720 (s). ^1H NMR δ_H (400 MHz, $CDCl_3$/ppm): 1.99 (s, 6 H, 16,16′-CH_3), 6.97 (t, J = 7.5 Hz, 1 H, 19-CH), 7.09 (d, J = 7.5 Hz, 2 H, 18,18′-CH), 7.42 (t, J = 7.4 Hz, 1 H, 4-CH), 7.52 (t, J = 7.4 Hz, 1 H, 5CH), 7.66 (t, J = 7.7 Hz, 1 H, 11-CH), 7.72 (t, J = 7.7 Hz, 1 H, 10-CH), 8.04 (m, 3 H, 3,6,9-CH), 8.47 (d, J = 7.8 Hz, 1 H, 12-CH). $^{13}C\{^{1}H\}$ NMR δ_C (155 MHz, $CDCl_3$/ppm): 18.2 (C-16,16′), 122.6 (C-17,17′), 122.7 (C-19), 123.5 (C-6), 123.6 (C-9), 127.7 (C-18, 18′) 128.2 (C-12), 128.8 (C-4), 129.4 (C-5), 129.6 (C-3), 132.3 (C-11), 135.5 (C-10), 150.3 (C-1), 179.9 (C14). UV-vis (ε, mol dm^{-3} cm^{-1}) (298 K, ∼10^{-5} M in MeCN): 566 nm (338), 396 nm (1459), 313 nm (4982). HRMS (ESI^+): m/z calcd. for $C_{22}H_{18}NO$: 312.1382, found 312.1388.

5.6.8 *N,N*-(2,3-Dimethylphenyl)-9,10-diiminophenanthrene (9)

Phenanthrenequinone (0.40 g, 1.92 mmol) and 2,3-dimethylaniline (0.47 g, 3.84 mmol) were reacted according to the method to yield **9** as a dark blue crystalline solid.

5.6.9 General Synthesis of *N*-(mono-substituted)-9,10-iminoalkoxy Semiquinone Radical Ions

The appropriate mono substituted iminophenanthrenequinone ligand was dissolved in dried PhMe. An excess of potassium metal was added, and the mixture left refluxed under Ar pressure for 12 h, during which time the colour of the solution turned from green to brown. The excess of unreacted potassium metal was removed by filtration and the

volume of the solution concentrated under vacuum. An excess of dried hexane was added to obtain a fine brown powder, which was stored under Ar pressure in the glove-box.

5.6.10 *N*-(2,6-diisopropylphenyl)-9,10-iminoalkoxyphenanthrene semiquinone [1•]$^{-}$

IR (ATR, ν/cm^{-1}) (Nujol mull, NaCl): 3089 (m, C-H Aryl), 2988 (w, C-H Methyl), 1532 (s, C=O), 1479 (s, C=N), 1288 (m), 1094 (s), 780 (m), 592 (w). UV-vis (ε, mol dm^{-3} cm^{-1}) (298 K, ~10^{-5} M in PhMe): 378 nm (2170), 290 nm (12188).

5.6.11 *N*-(4-chloro-2,6-diisopropylphenyl)-9,10-iminoalkoxyphenanthrene semiquinone [2•]$^{-}$

IR (ATR, ν/cm^{-1}) (Nujol mull, NaCl): 3034 (m, C-H Aryl), 2827 (m, C-H Methyl), 1566 (s, C=O), 1481 (s, C=N), 1428 (m), 1387 (m), 1168 (w), 867 (w), 724 (m). UV-vis (ε, mol dm^{-3} cm^{-1}) (298 K, ~10^{-5} M in PhMe): 362 nm (3606), 291 nm (15045).

5.6.12 *N*-(4-bromo-2,6-diisopropylphenyl)-9,10-iminoalkoxyphenanthrene semiquinone [3•]$^{-}$

IR (ATR, ν/cm^{-1}) (Nujol mull, NaCl): 3171 (m, C-H Aryl), 3028 (m, C-H Methyl), 1592 (s, C=O), 1478 (s, C=N), 1404 (s), 1334 (s), 1263 (m), 1200 (w), 1135 (w), 1053 (m), 998 (m), 916 (m), 757 (s), 619 (w). UV-vis (ε, mol dm^{-3} cm^{-1}) (298 K, ~10^{-5} M in PhMe): 345 nm (576), 291 nm (2394).

5.6.13 *N*-(4-iodo-2,6-diisopropylphenyl)-9,10-iminoalkoxyphenanthrene semiquinone [4•]$^{-}$

IR (ATR, ν/cm^{-1}) (Nujol mull, NaCl): 3025 (w, C-H Aryl), 2957 (m, C-H Methyl), 1475 (s, C=O), 1439 (s, C=N), 1380 (s), 1124 (s), 883 (w), 720 (m), 619 (m). UV-vis (ε, mol dm^{-3} cm^{-1}) (298 K, ~10^{-5} M in PhMe): 357 nm (596), 295 nm (2934).

5.6.14 *N*-(2,4,6-trimethylphenyl)-9,10-iminoalkoxyphenanthrene semiquinone [5•]$^{-}$

IR (ATR, ν/cm^{-1}) (Nujol mull, NaCl): 3178 (m, C-H Aryl), 2968 (m, C-H Methyl), 1596 (s, C=O), 1478 (s, C=N), 1432 (m), 1340 (m), 1250 (w), 1201 (m), 1134 (s), 1016 (m),

864 (w), 764 (m).). UV-vis (ε, mol dm^{-3} cm^{-1}) (298 K, ~10^{-5} M in PhMe): 352 nm (326), 293 nm (3066).

5.6.15 *N*-(2,6-dimethylphenyl)-9,10-iminoalkoxyphenanthrene semiquinone [6•]⁻

IR (ATR, *v*/cm^{-1}) (Nujol mull, NaCl): 3175 (m, C-H Aryl), 3001 (m, C-H Methyl), 1475 (s, C=O), 1439 (s, C=N), 1382 (m), 1367 (m), 1151 (w), 723 (m). UV-vis (ε, mol dm^{-3} cm^{-1}) (298 K, ~10^{-5} M in PhMe): 346 nm (2980), 290 nm (7879).

It was not possible to isolate single crystals of one of these radicals, although different strategies have been adopted. However, from the diffusion of dried hexane into a toluene solution of [**6**•]⁻, single crystals of *N*-(2,6-dimethylphenyl)formamide have been formed.

5.6.16 Reactions between *N*-(mono-substituted)-9,10-iminoalkoxy semiquinone radical ions and UCl_4

A green suspension of UCl_4 (100 mg, 0.263 mmol) in dried toluene (20 mL) was mixed with a brown toluene solution (15 mL) of a selected 9,10-iminoalkoxy semiquinone radical (*ca.* 2 equiv.). The mixture was stirred for two hours under reflux conditions and Ar pressure. A grey precipitate was formed and removed by filtration. The resulting brown solution was then reduced in volume under vacuum and crystals suitable for X-ray diffractions were grown by diffusion of dried hexane. Single crystals of $[K(H_2O)]_2[UO_2Cl_4]$ and *N*-(2,6-diisopropylphenyl)formamide) were obtained using, respectively, [**1**•]⁻ and [**2**•]⁻ as the radical-ligand.

5.7 References

[1] S. Demir, I.-R. Jeon, J. R. Long and T. D. Harris, *Coord. Chem. Rev.*, 2015, 289-290, 149-176

[2] a) C. G. Pierpont, *Coord. Chem. Rev.*, 2001, 219-221, 415-433; c) C. G. Pierpont and R. M. Buchanan, *Coord. Chem. Rev.*,1981, **38**, 45-87; d) A. Caneschi, D. Gatteschi, P. Rey, in: S. J. Lippard (Ed.), *Progress in Inorganic Chemistry*, John Wiley & Sons, Inc., 1991, pp. 331-429

[3] a) B. D. Koivisto and R. G. Hicks, *Coord. Chem. Rev.*, 2005, **249**, 2612-2630; b) K. E. Preuss, *Dalton Trans*, 2007, 2357-2369; c) N. Koga and S. Karasawa, *Bull. Chem. Soc. Jpn.*, 2005, **78**, 1384

[4] a) W. Kaim and M. Moscherosch, *Coord. Chem. Rev.*, 1994, **129**, 157; b) L. Ballester, A. Gutiérrez, M.F. Perpiñàn and M. T. Azcondo, *Coord. Chem. Rev.*, 1999, 190-192, 447-470; c) J. M. Manriquez, G. T. Yee, R. S. McLean, A. J. Epstein and J. S. Miller, *Science*, 1991, **252**,

1415; d) W. E. Broderick, J. A. Thompson, E. P. Day and B. M. Hoffman, *Science*, 1990, **249**, 401

[5] a) K. L. M. Harriman, J. L. Brosmer, L. Ungur, P. L. Diaconescu and M. Murugesu, *J. Am. Chem. Soc.*, 2017, **139**, 1420; b) C. A. P. Goodwin, F. Ortu, D. Reta, N. F. Chilton and D. P. Mills, *Nature*, 2017, **548**, 439; c) Y.-C. Chen, J.-L. Liu, Y. Lan, Z.-Q. Zhong, A. Mansikkamaki, L. Ungur, Q.-W. Li, J.-H Jia, L. F. Chibotaru, J.-B Han, W. Wernsdorfer, X.-M Chen and M.-L. Tong, *Chem. Eur. J.*, 2017, **23**, 5708; d) T. Puch, N. F. Chilton and R. A. Layfield, *Angew. Chem., Int. Ed.*, 2016, **55**, 11082; e) J. Liu, Y.-C. Chen, J.-L. Liu, V. Vieru, L. Ungur, J.-H. Jia, L. F. Chibotaru, Y. Lan, W. Wernsdorfer, S. Gao, X.-M. Chen and M.-L. Tong, *J. Am. Chem. Soc.* 2016, **138**, 5441; f) K. E. Preuss, *Coord. Chem. Rev.*, 2015, 289-290, 49-61; g) C. Benelli, A. Caneschi, D. Gatteschi and L. Pardi, *J. Appl. Phys.* 1990, **67**, 5613; h) A. Caneschi, D. Gatteschi N. Lalioti, C. Sangregorio, R. Sessoli, G. Venturi, A. Vindigni, A. Rettori, M. G. Pini and M. A. Novak, *Europhys. Lett.* 2002, **58**, 771; i) F.-S. Guo and R. A. Layfield, *Chem. Commun.*, 2017, **53**, 3130; l) J. R. Hickson, S. J. Horsewill, J. McGuire, C. Wilson, S. Sproules and J. H. Farnaby, *Chem. Commun.*, 2018, **54**, 11284

[6] W. W. Lukens and M. D. Walter, *Inorg. Chem.*, **49**, 2010, 4458

[7] O. P. Lam, C. Anthon, F. W. Heinemann, J. M. O'Connor and K. Meyer, *J. Am. Chem. Soc.*, 2008, **130**, 6567

[8] O. P. Lam, P. L. Feng, F. W. Heinemann, J. M. O'Connor and K. Meyer, *J. Am. Chem. Soc.*, 2008, **130**, 2806

[9] I. Castro-Rodriguez, H. Nakai, L. N. Zakharov, A. L. Rheingold and K. Meyer, *Science*, 2004, **305**, 1757

[10] M. A. Antunes, J. T. Coutinho, I. C. Santos, J. Marçalo, M. Almeida, J. J. Baldovì, L. C. J. Pereira, A. Gaita-Ariño and E. Coronado, *Chem. Eur. J.*, 2015, **21**, 17817

[11] E. M. Matson, S. M. Franke, N. H. Anderson, T. D. Cook, P. E. Fanwick and S. C. Bart, *Organometallics*, 2014, **33**, 1964

[12] S. Hohloch, J. R. Pankhurst, E. E. Jaekel, B. F. Parker, D. J. Lussier, M. E. Garner, C. H. Booth, J. B. Love and J. Arnold, *Dalton Trans.*, 2017, **46**, 11615

[13] D. R. Kindra and W. J. Evans, *Chem. Rev.*, 2014, **114**, 8865

[14] O. P. Lam, C. Anthon, F. W. Heinemann, J. M. O'Connor and K. Meyer, *J. Am. Chem. Soc.*, 2008, **130**, 6567

[15] a) W. Ren, G. Zi and M. D. Walter, *Organometallics*, 2012, **31**, 672; b) W. Ren, H. Song, G. Zi and M. D. Walter, *Dalton Trans.*, 2012, **41**, 5965

[16] a) C. H. Booth, M. D. Walter, D. Kazhdan, Y. J. Hu, W. W. Lukens, E. D. Bauer, L. Maron, O. Eisenstein and R. A. Andersen, *J. Am. Chem. Soc.*, 2009, **131**, 6480; b) N. A. G. Bandeira, C. Daniel, A. Trifonov and M. Calhorda, *Organometallics*, 2012, **31**, 4693

[17] S. A. Pattenaude, K. C. Mullane, E. J. Schelter, M. G. Ferrier, B. W. Stein, S. E. Bone, J. S. Lezama Pacheco, S. A. Kozimor, P. E. Fanwick, M. Zeller and S. C. Bart, *Inorg. Chem.*, 2018, **57**, 6530

[18] a) G. Christou, D. Gatteschi, D. N. Hendrickson and R. Sessoli, *MRS Bull.*, 2000, **25**, 66; b) R. Bagai and G. Christou, *Chem. Soc. Rev.*, 2009, **38**, 1011

[19] a) L. Bogani and W. Wernsdorfer, *Nat. Mater.*, 2008, **7**, 179; b) W. Liang, M. P. Shores, M. Bockrath, J. R. Long and H. Park, *Nature*, 2002, **417**, 725; c) M.-H. Jo, J. E. Grose, K. Baheti, M. M. Deshmukh, J. J. Sokol, E. M. Rumberger, D. N. Hendrickson, J. R. Long, H. Park, D. C. Ralph, *Nano Lett.*, 2006, **6**, 2014; d) H. B. Heersche, Z. de Groot, J.A. Folk, H. S. J. van der

Zant, C. Romeike, M. R. Wegewijs, L. Zobbi, D. Barreca, E. Tondello, A. Cornia, *Phys. Rev. Lett.*, 2006, **96**, 206801

[20] a) S. G. McAdams, A.-M. Ariciu, A. K. Kostopoulos, J. P. S. Walsh and F. Tuna, *Coord. Chem. Rev.*, 2017, **346**, 216; b) F. Pointillart, B. Le Guennic, T. Gauchy, S. Golhen, O. Cador, O. Maury and L. Ouahab, *Inorg. Chem.*, 2013, **52**, 5978; c) F. Pointillart, S. Klementieva, V. Kuropatov, Y. Le Gal, S. Golhen, O. Cador, V. Cherkasov and L. Ouahab, *Chem. Commun.*, 2012, **48**, 714; d) F. Pointillart, V. Kuropatov, A. Mitin, O. Maury, Y. Le Gal, S. Golhen, O. Cador, V. Cherkasov and L. POuahab, *Eur. J. Inorg. Chem.*, 2012, **48**, 714

[21] N. Magnani, *Int. J. Quantum Chem.*, 2014, **114**, 755; b) K. R. Meihaus and J. R. Long, *Dalton Trans.*, 2015, **44**, 2517

[22] L. C. J. Pereira, C. Camp, J. T. Coutinho, L. Chatelain, P. Maldivi, M. Almeida and M. Mazzanti, *Inorg. Chem.*, 2014, **53**, 11809; b) C. A. P. Goodwin, F. Tuna, E. J. L. Mclnnes, S. T. Liddle, J. McMaster, I. J. Vitorica-Yrezabal and D. P. Mills, *Chem. Eur. J.*, 2014, **20**, 14579; c) D. P. Mills, F. Moro, J. McMaster, J. van Slageren, W. Lewis, A. J. Blake and S. T. Liddle, *Nat. Chem.*, 2011, **3**, 454; d) F. Moro, D. P. Mills, S. T. Liddle and J. van Slageren, *Angew. Chem. Int. Ed.*, 2013, **52**, 3430

[23] V. Mougel, L. Chatelain, J. Pecaut, R. Caciuffo, E. Colineau, J. C. Griveau and M. Mazzanti, *Nat. Chem.*, 2012, **4**, 1011

[24] N. M. Edelstein, G. H. Lander, in: L. R. Morss, N. M. Edelstein, J. Fuger (Eds.), *The Chemistry of Actinide and Transactinide Elements*, third ed., vol 4, Springer, Dordrecht, 2006, (chap. 20)

[25] B. Gao, X. Luo, W. Gao, L. Huang, S.-M.Gao, X. Liu and Q. Wu, Y. Mu, *Dalton Trans.*, 2012, **41**, 2755

[26] K. A. Kreisel, G. P. A. Yap and K. H. Theopold, *Inorg. Chem.*, 2008, **47**, 5293

[27] B. Gao, L. Xin, W. Gao, Z.-Q. Hao, X.-Z. Xin, Q.-L. Wu and Y. Mu, *Polyhedron*, 2013, **63**, 91

[28] B. Xu, A. Ma, T. Jia, Z. Hao, W. Gao and Y. Mu, *Dalton Trans.,* 2016, **45**, 17966

[29] a) O. Takahashi, Y. Kohno and M. Nishio, *Chem. Rev.*, 2010, **110**, 6049; b) M. Nishio, *Phys. Chem. Chem. Phys,* 2011, **13**, 13873; c) T. J. Mooibroek and P. Gamez, *CrystEngComm*, 2012, **14**, 8462

[30] C. A. Hunter and J. K. M. Sanders, *J. Am. Chem. Soc.*, 1990, **112**, 5525

[31] S. E. Wheeler and K. N. Houk, *J. Am. Chem. Soc.*, 2008, **130**, 10854

[32] a) A. J. Neel, M. J. Hilton, M. S. Sigman and F. D. Toste, *Nature*, 2017, **543**, 637; b) J. W. Hwang, P. Li and K. D. Shimiza, *Org. Biomol. Chem.*, 2017, **15**, 1554; c) S. E. Wheeler and J. W. G. Bloom, *J. Phys. Chem. A*, 2014, **118**, 6133; d) C. R. Martinez and B. L. Iverson, *Chem. Sci.* 2012, **3**, 2191

[33] a) G. Cavallo, P. Metrangolo, R. Milani, T. Pilati, A. Priimagi, G. Resnati and G. Terraneo, *Chem. Rev.*, 2016, **116**, 2478; b) A. Bauzá, T. J. Mooibroek and A. Frontera, *ChemPhysChem*, 2015, **16**, 2496; c) R. W. Troff, T. Makela, F. Topic, A. Valkonen, K. Raatikainen and K. Rissanen, *Eur. J. Org. Chem.*, 2013, 1617

[34] For recent reviews see: a) L. C. Gilday, S. W. Robinson, T. A. Barendt, M. J. Langton, B. R. Mullaney and P. D. Beer, *Chem. Rev.*, 2015, **115**, 7118; b) R. Bishop, *CrystEngComm*, 2015, **17**, 7448; c) G. Berger, J. Soubhye and F. Meyer, *Polym. Chem.*, 2015, **6**, 3559; d) A. Mukherjee, S. Tothadi and G. R. Desiraju, *Acc. Chem. Res.*, 2014, **47**, 2514; e) A. Priimagi, G. Cavallo, P. Metrangolo and G. Resnati, *Acc. Chem. Res.*, 2013, **46**, 2686; f) F. Meyer and P. Dubois, *CrystEngComm*, 2013, **15**, 3058

[35] P. Frøyen, *Phosphorus Sulfur Silicon Relat. Elem.*, 1993, **81**, 37

[36] L. Li, M. Jeon and S. Y. Kim, *J. Mol. Catal. A.: Chem.*, 2009, **303**, 110

[37] T. J. Mooibroek, P. Gamez and J. Reedijk, *CrystEngComm*, 2008, **10**, 1501

[38] a) A. D. Rae and A. C. Willis, *Z. Kristallogr.*, 2003, **218**, 221; b) S. Y. Matsuzaki, M. Gotoh and A. Kuboyama, *Mol. Cryst. Liq. Cryst.*, 1987, **142**, 127; c) M. Alleaume, R. Darrouy and J. Housty, *Acta Crystallogr.*, 1961, **14**, 1202

[39] a) A. Gavezzotti and L. Lo Presti, *Cryst. Growth Des.*, 2016, **16**, 2952; b) R. Taylor, *Cryst. Growth Des.* 2016, **16**, 4165

[40] a) S. K. Singh and A. Das, *Phys. Chem. Chem. Phys.*, 2015, **17**, 9596; b) H. R. Khavasi, A. Ghanbarpour and A. A. Tehrani, *CrystEngComm*, 2014, **16**, 749; c) T. J. Mooibroek and P. Gamez, *CrystEngComm,* 2012, **14**, 1027; d) T. J. Mooibroek, P. Gamez and J. Reedijk, *CrystEngComm*, 2008, **10**, 1501

[41] G. R. Desiraju and R. Parthasarathy, *J. Am. Chem. Soc.* 1989, **111**, 8725

[42] O. V. Shishkin, *Chem. Phys. Lett.*, 2008, **458**, 96

[43] K. E. Riley, M. Vazquesz, C. Umemura, C. Miller and K.-A. Tran, *Chem. Eur. J.*, 2016, **22**, 17690

[44] a) A. J. Neel, M. J. Hilton, M. S. Sigman and F. D. Toste, *Nature*, 2017, **543**, 637; b) S. K. Singh, S. Kumar and A. Das, *Phys. Chem. Chem. Phys.*, 2014, **16**, 8819

[45] P. Politzer and J. S. Murray, *Cryst. Growth Des.*, 2015, **15**, 3767

[46] See for example a) N. Mohan and C. H. Suresh, *J. Phys. Chem. A*, 201**4**, **118**, 4315; b) N. Mohan, C. H. Suresh, A. Kumar and S. R. Gadre, *Phys. Chem. Chem. Phys*., 2013, **15**, 18401; c) Y. Lu, Y. Liu, H. Li, X. Zhu, H. Liu and W. Zhu, *J. Phys. Chem. A*, 2012, **116**, 2591; d) C. Estarellas, A. Frontera, D. Quinonero and P. M. Deya, *Cent. Eur. J. Chem.*, 2011, **9**, 25.

[47] M. P. Waller, A. Robertazzi, J. A. Platts, D. E. Hibbs and P. A. Williams, *J. Comput. Chem.*, 2006, **27**, 491

[48] a) J. J. McKinnon, M. A. Spackman and A. S. Mitchell, *Acta Crystallogr., Sect. B: Struct. Sci.*, 2004, **60**, 627; b) M. A. Spackman and J. J. McKinnon, *CrystEngComm*, 2002, **4**, 378; c) S. K. Wolff, D. J. Grimwood, J. J. McKinnon, M. J. Turner, D. Jayatilaka and M. A. Spackman, *CrystalExplorer* (Version 3.1), University of Western Australia, **2012**.

[49] a) L. A. Cameron, J. W. Ziller, A. F. Heyduk, *Chem. Sci.*, 2016, **7**, 1807; b) G. Szigethy, A. F. Heyduk, Dalton Trans. 2012, **41**, 8144; c) D. M. Togashi, D. E. Nicodem, *Spectrochim. Acta Part A*, 2004, **60**, 3205

[50] a) Ş. Nardali, F. Ucun, and M. Karakaya, Russ. J. Phys. Chem. A., 2017, **9**, 2137; b) L. Hermosilla, J. M. Garcìa de la Vega, C. Sieiro and P. Calle, *J. Chem. Theory. Comput.*, 2011, **7**, 169; c) H. M. Tuononen and A. F. Armstrong, *Inorg. Chem.*, 2005, **44**, 8277; d) P. Ludwing, T. Layloff and R. N. Adams, *J. Am. Chem. Soc*., 1964, **86**, 4568

[51] B. Omondi, A. Lemmerer, M. A. Fernandes, D. C. Levendis and M. Layh, *Acta Cryst.*, 2014, **70**, 106

[52] D. J. Watkin, R. G. Denning and K. Prout, *Acta Crystallogr., Sect. C: Cryst. Struct. Commun.*, 1991, **47**, 2517

[53] B. Xu, A. Ma, T. Jia, Z. Hao, W. Gao and Y. Mu, *Dalton Trans.*, 2016, **45**, 17966

[54] C. Popeney and Z. B. Guan, *Organometallics*, 2005, **24**, 1145

[55] J. H. Oskam, H. H. Fox, K. B. Yap, D. H. McConville, R. O'Dell, B. J. Lichtenstein and R. R. Schrock, *J. Organomet. Chem.*, 1993, **459**, 185

[56] S. Meiries and S. Nolan, *Synlett*, 2014, **25**, 393

[57] S. V. Kudrevich, M. G. Galpern, E. A. Luk and J. E. Van Lier, *Can. J. Chem.*, 1996, **74**, 508

[58] K. Momma and F. Izumi, *J. Appl. Crystallogr.*, 2011, **44**, 1272

[59] M. J. Frisch, G. W. Trucks, H. B. Schlegel, G. E. Scuseria, M. A. Robb, J. R. Cheeseman, G. Scalmani, V. Barone, B. Mennucci, G. A. Petersson, H. Nakatsuji, M. Caricato, X. Li, H. P. Hratchian, A. F. Izmaylov, J. Bloino, G. Zheng, J. L. Sonnenberg, M. Hada, M. Ehara, K. Toyota, R. Fukuda, J. Hasegawa, M. Ishida, T. Nakajima, Y. Honda, O. Kitao, H. Nakai, T. Vreven, J. A. Montgomery Jr., J. E. Peralta, F. Ogliaro, M. Bearpark, J. J. Heyd, E. Brothers, K. N. Kudin, V. N. Staroverov, R. Kobayashi, J. Normand, K. Raghavachari, A. Rendell, J. C. Burant, S. S. Iyengar, J. Tomasi, M. Cossi, N. Rega, J. M. Millam, M. Klene, J. E. Knox, J. B. Cross, V. Bakken, C. Adamo, J. Jaramillo, R. Gomperts, R. E. Stratmann, O. Yazyev, A. J. Austin, R. Cammi, C. Pomelli, J. W. Ochterski, R. L. Martin, K. Morokuma, V. G. Zakrzewski, G. A. Voth, P. Salvador, J. J. Dannenberg, S. Dapprich, A. D. Daniels, Ö. Farkas, J. B. Foresman, J. V. Ortiz, J. Cioslowski and D. J. Fox, *Gaussian 09, Revision C.01, Gaussian,* Inc., Wallingford CT, 2010

[60] Y. Zhao and D. G. Truhlar, *Theor. Chem. Acc.*, 2008, **120**, 215

[61] F. Weigend and R. Ahlrichs, *Phys. Chem. Chem. Phys.*, 2005, **7**, 3297

[62] S. F. Boys and F. Bernardi, *Mol. Phys.*, 1970, **19**, 553

[63] *AIMAll* (Version 12.06.03), Todd A. Keith, TK Gristmill Software, Overland Park KS, USA, 2012

Chapter 6

CONCLUSIONS

and

FUTURE WORK

In this thesis a series of high symmetry uranium(IV) and thorium(IV) thiocyanate compounds of formula $A_4[An(NCS)_8]$ (A = Me_4N, Et_4N, $^nPr_4N$, Cs; An = U, Th) have been structurally and spectroscopically characterized. It has been shown that crystal packing forces are energetically more important than crystal field splitting and, thus, the shape and size of the counteraction determine the coordination symmetry around the actinide ion. Notably, this effect proved to have a significant influence on the electronic structure of the $[U(NCS)_8]^{4-}$ ion and consequently on its magnetic behaviour. In particular, the low temperature (2 K) effective magnetic moment of $Cs_4[U(NCS)_8]$ was found significantly higher compared to the other samples.

In this study, it has been shown that the combination between the computational framework CONDON and advanced spectroscopic techniques, such as INS and FIR spectroscopy, is a very powerful approach to delineate the low-lying energy level electronic structure of these $A_4[U(NCS)_8]$ compounds. In particular, the results of this analysis, in agreement with the spectroscopic and magnetic data, suggest a triplet electronic ground state for $Cs_4[U(NCS)_8]$, which represents the first of its type in U(IV) chemistry. At this point, it could be useful to expand further the study toward other counter cations; it could be also important to isolate and characterize single crystals of $Cs_4[Th(NCS)_8]$.

Moreover, from the CONDON approach for the determination of the energy levels of the electronic structure of the uranium compounds, it was not possible to derive a reliable set of Slater-Condon parameters and spin-orbit coupling constants, although the spectroscopic data from the INS and FIR measurements were included in the calculations. These parameters, indeed, have been fixed for all compounds as mean values from analysis on various U(IV) compounds (Table 2.8), but this approximation affected significantly the energies of the higher excited states (> 1000 cm^{-1}). Therefore, in order to better fit these parameters, magnetic circular dichroism (MCD) measurements in the UV-vis region have been performed on the Et_4N, $^nPr_4N$, Cs compounds. MCD measurements, indeed, can detect transitions that are too weak to be seen in conventional optical absorption spectra or that are buried under a stronger transition. This analysis has been carried out by Dr. M. L. Neidig at University of Rochester and the results are shown in Figure 6.1, although they have not been analysed yet.

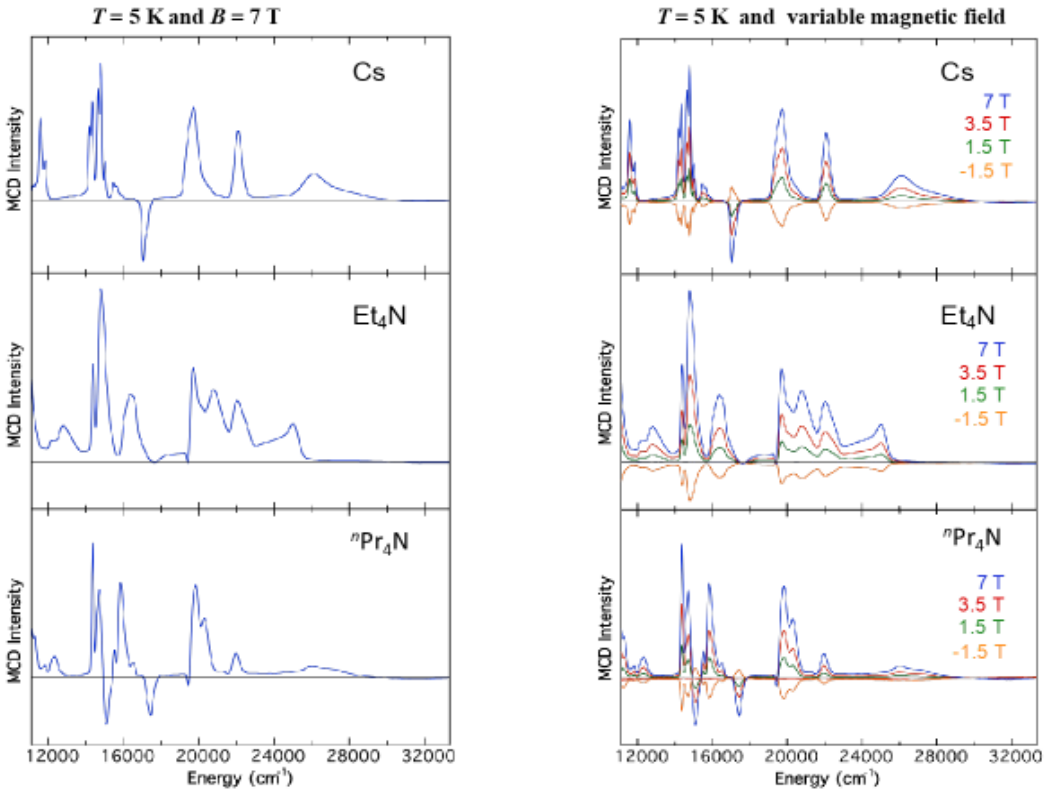

Figure 6.1. Magnetic circular dichroism spectra in the UV-vis region of $A_4[U(NCS)_8]$ (A = Cs, Et_4N, $^nPr_4N$), measured at (left) 5 K, with B = 7 T, and at (right) 5 K, with a variable magnetic field.

In this thesis, it has been shown that a small variation of the ligand field from $[U(NCS)_8]^{4-}$ to $[U(NCSe)_8]^{4-}$, with the $[NCSe]^-$ ligands being less electron donating than $[NCS]^-$, does not strongly affect the electronic structure of the $[U(NCS(e))_8]^{4-}$ ion. In fact, the spectroscopic and magnetic properties of $[Et_4N]_4[U(NCSe)_8]$ and $[^nPr_4N]_4[U(NCSe)_8]$ were comparable to those exhibited by the isostructural thiocyanate equivalents. However, it could be important to probe the low-lying energy level electronic structure of the two selenocyanate complexes by using the combination of INS and FIR spectroscopy, while specific heat capacity measurements would also be useful for this purpose. Moreover, in light of the unusual magnetic profile of $Cs_4[U(NCS)_8]$, it could be interesting to study the magnetic properties of the selenocyanate equivalent $Cs_4[U(NCSe)_8]$. However, the synthesis of this compound appeared to be more challenging, most probably due a large light and air sensitivity displayed by this sample.

The reactivity of the $[U(NCS)_8]^{4-}$ ion toward different counter-cations in non-aqueous media has also been explored in this project. Two mixed valent uranium species, that may have relevance for the oxidation of U(IV) to U(VI) from SNF, have been described and it has been proved that it is possible to isolate the unusual $[UO_2]^+$ ion using coordinating ligands and starting from a U(IV) species. However, the mechanism is not clear from this study and further investigation are necessary. Moreover, it has been confirmed that emission spectroscopy can be successfully used to recognize the presence of U(IV) ions in mixed valent uranium compounds.

A reaction between $[U(NCS)_8]^{4-}$ and $[Co(bipy)_3]^{2+}$ led to the isolation of a complex of formula $[Co(bipy)_3][U(NCS)_8]$, for which spectroscopic and magnetic data are indicative of a Co(III)-U(V) configuration; however, the mechanism of this reaction is not clear from our results. This U(V) compound has been also sent to Professor Frantisek Hartl from University of Reading, where accurate spectroelectrochemistry measurements will be performed. A comparison with the electrochemistry data belonging to the U(IV) compounds will be also useful. Moreover, it could be very interesting to use FIR spectroscopy to examine the low-lying energy level electronic structure of this mixed metal Co(III)-U(V) system.

Clearly, in this project, it has been proved that π-donor $[NCS]^-$ ligands are able to stabilize U(VI), U(V), U(IV) ions, but not also U(III). This has also been confirmed spectroelectrochemically and, in addition, theoretical approaches have revealed an enhanced ionicity for the U(III)–N bond compared to the U(IV)–N equivalent.

A series of uranyl thiocyanate and selenocyanate compounds have been structurally and spectroscopically characterized, with the aim of investigating the corresponding supramolecular noncovalent interactions. In some of the structures, chalcogenide interactions have also been observed; they have been described adopting the σ-hole bonding scheme and are more important in the $[NCSe]^-$ than in the $[NCS]^-$ series, in line of the increased polarizability of Se with respect to S. C—H···O=U hydrogen bonds have also been recognized, but they were weak and did not affect the electronic structure of the uranyl(VI) system. This result confirms the nature of the -yl oxygens as weak Lewis basis. Luminescence spectroscopy proved to be a powerful technique to analyse these species. The differences in the position of the emission bands between the $[NCS]^-$ and $[NCSe]^-$ compounds, are in line with the $[NCS]^-$ ion being more

electron donating than $[NCSe]^-$ toward the $[UO_2]^{2+}$ system; moreover, interestingly the coupling between the δ(NCS) and δ(NCSe) vibrational modes and the uranyl mode has been observed in the emission spectra measured in solid state at 77 K.

In this thesis, it has been clearly proved that in thiocyanate and selenocyanate uranium compounds it is not possible to assign the formal oxidation state of the uranium metal only on the basis of crystallographic data, but several spectroscopic techniques are necessary. In table 6.1, indeed, are listed the averages of the U–N, N=C and C=S(e) bond lengths for the uranium thiocyanate and selenocyanate compounds discussed in this thesis and, although the formal oxidation state of uranium is changed, there are no significant differences in the values of these bond lengths.

Table 6.1. U–N, C=N, C=S(e) average bond lengths (Å) for uranium thiocyanate and selenocyanate compounds, with the uranium ion in different oxidation states.

Compounds	**Uranium oxidation state**	**U–N**	**C=N**	**C=S**	**C=Se**
$[A]_4[U(NCS)_8]$ A = Me_4N, Et_4N, $^nPr_4N$, Cs, $^nBu_4N$, H_2(2.2.2-cryptand)	IV	2.425(1)	1.163(1)	1.621(1)	-
$Cs_5[U(NCS)_9][NCS]$	IV	2.475(2)	1.163(3)	1.631(3)	-
$[A]_4[U(NCSe)_8]$ A = $[Et_4N]$, $[^nPr_4N]$	IV	2.424(2)	1.148(2)	-	1.770(2)
U-DMF	Uranyl(V)	2.458(2)	1.166(3)	1.625(3)	-
$[Co(bipy)_3]$ $[U(NCS)_8]$	V	2.43(2)	1.16(1)	1.62(1)	-
$[A]_3[UO_2(NCS)_5]$ A = Me_4N, Et_4N, $^nPr_4N$, $^nBu_4N$, Me_3NBz, Et_3NBz, Na(2.2.2-cryptand), Na(18-crown-6)	VI	2.45 (1)	1.15(1)	1.63(1)	-
$[A]_3[UO_2(NCSe)_5]$ A = Me_4N, Et_4N, $^nPr_4N$, Et_3NBz	VI	2.46(1)	1.15(1)	-	1.79(1)

Finally, a series of *N*-Aryl-9,10-phenanthreneimines compounds have been structurally and spectroscopically described, and the noncovalent interactions shown

by their solid-state crystal structures have been fully discussed. From these ligands, iminoalkoxy semiquinone radicals have also been prepared and initial spectroscopic characterization confirm the formation of radical systems. At this point, it could be very useful to isolate and study the crystal structure of these radicals and compare the data with the structures of the neutral ligands. For future analysis, all the radicals have been sent to Dr. Damien Murphy (Cardiff University) for low-temperature EPR and Electron Nuclear Double Resonance (ENDOR) measurements. The interplay between these techniques will help to obtain information on the spin density distribution.

A U(IV) complex with these radicals could show unusual magnetic properties due to magnetic coupling interactions between the radical system and the two *5f* unpaired electrons of U(IV). Unfortunately, our attempts at the isolation of these complexes have failed, while these products have proved to be very air and moisture sensitive. Potassium metal has been used for the reduction process of the neutral ligands where the probable coprecipitation of KCl could drive forward the reaction. However, potassium metal is a very strong one-electron reducing reagent; thus, perhaps the use of a weaker reducing reagent could lead to the isolation of the desired radicals.

Appendix 1

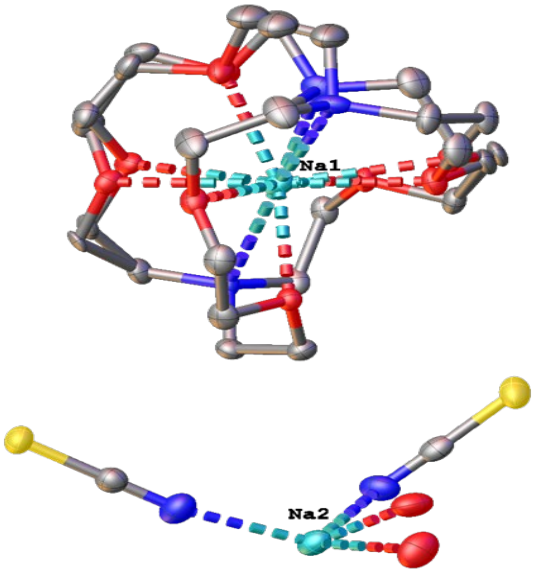

Figure 7.1. Asymmetric unit of [Na(2.2.2-cryptand)][Na(H_2O)($NCS)_2$] with atomic displacement shown at 50% probability. Hydrogen atoms omitted, and only sodium atoms labelled for clarity. Colour code: Na – light blue, N – blue, C – grey, O – red, S – yellow.

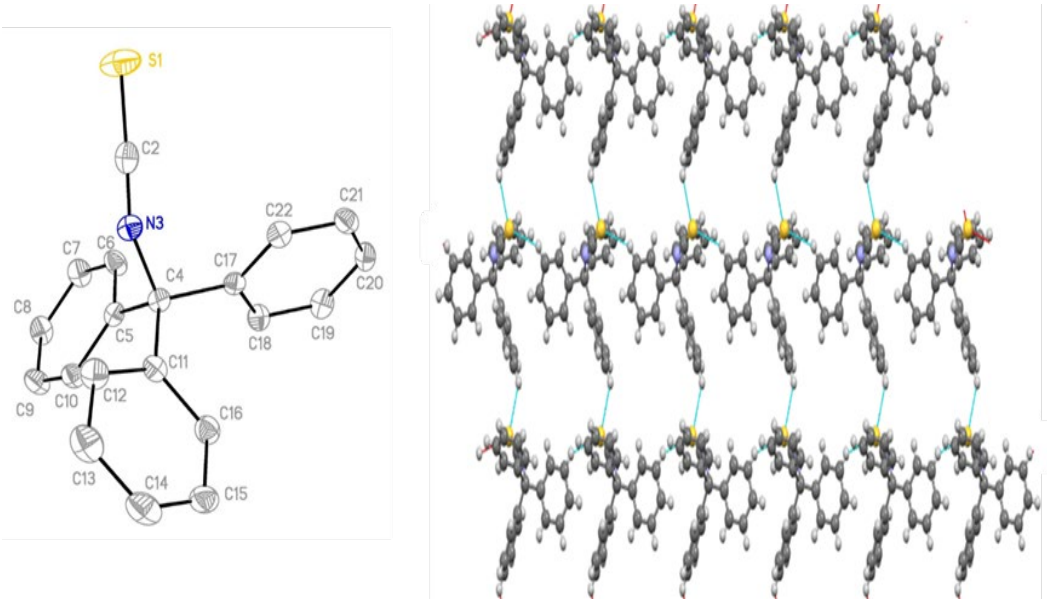

Figure 7.2. (Left) Asymmetric unit of Ph_3CNCS, with atomic displacement shown at 50% probability and hydrogen atoms omitted for clarity; (right) packing diagram of Ph_3CNCS view down the crystallographic *c* axis, with hydrogen bonding highlighted with blue dotted lines.

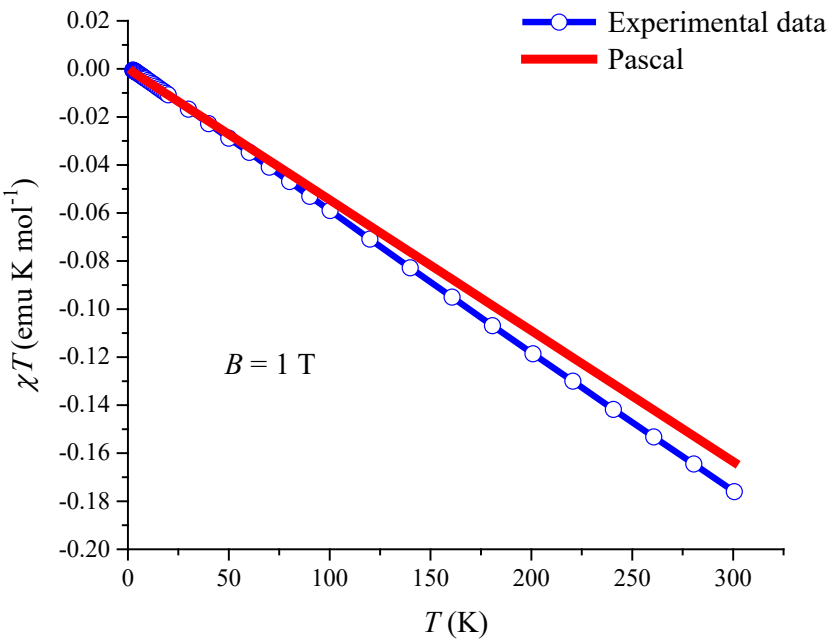

Figure 7.3. Magnetic susceptibility of $[Et_4N]_4[Th(NCS)_8]$ (as example of the Th compounds), plotted as χT vs T, for B = 1 T.

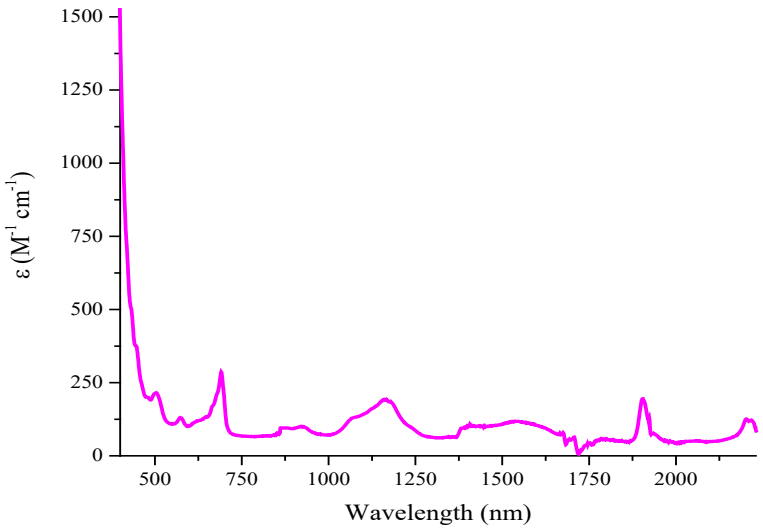

Figure 7.4. Vis-NIR absorption spectrum of $[Et_4N]_4[U(NCS)_8]$, measured at room temperature in MeCN solutions (1 x 10^{-4} M).

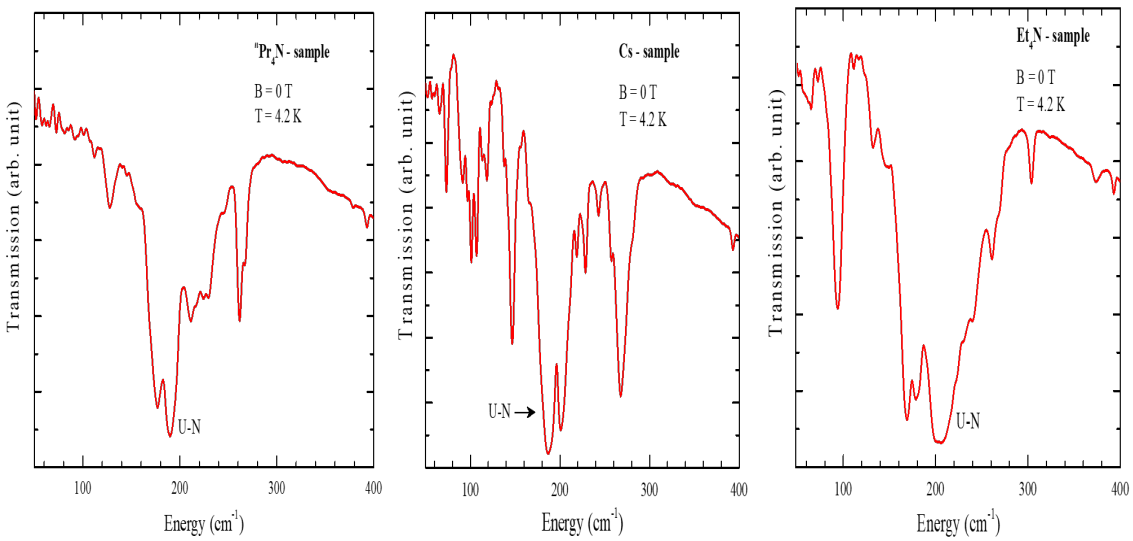

Figure 7.5. FIR spectra of (from left to right) $[^{n}Pr_4N]_4[U(NCS)_8]$, $Cs_4[U(NCS)_8]$ and $[Et_4N]_4[U(NCS)_8]$, acquired with B = 0 T and at T = 4.2 K, and showing the IR active ν(U–N) vibrational mode.

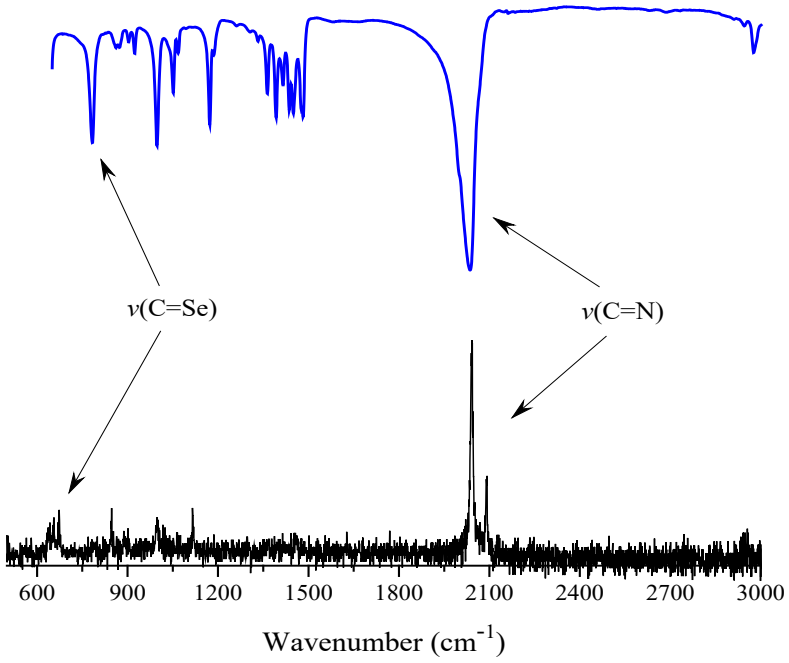

Figure 7.6. IR (top) and Raman (bottom) spectra of $[Et_4N]_4[U(NCSe)_8]$ in solid state.

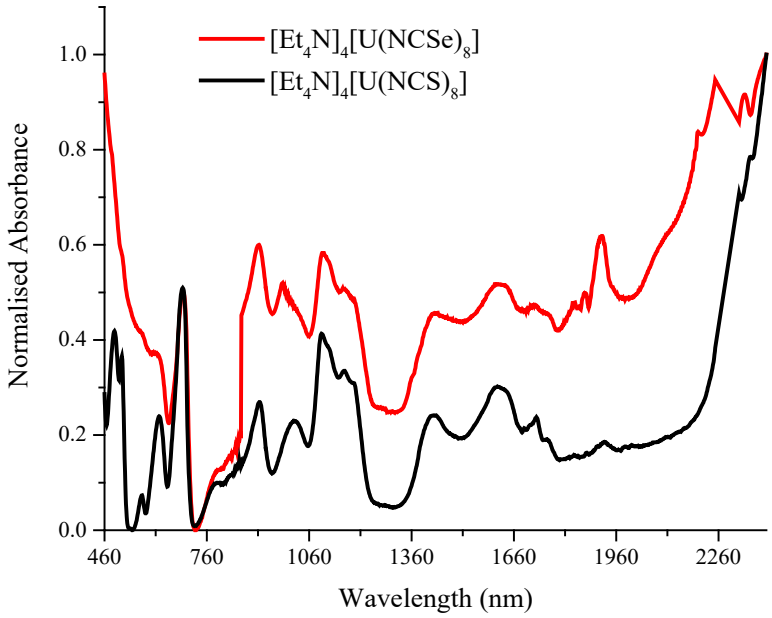

Figure 7.7. Vis-NIR spectra of $[Et_4N]_4[U(NCSe)_8]$ (red) and $[Et_4N]_4[U(NCS)_8]$ (black), measured in solid state.

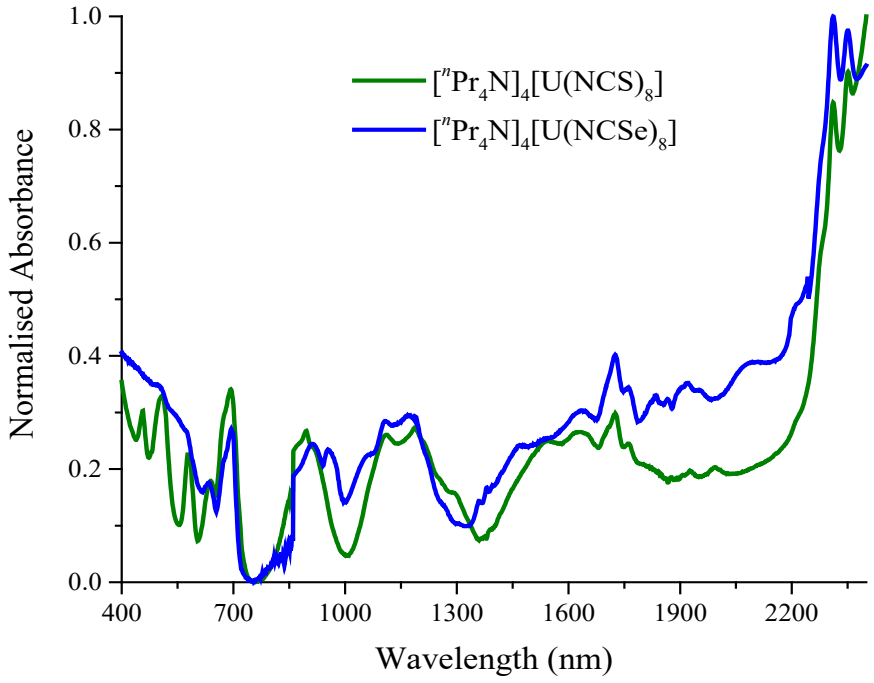

Figure 7.8. Vis-NIR spectra of $[^nPr_4N]_4[U(NCSe)_8]$ (blue) and $[^nPr_4N]_4[U(NCS)_8]$ (green), measured in solid state.

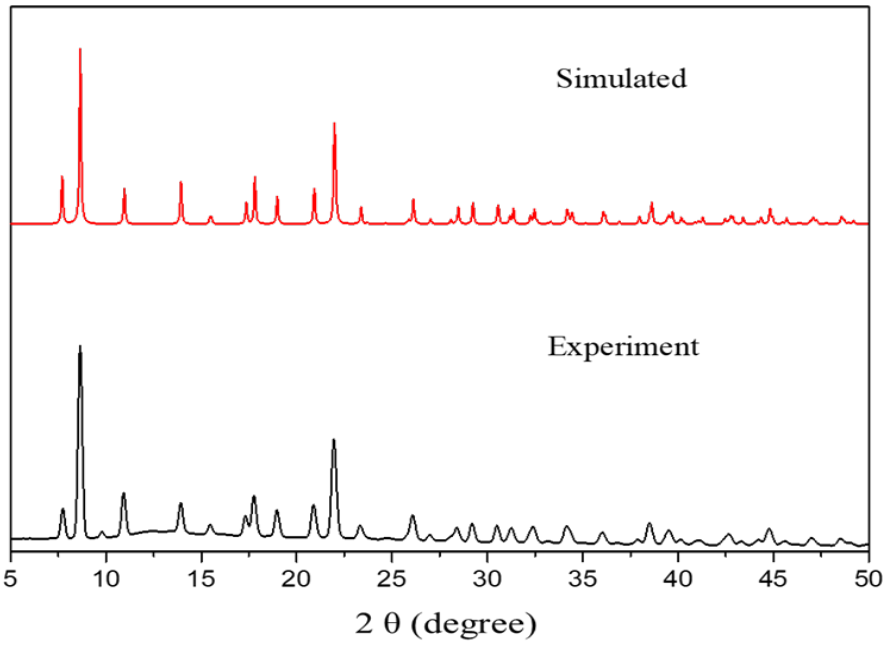

Figure 7.9. (Red line) Simulated powder pattern from the crystal structure and (black line) powder X-ray diffraction pattern of $[Et_4N]_4[U(NCS)_8]$.

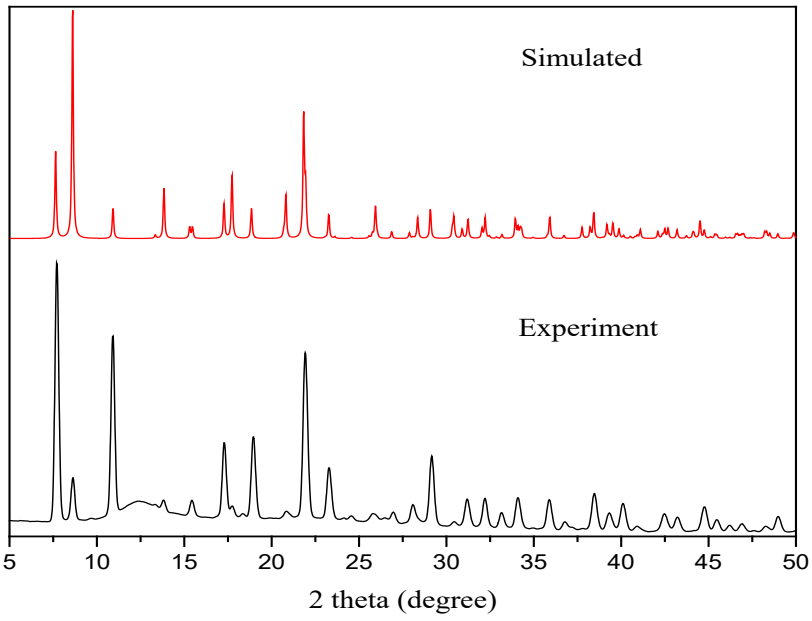

Figure 7.10. (Red line) Simulated powder pattern from the crystal structure and (black line) powder X-ray diffraction pattern of $[Et_4N]_4[Th(NCS)_8]$.

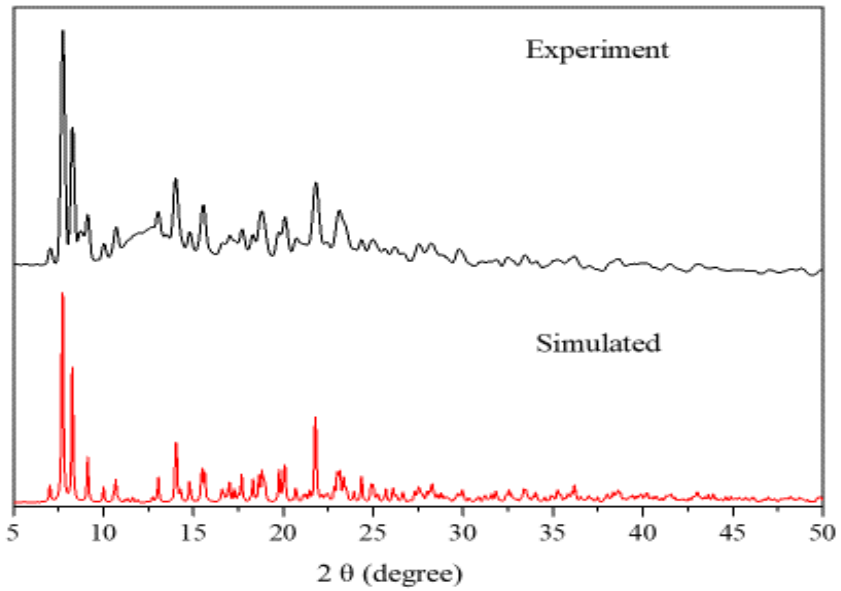

Figure 7.11. (Red line) Simulated powder pattern from the crystal structure and (black line) powder X-ray diffraction pattern of $[^{n}Pr_4N]_4[Th(NCS)_8]$.

Inelastic Neutron Scattering Measurements

Inelastic neutron scattering spectra were obtained using the MERLIN and MARI spectrometers at the ISIS Neutron and Muon Facility in Harwell (UK). Approximately 3g for each compound were wrapped in an aluminium foil packed (1) and (2), placed into a vanadium can sample holder (3) and sealed using In wire under a He atmosphere (4). These steps are illustrated in Figure 7.12; the pictures have been taken in air and using crystals of $[Cu(SO_4)_2]\cdot 5H_2O$, as example, but for the thorium and uranium samples all the procedure was carried out in a glove box.

Measurements of $Cs_4[An(NCS)_8]$ used MARI, running with the Gd chopper at 250 Hz with an incident energy of 40 meV. Measurements of $[Et_4N]_4[An(NCS)_8]$ used MERLIN, running with the Gd chopper at 600 Hz in repetition rate multiplication mode with a principle incident energy of 170 meV. The datasets are available at doi:10.5286/ISIS.E.73944367. After measurements and a sufficient time for the induced activity to decay (*ca.* two years), the samples were taken out from the vanadium cans and their purity checked by vibrational spectroscopy, confirming that no oxidation or decomposition had occurred during the measurement.

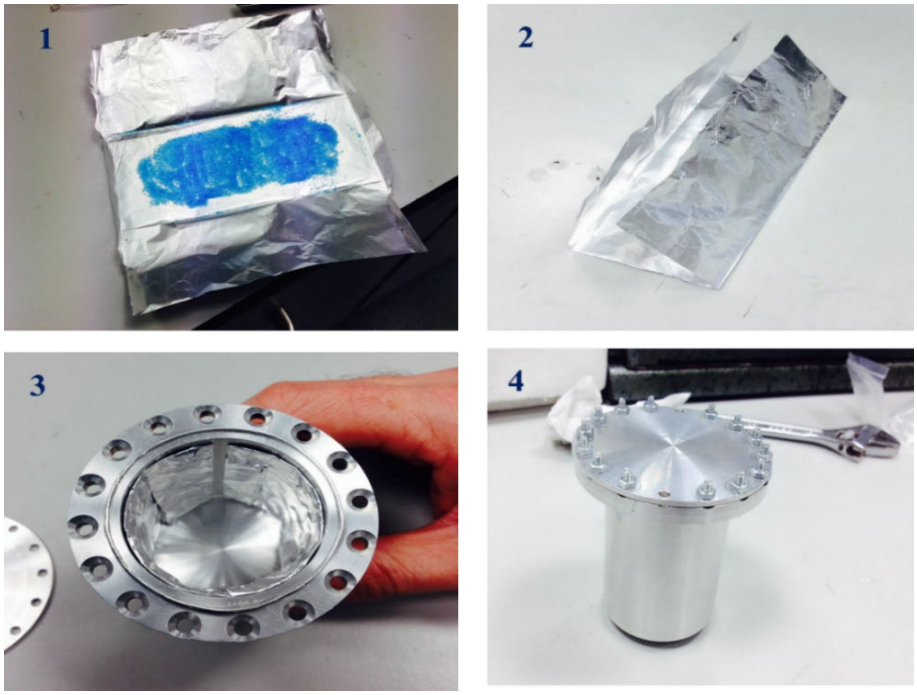

Figure 7.12. Sequence of steps to prepare samples for INS measurements.

Powder Neutron Diffraction Analysis

To resolve ambiguities arising from probable twinning in the neutron single-crystal data, high-resolution neutron powder diffraction data were acquired as a function of temperature. These measurements were carried out by Dr. Dominc Fortes, using HRPD at the ISIS Neutron and Muon Facility in Harwell (UK).[1] The instrument's 95 m flightpath and detector banks at high backscattering angles (mean $2\theta = 168°$) provides one of the highest $\Delta d/d$ resolutions available in the world (~ 6×10^{-4} for data integrated across the whole backscattering bank). The sample $[d_{20}\text{-}Et_4N]_4[U(NCS)_8]$ was loaded into an Al-alloy slab of internal dimensions 18 x 23 mm perpendicular to the incident beam and depth 5 mm parallel to the beam. Vanadium foil windows were screwed to the front and back of the sample holder, these being sealed with indium wire. Pictures of the sample-holder, before and during the measurements, are shown below in Figure 7.13.

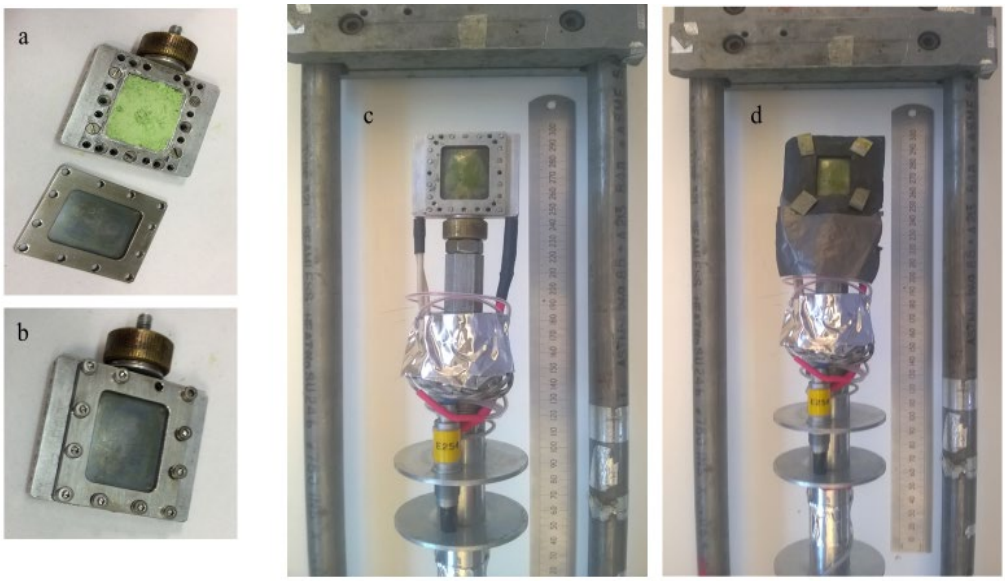

Figure 7.13. (a, b) The Al-alloy slab used to load the green powder of $[d_{20}\text{-}Et_4N]_4[U(NCS)_8]$; (c, d) pictures (front and back) of this slab containing the sample and mounted into the spectrometer before the neutron powder diffraction measurements.

Accurate and precise temperature control of the specimen was achieved with a 60 W cartridge heater inserted into one side of the Al frame and a fully ITS-1990 calibrated RhFe resistance thermometer inserted in the opposite side. Cooling was achieved using an 'Orange' He cryostat mounted on the HRPD beamline.[2] Data were measured in HRPD's 'long' 100-200 ms time-of-flight window (providing access to d-spacings from 2.2 - 3.9 Å in backscattering), this being judged to be most effective for determination of the correct cell symmetry and refinement of precise dimensions considering the quite large unit cell. At 4.7 K, data were collected for 6.5 hr (equivalent to 240 μA of proton beam current), at 100 K for 120 μA and at 200 K for 150 μA. With the *Mantid* program,[3] the data were normalized to the incident spectrum and corrected for instrument efficiency using a V:Nb standard and exported in a format suitable for profile refinement. In the absence of complete structures at low-temperature, the powder data were fitted by the LeBail method[4] in *GSAS/Expgui*[5] to obtain precise unit-cell parameters. These data show that the cell retains tetragonal symmetry down to 4.7 K and exhibits no detectable superlattice reflections. Refined unit cell parameters are reported in Table 2.4 (page 64). Data is available at https://doi.org/10.5286/ISIS.E.89608894.

Single Crystal Neutron Diffraction

Neutron diffraction data for both Th and U compounds were collected by Dr. Silvia Capelli on the SXD instrument[6] at the ISIS Neutron and Muon Facility in Harwell (UK), using the time-of-flight (TOF) Laue diffraction method.

For $[Et_4N]_4[U(NCS)_8]$, a single crystal of about 5 x 4 x 2 mm size (Figure 2.11) was attached with aluminium tape on the tip of an aluminium pin and mounted on the central stick of a Top-Loading helium Cryo-Cooled Refrigerating (TL-CCR) device, already held at 100 K. For the $[Et_4N]_4[Th(NCS)_8]$ compound, which is less stable in air than the U one, a single crystal of about 2.2 x 1.7 x 1 mm size (Figure 2.11, right) was wrapped in an Al foil and sealed in a Vanadium can of 6 mm diameter under helium atmosphere. The V-can was then mounted on the central stick of the CCR. Once the stick was in position in the CCR, the sample chamber was evacuated to 10^{-5} bar and purged with 400 mbar of He gas a couple of times in order to remove air and moisture; this is because air could give additional background scattering in the diffraction pattern and moisture from the air would freeze and block the rotation mechanism of the central stick. After the purging process, the CCR was cooled to the operating temperature of 4 K, where Bragg intensities were collected in a series of 5 (for the uranium) and 6 (for the thorium) angular orientations of the crystal around the vertical axis of the instrument, with exposure times of 3h 30m (for the uranium) and 11h (for the thorium) per orientation.

Reflection intensities were integrated using a 3D profile fitting procedure,[7] as implemented in the computer program *SXD2001*.[8] Data were corrected for Lorentz effect but no absorption correction was applied. The unit cells used for the structural refinements were taken from high resolution powder diffraction measurements of the same compounds performed on the HRPD instrument at the ISIS Neutron and Muon Facility in Harwell (UK). The initial structural models used for the refinement were based on the atomic coordinates of the thiocyanate core from the X-ray measurement of the Th compound, while the atoms in the tetraethylammonium counterions were located by Fourier difference maps. Both structures were refined by full matrix least squares on F^2 using SHELXL,[9] with anisotropic displacement parameters only for the thiocyanate core. The tetraethylammonium groups showed positional disorder due to the 4-fold symmetry of the nitrogen site that was modelled with splitted atomic positions of the first carbon of the ethyl chain, while the rotational disorder of the terminal methyl group, which was

visible in the Fourier difference maps, was taken into account with a riding refinement of the hydrogen atoms, which resulted in slightly increased isotropic thermal parameters.

Crystal data and structure refinement for [Na(2.2.2-cryptand)][Na(H_2O)($NCS)_2$], [H_2(2.2.2-cryptand)]$_2$[U($NCS)_8$] and [$Me_4N]_4$[U($NCS)_8$].

Compound	[Na(2.2.2-cryptand)][Na(H_2O)($NCS)_2$]	[H_2(2.2.2-cryptand)]$_2$[U($NCS)_8$]	[$Me_4N]_4$[U($NCS)_8$]·CH_3CN
Empirical formula	$C_{20}H_{38}N_4Na_2O_7S_2$	$C_{48}H_{82}N_{14}O_{12}S_8U$	$C_{26}H_{51}N_{13}S_8U$
Formula weight	556.64	1541.78	1040.30
Temperature	100(2) K	100(2) K	100(2) K
Wavelength	0.71073 Å	0.71073 Å	0.71073 Å
Crystal system	Monoclinic	Monoclinic	Monoclinic
Space group	$P2_1/n$	C2/c	$P2_1/c$
Unit cell dimensions	a = 12.5648(4) Å α = 90°. b = 10.3498(3) Å β = 102.8369(13)°. c = 21.5344(7) Å γ = 90°.	a = 23.3788(13) Å α = 90°. b = 13.3839(8) Å β = 117.9024(14)°. c = 24.5668(15) Å γ = 90°.	a = 24.5670(11) Å α = 90° b = 18.8842(8) Å β = 112.9257(12)° c = 21.6872(9) Å γ = 90°
Volume	2730.41(15) $Å^3$	6793.3(7) $Å^3$	9266.6(7) $Å^3$
Z	4	4	8
Density (calculated)	1.354 Mg/m^3	1.507 Mg/m^3	1.491 Mg/m^3
Absorption coefficient	0.272 mm^{-1}	2.698 mm^{-1}	3.897 mm^{-1}
F(000)	1184	3136	4144
Crystal size	0.23 x 0.15 x 0.1 mm^3	0.13 x 0.1 x 0.08 mm^3	0.18 x 0.17 x 0.14 mm^3
Theta range for data collection	2.880 to 26.486°.	2.243 to 25.248°.	2.530 to 26.498°
Index ranges	-15≤h≤15, -12≤k≤12, -27≤l≤26	-27≤h≤28, -16≤k≤16, -29≤l≤29	-30≤h≤30, -23≤k≤23, -26≤l≤26
Reflections collected	36968	60883	129562
Independent reflections	5610 [R(int) = 0.0475]	6145 [R(int) = 0.0671]	19114 [R(int) = 0.0551]
Completeness to theta = 26.000°	99.9 %	99.9 %	99.9 %
Absorption correction	Semi-empirical from equivalents	Semi-empirical from equivalents	Semi-empirical from equivalents
Max. and min. transmission	0.7454 and 0.6858	0.2598 and 0.2292	0.7454 and 0.6874
Refinement method	Full-matrix least-squares on F^2	Full-matrix least-squares on F^2	Full-matrix least-squares on F^2
Data / restraints / parameters	5610 / 138 / 436	6145 / 1048 / 749	19114 / 152 / 980
Goodness-of-fit on F^2	2.880 to 26.486°.	1.084	1.031
Final R indices [I>2σ(I)]	-15≤h≤15, -12≤k≤12, -27≤l≤26	R1 = 0.0964, wR2 = 0.2575	R1 = 0.0416, wR2 = 0.0878
R indices (all data)	36968	R1 = 0.1137, wR2 = 0.2846	R1 = 0.0630, wR2 = 0.0992
Largest diff. peak and hole	0.817 and -0.762 e.$Å^{-3}$	2.827 and -1.920 e.$Å^{-3}$	2.161 and -1.588 e.$Å^{-3}$

Crystal data and structure refinement for Ph_3CNCS, $[Me_4N]_4[Th(NCS)_8]\cdot CH_3CN$ and $[^nPr_4N]_4[U(NCS)_8]$.

Compound	Ph_3CNCS	$[Me_4N]_4[Th(NCS)_8]\cdot CH_3CN$	$[^nPr_4N]_4[U(NCS)_8]\cdot 2CH_2Cl_2$
Empirical formula	$C_{20}H_{15}NS$	$C_{26}H_{51}N_{13}S_8Th$	$C_{58}H_{116}Cl_4N_{12}S_8U$
Formula weight	$C_{20}H_{15}NS$	1034.31	1617.93
Temperature	301.39	100(2) K	100(2) K
Wavelength	100(2) K	0.71073 Å	0.71073 Å
Crystal system	0.71073 Å	Monoclinic	Monoclinic
Space group	Monoclinic	$P2_1/c$	C2
Unit cell dimensions	a = 9.1543(8) Å α = 90°. b = 17.5141(16) Å β = 106.852(2)°. c = 10.2105(9) Å γ = 90°.	a = 24.6776(11) Å α = 90° b = 18.9100(9) Å β = 112.9332(14)° c = 21.7193(9) Å γ = 90°	a = 20.2216(7) Å α = 90° b = 16.3196(6) Å β = 114.7570(10)° c = 13.2959(5) Å γ = 90°
Volume	1566.7(2) $Å^3$	9334.3(7) $Å^3$	3984.5(3) $Å^3$
Z	4	8	2
Density (calculated)	1.278 Mg/m^3	1.472 Mg/m^3	1.349 Mg/m^3
Absorption coefficient	0.202 mm^{-1}	3.586 mm^{-1}	2.422 mm^{-1}
F(000)	632	4128	1672
Crystal size	0.170 x 0.100 x 0.090 mm^3	0.13 x 0.12 x 0.07 mm^3	0.150 x 0.080 x 0.080 mm^3
Theta range for data collection	2.326 to 25.750°.	2.333 to 26.542°.	1.669 to 29.173°
Index ranges	-9≤h≤11, -21≤k≤21, -12≤l≤12	-30≤h≤31, -23≤k≤23, -27≤l≤26	-27≤h≤27, -22≤k≤22, -18≤l≤18
Reflections collected	33451	211541	79063
Independent reflections	2992 [R(int) = 0.0605]	19320 [R(int) = 0.0969]	10649 [R(int) = 0.0409]
Completeness to theta = 26.000°	100.0 %	99.9 %	100.0 %
Absorption correction	Numerical	Semi-empirical from equivalents	Semi-empirical from equivalents
Max. and min. transmission	0.9925 and 0.8135	0.7243 and 0.6203	0.4947 and 0.4229
Refinement method	Full-matrix least-squares on F^2	Full-matrix least-squares on F^2	Full-matrix least-squares on F^2
Data / restraints / parameters	2992 / 0 / 199	19320 / 431 / 1121	10649 / 1 / 386
Goodness-of-fit on F^2	1.031	1.036	1.016
Final R indices [I>2σ(I)]	R1 = 0.0375, wR2 = 0.0871	R1 = 0.0526, wR2 = 0.0988	R1 = 0.0182, wR2 = 0.0361
R indices (all data)	R1 = 0.0551, wR2 = 0.0943	R1 = 0.0867, wR2 = 0.1165	R1 = 0.0188, wR2 = 0.0362
Largest diff. peak and hole	0.240 and -0.293 $e.Å^{-3}$	2.577 and -1.920 $e.Å^{-3}$	0.920 and -0.813 $e.Å^{-3}$

Crystal data and structure refinement for $[Me_4N]_4[Th(NCS)_8(H_2O)]$, $[^nPr_4N]_4[Th(NCS)_8]$ and $[Me_4N]_4[Th(NCS)_7(NO_3)]\cdot 2CH_3CN$.

Compound	$[Me_4N]_4[Th(NCS)_8(H_2O)]$	$[^nPr_4N]_4[Th(NCS)_8]$	$[Me_4N]_4[Th(NCS)_7(NO_3)]\cdot 2CH_3CN$
Empirical formula	$C_{24}H_{50}N_{12}O_1S_8Th$	$C_{56}H_{112}N_{12}S_8Th$	$C_{27}H_{54}N_{14}O_3S_7Th$
Formula weight	958.18	1442.09	1079.30
Temperature	100(2) K	100(2) K	99.98 K
Wavelength	0.71073 Å	0.71073 Å	0.71073 Å
Crystal system	Monoclinic	Monoclinic	Monoclinic
Space group	C2/c	$P2_1/n$	$P2_1/n$
Unit cell dimensions	a = 18.4717(5) Å α = 90° b = 18.0031(5) Å β = 99.1900(10)° c = 24.6384(7) Å γ = 90°	a = 19.5075(11) Å α = 90° b = 16.5441(8) Å β = 97.0069(17) c = 23.1161(12) Å γ = 90°	a = 14.3721(4) Å α = 90°. b = 21.8074(6) Å β = 90.2733(11)°. c = 15.1495(4) Å γ = 90°.
Volume	8088.3(4) $Å^3$	7404.6(7) $Å^3$	4748.1(2) $Å^3$
Z	8	4	4
Density (calculated)	1.574 Mg/m^3	1.294 Mg/m^3	1.510 Mg/m^3
Absorption coefficient	4.113 mm^{-1}	2.280 mm^{-1}	3.491 mm^{-1}
F(000)	3799	3000	2160
Crystal size	0.28 x 0.12 x 0.11 mm^3	0.25 x 0.16 x 0.13 mm^3	0.34 x 0.17 x 0.13 mm^3
Theta range for data collection	2.815 to 27.499°.	2.160 to 26.533°.	2.700 to 27.498°.
Index ranges	-23≤h≤24, -23≤k≤23, -32≤l≤32	-24≤h≤24, -20≤k≤20, -28≤l≤28	-18≤h≤18, -28≤k≤28, -18≤l≤19
Reflections collected	175580	129981	69598
Independent reflections	9284 [R(int) = 0.0458]	15324 [R(int) = 0.0927]	10890 [R(int) = 0.0318]
Completeness to theta = 26.000°	99.9 %	99.9 %	99.9 %
Absorption correction	Semi-empirical from equivalents	Semi-empirical from equivalents	Semi-empirical from equivalents
Max. and min. transmission	0.7461 and 0.5271	0.7454 and 0.6369	0.7462 and 0.5979
Refinement method	Full-matrix least-squares on F^2	Full-matrix least-squares on F^2	Full-matrix least-squares on F^2
Data / restraints / parameters	9284 / 81 / 422	15324 / 303 / 983	10890 / 0 / 487
Goodness-of-fit on F^2	1.089	1.075	1.049
Final R indices [I>2σ(I)]	R1 = 0.0265, wR2 = 0.0564	R1 = 0.0413, wR2 = 0.0691	R1 = 0.0192, wR2 = 0.0387
R indices (all data)	R1 = 0.0336, wR2 = 0.0598	R1 = 0.0775, wR2 = 0.0843	R1 = 0.0256, wR2 = 0.0410
Largest diff. peak and hole	2.444 and -1.422 $e.Å^{-3}$	1.822 and -1.482 $e.Å^{-3}$	1.877 and -1.331 $e.Å^{-3}$

Crystal data and structure refinement for $[Me_4N]_4[Th(NCS)_6(NO_3)_2]$, $[Et_4N][UO_2(NO_3)_3]$ and $[Et_4N]_4[U(NCSe)_8]$.

Compound	$[Me_4N]_4[Th(NCS)_6(NO_3)_2]\cdot 2\,CH_3CN$	$[Et_4N][UO_2(NO_3)_3]$	$[Et_4N]_4[U(NCSe)_8]$
Empirical formula	$C_{26.95}H_{54}N_{14}O_{3.15}S_{6.95}Th$	$C_8H_{20}N_4O_{11}U$	$C_{40}H_{80}N_{12}Se_8U$
Formula weight	1079.50	586.31	1598.87
Temperature	100(2) K	296.15 K	100.01 K
Wavelength	0.71073 Å	0.71073 Å	0.71073 Å
Crystal system	Monoclinic	Orthorhombic	Tetragonal
Space group	$P2_1/n$	$Pna2_1$	I4/m
Unit cell dimensions	a = 14.3596(6) Å α = 90°. b = 21.8122(9) Å β = 90.2647(14)°. c = 15.1654(7) Å γ = 90°.	a = 16.0843(14) Å α = 90° b = 10.1067(9) Å β = 90° c = 11.1346(10) Å γ = 90°	a = 11.6968(5) Å α = 90° b = 11.6968(5) Å β = 90° c = 23.2018(9) Å γ = 90°
Volume	4750.0(4) $Å^3$	1810.0(3) $Å^3$	3174.4(3) $Å^3$
Z	4	4	2
Density (calculated)	1.510 Mg/m^3	2.152 Mg/m^3	1.673 Mg/m^3
Absorption coefficient	3.488 mm^{-1}	9.025 mm^{-1}	7.178 mm^{-1}
F(000)	2160	1104	1536
Crystal size	0.26 x 0.14 x 0.11 mm^3	0.16 x 0.12 x 0.1 mm^3	0.22 x 0.08 x 0.06 mm^3
Theta range for data collection	2.686 to 28.453°.	2.380 to 27.580°	1.755 to 30.070°.
Index ranges	-19≤h≤19, -29≤k≤29, -16≤l≤20	-20≤h≤13, -12≤k≤13, -14≤l≤14	-16≤h≤16, -15≤k≤16, -32≤l≤32
Reflections collected	91088	15404	18676
Independent reflections	11919 [R(int) = 0.0701]	4183 [R(int) = 0.0391]	2397 [R(int) = 0.0445]
Completeness to theta = 26.000°	99.8 %	100.0 %	100.0 %
Absorption correction	Semi-empirical from equivalents	Semi-empirical from equivalents	Semi-empirical from equivalents
Max. and min. transmission	0.7457 and 0.6315	0.7456 and 0.6332	0.7460 and 0.5096
Refinement method	Full-matrix least-squares on F^2	Full-matrix least-squares on F^2	Full-matrix least-squares on F^2
Data / restraints / parameters	11919 / 6 / 496	4183 / 7 / 222	2397 / 12 / 107
Goodness-of-fit on F^2	1.022	0.931	1.093
Final R indices [I>2σ(I)]	R1 = 0.0267, wR2 = 0.0418	R1 = 0.0271, wR2 = 0.0450	R1 = 0.0289, wR2 = 0.0714
R indices (all data)	R1 = 0.0440, wR2 = 0.0455	R1 = 0.0521, wR2 = 0.0513	R1 = 0.0367, wR2 = 0.0744
Largest diff. peak and hole	0.856 and -0.788 $e.Å^{-3}$	0.010(12)	2.140 and -0.820 $e.Å^{-3}$

Appendix 2

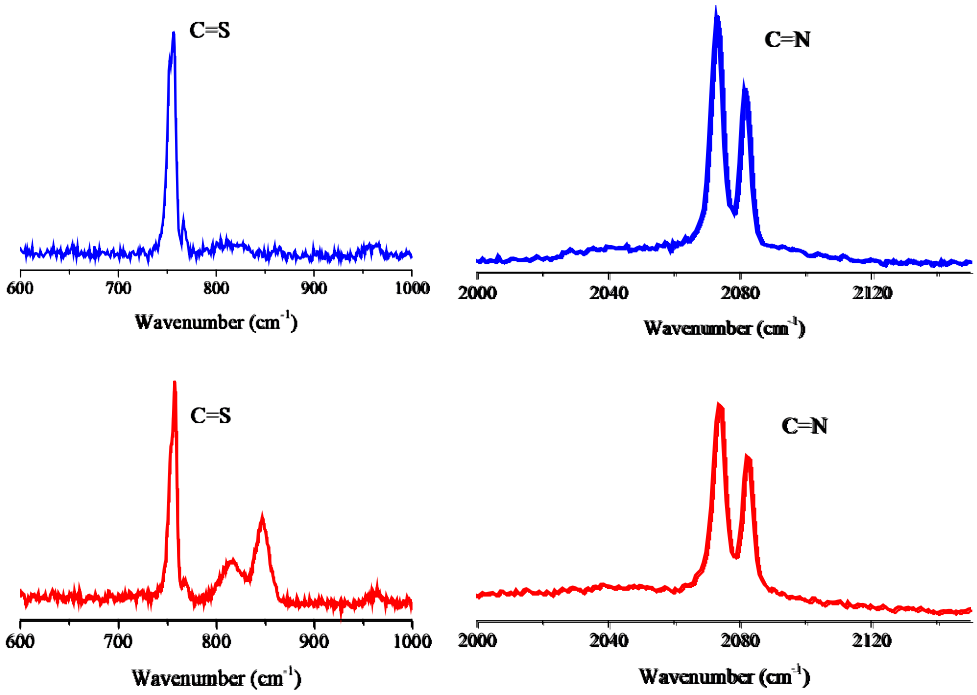

Figure 7.14. Raman spectra of **Co-Th** (blue) and **Co-U** (red) in solid-state, showing (left) the *ν*(C=S) and (right) the *ν*(C=N) Raman active stretches.

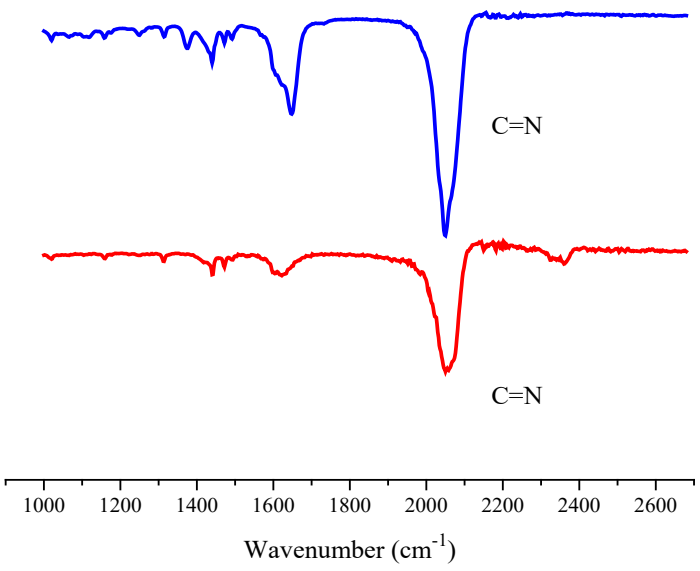

Figure 7.15. IR spectra of **Co-Th** (blue line) and **Co-U** (red line) displaying the *ν*(C=N) IR active stretch.

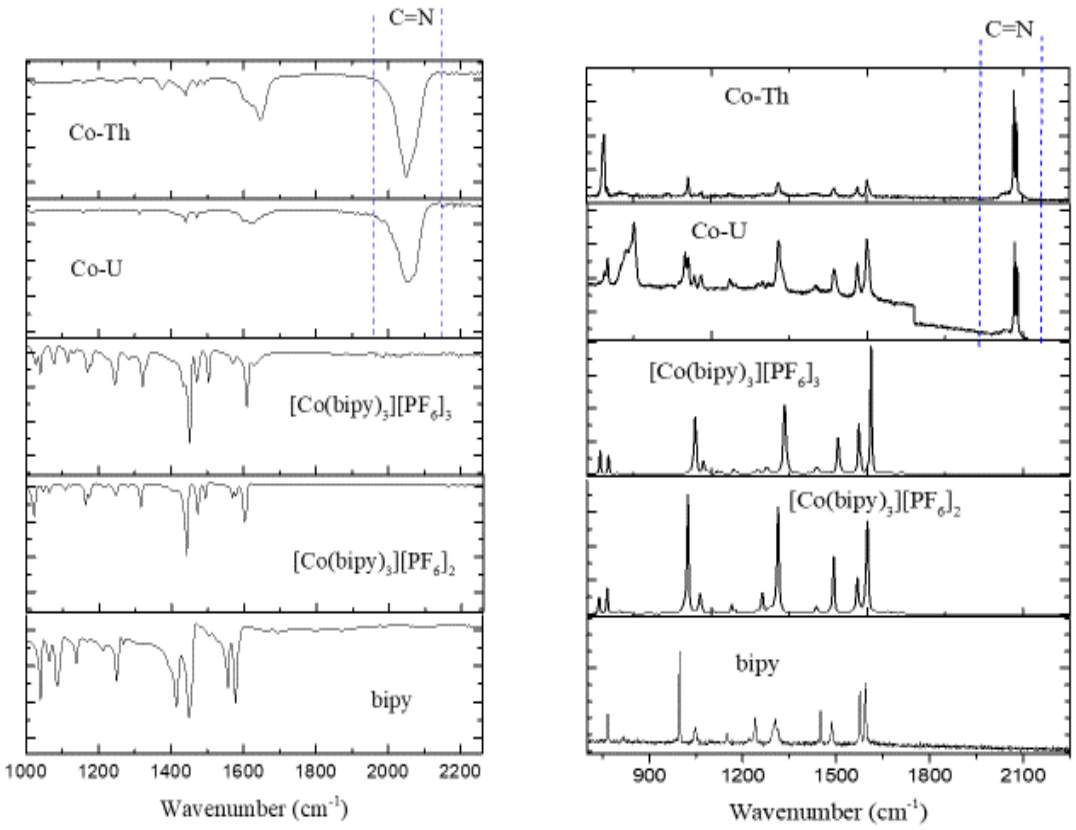

Figure 7.16. (Left) IR and (right) Raman spectra of **Co-Th**, **Co-U**, $[Co(bipy)_3][PF_6]_3$, $[Co(bipy)_3][PF_6]_2$ and bipy, measured in solid state.

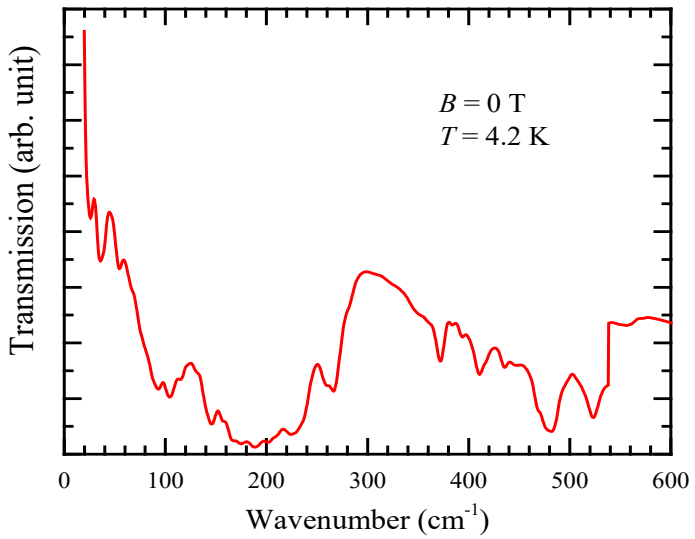

Figure 7.17. FIR spectra of $[Cs_5U(NCS)_9(NCS)]$, dispersed in eicosane, with $B = 0$ T and at $T = 4.2$ K.

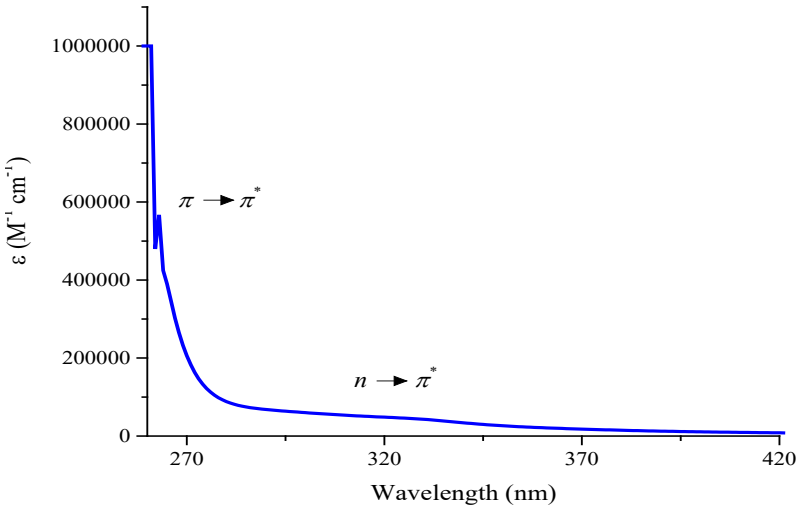

Figure 7.18. UV-vis absorption spectrum of $Cs_5[Th(NCS)_9][NCS]$ (2.1 x 10^{-6} M) in MeCN.

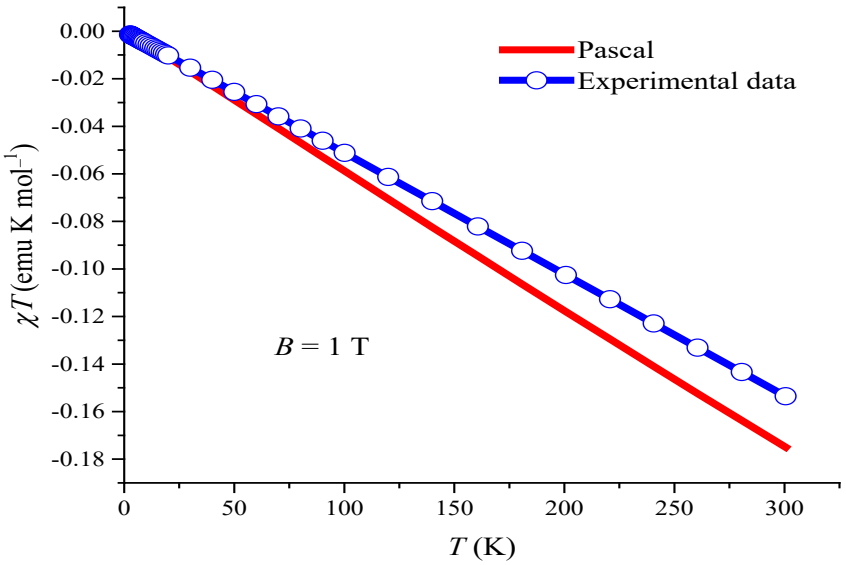

Figure 7.19. Magnetic susceptibility measurements for $Cs_5[Th(NCS)_9][NCS]$, collected at B = 1T and plotted as χT *vs* *T*. Calculated Pascal diamagnetism (red line) is in good agreement with the experimental data (dotted blue line).

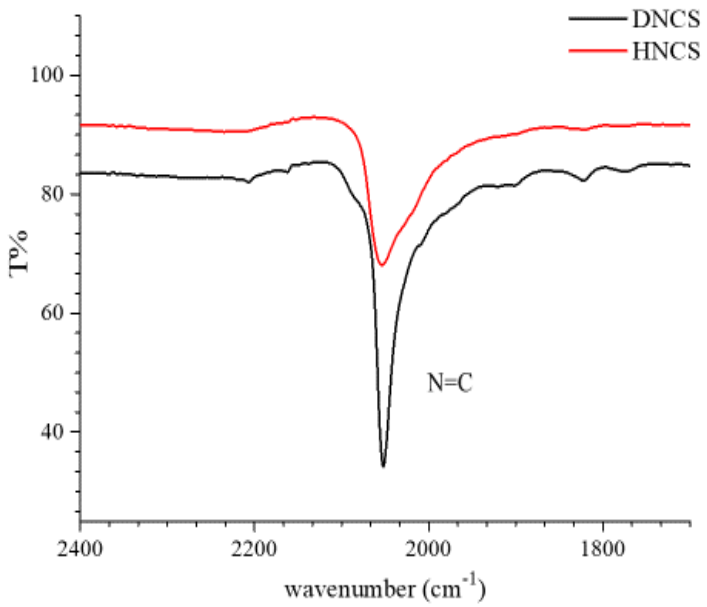

Figure 7.20. IR spectra of [Ph_4P][NCS][HNCS] (red line) and [Ph_4P][NCS][DNCS] (black line) showing the region with the *ν*(N=C) stretch.

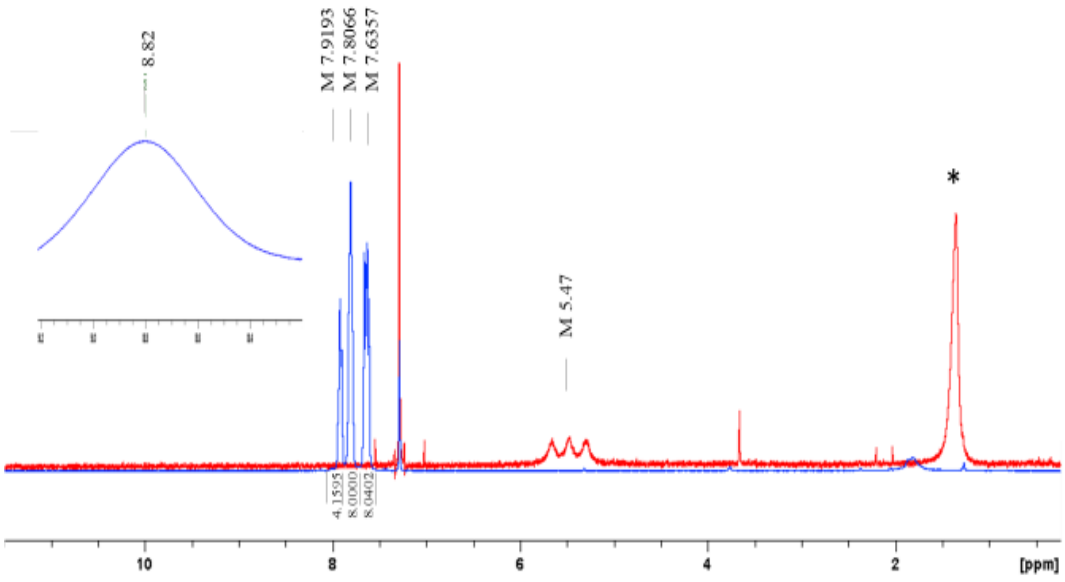

Figure 7.21. (Blue line) ^{1}H NMR spectrum of [Ph_4P][NCS][HNCS] in $CDCl_3$; insert shows the [HNCS] resonance at 8.82 ppm. (Red line) ^{1}H NMR spectrum of $[HNCS]_{(g)}$ dissolved in $CDCl_3$ (* indicates water).

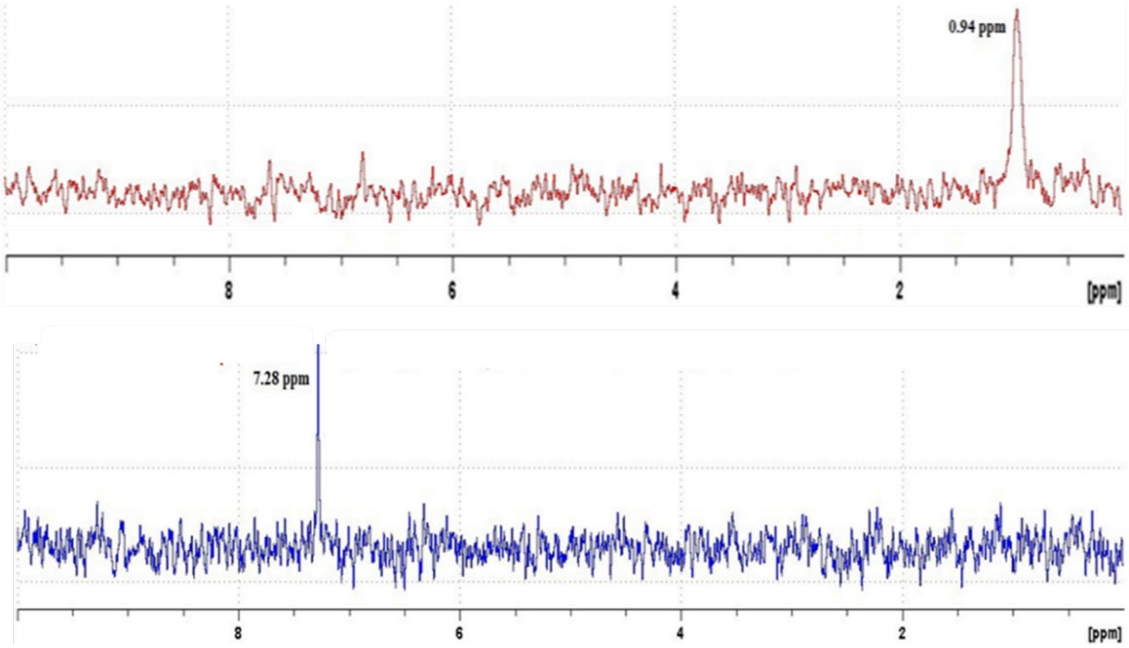

Figure 7.22. (Top) ^{2}H NMR spectrum of [DNCS] in $CHCl_3$. (Bottom) ^{2}H NMR spectrum of $[Ph_4P][NCS][DNCS]$ in $CHCl_3$.

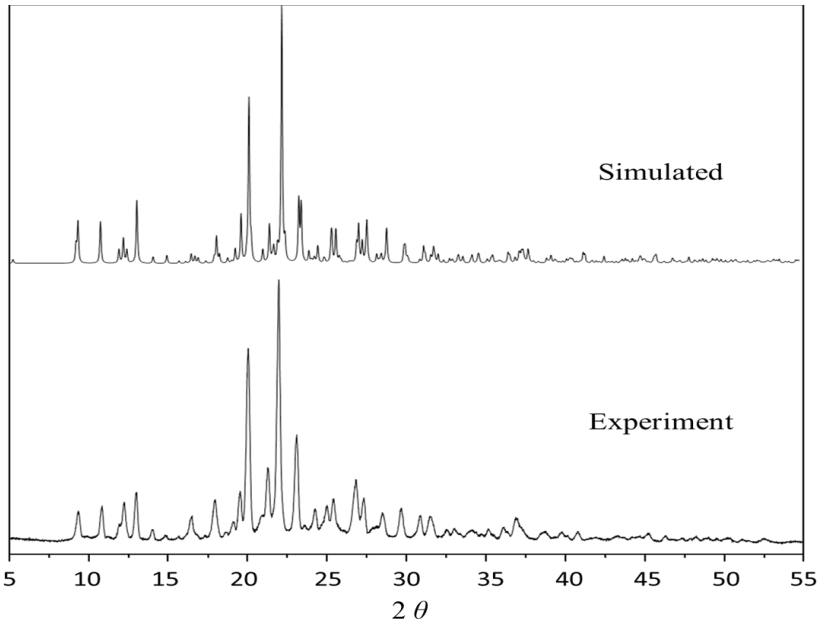

Figure 7.23. Experimental (bottom) and simulated (up) powder X-ray diffraction pattern of $[Ph_4P][NCS][HNCS]$.

Crystal data and structure refinement for **U-DMF**, **U-MeCN** and **Co-U**.

Compound	**U-DMF**	**U-MeCN**	**Co-U**
Empirical formula	$C_{56}H_{105}N_{26}O_{19}S_{11}U_4$	$C_{112}H_{38}Cs_{56}N_{112}O_{27}S_{112}U_{16}$	$C_{88}H_{59}Co_2N_{31}S_{16}U_2$
Formula weight	2751.43	18226.70	2657.54
Temperature	100(2) K	100(2) K	100(2) K
Wavelength	0.71073 Å	0.71073 Å	0.71073 Å
Crystal system	Monoclinic	Orthorhombic	Triclinic
Space group	$P2_1/n$	$Pna2_1$	$P\bar{1}$
Unit cell dimensions	a = 16.7660(7) Å α = 90° b = 13.2785(6) Å β = 94.9093(14)° c = 44.239(2) Å γ = 90°	a = 27.5717(9) Å α = 90° b = 27.5456(8) Å β = 90° c = 13.5609(5) Å γ = 90°	a = 13.0521(6) Å α = 94.4338(16)°. b = 19.9142(8) Å β = 102.7497(15)°. c = 22.4916(9) Å γ = 104.6416(17)°
Volume	9812.7(7) $Å^3$	10299.2(6) $Å^3$	5461.6(4) $Å^3$
Z	4	1	2
Density (calculated)	1.862 Mg/m^3	2.939 Mg/m^3	1.616 Mg/m^3
Absorption coefficient	6.884 mm^{-1}	11.764 mm^{-1}	3.618 mm^{-1}
F(000)	5276	8054	2596
Crystal size	0.19 x 0.18 x 0.12 mm^3	0.317 x 0.048 x 0.045 mm^3	0.39 x 0.03 x 0.03 mm^3
Theta range for data collection	2.067 to 26.526°.	2.336 to 26.126°.	2.023 to 25.857°.
Index ranges	$-16\leq h\leq 21$, $-16\leq k\leq 16$, $-55\leq l\leq 55$	$-34\leq h\leq 34$, $-34\leq k\leq 34$, $-16\leq l\leq 16$	$-14\leq h\leq 16$, $-24\leq k\leq 24$, $-27\leq l\leq 27$
Reflections collected	124715	169315	67259
Independent reflections	20281 [R(int) = 0.0468]	20437 [R(int) = 0.0543]	21025 [R(int) = 0.1267]
Completeness to theta = 26.000°	99.7 %	99.8 %	99.9 %
Absorption correction	Semi-empirical from equivalents	Semi-empirical from equivalents	Semi-empirical from equivalents
Max. and min. transmission	0.2602 and 0.1626	0.7453 and 0.1322	0.2602 and 0.1626
Refinement method	Full-matrix least-squares on F^2	Full-matrix least-squares on F^2	Full-matrix least-squares on F^2
Data / restraints / parameters	20281 / 0 / 1075	20437 / 51 / 1007	21025 / 901 / 1587
Goodness-of-fit on F^2	1.229	1.121	0.986
Final R indices [$I>2\sigma(I)$]	R1 = 0.0423, wR2 = 0.0893	R1 = 0.0290, wR2 = 0.0558	R1 = 0.0634, wR2 = 0.1069
R indices (all data)	R1 = 0.0505, wR2 = 0.0920	R1 = 0.0364, wR2 = 0.0589	R1 = 0.1501, wR2 = 0.1337
Largest diff. peak and hole	2.264 and -2.124 $e.Å^{-3}$	2.413 and -2.373 $e.Å^{-3}$	1.580 and -1.375 $e.Å^{-3}$

Crystal data and structure refinement for **Co-Th**, $[Co(bipy)_3][PF_6]_3$ and $[Na(H_2O)_4]_2[Co(NCS)_4]$

Compound	**Co-Th**	$[Na(H_2O)_4]_2[Co(NCS)_4]$	$[Co(bipy)_3][PF_6]_3 \cdot MeCN$
Empirical formula	$C_{87}H_{67}Co_2N_{30}O_{3.50}S_{15}Th_2$	$C_4H_{16}CoN_4Na_2O_8S_4$	$C_{32.17}H_{27.25}CoF_{18}N_{7.08}P_3$
Formula weight	2651.54	481.36	1006.87
Temperature	100(2) K	100(2) K	100(2) K
Wavelength	0.71073 Å	1.54178 Å	0.71073 Å
Crystal system	Triclinic	Monoclinic	Trigonal
Space group	$P\bar{1}$	$P2_1/n$	R3c
Unit cell dimensions	a = 12.620(4) Å α = 80.130(9)°. b = 17.505(4) Å β = 80.165(7)°. c = 24.000(7) Å γ = 83.345(7)°	a = 5.4063(4) Å α = 90° b = 19.1798(14) Å β = 91.501(5)°. c = 18.7722(13) Å γ = 90°.	a = 31.0315(11) Å α = 90° b = 31.0315(11) Å β = 90°. c = 21.0809(8) Å γ = 120°.
Volume	5126(2) $Å^3$	1945.9(2) $Å^3$	17580.3(14) $Å^3$
Z	2	4	18
Density (calculated)	1.718 Mg/m^3	1.643 Mg/m^3	1.712 Mg/m^3
Absorption coefficient	3.579 mm^{-1}	11.728 mm^{-1}	0.685 mm^{-1}
F(000)	2602	980	9069
Crystal size	0.12 x 0.11 x 0.09 mm^3	0.35 x 0.03 x 0.03 mm^3	0.27 x 0.19 x 0.15 mm^3
Theta range for data collection	2.575 to 25.859°.	3.295 to 70.149°.	2.899 to 26.102°.
Index ranges	-15≤h≤15, -21≤k≤21, -29≤l≤29	-6≤h≤6, -23≤k≤22, -22≤l≤22	-38≤h≤30, -36≤k≤38, -26≤l≤26
Reflections collected	66629	16300	38327
Independent reflections	19635 [R(int) = 0.1294]	3659 [R(int) = 0.0834]	7740 [R(int) = 0.0381]
Completeness to theta = 26.000°	99.8 %	99.8 %	99.8 %
Absorption correction	Semi-empirical from equivalents	Semi-empirical from equivalents	Semi-empirical from equivalents
Max. and min. transmission	0.7453 and 0.6743	0.7533 and 0.4103	0.7453 and 0.6649
Refinement method	Full-matrix least-squares on F^2	Full-matrix least-squares on F^2	Full-matrix least-squares on F^2
Data / restraints / parameters	19635 / 746 / 1474	3659 / 0 / 216	7740 / 298 / 620
Goodness-of-fit on F^2	1.009	1.055	1.062
Final R indices [I>2σ(I)]	R1 = 0.0692, wR2 = 0.1550	R1 = 0.0574, wR2 = 0.1541	R1 = 0.0521, wR2 = 0.1448
R indices (all data)	R1 = 0.1552, wR2 = 0.1973	R1 = 0.0716, wR2 = 0.1637	R1 = 0.0565, wR2 = 0.1484
Largest diff. peak and hole	1.893 and -1.272 $e.Å^{-3}$	0.566 and -0.498 $e.Å^{-3}$	0.014(5)

Crystal data and structure refinement for $[bipyH]_3[UO_2(NCS)_5][bipy]$, $[Co(bipy)_2(NCS)_2]$ and $Cs_5[U(NCS)_9][NCS]$.

Compound	$[bipyH]_3[UO_2(NCS)_5][bipy]$	$[Co(bipy)_2(NCS)_2]$	$Cs_5[U(NCS)_9][NCS]$
Empirical formula	$C_{35}H_{27}N_{11}O_2S_5U$	$C_{22}H_{16}CoN_6S_2$	$C_{10}Cs_5N_{10}S_{10}U$
Formula weight	1032.00	487.46	1483.38
Temperature	100(2) K	100(2) K	99.99 K
Wavelength	0.71073 Å	0.71073 Å	0.71073 Å
Crystal system	Monoclinic	ic	Monoclinic
Space group	P2/n	Pbca	$P2_1/c$
Unit cell dimensions	a = 11.444(2) Å α = 90° b = 11.877(2) Å β = 102.221(5)°. c = 15.088(2) Å Å γ = 90°	a = 15.8471(10) Å α = 90°. b = 15.7469(9) Å β = 90°. c = 16.6968(11) Å γ = 90°	a = 15.4437(4) Å α = 90°. b = 11.2764(3) Å β = 92.3462(13)°. c = 20.0016(6) Å γ = 90°.
Volume	2004.2(6) $Å^3$	4166.6(4) $Å^3$	3480.34(17) $Å^3$
Z	2	8	4
Density (calculated)	1.710 Mg/m^3	1.554 Mg/m^3	2.831 Mg/m^3
Absorption coefficient	4.357 mm^{-1}	1.047 mm^{-1}	10.439 mm^{-1}
F(000)	1004	1992	2628
Crystal size	0.12 x 0.07 x 0.06 mm^3	0.26 x 0.09 x 0.04 mm^3	0.2 x 0.13 x 0.11 mm^3
Theta range for data collection	2.763 to 25.498°.	2.758 to 27.540°.	2.724 to 27.608°.
Index ranges	-13≤h≤12, -14≤k≤8, -13≤l≤18	-20≤h≤20, -20≤k≤19, -21≤l≤21	-20≤h≤20, -14≤k≤14, -22≤l≤26
Reflections collected	6198	29781	32364
Independent reflections	3681 [R(int) = 0.0273]	4788 [R(int) = 0.0997]	8053 [R(int) = 0.0262]
Completeness to theta = 26.000°	98.7 %	99.9 %	99.9 %
Absorption correction	Semi-empirical from equivalents	Semi-empirical from equivalents	Semi-empirical from equivalents
Max. and min. transmission	0.7454 and 0.6083	0.7456 and 0.6196	0.2251 and 0.1507
Refinement method	Full-matrix least-squares on F^2	Full-matrix least-squares on F^2	Full-matrix least-squares on F^2
Data / restraints / parameters	3681 / 397 / 365	4788 / 0 / 280	8053 / 0 / 325
Goodness-of-fit on F^2	1.056	1.037	1.051
Final R indices [I>2σ(I)]	R1 = 0.0337, wR2 = 0.0755	R1 = 0.0419, wR2 = 0.0746	R1 = 0.0333, wR2 = 0.0784
R indices (all data)	R1 = 0.0418, wR2 = 0.0792	R1 = 0.0824, wR2 = 0.0883	R1 = 0.0413, wR2 = 0.0824
Largest diff. peak and hole	1.018 and -0.896 $e.Å^{-3}$	0.479 and -0.463 $e.Å^{-3}$	4.543 and -3.258 $e.Å^{-3}$

Crystal data and structure refinement for $Cs_5[Th(NCS)_9][NCS]$, $[Ph_4P][NCS][HNCS]$ and $[Ph_4P][NCSe]$.

Compound	$Cs_5[Th(NCS)_9][NCS]$	$[Ph_4P][NCS][HNCS]$	$[Ph_4P][NCSe]$
Empirical formula	$C_{10}Cs_5N_{10}S_{10}Th$	$C_{26}H_{21}N_2PS_2$	$C_{25}H_{20}NPSe$
Formula weight	1477.06	456.54	444.35
Temperature	99.99 K	100(2) K	100(2) K
Wavelength	0.71073 Å	0.71073 Å	0.71073 Å
Crystal system	Monoclinic	Monoclinic	Tetragonal
Space group	$P2_1/c$	$P2_1/c$	$P\bar{4}$
Unit cell dimensions	a = 15.5256(5) Å α = 90°. b = 11.3293(4) Å β = 92.459(2)°. c = 19.9661(7) Å γ = 90°.	a = 16.6614(5) Å α = 90°. b = 7.5194(2) Å β = 105.5766(11)°. c = 19.3601(6) Å γ = 90°.	a = 11.8142(5) Å α = 90°. b = 11.8142(5) Å β = 90°. c = 7.2500(3) Å γ = 90°.
Volume	3508.7(2) $Å^3$	2336.42(12) $Å^3$	1011.92(10) $Å^3$
Z	4	4	2
Density (calculated)	2.796 Mg/m^3	1.298 Mg/m^3	1.458 Mg/m^3
Absorption coefficient	9.976 mm^{-1}	0.312 mm^{-1}	1.945 mm^{-1}
F(000)	2619	952	452
Crystal size	0.18 x 0.15 x 0.12 mm^3	0.290 x 0.140 x 0.090 mm^3	0.3 x 0.17 x 0.13 mm^3
Theta range for data collection	2.721 to 29.443°.	2.184 to 27.636°.	2.810 to 27.148°.
Index ranges	$-21\leq h\leq 21$, $-15\leq k\leq 15$, $-27\leq l\leq 27$	$-21\leq h\leq 21$, $-9\leq k\leq 9$, $-25\leq l\leq 25$	$-14\leq h\leq 15$, $-15\leq k\leq 15$, $-9\leq l\leq 9$
Reflections collected	89763	108909	11023
Independent reflections	9656 [R(int) = 0.0376]	5414 [R(int) = 0.0473]	2231 [R(int) = 0.0276]
Completeness to theta = 26.000°	99.9 %	100.0 %	99.8 %
Absorption correction	Semi-empirical from equivalents	Semi-empirical from equivalents	Semi-empirical from equivalents
Max. and min. transmission	0.7458 and 0.5311	0.7456 and 0.7067	0.7455 and 0.6466
Refinement method	Full-matrix least-squares on F^2	Full-matrix least-squares on F^2	Full-matrix least-squares on F^2
Data / restraints / parameters	9656 / 1 / 334	5414 / 0 / 284	2231 / 0 / 129
Goodness-of-fit on F^2	1.070	1.025	1.061
Final R indices [$I>2\sigma(I)$]	R1 = 0.0310, wR2 = 0.0661	R1 = 0.0338, wR2 = 0.0813	R1 = 0.0200, wR2 = 0.0469
R indices (all data)	R1 = 0.0383, wR2 = 0.0690	R1 = 0.0491, wR2 = 0.0906	R1 = 0.0224, wR2 = 0.0480
Largest diff. peak and hole	1.531 and -2.546 $e.Å^{-3}$	0.386 and -0.379 $e.Å^{-3}$	0.194 and -0.354 $e.Å^{-3}$

Appendix 3

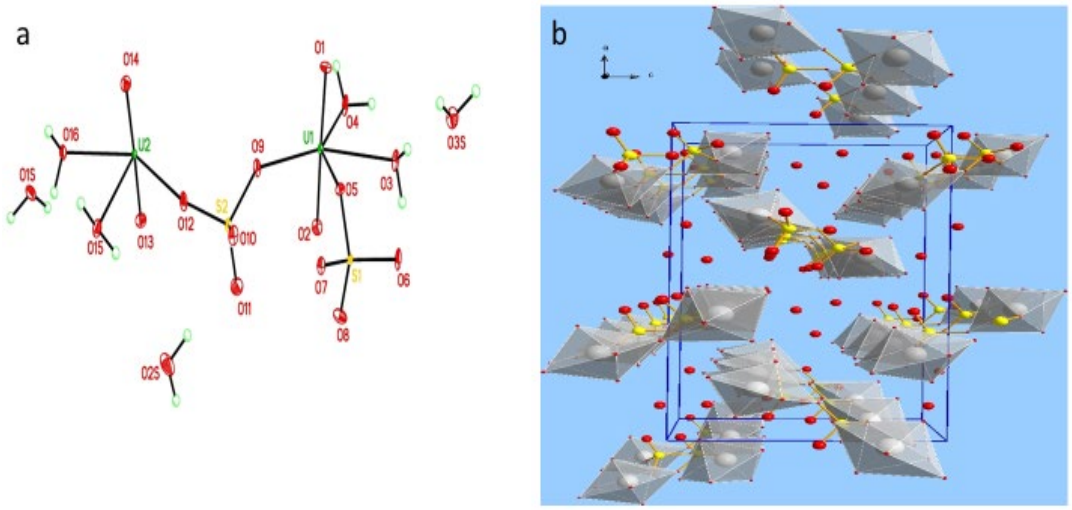

Figure 7.24. (a) Asymmetric unit of $[(UO_2)_2(SO_4)_2(H_2O)_4].3H_2O$, with atomic displacement parameters shown at 50% probability. (b) Packing diagram viewed down the crystallographic *b*-axis, with polyhedral centred on the U atom only and hydrogen atoms omitted for clarity.

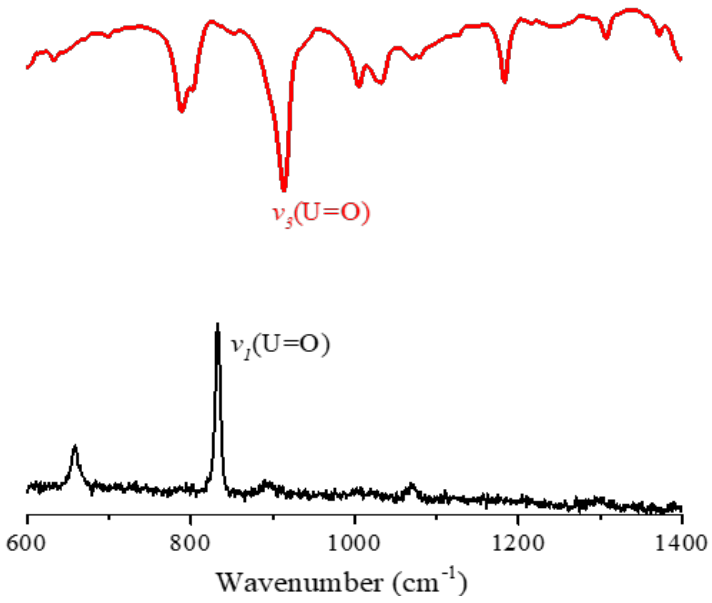

Figure 7.25. (Bottom) Raman and (up) IR spectra of $[Et_4N][UO_2Cl_4][CuCl_4]$, measured in solid state.

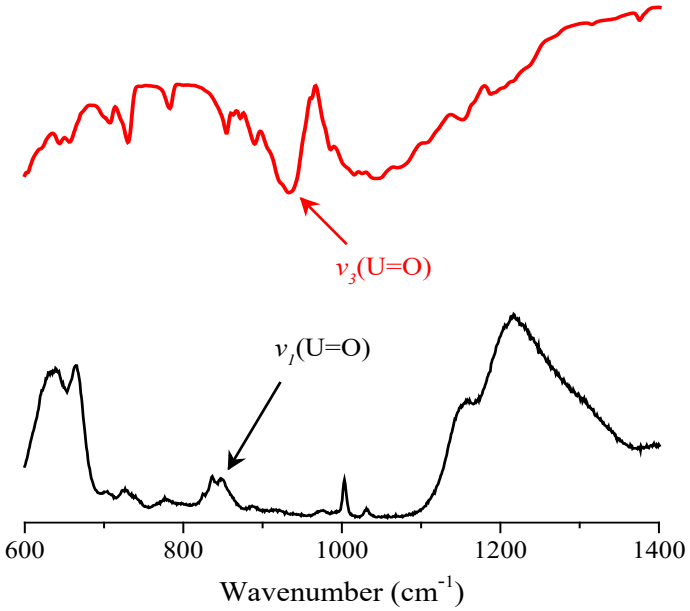

Figure 7.26. (Bottom) Raman and (up) IR spectra of $[Me_3NBz]_2[UO_2Cl_4]$.

Crystal data and structure refinement for $[^{n}Bu_4N]_3[UO_2(NCS)_5]$, $[Et_3NBz]_3[UO_2(NCS)_5]$ and $[Me_3NBz]_3[UO_2(NCS)_5]$

Compound	$[^{n}Bu_4N]_3[UO_2(NCS)_5]\cdot MeCN$	$[Et_3NBz]_3[UO_2(NCS)_5]$	$[Me_3NBz]_3[UO_2(NCS)_5]$
Empirical formula	$C_{55}H_{111}N_9O_2S_5U$	$C_{44}H_{66}N_8O_2S_5U$	$C_{35}H_{48}N_8O_2S_5U$
Formula weight	1328.85	1137.37	981.33
Temperature	100.0 K	100(2) K	100(2) K
Wavelength	0.71073 Å	0.71073 Å	0.71073 Å
Crystal system	Orthorhombic	Orthorhombic	triclinic
Space group	$Cmc2_1$	$P2_12_12_1$	$P\bar{1}$
Unit cell dimensions	a = 21.1287(7) Å α = 90°. b = 16.0301(5) Å β = 90°. c = 20.4548(6) Å γ = 90°.	a = 9.1688(3) Å α = 90°. b = 16.3362(5) Å β = 90°. c = 34.0546(10) Å γ = 90°.	a = 11.409(7) Å α = 119.154(10)° b = 14.977(7) Å β = 101.038(18)° c = 15.295(8) Å γ = 100.197(18)°
Volume	6927.9(4) $Å^3$	5100.8(3) $Å^3$	2126(2)
Z	4	4	2
Density (calculated)	1.274 Mg/m^3	1.481 Mg/m^3	2
Absorption coefficient	2.535 mm^{-1}	3.429 mm^{-1}	3.589 mm^{-1}
F(000)	2768	2296	2343
Crystal size	0.29 x 0.23 x 0.2 mm^3	0.202 x 0.175 x 0.144 mm^3	0.29 x 0.09 x 0.03 mm^3
Theta range for data collection	2.551 to 28.486°.	2.564 to 26.487°.	3.895 to 30.468°
Index ranges	-28≤h≤28, -21≤k≤21, -27≤l≤27	-11≤h≤11, -20≤k≤20, -42≤l≤42	-25≤h≤55, -76≤k≤19, -24≤l≤20
Reflections collected	104249	88554	72006
Independent reflections	8932 [R(int) = 0.0593]	10513 [R(int) = 0.0463]	7278 [R(int) = 0.0327]
Completeness to theta = 26.000°	99.9 %	99.8 %	99.9 %
Absorption correction	Semi-empirical from equivalents	Numerical	Semi-empirical from equivalents
Max. and min. transmission	0.7457 and 0.6651	0.9941 and 0.5583	0.7478 and 0.6445
Refinement method	Full-matrix least-squares on F^2	Full-matrix least-squares on F^2	Full-matrix least-squares on F^2
Data / restraints / parameters	8932 / 145 / 349	10513 / 0 / 550	7289 / 0 / 345
Goodness-of-fit on F^2	1.129	0.978	1.126
Final R indices [I>2σ(I)]	R1 = 0.0518, wR2 = 0.1162	R1 = 0.0174, wR2 = 0.0357	R1 = 0.0454, wR2 = 0.1344
R indices (all data)	R1 = 0.0670, wR2 = 0.1238	R1 = 0.0198, wR2 = 0.0364	R1 = 0.05653, wR2 = 0.1356
Largest diff. peak and hole	1.104 and -2.241 $e.Å^{-3}$	0.739 and -0.612 $e.Å^{-3}$	4.147 and -1.917 $e.Å^{-3}$

Crystal data and structure refinement for $[Me_3NBz]_3[UO_2(NCS)_5]$, $[(18\text{-}C\text{-}6)Na]_3[UO_2(NCS)_5]$ and $[(2.2.2\text{-}crypt)Na]_3[UO_2(NCS)_5]$

Compound	$[Me_3NBz]_3[UO_2(NCS)_5]$	$[(18\text{-}C\text{-}6)Na]_3[UO_2(NCS)_5]$	$[(2.2.2\text{-}crypt)Na]_3[UO_2(NCS)_5]$
Empirical formula	$C_{35}H_{48}N_8O_2S_5U$	$C_{82}H_{161}N_{10}Na_6O_{49.50}S_{10}U_2$	$C_{59}H_{108}N_{11}Na_3O_{20}S_5U$
Formula weight	981.33	3013.80	1758.86
Temperature	100(2) K	100(2) K	100(2) K
Wavelength	0.71073 Å	1.54178 Å	1.54178 Å
Crystal system	triclinic	Triclinic	Monoclinic
Space group	$P\bar{1}$	$P\bar{1}$	$P2_1/n$
Unit cell dimensions	a = 11.409(7) Å α = 119.154(10)° b = 14.977(7) Å β = 101.038(18)° c = 15.295(8) Å γ = 100.197(18)°	a = 10.733(2) Å α = 88.98(3)°. b = 23.783(5) Å β = 88.32(3)°. c = 25.859(5) Å γ = 88.90(3)°.	a = 14.332(3) Å α = 90°. b = 21.664(5) Å β = 102.370(8)°. c = 25.867(6) Å γ = 90°.
Volume	2126(2)	6596(2) $Å^3$	7845(3) $Å^3$
Z	2	2	4
Density (calculated)	2	1.517 Mg/m^3	1.489 Mg/m^3
Absorption coefficient	3.589 mm^{-1}	9.242 mm^{-1}	7.834 mm^{-1}
F(000)	2343	3058	3616
Crystal size	0.29 x 0.09 x 0.03 mm^3	0.17 x 0.07 x 0.05 mm^3	0.14 x 0.04 x 0.04 mm^3
Theta range for data collection	3.895 to 30.468°	1.709 to 68.997°.	2.687 to 68.322°.
Index ranges	-25≤h≤55, -76≤k≤19, -24≤l≤20	-12≤h≤12, -28≤k≤28, -2≤l≤31	-17≤h≤17, -26≤k≤26, -31≤l≤31
Reflections collected	72006	23895	83403
Independent reflections	7278 [R(int) = 0.0327]	23895 [R(int) = ?]	14371 [R(int) = 0.0872]
Completeness to theta = 26.000°	99.9 %	99.1 %	100.0 %
Absorption correction	Semi-empirical from equivalents	Semi-empirical from equivalents	Semi-empirical from equivalents
Max. and min. transmission	0.7478 and 0.6445	0.7531 and 0.4512	0.7531 and 0.5690
Refinement method	Full-matrix least-squares on F^2	Full-matrix least-squares on F^2	Full-matrix least-squares on F^2
Data / restraints / parameters	7289 / 0 / 345	23895 / 865 / 1522	14371 / 1380 / 1363
Goodness-of-fit on F^2	1.126	1.139	1.027
Final R indices [I>2σ(I)]	R1 = 0.0454, wR2 = 0.1344	R1 = 0.1477, wR2 = 0.3599	R1 = 0.0605, wR2 = 0.1655
R indices (all data)	R1 = 0.05653, wR2 = 0.1356	R1 = 0.1688, wR2 = 0.3725	R1 = 0.0790, wR2 = 0.1838
Largest diff. peak and hole	4.147 and -1.917 $e.Å^{-3}$	3.590 and -5.158 $e.Å^{-3}$	1.830 and -1.069 $e.Å^{-3}$

Crystal data and structure refinement for $[(2.2.2\text{-crypt})Na]_3[UO_2(NCS)_5]$, $[Ph_4P]_2[UO(NCS)_3(NO_3)_2]$ and $[Et_3NBz]_3[UO_2(NCSe)_5]$

Compound	$[(2.2.2\text{-crypt})Na]_3[UO_2(NCS)_5]$	$[Ph_4P]_2[UO(NCS)_3(NO_3)_2]$	$[Et_3NBz]_3[UO_2(NCSe)_5]$
Empirical formula	$C_{59}H_{108}N_{11}Na_3O_{20}S_5U$	$C_{51}H_{40}N_4O_5P_2S_3U$	$C_{44}H_{66}N_8O_2Se_5U$
Formula weight	1758.86	1185.02	1371.87
Temperature	100(2) K	99.99 K	100.02 K
Wavelength	1.54178 Å	0.71073 Å	0.71073 Å
Crystal system	Monoclinic	Monoclinic	Orthorhombic
Space group	$P2_1/n$	C2/c	$P2_12_12_1$
Unit cell dimensions	a = 14.332(3) Å α = 90°. b = 21.664(5) Å β = 102.370(8)°. c = 25.867(6) Å γ = 90°.	a = 25.2809(10) Å α = 90°. b = 14.1091(6) Å β = 129.534(2)°. c = 17.7231(7) Å γ = 90°.	a = 9.388(6) Å α = 90°. b = 16.318(10) Å β = 90° c = 34.35(2) Å γ = 90°.
Volume	7845(3) $Å^3$	4875.6(4) $Å^3$	5263(6) $Å^3$
Z	4	4	4
Density (calculated)	1.489 Mg/m^3	1.614 Mg/m^3	1.731 Mg/m^3
Absorption coefficient	7.834 mm^{-1}	3.574 mm^{-1}	6.584 mm^{-1}
F(000)	3616	2336	2656
Crystal size	0.14 x 0.04 x 0.04 mm^3	0.21 x 0.08 x 0.05 mm^3	0.18 x 0.08 x 0.05 mm^3
Theta range for data collection	2.687 to 68.322°.	2.845 to 30.218°.	2.566 to 26.820°.
Index ranges	$-17\leq h\leq 17$, $-26\leq k\leq 26$, $-31\leq l\leq 31$	$-35\leq h\leq 35$, $-19\leq k\leq 19$, $-24\leq l\leq 24$	$-11\leq h\leq 11$, $-20\leq k\leq 20$, $-43\leq l\leq 43$
Reflections collected	83403	70615	77755
Independent reflections	14371 [R(int) = 0.0872]	7201 [R(int) = 0.0487]	11221 [R(int) = 0.1189]
Completeness to theta = 26.000°	100.0 %	99.7 %	99.8 %
Absorption correction	Semi-empirical from equivalents	Semi-empirical from equivalents	Semi-empirical from equivalents
Max. and min. transmission	0.7531 and 0.5690	0.7460 and 0.6411	0.7454 and 0.6267
Refinement method	Full-matrix least-squares on F^2	Full-matrix least-squares on F^2	Full-matrix least-squares on F^2
Data / restraints / parameters	14371 / 1380 / 1363	7201 / 0 / 301	11221 / 6 / 550
Goodness-of-fit on F^2	1.027	1.126	1.032
Final R indices [$I>2\sigma(I)$]	R1 = 0.0605, wR2 = 0.1655	R1 = 0.0469, wR2 = 0.1264	R1 = 0.0403, wR2 = 0.0567
R indices (all data)	R1 = 0.0790, wR2 = 0.1838	R1 = 0.0583, wR2 = 0.1349	R1 = 0.0598, wR2 = 0.0610
Largest diff. peak and hole	1.830 and -1.069 $e.Å^{-3}$	4.107 and -1.917 $e.Å^{-3}$	0.770 and -1.029 $e.Å^{-3}$

Crystal data and structure refinement for $[Et_3NBz]_3[UO_2(NCSe)_5]$, and $[^nPr_4N]_3[UO_2(NCSe)_5]$.

Compound	$[Et_3NBz]_3[UO_2(NCSe)_5]$	$[^nPr_4N]_3[UO_2(NCSe)_5]$	$[Et_4N]_3[UO_2(NCSe)_5][NCSe]$
Empirical formula	$C_{44}H_{66}N_8O_2Se_5U$	$C_{41}H_{84}N_8O_2Se_5U$	$C_{38}H_{80}N_{10}O_2Se_6U$
Formula weight	1371.87	1353.99	1420.91
Temperature	100.02 K	99.99 K	100(2) K
Wavelength	0.71073 Å	0.71073 Å	0.71073 Å
Crystal system	Orthorhombic	Monoclinic	Triclinic
Space group	$P2_12_12_1$	$P2_1/n$	$P\bar{1}$
Unit cell dimensions	a = 9.388(6) Å α = 90°. b = 16.318(10) Å β = 90° c = 34.35(2) Å γ = 90°.	a = 10.7904(3) Å α = 90°. b = 19.4146(5) Å β = 98.7490(12)°. c = 27.0052(6) Å γ = 90°.	a = 13.7730(5) Å α = 91.2012(11)°. b = 15.1019(6) Å β = 114.1718(10)°. c = 15.2571(6) Å γ = 105.8632(10)°.
Volume	5263(6) $Å^3$	5591.5(2) $Å^3$	2752.84(19) $Å^3$
Z	4	4	2
Density (calculated)	1.731 Mg/m^3	1.608 Mg/m^3	1.714 Mg/m^3
Absorption coefficient	6.584 mm^{-1}	$^{-1}$	6.953 mm^{-1}
F(000)	2656	2656	1380
Crystal size	0.18 x 0.08 x 0.05 mm^3	0.25 x 0.2 x 0.17 mm^3	0.150 x 0.050 x 0.012 mm^3
Theta range for data collection	2.566 to 26.820°.	2.595 to 28.446°.	1.418 to 27.843°.
Index ranges	-11≤h≤11, -20≤k≤20, -43≤l≤43	-14≤h≤14, -26≤k≤23, -33≤l≤36	-18≤h≤17, -19≤k≤19, -17≤l≤20
Reflections collected	77755	67644	65715
Independent reflections	11221 [R(int) = 0.1189]	14033 [R(int) = 0.0494]	13054 [R(int) = 0.0449]
Completeness to theta = 26.000°	99.8 %	99.9 %	100.0 %
Absorption correction	Semi-empirical from equivalents	Semi-empirical from equivalents	Semi-empirical from equivalents
Max. and min. transmission	0.7454 and 0.6267	0.7457 and 0.5396	0.7456 and 0.5925
Refinement method	Full-matrix least-squares on F^2	Full-matrix least-squares on F^2	Full-matrix least-squares on F^2
Data / restraints / parameters	11221 / 6 / 550	14033 / 0 / 526	13054 / 38 / 640
Goodness-of-fit on F^2	1.032	1.028	1.008
Final R indices [I>2σ(I)]	R1 = 0.0403, wR2 = 0.0567	R1 = 0.0270, wR2 = 0.0439	R1 = 0.0271, wR2 = 0.0531
R indices (all data)	R1 = 0.0598, wR2 = 0.0610	R1 = 0.0412, wR2 = 0.0467	R1 = 0.0468, wR2 = 0.0584
Largest diff. peak and hole	0.770 and -1.029 $e.Å^{-3}$	0.912 and -0.737 $e.Å^{-3}$	1.430 and -1.206 $e.Å^{-3}$

Crystal data and structure refinement for $[Et_4N]_3[UO_2(NCSe)_5][NCSe]$ and $[Me_4N]_3[UO_2(NCSe)_5][H_2O]$.

Compound	$[Et_4N]_3[UO_2(NCSe)_5][NCSe]$	$[Me_4N]_3[UO_2(NCSe)_5][H_2O]$	$[Et_4N]_4[UO_2Cl_4][CuCl_4]$
Empirical formula	$C_{38}H_{80}N_{10}O_2Se_6U$	$C_{34}H_{73}N_{16}O_{4.50}Se_{10}U_2$	$C_{32}H_{80}Cl_8CuN_4O_2U$
Formula weight	1420.91	2043.74	1138.17
Temperature	100(2) K	99.97 K	100(2) K
Wavelength	0.71073 Å	0.71073 Å	0.71073 Å
Crystal system	Triclinic	Triclinic	Tetragonal
Space group	Pī	$P\bar{1}$	P4/n
Unit cell dimensions	a = 13.7730(5) Å α = 91.2012(11)°. b = 15.1019(6) Å β = 114.1718(10)°. c = 15.2571(6) Å γ = 105.8632(10)°.	a = 9.035(4) Å α = 94.87(3)°. b = 16.740(8) Å β = 97.711(19)°. c = 22.507(19) Å γ = 94.666(9)°.	a = 14.0062(3) Å α = 90°. b = 14.0062(3) Å β = 90°. c = 12.2740(3) Å γ = 90°.
Volume	2752.84(19) $Å^3$	3347(4) $Å^3$	2407.83(11) $Å^3$
Z	2	2	2
Density (calculated)	1.714 Mg/m^3	2.028 Mg/m^3	1.570 Mg/m^3
Absorption coefficient	6.953 mm^{-1}	10.315 mm^{-1}	4.275 mm^{-1}
F(000)	1380	1898	1146
Crystal size	0.150 x 0.050 x 0.012 mm^3	0.15 x 0.13 x 0.05 mm^3	0.2 x 0.16 x 0.08 mm^3
Theta range for data collection	1.418 to 27.843°.	2.453 to 25.499°.	2.206 to 27.471°.
Index ranges	-18≤h≤17, -19≤k≤19, -17≤l≤20	-11≤h≤11, -19≤k≤20, -27≤l≤27	-18≤h≤18, -18≤k≤18, -15≤l≤15
Reflections collected	65715	41039	44630
Independent reflections	13054 [R(int) = 0.0449]	12380 [R(int) = 0.0500]	2773 [R(int) = 0.0514]
Completeness to theta = 26.000°	100.0 %	99.5 %	99.9 %
Absorption correction	Semi-empirical from equivalents	Semi-empirical from equivalents	Semi-empirical from equivalents
Max. and min. transmission	0.7456 and 0.5925	0.7453 and 0.5681	0.7459 and 0.6002
Refinement method	Full-matrix least-squares on F^2	Full-matrix least-squares on F^2	Full-matrix least-squares on F^2
Data / restraints / parameters	13054 / 38 / 640	12380 / 54 / 632	2773 / 31 / 111
Goodness-of-fit on F^2	1.008	1.205	1.059
Final R indices [I>2σ(I)]	R1 = 0.0271, wR2 = 0.0531	R1 = 0.0441, wR2 = 0.0741	R1 = 0.0534, wR2 = 0.1414
R indices (all data)	R1 = 0.0468, wR2 = 0.0584	R1 = 0.0664, wR2 = 0.0786	R1 = 0.0548, wR2 = 0.1428
Largest diff. peak and hole	1.430 and -1.206 $e.Å^{-3}$	1.372 and -1.294 $e.Å^{-3}$	4.299 and -2.439 $e.Å^{-3}$

Crystal data and structure refinement for $[Et_4N]_4[UO_2Cl_4][CuCl_4]$ and $[Me_3NBz]_2[UO_2Cl_4]$.

Compound	$[Et_4N]_4[UO_2Cl_4][CuCl_4]$	$[Me_3NBz]_2[UO_2Cl_4]$
Empirical formula	$C_{32}H_{80}Cl_8CuN_4O_2U$	$C_{20}H_{32}Cl_4N_2O_2U$
Formula weight	1138.17	712.30
Temperature	100(2) K	100(2) K
Wavelength	0.71073 Å	0.71073 Å
Crystal system	Tetragonal	Triclinic
Space group	P4/n	$P\bar{1}$
Unit cell dimensions	a = 14.0062(3) Å α = 90°. b = 14.0062(3) Å β = 90°. c = 12.2740(3) Å γ = 90°.	a = 8.5670(5) Å α = 85.7675(16)°. b = 8.8818(5) Å β = 87.9567(16)°. c = 10.4958(6) Å γ = 62.6455(14)°.
Volume	2407.83(11) $Å^3$	707.39(7) $Å^3$
Z	2	1
Density (calculated)	1.570 Mg/m^3	1.672 Mg/m^3
Absorption coefficient	4.275 mm^{-1}	6.130 mm^{-1}
F(000)	1146	342
Crystal size	0.2 x 0.16 x 0.08 mm^3	0.35 x 0.15 x 0.07 mm^3
Theta range for data collection	2.206 to 27.471°.	2.741 to 27.669°.
Index ranges	-18≤h≤18, -18≤k≤18, -15≤l≤15	-11≤h≤11, -11≤k≤11, -13≤l≤13
Reflections collected	44630	13282
Independent reflections	2773 [R(int) = 0.0514]	3289 [R(int) = 0.0368]
Completeness to theta = 26.000°	99.9 %	99.6 %
Absorption correction	Semi-empirical from equivalents	Semi-empirical from equivalents
Max. and min. transmission	0.7459 and 0.6002	0.7456 and 0.4270
Refinement method	Full-matrix least-squares on F^2	Full-matrix least-squares on F^2
Data / restraints / parameters	2773 / 31 / 111	3289 / 103 / 259
Goodness-of-fit on F^2	1.059	1.130
Final R indices [I>2σ(I)]	R1 = 0.0534, wR2 = 0.1414	R1 = 0.0337, wR2 = 0.0876
R indices (all data)	R1 = 0.0548, wR2 = 0.1428	R1 = 0.0338, wR2 = 0.0876
Largest diff. peak and hole	4.299 and -2.439 $e.Å^{-3}$	2.020 and -1.501 $e.Å^{-3}$

Appendix 4

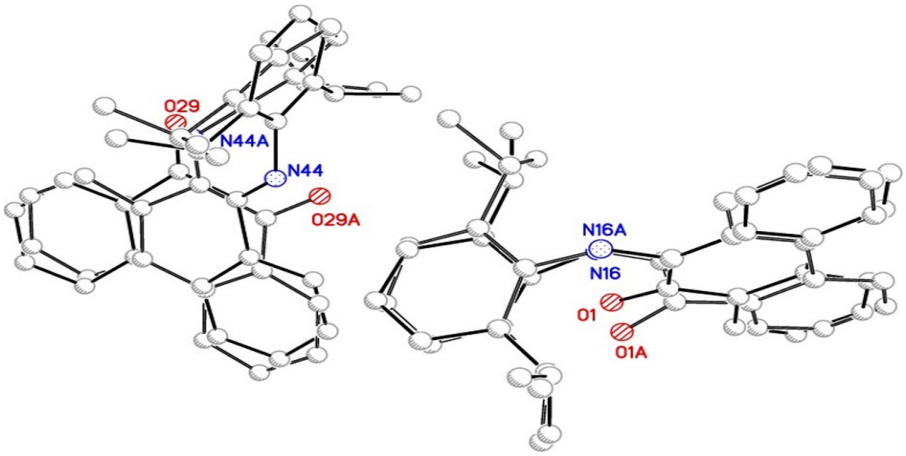

Figure 7.27. Molecular structure of **1**, showing the whole molecule disorder (60:40 and 52:48%). Only non-carbon atoms labelled and hydrogen atoms omitted for clarity. Atomic displacement shown at 50% probability.

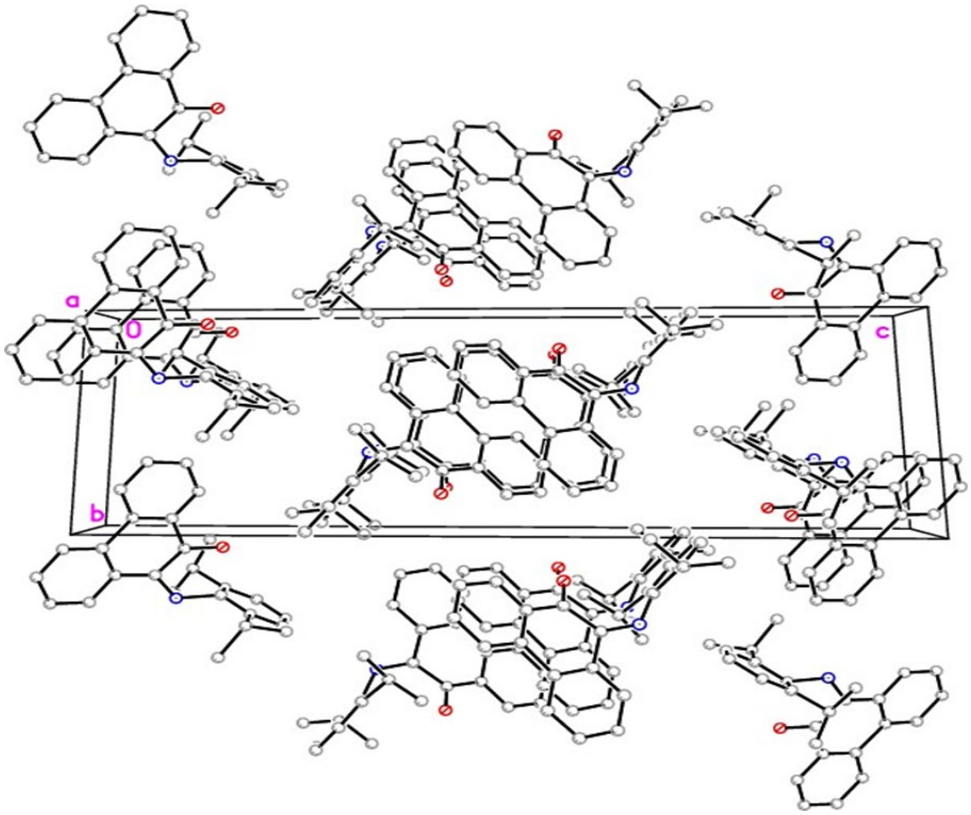

Figure 7.28. Packing diagram of major disordered moiety of **1**, viewed normal to the a-axis. Hydrogen atoms omitted for clarity.

Crystal data and structure refinement for 10-[(2,6-diisopropylphenyl)imino]phenanthren-9-one (**1**), 10-[(4-chloro-2,6-diisopropylphenyl)imino]phenanthren-9-one (**2**) and 10-[(4-bromo-2,6-diisopropylphenyl)imino]phenanthren-9-one (**3**).

Compound	10-[(2,6-diisopropylphenyl)imino]phenanthren-9-one (**1**)	10-[(4-chloro-2,6-diisopropylphenyl)imino]phenanthren-9-one (**2**)	10-[(4-bromo-2,6-diisopropylphenyl)imino]phenanthren-9-one (**3**)
Empirical formula	C26H25NO	$C_{26}H_{24}ClNO$	$C_{26}H_{24}BrNO$
Formula weight	367.47	401.91	446.37
Temperature	100(2) K	100(2) K	100(2) K
Wavelength	1.54178 Å	1.54178 Å	0.71073 Å
Crystal system	triclinic	Monoclinic	Monoclinic
Space group	$P1^{-}$	$P2_1/c$	$P2_1/c$
Unit cell dimensions	a = 12.8736(3) Å α = 86.914(4) ° b = 14.1644(3) Å β = 83.286(4)°. c = 23.9071(6) Å γ = 65.873(4)°	a = 8.0689(3) Å, α = 90°. b = 14.3634(5) Å, β = 95.1407(19)°. c = 37.0823(11) Å, γ = 90°.	a = 9.1013(4) Å α = 90°. b = 14.0300(6) Å β = 91.0340(10)°. c = 16.4292(6) Å γ = 90°.
Volume	86.914(4)	4280.4(3) $Å^3$	2097.52(15) $Å^3$
Z	83.286(4)	8	4
Density (calculated)	65.873(4)	1.247 Mg/m^3	1.414 Mg/m^3
Absorption coefficient	2020.7(3)	1.695 mm^{-1}	1.977 mm^{-1}
F(000)	4	1696	920
Crystal size	100	0.260 x 0.070 x 0.050 mm^3	0.260 x 0.170 x 0.080 mm^3
Theta range for data collection	1.208	2.393 to 68.341°.	1.909 to 30.058°.
Index ranges	0.560	-9≤h≤8, -17≤k≤17, -44≤l≤44	-12≤h≤12, -19≤k≤19, -23≤l≤20
Reflections collected	784	39019	37924
Independent reflections	0.11 × 0.09 × 0.03	7776 [R(int) = 0.0718]	6151 [R(int) = 0.0374]
Completeness to theta = 26.000°	1.620 to 68.528	99.5 %	100.0 %
Absorption correction	$–10 \le h \le 10$	Semi-empirical from equivalents	Semi-empirical from equivalents
Max. and min. transmission	$–10 \le k \le 11$	0.7531 and 0.6090	0.7460 and 0.6544
Refinement method	$–32 \le l \le 33$	Full-matrix least-squares on F^2	Full-matrix least-squares on F^2
Data / restraints / parameters	24243	7776 / 0 / 531	6151 / 0 / 266
Goodness-of-fit on F^2	7090 [R(int) = 0.0855]	1.017	1.015
Final R indices [I>2σ(I)]	95.8	R1 = 0.0542, wR2 = 0.1478	R1 = 0.0323, wR2 = 0.0707
R indices (all data)	full-matrix least-squares	R1 = 0.0711, wR2 = 0.1604	R1 = 0.0466, wR2 = 0.0755
Largest diff. peak and hole	on F^2	0.643 and -0.673 $e.Å^{-3}$	0.677 and -0.382 $e.Å^{-3}$

Crystal data and structure refinement for 10-[(4-Iodo-2,6-diisopropylphenyl)imino]phenanthren-9-one (**4**), 10-[(2,4,6-trimethylphenyl)imino]phenanthren-9-one (**5**) and 10-[(2,6-dimenthylphenyl)imino]phenanthren-9-one (**6**).

Compound	10-[(4-Iodo-2,6-diisopropylphenyl)imino] phenanthren-9-one (**4**)	10-[(2,4,6-trimethylphenyl)imino] phenanthren-9-one (**5**)	10-[(2,6-dimenthylphenyl)imino]phenanthren-9-one (**6**)
Empirical formula	$C_{26}H_{24}INO$	$C_{23}H_{19}NO$	$C_{22}H_{17}NO$
Formula weight	493.36	325.39	311.36
Temperature	100(2) K	99.99 K	100.0 K
Wavelength	0.71073 Å	0.71073 Å	0.71073 Å
Crystal system	Monoclinic	Triclinic	Triclinic
Space group	$P2_1/c$	$P\bar{1}$	$P\bar{1}$
Unit cell dimensions	a = 9.2399(5) Å α = 90°. b = 14.2091(8) Å β = 95.564(2)°. c = 16.7858(9) Å γ = 90°.	a = 8.1026(9) Å α = 107.042(4)°. b = 9.4866(11) Å β = 91.991(5)°. c = 12.3706(14) Å γ = 113.538(5)°.	a = 8.5936(11) Å α = 74.172(5)°. b = 9.2038(11) Å β = 73.961(5)°. c = 10.8711(13) Å γ = 77.487(5)°.
Volume	2193.4(2) $Å^3$	820.89(16) $Å^3$	785.70(17) $Å^3$
Z	4	2	2
Density (calculated)	1.494 Mg/m^3	1.316 Mg/m^3	1.316 Mg/m^3
Absorption coefficient	1.476 mm^{-1}	0.080 mm^{-1}	0.080 mm^{-1}
F(000)	992	344	328
Crystal size	0.230 x 0.130 x 0.090 mm^3	0.145 x 0.1 x 0.06 mm^3	0.38 x 0.13 x 0.04 mm^3
Theta range for data collection	1.881 to 29.000°.	2.784 to 28.416°.	2.815 to 25.578°.
Index ranges	-12≤h≤12, -19≤k≤19, -22≤l≤22	-10≤h≤10, -12≤k≤12, -16≤l≤16	-10≤h≤10, -10≤k≤11, -13≤l≤13
Reflections collected	42398	12392	6469
Independent reflections	5834 [R(int) = 0.0446]	1]	2911 [R(int) = 0.0672]
Completeness to theta = 26.000°	100.0 %	99.7 %	98.4 %
Absorption correction	Semi-empirical from equivalents	Semi-empirical from equivalents	Semi-empirical from equivalents
Max. and min. transmission	0.7460 and 0.6673	0.7457 and 0.6677	0.7452 and 0.6050
Refinement method	Full-matrix least-squares on F^2	Full-matrix least-squares on F^2	Full-matrix least-squares on F^2
Data / restraints / parameters	5834 / 11 / 266	4110 / 0 / 229	2911 / 0 / 219
Goodness-of-fit on F^2	1.082	0.998	1.013
Final R indices [I>2σ(I)]	R1 = 0.0474, wR2 = 0.1143	R1 = 0.0611, wR2 = 0.1249	R1 = 0.0598, wR2 = 0.1427
R indices (all data)	R1 = 0.0623, wR2 = 0.1200	R1 = 0.1337, wR2 = 0.1499	R1 = 0.1290, wR2 = 0.1783
Largest diff. peak and hole	0.770 and -1.391 $e.Å^{-3}$	0.242 and -0.267 $e.Å^{-3}$	0.285 and -0.297 $e.Å^{-3}$

Crystal data and structure refinement for 10-[(phenyl)imino]phenanthren-9-one (**7**) 2,7-di-*tert*-butylphenanthrene-9,10-dione (**8**) *N,N′*-(2,3-dimethylphenyl)-9,10-diiminophenanthrene (**9**).

Compound	10-[(phenyl)imino]phenanthren-9-one (**7**)	2,7-di-*tert*-butylphenanthrene-9,10-dione (**8**)	*N,N′*-(2,3-dimethylphenyl)-9,10-diiminophenanthrene (**9**)
Empirical formula	$C_{20}H_{13}NO$	$C_{22}H_{24}O_2$	C30 H26 N2
Formula weight	283.31	320.41	414.53
Temperature	100(2) K	100(2) K	100(2) K
Wavelength	0.71073 Å	0.71073 Å	1.54178 Å
Crystal system	Triclinic	Monoclinic	Orthorhombic
Space group	P1	$P2_1/n$	Pbca
Unit cell dimensions	a = 5.5249(4) Å α = 108.522(3)°. b = 11.3719(8) Å β = 102.295(3)°. c = 12.4821(9) Å γ = 100.532(4)°.	a = 8.3639(4) Å α = 90°. b = 11.6869(6) Å β = 94.8536(19)°. c = 18.6543(9) Å γ = 90°.	a = 12.8736(3) Å α = 90°. b = 14.1644(3) Å β = 90°. c = 23.9071(6) Å γ = 90°.
Volume	699.50(9) $Å^3$	1816.88(15) $Å^3$	4359.38(18) $Å^3$
Z	2	4	8
Density (calculated)	1.345 Mg/m^3	1.171 Mg/m^3	1.263 Mg/m^3
Absorption coefficient	0.083 mm^{-1}	0.073 mm^{-1}	0.562 mm^{-1}
F(000)	296	688	1760
Crystal size	0.16 x 0.12 x 0.09 mm^3	0.380 x 0.070 x 0.070 mm^3	0.21 x 0.15 x 0.03 mm^3
Theta range for data collection	3.116 to 25.633°.	2.058 to 26.000°.	4.997 to 69.936°.
Index ranges	-6≤h≤6, -13≤k≤13, -15≤l≤15	-10≤h≤10, -14≤k≤14, -23≤l≤21	-15≤h≤15, -17≤k≤14, -29≤l≤29
Reflections collected	16171	63057	37968
Independent reflections	5236 [R(int) = 0.0859]	3573 [R(int) = 0.0548]	4121 [R(int) = 0.0595]
Completeness to theta = 26.000°	99.6 %	100.0 %	99.9 %
Absorption correction	Semi-empirical from equivalents	Semi-empirical from equivalents	Semi-empirical from equivalents
Max. and min. transmission	0.7452 and 0.6097	0.7456 and 0.6963	0.7533 and 0.6367
Refinement method	Full-matrix least-squares on F^2	Full-matrix least-squares on F^2	Full-matrix least-squares on F^2
Data / restraints / parameters	5236 / 42 / 362	3573 / 0 / 223	4121 / 0 / 293
Goodness-of-fit on F^2	1.021	1.023	1.027
Final R indices [I>2σ(I)]	R1 = 0.0657, wR2 = 0.1401	R1 = 0.0465, wR2 = 0.1173	240
R indices (all data)	R1 = 0.1210, wR2 = 0.1666	R1 = 0.0724, wR2 = 0.1339	R1 = 0.0601, wR2 = 0.1344
Largest diff. peak and hole	0.585 and -0.442 $e.Å^{-3}$	0.273 and -0.160 $e.Å^{-3}$	0.191 and -0.251 $e.Å^{-3}$

Crystal data and structure refinement for N-(2,6-dimethylphenyl)formamide, $[K(H_2O)]_2[UO_2Cl_4]$ and *N*-(2,6-diisopropylphenyl)formamide.

Compound	*N*-(2,6-dimethylphenyl)formamide	$[K(H_2O)]_2[UO_2Cl_4]$	*N*-(2,6-diisopropylphenyl)formamide
Empirical formula	$C_9H_{11}NO$	$Cl_4H_4K_2O_4U$	$C_{27}H_{40}N_2O_2$
Formula weight	149.19	526.06	424.61
Temperature	100(2) K	100(2) K	100(2) K
Wavelength	0.71073 Å	0.71073 Å	1.54178 Å
Crystal system	Orthorhombic	Triclinic	Hexagonal
Space group	$P2_12_12_1$	$P\bar{1}$	$P6_1$
Unit cell dimensions	a = 4.4973(2) Å α = 90°. b = 8.5091(4) Å β = 90°. c = 20.6673(11) Å γ = 90°.	a = 6.6400(3) Å α = 92.5827(14)°. b = 6.7144(3) Å β = 101.6968(13)°. c = 7.2226(4) Å γ = 118.7540(12)°.	a = 16.7613(5) Å α = 90°. b = 16.7613(5) Å β = 90°. c = 8.4038(3) Å γ = 120°.
Volume	790.90(7) $Å^3$	272.60(2) $Å^3$	2044.66(14) $Å^3$
Z	4	1	3
Density (calculated)	1.253 Mg/m^3	3.204 Mg/m^3	1.035 Mg/m^3
Absorption coefficient	0.082 mm^{-1}	16.597 mm^{-1}	0.500 mm^{-1}
F(000)	320	234	696
Crystal size	0.25 x 0.1 x 0.1 mm^3	0.19 x 0.12 x 0.06 mm^3	0.33 x 0.03 x 0.03 mm^3
Theta range for data collection	3.101 to 25.762°.	3.510 to 28.480°.	3.044 to 68.200°.
Index ranges	-5≤h≤5, -10≤k≤10, -24≤l≤25	-8≤h≤8, -8≤k≤8, -9≤l≤9	-20≤h≤17, -20≤k≤20, -9≤l≤10
Reflections collected	5131	10339	16886
Independent reflections	1527 [R(int) = 0.0269]	1371 [R(int) = 0.0365]	2488 [R(int) = 0.0936]
Completeness to theta = 26.000°	99.8 %	99.9 %	99.9 %
Absorption correction	Semi-empirical from equivalents	Semi-empirical from equivalents	Semi-empirical from equivalents
Max. and min. transmission	0.7453 and 0.6770	0.7457 and 0.3950	0.7530 and 0.5988
Refinement method	Full-matrix least-squares on F^2	Full-matrix least-squares on F^2	Full-matrix least-squares on F^2
Data / restraints / parameters	1527 / 0 / 106	1371 / 2 / 58	2488 / 2 / 156
Goodness-of-fit on F^2	1.077	1.197	1.068
Final R indices [I>2σ(I)]	R1 = 0.0314, wR2 = 0.0742	R1 = 0.0166, wR2 = 0.0419	R1 = 0.0680, wR2 = 0.1721
R indices (all data)	R1 = 0.0358, wR2 = 0.0775	R1 = 0.0166, wR2 = 0.0419	R1 = 0.0914, wR2 = 0.1940
Largest diff. peak and hole	0.134 and -0.208 $e.Å^{-3}$	1.104 and -2.324 $e.Å^{-3}$	0.0(8)

[1] R. M. Ibberson, *Nucl. Instrum. Methods Phys. Res., Sect. A.,* 2009, **600**, 47

[2] R. M. Ibberson, 2009, Design and performance of the new supermirror guide on HRPD at ISIS. *Nuclear Instruments and Methods in Physics Research A,* **600**, 47; R. M. Ibberson, W. I. F. David and K. S. Knight, 1992, The high resolution neutron powder diffractometer (HRPD) at ISIS – a user guide. RAL-92-031. Rutherford Appleton Laboratory, UK.

[3] Mantid, Manipulation and Analysis Toolkit for Instrument Data; Mantid Project, (http://dx.doi.org/10.5286/SOFTWARE/MANTID), O. Arnold and 27 co-authors (2014) Mantid-Data analysis and visualization package for neutron scattering and μSR experiments. *Nucl. Instrum. Methods Phys. Res. A*, **764**, 156

[4] A. Le Bail, Pwder Diff., 2005, **20**, 316

[5] A. C. Larson and R. B. Von Dreele, *General Structure Analysis System (GSAS)*, 1994,. Los Alamos National Laboratory Report, Laur 86-748. B. H. Toby, 2001, EXPGUI, a graphical user interface for GSAS, *J. Appl. Crystallogr.*, **34**, 210

[6] D. A. Keen, M. J. Gutmann and C. C. Wilson, *J. Appl. Crystallogr.*, 2006, **39**, 714

[7] M. J. Gutmann, *Nucl. Instrum. Meth. A.*, 2017, **848**, 170

[8] M. J. Gutmann, *SXD*2001, 2005, ISIS Neutron and Muon Facility, Rutherford Appleton Laboratory, Harwell Science Campus, Oxfordshire, UK

[9] G. M. Sheldrick, *Acta Crystallogr.*, 2008, **64**, 112